

Lecture Notes in Civil Engineering

Vincenzo Gattulli
Marco Lepidi
Luca Martinelli *Editors*

Dynamics and Aerodynamics of Cables

ISDAC 2023

 Springer

Lecture Notes in Civil Engineering

Volume 399

Series Editors

Marco di Prisco, Politecnico di Milano, Milano, Italy

Sheng-Hong Chen, School of Water Resources and Hydropower Engineering,
Wuhan University, Wuhan, China

Ioannis Vayas, Institute of Steel Structures, National Technical University of
Athens, Athens, Greece

Sanjay Kumar Shukla, School of Engineering, Edith Cowan University, Joondalup,
WA, Australia

Anuj Sharma, Iowa State University, Ames, IA, USA

Nagesh Kumar, Department of Civil Engineering, Indian Institute of Science
Bangalore, Bengaluru, Karnataka, India

Chien Ming Wang, School of Civil Engineering, The University of Queensland,
Brisbane, QLD, Australia

Zhen-Dong Cui, China University of Mining and Technology, Xuzhou, China

Lecture Notes in Civil Engineering (LNCE) publishes the latest developments in Civil Engineering—quickly, informally and in top quality. Though original research reported in proceedings and post-proceedings represents the core of LNCE, edited volumes of exceptionally high quality and interest may also be considered for publication. Volumes published in LNCE embrace all aspects and subfields of, as well as new challenges in, Civil Engineering. Topics in the series include:

- Construction and Structural Mechanics
- Building Materials
- Concrete, Steel and Timber Structures
- Geotechnical Engineering
- Earthquake Engineering
- Coastal Engineering
- Ocean and Offshore Engineering; Ships and Floating Structures
- Hydraulics, Hydrology and Water Resources Engineering
- Environmental Engineering and Sustainability
- Structural Health and Monitoring
- Surveying and Geographical Information Systems
- Indoor Environments
- Transportation and Traffic
- Risk Analysis
- Safety and Security

To submit a proposal or request further information, please contact the appropriate Springer Editor:

- Pierpaolo Riva at pierpaolo.riva@springer.com (Europe and Americas);
- Swati Meherishi at swati.meherishi@springer.com (Asia—except China, Australia, and New Zealand);
- Wayne Hu at wayne.hu@springer.com (China).

All books in the series now indexed by Scopus and EI Compendex database!


Vincenzo Gattulli · Marco Lepidi · Luca Martinelli
Editors

Dynamics and Aerodynamics of Cables


ISDAC 2023

 Springer

Editors

Vincenzo Gattulli 
DISG
Sapienza University of Rome
Rome, Italy

Marco Lepidi 
DICCA
University of Genoa
Genoa, Italy

Luca Martinelli 
DICA
Politecnico di Milano
Milan, Italy

ISSN 2366-2557 ISSN 2366-2565 (electronic)
Lecture Notes in Civil Engineering
ISBN 978-3-031-47151-3 ISBN 978-3-031-47152-0 (eBook)
<https://doi.org/10.1007/978-3-031-47152-0>

© The Editor(s) (if applicable) and The Author(s), under exclusive license to Springer Nature Switzerland AG 2024

This work is subject to copyright. All rights are solely and exclusively licensed by the Publisher, whether the whole or part of the material is concerned, specifically the rights of translation, reprinting, reuse of illustrations, recitation, broadcasting, reproduction on microfilms or in any other physical way, and transmission or information storage and retrieval, electronic adaptation, computer software, or by similar or dissimilar methodology now known or hereafter developed.

The use of general descriptive names, registered names, trademarks, service marks, etc. in this publication does not imply, even in the absence of a specific statement, that such names are exempt from the relevant protective laws and regulations and therefore free for general use.

The publisher, the authors, and the editors are safe to assume that the advice and information in this book are believed to be true and accurate at the date of publication. Neither the publisher nor the authors or the editors give a warranty, expressed or implied, with respect to the material contained herein or for any errors or omissions that may have been made. The publisher remains neutral with regard to jurisdictional claims in published maps and institutional affiliations.

This Springer imprint is published by the registered company Springer Nature Switzerland AG
The registered company address is: Gewerbestrasse 11, 6330 Cham, Switzerland

Paper in this product is recyclable.

Organization

Conference Chairs

Vincenzo Gattulli, Sapienza University of Rome, Italy
Luca Martinelli, Politecnico di Milano, Italy
Marco Lepidi, University of Genoa, Italy

Scientific Committee

Alberto Zasso, Politecnico di Milano, IT
Allan Larsen, Technical University of Denmark, DK
Annick D'Auteuil, National Research Council Canada, CA
Christian Cremona, Bouygues Construction & Bouygues Travaux Publics, FR
Christos Georgakis, Aarhus University, DK
Claude Henri Lamarque, University of Lyon, FR
Daniele Zulli, University of L'Aquila, IT
Delong Zuo, Texas Tech University, USA
Elsa Caetano, University of Porto, PT
Guy Larose, Carleton University, CA
Heidi Christiansen, Svend Ole Hansen ApS, DK
Helmut Wenzel, Vienna Consulting Engineers, AT
Jasna B. Jakobsen, University of Stavanger, NO
Jungao Wang, Statens Vegvesen, NO
Luca Caracoglia, Northeastern University, USA
Masaru Matsumoto, Kyoto University, JP
Olivier Flamand, Scientific and Technical Center for Building, FR
Sean McTavish, University of Sherbrooke, CA
Sebastien Langlois, University of Udine, Italy
Tieding Guo, Hunan University, CN

Tomomi Yagi, Kyoto University, JP
Vincent Denoël, University of Liège, BE
Vincenzo Gattulli, Sapienza University of Rome, IT
Wen-li Chen, Harbin Institute of Technology, CN
Yozo Fujino, Josai University, JP

Local Committee

Daniela Addressi, Sapienza University of Rome, IT
Andrea Arena, Sapienza University of Rome, IT
Marianna Crognale, Sapienza University of Rome, IT
Melissa De Iuliis, Sapienza University of Rome, IT
Francesco Foti, Politecnico di Milano, IT
Egidio Lofrano, Sapienza University of Rome, IT
Francesco Potenza, University G. d'Annunzio of Chieti-Pescara, IT
Cecilia Rinaldi, Sapienza University of Rome, IT
Daniele Sivori, University of Genoa, IT

Sponsors



BEST DESIGN



Abstracts of Keynotes

Suspension Bridges and Their Main Cables, from the Industrial Revolution to Present

Fabio Brancaleoni

E.D.IN. Ltd, Consulting Engineers, former Full Professor of Structural Engineering
f.brancaleoni@ediningegneria.com

Abstract

The presentation is devoted to an overview of the development of technologies, materials, and methods for the erection of suspension bridges' main cables in the contemporary age, from the drive given by the Industrial Revolution to the present times. For a wider scenario, fundamental aspects of the conception of suspension bridges in the same period are also outlined. In the first part, attention is given to the development of chain bridges and to the transition toward wires as the basic unit for cable forming. The respective roles of the European and the American civil engineering environments are discussed, with the first pioneers and their works, be they successes or failures. The difficulties in cable erection are described, until the European invention of the aerial spinning technique, which became in turn the premise of the great "American Century" from half Eighteenth to half Nineteenth Century. Of this magnificent period in the history of bridge construction figures of engineers, accomplishments and technical solutions are presented. In the second part, the progress brought up to the present is followed, outlining the respective role of technological and scientific development. Going through the bridges built in the first half of the Nineteenth century, the improvements in cable erection methodologies are commented on, with the first bridges built adopting the successful novel approach based on the adoption of prefabricated parallel wire strands (PPWS) and with the subsequent improvements for on-site spinning methods, with the so-called modified aerial spinning. These two methods are nowadays dominant in the construction industry, with spiral ropes adopted as a rare and minor exception. As a conclusion, a short brief is given to the overall concepts that allow the possibility of super-long spans, today with the 2023 m of the "1915" suspension bridge on the Dardanelles and with possible larger spans worldwide, such as the known design for a 3300 m span on the Strait of Messina, whose main cable layout is commented, together with some aspects of interest both for future research and innovative engineering solutions.

A Learning Framework for Pragmatic Management of the Dynamic Performance of Infrastructure Assets

Colin Taylor

Department of Civil Engineering, University of Bristol

Colin.Taylor@bristol.ac.uk

Abstract

The dynamic performance of infrastructure assets, such as cable-stayed and suspension bridges, guyed masts, and aging nuclear reactor cores, is often complex, intricate, and nonlinear, with highly uncertain loading conditions and asset properties. Analysis requires imaginative theorization and often very large, time-consuming, computation to explore the performance space. However, usually, the asset management decision resolves simply to the selection of one option from a small number of viable courses of remedial action. The asset manager only needs parsimonious information from dynamic analysis that is necessary and sufficient, first, to choose the option, and second, to refine and execute the chosen course of action to achieve the desired outcomes at an affordable cost. This paper describes an outcomes-focused learning framework that helps accelerate progress toward this asset management goal. Based on modern cognitive and learning science, the framework was developed and tested in the context of the seismic performance of aging graphite cores in nuclear power plants, the dynamic performance of the historic Clifton Suspension Bridge, and even customer switching between bank current accounts. The framework is applicable to any kind of outcomes-focused decision-making and is valuable for guiding impactful research. The framework principles will be illustrated by reference to typical cable dynamics problems.

Preface

This book contains the Proceedings of the papers presented at the 3rd International Symposium of Dynamics and Aerodynamics of Cables (ISDAC 2023). The conference was held at SAPIENZA University of Rome, Italy, on June 15–17, 2023.

At its inaugural edition organized in Liège, Belgium (1995), the Conference was called the *International Symposium on Cable Dynamics (ISCD)*. The Conference was then held every two years until 2011 with the editions taking place in Tokyo, Japan (1997), Trondheim, Norway (1999), Montreal, Canada (2001), Santa Margherita Ligure, Italy (2003), Charleston, USA (2005), Vienna, Austria (2007), Paris, France (2009), and Shanghai, China (2011). In 2014, the Conference was renamed *Cable Dynamics and Aerodynamics Symposium (SDAC)* and was held in Kongens Lyngby, Denmark. From 2017 to the present, the Conference has been established as the *International Symposium on Dynamics and Aerodynamics of Cables (ISDAC)* and is currently attended by scholars and researchers from several relevant institutions from all over the world.

In continuity with the scientific tradition of past editions, the Symposium has promoted the development of all the traditional and emerging areas related to the Dynamics and Aerodynamics of Cables. The conference was held in Porto, Portugal (2017) and in Stavanger, Norway (2021). The ISDAC 2023 edition was hosted by the DISG—Department of Structural and Geotechnical Engineering of Sapienza University of Rome (Italy), and organized in collaboration with DICA—Department of Civil and Environmental Engineering of Politecnico di Milano (Italy), and DICCA—Department of Civil, Chemical and Environmental Engineering of University of Genoa (Italy).

The main topics of the conference have included nonlinear cable dynamics, cable structures and moving cables, cable aging, fatigue, degradation and failure mechanisms, laboratory testing of cable dynamics and aerodynamics, field investigations of cable dynamics and aerodynamics, computational models for cable dynamics and fluid-structure interaction, cable vibration control, cable-driven parallel manipulators and cable cranes, monitoring of cable performance, environmental and anthropic loads on cable structures, new materials for structural cables, and design performance criteria. The volume is organized, according to the Symposium sessions, in

five thematic sections, namely: (i) *cable structures*, (ii) *aerodynamics and nonlinear dynamics*, (iii) *monitoring and testing*, (iv) *identification and control*, and (v) *models*.

The papers published in this volume have been selected among those submitted by the participants after a rigorous review process by expert referees and members of the International Scientific Committee. This process ensured a high quality of the publication, highlighting how research conducted with different backgrounds finds a common interest in the physical phenomena of cable vibrations, ultimately leading to a fruitful exchange of multidisciplinary knowledge and expertise.

Thriving for excellence, gender diversity has been considered during the Symposium as a contribution to promoting gender equality in research and innovation.

We would like to thank Fabio Brancaloni, *EDIN Ltd, Consulting Engineers, former Full Professor of Structural Engineering of ROMA TRE University, Italy*, for his lovely opening lecture, Colin Taylor, *Emeritus Professor of Earthquake Engineering at the University of Bristol, UK*, for his first keynote lecture, a window into the future, Shaohong Cheng, *Full Professor at the Department of Civil and Environment Engineering, University of Windsor, Canada*, for her second keynote lecture of excellent inspirational and motivational value for young and experienced researchers.

On behalf of ISDAC 2023, we would like to express our great appreciation to all the supporting institutions, sponsors, scientific committee members, organizing committee members, and participants of this scientific event. We also express our special thanks to all the people who contributed to the success of the Conference.

The Local Organizing Committee, coordinated by Prof. Andrea Arena, worked very hard and gave us enormous and decisive support for the organization of the Symposium and its Proceedings. We wish to express our sincere gratitude for that.

Rome, Italy
Milan, Italy
Genoa, Italy
September 2023

Vincenzo Gattulli
Luca Martinelli
Marco Lepidi

Contents

Keynotes

Explore Essential Elements in the Generation Mechanisms of Wind-Induced Cable Vibrations: An Insight Offered by Numerical Techniques	3
Shaohong Cheng and Ran Wang	

Cable Structures

Novel Position Control for Ensuring Feasible Tension Distribution of Cable-Driven Parallel Manipulators	19
Andrea Martín-Parra, Jorge Muñoz, Francisco Moya-Fernández, David Rodríguez-Rosa, Sergio Juárez-Pérez, and Concepción A. Monje	
Kinetostatic Analysis of a Novel Planar Cable-Driven Robot with a Single Cable Loop	31
Sergio Juárez-Pérez, Andrea Martín-Parra, Francisco Moya Fernández, David Rodríguez Rosa, and Antonio González Rodríguez	
Dynamic Testing of a Long-Span Suspension Cable Net	41
Robert Soltys, Michal Tomko, Stanislav Kmet, and Christos Thomas Georgakis	
Vibration Mitigation of Catenary Bridges	49
Gergely Szabó and Gábor Hochrein	
Field Observation of Global and Local Dynamics of a Cable-Stayed Bridge	61
Jasna Bogunović Jakobsen, Jónas Þór Snæbjörnsson, and Nicolo Daniotti	

Aerodynamics and Nonlinear Dynamics

Wake Galloping Suppression in Two Closely Spaced Cylinders with Surface Modification	75
---	----

Thu Dao, Tomomi Yagi, Kyohei Noguchi, and Gabriel Mohallem

Comparison of Observed and Simulated Galloping Responses of a Four-Bundled Conductor Under Wet Snow Accretion	85
--	----

Hisato Matsumiya, Saki Taruishi, Hiroki Matsushima, and Teruo Aso

Statistical Study of Aeolian Vibration Characteristics of Overhead Conductor	99
---	----

Shaoqi Yang, Luc Chouinard, Sébastien Langlois, Josée Paradis, and Pierre Van Dyke

Three-Dimensional Flow Characterizations for Yawed and Inclined Circular Cylinders for Bridge Cable Stays	109
--	-----

Michael Hoftyzer and Elena Dragomirescu

Propagation of the Uncertainty in the Dynamic Behavior of OPGW Cables Under Stochastic Wind Load	121
---	-----

Damián Campos, Andrés Ajras, and Marcelo Piovan

Investigation of Ice Accretion Conditions in Observed Galloping Events of Four-Bundled Conductor	133
---	-----

Saki Taruishi and Hisato Matsumiya

The Influence of Ice Accretion Thickness on the Aerodynamic Behaviour of Stay Cables of Bridges	145
--	-----

Annick D'Auteuil, Sean McTavish, Arash Raeesi, and Krzysztof Szilder

Non-linear Dynamic Response of a Small-sag Cable Model of a Guy Line of a Guyed Tower to Stochastic Wind Excitation	157
--	-----

Hanna Weber, Anna Jabłonka, and Radosław Iwankiewicz

Review Study on Nonlinear Modeling Issues Associated with the Dynamics of In-Plane Cable Networks	171
--	-----

Luca Caracoglia and Gian Felice Giaccu

Monitoring and Testing

Force Measurements on Flexible Sagged Cable Undergoing Forced Vibration at a Single Point	185
--	-----

Dániel Dorogi and László E. Kollár

Wave Propagation-Based Assessment of Damage in Laboratory Samples of a Cable	195
---	-----

João Rodrigues, Elsa Caetano, Carlos Moutinho, and Raphael Mendonça

Full-Size Testing of Stay Cable Damping for the Assessment of Viscous Damper Efficiency 207
 Max Vollmering and Werner Brand

Vibration Excitation and Damping of Suspension Bridge Hanger Cables 217
 Allan Larsen

Cable-Stayed Bridge Model Updating Through Analytical Formulation, Finite Element Model and Experimental Measurements 229
 Cecilia Rinaldi, Marco Lepidi, Francesco Potenza, and Vincenzo Gattulli

Identification and Control

Bayesian Identification of the Axial Forces, the Bending Stiffnesses, and the Connecting Point in Crossed Cables 243
 D. Piciuccio, F. Foti, V. Denoël, T. Auguste, S. Hoffait, and M. Geuzaine

Comparison of Fatigue Lifetime Estimation of a Conductor Based on a Standard Vibration Device and Other Structural Health Monitoring System Sensors 255
 Raphael Mendonça, Elsa Caetano, Carlos Moutinho, Omar As Saadi, and João Rodrigues

On the Assessment and Mitigation of Vortex-Induced-Vibrations of Overhead Electrical Conductors 267
 F. Foti and L. Martinelli

A Numerical Investigation on the Dynamic Response of Short Slack Cables 277
 S. Corazza, F. Foti, and L. Martinelli

Comparing Different Techniques of Determining Cable Forces from Vibration Measurements on a Cable-Stayed Arch Bridge 289
 Stefan Verdenius

Models

On the Seismic Response of Anchoring Elements for Submerged Floating Tunnels 303
 S. Corazza, M. Geuzaine, F. Foti, V. Denoël, and L. Martinelli

3D Finite Element Modelling of Conductor-Clamp Assemblies Under Cyclic Bending: Sensitivity Analysis of Wire Contact Coefficient of Friction 315
 Sébastien Lalonde, Leticia Kared, Raynald Guilbault, and Sébastien Langlois

Numerical Characterization of Overhead Conductor Local Loading Conditions at Wire Contact Points in the Vicinity of Suspension Clamps 327
Liticia Kared, Sébastien Lalonde, Sébastien Langlois, and Raynald Guilbault

General Modelling of Cable Vibrations Using Data Extracted from Physical Simulation 339
John A. Redford, Maxime Gueguin, Fikri Hafid, Matthieu Ancellin, and Jean-Michel Ghidaglia

Parametric Dynamic Modeling of Cable-Driven Parallel Manipulators 351
Andrea Arena, Erika Ottaviano, and Vincenzo Gattulli

Catenary Solutions for Inextensible Cables: A Perturbation-Based High-Order Approximation 363
Marco Lepidi

Author Index 375

Keynotes

Explore Essential Elements in the Generation Mechanisms of Wind-Induced Cable Vibrations: An Insight Offered by Numerical Techniques



Shaohong Cheng and Ran Wang

Abstract The inclined and/or yawed orientation of bridge stay cables results in the formation of secondary axial flow on the leeward side of cable surface, the intensity of which depends on the effective attack angle. On the other hand, the cross-sectional shape of a real stay cable is usually not perfectly round. It is believed that the presence of axial flow and roundness imperfection would contribute to trigger some unique wind-induced cable vibration phenomena. To clarify their respective role in the excitation mechanisms, a delayed detached eddy simulation (DDES) is performed in OpenFOAM on an inclined circular cylinder. The effect of cable orientation is studied for $\alpha = 0^\circ, 30^\circ, 45^\circ, 60^\circ$ at $Re = 1.0 \times 10^4$ and 1.4×10^4 , whereas the impact of cable cross-sectional shape is examined for four different levels of roundness imperfection. Results show that the interaction between Kármán vortex and axial vortex causes an “S” pattern movement of a low C_p region along cable leeward surface, which generated an intermittently amplified transverse lift. This could be the source which triggers unstable cable motion. Further, the strength of axial flow is found critical to its interaction with Kármán vortex. This explains why aerodynamic instability of a cable was only observed at certain cable orientations in lab and on site. In addition, an imperfectly round cable is observed to have a smaller recirculation region in the wake, which helps to trap more axial flow close to the cable leeward surface and may enhance the interaction between axial and Kármán vortices.

Keywords Stay cable · Axial flow · Kármán vortex · Intermittent amplification

S. Cheng (✉) · R. Wang
University of Windsor, Windsor, ON, Canada
e-mail: shaohong@uwindsor.ca

R. Wang
e-mail: wang1hf@uwindsor.ca

1 Introduction

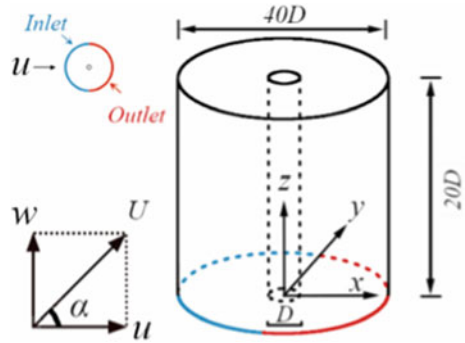
Stay cables on cable-stayed bridges are susceptible to dynamic excitations such as wind. Over the past three decades, many experimental and analytical studies have been conducted to investigate wind-induced vibrations occurred with and without precipitations. While mechanisms associated with rain-wind-induced cable vibrations are better understood than before, the cause of wind-induced oscillations of dry cables still require intensive research effort. Existing studies on dry cables show that: (a) the emergence of critical Reynolds number regime [1, 2]; and (b) the presence of axial flow [3] would affect the aerodynamic forces acting on a cable; (c) the correlation of sectional aerodynamic forces [4] can decide how well they collaborate along cable span to excite a cable; and (d) the sustained duration of critical condition [5] would govern the built-up amplitude of cable response. The contributions made by (a), (c), and (d) are supported by experimental and analytical results, whereas the role of axial flow is yet to be clarified. The strength of axial flow and the level of its impact on the surrounding flow structure are affected by the cable orientation. In addition, the imperfectly round cross-sectional shape of a real stay cable would also have an influence on the surrounding flow. Although much progress has been made in identifying the contributing factors for triggering unstable cable response, the obtained information regarding the surrounding flow and how it is affected by cable orientation and geometric imperfection through wind tunnel tests and site measurements is still limited.

The Computational Fluid Dynamics (CFD) simulation grants the access to rich information in the entire flow field with unlimited level of details. Further, it offers the possibility of conducting investigations beyond the conditions that are achievable in lab environment. This allows to explain the physics associated with the excitation mechanisms in more depth. In the current study, we use the delayed detached eddy simulation (DDES) in OpenFOAM version 4.1 (Open source Field Operation and Manipulation) to scrutinize how flow surrounding an inclined cable is affected by cable orientation and geometric imperfection, and thus impact on its aerodynamic response.

2 Role of Cable Orientation

Aerodynamic behaviour of an inclined circular cylinder has been extensively studied by many researchers through wind tunnel tests and numerical simulations [e.g. 2, 6–9]. It has been found that the relative angle between the oncoming flow and the cylinder axis had a decisive impact on the aerodynamic stability of a cylinder. Literature data indicate that unstable cable motion is possible to occur in the sub-critical and critical Reynolds number range when the equivalent attack angle is within the range of $\alpha = 20^\circ$ and 60° , and mostly reported at $\alpha = 30^\circ$ and 45° . To find out what is special in the surrounding flow structure within this cable orientation

Fig. 1 Computational model



range, CFD simulation is conducted at $Re = 1.4 \times 10^4$ for four attack angles of $\alpha = 0^\circ, 30^\circ, 45^\circ, 60^\circ$.

2.1 Numerical Model

The computational domain has a cylindrical geometry (Fig. 1). A rigid circular cylinder is located at the center of the computational domain whose diameter is 40 times that of the cylinder. The x -axis represents the stream-wise direction for the case $\alpha = 0^\circ$, and it will not change its direction for the other cases; the z -axis coincided with the axis of the circular cylinder; and the y -axis is perpendicular to the x - and z -axes. A turbulent inlet with an intensity of 1% is adopted. The surface pressure and velocity gradient at the outlet are set as zero. A no-slip condition is applied to the cylinder surface wall and the periodic condition is prescribed at the span-wise wall. The non-dimensional time is defined as $t^* = tU_\infty/D$, where t is the dimensional time, U_∞ is the free-stream velocity, and D is the diameter of the circular cylinder. For more details of the numerical model, such as model validation, duration for the sampling window, and turbulence model, please refer to [9].

2.2 Near Wake Structure

Figure 2 shows the wake vertical vorticity, ω_z , of a cylinder at four different attack angles. The direction of the vertical vorticity is perpendicular to the streamwise direction. It enables to visualize the detached shear layers in the streamwise direction. It can be seen that as α increases, the shear layers become less curved and more stable. If placing a probe in the vicinity of the shear layer to measure cross-flow velocity at this point and perform a spectrum analysis, the strength of Kármán vortex shedding is found to gradually weaken as the attack angle increases (Fig. 3). In Fig. 3, the horizontal axis represents the Strouhal number based on the normal component of

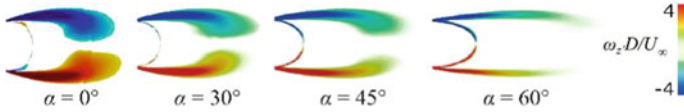


Fig. 2 Time-averaged vertical vorticity

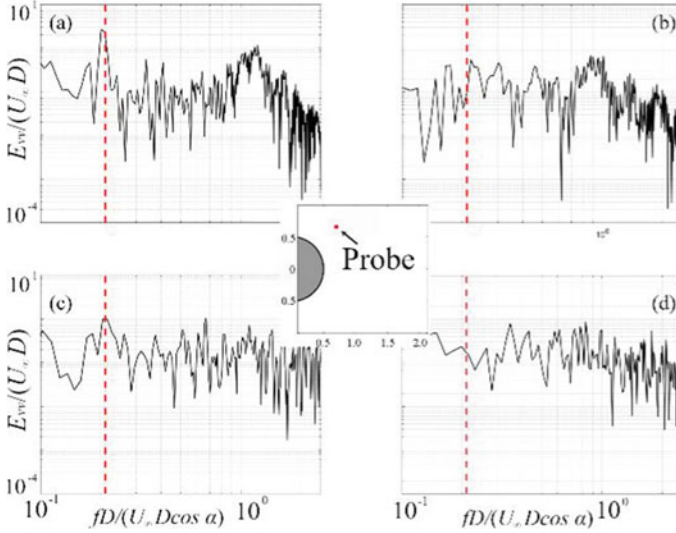


Fig. 3 Spectra of cross-flow velocity in the vicinity of shear layer

the free-stream velocity U_∞ , and the vertical axis for the cross-flow velocity spectral energy normalized by the free-stream velocity U_∞ and the cylinder diameter D .

2.3 Sectional Lift

Figure 4 describes the evolution of the sectional lift along the entire span during the studied time frame when the cylinder is inclined at four different attack angles at $Re = 1.4 \times 10^4$. The presence of Kármán vortex shedding can be recognized from the periodic pattern of the red/blue or yellow/cyan stripes. It is noticed that when $\alpha = 30^\circ$, there exists a moving pattern of “peak lift” in the lift contour, implying the propagation of a strong Kármán vortex shedding along the cylinder span over time. This kind of propagation becomes weaker and discontinued at relatively larger angle of attack.

To have a better understanding of the cause of this moving pattern of peak lift, the time variation of sectional lift at 100 equal-spaced span-wise locations along the cylinder span were investigated. Figure 5 depicts a sample sectional lift coefficient

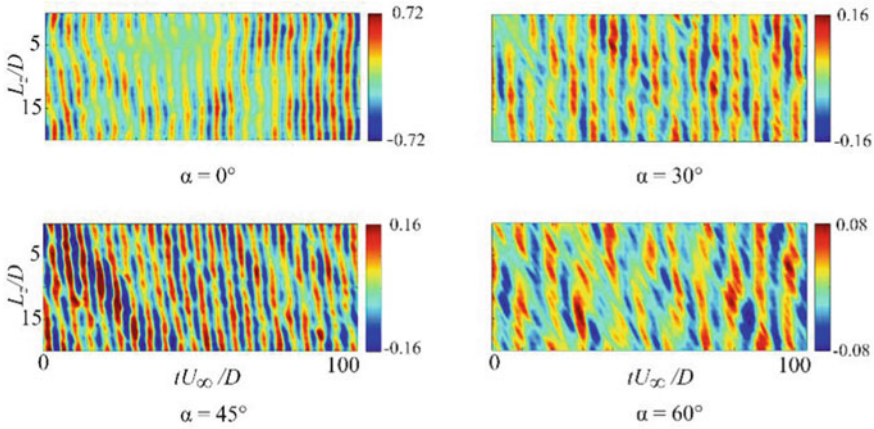


Fig. 4 Sectional lift coefficient contour at $Re = 1.4 \times 10^4$

time history at section 60, which shows a periodic time variation of lift with the same frequency as Kármán vortex shedding. Besides, the existence of a low frequency variation is also observed from the figure such that the sectional lift is enhanced once every few Kármán vortex shedding cycles. This can be seen more clearly from the red envelope curve and is also confirmed by the power spectrum analysis results given in Fig. 6, where two peaks, one corresponding to Kármán vortex shedding ($St = 0.2$), and another (designated by the red broken line) at a frequency a fraction of the former, are present. It is worth noting that the low frequency peak is slightly broad-banded and centered roughly at $St = 0.05$. An examination of the power spectrum of sectional lift at all 100 span-wise locations reveals the presence of these two peaks in all sections.

The time variation of sectional lift at different span-wise locations are then compared. Figure 7 shows the sectional lift time history from section 43 to 78, which covers close to 40% of the cylinder length in the mid-portion. The enhanced lift event at a specific span-wise location is observed to propagate along the cylinder span, indicating that the occurrence of strong vortex shedding events along cylinder span has a slight time lag.

The span-wise propagation velocity of the enhanced lift event can be calculated based on the distance between the sections and the time interval between the events.

Fig. 5 Time history of lift coefficient at section 60 when $\alpha = 30^\circ$ at $Re = 1.4 \times 10^4$

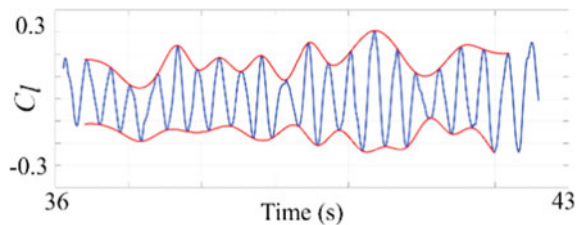


Fig. 6 Power spectrum of lift at section 60

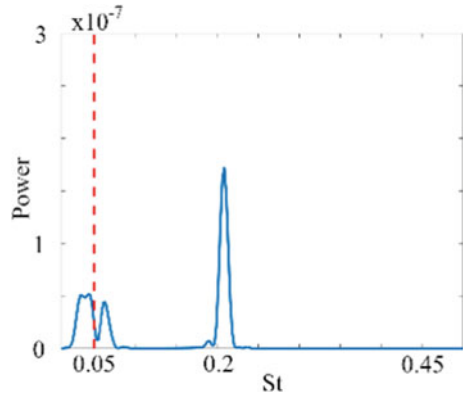
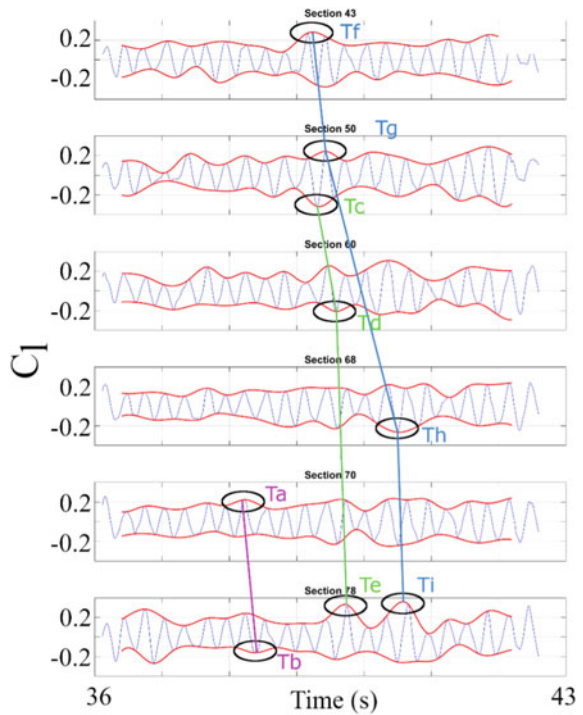
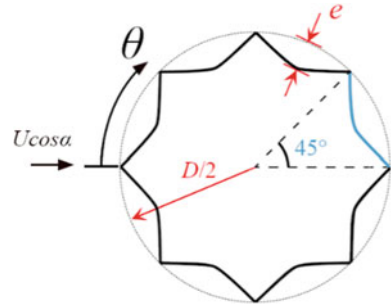


Fig. 7 Time history of lift coefficient at sections in the mid-portion of a cylinder inclined at 30° when $Re = 1.4 \times 10^4$



For example, for Events A and B shown in Fig. 7, the span-wise spacing between sections 43 and 50 is 0.112 m, and the time interval between their occurrence is 0.14 s, this gives a propagation speed from A to B as 0.80 m/s. If conducting the same calculation for the rest events, an average propagation speed of 0.82 m/s can be obtained. This is nearly identical to the axial component of the free-stream velocity,

Fig. 8 Numerical model of an imperfectly round cable cross section



which is 0.83 m/s, implying that axial flow is responsible for the moving pattern of peak lift appeared in the lift contour.

3 Effect of Roundness Imperfection

3.1 Numerical Model

Due to manufacturing precision, assembling processes, and deformations during shipping and storage, surface irregularities exist in HDPE tubes of stay cables, so the cross-sectional shape of a real stay cable usually is not perfectly round. A similar definition of roundness used in an existing experimental study [10] is adopted. In the numerical model, the cross-sectional shape of the cylinder is formed by superimposing a half-sine curve on 1/8 of a circle. This pattern repeats every 45° of axial rotation until the entire cross section is formed, as depicted in Fig. 8. The control variable of roundness is defined as the ratio between the maximum groove depth, e , and the cylinder diameter, D . Flow around a cylinder inclined at 45° was studied for $e/D = 0, 1\%, 4\%$ and 10% at $Re = 1.0 \times 10^4$, with $e/D = 0$ for a perfectly round circular cylinder.

3.2 Sectional Lift

Figure 9 illustrates the spatial and temporal distribution of sectional lift coefficient at $\alpha = 0^\circ$ and 45° . The non-dimensional parameter L_z/D is used to define the span-wise location of a section, where L_z is the z -coordinate. The color scale provides the magnitude of the lift coefficient. The presence of Kármán vortex shedding can be recognized from the periodic pattern of the yellow (or red) and cyan (or blue) stripes. In the normal flow case, the stripes are generally perpendicular to the horizontal axis of time in the contour, indicating that the roundness imperfection defined in the current study has negligible impact on the synchronization of Kármán vortex

shedding over the cylinder span. For $e/D = 4\%$, sectional lift has very large absolute values over most part of the cylinder or even the entire cylinder, suggesting the presence of strong Kármán vortex shedding events along the cylinder span.

At $\alpha = 45^\circ$, the sectional lift contour has two important features: In all four roundness imperfection cases, the color stripes representing Kármán vortex shedding events are tilted against the horizontal axis of time, which indicates the occurrence of Kármán vortex shedding along the cylinder span has a time lag. This is believed to be caused by the inclined orientation of the cylinder. In addition, a moving pattern of peak lift can be seen in the contour. It is most distinctive when $e/D = 4\%$, and becomes less obvious when the roundness imperfection becomes less or more sizable.

By examining the sectional lift contour for the 4% roundness imperfection case over a longer time period (Fig. 10), it is found that the appearance of moving pattern of peak lift have an irregular intermittent characteristic, with the time interval between the two successive ones varies between roughly three to six times of a conventional Kármán vortex shedding period. This would lead to an intermittent amplification of sectional lift at a frequency much lower than that of Kármán vortex shedding. This irregular intermittency is consistent with the slight broad-banded low frequency peak observed earlier in the sectional lift contour. A similar moving pattern of peak lift has also been observed for a perfectly round cylinder at $\alpha = 30^\circ$ and $Re = 1.4 \times 10^4$

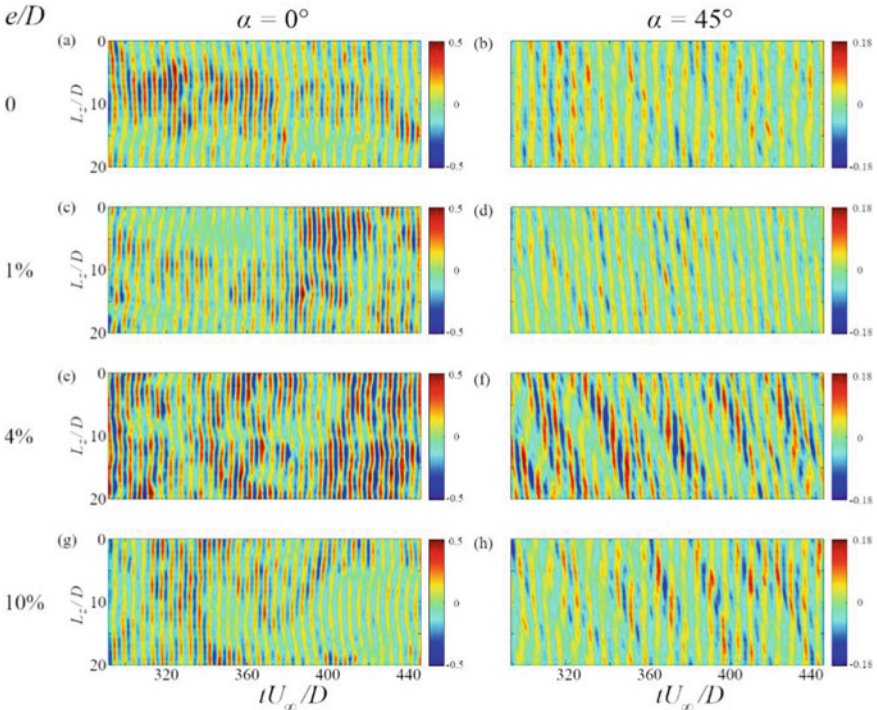
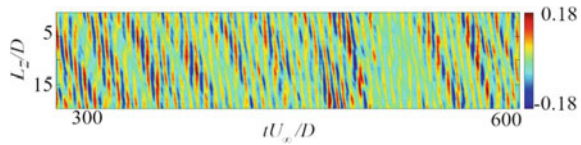


Fig. 9 Sectional lift coefficient contour at $\alpha = 0^\circ$ and 45° when $Re = 1.0 \times 10^4$

Fig. 10 Sectional lift coefficient contour when $e/D = 4\%$ ($\alpha = 45^\circ$, $Re = 1.0 \times 10^4$)



in Sect. 2.3. We speculate that the roundness imperfection might disturb the flow in a similar way as the combined effect of the Reynolds number and the attack angle.

To evaluate the coordination of sectional lift along the cylinder span, the cross-correlation of sectional lift at five span-wise locations with a spatial interval of D to $4D$ are analyzed. The spatial interval between sections i and j ($i = 1$ to 5 , $j = i + 1$ to 5) is designated by S_{ij} . As shown in Fig. 11, for all four roundness imperfection levels in $\alpha = 0^\circ$ and 45° cases, the periodicity of the local maximum in the correlogram of sectional lift matches the Strouhal number deduced based on the span-wise averaged lift. When $\alpha = 45^\circ$, although the Strouhal number of the $e/D = 4\%$ and $e/D = 0$ cases are the same, the sectional C_L contour of these two cases are found to exhibit considerably different patterns. The correlogram of sectional lift for $e/D = 4\%$ also show a low frequency fluctuation that the correlation of sectional lift is much enhanced once every few Kármán vortex shedding cycles, the interval between which is found to associate with the moving pattern of peak lift.

3.3 Surface Pressure

The instantaneous C_p contour of a cylinder at $\alpha = 45^\circ$ with $e/D = 4\%$ is portrayed in Fig. 12 for time instants $t^* = 565, 569, 572, 576, 579$, and 582 . The x -axis represents the angular position along the cylinder circumference direction, and the y -axis represents the span-wise location. The two red regions ($0^\circ < \theta < 30^\circ$ and $330^\circ < \theta < 360^\circ$) in the surface pressure plots are under pressure, whereas the rest of the cylinder surface is subjected to suction (in green or blue). The low C_p (or high suction) region is denoted by a red rectangular box and the local minimum C_p is denoted by a red cross. If using a black dashed line to connect the locations of local minimum C_p at different time instants, an “S” shaped motion trajectory of the low C_p region can be identified, which has strong three-dimensional characteristics. The motion can be decomposed into two components, with one being tangent to the cylinder circumference and the other along the cylinder axis.

If we estimate the moving speed of the low C_p region along the cylinder axial direction using the geometric center of the regions enclosed by the red rectangular box and the time lag between the leftmost and the rightmost points on the “S” pattern, this speed is determined to be 1.25 m/s. On the other hand, the free-stream velocity component in the cylinder span-wise direction is 1.17 m/s. The close match between these two suggests that the formation of the “S” pattern motion path is strongly related to the near-wake flow along the cylinder axial direction. Further, the frequency of

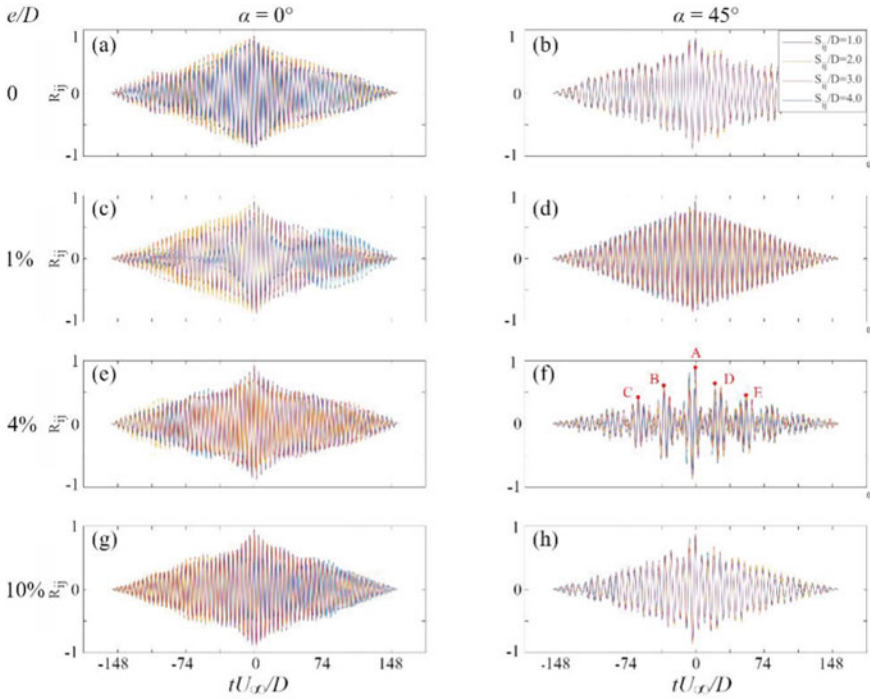


Fig. 11 Cross-correlogram of sectional lift for $\alpha = 0^\circ$ and 45° when $Re = 1.0 \times 10^4$ and $e/D = 0, 1\%, 4\%$ and 10%

the tangential movement is found to agree well with the Strouhal number. These clearly indicate that this unique “S”-shaped flow structure in the cylinder near wake is generated under the combined effect of Kármán vortex and axial flow.

3.4 Stream Trace

The instantaneous stream-trace of a cylinder inclined at 45° with $e/D = 0$ and 4% is shown in Fig. 13. It is seen that when flow approaches and passes the cylinder at a non-zero attack angle, at any arbitrary cross section of the cylinder, part of the flow is trapped within the recirculation zone and travels downward along the cylinder axial direction, which is indicated by the black arrow A and often referred to as the axial flow. The presence of roundness imperfection would reduce the size of the recirculation zone so the axial flow would be retained closer to the cylinder leeward surface and thus enhance its strength. Axial flow “pushes” the flow around the leeward side of the cylinder surface and that in the near-wake to move along the cylinder axial direction. Thus, as time progresses, the low C_p region would not only alternate its location along the tangential direction of the cylinder circumference

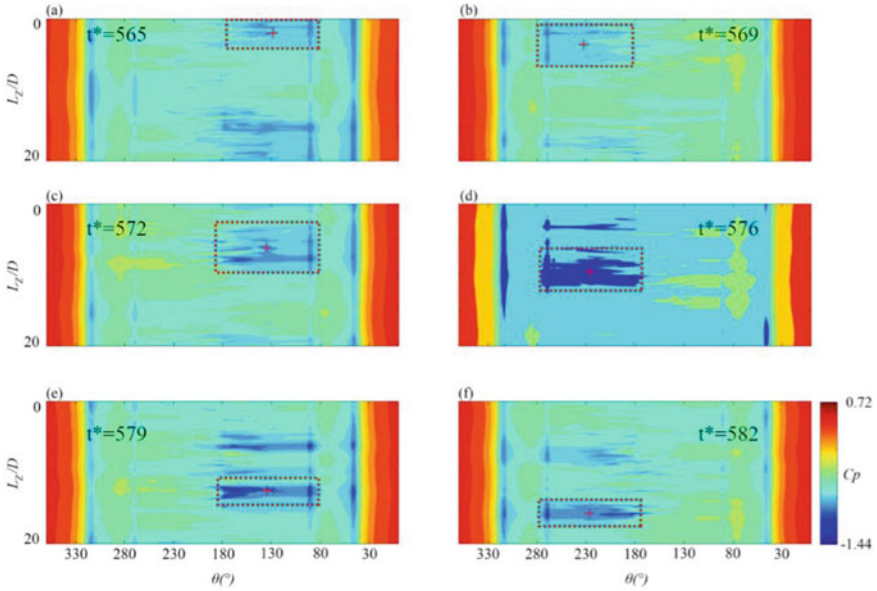


Fig. 12 Instantaneous C_p contour at $\alpha = 45^\circ$ for $e/D = 4\%$

but also continuously travel along the cylinder axial direction, which leads to the formation of a unique flow structure that moves in an “S” pattern in the cylinder near-wake.

Besides, it is observed that this newly formed axial flow is not stable. Instead of remaining in the recirculation zone while moving along the cylinder axial direction, it would “escape” after a short while by forming vortices and shedding from the cylinder surface, as indicated by the black arrow B. The formation and shedding of the axial vortices would interact with other flow structures, i.e., the von Kármán vortices. If the shedding of the axial vortex and Kármán vortex happen to occur at the same time, the interaction between the two would lead to the amplification of the Kármán vortex shedding and thus enhance the transverse lift. Since the frequency of axial vortex formation and shedding is found to be a fraction of that of Kármán

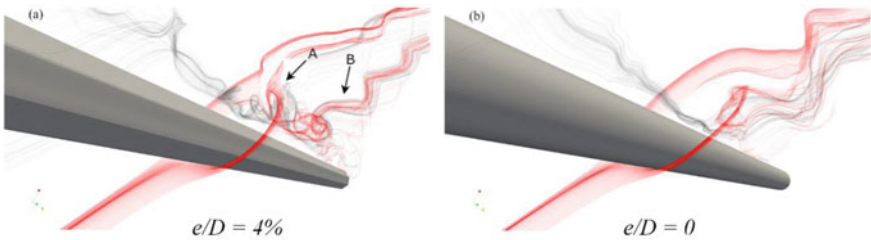


Fig. 13 Stream-trace of a cylinder inclined at $\alpha = 45^\circ$ when $e/D = 0$ and 4%

vortex, so the transverse lift is amplified intermittently. If such kind of intermittently amplified lift events occur continuously and also at different cross-sections along the span, it is possible to become an excitation source to trigger unstable cable motion.

It is also observed that if the roundness imperfection is considerable, then the formed axial flow would be “too strong” such that instead of interacting with the Kármán vortex shedding and amplify it intermittently, it would suppress the formation and shedding of the Kármán vortex instead.

4 Concluding Remarks

A series of CFD simulations have been conducted in the current study at $Re = 1.0 \times 10^4$ and 1.4×10^4 to explore the role of axial flow and roundness imperfection of cable cross-sectional shape on the generation mechanisms of wind-induced vibrations of dry cables. Results showed that the intensity of the axial flow, which depends on the cable orientation and the level of roundness imperfection of the cable cross-sectional shape, is critical to the occurrence of intermittently amplified lift for triggering wind-induced vibrations of dry cables. The axial flow cannot be too weak for forming axial vortex, and meanwhile cannot be too strong to suppress Kármán vortex. The suitable level of axial flow intensity which allows to interact with and intermittently enhance Kármán vortex formation and shedding can only be satisfied for certain range of cable orientation and certain level of geometric imperfection. This explains why aerodynamic instability of a cable was only observed at certain cable orientations in lab and on site.

References

1. Macdonald J, Larose GL (2006) A unified approach to aerodynamic damping and drag/lift instabilities, and its application to dry inclined cable galloping. *J Fluids Struct* 22:229–252. <https://doi.org/10.1016/j.jfluidstructs.2005.10.002>
2. Cheng S, Larose GL, Savage MG, Tanaka H, Irwin PA (2008) Experimental study on the wind-induced vibration of a dry inclined cable—Part I: phenomena. *J Wind Eng Ind Aerodyn* 96:2231–2253. <https://doi.org/10.1016/j.jweia.2008.01.008>
3. Matsumoto M, Yagi T, Hatsuda H, Shima T, Tanaka M, Naito H (2010) Dry galloping characteristics and its mechanism of inclined/yawed cables. *J Wind Eng Ind Aerodyn* 98:317–327
4. Cheng S, Tanaka H (2005) Correlation of aerodynamic forces on an inclined circular cylinder. *Wind Struct* 8(2):135–146
5. Raeesi A, Cheng S, Ting DS-K (2014) A two-degree-of-freedom aeroelastic model for the vibration of dry cylindrical body along unsteady air flow and its application to aerodynamic response of dry inclined cables. *J Wind Eng Ind Aerodyn* 130:108–124. <https://doi.org/10.1016/j.jweia.2014.04.007>
6. Saito M, Matsumoto T, Kitazawa M (1994) Rain-wind excitation of cables of cable-stayed Higashi–Kobe Bridge and cable vibration control. In: Proceedings of international conference on cable-stayed and suspension bridges (AFPC). Deauville, France, pp 507–514

7. McTavish S, Raeesi A, D'Auteuil A, Yamauchi K, Sato H (2018) An investigation of the mechanisms causing large-amplitude wind-induced vibrations in stay cables using unsteady surface pressure measurements. *J Wind Eng Ind Aerodyn* 183:19–34
8. Yeo D, Jones NP (2008) Investigation on 3-D characteristics of flow around a yawed and inclined circular cylinder. *J Wind Eng Ind Aerodyn* 96:1947–1960
9. Wang R, Cheng S, Ting DS-K (2019) Effect of yaw angle on flow structure and cross-flow force around a circular cylinder. *Phys Fluids* 31:014107
10. Wang J, Jakobsen JB, McTavish S, Larose GL (2019) Aerodynamic performance of a grooved cylinder in flow conditions encountered by bridge stay cables in service. *J Wind Eng Ind Aerodyn* 188:80–89

Cable Structures

Novel Position Control for Ensuring Feasible Tension Distribution of Cable-Driven Parallel Manipulators



Andrea Martín-Parra , Jorge Muñoz , Francisco Moya-Fernández ,
David Rodríguez-Rosa , Sergio Juárez-Pérez , and Concepción A. Monje 

Abstract Cable-Driven Parallel Robots are considered an effective automated solution to tackle some open industrial problems such as the manipulation of large payloads into a large workspace. They are considered fully-constrained when the n degrees-of-freedom of the end-effector are commanded by means of $n + 1$ cables. The dynamics of this extended configuration is strongly non-linear and, in addition, position control strategies must face the problem of maintaining cable tensions within an acceptable range. This paper proposes a simple but effective and robust control strategy based on adding a control signal offset to the output of a linear PID type control. Simulation results show that this proposal provides an excellent tracking of the end-effector pose in a planar case maintaining all cable tensions into the allowed range. The results presented in this work can be easily applied to spatial configurations.

Keywords Cable-driven robot · Dynamic model · Position control · Tension distribution

A. Martín-Parra (✉) · F. Moya-Fernández · D. Rodríguez-Rosa · S. Juárez-Pérez
School of Industrial and Aerospace Engineering, 45071, Toledo, Spain
e-mail: Andrea.Martin@uclm.es

F. Moya-Fernández
e-mail: Francisco.Moya@uclm.es

D. Rodríguez-Rosa
e-mail: DavidRRosa@uclm.es

S. Juárez-Pérez
e-mail: Sergio.Juarez@uclm.es

J. Muñoz · C. A. Monje
Robotics Lab, Department of Systems Engineering and Automation, Universidad Carlos III de Madrid, Av. Universidad 30, 28911 Madrid, Spain
e-mail: jmyanezb@ing.uc3m.es

C. A. Monje
e-mail: cmonje@ing.uc3m.es

1 Introduction

Cable-driven parallel robots (CDPRs) are a type of parallel manipulator where the end-effector is supported by flexible cables instead of rigid links [1]. This particular property of cables provides CDPRs several advantages such as smaller inertia and higher payload to weight ratio, which allows high speed and acceleration of the end-effector. The limitations of cables, which can only be driven by tension rather than compression, restrict the robot's workspace and make defining the motion range very important [1]. The robot's equilibrium equation can only be solved for positive cable tensions, and the cable forces must be kept within certain limits to prevent sagging and to avoid exceeding the torque limits of the actuators. Cable sagging is not usually taken into account (see [2]), but it is a complex issue that affects end-effector positioning and cable coiling. Other issues such as positioning accuracy, stiffness and vibration of CDPRs are caused by cable flexibility and compliance. Generally, CDPRs with n degrees-of-freedom (DOFs) driven by m cables can be classified according to their mobility and statics. CDPRs are under-constrained when $n + 1 > m$, fully-constrained when $n + 1 = m$, and redundantly or over-constrained when $n + 1 < m$. In the case of fully and over-constrained CDPRs there is an infinite number of force distributions that satisfy the force equilibrium equation for a certain end-effector pose and externally applied wrench. Therefore, the underlying mathematical problem is undetermined. In the last decade, several researches have proposed algorithms to compute force distributions for cable-driven parallel robots. These algorithms include interval analysis and gradient-based optimization [3], real-time control algorithms [4], including finding a closed-form solution [5]. Later, in [6] Pott compared the most studied methods to compute tension distributions and presented his new improved closed-form algorithm. The desirable characteristics of these algorithms include their computational cost, ability to deliver continuous tension along a trajectory, and ability to adjust tension levels from highly antagonistic to minimally antagonistic to achieve high stiffness or low power consumption [7]. Most control strategies for CDPRs involve linearization of the non-linear dynamic equations that describe the behaviour of the robot using feedforward linearization or inverse dynamics techniques (see [8]). Other approaches include sliding mode control [9], adaptive control [10] or model predictive control [11]. Hybrid position-force control strategies are also used to maintain cable forces within certain limits while controlling the end-effector pose [12].

This paper presents a new and simpler control technique for CDPRs, which adds a control signal offset to the output of a robust cascade PID controller. Compared to more complex algorithms for cable force distribution or advanced control techniques such as fuzzy-logic or adaptive control, this novel and robust control strategy has proved to be as efficient and achieve proper performance of end-effector positioning and trajectory tracking while maintaining tension within the allowed range. The technique is implemented for a conventional CDPR for comparative purposes and can be easily applied to any configuration or spatial case.

2 Cable-Driven Parallel Robot Modelling

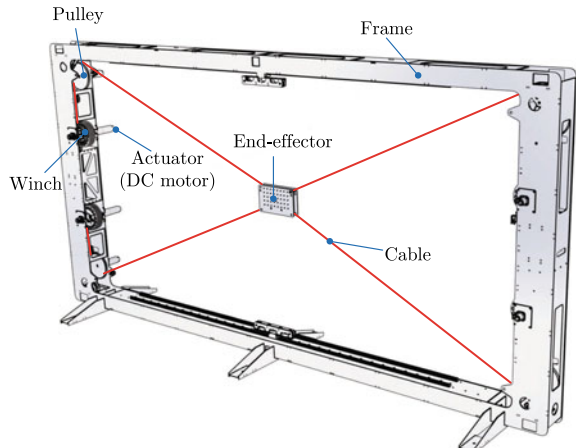
2.1 Kinematic and Static Models

Consider the planar conventional CDPR shown in Fig. 1. This manipulator possesses 4 cables of equal length, $m = 4$, allowing for 2 translational and 1 rotational DOFs, $n = 3$. The main elements of the robot, which can be seen in Fig. 1, are: fixed frame, end-effector, cables, actuation system using DC motors/gear boxes, and transmission system composed of pulleys that drive the cables to the end-effector. The actuation system is fixed to the upper and lower corners of the frame, and a winch mechanism converts the motor rotational motion into linear displacement to retract and release the cables.

Figure 2 shows important points to formulate the robot geometry. Distances W , H , and w , h are the width and height of the frame and the end-effector, respectively. $\mathbf{T} = [T_1, \dots, T_m]^T$ is the cable tension array, and the pose of the end-effector, $\mathbf{Q}_e = [x_e, y_e, \delta_e]$, is defined by its position ($\mathbf{q}_e = [x_e, y_e]$) and orientation (δ_e).

The geometry of the frame is defined by the proximal anchor points, PAP, $\mathbf{A}_i \in R^2 (i = 1, \dots, m)$ w.r.t. the world reference system, whereas the end-effector geometry is defined by distal anchor points, DAP, $\mathbf{b}_i \in R^2 (i = 1, \dots, m)$, w.r.t the local reference system of the end-effector. In this sense, the position of the DAP w.r.t the world reference system is obtained as $\mathbf{B}_i = \mathbf{q}_e + \mathbf{R}_z(\delta_e) \cdot \mathbf{b}_i$, where $\mathbf{R}_z(\delta)$ is the rotation matrix around the z axis. The kinematic model relates the joint angles, α , to the end-effector pose, \mathbf{Q}_e . This relationship is split into two: one relates joint angles α to cables lengths $\mathbf{L} = [L_1, \dots, L_m]$, and the other one relates the cable lengths \mathbf{L} to the end-effector pose \mathbf{Q}_e . In this way, motor angles can be obtained as $\alpha = \frac{\Delta L}{r} = \frac{L - L_0}{r}$, where r is the combined winch radius that considers the effective winch radius and the gear box connected to the actuators, and the cables lengths, \mathbf{L} , are obtained as $\mathbf{L} = \phi^{IK}(\mathbf{Q}_e)$, being ϕ^{IK} the inverse kinematic transform considering mass-less

Fig. 1 Planar fully constrained CDPR



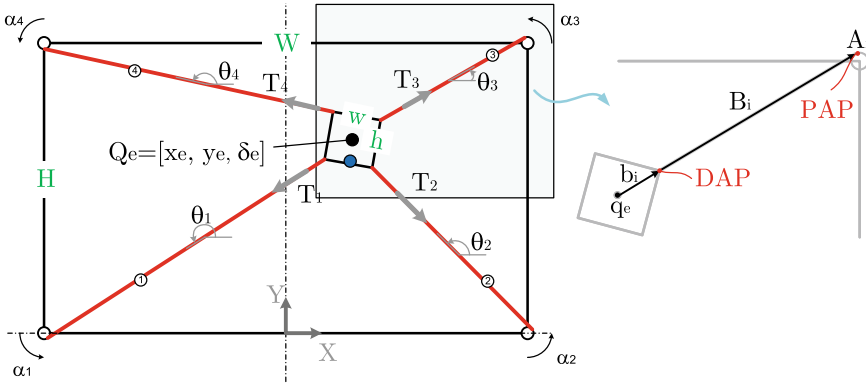


Fig. 2 Geometry of the CDPR

cables. As it can be seen, the solution of the inverse kinematic function always exists, it is always unique (ignoring the solutions that provide negative lengths), and it exists for arbitrary end-effector poses, \mathbf{Q}_e .

The static model of the robot is composed by the sum of external forces acting on the end-effector, i.e., the force equilibrium in the x and y axes, and the torque equilibrium around the z axis. In the static situation, the cable tension is equal along the cable path. The equilibrium of the system is formed by the following set of equations:

$$\mathbf{A}_e^T(\mathbf{Q}_e)\mathbf{T} + \mathbf{W}_e = 0 \quad (1)$$

where \mathbf{A}_e^T is the structure matrix containing the directions in which cables exert force and torque to the end-effector. It is a $n \times m$ matrix that yields:

$$\mathbf{A}_e^T = \begin{bmatrix} \mathbf{u}_1 & \dots & \mathbf{u}_m \\ \mathbf{R}_z(\delta_z)\mathbf{b}_1 \times \mathbf{u}_1 & \dots & \mathbf{R}_z(\delta_z)\mathbf{b}_m \times \mathbf{u}_m \end{bmatrix} \quad (2)$$

defining $\mathbf{u}_i = \frac{A_i - B_i}{L_i}$ as the unity vector containing the direction in which cable forces are exerted on the end-effector. On the other hand, \mathbf{W}_e is a vector containing the external wrench applied on the end-effector, and if the end-effector is only subjected to its own weight: $\mathbf{W}_e = [0, -m_e \cdot g, 0]^T$, being m_e the end-effector mass and g the gravity acceleration. The static equilibrium of the system contains n equations and m unknowns, this means that with $m = n + 1$ and an arbitrary end-effector pose, the problem is under-determined and the redundancy remains $r = m - n = 1$. In an under-constrained system of equations exists infinite solutions. In this way, a lot of efforts of the CDPR community are focused on proposing a proper tension (force) distribution among all the feasible solutions.

2.2 Dynamic Model

As it has been mentioned, CDPRs are an effective solution in works that require large workspace and high payload capabilities. Modelling and simulating the dynamic behaviour is basic to analyse such extreme scenarios quickly, without risk, and in a cost-efficient way. The input variables to the system are the torques exerted by motors, $\boldsymbol{\tau}$, and the output is the end-effector pose \mathbf{Q}_e . Assuming that the only forces acting over the end-effector are those exerted by cables and the gravity, the dynamic behaviour of the end-effector is obtained using the Newton-Euler formulation:

$$\mathbf{M}_e \ddot{\mathbf{Q}}_e = \mathbf{A}_e^T(\mathbf{Q}_e) \mathbf{T} + \mathbf{W}_e \quad (3)$$

where \mathbf{M}_e is the diagonal mass/inertia matrix. On the other hand, the motor/gear box/winch set dynamic expression yields:

$$\boldsymbol{\tau} = \mathbf{J} \ddot{\boldsymbol{\alpha}} + \mathbf{b}_m \dot{\boldsymbol{\alpha}} + r \mathbf{T} \quad (4)$$

with \mathbf{J} the rotational inertia matrix and \mathbf{b}_m the viscous friction coefficient. Equations (3) and (4) constitute the dynamic model of the robot. To obtain the control scheme that allows the design of a controller for each actuator, the following coupled dynamic model is employed:

$$\begin{aligned} \mathbf{M}_e \ddot{\mathbf{Q}}_e &= \mathbf{A}_e^T(\mathbf{Q}_e) \mathbf{T} + \mathbf{W}_e \\ \boldsymbol{\tau} &= \mathbf{J} \ddot{\boldsymbol{\phi}}^{IK}(\mathbf{Q}_e) + \mathbf{b}_m \dot{\boldsymbol{\phi}}^{IK}(\mathbf{Q}_e) + r \mathbf{T} \end{aligned} \quad (5)$$

Dynamic model (5) can be expressed in both, Cartesian and joints coordinates. The second one is commonly used mainly because joint coordinates control is much more easier to implement than Cartesian coordinates control.

2.3 Workspace Limitation and Control Requirements

A procedure to find solutions of the static equilibrium equations is required to determine the workspace. These solutions are restricted by the maximum, T_{max} , and minimum, T_{min} , allowed cable tension. T_{max} is determined by the maximum torque the motor is able to exert and the break limit of the cable, whereas T_{min} is restricted by the sagging effect of the cables (see e.g. [2]). Defining $\kappa = \frac{T_{max}}{T_{min}}$, the workspace is directly defined by κ . For a planar fully constrained scheme, Fig. 3 represents the static workspace for different values of κ with and without gravity ($\delta_e = 0^\circ$).

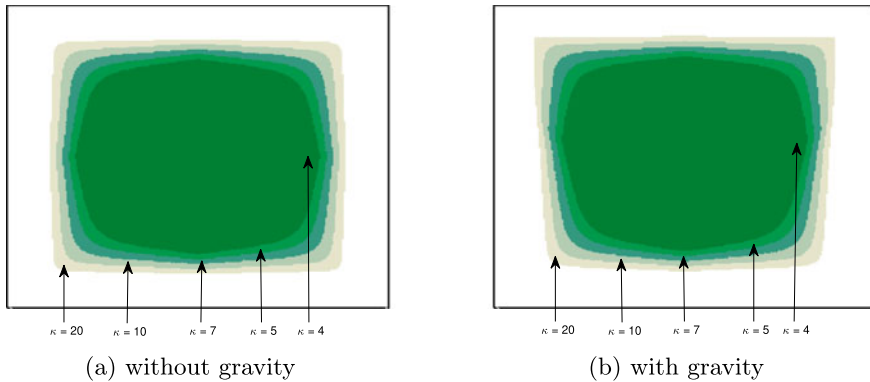


Fig. 3 Workspace for a planar fully constrained CDPR ($\delta_e = 0^\circ$)

3 Control System Design

3.1 Preliminaries

During the last two decades a lot of control strategies have been proposed for the position control of cable-driven parallel robots. The main open problems are: (a) The dynamic model is strongly non-linear. Some tensions near the edge of the workspace are high, while in the central workspace positions, a much lower force distribution is possible.

A linear controller can be tuned for one of these areas but its behaviour deteriorates in the others. This issue yields to adaptive controllers or non-linear controllers; (b) All cable tension shall be in the desired range $[T_{min}, T_{max}]$. The most extended tendency is to determine a feasible tension distribution inside this range for the actual/reference position of the end-effector. This is normally addressed with hybrid force/position control strategies. The following section propose a simple but effective control strategy which is able to tackle both problems using a linear controller, such a cascade PID without any online tension distribution (e.g., [13]).

3.2 Novel Proposal

The main goal of the control scheme in a CDPR is to effectively track a target end-effector pose, \mathbf{Q}_e , along a manoeuvre while maintaining cable tensions within the range $[T_{min}, T_{max}]$. Joint coordinates control requires the inverse kinematic for generating the joints reference, $\alpha^* = [\alpha_1^*, \alpha_2^*, \alpha_3^*, \alpha_4^*]^T$. The control block is a diagonal matrix of 4×4 , so SISO controllers can be tuned for each motor. Furthermore, given that finding the motor positions is easy by means of encoders, the control vari-

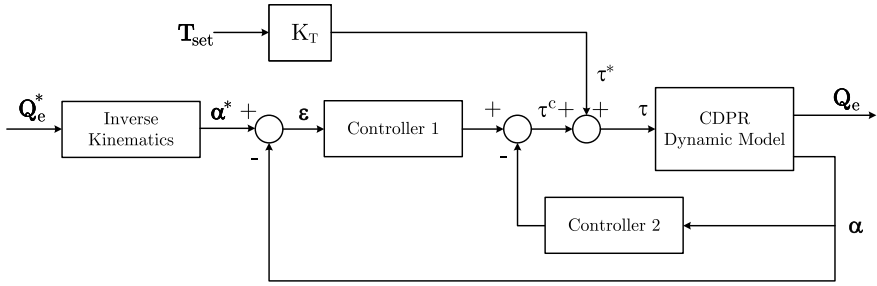


Fig. 4 Proposed control scheme

ables are joint positions. Figure 4 represents the proposed control approach, where $\mathbf{Q}_e^* = [x_e^*, y_e^*, \delta_e^*]^T$ is the end-effector position reference and ε the error signal.

In order to maintain cables tension inside the allowed range $[T_{min}, T_{max}]$ and to ensure a good behaviour of the controlled system in all the workspace, a reference value of control signal, $\boldsymbol{\tau}^* = [\tau_1^*, \tau_2^*, \tau_3^*, \tau_4^*]^T$, has been added to the output of the linear controller, $\boldsymbol{\tau}^c = [\tau_1^c, \tau_2^c, \tau_3^c, \tau_4^c]^T$. In this sense, the new control signal yields $\boldsymbol{\tau} = \boldsymbol{\tau}^c + \boldsymbol{\tau}^*$. This work proposes to compute the reference torque value as $\boldsymbol{\tau}^* = r\mathbf{T}_{set}$, being $\mathbf{T}_{set} = [T_{set1}, T_{set2}, T_{set3}, T_{set4}]^T$ the reference value of cable tensions that can be fixed to any tension value inside of $[T_{min}, T_{max}]$ in the same way as all distribution tension algorithm (e.g., [14]). This proposal is based on adding to the torque control signal the equivalent torque to apply a T_{set} force under static condition ($K_T = r$).

3.3 Controller Tuning

For each actuator i the PID constants, K_p, K_i, K_d , are selected to ensure a high performance trajectory tracking with zero steady state error, fast time response and no overshoot in its transient response. For illustrative purpose, a frequency domain tuning method has been selected. Neglecting the non-linear terms of (4), the transfer function of the actuator i with $i = 1, \dots, 4$, can be written as $G_i = \frac{K_i}{s(T_i s + 1)}$, being $K_i = 1/b_{mi}$ and $T_i = J_i/b_{mi}$. Denoting the transfer function of controllers 1 and 2 (see Fig. 4) as $R_1(s)$ and $R_2(s)$, respectively, the equivalent open-loop transfer function, $G_{OL}(s)$, for each actuator is $G_{OL}(s) = G_i(s)(R_1(s) + R_2(s))$ and the complex tuning equation in frequency-domain is therefore:

$$(R_1(j\omega_c) + R_2(j\omega_c))G_i(j\omega_c) = -e^{j\varphi} \quad (6)$$

being ω_c the gain crossover frequency and φ the phase margin. Constants K_p and K_d can be easily obtained with the frequency-domain tuning equations, whereas K_i can be selected to fulfil an additional requirement.

4 Simulation Results

4.1 Preliminaries

In order to validate the novel control technique performance, the CDPR dynamic model described in Sect. 2.2 has been modeled using Matlab® and Simulink®. A fixed sample time of 1ms has been set while using ode45 solver (Dormand-Prince). The main parameters of the robot are: frame size [2.224, 1.112] m, end-effector size [0.281, 0.287] m, end-effector mass and inertia, 1 kg and $1 \cdot 10^{-1} \text{kgm}^2$, and motors/winch set with a pulley radius, $r = 0.06$ m, and dynamics parameters $K = 0.0137$ and $T = 0.03$.

4.2 Controller Tuning

As the robot is mechanically symmetric, all controllers are tuned identically. The equivalent linear transfer function of the motors is $G(s) = \frac{0.4574}{s(s+33.3)}$. Using a fixed gain crossover frequency, $\omega_c = 10$ rad/s, and phase margin, $\varphi = 70^\circ$, to reach a rapid and damped response of the controlled system, the resulting controller parameters are $K_p = 758.87$, and $K_d = 8.1450$. On the other hand, the value of K_i is increased till the best controller for any metrics is found. In this sense, the maximum value of the integral constant before hunting effect is $K_i = 1250.0$. Assuming a reasonable maximum torque of 17.7 Nm, the maximum allowed tension is $T_{max} = 295$ N. On the other hand, a minimum tension value of $T_{min} = 10$ N has been fixed to avoid the sagging cable effect. In this way, T_{set} has been selected in the middle of the allowed range [10, 295] N, i.e., $T_{set} = 152.5$ N.

4.3 Trajectory Tracking Results

For validating the proposed control scheme, several trajectories along the WFW of the robot are executed. To measure the kindness/performance of the novel control, the end-effector travelling and cable tensions are tracked and the Integral Absolute Error (IAE), γ , between the end-effector pose, \mathbf{Q}_e , and its reference, \mathbf{Q}_e^* , is computed. Dynamic model (5) is a second order system, so 8th Bezier trajectories are implemented to ensure smooth trajectories and avoid abrupt changes in the control signal value. For illustrative purpose, a set of 10 non-oriented trajectories are executed within the limits of the WFW of the robot. All these trajectories are executed in $t_s = 3$ s. Figure 5 represents the set of the 10 trajectories used for checking the control strategy performance. Note that most of them have been configured to travel near the workspace limit where the difference between cables tensions are maximum (worst case).

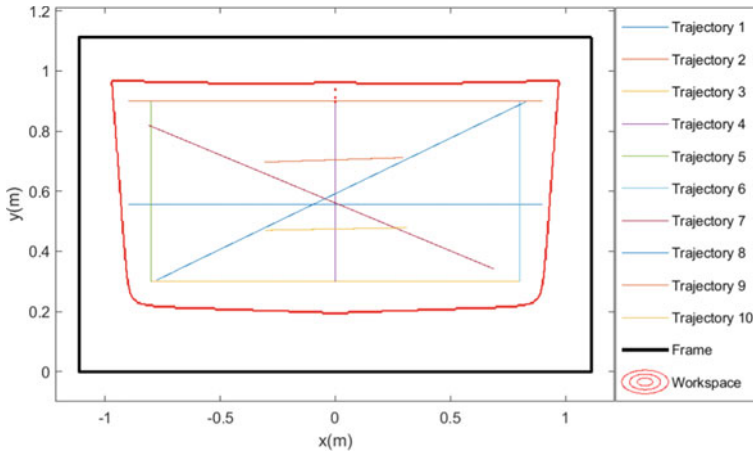


Fig. 5 Trajectories for control strategy validation

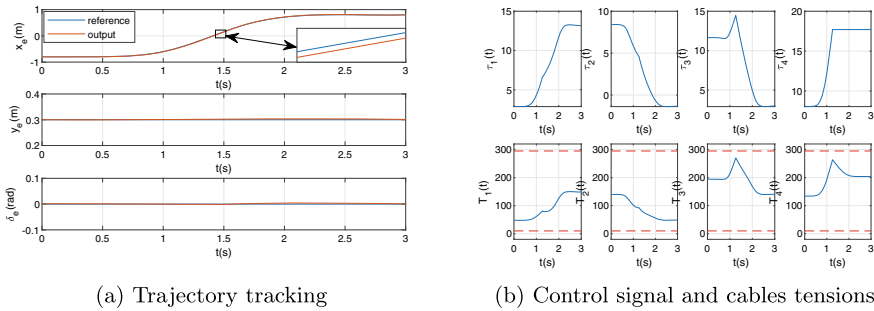


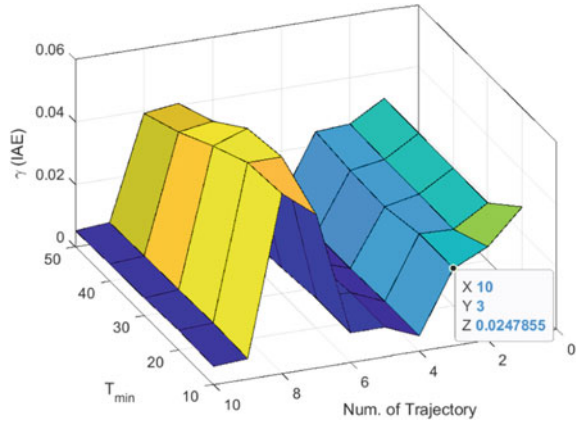
Fig. 6 Results of the end-effector position tracking (Trajectory 3)

Figure 6a represents the end-effector trajectory tracking for Trajectory 3 and Fig. 6b shows the control signal of the motors and the cables tension, which are inside the allowed limit $[T_{min}, T_{max}] = [10, 295]$ N. The obtained IAE of the trajectory tracking is $\gamma = 0.02479$.

In order to check the control strategy performance, IAE γ has been obtained for all trajectories and for $T_{min} = 10, 20, 30, 40$ and 50 N. Figure 7 represents the obtained γ values.

For all trajectories cables tension remains into the allowed range $[T_{min}, T_{max}]$ and the obtained γ results allow concluding a good trajectory tracking in all workspace areas.

Fig. 7 IAE results for all trajectories and different values of T_{min}



5 Conclusions

In this work, a novel control technique for CDPRs based on adding an offset to the output of a robust cascade PID controller is proposed. First, the kinematic and dynamic model of a conventional CDPR is presented together with one of its main disadvantages, i.e., the workspace reduction due to cable tensions restrictions. Then, the control scheme and the control strategy, together with the election of the appropriate offset set, are introduced. In order to test the performance of the proposed control strategy in terms of robustness, several trajectories are executed inside the workspace of the robot while tracking the end-effector trajectory and computing the IAE. Results show that the proposed simple control approach for CDPRs allows an accurate position control of the robot maintaining all cable tensions inside the allowed range $[T_{min}, T_{max}]$. It is notable how the travelling dexterity of the end-effector improves, even in complicated zones such as the workspace borders. In addition, this novel strategy improves the overall stiffness of the end-effector, specially near the workspace borders.

Acknowledgements Authors wish to thank the University of Castilla-La Mancha, Spain for the financial support provided by the pre-doctoral grant 2020-PREDUCLM-16080 and to the regional government Junta de Comunidades de Castilla-La Mancha (European Regional Development Fund) by the grant SBPLY/21/180501/000238.

References

1. Qian S, Zi B, Shang W-W, Xu Q-S (2018) A review on cable-driven parallel robots. Chin J Mech Eng 31(1):1–11
2. Ottaviano E, Arena A, Gattulli V (2021) Geometrically exact three-dimensional modeling of cable-driven parallel manipulators for end-effector positioning. Mech Mach Theory 155:104102

3. Bruckmann T, Pott A, Hiller M (2006) Calculating force distributions for redundantly actuated tendon-based Stewart platforms. In: *Advances in robot kinematics: mechanisms and motion*. Springer, pp 403–412
4. Ouyang B, Shang W (2016) Rapid optimization of tension distribution for cable-driven parallel manipulators with redundant cables. *Chin J Mech Eng* 29(2):231–238
5. Pott A, Bruckmann T, Mikelson L (2009) Closed-form force distribution for parallel wire robots. In: *Computational kinematics: proceedings of the 5th international workshop on computational kinematics*. Springer, pp 25–34
6. Pott A (2014) An improved force distribution algorithm for over-constrained cable-driven parallel robots. In: *Computational kinematics: proceedings of the 6th international workshop on computational kinematics (ck2013)*. Springer, pp 139–146
7. Côté AF, Cardou P, Gosselin C (2016) A tension distribution algorithm for cable-driven parallel robots operating beyond their wrench-feasible workspace. In: *2016 16th international conference on control, automation and systems (ICCAS)*. IEEE, pp 68–73
8. Zheng Y-Q (2006) Feedback linearization control of a wire-driven parallel support system in wind tunnels. In: *Sixth international conference on intelligent systems design and applications*, vol. 3. IEEE, pp 9–13
9. Ren P, Sun Y (2018) Sliding mode set point control of a six-dof cable-suspended parallel robot with tension constraints and uncertain disturbances. In: *International design engineering technical conferences and computers and information in engineering conference*, vol 51814. American Society of Mechanical Engineers, p V05BT07A018
10. Babaghasabha R, Khosravi MA, Taghirad HD (2015) Adaptive control of kntu planar cable-driven parallel robot with uncertainties in dynamic and kinematic parameters. In: *Cable-Driven parallel robots: proceedings of the second international conference on Cable-Driven parallel robots*. Springer, pp 145–159
11. Qi R, Rushton M, Khajepour A, Melek WW (2019) Decoupled modeling and model predictive control of a hybrid cable-driven robot (HCDR). *Robot Auton Syst* 118:1–12
12. Jun J, Jin X, Pott A, Park S, Park J-O, Ko SY (2016) Hybrid position/force control using an admittance control scheme in cartesian space for a 3-DOF planar cable-driven parallel robot. *Int J Control Autom Syst* 14(4):1106–1113
13. Zhang B, Shang W, Cong S, Li Z (2022) Dual-loop dynamic control of cable-driven parallel robots without online tension distribution. *IEEE Trans Syst Man Cybern Syst* 52(10):6555–6568
14. Fabritius M, Rubio-Gómez G, Martin C, Santos JC, Kraus W, Pott A (2023) A nullspace-based force correction method to improve the dynamic performance of cable-driven parallel robots. *Mech Mach Theory* 181:105177

Kinetostatic Analysis of a Novel Planar Cable-Driven Robot with a Single Cable Loop



Sergio Juárez-Pérez , Andrea Martín-Parra ,
Francisco Moya Fernández , David Rodríguez Rosa ,
and Antonio González Rodríguez 

Abstract One of the main problems of Cable-Driven Robots is the limited workspace in comparison to the frame area (in planar cases) or frame volume (in spatial cases). Depending on the presence of external force and the minimum and maximum allowed tension values, the workspace can be significantly decreased. Previous works focused on solving kinematic or dynamic problems when cables are sagging and, as a consequence, to include these end-effector poses into the usable workspace of the robot. In this paper, we tackle the problem of increasing the workspace of cable-driven robots by means of two mechanical modifications: adding passive carriages to the frame and using a single cable loop to command the end-effector pose. The workspace gain for a planar case is presented taking into account the different robot parameters.

Keywords Cable-driven robot · Parallel robot · Kinematics · Statics · Workspace

1 Introduction

Cable Driven Parallel Robots (CDPRs) are parallel manipulators in which conventional rigid links are replaced by cables. The use of cables to constrain a moving platform (end-effector) offers a number of advantages that stem mainly from the

S. Juárez-Pérez · A. Martín-Parra (✉) · F. Moya Fernández · D. Rodríguez Rosa ·
A. González Rodríguez
School of Industrial and Aerospace Engineering, University of Castilla-La Mancha, 45071
Toledo, Spain
e-mail: Andrea.Martin@uclm.es

S. Juárez-Pérez
e-mail: Sergio.Juarez@uclm.es

F. Moya Fernández
e-mail: Francisco.Moya@uclm.es

D. Rodríguez Rosa
e-mail: David.RRosa@uclm.es

A. González Rodríguez
e-mail: Antonio.Gonzalez@uclm.es

lightweight design of the robot. Each link is driven by a single actuator, so that no single actuator carries the weight of another actuator. Furthermore, when the actuator is attached to the robot frame, only the passive structure of the machine needs to be lifted, balanced and accelerated, i.e. smaller actuators and lighter links can be used.

CDPRs may achieve high precision, high end-effector speed and acceleration (due to much lower inertia and higher payload-to-weight ratio), large achievable working space and greater flexibility [1]. However, the cables can only act unilaterally through tension which limits the moment resisting and exertion capabilities [2]. One of the main problems of this type of robot is to keep the cable forces or tensions within reasonable limits [3]. Cable tensions must be kept above a certain value to avoid cable sagging, and below a certain maximum due to the maximum possible torque exerted by the actuators. Cable sagging is one of the main drawbacks of CDPRs, as it reduces positioning accuracy in large workspace applications [4].

A common kinematic classification of CDPRs is presented in [5]. It is based on the number of cables, m , and degrees of freedom (DOF), n , and distinguishes between under-constrained ($m \leq n \leq 6$) or *incompletely restrained positioning mechanism* (IRPM), fully-constrained ($n + 1 = m$) or *completely restrained positioning mechanisms* (CRPM), and redundantly constrained ($n + 1 < m$) or *redundantly restrained positioning mechanisms* (RRPM). The case where $n = m$ is also special because the robot would be kinematically fully-constrained, although the force equilibrium depends on external forces, such as gravity. If the robot relies on gravity for balancing and its workspace is mostly below the robot frame, then it is commonly referred to as a suspended or crane configuration.

For fully-constrained and over-constrained CDPRs, there are an infinite number of force distributions that satisfy the equilibrium equation for a given pose and acceleration of the end-effector and an externally applied wrench. The indeterminacy of the force distribution has implications not only on the size of the wrench feasible workspace (WFW) of the robot, but also on the control approach to be used. In the case of conventional CDPRs, limiting the cable tensions significantly reduces the WFW compared to the area of its frame [6]. Specifically, in planar CDPRs, the reduction in the size of the WFW occurs both at the top of the frame, due to the maximum allowable tension, and at the sides, due to the minimum value of these limits. A solution to not losing so much WFW would be to extend the tension limits, but this requires much larger actuators or to take sagging into account when modelling the system. This problem can be tackled in three ways: Using algorithms for the calculation of the force distribution [7, 8], adding passive elements to the robot to improve overall dexterity [9, 10], or adding active elements to the robot design [11] in order to reconfigure the position of the anchor points of the cables in the end-effector. Finally, previous works have proven that it is not necessary to add more actuators to the design, instead, adding passive elements to the robot design increase the WFW of the robot immensely. In [12, 13] the addition of passive carriages, that move freely along linear guides in the robot frame, is shown to provide a significant increase of the robot WFW. These carriages are fitted with pulleys that redirect the cable towards the end-effector, reducing the variation in the direction of the cables during end-effector travel. The result of using passive carriages is that the required cable

tension is lower, so that reasonable tension limits are achieved, providing a much higher WFW. In [13] the kinetostatic analysis of a CDPR with passive carriages is presented together with other studies that influence the size of the WFW of the robot, such as the modification of geometrical parameters and stiffness analysis. The main issue of the design is the loss of stiffness along the x-axis.

In this paper, a second mechanical modification is introduced to reduce vibrations when the end-effector manoeuvres. The novel mechanical modification is to use a single cable loop to command the end-effector pose together with the passive carriages. Both modifications obtain an enlargement of the WFW while maintaining constant robot stiffness. This paper presents the new mechanical concept, the mathematical foundations and the comparison of the WFW of the robot with respect to that of a conventional CDPR. Finally, a control strategy is proposed and simulated results are presented.

The following sections are organised as follows. Section 2 presents the new mechanical concept and analyses the workspace gains of the novel proposal. Section 3 develops the mathematical model of the robot. Section 4 proposes a kinematic control to validate the mathematical foundations. Section 5 shows the simulation results and, finally, Sect. 6 summarises the conclusions of this work.

2 System Description

Conventional CDPRs as shown in Fig. 1 exhibit a reduced WFW because of cable tensions which have to be kept within certain limits in order not to degrade performance. This is shown in Fig. 2 where static workspace of a conventional CDPR is obtained using the same geometric parameters as in simulations (see Sect. 5), a maximum tension, T_{max} , determined by the maximum holding torque of the motors and the breaking strength of the cables, and different minimum tension limits T_{min} . It must be pointed out that the borders/boundaries of the WFW are delicate zones to manoeuvre because of undesired vibrations of the end-effector, i.e., loss of stiffness.

This paper proposes a solution for both problems using a single cable loop CDPR (sCDPR), as shown in Fig. 3. It uses passive carriages as presented in [13], but with a twist. Instead of using four independent cables, this new mechanical concept employs a single cable loop. The loop is driven by two actuators placed at the lower corners of the frame that change the pose of the end-effector through a set of driven pulleys. One remarkable characteristic of this modification is that the cable length remains constant for every end-effector pose.

The dimensions of the frame are determined by its width, W , and height, H , while the end-effector is determined by its width, w , and height, h , as well. Other dimensional parameters are the widths of the upper carriage w_{uc} and lower carriage w_{lc} , and the radius of the driven pulleys, r , attached to both actuators.

To further develop the kinetostatic model, the generalized coordinates of the system are: x_e , for the horizontal coordinate of the end-effector, and y_e for the vertical

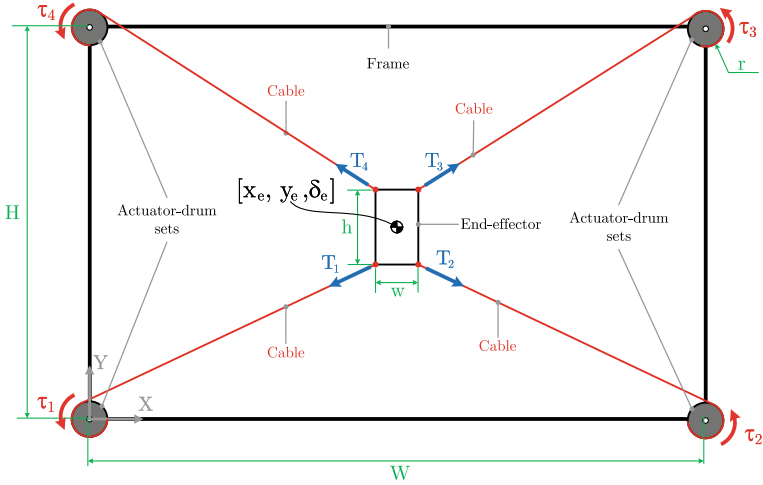


Fig. 1 Conventional planar CDPR

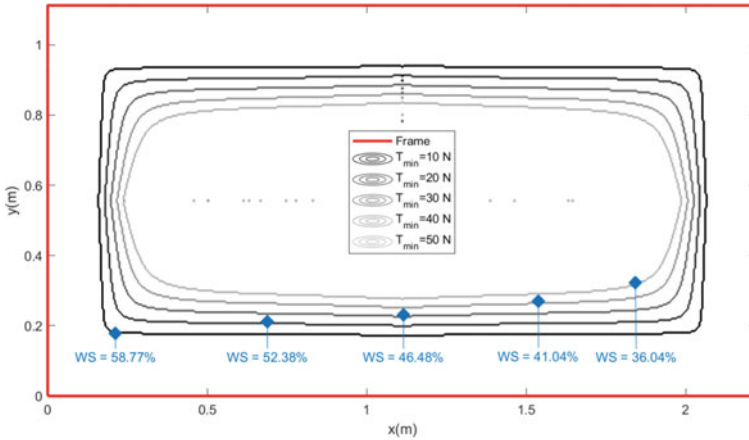


Fig. 2 Workspace of the conventional planar CDPR

coordinate of the end-effector. In this proposal, the carriages are considered to be aligned with the end-effector at all times, so there is no rotation of the end-effector. As for the actuators, their angular coordinates are θ_1 and θ_2 , respectively for the left and right actuator, and the input torque exerted by both motors are, τ_1 and τ_2 .

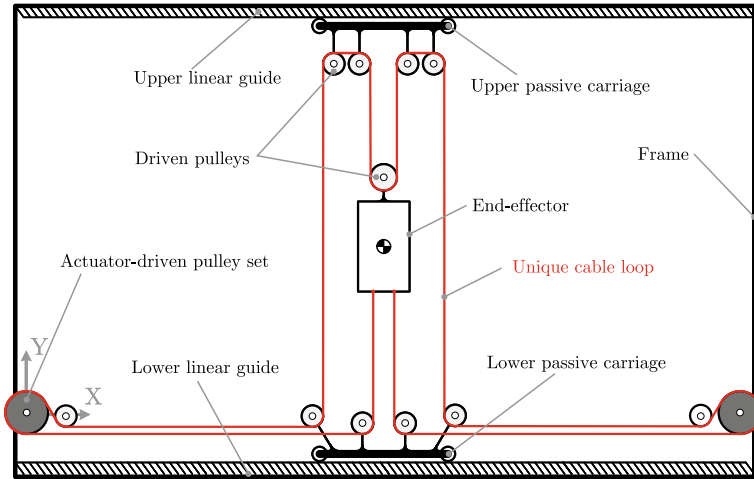


Fig. 3 Single cable loop planar CDRP proposal: sCDPR

2.1 Workspace Gain

The CDRP workspace is an important parameter for designing the robot structure, calculating the stiffness, as well as controlling the moving trajectory of the end-effector. There are three commonly used methods to define the workspace of a CDRP: The pointwise method that considers whether a finite set of discrete points satisfy the workspace constraints, the continuous method with the most commonly used algorithm being interval analysis, and the analytical method that focuses on defining the boundary (geometrical shape) of the workspace. The advantage of this method is that it gives a visual look at the geometry of the workspace [14].

With the novel proposal, assuming that after a manoeuvre both carriages are aligned with the end-effector, the equilibrium of forces is guaranteed, so the end-effector should be able to reach most of the frame area. The reachability is restricted by the static conditions:

$$\begin{aligned} \frac{w_{lc}}{2} \leq x \leq W - \frac{w_{lc}}{2} \\ b \leq y \leq H - a \end{aligned} \tag{1}$$

being a the distance between the end-effector and the upper pulley centres, and $b = \frac{w}{2}$.

The feasible workspace of the new design is formed by all the coordinates of the end-effector satisfying (1). In this proposal the workspace only depends on the geometry of the frame and end-effector, so the analytical method is easy to apply. Figure 4 represents the static workspace of the novel sCDPR using the same parameters as in the simulations presented in Sect. 5.

It should be noted that, unlike the workspace of a conventional CDRP (see Fig. 2), the workspace of the sCDPR is not limited by the cable tensions or system pretension.

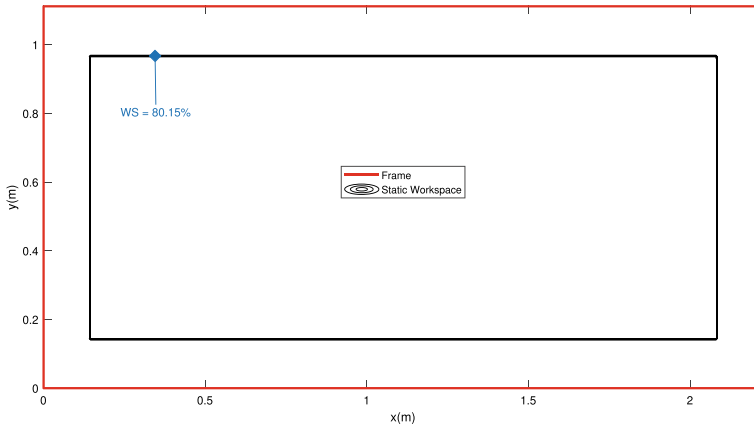


Fig. 4 Workspace of the sCDPR

The workspace of a sCDPR can be adjusted by changing the geometry of the mechanical elements of the design. This offers scalability advantages over its conventional CDPR counterpart.

3 Mathematical Model

3.1 Kinetostatic Model

One of the advantages of a design with a single cable loop is that the complexity of its kinematic formulation is significantly reduced. The change in the end-effector position is only influenced by the angle variation in the actuators that roll or unroll a certain amount of cable. Therefore, forward and inverse kinematic expressions yield:

$$\begin{aligned} [\Delta x_e, \Delta y_e] &= \phi^{FK}(\Delta\theta_1, \Delta\theta_2) \\ [\Delta\theta_1, \Delta\theta_2] &= \phi^{IK}(\Delta x_e, \Delta y_e), \end{aligned} \quad (2)$$

being $\phi^{FK} = \left[\frac{r(\Delta\theta_1 + \Delta\theta_2)}{2}, \frac{r(\Delta\theta_1 - \Delta\theta_2)}{2} \right]$ and $\phi^{IK} = \left[\frac{(\Delta x_e - \Delta y_e)}{r}, \frac{(\Delta x_e + \Delta y_e)}{r} \right]$ the forward and inverse kinematic transforms respectively.

Tension or pretension of the cables do not influence the kinematic positioning, however it greatly affects the system accuracy as it has direct consequences on the stiffness while manoeuvring the end-effector. On the other hand, the static model discussed in the previous section guarantees the equilibrium of forces. It is not necessary to solve a static equilibrium system in order to choose the tension values that remain within the tension limits while complying with the kinetostatic equilibrium.

4 Kinematic Control

As this paper only addresses the kinetostatic behaviour of the novel proposal, a kinematic control scheme is used in order to validate the kinematic model presented. Joint coordinates ($\theta = [\theta_1, \theta_2]^T$) will be used in the feedback loop of the control scheme. They are selected in preference to Cartesian coordinates ($\mathbf{Q}_e = [x_e, y_e]^T$) because measurable variables are the angular position of the motors. Therefore it only requires the inverse kinematics to generate the joints references, θ^* . In this sense, the controller block is a 2×2 diagonal matrix and SISO controllers are tuned for each motor. Dynamics of actuator i can be written as:

$$\tau_i(t) = J_i\ddot{\theta}_i + b_i\dot{\theta}_i + \tau_c(t) \tag{3}$$

where J_i is the motor inertia, b_i is the viscous friction coefficient and $\tau_c(t)$ the torque due to Coulomb friction. Disregarding the Coulomb torque, the dynamics of the actuators becomes linear and the Laplace transform can be applied to (3), to obtain the dynamic model of the motors:

$$\tau_i(s) = J_i\theta_i(s)s^2 + b_i\theta_i(s)s \tag{4}$$

Finally, the transfer function of the system can be written as:

$$G_i(s) = \frac{\theta_i(s)}{\tau_i(s)} = \frac{A_i}{s(s + B_i)} \tag{5}$$

being $A_i = \frac{1}{J_i}$ and $B_i = \frac{b_i}{J_i}$. These parameters are specific to each motor and should be determined experimentally. Figure 5 shows an schematic of the control scheme employed.

Assuming PID controllers, $R(s) = K_p + K_d s + K_i \frac{1}{s}$, where K_p , K_d and K_i are the proportional, derivative and integral gains [15], conventional frequency domain tuning method has been used to obtain the controllers gains. In this sense, by fixing the desired values of gain crossover frequency, w_{cg} , and phase margin, φ_m , (see [16]), the best PID gains were found to be $K_p = 2.2791$, $K_d = 0.8972$ and no integral action for a gain crossover value of $w_{cg} = 80$ rad/s and phase margin of $\varphi_m = \pi/2$ rad.

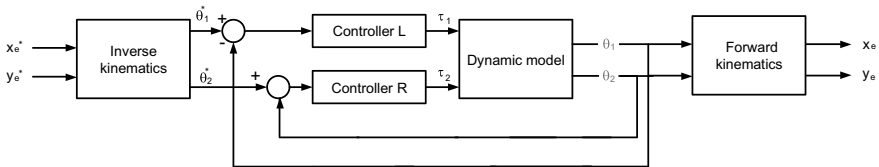


Fig. 5 Control scheme for positioning the end-effector

5 Simulation Results

Simulations are developed using Matlab[®] and Simulink[®]. The sample time is set to 1 ms using ode8 (Dormand-Prince) as solver. The model parameters considered for the study are shown in side table of Fig. 7.

As the actuators dynamics model (3) is of second order, Bezier trajectories of 4th order have been implemented to ensure smooth end-effector trajectories. These kind of trajectories avoid abrupt changes in the control signal values, which could yield to non-desirable vibrations of the end-effector. In order to illustrate the kinematic behaviour of the novel proposal, several simulated trajectories are presented along this section.

Figures 6 and 7 shows the tracking results of a horizontal, vertical and diagonal movement from [0.1585, 0.5560] m to [2.0655, 0.5560] m, [1.112, 0.1865] m to [1.112, 0.9255] m and [0.1585, 0.1865] m to [2.0655, 0.9255] m, respectively. Note

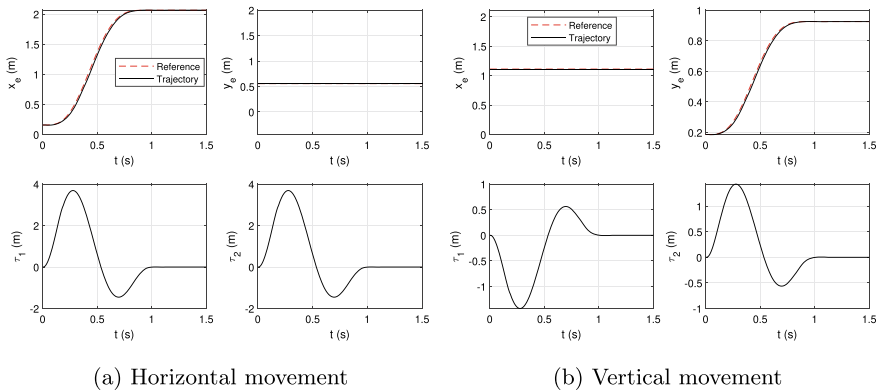


Fig. 6 Horizontal and vertical movement of the sCDPR

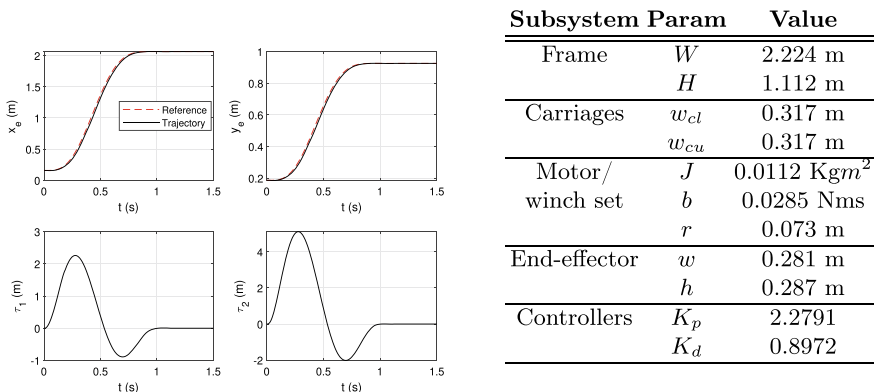


Fig. 7 Diagonal movement and simulation parameters for the sCDPR

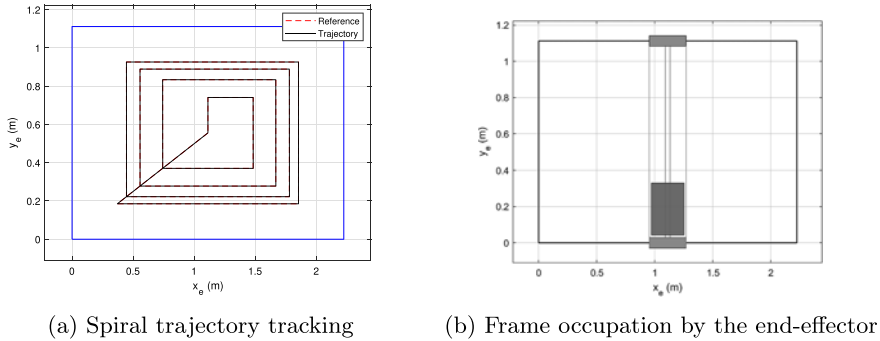


Fig. 8 Spiral movement of the sCDPR

that the trajectories cover a large area of the workspace, since they start from its boundaries and go all the way to the other side. In addition, the tracked integral absolute error (IAE) [17] for each trajectory are of 0.0238, 0.0092 and 0.0330 m.

Finally, Fig. 8 shows the trajectory tracking of a spiral type trajectory which starts and ends in the middle of the frame, the IAE error is of 0.1751 m.

These results show the feasibility of the proposal and evidence that the novel design is capable of reaching most of the entire frame area.

6 Conclusions

This paper proposes a novel design for fully-constrained CDPRs with 3 DOFs based on adding a second mechanical modification to the design with passive carriages presented in [13]. The new modification consists of using a single cable loop to command the robot. The main goal of the new design is to reduce vibrations, i.e. the loss of stiffness along the x-axis, while maintaining the WFW improvement achieved adding the passive carriages to the design.

The kinematic and static models of the novel design are presented. It is remarkable how this second modification greatly reduces the kinetostatic complexity of the model compared to that of the previous novel design, and even to that of a conventional CDPR. The single cable loop reduces the kinematics to expressions where the variation of pose of the end-effector is directly related to the variation of angle suffered on the motors.

Regarding the main setback of the passive carriages design, the single cable loop provides more robustness to the design. In order to prove this, several simulated trajectories are executed and tracked. Results evidence the high reachability of the proposal within the sCDPR workspace, while the kinematic control provides good accuracy when manoeuvring the end-effector.

Taking into account all of the above, it could be interesting to study the dynamic behaviour of the sCDPR, and design new control strategies that suits the requirements of the new design, together with the requirements of the task they are going to perform. In fact, this type of CDPRs, because of its performance, are thought to be very useful in logistic tasks such as picking and automatic storage.

Acknowledgements Authors wish to thank the University of Castilla-La Mancha for the financial support provided by the pre-doctoral grant 2020-PREDUCLM-16080 and to European Regional Development Fund and Junta de Comunidades de Castilla-La Mancha for grant SBPLY/21/180501/000238.

References

- Berti A, Merlet J-P, Carricato M (2016) Solving the direct geometrico-static problem of under-constrained cable-driven parallel robots by interval analysis. *Int J Robot Res* 35(6):723–739
- Qian S, Zi B, Wang D, Li Y (2018) Development of modular cable-driven parallel robotic systems. *IEEE Access* 7:5541–5553
- Pott A (2018) Geometric and static foundations. In: *Cable-driven parallel robots*. Springer tracts in advanced robotics. Springer International Publishing, Cham, pp 15–44
- Qian S, Zi B, Shang W-W, Xu Q-S (2018) A review on cable-driven parallel robots. *Chin J Mech Eng* 31(1):1–11
- Pott A (2018) Classification and architecture. *Cable-driven parallel robots: theory and application*, pp 15–43
- Pott A, Pott A (2018) Workspace. *Cable-driven parallel robots: theory and application*, pp 157–227
- Hassan M, Khajepour A (2011) Analysis of bounded cable tensions in cable-actuated parallel manipulators. *IEEE Trans Robot* 27(5):891–900
- Pott A (2014) An improved force distribution algorithm for over-constrained cable-driven parallel robots. In: *Computational kinematics: proceedings of the 6th international workshop on computational kinematics (CK2013)*. Springer, pp 139–146
- Youssef K, Otis MJ-D (2020) Reconfigurable fully constrained cable driven parallel mechanism for avoiding interference between cables. *Mech Mach Theory* 148:103781
- An H, Yuan H, Tang K, Xu W, Wang X (2022) A novel cable-driven parallel robot with movable anchor points capable for obstacle environments. *IEEE/ASME Trans Mechatron* 27(6):5472–5483
- Barbazza L, Oscari F, Minto S, Rosati G (2017) Trajectory planning of a suspended cable driven parallel robot with reconfigurable end effector. *Robot Comput-Integr Manuf* 48:1–11
- Rubio-Gómez G, Juárez S, Rodríguez-Rosa D, Bravo E, Ottaviano E, Gonzalez-Rodriguez A, Castillo-García FJ (2021) Addition of passive-carriage for increasing workspace of cable robots: automated inspection of surfaces of civil infrastructures. *Smart Struct Syst* 27(2):387
- Martin-Parra A, Juarez-Perez S, Gonzalez-Rodriguez A, Gonzalez-Rodriguez AG, Lopez-Diaz AI, Rubio-Gomez G (2023) A novel design for fully constrained planar cable-driven parallel robots to increase their wrench-feasible workspace. *Mech Mach Theory* 180:105159
- Tho TP, Thinh NT (2022) An overview of cable-driven parallel robots: workspace, tension distribution, and cable sagging. *Math Probl Eng* 2022
- Ogata K et al (2010) *Modern control engineering*, vol 5. Prentice Hall, Upper Saddle River, NJ
- Feliu-Batlle V, Castillo-García FJ (2014) On the robust control of stable minimum phase plants with large uncertainty in a time constant. A fractional-order control approach. *Automatica* 50(1):218–224
- Feliu-Batlle V, Rivas-Perez R, Castillo-García F (2021) Design of a $pi\alpha$ controller for the robust control of the steam pressure in the steam drum of a bagasse-fired boiler. *IEEE Access* 9:95123–95134

Dynamic Testing of a Long-Span Suspension Cable Net



Robert Soltys , Michal Tomko , Stanislav Kmet ,
and Christos Thomas Georgakis 

Abstract This paper presents a study of dynamic testing conducted on a long-span suspension cable net, which serves as the supporting structure for a lightweight roof. The original suspended cable net was replaced with this new structure, and the shape and stress state of the cable net depend on various factors, such as the geometry of circumferential supports, cable lengths, and cable prestress. The structural behaviour is significantly influenced by system nonlinearity, prestress, mass, service loading, flexibility of the circumferential supports, creep effects of cable elements, structural and geometrical symmetry, stiffness of upper non-structural layers, and temperature, which have been considered in the structural design of the new roof. Obtaining the modal parameters of the roof will be important for validating the real structure with a numerical model created for structural design purposes, both immediately after the final construction and during its lifecycle. The identified modal parameters estimated through in-situ dynamic testing are discussed. The dynamic tests were conducted immediately after the final construction stage of the cable net to estimate the roof modal parameters, serving as a reference for further analysis during the lifecycle of the roof. The paper focuses on discussing the estimated modal parameters, including the natural frequencies and natural modes. Finally, the continuous dynamic monitoring of the cable net is presented, enabling the analysis of the dynamic behaviour throughout its entire lifecycle.

Keywords Cable net · Prestress · Suspension roof · Dynamic test

R. Soltys (✉) · M. Tomko · S. Kmet
Technical University of Kosice, Kosice 040 01, Slovakia
e-mail: robert.soltys@tuke.sk

C. T. Georgakis
Aarhus University, Aarhus C, 8000 Aarhus, Denmark

1 Introduction

Cable nets are widely used as structural systems to cover large buildings, such as stadiums and velodromes, due to their structural efficiency. Their specific shape created by a double curvature stabilises the roof structure under external loadings while the cables act only in tension. This allows the system to balance entire structural frames, and applying tension to these cables can make structural members resistant to compression [5]. The susceptibility of cable structures to vibrations has sparked interest in assessing their structural condition through permanent dynamic monitoring [3].

The role of dynamic testing was discussed in [3]. In [4] full-scale measurements of wind effects on a long-span cable-supported roof were presented. The wind-induced response data were analysed in the time–frequency domain. Other full-scale measurements of long-span roofs can also be found in [6, 8, 10]. Rizzo et al. [9] discussed the dynamic modal identification and the FEM (Finite Element Method) predictive numerical modelling of flexible hyperbolic paraboloid roofs of scaled aeroelastic models. Vassilopoulou presented extensive research of dynamic behaviour of saddle-form cable nets [11].

Temperature increase and the creep effect of cables lead to an increase in cable length, resulting in an increment of the sag of the carrying cables. This, in turn, leads to a decrease in the prestress of stabilising cables and an overall reduction in cable tension, resulting in a decrease in the natural frequencies of the suspended cable roof.

The paper presents a study of a dynamic test of a new long-span cable net, which replaced the original one in 2020 after reaching its lifecycle. The dynamic test was performed immediately after the final construction of the roof. The identified modal parameters obtained using the FDD method are presented and will serve as reference values for further analysis of the structural health of the roof. It is believed, that by extracting the modal parameters of the roof during its lifecycle, it will be possible to detect a decrease of prestress of the stabilising cables and possible asymmetry of the stress state of the cable net.

The identified modal parameters calculated from the performed in-situ dynamic test represent the reference values for further dynamic analysis of the roof with a focus on effects influencing its structural response. These effects include wind-induced vibrations, the influence of temperature changes, and the creep effects of cables, which are supplemented by numerical simulations as studied in previous research.

2 Characteristics of the Structure

The Ice hockey stadium in Presov was built in 1966 with a seating capacity of 5500 people. A digital visualization of the hall is shown in Fig. 1. The prestressed cable net (Figs. 2 and 3) is anchored into massive reinforced concrete arches with

dimensions of 77.4×92.0 m. The arches are supported with concrete columns with a circular cross-section and ends which are anchored into concrete pylons to stabilise the whole structure [7]. The carrying cables consist of spiral two-layered strands with a nominal diameter of 24 mm and stabilising cables with the same structure and a nominal diameter of 12 mm. The cladding was installed after prestressing the stabilising cables of the cable net to a desired force of 30 kN, estimated by the computational form-finding technique proposed by [1]. The cable net was replaced in 2020 after the original reached the end of its lifecycle. The cables form a plan view raster of squares with side length of 1.0 m. The structural system of the new roof was designed by Technical University of Kosice.

In contrast to the previous cable roof, which included a relatively heavyweight sprayed concrete layer used as roof cladding [7], the new roof was designed to use a thin trapezoidal sheet as cladding. The difference in mass between the previous roof and the new roof resulted in a different cable net geometry with respect to the position

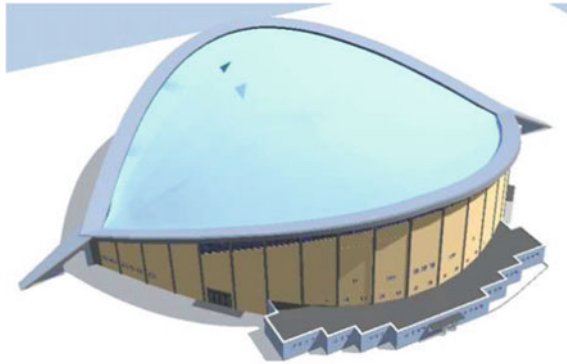


Fig. 1 Visualisation of the Ice hockey stadium of Presov



Fig. 2 Side view of the cable net



Fig. 3 View of the cable net from inside the structure

and angles of inclination of the holes in the concrete arches for anchoring the cables and sag of the cables in the post construction stage, i.e. with all permanent loadings in place. The cable net was designed to be symmetrical in terms of geometry and its stress state exhibiting specified tension forces in each cable during the structural design phase. Due to the limited number of force sensors installed in the cable net, the estimation of modal parameters using the dynamic test was performed to visually assess the symmetry of the stress state of the cable net through the visualisation of the identified natural modes.

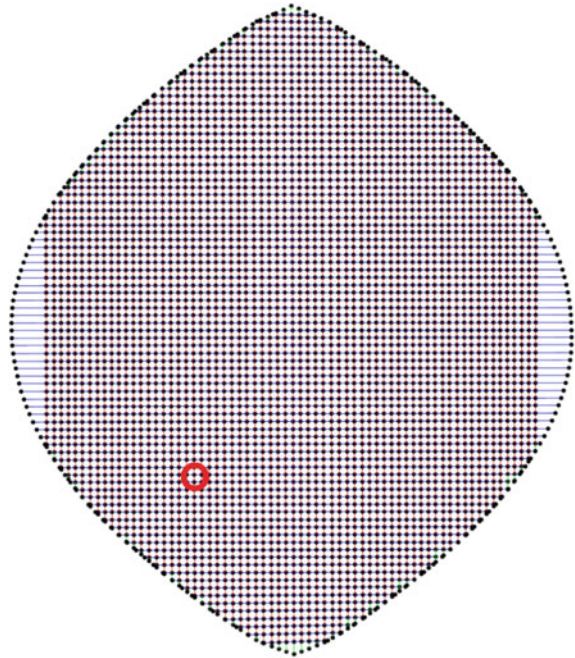
2.1 Monitoring System and Dynamic Test

A total of 17 accelerometers were installed in the roof with a recording frequency of 20 Hz connected to two HBM MX840BR transducers. The measured data are permanently recorded using HBM DataRecorder CX22BR type and are available online via Ethernet connection. The frequency domain decomposition (FDD) technique [2] was applied to data to extract the dynamic properties of the structure.

In the FDD, a cross power spectral density (CPSD) matrix is calculated from the measured acceleration and decomposed into singular values and singular vectors at each frequency point using singular value decomposition (SVD) [6].

Vibration of the roof was excited by a suddenly released mass of 350 kg (Fig. 5) hanging at the node of the cable net (Fig. 4). The position of the excitation was specified to avoid locations where vibration nodes were expected to occur (a node in vibration is a point where no vibration occurs). A single excitation (i.e. mass release) was performed at a specified location, allowing for the excitation of a wide range of natural modes simultaneously. Data from all 17 installed accelerometers

Fig. 4 Plan view of the cable net with the location of the hanging mass (circle in red) before release



were collected. The position and numbering of all 17 accelerometers correspond to intersections of the red lines marked as points 1 to 17, as is shown in Fig. 7. Figure 6 shows measured accelerations from four selected accelerometers marked 1, 3, 7 and 9, as is depicted in Fig. 7. Identified natural modes of the roof using the FDD technique applied on the recorded acceleration data are shown in Fig. 7 and corresponding natural frequencies are shown in Table 1.

The first natural frequency $f_{0,1} = 0.688$ Hz was identified and the symmetry of the roof is evident from the identified natural modes.

3 Conclusions

The presented study deals with modal identification of the cable roof of the Ice hockey stadium in Presov using the FDD technique. The natural modes and natural frequencies of the structure were successfully identified from the free-decay vibration excited by the release of a mass. These values are a part of the permanent structural health monitoring system of the structure to increase its safety and lifecycle.

In future, the identified modal values will be compared to those obtained from numerical simulations using the finite element method and the damping from the free decay vibration will be calculated.



Fig. 5 View of the hanging mass before release

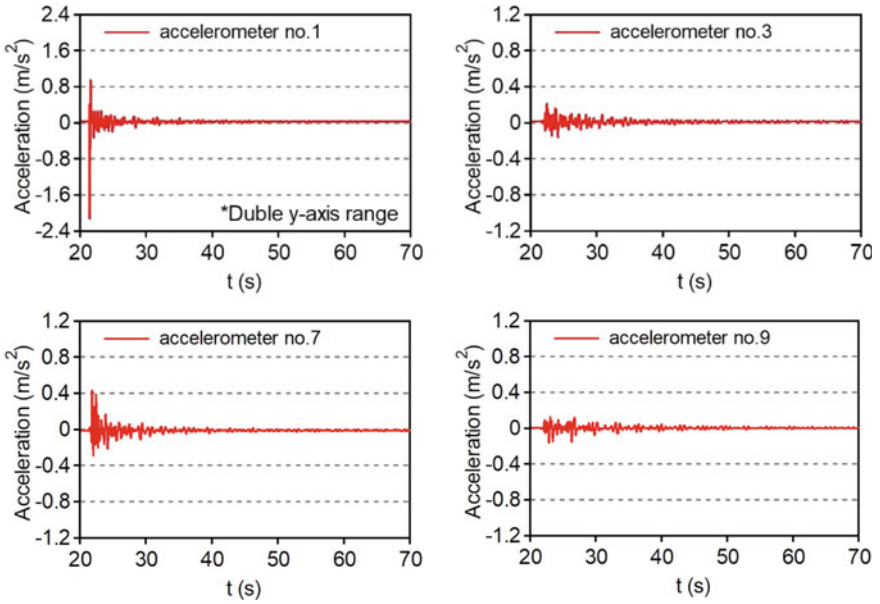


Fig. 6 Time-histories of the measured accelerations from accelerometers no. 1, 3, 7 and 9

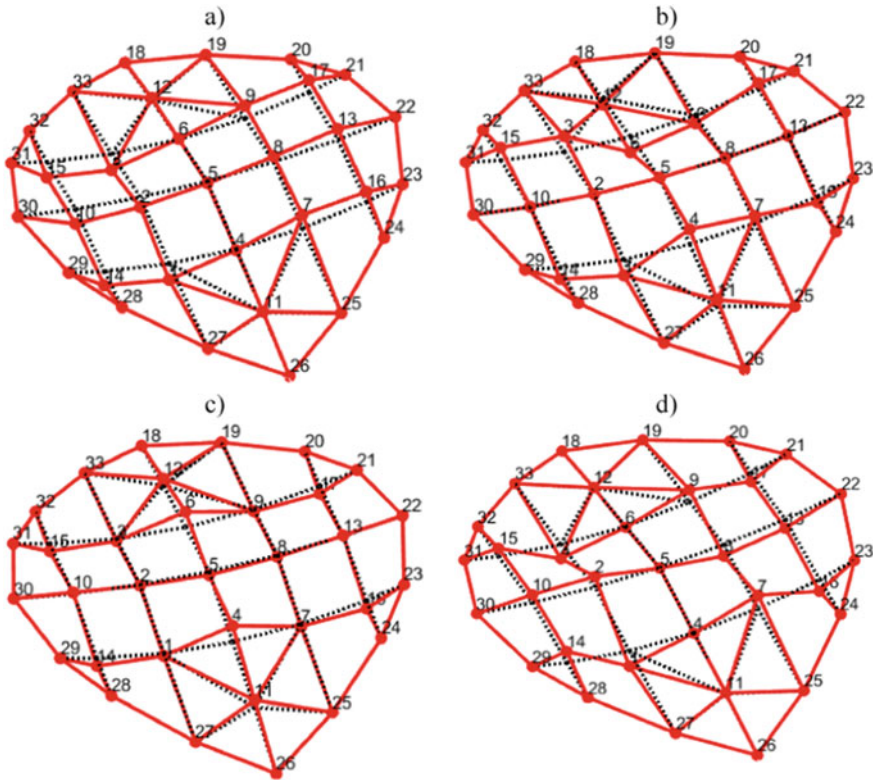


Fig. 7 Identified natural modes using the FDD technique of the roof: **a** 1st mode, **b** 2nd mode, **c** 3rd mode and **d** 4th mode. Black dashed lines represent the characteristic geometry lines of the roof while the red lines represent identified natural mode. The positions of 17 accelerometers are marked with numbers from 1 to 17

Table 1 Identified natural frequencies

Natural frequency (Hz)	$f_{0,1}$	$f_{0,2}$	$f_{0,3}$	$f_{0,4}$
Measurement—FDD	0.688	0.864	0.988	1.129

Acknowledgements The paper is carried out within the project No. 1/0129/20, partially funded by the Science Grant Agency of the Ministry of Education of Slovak Republic and the Slovak Academy of Sciences.

References

1. Bletzinger KU, Ramm E (1999) A general finite element approach to the form finding of tensile structures by the updated reference strategy. *Int J Space Struct* 14(2):131–146
2. Brincker R, Zhang L, Andersen P (2000) Modal identification from ambient responses using frequency domain decomposition. In: *Proceedings of the 18th international modal analysis conference (IMAC)*, San Antonio, Texas, pp 625–630
3. Caetano E, Cunha Á (2015) Dynamic testing of cable structures. In: *EVACES'15, 6th international conference on experimental vibration analysis for civil engineering structures*, vol 24. MATEC Web of Conferences, pp 1–15
4. Chen B, Wu T, Yang Y, Yang Q, Li Q, Kareem A (2016) Wind effects on a cable-suspended roof: Full-scale measurements and wind tunnel based predictions. *J Wind Eng Ind Aerodyn* 155:159–173
5. Hosozawa O, Shimamura K, Mizutani T (1999) The role of cables in large spatial structures: introduction of recent space structures with cables in Japan. *Eng Struct* 21:795–804
6. Kim JY, Yu E, Kim DY, Tamura Y (2011) Long-term monitoring of wind-induced responses of a large-span roof structure. *J Wind Eng Ind Aerodyn* 99:955–963
7. Kmet S, Tomko M, Soltys R, Rovnak M, Demjan I (2019) Complex failure analysis of a cable-roofed stadium structure based on diagnostics and tests. *Eng Fail Anal* 103:443–461
8. Magalhaes F, Caetano E, Cunha A (2008) Operational modal analysis and finite element model correlation of the Braga Stadium suspended roof. *Eng Struct* 30:1688–1698
9. Rizzo F, Sadhu A, Abasi A, Pistol A, Flaga Ł, Venanzi I, Ubertini F (2023) Construction and dynamic identification of aeroelastic test models for flexible roofs. *Arch Civ Mech Eng* 23
10. Tamura Y, Yoshida A, Zhang L (2005) Damping in buildings and estimation techniques. In: *Proceedings of the 6th Asia-Pacific conference on wind engineering*. Seoul, Korea, pp 193–213
11. Vassilopoulou I, Petrini F, Gantes CJ (2017) Nonlinear dynamic behavior of cable nets subjected to wind loading. *Structures* 10:170–183

Vibration Mitigation of Catenary Bridges



Gergely Szabó and Gábor Hochrein

Abstract Catenary pedestrian bridges are apparently spreading all over the world. These structures are highly popular as they provide the pedestrians with excitement and adventure. Consequently, there is a need to increase the span length, which might lead to the reconsideration of the conventional approaches. A novel structural configuration was proposed with special focus on the feasibility and proper static and dynamic performance of slender catenary bridges. A dedicated physical model was built and measured as a demonstration. The behavior of this model was also investigated by using numerical simulation.

Keywords Catenary bridge · Geometrically non-linear dynamics · Iso-tensioning

1 Introduction

1.1 Catenary Bridge Structures

The main elements of these bridges are the catenary cables that are fixed at both ends. These cables carry the vertical loads, such as the self-weight or ice loading. When necessary, wind cables and connecting cables are also involved in order to provide extra stiffness to the whole structure, which was studied in detail in [1, 2]. The problem with these bridges is that the connecting cables are complicated to tension evenly due to their mutual interaction. There can be loose cables that may vibrate, and the others can be overloaded. In addition, the overall structural behavior is strongly temperature dependent. To overcome the above mentioned problems, a novel structural configuration is proposed shown in Fig. 1. In contrast to conventional catenary bridges, the evenly distributed and temperature independent connecting cable forces can be conveniently ensured by adopting pulleys that are used for railway overhead electric wires for instance. Post-tensioning cables on both sides of the

G. Szabó (✉) · G. Hochrein
Pont-TERV Ltd., Mohai út 38, 1119 Budapest, Hungary
e-mail: mr.gergely.szabo@gmail.com

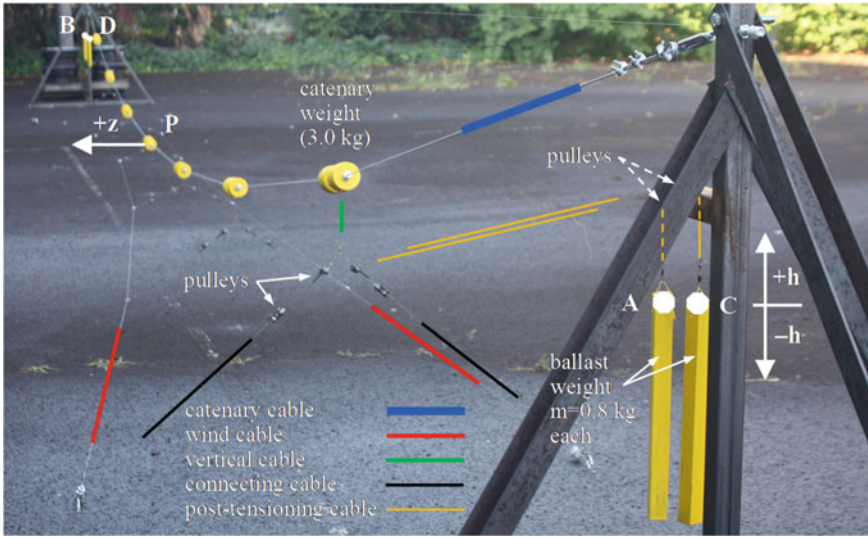


Fig. 1 The 14 m long physical model with the monitored points and the colored cable types

catenary with ballasts at their end points are used to adjust the desired pre-stressing to the structure. The novel approach has been first introduced at the WIBE (World Innovation in Bridge Engineering) prize competition. The main criterion was to propose a novel structural solution in the field of bridge engineering, with physical model as a demonstration. In this paper the fabrication and the test of this model are addressed. Numerical modeling and simulation are also introduced. The results of the measurements and the computational results are compared. Based on the results acquired from the physical and numerical models, the proposed novel configuration appears to be promising for catenary bridge structures.

2 Physical Model

2.1 Model Fabrication

The feasibility and the principle of the proposed novel structure were demonstrated on a physical model shown in Fig. 1. Steel wire ropes were used for the main catenary as well as for the wind cables. Soft fishing line was used for the post-tensioning and the connecting cables. The multi-strand fishing line is advantageous due to its bending flexibility, which reduces the overall friction of the pulley system. The different cable types are highlighted by using coloring. The span of the main catenary cable is $L = 14$ m. The diameter of the catenary cables is 3.0 mm ($EA = 560$ kN), and that of the wind cables is 1.0 mm ($EA = 75$ kN). The fishing line diameter of the post-tensioning

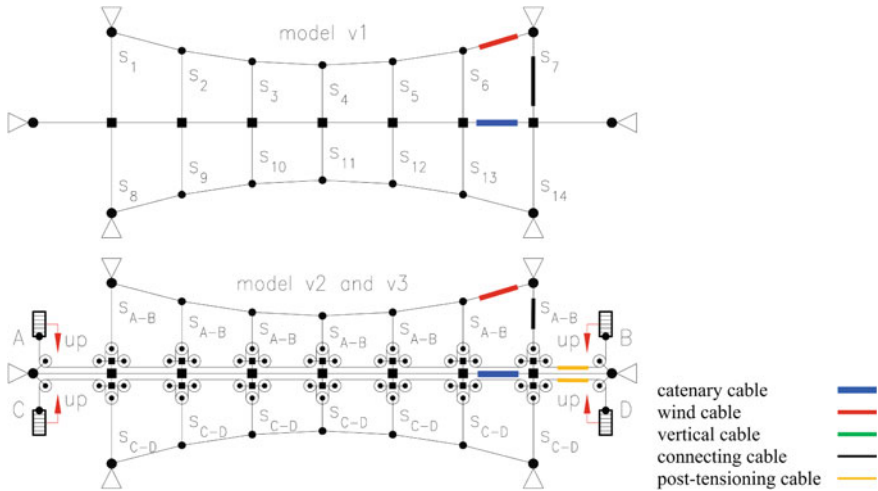


Fig. 2 Conventional (top) and the proposed structural system with the connecting cable forces

and the connecting cables is 0.40 mm ($EA = 2 \text{ kN}$). When the bridge was ready and the ballasts were released, the spatial pre-stressed structure was qualitatively studied; the connecting cable forces were indeed close together as desired, loose cables were not found.

The projected schematic top view of the original and the proposed structural configuration is shown in Fig. 2. In case of the conventional structure, the connection between the main catenary cable and the wind cables is ensured by using connecting cables (see Fig. 1). The desired internal forces can be adjusted by pre-stressing the wind cables and the connecting cables, which is practically complicated to carry out precisely due to the mutual interaction of the cables. The connecting cable force distribution depends on the stiffness properties of the whole structure and the pre-stress applied to the cables. In case of conventional catenaries, no post-tensioning cables are used, which will be referred to as model v1 in this paper.

2.2 Principles of the Proposed Structural Arrangement

The proposed system requires ballast weights in order to set the desired cable forces. In contrast to model v1, the connecting cables do not connect the wind cables and the catenary directly. Instead, two post-tensioning cables are included in the whole system belonging to the two wind cables on the two sides of the catenary. The post-tensioning cables are referred to as A-B and C-D, according to the points on the ballast weights. The whole system of a post-tensioning cable and the belonging connecting cables are referred to as branches A-B and C-D. There are two versions of the proposed system; in case of model v2, all the four ballast weights move

independently from each other. Model v3 is different, as the neighboring ballasts are connected together; the motion of ballasts A and C is not independent, instead a common upward or downward motion is allowed only. The same applies to ballasts B and D. Model v2 and v3 both produce equal connecting cable forces within a branch if the friction of the pulleys is neglected. For model v2 the connecting cable forces of the two branches are equal: $S_{A-B} = S_{C-D}$. The pulley system gives an additional flexibility to the system, which may reduce the horizontal stiffness of the main catenary. Therefore, it was of utmost importance to compare the static and dynamic behavior of the proposed models v2 and v3 to the original one named v1. The physical model was constructed with special attention to this need; the pulley system was equipped with a constraint that was capable of fixing the post-tensioning cables, which made it feasible to investigate and compare the behavior of model v1, v2 and v3. The structural details of the physical model are shown in Fig. 3. The slender catenary bridges are sensitive to wind loading; therefore the behavior due to horizontal static loading was studied and compared. Every catenary nodes was loaded horizontally. The load test can be seen in Fig. 4. All the three configurations were tested. Model v1 was set by fixation of the post-tensioning cables around the pulleys.

The connecting cable forces are independent from each other in this case. For model v2 the above mentioned fixation was released. Model v3 was set by joining

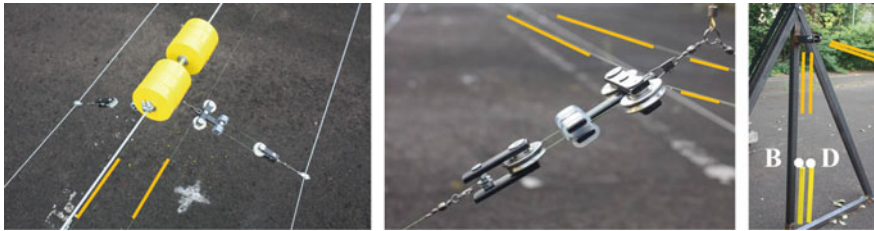


Fig. 3 Structural details of the physical model: catenary node, pulleys and the ballast weights

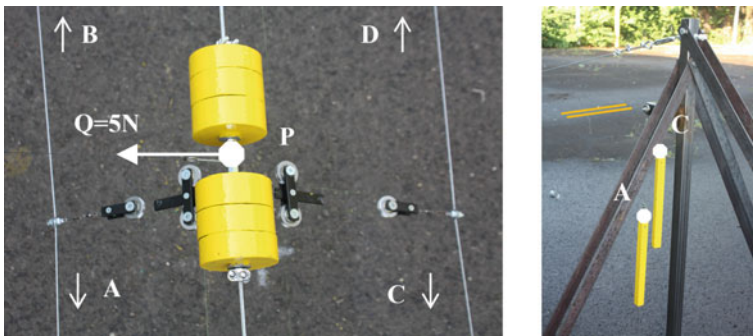


Fig. 4 Horizontal static deflection of the catenary and the vertical displacement of the ballast

the neighboring ballasts together. The pulley friction can be an important factor in the proposed system; therefore the initial friction value was measured by applying force difference onto the two ends of a test cable hanging on the two sides of a single V-groove ball bearing. The force difference reached 5% at the boundary of stall and motion, but drops to 1–2% when even moderate motion appears. Time-dependent behavior was also observed, which was explained by the presence of grease in the bearings. Due to the friction and viscous properties of the pulleys, the whole structure was given slight vibration at each static measurement in order to help the pulleys and the post-tensioning cables arrange and approach the ideal frictionless state. This was particularly important for model v2. In case of model v1, the ballast weights do not move and there is no pulley rotation either. In case of model v2, however, as the distance between the catenary and the wind cable changes, the ballasts move accordingly. The horizontal displacement of the catenary results in vertical displacements of ballasts A and C in the opposite direction (see Fig. 4). In case of model v3 the neighboring ballasts are joined together, therefore no significant ballast motion was observed. By using an accelerometer, the horizontal vibration of point P was monitored in a dynamic test. The first sway mode was excited by hand, which resulted in a free decay motion for each model.

3 Static Numerical Model

3.1 Introduction of the Numerical Approach

The static behavior was studied on a 72 DOFs numerical model (24 nodes with 3DOFs each), which was written in Octave (see Fig. 5). The model consists of two-node spatial truss elements with tension capabilities only. The structural elements are the main catenary cable, the wind cables on both sides, the connecting cables and the vertical elements. The post-tensioning cables and the ballasts are not shown in this model, but their effects are included as described below.

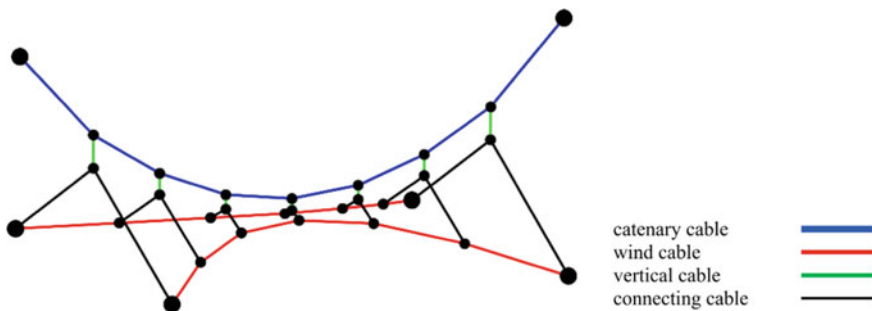


Fig. 5 Spatial view of the numerical model (post-tensioning cables are not shown)

3.2 Static Equations of the Geometrically Non-linear Structure

The considered mechanical system involves geometrical non-linearity; therefore the Newton–Raphson iterative approach was applied to find static equilibrium (Eq. 1), which was carried out in two steps.

$$\mathbf{K}_i(\mathbf{x}_i)\Delta\mathbf{x}_i = \Delta\mathbf{q}_{red,i} \quad (1)$$

At the first construction stage the main catenary cable was activated with its self-weight, which was complemented by the wind cables and the connecting cables at the second stage. Therefore, the sizes of the matrices and vectors are different in these two construction stages. The results of the first stage (e.g. cable length and forces, geometry and stiffness matrices) are used as initial condition for the second one. The first stage is the same for the three models. In case of model v1, the pre-stressing is defined to the wind cables and the connecting cables as kinematic loads, i.e. cable shortening. The connecting cable force distribution strongly depends on the kinematic loads. In case of model v2 and v3, however, the connecting cable forces are the same in every cable and depend on the ballast weight only. The additional horizontal forces are applied at stage two. The key step during the Newton–Raphson process is the formulation of the tangential stiffness matrix that belongs to the actual state of the structure, which can be assembled from the element stiffness matrices. Spatial truss elements were used with an element stiffness matrix according to Eq. 2.

$$\mathbf{K}_e = \left[k - \frac{s}{L} \right] \mathbf{e} \cdot \mathbf{e}^T + \frac{s}{L} \cdot \mathbf{I} \quad (2)$$

The spring stiffness is $k = EA/L$, with $EA =$ normal stiffness; $L =$ cable length; $\mathbf{e} =$ cable orientation unit vector; $s =$ cable force; $\mathbf{I} =$ identity matrix. The element matrix takes structural and geometrical stiffness into account. For model v1 the formulation of the element matrices is straightforward, the internal force variation of the j^{th} connecting cable is $\Delta s_j = f(\Delta L_j)$, which is the function of the length variation. For model v2 and v3, however, special further considerations have to be made. The force of the j^{th} connecting cable depends not only on the displacement of the nodes of its two end points, but that of every connecting cable. Therefore, a compatibility equation of the coupled system of the post-tensioning and connecting cables has to be solved at each iteration step in order to obtain the cable force changes based on the nodal displacement variation vector $\Delta\mathbf{x}_i$. The arrangement of branch A-B can be seen in Fig. 6.

The forces in the connecting cables of a branch are equal, provided that pulley friction is neglected, which leads to the analogy of serial coupling in electricity. By using this principle, the cable-mass-pulley system (see Fig. 6) was reduced into an inhomogeneous spring, which includes all the connecting cables and the tensioning cable belonging to branch A-B (see Fig. 7). The points M_j were merged into point M , and points A and B into point A-B. The total displacement variation reduced to point

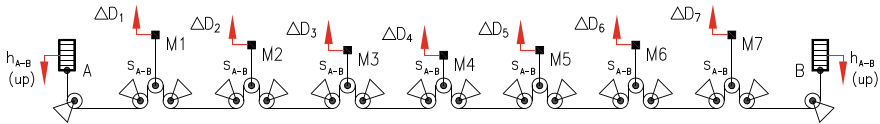


Fig. 6 Top view of the of branch A-B (D and h are displacement values, s is the cable force)

M is calculated as $\Delta x_{A-B} = \sum \Delta D_j$, where $\Delta D_j =$ end points distance variation (see Fig. 8) of the j^{th} connecting cable of the branch A-B. The linear reduced stiffness can be calculated by using a reciprocal formula for the serially coupled linear springs of branch A-B:

$$k_{red,A-B} = \frac{1}{\sum \frac{L_j}{EA_j} + \frac{L_{A-B}}{4EA_{A-B}}} \tag{3}$$

In Eq. 3 $L_j =$ length of a connecting cable; $EA_j =$ normal stiffness of a connecting cable, $L_{A-B} =$ length of the post-tensioning cable, $EA_{A-B} =$ normal stiffness of the post-tensioning cable. Branch C-D can be handled likewise. Symmetrical horizontal loading was considered only.

If there is no horizontal load, models v2 and v3 can be considered equivalent as the force is $s = 2 mg$ in every connecting cable, where $m =$ weight of one ballast and $g = 9.81 \text{ m/s}^2$. The behavior of these two models, however, is different if horizontal load is also applied, which is illustrated in Fig. 9. In case of model v2, branches A-B and C-D are independent; therefore the ballast weights can move freely. Consequently

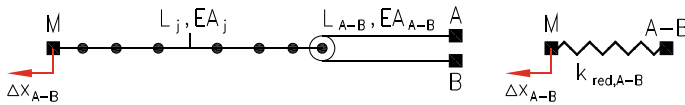


Fig. 7 Derivation of the idealized spring (left) and its reduced model (right)

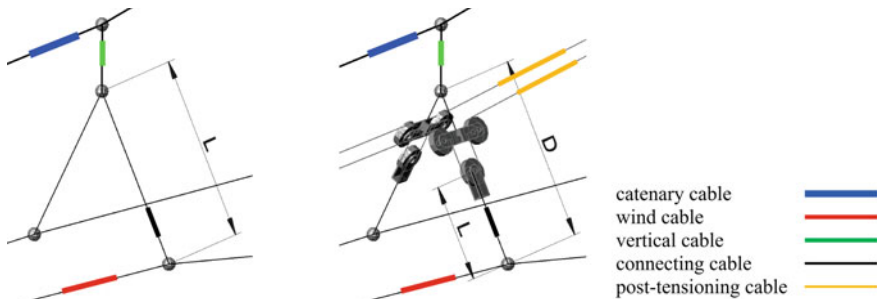


Fig. 8 Connecting cables of model v1 (left) and v2-v3 (right)

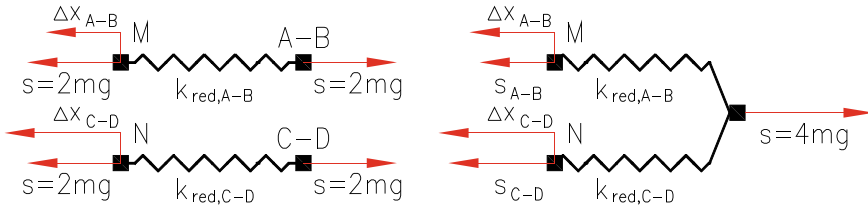


Fig. 9 Difference between the behavior of model v2 (left) and v3 (right)

the connecting cable forces do not change due to any structural displacement field, that is $\Delta s_{A-B} = 0$ and $\Delta s_{C-D} = 0$. This can be modeled by simply eliminating term k in the element stiffness matrix of the connecting cables (Eq. 2), which means that the geometrical stiffness belonging to the constant connecting cable forces exists only. In case of model v3 points A-C and B-D are connected together; the two inhomogeneous springs belonging to the branches A-B and C-D are now coupled in a parallel way.

The internal force variation for branch A-B is $\Delta s_{A-B} = f(\Delta D_j, j = 1..2n)$ and that for the branch C-D is $\Delta s_{C-D} = g(\Delta D_j, j = 1..2n)$, where $n =$ number of the connecting cables on one side, namely 7 in our case. Unlike model v2, the connecting cable forces are not invariant with respect to the reduced displacement variation in case of model v3. If the reduced displacement variation of Δx_{A-B} and Δx_{C-D} are not equal, a difference will appear between the connecting cable forces of the two branches due to the constraint caused by the connection of the corresponding ballast weights. The reduced displacement variations for branch A-B can be calculated as $\Delta x_{red,A-B} = \Delta x_{A-B} - (\Delta x_{A-B} + \Delta x_{C-D})/2$ and that for branch C-D is $\Delta x_{red,C-D} = \Delta x_{C-D} - (\Delta x_{A-B} + \Delta x_{C-D})/2$. If symmetrical horizontal forces are applied, the connecting cable force variations are calculated as $\Delta s_{A-B} = \Delta x_{red,A-B} \cdot k_{red,A-B}$ and $\Delta s_{C-D} = \Delta x_{red,C-D} \cdot k_{red,C-D}$. Compared to model v2, stiffness k in the element stiffness matrix is not zero. The normal stiffness values k for each connecting cable of branch A-B and C-D are $n \cdot k_{red,A-B}$ and $n \cdot k_{red,C-D}$; respectively.

4 Dynamic Numerical Model

The dynamic behavior of the three models was studied by extending the static equations with the inertia and damping forces. A non-iterative incremental time advancement version of the Leap-frog scheme was used instead of a more complicated nested Newton-Raphson scheme. Model v1 required to solve Eq. 4.

$$\mathbf{M}\Delta \mathbf{a}_i + \mathbf{C}\Delta \mathbf{v}_i + \mathbf{K}_i(\mathbf{x}_i)\Delta \mathbf{x}_i = \Delta \mathbf{Q}_i \quad (4)$$

In Eq. 4 \mathbf{M} = mass matrix; \mathbf{C} = damping matrix; \mathbf{a} = acceleration vector; \mathbf{v} = velocity vector; \mathbf{x} = displacement vector; \mathbf{Q} = external load vector. As the structure is geometrically non-linear, the stiffness matrix has to be updated at each time step

based on the geometrical position of the nodes (see Fig. 5) and the cable forces. Although the explicit scheme was easy to implement, the time step necessary for a stable and accurate solution was typically 10 times less than usual in linear dynamics. The dynamic behavior of model v2 is different from the static one. Since the structural nodes have accelerations, so have the ballasts, therefore the variations in the connecting cable forces appear during the dynamic load conditions. To handle this, a separate dynamic equation has to be solved for the vertical dynamic motion of the ballast weights. Model v3 does not differ from the principles of the static modeling. More details of the dynamic formulations of model v2 and v3 can be found in [3].

5 Validation

In the previous chapters the proposed structural system was investigated by means of physical and numerical approaches. The input for the numerical simulation was set in accordance with the properties of the physical model. A horizontal static load of 5 N was applied to the catenary nodes. In Table 1 the measured and calculated horizontal displacement of point P (see Fig. 10) and vertical displacement of ballast points A and C are compared. The measured and simulated displacement values are in good agreement for models v1 and v3. The results based on model v1 and v3 are close together, which means that there is no significant loss in the overall stiffness due to the dominant horizontal loading by applying the proposed post-tensioning system of model v3. Model v2, however, gave 2–3 times larger displacement, which can be explained by the unconstrained vertical displacement of the ballasts and the consequently constant connecting cable forces. The connecting cables with constant forces need to change spatial orientation in order to balance the horizontal load, which is the source of the significantly larger horizontal displacement. The measured horizontal displacement is lower by 35 per cent than the calculated one due to the friction of the pulleys. The ballast displacement shows the difference between models v2 and v3; points A and C move in the opposite direction and so do points B and D in case of model v2. On the other hand, in case of model v3, points A-C and B-D are connected together, resulting in a small common displacement, which constrains the horizontal displacement of the catenary.

Table 1 Measured and calculated displacement of point P and ballast points A and C in mm

Model	Physical			Numerical		
	P_hor	A_vert	C_vert	P_hor	A_vert	C_vert
v1	21	–	–	22	–	–
v2	50	–190	178	67	–276	276
v3	28	3	3	29	8	8

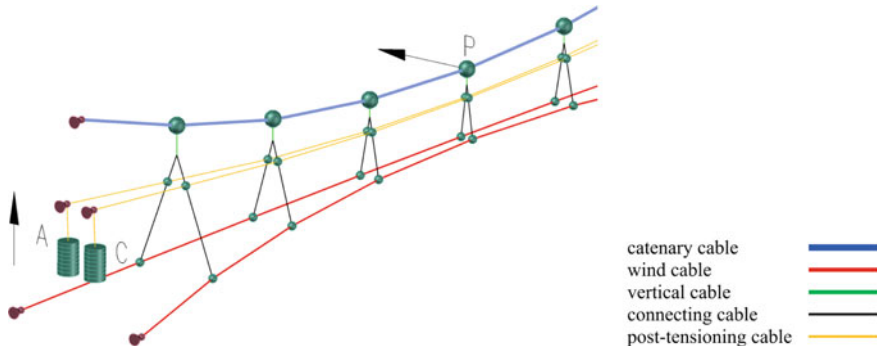


Fig. 10 Monitored points and the directions of the displacements

The developed dynamic numerical method was also validated. The natural frequencies were determined by using FFT analysis of the time series of the geometrically non-linear time stepping method. The simulation was started on the completed bridge structure as a result of the nonlinear static calculation. The time-dependent horizontal load was applied to each catenary node; it was ramped up in a quasi-steady manner and then set to zero in one time step, obtaining a free decay oscillation to study.

The results are shown in Table 2 for the three models extended with stage1 for the catenary alone state. The measured and simulated natural frequencies of the sway mode are in good agreement. According to expectations, model v1 has the highest frequency as it has the highest stiffness. Model v3 showed somewhat higher static deflection and the frequency is consequently lower. Model v2 is interesting as the sway mode has a frequency close to that of models v1 and v3. On the other hand, the extra freedom of the ballasts provided a slow vibration mode that belongs to the vertical motion of the ballasts and the horizontal motion of the catenary. The frequency is around 0.30 Hz, which is shown in Table 2 in parentheses. This mode was spotted numerically but did not show up in the measurements, which is explained by the behaviour of the pulleys; the bearings of this size give relatively high friction and viscosity, which might hinder the whole pulley system from accommodating this vibration mode. On the qualitative observation of the behaviour of model v2 it was found that the motion of the ballasts might be mitigated by using viscous dampers. By using such elements, the damping of the whole bridge is hoped to be increased, which could effectively contribute to the span length maximization [4].

Table 2 Natural frequencies of the symmetrical sway mode in Hz

Model	Physical	Numerical
Stage1	0.68	0.66
v1	1.50	1.44
v2	1.37	1.30 (0.30)
v3	1.38	1.28

6 Conclusions

In this paper a novel post-tensioning method was proposed for long-span catenary bridges. The system involves pulleys, which have a number of advantages. First of all, the pre-stressing is temperature-independent. Secondly, the connecting cable forces are evenly distributed, therefore any vibration of a loose cable is unlikely. The proposed structural configuration was demonstrated and tested on a physical model. The evenly distributed connecting cable forces were indeed observed, which was our main goal to achieve. Static and dynamic numerical models were also developed. Three structural configurations were investigated; the conventional one named model v1, and the novel pulley-based system with and without fixing the neighboring ballasts together, named models v3 and v2; respectively. The measured and calculated results were in good agreement. It was found that model v2 has more flexibility due to the unconstrained motion of the ballasts, which is a drawback of this configuration. Each ballast, however, can be equipped with hydraulic dampers, which are believed to be capable of adding extra damping to the whole structure. The increase of damping is of utmost importance in case of slender steel structures, which will be our main goal to achieve in the forthcoming research projects. Also, our numerical models are planned to be updated in order to include the friction of the pulleys both under static and dynamic conditions.

References

1. Huang MH, Thambiratnam DP, Perera NJ (2005) Vibration Characteristics of Shallow Suspension Bridge with Pre-tensioned Cables. *Eng Struct* 27(8):1220–1233
2. Szabó G, Pálóssy M, Mátyássy L (2017) Static and dynamic study of a 700 m long catenary bridge. In: *IABSE symposium: Engineering the Future*, pp 548–555. IABSE, Vancouver, Canada
3. Szabó G, Gábor H (2020) Numerical and experimental study of a slender catenary bridge with a novel tensioning system. In: Papadrakakis, M., Fragiadakis, M., Papadimitriou, C. (eds.) *EURODYN 2020*, Athens, Greece
4. Ge YJ (2016) Aerodynamic challenge and limitation in long-span cable-supported bridges. In: *The 2016 World Congress on Advances in Civil, Environmental and Materials Research (ACEM16)*, Jeju Island, Korea

Field Observation of Global and Local Dynamics of a Cable-Stayed Bridge



Jasna Bogunović Jakobsen, Jónas Þór Snæbjörnsson, and Nicolo Daniotti

Abstract This work examines dynamic characteristics of a cable-stayed bridge, utilizing acceleration data from the bridge deck as well as the cables. A weather station installed on the bridge provides additional data for the interpretation of the observed wind and traffic induced vibrations. The measurement data are acquired on the Stavanger City Bridge. The bridge layout, combining steel and concrete girder segments supported by a tower and stay cables, makes it an interesting case for system identification analysis especially as all three parts of the bridge structured are monitored to some extent. Especially as cable vibration sensors are rarely included in long-term wind and structural health monitoring of the cable-stayed bridges. The data analysis investigates the characteristics of the suspended steel box and the supporting concrete girder, synchronization in response between the different structural components and the interaction between deck vibrations and cable vibrations. The paper explores the performance of system identification techniques for estimation of damping, which is challenging for damping levels as low as 0.05%, such as in the case of the stay cables. It is found that there is a strong interaction between the cables and the deck structure. Detailed identification of the cable properties showed a clear dependency between the total cable damping and the wind velocity, revealing the contribution of aerodynamic damping.

Keywords Cable-stayed bridge · Vibrations · Acceleration · System identification · Damping

J. B. Jakobsen (✉) · J. Þ. Snæbjörnsson · N. Daniotti
Department of Mechanical and Structural Engineering and Materials Science, University of Stavanger, Stavanger, Norway
e-mail: jasna.b.jakobsen@uis.no

J. Þ. Snæbjörnsson
e-mail: jonasthor@ru.is

N. Daniotti
e-mail: nid@sohansen.dk

J. Þ. Snæbjörnsson
Department of Engineering, Reykjavik University, Stavanger, Iceland

N. Daniotti
Svend Ole Hansen Aps, Hansen, Denmark

© The Author(s), under exclusive license to Springer Nature Switzerland AG 2024
V. Gattulli et al. (eds.), *Dynamics and Aerodynamics of Cables*, Lecture Notes in Civil Engineering 399, https://doi.org/10.1007/978-3-031-47152-0_6

1 Introduction

Large vibration amplitudes of the stay cables of the Stavanger City Bridge, in Norway, associated with the combined effects of wind and rain have been reported on different occasions [1]. Previous work [2, 3] has also established that the structural damping of the cable vibrations is very low, with damping ratios of the order of 10^{-4} . It is of interest to explore further the simultaneous bridge girder and stay cables dynamic response, with special attention to methods suitable for identification of low damping levels of stay cables. In the following, the key information about the studied cable-stayed bridge and the monitoring system is presented, followed by the analysis of the selected bridge girder and cable vibration data.

1.1 The Study Case

The central part of the Stavanger City bridge is a cable-stayed bridge with a suspended main span of 185 m supported by a 75 m-high A-shaped tower (see Fig. 1). The main span is a steel box girder of 15.5 m width and 2.4 m depth, whereas the rest of bridge consists of pre-stressed concrete side-spans supported by concrete columns [1].

Three sets of stay-cables at each side connect the pylon with the bridge deck. The length of the stays ranges from 61 to 141 m with constant diameter of 79 mm. The stay cables are of the locked-coil ropes type.

Two of the stay cable-sets on each side are comprised of four individual cables having a center-to-center distance of 320 mm and 480 mm to 580 mm with rigid connections between individual cables at two or three locations along the cable length, as depicted in Fig. 1b. The third and shortest cable stays are in a pair, with rigid connections placed in two locations along the stay span. Passive rubber dampers

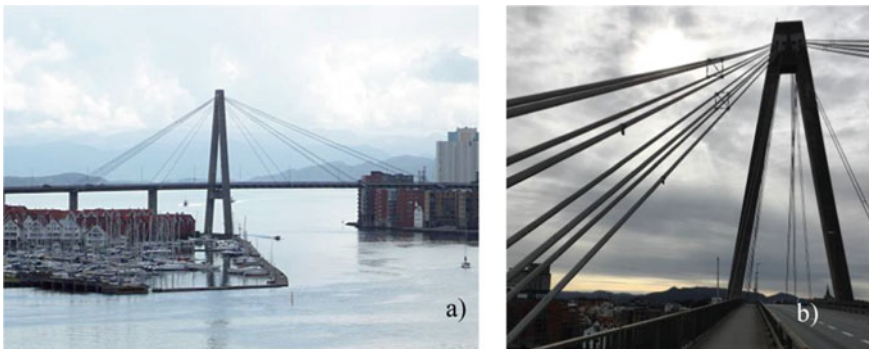


Fig. 1 The Stavanger City Bridge. **a** A side view from west. **b** A view towards south, showing the cable setup, the accelerometers on one side and the anemometer pole

at the ends of the stay cables are installed to reduce vibration effects on the anchor heads.

The following sections provide an overview of the bridge instrumentation, the acceleration data collected, and analysis of a relevant vibration event.

1.2 Instrumentation

The cable monitoring system is comprised of four wireless battery-powered tri-axial accelerometers (G-Link200-8G from Microstrain), which are installed on stay cables referred to as C1 and C2 (on each side of the deck) about 4 m above deck level, see Fig. 2a, b. The sampling frequency of the sensors is 64 Hz. The accelerations components of each sensor are normal to the cable axis along the in-plane (vertical) and out-of-plane (lateral) direction.

Two tri-axial accelerometers (CUSP-3D from Canterbury Seismic Instruments) are located inside the bridge deck on each side of the pylon. One is mounted on the east wall of the concrete deck north of the tower, 20.8 m from the anchor beam of the stay cables C1 and C2 whereas the other one is in the steel box girder 35 m south of the tower. The sampling frequency of the sensors is set to 50 Hz. The deck accelerometers north and south of the tower are denoted DN and DS, respectively, see Fig. 2.

A weather transmitter (WXT530 from Vaisala) is mounted on a 3.5 m-high pole between the anchors of cable C1-C2 and C3 on the east side of the bridge deck (Fig. 2). The instrument measures the horizontal wind components, the absolute temperature, relative humidity, pressure, and rain intensity with a sampling frequency up to 4 Hz.

Data from the accelerometers (DN & DS) inside the bridge deck and the weather station are gathered and synchronized using a single data acquisition unit whereas the wireless accelerometers installed on the cables transmit data to a dedicated logging unit. Synchronization between all signals is then carried out in the pre-processing phase, based on individual time stamps.

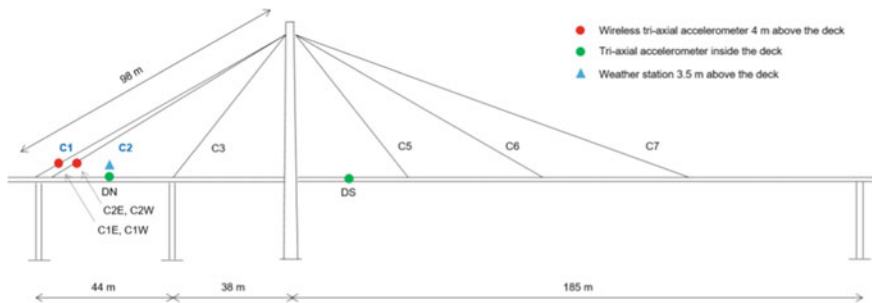


Fig. 2 Instrumentation of the Stavanger City Bridge

2 Data Analysis

The following data analyses are based on vibration data gathered over 24 h on 28.08.2019. The focus is on the dynamic properties of the bridge, including the natural frequencies, and damping of the cables.

Figure 3 shows the mean wind velocity and direction relative to the bridge axis over the 24-h period (UTC) on August 28, 2019. The velocity was in the range of 3 m/s to 9 m/s, and the wind direction varied from Southeast during the first 12 h toward South-southwest in the afternoon. It should be noted that the bridge axis lies about -18° from North, towards Northwest. It rained in the afternoon around 15:30 and again around 16:30, but as the mean wind velocity was below 5 m/s and the wind direction was along the bridge axis at the time, large wind-rain induced vibrations did not occur.

Figure 4 (left) shows the vibration time-series recorded by the tri-axial accelerometer in the steel deck at location (DS). As can be seen the acceleration amplitude generally follows the magnitude of the mean wind velocity. Traffic-induced vibrations of short duration are also noticeable as regular spikes on top of the wind-induced response. It is also clear that the vertical vibration is about three times the transversal vibration and close to 7 times higher than the axial vibrations in the deck. The accelerations in the concrete deck on the other side of the tower (DN), follow the same amplitude pattern, but the magnitude is about half of the acceleration levels at (DS) in the steel deck.

Figure 4 (right) shows the cable accelerations recorded during the 24-h period at cable location C1E. As can be seen the sway and heave accelerations are a magnitude larger than the axial vibrations. It is also clear that the sway and heave acceleration levels follow the wind velocity variations closely.

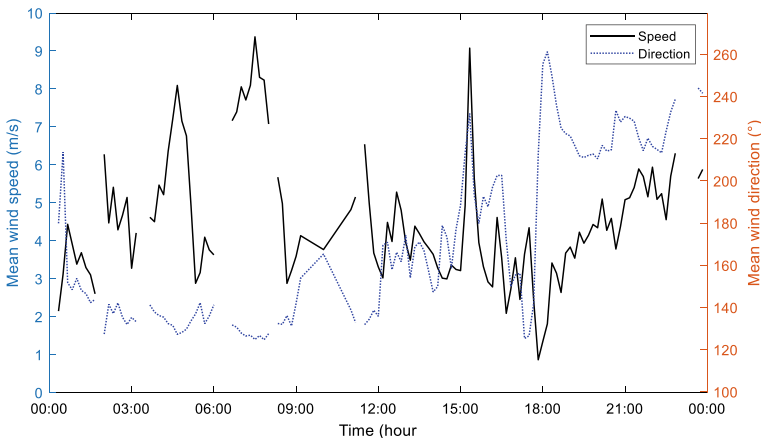


Fig. 3. 10-min mean wind velocity and wind direction relative to the bridge axis on 28.02.2019

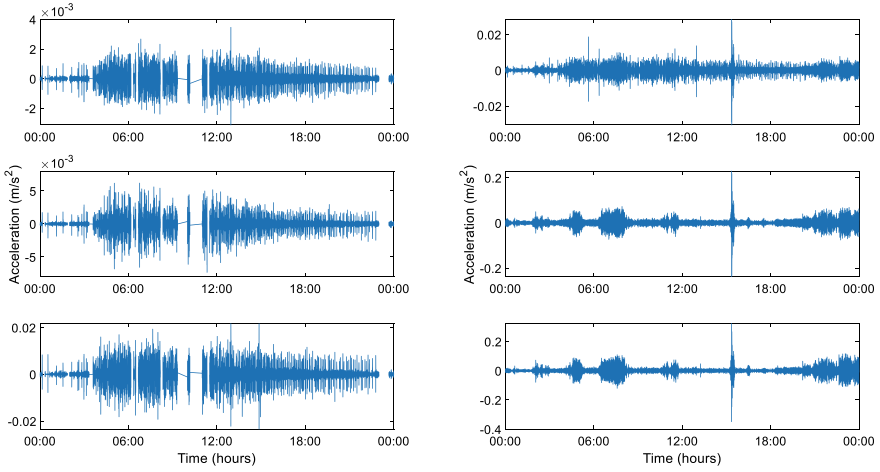


Fig. 4 Accelerations recorded on 28.8.2019 in the steel deck at DS (left) and on cable C1E (right). Axial component (top), sway component (middle) and heave component (bottom)

2.1 Spectral Analysis

The recorded signals were investigated in terms of their spectral properties, as illustrated in Fig. 5. The variance normalized spectra of three acceleration components in the steel and the concrete deck are shown, along with the associated co-coherence between the corresponding vibration components. The axial vibrations in both parts of the deck show a similar spectral pattern and have a relatively high coherence over the whole frequency range. Negative co-coherence is observed for the across-deck (y) accelerations below 5 Hz, whereas the co-coherence is largely positive at the lower frequencies for the along-deck (x) and the vertical (z) accelerations. This is partially linked to the influence from the cable vibrations, especially for the vertical acceleration. It is particularly the y-acceleration that clearly demonstrates some deck-modes that cannot be directly linked to the cable vibrations.

2.2 System Identification Using the SSI-COV Method

The modal properties of the cables and bridge deck were derived from each sensor system, i.e. the three channels, using an automated covariance-driven stochastic subspace identification algorithm (SSI-COV) toolbox from [4], which was inspired by [5].

A summary of the results for the cable vibrations is shown in Fig. 6 along with a typical stabilization diagram in Fig. 8. It was found that most of the spectral peaks gave several frequency values, as can be seen in Fig. 7, which affected the evaluated

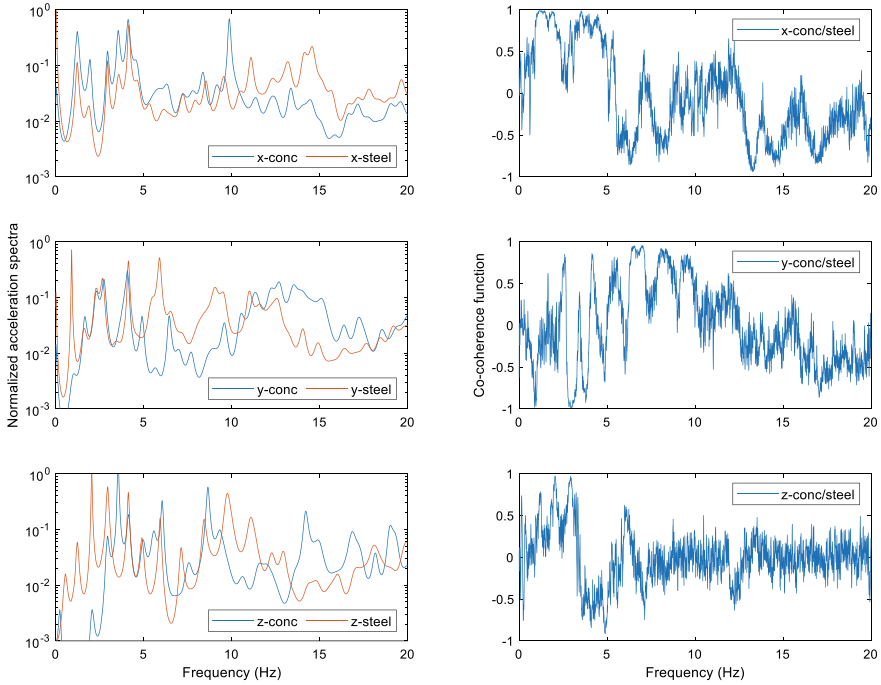


Fig. 5 Variance normalized spectra and coherence of accelerations in the concrete (DN) and steel (DS) parts of the bridge deck, based on 24-h of data from 28.08.2019

damping. The damping varies more when evaluated for all three components of motion than for a single component, see Sect. 2.3. However, it is seen that the damping is generally of the order of 10^{-3} and below 0.005, at least for the first three and last three of the eight cable modes reported. The variability in the damping estimation is found to be greatest for modes 4 and 5, which are likely more influenced by the deck structure than the other modes.

Although not apparent from Fig. 6, it was found that sensor C2W, gives the lowest damping on average and a slightly higher natural frequencies than the other sensors, indicating that the C2W cable may have somewhat higher tension than the other cables. Similarly, C2W showed the highest damping on average.

System identification results from the deck vibrations are shown in Fig. 8, for frequencies up to 21 Hz. As can be seen, the eigen-frequencies fall in many instances close to the cable frequencies, shown by dashed lines. This indicates the close coupling between the deck and the cables, particularly for the lower cable modes.

The analysis shows that the bridge deck is partly excited by the cable vibrations. Therefore, the vibrations recorded in the deck are to some extent forced vibrations, rather than ambient vibrations. An output only system identification method is therefore somewhat inadequate, when analyzing the deck vibrations, as it is difficult to

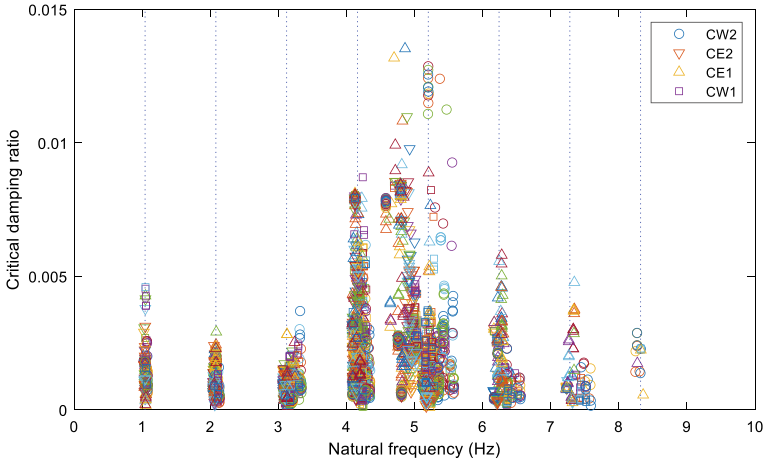


Fig. 6 Damping ratio as a function of natural frequency for the sway and heave motion from all cable sensors for each hour on 28.8.2019, estimated using the SSI-COV method. The vertical lines give a regular multiple of the first eigen frequency (1.04 Hz)

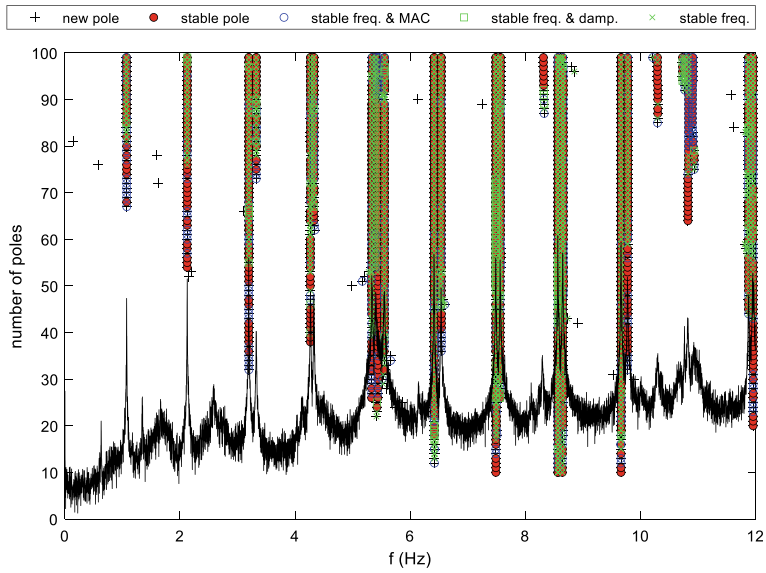


Fig. 7 An example of a stabilization diagram for the SSI-COV estimation process for cable C1E. The PSD estimate of the vertical response is superposed to the identified poles

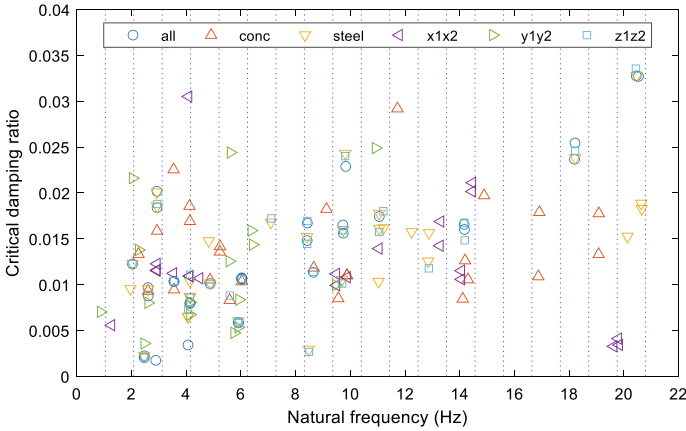


Fig. 8 Damping ratio as a function of natural frequency for different combinations of the components of deck vibrations from both sensors (DN & DS) over the 24-h period on 28.08.2019, estimated using the SSI-COV method

separate the deck modes and the cable modes since the steel deck is supported by the cables, which are then anchored in the concrete side span.

2.3 Cable Dynamics in Relation to Weather Conditions

The following describes a more detailed analysis of cable dynamic characteristics in relation to influencing parameters such as temperature and wind conditions, for the three lowest modes of the C1E cable. Distinct spectral peaks for the three sway and heave modes are utilized to isolate the resonant responses, in a 0.1 Hz wide frequency band centered at a considered peak frequency.

The eigen-frequencies and damping ratios are estimated considering one acceleration component at the time, using the eigen-value analysis (singular value decomposition) of the covariance block Hankel matrix [6, 7]. To ensure a robust analysis of the random signals in a limited frequency band, a convergence study of damping estimates was performed prior to an automatized analysis of all the signals. The range of identified eigen-frequencies and damping ratios are presented in Table 1. For the first mode, the mean heave frequency is 1% higher than the sway frequency, due to the cable sag effect [8]. The difference corresponds to a sag of about 0.25 m for the 98.3 m long cable, or a 2% increase in the effective tension force. For the second and the third mode, the average frequencies in the two directions differ by less than 0.1%.

In Fig. 9, the daily variation of all the six eigen-frequencies is displayed, together with the ambient temperature. A clear effect of temperature on the eigen-frequencies is demonstrated, with a temperature rise and fall giving a reduction and increase,

Table 1 Minimum, Mean and Maximum values of eigenfrequencies (f) and damping ratios (ξ) for the first three cable modes evaluated separately for heave and sway motion

	Mode 1				Mode 2				Mode 3			
	Heave		Sway		Heave		Sway		Heave		Sway	
	f Hz	ξ %	f Hz	ξ %	f Hz	ξ %	f Hz	ξ %	f Hz	ξ %	f Hz	ξ %
Min	1.032	0.027	1.022	0.066	2.041	0.033	2.043	0.038	3.068	0.031	3.071	0.042
Mean	1.038	0.090	1.028	0.139	2.055	0.082	2.056	0.101	3.088	0.078	3.091	0.098
Max	1.043	0.144	1.033	0.245	2.065	0.193	2.065	0.225	3.102	0.162	3.105	0.202

respectively, in the eigen-frequencies. This concurs with findings from another bridge [9].

In Figs. 10 and 11, the associated damping ratios for the three sway and heave modes during the 24 h are illustrated, together with the mean wind components in the two directions. A significant correlation between the magnitude of the relevant wind velocity components and damping can be observed, demonstrating the important contribution of aerodynamic damping to the estimated damping levels, which is largest for the lowest vibration mode. The results complement former field studies on wind-cable interaction [10] and [11]. In the absence of wind, pure structural damping is in the range 0.02% to 0.05%, in line with estimates from free vibration data analysis [3].

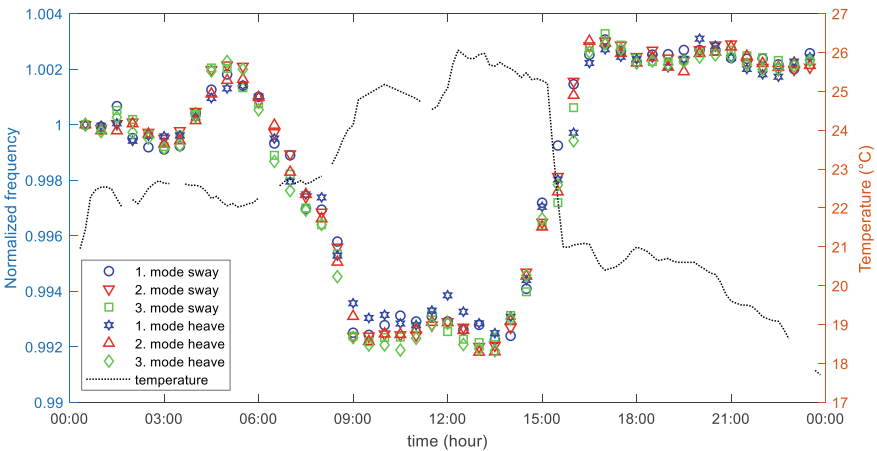


Fig. 9 Natural frequency for modes 1, 2 and 3 normalized by their initial value, as a function of time on 28.08.2019, along with 10 min mean values of atmospheric temperature

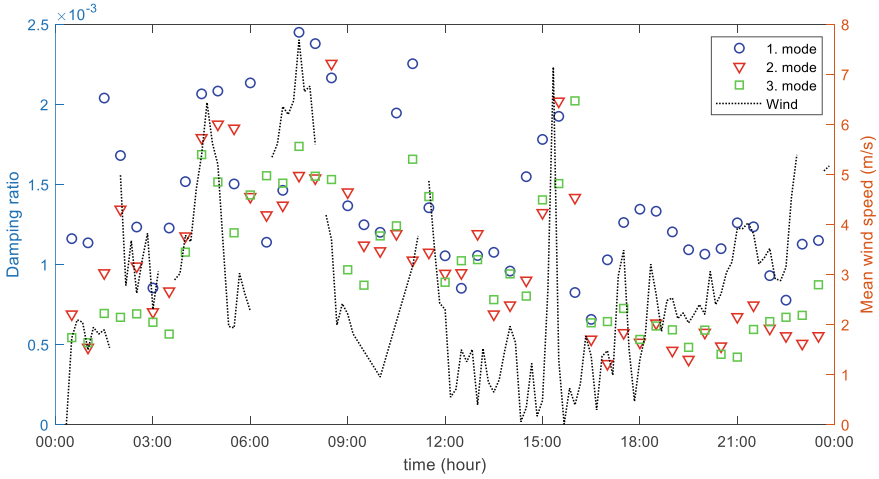


Fig. 10 Damping ratio for modes 1, 2 and 3, for sway motion evaluated based on 24 h acceleration data from 28.08.2019 plotted as a function of time, along with mean values over 10 min of the wind velocity acting horizontally across the cable

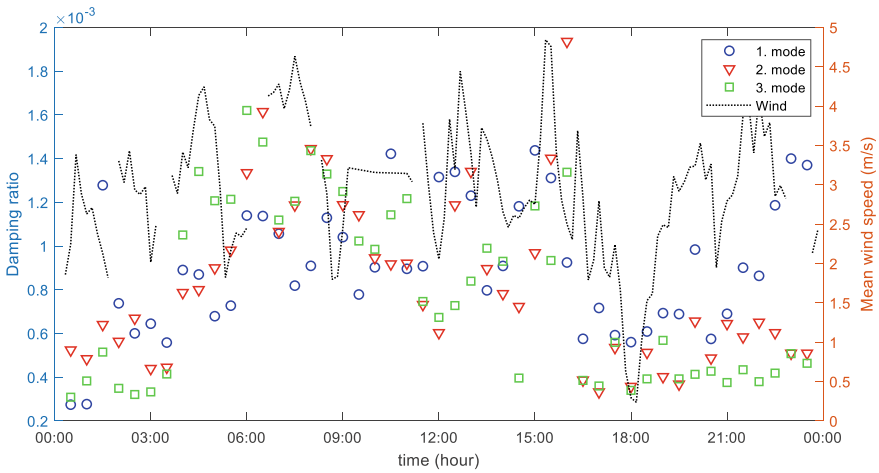


Fig. 11 Damping ratio for modes 1, 2 and 3 for heave motion, evaluated based on 24 h acceleration data from 28.08.2019, plotted as a function of time, along with mean values over 10 min of the wind velocity acting upward across the cable

3 Summary and Conclusions

The paper studies acceleration data from a cable stayed bridge, gathered over 24 h on 28.08.2019. Both deck and cable accelerations are studied. The bridge is a complex structure to analyze, as it combines a concrete deck and tower, that anchors and

supports the cable stayed steel deck providing the crossing over the entrance of Stavanger harbor.

The natural frequencies observed in the deck data are partly the same as the natural frequencies of the cable vibrations, indicating that the deck vibrations are to some extent forced by the cable actions, in addition to being induced by wind action and traffic.

Evaluation of the deck damping gave traditional values in the range of 1% to 2%. Whereas the cable damping was found to be more than an order of magnitude lower, except for modes with a frequency between 4 and 6 Hz, where there is likely a coupling between deck modes and cable modes.

The frequency and damping of the three lowest cable modes were studied in more detail for a single cable. It was found that the natural frequency of the cable was influenced by the ambient temperature changes over the 24 h, with higher ambient temperature resulting in lower natural frequencies. It was also found that the overall damping ratios of cable were strongly correlated with the variations in wind velocity during the 24-h, indicating the significance of aerodynamic damping.

Acknowledgements The support of the Norwegian Public Roads Administration and Rogaland County Municipality to the monitoring project is gratefully acknowledged, as well as contributions of the former master students, Sander Felberg and Vitor Pinto, to data analysis and numerical modelling.

References

1. Daniotti N, Jakobsen JB, Snæbjörnsson J, Cheynet E, Wang J (2021) Observations of bridge stay cable vibrations in dry and wet conditions: A case study. *J Sound Vib* 503:116106
2. Daniotti, N., Jakobsen, J.B., Snæbjörnsson, J., Cheynet, E. & Wang, J.: Full-scale observations of bridge stay cable vibrations in a wet state, In: Jakobsen (ed.), *Proc. of 2nd Int. Sym. on Dynamics and Aerodynamics of Cables*, pp. 107–114, University of Stavanger (2021).
3. Pinto VD (2022) Stay cables of Stavanger City bridge: damping estimation and mitigation of vibrations, Master thesis, University of Stavanger
4. Cheynet E (2020) Operational Modal Analysis with Automated SSI-COV Algorithm. Zenodo. <https://doi.org/10.5281/ZENODO.3774061>
5. Magalhães F, Cunha A, Caetano E (2009) Online automatic identification of the modal parameters of a long span arch bridge. *Mech Syst Sig Process* 23(2):316–329
6. Hoen Ch, Moan T, Remseth S (1993) System identification of structures exposed to environmental loads. In: Moan et al (eds), *Structural Dynamics – EURO DYN '93*, pp 835–844 Balkema
7. Bogunović Jakobsen J, Hjorth-Hansen E (1995) Determination of the aerodynamic derivatives by a system identification method. *J Wind Eng Ind Aerodyn* 57(2–3):295–305
8. Virlogeux M (1998) Cable-vibrations in cable-stayed bridges, In: Larsen A. & Eisdahl (eds.), *Proc. of Int. Symp. on Advances in Bridge Aerodynamics*, pp. 213–233, Balkema
9. Cheynet E, Snæbjörnsson J, Jakobsen JB (2017) Temperature Effects on the Modal Properties of a Suspension Bridge. *Dyanmic of Civil Structures*, Vol 2, pp 87–93. Springer

10. Macdonald JHG (2002) Separation of the contributions of aerodynamic and structural damping in vibrations of inclined cables. *J Wind Eng Ind Aerodyn* 90:19–39
11. Acampora A, Macdonald JHG, Georgakis CT, Nikitas N (2014) Identification of aeroelastic forces and static drag coefficients of a twin stay bridge cable from full-scale ambient vibration measurements. *J Wind Eng Ind Aerodyn* 124:90–98

Aerodynamics and Nonlinear Dynamics

Wake Galloping Suppression in Two Closely Spaced Cylinders with Surface Modification



Thu Dao , Tomomi Yagi , Kyohei Noguchi , and Gabriel Mohallem

Abstract Wake galloping is often observed in two closely-spaced circular cylinders. Previous studies have reported large amplitude transverse oscillation (galloping) in the downstream cylinder, where streamwise and transverse center-to-center distances between two cylinders were $3.0D$ – $3.5D$ and $0.3D$ – $0.5D$, respectively (D is the diameter of the cylinders). In this study, the mechanism and countermeasure of wake galloping of two cylinders in these arrangements are discussed. Due to the dynamics between the wake of the upstream cylinder and the oscillation of the downstream cylinder, the unsteady wake was hysteretic and initiated wake galloping in the downstream cylinder. Wake galloping, when occurred, depends on reduced velocity and not Reynolds number because both cylinders were in the subcritical Reynolds number regime at the wake galloping onset. A cylinder attached with twelve spiral protuberances at a 27° winding angle was introduced to suppress wake galloping. The modified cylinder with the spiral protuberances performed most effectively against wake galloping when it was placed on the downstream side. The aerodynamic forces on the cylinder with spiral protuberances did not generate negative damping. Therefore, the surface-modified cylinders successfully suppressed wake galloping.

Keywords Wake-induced vibration · Wake galloping · Parallel cylinders · Surface modification · Spiral protuberances

T. Dao (✉) · T. Yagi · K. Noguchi
Kyoto University, Kyotodaigaku-Katsura, Nishikyo-Ku, Kyoto 615-8540, Japan
e-mail: dao.thu.r42@kyoto-u.jp

G. Mohallem
Delft University of Technology, Mekelweg 5, 2628 CD Delft, Netherlands

1 Introduction

Parallel-twin-cylinder structures are susceptible to wake-induced vibrations. Studies on this topic have been conducted covering an extensive range of spacing scenarios between the two cylinders [1–4]. Wake galloping (WG) was observed in the downstream cylinder spaced at $3.0D$ – $3.5D$ longitudinally and $0.3D$ – $0.5D$ transversely from the upstream cylinder [1]. In another wind tunnel free vibration test, where the streamwise spacing between the two tandem cylinders ranged from $7.0D$ to $7.4D$, the downstream cylinder also underwent WG [5]. Surface helical wires/spiral protuberances on the cylinders have been introduced to suppress WG. Successful applications of such surface modifications were reported in [5–7]. However, elaborative discussion on the suppression mechanisms, especially those related to flow phenomena, are often overlooked.

This study focuses on WG in parallel cylinders, spaced at $3.0D$ in the streamwise direction, and $0.3D$ – $0.5D$ in the transverse direction. Twelve surface spiral protuberances were attached to the cylinders to suppress WG, following the original design proposed in [8] and subsequently utilized in [5]. The mechanism of WG in two plain cylinders is firstly discussed considering relevant flow phenomena. The performance of the cylinders with 12 spiral protuberances against WG is then evaluated. Finally, the suppression mechanism of the spiral protuberances is presented.

2 Wind Tunnel Tests

Aerodynamic pressure measurement tests were conducted in the room-circuit Eiffel-type wind tunnel at Kyoto University whose capacity was 30 m/s. The test section measures 1.0 m wide and 1.8 m high.

The cylinder models were two aluminum pipes of the same diameter $D = 0.7$ m and length $L = 0.9$ m. For the surface-modified cylinders, 12 rubber protuberances of dimensions 3.36 mm wide and 2.10 mm thick were glued to the surface of the cylinders in a spiral shape whose winding angle was $\gamma = 27^\circ$, calculated as in Eq. (1):

$$\gamma = \tan^{-1}(2D/P) = 27^\circ \quad (1)$$

where P [m] is the length of one spiral turn in the spanwise direction. The 12 spiral protuberances define the pitch $d = 22.9$ mm, the spanwise distance between two adjacent protuberances (Fig. 1).

On the downstream cylinder set a pressure ring consisting of 12 pressure taps distributed evenly along its circumference such that the protuberances were situated right in-between the protuberances. The angular position of the pressure taps was defined by θ [deg] from the stagnation point. The pressure ring was set at 0.4 and 0.5 m from the two ends of the cylinder. The position of pressure ring defined the origin

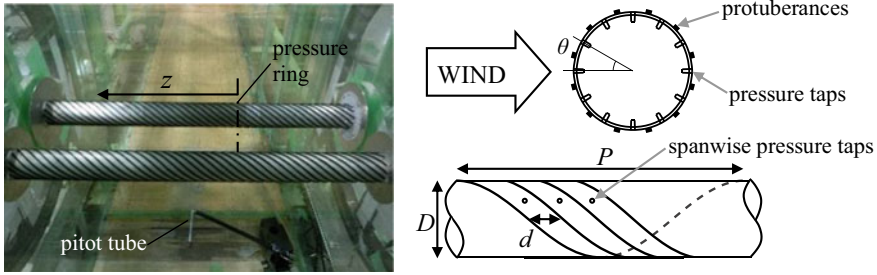


Fig. 1 Cylinders with 12 surface spiral protuberances

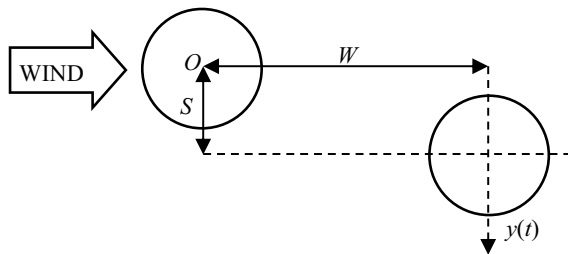
of the spanwise axis z , where a number of pressure taps lined up in z -direction. The spanwise pressure taps were spaced at d to accommodate the protuberances (Fig. 1).

The arrangement of the two cylinders in the tests is described in Fig. 2, where W [m] and S [m] denote the center-to-center distances between the two cylinders in the streamwise and transverse directions respectively. In the tests, both cylinders were normal to the incoming flow. The upstream cylinder was fixed to the walls of the wind tunnel so that no displacement was allowed. The downstream cylinder was assigned with transverse harmonic oscillations via an oscillating frame connected to a motor. The frequency of the prescribed oscillations was 0.673 Hz. The dimensionless transverse double amplitude was set at $2A = 0.4D$. In Fig. 2, $y(t)$ [m] is the instantaneous displacement of the downstream cylinder during the oscillation with reference to the upstream cylinder. For a downstream cylinder at $S/D = 0.5$, its displacement $y(t)$ during one oscillation cycle would range from $0.3D$ to $0.7D$. The displacement of the downstream cylinder was measured by two laser sensors at two ends. The downstream oscillated in the smooth flow with freestream velocity $U = 5.0\text{--}12.0$ m/s, resulting in a reduced velocity ranging from $U/fd = 106$ to 255 .

During the harmonic oscillations, unsteady surface pressure at each pressure tap was measured using a 1.2 m vinyl tube connected to a multipoint-pressure sensor. The measured unsteady pressure was made dimensionless by Eq. (2):

$$C_P(\theta, t) = \frac{P(\theta, t)}{0.5\rho U^2} \tag{2}$$

Fig. 2 Arrangement of two cylinders



where $P(\theta)$ [Pa] is the unsteady measured surface pressure at θ with reference to the static pressure in the test section which was obtained by placing the pitot tube below the downstream cylinder (Fig. 1), ρ [kg/m³] is the air density.

Conventionally, harmonic oscillations are prescribed to the solid body in the wind to extract flutter derivatives. In this study, H_1^* is the concerned flutter derivative, which is a transverse aerodynamic damping parameter and calculated as in Eq. (3):

$$H_1^* = \frac{-F_{L0} \sin \Psi}{\rho(0.5D)^2 \omega^2 A} \quad (3)$$

where F_{L0} [N] is the amplitude of the unsteady lift force, Ψ [deg] is the phase difference between the unsteady lift and displacement $y(t)$, ω [rad/s] is the angular frequency of the prescribed oscillation. In this study however, H_1^* can be evaluated in an integral manner, where it is calculated on small segments on the body of the cylinder. Therefore, segmental lift amplitude $L_{\theta 0}$ and segmental phase difference Ψ_{θ} are introduced, where $L_{\theta 0}$ is the amplitude of dimensionless unsteady lift acting on a unit surface area and calculated as in Eq. (4):

$$L_{\theta 0} = C_{p0} |\sin \theta| \quad (4)$$

where C_{p0} is the amplitude of dimensionless unsteady pressure at θ ; and Ψ_{θ} [deg] is the phase difference between the segmental unsteady lift at θ and the displacement $y(t)$.

3 Results and Discussion

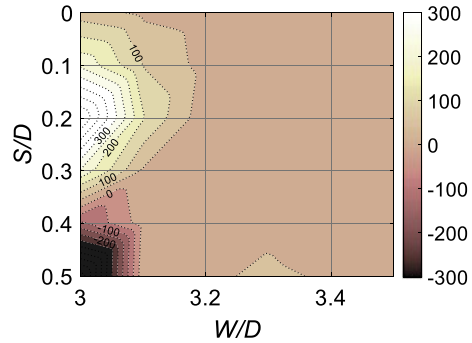
3.1 Wake Galloping in Two Plain Cylinders

Wake galloping in two cylinders at ($W/D = 3.0$, $S/D = 0.3$) reportedly occurred at $U/fD = 100$ [1]. Therefore, the following sections focus on the reduced velocity range of $U/fD \geq 100$.

The effect of spacing between the two cylinders on WG was discussed in [1] based on the values of the flutter derivative H_1^* . Figure 3 presents the contour map of H_1^* of the downstream cylinder spaced at ($3.0D$ – $3.5D$) in the streamwise direction, and ($0.0D$ – $0.5D$) in the transverse direction from the upstream cylinder at $U/fD = 136$. In Fig. 3, within $W/D = 3.0$ – 3.2 , the transverse distance of $S/D = 0.3$ – 0.4 marks a switch in value of H_1^* , where the downstream cylinder at $S/D < 0.3$ would gallop ($H_1^* > 0$), while it would be stable at $S/D > 0.4$ ($H_1^* < 0$).

Wake galloping in the downstream cylinder at ($W/D = 3.0$ – 3.2 , $S/D = 0.0$ – 0.4) is related to the evolution of the flow patterns around it upon small perturbation [7]. Figure 4 shows the instantaneous surface pressure distributions on the downstream cylinder at ($W/D = 3.0$, $S/D = 0.3$) when it oscillated transversely with a

Fig. 3 Flutter derivative H_1^* at $U/fD = 136$ in various spacing scenarios [1]



double amplitude of $0.4D$. The flow patterns are sketched based on stagnation pressure ($C_{P_{\max}}$) and circumferential pressure gradient ($\partial C_P/\partial\theta$). In Fig. 4a, b, when the downstream cylinder is spaced at $y = 0.5D$ and $0.3D$, respectively, from the upstream cylinder, large negative pressure with a significant negative pressure gradient is observed immediately following the stagnation region of $C_{P_{\max}}$, which suggests flow acceleration on the inner surface. This was probably achieved by squeezing the wake of the upstream cylinder into the space between two cylinders. Hence, such accelerated flow is called ‘gap flow’. For a thorough description of the flow fields, refer to [9]. When reaching $y = 0.1D$, the inner surface of the downstream cylinder exhibited a flat pressure gradient which indicates no flow, in other words, the upper half of the downstream cylinder was submerged in the wake of the upstream (Fig. 4c). Such flow evolution was hysteretic. The evolution of the flow on the approaching cylinder deviated from that on the departing cylinder. This is illustrated by Fig. 4b and d, where the downstream cylinder is at $y = 0.21D$ transversely from the upstream one but the two instantaneous pressure distributions noticeably differ. Firstly, the stagnation pressure in Fig. 4b is $C_{P_{\max}} \approx 0.9$, which means the velocity of the incoming flow was almost the same as the freestream. Conversely, the stagnation pressure in Fig. 4d is $C_{P_{\max}} \approx 0.4$, suggesting the incoming flow was slowed down by the wake of the upstream cylinder. Consequently, considering the pressure gradient, the gap flow on the inner surface in Fig. 4d was underdeveloped when compared to Fig. 4b. Secondly, the flow on the outer surface at $t = 0.7T$ sustained higher negative pressure than that at $t = 0.3T$. Such hysteresis resulted in positive work done by the flow where the downstream cylinder would extract energy from the flow and start galloping. Additionally, the hysteresis is absorbed into the phase difference Ψ in H_1^* calculation, such that WG onset was successfully determined by H_1^* . This mechanism is thoroughly discussed in [7].

The following section discusses the arrangement of ($W/D = 3.0$, $S/D = 0.5$), where $H_1^* < 0$, to highlight the spacing sensitivity of WG. Instantaneous pressure distributions on the downstream cylinder at four instants— $t = 0.0$, 0.25 , 0.5 , and $0.75T$ —during a transverse oscillation around ($W/D = 3.0$, $S/D = 0.5$) with a double amplitude of $0.4D$ are presented in Fig. 5 (other than equilibrium position, other parameters are the same as those in Fig. 4). Strong gap flow on the inner

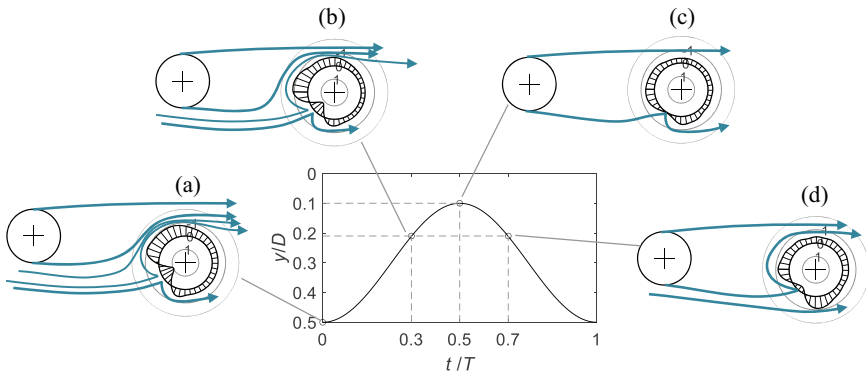


Fig. 4 Dimensionless instantaneous surface pressure and schematic flow patterns at four instants within one cycle at $U/lD = 183$, $W/D = 3.0$, $S/D = 0.3$

surface was observed at $t = 0.5 T$ when the downstream cylinder was at $y = 0.3D$, similar to the gap flow mechanism described in Fig. 4b. However, there are two major differences from the case in Fig. 4. Firstly, the stagnation region resided outside the wake of the upstream cylinder at all times, which is inferred from the stagnation pressure of $C_{Pmax} \approx 1.0$. Secondly, considering how the pressure distribution at $t = 0.25 T$ resembles that at $t = 0.75 T$, the flow evolution showed almost no hysteresis, leading to $H_1^* \leq 0$ as seen in Fig. 3.

To summarize, WG in parallel plain cylinders is sensitive to the traverse spacing between the two cylinders. In more detail, WG would occur in the downstream cylinder if its trajectory involved immersion into the wake of the upstream cylinder and vice versa.

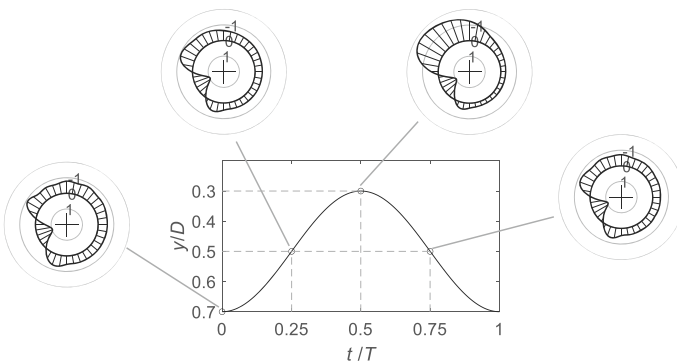


Fig. 5 Dimensionless instantaneous surface pressure at four instants within one cycle at $U/lD = 183$, $W/D = 3.0$, $S/D = 0.5$

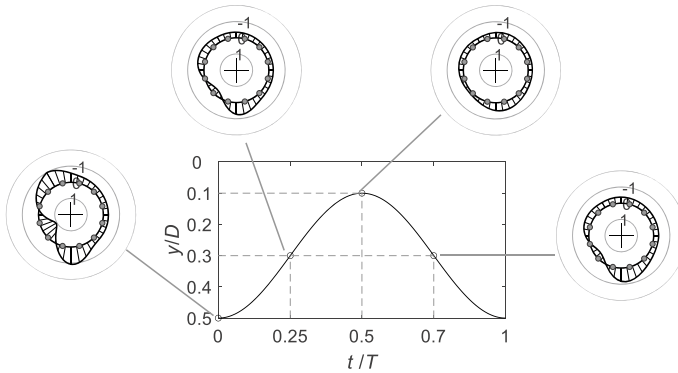


Fig. 6 Dimensionless instantaneous surface pressure on the downstream cylinder with spiral protuberances at four instants within one cycle at $U/fD = 183$, $W/D = 3.0$, $S/D = 0.3$

3.2 Wake Galloping Suppression by Cylinders with Spiral Protuberances

The performance of the surface-modified cylinders with spiral protuberances was reported in [7], where the surface-modified cylinder was most effective against WG when placed on the downstream side. Considering industrial applications, it is practical to focus on the case of two cylinders with spiral protuberances instead of a combination of two types of cylinders. Therefore, the following section elaborates on the case of two cylinders with spiral protuberances at $U/fD = 183$.

Unlike WG in two plain cylinders, the spacing sensitivity of WG was not found in the case of two modified cylinders with spiral protuberances. To illustrate this, two spacing scenarios—($W/D = 3.0$, $S/D = 0.3$) and ($W/D = 3.0$, $S/D = 0.5$)—are discussed. Figures 6 and 7 show the instantaneous surface pressure on the modified downstream cylinder whose equilibrium position was at ($W/D = 3.0$, $S/D = 0.3$) and ($W/D = 3.0$, $S/D = 0.5$) respectively.

In the case of ($W/D = 3.0$, $S/D = 0.3$), the downstream modified cylinder already immersed into the wake of the upstream at $y = 0.3D$, which was in sharp contrast to the plain cylinder at $y = 0.21D$ in Fig. 4b. The wake of the former was significantly less resistant to entrainment than that of the latter. This also holds in the case of ($W/D = 3.0$, $S/D = 0.5$) in Fig. 7. While the downstream plain cylinder at $S/D = 0.5$ remained outside the wake during the oscillation (Fig. 5), the inner surface of the modified cylinder in Fig. 7 advanced into the wake at the uppermost position $y = 0.3D$. In that perspective, the flow on the modified downstream cylinder experienced equally drastic evolution—inside and outside the wake of the upstream cylinder—as in the case of two plain cylinders in Sect. 3.1. However, hysteresis was not recorded in the downstream cylinder with spiral protuberances as the pressure distributions at $t = 0.25$ and $0.75 T$ were almost the same in both Figs. 6 and 7.

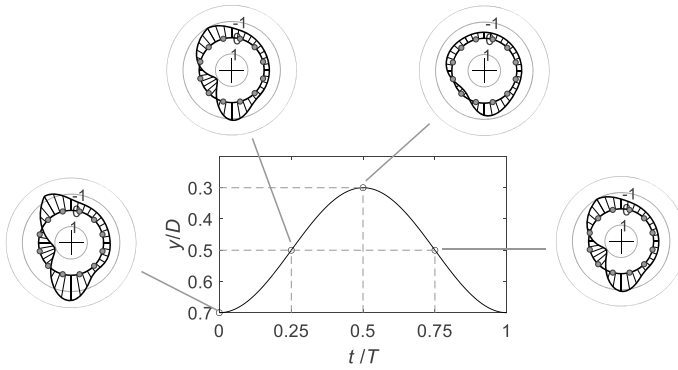


Fig. 7 Dimensionless instantaneous surface pressure on the downstream cylinder with spiral protuberances at four instants within one cycle at $U/fD = 183$, $W/D = 3.0$, $S/D = 0.5$

Upon the application of spiral protuberances, the theme of three-dimensional flow around a single cylinder with surface modification was explored in [8]. Three-dimensionality in the context of two parallel modified cylinders is also of interest. Figure 8 presents the segmental lift amplitudes $L_{\theta 0}$ and phase differences Ψ_{θ} along the span of the downstream cylinder at ($W/D = 3.0$, $S/D = 0.3$). Three angles— $\theta = 60^\circ$, 270° , and 300° —were chosen to represent the inner, outer, and stagnation regions respectively. While the segmental lift amplitudes at the same angle θ significantly vary spanwise for all three regions, the segmental phase differences are consistent along the span at either $\Psi_{\theta} = 0^\circ$, 180° , or -180° , and hence, $\sin \Psi \approx 0$, which results in $H_1^* \approx 0$. The only exception at ($\theta = 300^\circ$, $z = 3d$), where $\Psi_{\theta} = 53^\circ$, is because the segmental lift amplitude here was so small that it was difficult to detect the phase difference. This observation also holds for the case of ($W/D = 3.0$, $S/D = 0.5$).

Fig. 8 Segmental lift amplitude $L_{\theta 0}$ and phase difference Ψ_{θ} along the span at $U/fD = 183$, $W/D = 3.0$, $S/D = 0.3$, unfilled markers denote two cylinders with spiral protuberances, filled markers denote two plain cylinders

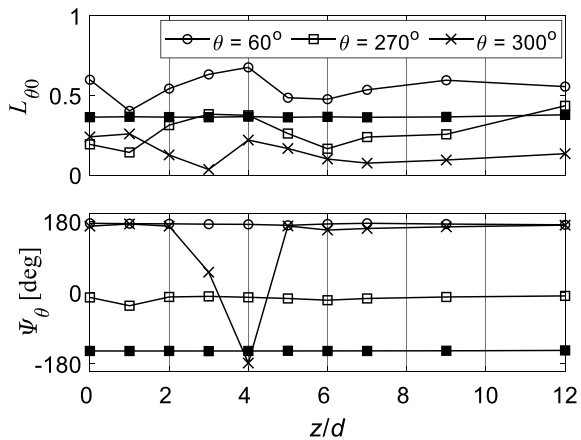
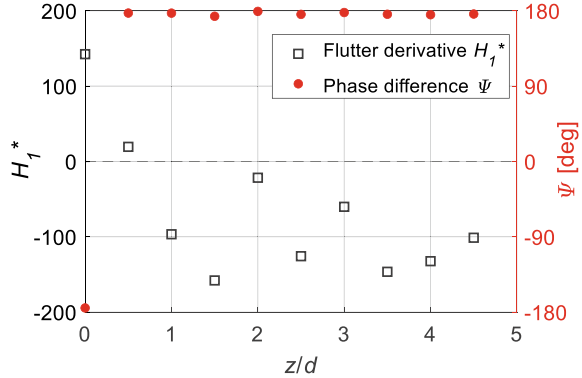


Fig. 9 Flutter derivative H_1^* and phase difference ψ along the span at $U/fD = 183$, $W/D = 3.0$, $S/D = 0.3$



In summary, the downstream modified cylinder with spiral protuberances can suppress WG by eliminating the hysteresis of the flow evolution when the spacing between two cylinders varied during oscillation. The flow properties seemingly varied spanwise due to the surface protuberances. However, the suppression mechanism can be explained in two-dimension, that is, flutter derivative H_1^* calculated at any cross-section along the span would be negative as shown in Fig. 9. Even though positive H_1^* was observed at some locations, their values are trivial for a reduced velocity of 183 (note that H_1^* is not normalized by wind speed, which means it should increase as the wind speed in-creases). In comparison, H_1^* in two smooth cylinders with the same spacings an reduced velocity is of order of 1000 [1].

4 Conclusions

This study explored the wake galloping phenomenon in the downstream cylinder which was spaced at $3.0D$ longitudinally, and $0.3D-0.5D$ transversely from the upstream cylinder. The concluding remarks are as follows:

- Wake galloping in the case of two plain cylinders was because of the hysteretic flow evolution when the downstream cylinder advanced into the wake of the upstream cylinder and then departed from it.
- Wake galloping did not occur in the case of two cylinders with 12 spiral protuberances. The surface protuberances eliminated the aforementioned hysteretic wake. Therefore, the modified cylinders were stable against wake galloping.
- Unsteady surface pressure on the downstream cylinder with 12 spiral protuberances varied spanwise in amplitudes because of the three-dimensional protuberances. However, wake galloping was suppressed at any two-dimensional cross-section along the span.

References

1. Fukushima H, Yagi T, Shimoda T, Noguchi K (2021) Wake-induced instabilities of parallel circular cylinders with tandem and staggered arrangements. *J Wind Eng Ind Aerodyn* (215):104697
2. Xu W, Wu H, Song Z, He Z, Wang E, Ge W et al (2022) Flow-induced vibrations of two staggered cylinders with a moderate spacing and varying incident angles at subcritical Reynolds numbers. *Ocean Eng* (258):111723
3. Li T, Ishihara T, Yang Q, Chen Q (2023) Numerical study on flow-induced vibration of two-degree-of-freedom staggered circular cylinders at subcritical Reynolds numbers. *Ocean Eng* (273):113908
4. Dubois R, Andrienne T (2023) Identification of distinct flow behaviours around twin rough cylinders at low wind incidence. *J Fluids Struct* (117):103815
5. Sakaki I, Yagi T, Ogawa S, Yuan Y, Shirato H (2017) Wake-induced vibration of parallel cables with spiral protuberances. In: International symposium on the dynamic and aerodynamic of cables on proceedings. Portugal, Porto, pp 83–90
6. Li T, Ishihara T (2021) Numerical study on wake galloping of tandem circular cylinders considering the effects of mass and spacing ratios. *J Wind Eng Ind Aerodyn* (210):104536
7. Dao T, Yagi T, Noguchi K, Fukushima H, Mohallem G, Do T (2022) Generation mechanism of wake galloping in two staggered circular cylinders in view of hysteretic flow phenomena. *J Wind Eng Ind Aerodyn* (229):105127
8. Yagi T, Okamoto K, Sakaki I, Koroyasu H, Liang Z, Narita S et al (2011) Modification of surface configurations of stay cables for drag force reduction and aerodynamic stabilization. In: 13th international conference on wind engineering on proceedings, Amsterdam, The Netherlands
9. Wu G, Du X, Wang Y (2020) LES of flow around two staggered circular cylinders at a high subcritical Reynolds number of 1.4×10^5 . *J Wind Eng Ind Aerodyn* (196):104044

Comparison of Observed and Simulated Galloping Responses of a Four-Bundled Conductor Under Wet Snow Accretion



Hisato Matsumiya , Saki Taruishi , Hiroki Matsushima, and Teruo Aso

Abstract Field observations of four-bundled conductors have been carried out at the Kushiro test line since 2014 to investigate the galloping characteristics caused by wet snow accretion on overhead transmission lines. On January 12, 2022, a large galloping was observed at this site. It was seen that the conductors mainly vibrated in the vertical two-loops/span mode coupled with the horizontal and torsional modes. The maximum total amplitude reached approximately 5.8 m in the vertical direction. Numerical simulation is an effective method for estimating the galloping response amplitude of full-scale overhead transmission lines; however, the simulated response amplitude is highly dependent on the input conditions, such as snow accretion shape and wind speed. Therefore, this study conducted a parametric analysis to evaluate the sensitivity of the response amplitudes to the input conditions by varying the snow accretion shape and its development angle in addition to wind speed. The results of the analysis under the snow accretion conditions closest to those observed on January 12, 2022, were found to approximately reproduce the observed response amplitudes.

Keywords Galloping · Wet snow accretion · Overhead transmission lines

1 Introduction

Galloping is occasionally observed in overhead transmission lines owing to ice accretion. Because the ice accretion shape can vary depending on the type, galloping characteristics and the effects of countermeasures might vary accordingly. Atmospheric icing is typically classified into two categories: in-cloud icing and precipitation icing, depending on its developmental process [1, 2]. In-cloud icing occurs in clouds containing supercooled droplets that remain in the liquid phase at temperatures

H. Matsumiya (✉) · S. Taruishi · H. Matsushima · T. Aso
Central Research Institute of Electric Power Industry, Abiko 1646, Abiko-shi, Chiba 270-1194,
Japan
e-mail: hisato-m@criepi.denken.or.jp

H. Matsumiya
Kyoto University, Kyotodaigaku-Katsura, Nishikyo-ku, Kyoto 615-8540, Japan

© The Author(s), under exclusive license to Springer Nature Switzerland AG 2024
V. Gattulli et al. (eds.), *Dynamics and Aerodynamics of Cables*, Lecture Notes in Civil
Engineering 399, https://doi.org/10.1007/978-3-031-47152-0_8

below 0 °C; therefore, in-cloud icing is likely to occur in high-altitude transmission lines. Depending on the cloud liquid water content, the size of distribution of the cloud droplets, air temperature, and wind speed, the ice accretion characteristics can be classified into soft rime and hard rime. In contrast, precipitation icing is caused by freezing rain and wet and dry snow, which can even occur in plain areas. Freezing rain falls under a specific temperature distribution with elevation, such as when a temperature inversion occurs in the lowest layer. Regarding freezing rain, glaze ice forms when the droplet freezing time is sufficiently long for a film of water to cover the accreting surface. Graze ice is compact, smooth, and usually transparent. Conversely, wet snowflakes, which precipitate at a temperature of approximately 0 °C, contain some liquid water and easily accrete to the conductor [3]. In addition, wet snow accretion is characterised by its occurrence even under strong winds, whereas dry-snow accretion occurs only under weak-to-calm winds. As mentioned above, the development direction and shape of icing vary significantly depending on the type of impacting droplets or particles and the wind speed. Galloping can occur under every condition except dry-snow accretion, when strong winds blow after icing but before the ice shedding. In Japan, galloping is often caused by in-cloud icing and wet snow accretion in the mountain and plain regions, respectively. Therefore, the authors have conducted field observations of full-scale transmission lines to investigate the accretion characteristics and dynamic response of the lines to galloping under in-cloud icing [4] and wet snow accretion [5, 6].

Furthermore, numerical simulation is an effective method for estimating the galloping response amplitude of full-scale overhead transmission lines. In general, the overhead transmission line is modelled using the finite element method, and the amplitude is estimated through time history response analysis [7, 8]. Aerodynamic force modelling has been investigated by wind tunnel tests [9] while structural modelling has been investigated by observations on full-scale test lines with an ideal and artificial snow accretion [10]. Therefore, the numerical simulation method has been validated to some extent. However, the simulated response amplitude depends highly on the input conditions such as icing shape and wind speed, as well as their distribution in the span. A parametric analysis has been performed when identifying the cause of a galloping accident where the icing shape is unknown and examining countermeasures based on the analysis by gradually varying the icing shape and its development angle as well as the wind speed. Moreover, to obtain a response amplitude, a parametric analysis with many different conditions can be performed; however, setting conditions that are not appropriate to the actual situation can result in excessive response amplitudes. Therefore, it is important to consider how to set input conditions based on the actual ice accretion and wind speed distribution to achieve an accurate amplitude estimation.

This study presents the observation result of noticeable galloping of four-bundled conductors at the Kushiro test line, where field observations for wet snow accretion have been carried out since 2014. Then, the sensitivity of the response amplitudes to the input conditions is indicated via a parametric analysis, wherein the icing shape and its development angle are varied gradually in addition to the wind speed.

Furthermore, the results of the analysis under the icing conditions closest to those of observation are compared to the observed response amplitudes.

2 Overview of the Kushiro Test Line

The Kushiro test line was constructed in 2013 in Kushiro City, Hokkaido, Japan, to enable field observations of galloping in overhead lines and wet snow accretion on conductors and insulators [6, 11]. During severe snowfall events at this site, by approaching a low pressure, precipitation at approximately 0 °C continues under moderate to strong winds. Figure 1 shows the Kushiro test line, which comprises three towers that are currently connected by two phases of four-bundled conductors (between the upper arms of Towers 1 and 2) and 11 phases of single conductors (between the middle arms of Towers 1 and 2 and the lower arms of Towers 1 and 3). The test line extends at 115° in the azimuthal direction.

The test line includes various meteorological instruments to measure wind speed and direction, air temperature, relative humidity, atmospheric pressure, precipitation, radiation balance, and snowfall drop size distribution and its falling velocity. Furthermore, tension metres for the conductors and web cameras are installed on the towers,

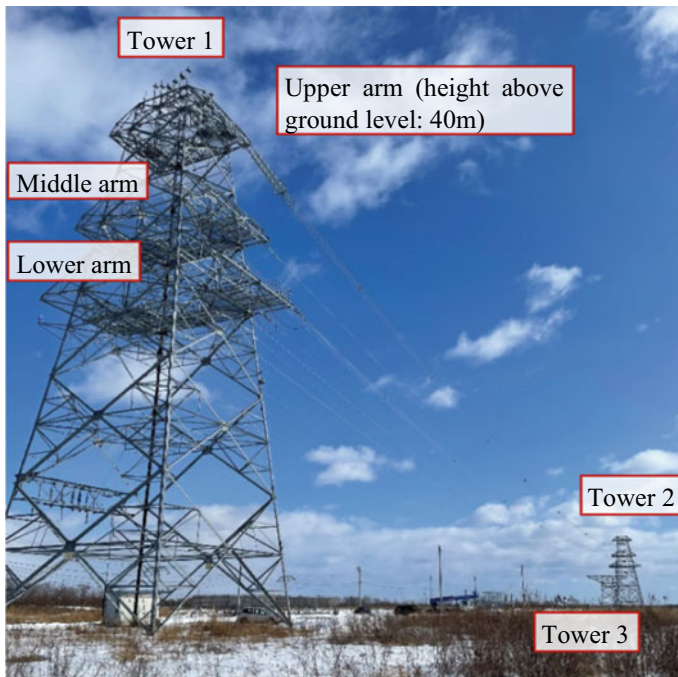


Fig. 1 Kushiro test line

Table 1 Structural condition

Conductor	ACSR410 mm ²
Diameter	28.5 mm
Distance of sub-conductors	400 mm
Span length	393.9 m
Sag*	15.2 m
Tension of sub-conductors*	22.5 kN

* At the temperature of 13.1 °C

and LED markers are installed in the span. The vertical, horizontal, and torsional displacements of the line can be obtained by analysing the images captured using the web cameras. Moreover, the cameras are set at the spacers in the span to capture the images and identify the snow-accreted conditions for bundled conductors.

This study subjects to the four-bundled conductor line without any anti-galloping device. The structural conditions of the line are shown in Table 1. Figures 2 and 3 show the type of spacers installed and the spacer spacing, respectively. These conditions are identical to those of a typical 500 kV transmission line in Japan.



Fig. 2 Normal spacer

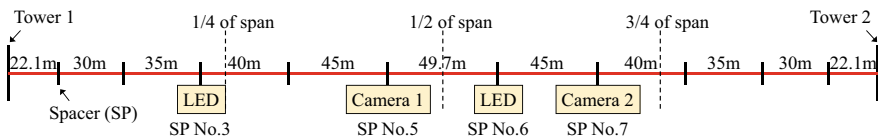


Fig. 3 Location of spacers and equipment in the span

3 Galloping Observed on January 12, 2022

3.1 Meteorological Conditions During the Development of Wet Snow Accretion

A well-developed low pressure approached the Kushiro test line resulting in severe snowfall from 11 to 12 January 2022. Figure 4 shows the time series of 10 min statistics of meteorological data and tension. Air temperature and relative humidity were measured at a height of 4 m above the ground, and the wind speed and direction were measured at 44 m from above the ground. The tension measured at two insulator support points on Tower 1 was added up, divided by the number of sub-conductors (four), and converted into tension per sub-conductor. The maximum, minimum, and mean values of tension were calculated every 10 min. Figure 5 shows the amount of snow accretion per unit length estimated from the mean tension. It is assumed that cylindrical snow accretion (snow density: 600 kg/m³, drag coefficient: 1.0) occurs uniformly across the span and the effect of an increase in the mean tension due to wind loads is excluded to estimate the snow accretion amount from the mean tension. Although it is necessary to consider the fact that the snow accretion is not uniformly distributed in the span and the drag coefficient varies depending on the shape of the snow accretion, the snow accretion amount can be approximately estimated in Fig. 5.

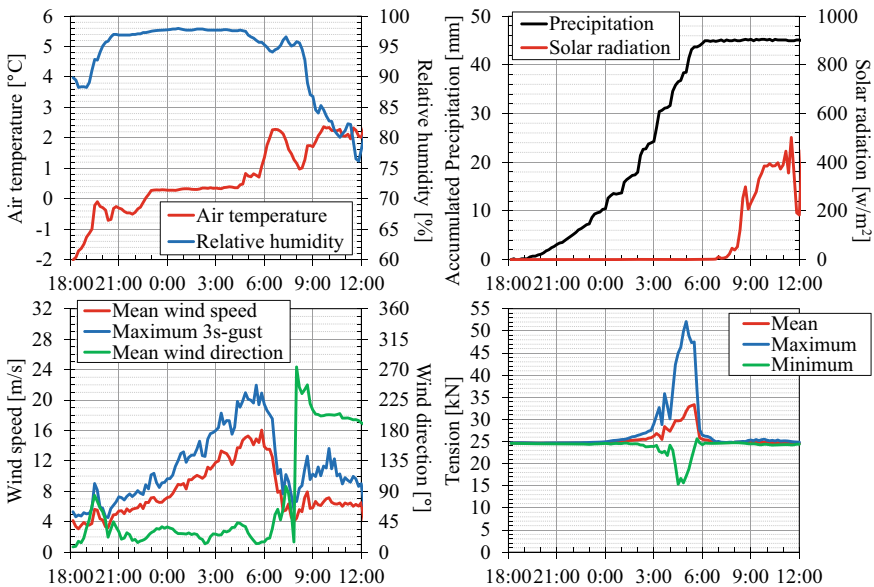
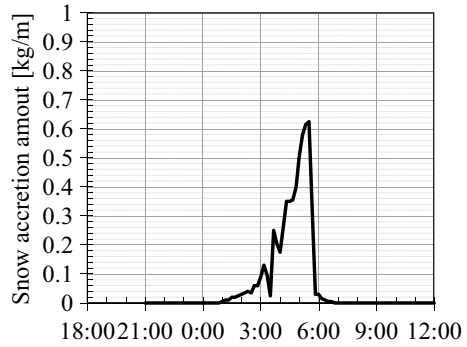


Fig. 4 Time series of a 10 min statistics of meteorological data and tension (2022/1/11 18:00–2022/1/12 12:00)

Fig. 5 Snow accretion amount calculated from tension



Snowfall started after 19:00 on the 11th, and snow accretion developed after 0:00 on the 12th at temperatures between 0–1 °C and relative humidity of 95% or higher. The wind speed gradually increased and maintained an average speed of 8–16 m/s until 6:00. During this period, the wind direction was close to the perpendicular direction of the line (azimuth angle: 25°), and the mean value of the turbulence intensity of the wind was 0.13. Based on the snow accretion classification method using temperature, humidity, and wind speed [12], this case was classified as a strong-wind wet snow accretion.

The amount of snow accretion increased until around 5:30, then decreased rapidly as the temperature increased, eventually decreasing completely by 6:00. Some cameras were able to capture the snow accretion situation just before snow shedding. The snow accretion situation captured by spacer camera 2 at spacer No. 7 looking in the direction of the Tower 1 is shown in Fig. 6. The remaining snow accretion on the upper left-hand conductor shows a triangular-shaped snow accretion developed on the upwind side (right-hand side) of the conductor. The height of snow accretion to the windward direction was approximately the same as the diameter of the sub-conductor. Furthermore, the surface of the accreted snow became smooth. It is speculated that the reason for this is that snowfall particles are compacted and attached to the snow body, which melts owing to the heat transfer from the air. In the case of in-cloud icing, when supercooled water droplets with small diameter impact conductors at relatively high wind speed, icing develops on the windward side of the conductor; however, the surface of the icing body is generally relatively rough [1, 2, 4]. In the case of freezing rain, the attached water droplets do not freeze immediately but develop by covering the conductor surface or in the direction where the droplets drop [1, 2]. Therefore, the accretion shape differs depending on the icing type.

Fig. 6 Snow accretion situation just before the snow shedding (2022/1/12, 6:00:05)



3.2 Response of the Four-Bundled Conductor Due to Galloping

As shown in Fig. 4, a large variation in tension (difference between maximum and minimum tension) can be observed, especially between 4:30 and 5:30, due to galloping. A time series of displacement at the LED markers installed in the spacers was calculated by conducting an image analysis from 21:00 to 5:30. Figure 7 shows the total amplitudes (difference between the maximum and minimum values every 10 min) of the vertical and horizontal displacements as well as the torsional angles of the four-bundled conductor. The vertical amplitude increased after 3:00, indicating the occurrence of galloping.

The video images showed that the two-loops/span mode (asymmetric first mode) was dominant in the observed galloping, with larger values at the spacer No. 3, which was close to the quarter of the span located at the antinode of this mode, compared to the spacer No. 6. The amplitude was particularly large between 4:30 and 5:30. The maximum amplitude at the spacer No. 3 was 5.8 m and 5.6 m for the vertical total amplitude and horizontal displacement total amplitude, respectively, and 216° for the torsional angle total amplitude. As an example of galloping response, Fig. 8 shows the time history waveforms of the vertical and horizontal displacement as well as the torsional angle at spacer No. 3 from 4:31:00 to 4:31:20, accompanied by the tension waveform. The vertical and horizontal displacements and the torsional

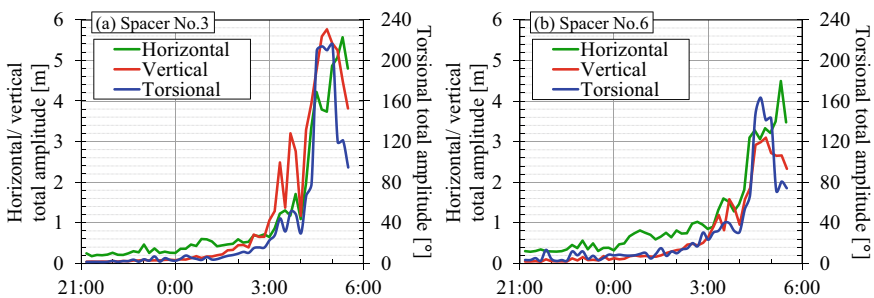


Fig. 7 Total amplitudes of displacements and torsional angles at spacers No. 3, 6

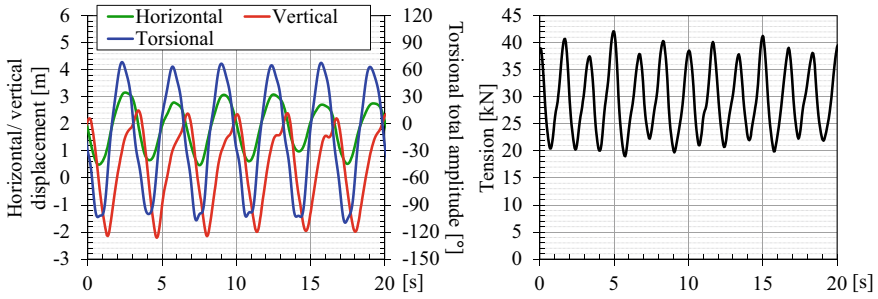


Fig. 8 Time history waveforms of displacements and torsional angles (4:31:00–20)

angles are coupled, resulting in a steady response. The coupled vibration in three degrees of freedom is a characteristic of the galloping of the four-bundled conductor. However, the waveforms of all displacements showed a slightly deformed shape from a sinusoidal wave, particularly in the vertical displacement, where a bump was observed in the waveform at the same timing of one cycle. This can be attributed to the effects of aerodynamic and structural (geometrical) non-linearity as the response reached a large amplitude. Additionally, the tension fluctuated at twice the frequency compared to the displacement, considering the tension increases when the conductor moves in either the positive or negative directions, which is characteristic of the even-loops/span modes (asymmetric modes).

Figure 9 shows the mean values of the torsional angle of the four-bundled conductor. Because the torsional angle is an angle from the horizontal plane, it has a value even without snow accretions. The occurrence characteristics of galloping are highly dependent on the direction of snow accretion (angle of attack to the wind) in addition to the shape of the snow accretion and the wind speed. If snow accretion develops on the windward side, galloping occurs when a certain angle of attack exists between the direction of snow accretion and the wind [4, 9]. As the spacers hold the sub-conductors without rotation, the torsional angle of the four-bundled conductor at the spacer position can be used to approximately determine the angle of attack to the wind in the span. Figure 10 shows the relationship between the mean torsional angle and the vertical total amplitude. Although the distribution of torsional angles in the span might affect the galloping onset characteristics, the effect of the torsional angle around the anti-nodes of the mode is dominant. Therefore, Fig. 10 indicates the relationship at spacer No. 3, which is near the quarter of the span and corresponds approximately to the antinode of the two-loops/span mode. A large amplitude was observed when the four-bundled conductor was rotated by approximately -10 to -20° (downwards) from the initial angle (-10°).

Figure 11 shows the relationship between the mean wind speed and the vertical total amplitude of displacement. Snow accretion developed when the wind speed increased in this case, and the wind speed range where galloping was observed (above about 12 m/s) corresponded approximately to the wind speed range where snow accretion occurred. Therefore, Figs. 10 and 11 show the cases where the snow

Fig. 9 Time series of mean torsional angle of four-bundled conductor

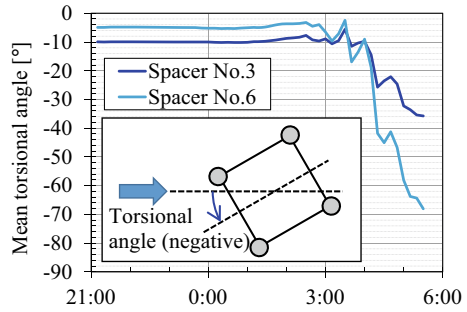


Fig. 10 Relationship between the mean torsional angle and vertical total amplitude at spacer No. 3

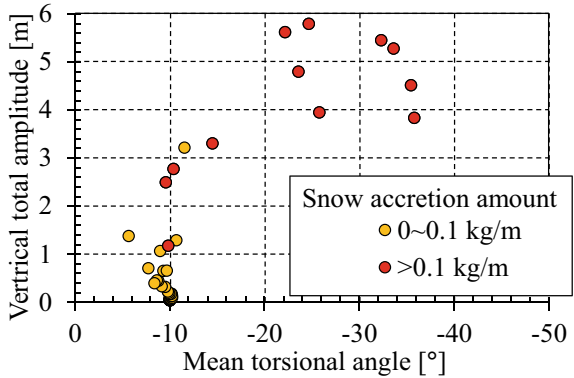
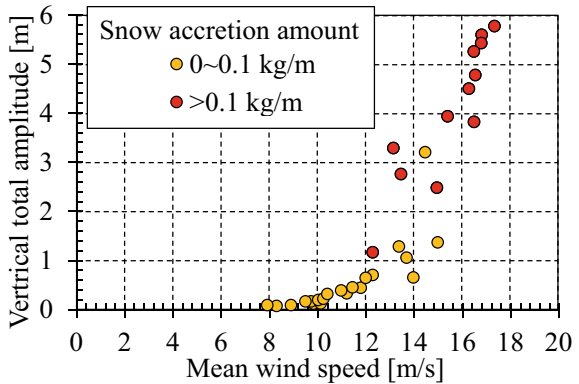


Fig. 11 Relationship between the mean wind speed and vertical total amplitude at spacer No. 3



accretion amount exceeds 0.1 kg/m and is less than 0.1 kg/m, respectively. Under the conditions where snow accretion occurred, the amplitude increases with the wind speed.

4 Comparison with Simulated Galloping

Time history response analyses was conducted to clarify the sensitivity of the response amplitudes of galloping to the snow accretion shape and its development angle using the three-dimensional nonlinear finite element analysis code called ‘CAFSS’ [10]. The analysis model was validated for natural frequencies and structural damping characteristics by conducting excitation tests on the Kushiro test line [13]. The aerodynamic forces acting on each sub-conductor were modelled by a quasi-steady aero dynamic force model [9] and calculated using the aerodynamic force coefficients for a single conductor with triangular-shaped snow accretion [14]. Fluctuating wind waveforms in the span were generated using a multidimensional autoregressive model with a specific power spectrum and coherence [15]. The turbulence intensity was 0.15. The vertical total amplitude was calculated from the difference between the maximum and minimum values over the latter 600 s of each 660 s analysis time period.

Figure 12 shows the vertical total amplitudes at spacer No. 3 for each snow accretion height and angle. The snow accretion angle corresponded to the angle without wind, and hence, changes as the wind speed increased. The maximum values of amplitude were compared when the snow accretion angle was set within the respective angle range (in every 2° intervals). For all snow accretion heights, the response amplitude increased up to a certain range of the snow accretion angle (approximately 30°); however, the maximum response amplitude does not increase when the angle range was greater than 50° . The larger the snow accretion height, the larger was the response amplitude, and the maximum amplitude could be obtained even for a small snow accretion angle. Furthermore, the amplitude increased as the wind speed increased.

Figure 13 compares the vertical total amplitude at spacer No. 3 between time history analysis for three accretion heights (snow accretion angle range: 0 to -10° or 0 to -30°) and the field observation. When there was snow accretion (over 0.1 kg/m), the observed results showed a trend close to the analysis results with $S = D/2 \sim D$. On comparing the snow accretion situation observed in Fig. 6, it was observed that the snow accretion conditions with close response amplitudes were close to the actual conditions. Therefore, the analysis based on the assumption of ideal triangular snow accretion showed that reasonable amplitudes can be obtained.

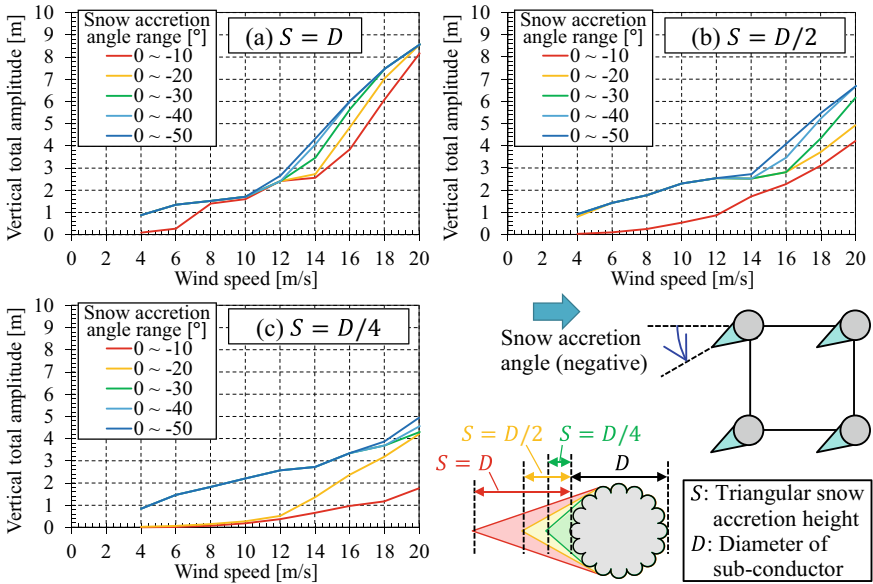
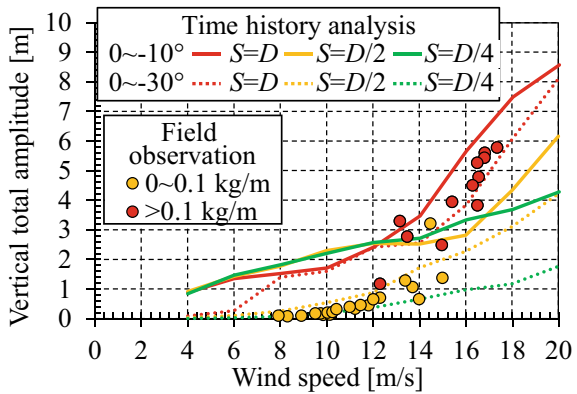


Fig. 12 Comparison of maximum response amplitudes at spacer No. 3 for each snow accretion angle range and snow accretion height (results of CAFSS)

Fig. 13 Comparison of vertical total amplitude at spacer No. 3 between time history analysis and field observation



5 Conclusions

The large galloping of a four-bundle conductor under wet snow accretion was observed at Kushiro test lines. The conductors, without any countermeasures, vibrated mainly in the vertical two-loops/span mode coupled with the horizontal and torsional modes, where the maximum total amplitude reached approximately 5.8 m in the vertical direction. Simultaneously, triangular-shaped snow accretion occurred on the windward side of the conductors. Furthermore, when the direction of the snow

accretion faced downwards owing to the rotation of the four-bundled conductor, a large amplitude was observed. Under the conditions where snow accretion occurred, the amplitude increased as the wind speed increased.

Through time history analysis, the sensitivity of the response amplitudes of galloping to the snow accretion shape and its development angle were indicated using the three-dimensional nonlinear finite element analysis code ‘CAFSS’. The larger the snow accretion height was, the larger was the response amplitude, and the maximum amplitude could be obtained even for a small snow accretion angle. Furthermore, the results of the analysis under the snow accretion conditions closest to those observed were found to approximately reproduce the observed response amplitudes.


References

1. Poots G (1996) Ice and snow accretion on structures. Research Studies Press, Taunton
2. Farzaneh M (2008) Atmospheric icing of power networks. Springer, Dordrecht
3. Sakamoto Y (2000) Snow accretion on overhead wires. *Phil Trans R Soc A* 358:2941–2970
4. Matsumiya H, Yukino T, Shimizu M, Nishihara T (2022) Field observation of galloping on four-bundled conductors and verification of countermeasure effect of loose spacers. *J Wind Eng Ind Aerodyn* 220
5. Matsumiya H, Ichikawa H, Aso T, Shugo M, Nishihara T, Shimizu M, Sugimoto S (2019) Field observation of wet snow accretion and galloping on a single conductor transmission line. In: Proceedings of international workshop on atmospheric icing of structures, Reykjavik, Iceland
6. Matsumiya H, Matsushima H, Aso T, Nishihara T, Sugimoto S (2021) Field observations of snow damage to overhead transmission lines at the Kushiro test line. In: Proceedings of international workshop on atmospheric icing of structures, Montreal, Canada
7. Desai YM, Yu P, Shah AH, Popplewell N (1996) Perturbation-based finite element analysis of transmission line galloping. *J Sound Vib* 191:469–489
8. Shimizu M, Shugo M, Sato J (1998) A geometric nonlinear analysis of transmission lines’ galloping (in Japanese). *J Struct Eng* 44A:951–960
9. Matsumiya H, Nishihara T, Yagi T (2018) Aerodynamic modeling for large-amplitude galloping of four-bundled conductors. *J Fluids Struct* 82:559–576
10. Shimizu M, Sato J (2001) Galloping observation and simulation of a 4-conductor bundle transmission line (in Japanese). *J Struct Eng* 47A:479–488
11. Nishihara T, Matsumiya H, Sugimoto S, Hashimoto A, Ichikawa H, Aso T, Shugo M (2017) Field observation of snowstorm damage to overhead transmission lines at Kushiro test line—Construction of full-scale test lines and analysis of typical snow accretion during two winter seasons (in Japanese). CRIEPI research report, N16003
12. Sugimoto S, Aso T, Saeki M (2012) Proposal of a type classification method for snow accretion on overhead transmission line using meteorological data (in Japanese). CRIEPI research report, N11059
13. Taruishi S, Matsumiya H, Matsushima H, Shimizu M (2019) Evaluation of validity of method for making FEM model of a four-bundled conductor by excitation tests and simulations. In: Proceedings of second international symposium on dynamics and aerodynamics of cables. Stavanger, Norway, pp 183–190
14. Matsumiya H, Nishihara T, Shimizu M () Aerodynamic characteristics of ice and snow accreted conductors of overhead transmission lines. In: Proceedings of 13th International Conference on Wind Engineering, Amsterdam, Netherlands

15. Iwatani Y (1982) Simulation of multidimensional wind fluctuations having any arbitrary power spectra and cross spectra (in Japanese). *J Wind Eng* 1982(11):5-18

Statistical Study of Aeolian Vibration Characteristics of Overhead Conductor



Shaoqi Yang , Luc Chouinard, Sébastien Langlois, Josée Paradis, and Pierre Van Dyke

Abstract Overhead transmission conductors are vulnerable to fretting fatigue due to aeolian vibrations. Accurate estimation of vibration severity is essential to determine the residual life of in-service lines and to schedule timely maintenance or replacement. For most transmission line networks, vibration monitoring systems are not available, and thus the vibration hazards must be derived from local wind conditions. The most widely accepted estimation procedure of the severity of aeolian vibration is by calculating the maximum oscillation amplitudes of the conductor based on the Energy Balance Principle (EBP), which establishes the balance between the energy transmitted to the conductor by the wind and the energy dissipated by self-damping of the conductor and dampers. However, the EBP is based on wind tunnel results where only one frequency is excited, while observations and experimental results show that multiple resonant modes are excited simultaneously. Furthermore, the distribution of vibration amplitudes and number of cycles for each amplitude are required to calculate cumulative damage due to fretting fatigue. In this paper, vibration data from an experimental undamped ACSR test line in Quebec, Canada, is analyzed in conjunction with concurrent winds over a 2-month period. The first step of the analysis is to identify observations corresponding to aeolian vibrations in both the time and frequency domains. For each record of aeolian vibrations, amplitudes are fitted to a Rayleigh distribution based on the narrow-band assumption. The number of cycles and Rayleigh parameter are then related to wind conditions through a modified Strouhal frequency and EBP methodology. A statistical model is proposed to understand the relationship between vibration profiles and wind input, taking into consideration the influence of wind speed and turbulence intensity, as well as the influence of conductor tension.

S. Yang (✉) · L. Chouinard
Department of Civil Engineering, McGill University, Montreal, Canada
e-mail: shaoqi.yang@mail.mcgill.ca

S. Langlois
Department of Civil Engineering, Université de Sherbrooke, Sherbrooke, Canada

J. Paradis · P. Van Dyke
Institut de Recherche d'Hydro-Québec (IREQ), Varennes, Canada

Keywords Overhead conductor · Aeolian vibration · Vibration profile · Damage accumulation · Residual life

1 Introduction

Wind-induced vibrations on overhead transmission lines are a well-known topic. Of these, aeolian vibration induced by vortex shedding can lead to fretting fatigue near the fixed location of conductors [1]. Aeolian vibration amplitudes are usually controlled by installing the conductor at a tension below the safe design tension (H/w), as well as adding an adequate damping system. Such threshold is meant to ensure that fatigue cannot occur during the service life of the conductor. However, in practice, an accurate estimation of the residual fatigue life of the conductors is desired to support the maintenance of transmission networks.

The fatigue of conductors is often evaluated by the stress-life (S–N) approach [2], while the stress levels are calculated from Y_b , the bending amplitude measured at a distance of 89 mm from Last Point of Contact (LPC) [3] or $f_{y_{max}}$, the product of vibration frequency by antinode amplitude [2]. Due to its close correlation with the stress at the uppermost surface of the conductor near the suspension clamp, and its accessible location, Y_b is widely used as an indicator of fatigue exposure severity. Considering a specific span of conductor in service, a profile of Y_b , in terms of number of cycles at each amplitude levels, is only available through onsite measurements. Despite the advance in monitoring hardware [4], it is still impossible to install monitoring system to the entire network. Thus, a methodology for estimating Y_b profiles directly from wind data is required.

The two most common procedures to calculate aeolian vibrations are dynamic analyses and the Energy Balance Principle (EBP). The dynamic analyses, either analytical [5, 6] or numerical [7, 8] are not applicable to estimate a Y_b profile, given that the input wind excitation is spatiotemporally random. The EBP is based on experimental measurements of wind energy input and energy dissipated by the conductor self-damping and dampers. When applying EBP in practice, the frequency of vibration is first determined using the Strouhal number:

$$f_s = 0.185 v/D \quad (1)$$

where f_s is the frequency of vibration, v is the wind speed (in m/s) perpendicular to the line, and D (in meters) is the diameter of the conductor. An estimate of the maximum amplitude corresponding to f_s can be obtained from the wind energy input and damping curves [9, 10]. However, the EBP is based on wind tunnel results where only one frequency is excited, while observations and experimental results show that multiple resonant modes are excited simultaneously.

Since the 1980s, researchers and engineers [11–14] have been attempting to incorporate statistical modifications into EBP in order to account for the randomness of wind excitation, specifically in terms of turbulence intensity, and Y_b profile. As shown

in sections below, the dominant frequencies of aeolian vibrations are located within a narrow band of 10 Hz, which leads to a reasonable assumption that aeolian vibration is a stationary narrow-band random vibration [15] within a short time duration T . The narrow-band assumption allows for the estimation of the number of cycles from the frequency domain when multiple frequencies are excited. Furthermore, assuming that the instantaneous vertical displacement $y_b(t)$ is a stationary Gaussian process, the bending amplitude Y_b obtained from $y_b(t)$ can be shown to be a Rayleigh random variable [16]. In this paper, vibration and wind data from an experimental undamped ACSR test line in Quebec, Canada, are analyzed over a 2-month period. Several statistics from both vibration and wind observations are estimated and analyzed, and a novel method for estimating number of cycles and Rayleigh parameter of Y_b from wind data is proposed.

2 Test Setup and Data Structure

A statistical analysis was performed on experimental data from the Hydro-Québec test line located near Varennes, Quebec [17]. The line was a single ACSR Bersfort 48/7 conductor without any dampers. A brief description of conductor properties is provided in Table 1. The experiment was conducted from 2019-09-09 to 2019-10-11 with a tensile force of 27 kN, which is 15% of the conductor rated tensile strength (RTS), and again from 2019-10-30 to 2019-11-29 with a tensile force of 45 kN (25% RTS).

Wind conditions and conductor motion in the 450 m central span (Fig. 1) were recorded by multiple sensors. Among those, two data sets are analyzed in this paper: (1) $y_b(t)$: the relative displacement between clamp and conductor at 89 mm from LPC at NW end of the central span; (2) $v(t)$: the horizontal wind speed perpendicular to the line direction measured by the nearest anemometer. The anemometer is positioned at the line level, 150 m away from the northwest end of the central span. The height of the line and the anemometer height vary under different tension forces.

Every 10 min, the wind speed and direction were recorded for 5 min with an acquisition rate of 10 Hz, and the displacement was recorded for 71.4 s with an acquisition rate of 420 Hz. According to their acquisition speed and duration, the start time of every record is adjusted so that both acquisition end simultaneously. The wind speed and direction were then converted to the horizontal wind speed perpendicular to the line direction. And the displacement data was processed by a 2–50 Hz bandpass filter to remove the constant term and any high frequency noise.

Table 1 Mechanical properties of conductor

Designation	Stranding	Diameter	Linear weight	RTS
ACSR Bersfort	48 × 3.32 mm steel, 7 × 4.27 mm aluminum	35.56 mm	2.369 kg/m	180.1 kN

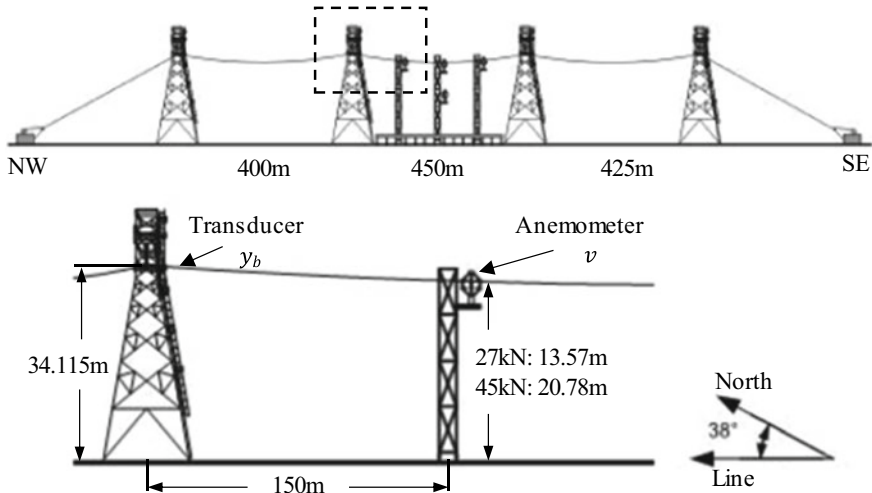


Fig. 1 Test setup of Hydro-Québec’s Varennes test line

For the analysis, both $y_b(t)$ and $v(t)$ were separated into short time intervals. As a dynamic system, the vibration amplitude is delayed in response to variations of the wind speed due to inertia of the line. Thus, if y_b is observed for an interval from t_0 to $(t_0 + T)$, the corresponding v interval is sampled from $(t_0 - \Delta t)$ to $(t_0 + T)$. The optimal combination was found to be $T = 50s$ and $\Delta t = 20s$ and an example of intervals is provided in Fig. 2. More details regarding T and Δt are given in Sect. 3.2.

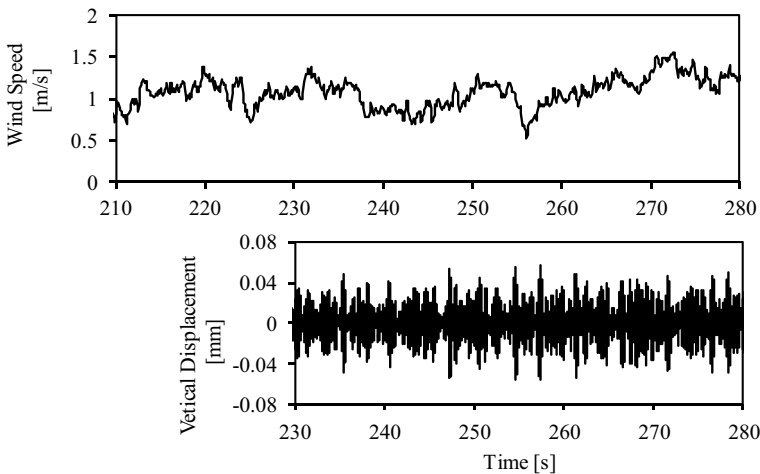


Fig. 2 An example of record intervals with $T = 50s$, $\Delta t = 20s$. Top: $v(t)$, horizontal wind speed normal to the line direction, bottom: $y_b(t)$, the relative displacement between clamp and conductor at 89 mm from LPC

3 Statistical Characteristics of Aeolian Vibration

3.1 Preliminary Analysis

For each $T + \Delta t$ wind speed interval, the mean and standard deviation (SD) were first calculated. A histogram was also constructed and saved for further use. For corresponding vibration interval, the amplitudes of vibration (peak and valley in each cycle) were first extracted. Since Y_b is defined as peak-to-peak amplitude in aeolian vibration, the amplitudes are referred as $Y_b/2$ hereafter. The mean and SD of normal wind speed are plotted against the maximum amplitude in Fig. 3a, b. A larger amplitude level can be observed for the 45 kN line, which agrees with the theory that higher tension in the conductor results in lower self-damping. For both 27 kN and 45 kN cases, the data points at the top-left corner of the figures correspond to intervals that are not aeolian vibrations, a clear boundary can be observed at the 0.025 mm amplitude level.

The Fast Fourier Transform (FFT) was applied to each sampled interval. Let y_0, \dots, y_N be the observations in a given time interval for y_b , the FFT is:

$$\mathcal{F}(f_k) = \frac{1}{N} \left| \sum_{n=0}^{N-1} y_n e^{-i2\pi kn/N} \right|, k = 0, 1, \dots, N - 1 \tag{2}$$

where $f_k = k/T$ is the k th frequency components and $N = 420T$ is the total number of data points in the interval. The energy contribution of each frequency component can be evaluated as

$$EC(f_k) = \frac{\mathcal{F}(f_k)^2}{RMS} \tag{3}$$

where RMS is the root-mean-square of y_b . The frequencies which contribute more than 5% to the RMS are considered *major frequencies*. For $T = 50$ s and $\Delta t = 20$ s, the major frequencies are usually limited in a band of 10 Hz (Fig. 3c), and the total energy contribution (Fig. 3d) is higher than 50%. The 0.025 mm amplitude level boundary can also be seen clearly.

The major frequencies can be used to estimate the total number of cycles. In the time domain, for each interval, a nominal frequency f_{no} is defined as

$$f_{no} = \frac{\text{observed number of cycles}}{T} \tag{4}$$

And a central frequency f_c can be calculated from the FFT spectrum as,

$$f_c = \frac{\sum \mathcal{F}(f_i)^2 \cdot f_i}{\sum \mathcal{F}(f_i)^2} \tag{5}$$

where f_i are the major frequencies. This approach was found to be very accurate in both 27 kN and 45 kN cases (Fig. 4).

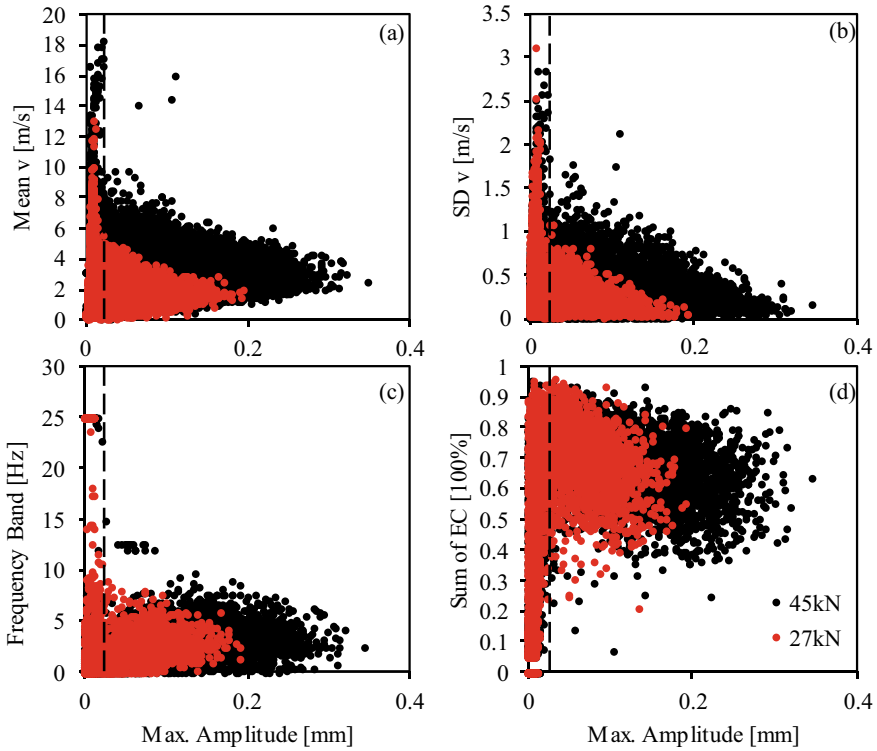


Fig. 3 Experimental data plot ($T = 50$ s, $\Delta t = 20$ s). Horizontal axis is the maximum amplitude level observed, vertical axis are: **a** mean of the normal wind speed, **b** standard deviation of the normal wind speed, **c** bandwidth of major frequencies, and **d** the total energy contribution of major frequencies. The black dashed lines are the 0.025 mm amplitude level

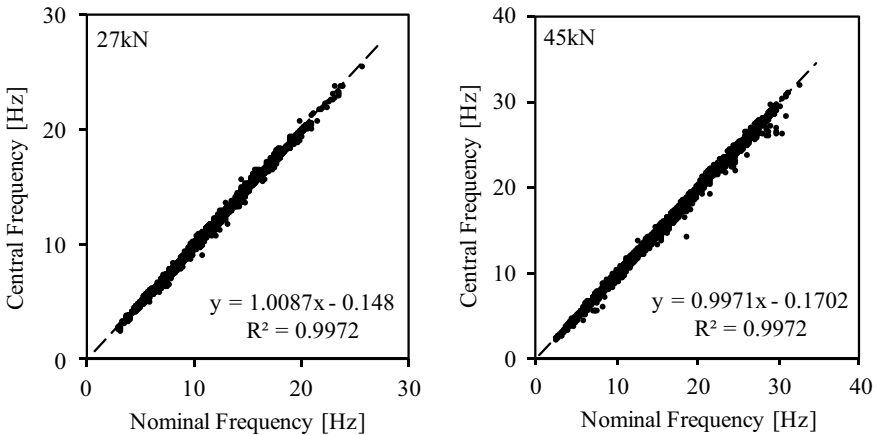


Fig. 4 Comparison of observed nominal frequency and central frequency calculated from FFT

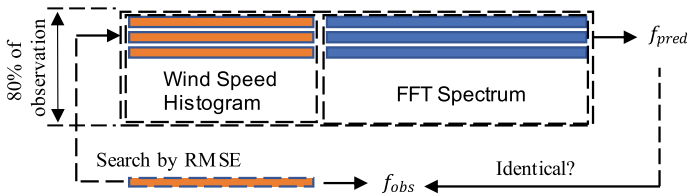


Fig. 5 The workflow for validation and selection of T and Δt

3.2 The Optimal T and Δt

The idea of determining nominal frequency from wind histogram was tested in conjunction with the search for the optimal T and Δt . The algorithm is illustrated in Fig. 5 and the results are shown in Fig. 6. For both 27 kN and 45 kN cases, all combinations of T ranging from 30 to 60 s, and Δt from 0 to 30 s, were tested in the following manner: Given a specific T and Δt pair, all the aeolian vibration intervals (i.e., maximum amplitude > 0.025 mm) were first identified. A randomly selected set comprising 80% of the records were used as training set and the remaining 20% were used as testing set. For each wind histogram in the testing set, its nearest approximation was located in the training set (the orange matrix in Fig. 5) based on the root-mean-square difference. Once the nearest wind histogram is located, the corresponding FFT spectrum in training set (the blue matrix in Fig. 5) was used as the predicted FFT for the testing wind histogram. The central frequencies calculated from the predicted FFT spectrum were compared to the nominal frequencies of the testing set to check the quality of prediction by the R^2 score. The algorithm verified that two similar wind histograms always lead to a similar nominal frequency, but the optimal duration for the 27 kN and 45 kN were found to be different. Since 45 kN case is more important, the 50 s + 20 s combination was selected and used for both cases for consistency. Further study will be conducted to consider not only the tension force, but also the frequency and damping.

3.3 Rayleigh Distribution and Y_b

The Rayleigh distribution has a probability density function (PDF)

$$f(x; s) = \frac{x}{s^2} e^{-\frac{x^2}{2s^2}} \tag{6}$$

where x is the random variable and s is the distribution parameter. The theoretical mean, standard deviation and coefficient of variance are

$$\mu = \sqrt{\frac{\pi}{2}}s, \sigma = \sqrt{\frac{4-\pi}{2}}s, cov = \sqrt{\frac{4-\pi}{\pi}} = 0.523 \tag{7}$$

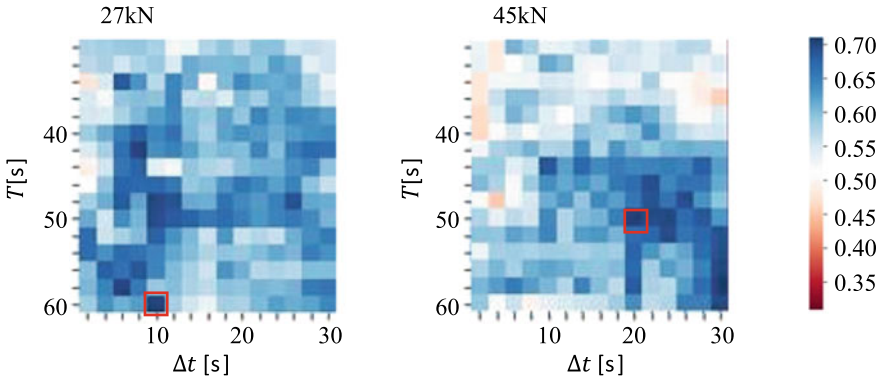


Fig. 6 The quality of prediction in terms of R^2 between the predicted central frequency and the observed nominal frequency

If the instantaneous vertical displacement $y_b(t)$ is a stationary Gaussian process $N(0, \sigma_B)$, the bending amplitude Y_b is a Rayleigh random variable with $s = \sqrt{2}\sigma_b$ [16]. The maximum, mean and standard deviation of observed Y_b are plotted in Fig. 7. For both 27 kN and 45 kN case, the max-mean and SD-mean were found linearly correlated with very high R^2 scores. The constant max/mean and SD/mean ratio suggest Y_b follows a same distribution despite of the change of tension. Furthermore, the observed *cov* is 0.5343 for 27 kN and 0.5313 for 45 kN, both agree with the theoretical value of 0.523, which is a strong evidence supporting the Rayleigh assumption. And the max/mean ration (2.73 and 2.70) suggests the maximum value is the 99.67% percentile of Rayleigh distribution.

Similar to the nominal frequency, the Rayleigh parameter s can also be estimated from the frequency domain. Given Y_b is a Rayleigh random variable with $s = \sqrt{2}\sigma_b$,

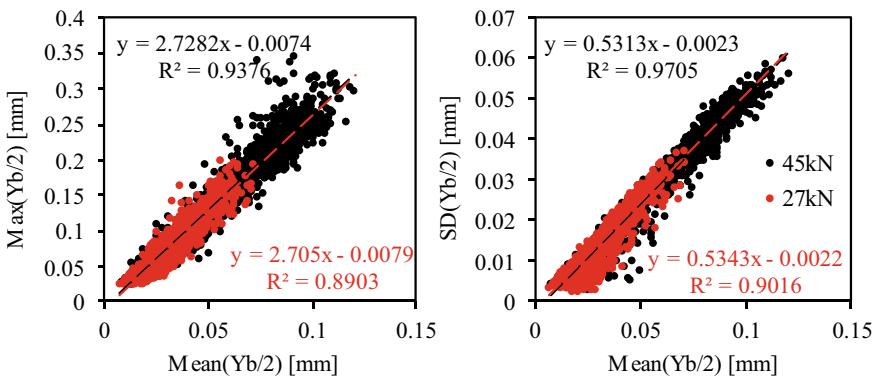
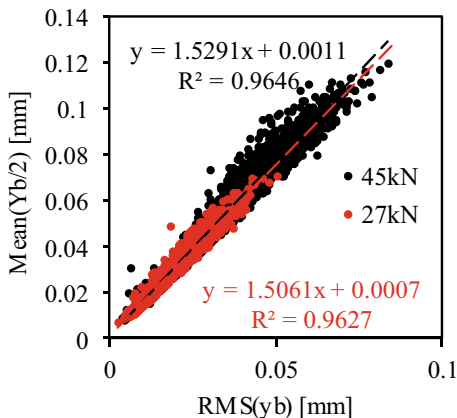


Fig. 7 Relationship between the statistics of bending amplitude Y_b . Left: maximum amplitude versus the mean of Y_b in each interval; Right: standard deviation of Y_b versus the mean of Y_b in each interval. Simple linear regression line and R^2 scores are provided in the plots

Fig. 8 Relationship between mean of Y_b and the root-mean-squared value of y_b (or the left-hand side term in Eq. 9) in each slice



the expected value of Y_b is

$$E(Y_b) = \sqrt{\frac{\pi}{2}}s = \sqrt{\pi}\sigma_b \tag{8}$$

On the other hand, Parseval’s theorem indicates that

$$\sqrt{2 \sum \mathcal{F}(f_i)^2} \approx RMS[y_b(t)] \tag{9}$$

where f_i are the major frequencies, and RMS stands for the root-mean-square value. Since $y_b(t)$ is a Gaussian process $N(0, \sigma_B)$, its RMS is equal to its standard deviation σ_B . Combining the above equation yields that

$$E(Y_b) = \sqrt{\pi}\sigma_b = \sqrt{\pi}RMS[y_b(t)] = \sqrt{\pi}\sqrt{2 \sum \mathcal{F}(f_i)^2} \tag{10}$$

As shown in Fig. 8, the linear relationship described by the above equations is observed in the data. While the ratios (1.5291 for 45 kN and 1.5061 for 27 kN) are again very close to the theoretical value of $\sqrt{\pi}(\approx 1.77)$, further study will be conducted to address the difference between observed and theoretical values.

4 Conclusion

Several statistical and probabilistic analyses were conducted on the aeolian vibration data. By appropriately selecting a record duration of 50 s + 20 s, it was determined that the bending amplitude Y_b followed a Rayleigh distribution. Furthermore, the two significant parameters, nominal frequency and Rayleigh parameter, were calculated from the frequency domain. The wind speed histogram was utilized to forecast primary frequencies and demonstrated a positive potential for estimating the nominal

frequency. Future research will focus on refining the estimation of the Rayleigh parameter and completing the entire method to evaluate the number of cycles and amplitude of vibrations given a certain wind distribution and line configuration.

References

1. Diana G (ed) (2018) Modelling of vibrations of overhead line conductors. Springer International Publishing, Cham
2. Cloutier L, Goudreault S, Cardou A (2006) Fatigue of overhead conductors. In: Chan JK, Havard DG, Rawlins CB, Weisel J (eds) EPRI Transmission Line Reference Book: Wind induced Conductor Motion, 2nd edn. EPRI, Palo Alto
3. Poffenberger JC, Swart RL (1965) Differential displacement and dynamic conductor strain. *IEEE Trans Power Apparatus Syst* 84(4):281–289
4. Diana G, Tarsitano D, Mauri M, Dezza FC, Zanelli F, Manenti A, Ripamonti F (2021) A wireless monitoring system to identify wind induced vibrations in HV transmission lines. In: 3rd SEERC conference, paper no 1129, Vienna
5. Diana G, Cheli F, Fossati F, Manenti A (1993) Aeolian vibrations of overhead transmission lines: computation in turbulence conditions. *J Wind Eng Ind Aerodyn* 46–47:639–648
6. Ibrahim RA (2004) Nonlinear vibrations of suspended cables—Part III: random excitation and interaction with fluid flow. *Appl Mech Rev* 57(6):515–549
7. Lalonde S, Guilbault R, Langlois S (2017) Modeling multilayered wire strands, a strategy based on 3D finite element beam-to-beam contacts—Part II: Application to wind-induced vibration and fatigue analysis of overhead conductors. *Int J Mech Sci* 126:297–307
8. Liu J, Yan B, Mou Z, Gao Y, Niu G, Li X (2022) Numerical study of aeolian vibration characteristics and fatigue life estimation of transmission conductors. *PLoS ONE* 17(1):e0263163
9. IEC 61897-2020: Overhead lines - Requirements and tests for Aeolian vibration dampers, International Electrotechnical Commission (2020)
10. IEC 60826-2017: Overhead transmission lines—Design criteria. International Electrotechnical Commission (2017)
11. Noiseux DU, Hardy C, Houle S (1987) Statistical methods applied to Aeolian vibrations of overhead conductors. *J Sound Vib* 113(2):245–255
12. CIGRE SC22 WG01: Report on Aeolian Vibration (Rapport sur les vibrations éoliennes) (1989)
13. Noiseux DU, Houle S, Beauchemin R (1988) Transformation of wind tunnel data on aeolian vibrations for application to random conductor vibrations in a turbulent wind. *IEEE Trans Power Deliv* 3(1):265–271
14. Hardy C, Noiseux DU, Leblond A, Brunelle J, Van Dyke P (1996) Modelling of single conductor-damper system response—Volume 1: theoretical and validation manual. Canadian electrical association, Rapport technique No. 372 T 823
15. Lalanne C (2014) Mechanical vibration and shock analysis: random Vibration, 3rd edn. ISTE Ltd./John Wiley and Sons Inc., Hoboken, NJ
16. Yang J-N, Shinozuka M (1971) On the first excursion probability in stationary narrow-band random vibration. *J Appl Mech* 38(4):1017–1022
17. Paradis J (2022): Étude de l’amortissement interne des conducteurs excités selon plusieurs fréquences simultanément (PhD Thesis). Université de Sherbrooke, Sherbrooke (Québec) Canada

Three-Dimensional Flow Characterizations for Yawed and Inclined Circular Cylinders for Bridge Cable Stays



Michael Hoftyzer and Elena Dragomirescu

Abstract The vibrations induced by the wind on inclined cables of cable stayed bridges has been well established with both experimental and numerical investigations following observations made in the field of under construction and in-service long span structures. The characteristics and the patterns of the axial flow formed on the leeward surface of stay cables inclined and yawed to the direction of main wind flow is investigated in this study. To supplement the experimental and numerical work in this area, CFD simulations were performed on various cylinder models with cable inclination angles of 0° – 60° , and yaw angles of 0° – 40° . To determine the effect of the axial flow on the leeward side of the circular cylinder and the pressure induced on the cylinder the pressure coefficients distributions along the downstream surface of the circular cylinder model were investigated. From these it was noted that the change in the orientation of the cylinder, with both inclination and yaw as described above, changes the pressure distribution along with the development of rotational variations (appearance of rotating flow) of the flow along the leeward side of the circular cylinder. A frequency domain analysis was performed for characterizing the flow along the leeward side of the cylinder providing additional information compared to the time domain analysis. The coherence between the frequency components of the lift coefficient, the pressure coefficient along the leeward side of the cylinder, and the velocity near the leeward side of the cylinder was calculated, to determine the level of interaction between these parameters.

Keywords Cable-Stayed bridges · Bluff-Body aerodynamics · Yawed and inclined circular cylinder · High Reynolds number flows · 3D cylinder flows

M. Hoftyzer (✉)
Parsons Corporation, Ottawa, ON, Canada
e-mail: mhoft084@uottawa.ca

E. Dragomirescu
Department of Civil Engineering, University of Ottawa, Ottawa, ON K1N 6N5, Canada
e-mail: Elena.Dragomirescu@uottawa.ca

1 Introduction

For long span bridge construction cable-stayed bridges are the preferred option, over the more expensive suspension bridge. This has led to the construction of cable-stayed bridges to expand over the past number of years. As a result of their long and slender shape, stayed cables of these long span structures are known to vibrate during both the construction phase of the project and/or upon completion and opening of these massive bridges. The vibration of the slender cables may be a result of several known fluid–structure interactions such as rain-wind effect, wind buffeting turbulent effect, parametric excitations, wake effects, or by a combination of these above mechanisms. Wind engineers and aerodynamists are of particular interest in the stay cables vibration phenomenon, known as dry cable galloping, as it is not well understood. Thorough experimental programs have been carried out by several researchers to better understand this phenomenon including [1, 5, 6, 8] and others. Dry cable galloping, the aerodynamic instability of the structural stay cables, has been noted to occur around the Reynolds number of $Re = 2.2 \times 10^5$ for a cable inclination at the angles of 57° and higher [6]. Based on the variation of aerodynamic coefficients with the Reynolds number and the inclination of the inclined cable, a formulation has been offered for the aerodynamic forces applied to a cable in the attempt to predict the galloping condition [7]. A structural damping recommendation has been established by FHWA [3] for cable-stayed bridges in an attempt to lower the occurrence of stay cable galloping. However, tests performed in the wind tunnel and results obtained in field observations on similar cable models tested within the similar Reynolds number range have led to different aerodynamic coefficients resulting in different structural responses [1, 5, 15]. Increasing the structural damping of inclined stay cables is not necessarily effective in reducing the dry inclined cable galloping vibration, which is of concern for both bridge designers and bridge builders around the world [11].

To assist in better understanding the flow around an inclined circular cylinder, many visualization techniques have been used in the laboratory with the assistance of flow visualization. In the wind tunnel oil film visualization techniques were used, which resulted in noting the presence of an axial flow on the leeward side of the cylinder inclined at 42.5° and yaw varying between 0° and 45° for a Reynolds number of $Re = 1.5 \times 10^5$ [8], and also noted in similar studies performed by Matsumoto et al. [9] for up to $Re = 1.65 \times 10^5$. The presence of the axial flow along the leeward side of the inclined stay cable has been linked to the on-set wind speed for dry inclined cable galloping. The development of the axial flow along the leeward side of the cylinder has been connected to the on-set of rain-wind vibration caused by the presence of the water rivulet along the length of the stay cable, though the Reynolds number and the inclination of the cables for which the two phenomena are different: dry inclined galloping, and rain-wind vibration [10].

Presented in this paper are some of the results from a study where the flow was numerically simulated around an inclined circular cylinder representing a section of an inclined stayed cable. This was completed to assist in clarifying the conditions for the occurrence of dry cable galloping of inclined cables and a connection between

the axial flow along the leeward side of the cylinder. The results presented are part of a study for cases with Reynolds numbers varying between 1.1×10^5 to 5.5×10^5 and with cylinder inclination angles (α) of 0° to 60° and yaw angles (β) of 0° to 40° ; cases $\alpha = 60^\circ$, $\beta = 0^\circ$, $\phi = 60^\circ$; and $\alpha = 50^\circ$, $\beta = 40^\circ$, $\phi = 60.5^\circ$; for $Re = 1.1 \times 10^5$ and 3.3×10^5 presented.

The angle between the flow and the cylinder measured in the plane of the flow is defined as the relative angle of attack (ϕ) between the incoming flow and the cylinder [1] where the angle ϕ is a unique value for a given set of inclination angles (α) and yaw angles (β). This is an important parameter in the interpolation of the results as it best describes how the wind interacts, or ‘sees’, the cylinder as it approaches and influences the resulting flow around the cylinder.

2 Computational Model

A closed space rectangular computational domain was employed in this study to model the flow around a circular cylinder, as illustrated in Fig. 1 below. The computational domain consisted of the following dimensions: the flow field extending $30D$ along the length of the cylinder; $22.5D$ in the direction of flow, $11.25D$ upstream and downstream from the center of the cylinder; and $22.5D$ in the direction perpendicular to the direction of flow centered around the cylinder. With the inclination of the cylinder the height of the domain changes to correspond to the cylinder length of $30D$. Over 3,000,000 cells were used to mesh the entire computational domain with over 200,000 elements used to mesh the face of the cylinder surface with a sample of the mesh used shown in Fig. 1. High Reynolds numbers of $Re = 1.1 \times 10^5$ to 5.5×10^5 were used in this study resulting from wind speeds ranging between 18.0 m/s and 90.3 m/s. These Reynolds number values correspond to the precritical regime of the TrBL (Transition in Boundary Layers) flow regime as defined by Zdravkovich [14] which is known for the abrupt decrease in drag force with an increase in wind speed and is defined as the drag crisis [12, 14].

For this research the LES turbulence model is used throughout the entire domain with Smagorinsky model used for turbulent viscosity. The flow perpendicular and inclined/yawed to circular cylinders were studied in this research with a cylinder diameter $D = 0.089$ m and cylinder length of $30D = 2.67$ m investigated (Fig. 1). The resulting aerodynamic characteristics of inclined/yawed slender circular cylinders were calculated from the simulations, and the three-dimensional characteristics of the axial flow which materialized were visualized.

The size of the computational mesh was a balance between the convergence rate of the model, computational time of the model, and accuracy of the model as outline in [4].

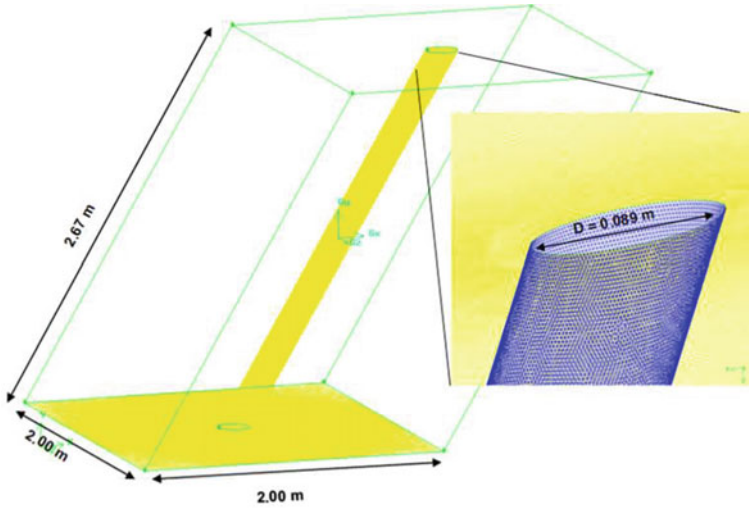


Fig. 1 Computational domain and mesh details

3 Pressure Distribution Around the Cable Model

To determine the effect of the flow pattern around a circular cylinder on the pressure induced at the surface of the cylinder the pressure distributions upstream and downstream of the cylinder is shown in Figs. 2 and 3 for the two cases presented: $\alpha = 60^\circ$, $\beta = 0^\circ$, $\phi = 60^\circ$, $Re = 1.1$ and 3.3×10^5 ; and for $\alpha = 50^\circ$, $\beta = 40^\circ$, $\phi = 60.5^\circ$, $Re = 1.1$ and 3.3×10^5 . The pressure distributions are shown in the visualizations on a plane parallel to the approaching flow and passing through the center of the cylinder for the cylinder's entire length.

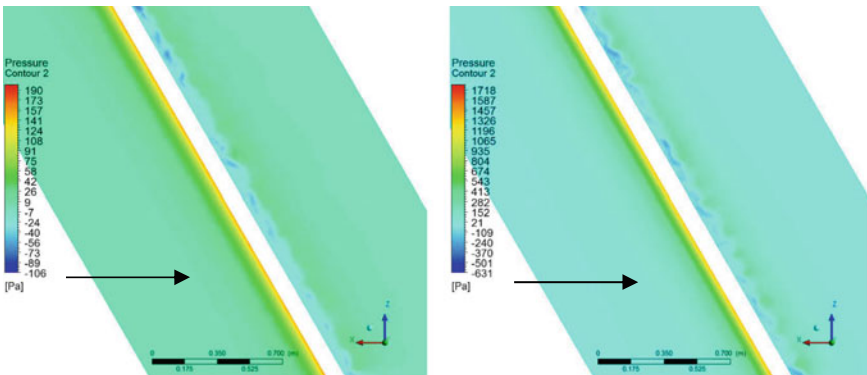


Fig. 2 Pressure distribution around the cylinder: $\phi = 60^\circ$; $\alpha = 60^\circ$, $\beta = 0^\circ$; (i) $Re = 1.1 \times 10^5$, (ii) $Re = 3.3 \times 10^5$. The approaching flow is marked with a black arrow

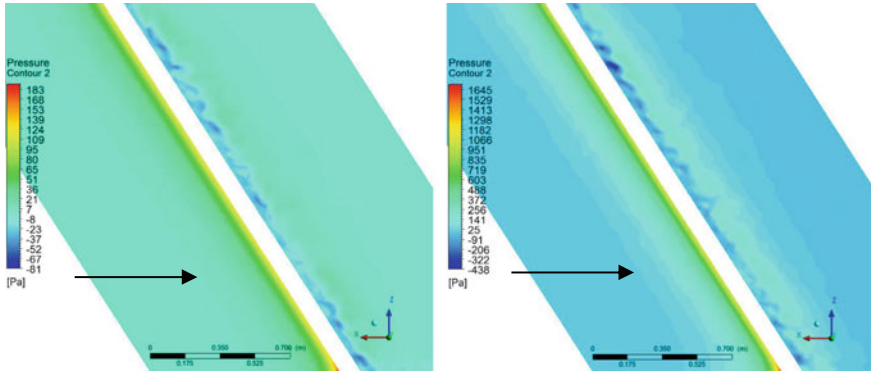


Fig. 3 Pressure distribution around the cylinder: $\phi = 60.5^\circ$; $\alpha = 50^\circ$, $\beta = 40^\circ$; (i) $Re = 1.1 \times 10^5$, (ii) $Re = 3.3 \times 10^5$. The approaching flow is marked with a black arrow

Starting with the well-known case of flow perpendicular to the cylinder, an area of high negative pressure develops along the leeward side of the cylinder. The results for this case are presented in Hoftzyer and Dragomirescu [4]. The developing vortices from the flow around the perpendicular circular cylinder leads to this build-up of pressure on the leeward face of the cylinder before the flow continues downstream. This variation in pressure along the length of the cylinder is due to the known three-dimensionality of the flow around circular cylinders perpendicular to the flow for this Reynolds number.

With the cylinder inclined to the flow the pressure surrounding the cylinder produces a rotational variation (appearance of rotating flow) of the pressure along the length of the leeward side of the circular cylinder. This rotational variation differs for different Reynolds numbers and angles of inclination and yaw tested with some rotational formations closely spaced while others are more spread along the length of the cylinder.

Examining the pressure distributions for the cases presented in Figs. 2 and 3, it is noted that there are regions of weak layer pressure variations along the leeward length of the cylinder including a non-periodic variation in the pressure distribution recorded in this area for cases $\alpha = 60^\circ$, $\beta = 0^\circ$, $\phi = 60^\circ$, $Re = 1.1 \times 10^5$, and $\alpha = 60^\circ$, $\beta = 0^\circ$, $\phi = 60^\circ$, $Re = 3.3 \times 10^5$ shown in Fig. 2.

In contrast, the velocity distribution along the leeward length of the cylinder shows rotational formations of low velocity intensity generated along the leeward side of the cylinder. These formations are closely spaced for the cases resulting in high negative pressures being reported along the leeward side of the cylinder: $\alpha = 50^\circ$, $\beta = 40^\circ$, $\phi = 60.5^\circ$, $Re = 1.1 \times 10^5$ and $\alpha = 50^\circ$, $\beta = 40^\circ$, $\phi = 60.5^\circ$, $Re = 3.3 \times 10^5$ shown in Fig. 3 for very similar angle of attack to the cases presented in Fig. 2: $\alpha = 60^\circ$, $\beta = 0^\circ$, $\phi = 60^\circ$.

4 Velocity Distribution Around the Cable Model

The velocity distribution is shown on the same plane defined above for the flow field upstream and downstream of the circular cylinders through the center of the cylinder for its entire length as shown in Figs. 4 and 5 for the previously defined cases. This was completed to aid in establishing the effect the flow pattern has on the pressure induced at the surface of the cylinder, in particular the flow along the leeward side of the cylinder.

Rotational formations are noted in the velocity distributions presented are of low velocity intensity along the leeward side of the cylinder. These formations are low intensity rotational formations with more widely spaced with gaps between them for areas of lower negative pressure: $\alpha = 60^\circ, \beta = 0^\circ, \phi = 60^\circ$ for both Reynolds number presented, $Re = 1.1 \times 10^5$ and $Re = 3.3 \times 10^5$, as shown in Fig. 4.

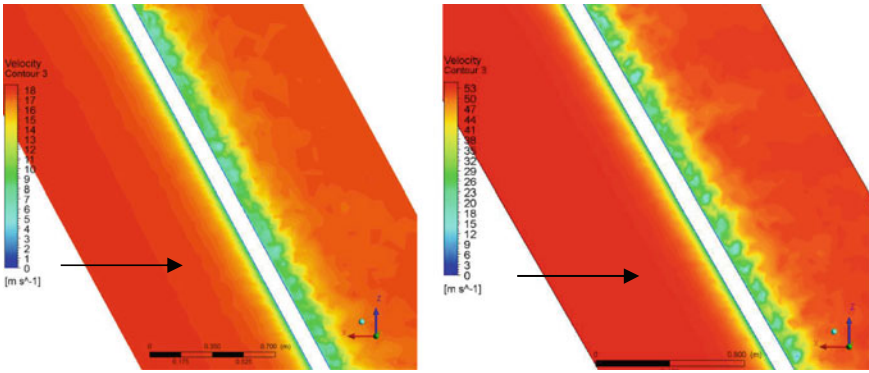


Fig. 4 Velocity distribution around the cylinder: $\phi = 60^\circ; \alpha = 60^\circ, \beta = 0^\circ$; (i) $Re = 1.1 \times 10^5$, (ii) $Re = 3.3 \times 10^5$. The approaching flow is marked with a black arrow

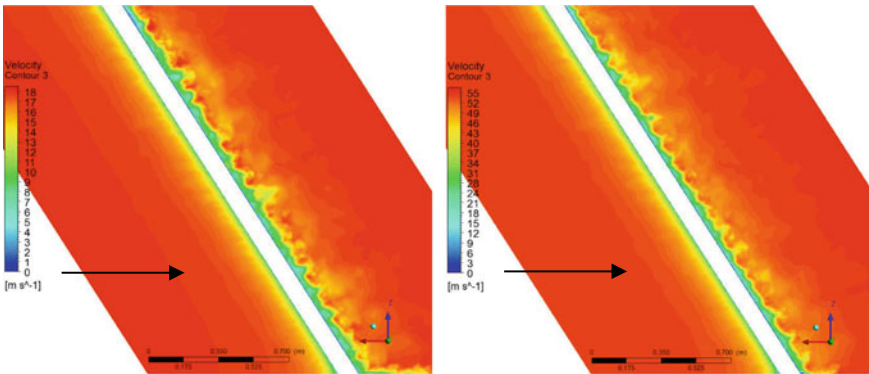


Fig. 5 Velocity distribution around the cylinder: $\phi = 60.5^\circ; \alpha = 50^\circ, \beta = 40^\circ$; (i) $Re = 1.1 \times 10^5$, (ii) $Re = 3.3 \times 10^5$. The approaching flow is marked with a black arrow

These formations are closely spaced for the cases where high negative pressures were reported: $\alpha = 50^\circ$, $\beta = 40^\circ$, $\phi = 60.5^\circ$, $Re = 1.1 \times 10^5$ and $\alpha = 50^\circ$, $\beta = 40^\circ$, $\phi = 60.5^\circ$, $Re = 3.3 \times 10^5$ shown in Fig. 5.

5 Pressure Distribution on the Leeward Side of the Cylinder

As noted above, the pressure distributions within the flow shows the development of a rotational variation of the flow along the leeward side of the circular cylinder. This rotational flow variation changes along the length of the circular cylinder with the change in Reynolds number, angle of inclination (α), and yaw of the cylinder (β) tested. Some of the rotational formations are noted to be closely spaced while others spread out widely over the length of the cylinder.

For the flow perpendicular to the cylinder, $\alpha = 0^\circ$, $\beta = 0^\circ$, $\phi = 0^\circ$, $Re = 1.1$ and 3.3×10^5 there were alternating pressures from negative to positive noted without presenting any identifiable pattern along the length of the cylinder [4]. This is not surprising with the well-known variation in pressure distribution along the length of the cylinder is due to the three-dimensionality of the flow.

With the entire leeward surface of the inclined and/or yawed cylinder presented, it is noted that the width of the pressure distribution along the leeward side of the cylinder also varied for the different cases. The pressure distribution varied as follows: from a narrow band for some cases, to a relative fairly wide band (for the cases $\alpha = 60^\circ$, $\beta = 0^\circ$, $\phi = 60^\circ$, for $Re = 1.1$ and 3.3×10^5 ; and $\alpha = 50^\circ$, $\beta = 40^\circ$, $\phi = 60.5^\circ$, for $Re = 1.1$ and 3.3×10^5 ; presented here in Figs. 6 and 7), or up to very wide band for other cases.

Small areas of low-pressure intensity, alternating with high intensity pressure along the length of the cable, formed wave shapes for the cases $\alpha = 50^\circ$, $\beta = 40^\circ$, $\phi = 60.5^\circ$, for $Re = 1.1$ and 3.3×10^5 , as shown in Fig. 7.

A possible change in flow regime may be encountered with the noted differences in the pressure distributions and associated flow patterns around the cylinder. These changes in regimes include variations in flow properties such as lower pressure along the leeward side of the cylinder, higher pressure along the leeward side of the cylinder, and altering between lower and higher pressure along the leeward side of the cylinder.

6 Cross-Coherence

In most of the experimental and numerical investigations carried out on the flow around circular cylinders the time domain analysis is the primary focus in evaluating the study results including the vortices in the wake of the inclined circular cylinder.

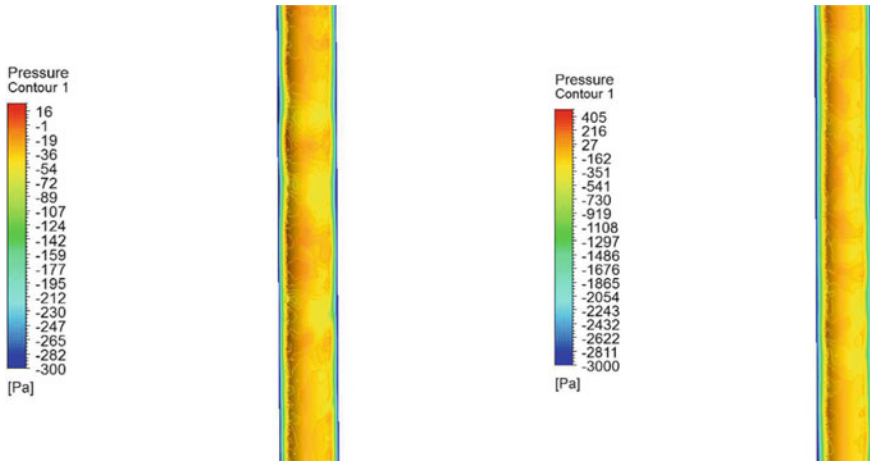


Fig. 6 Pressure distribution on the leeward side of the cylinder model: $\phi = 60^\circ$; $\alpha = 60^\circ$, $\beta = 0^\circ$; (i) $Re = 1.1 \times 10^5$, (ii) $Re = 3.3 \times 10^5$

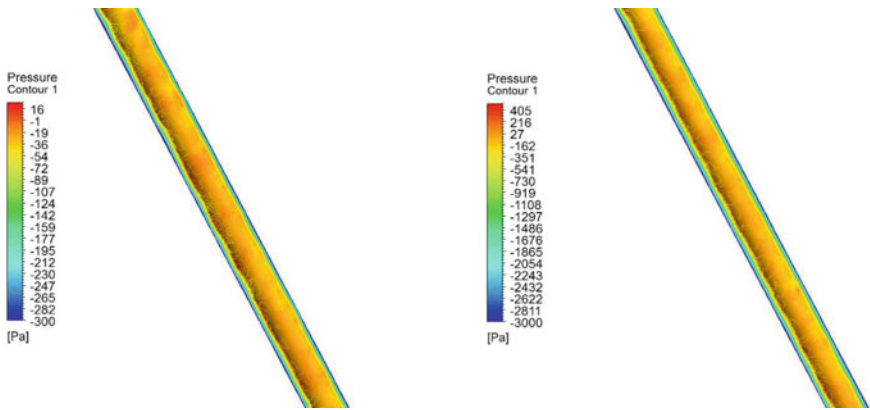


Fig. 7 Pressure distribution on the leeward side of the cylinder model: $\phi = 60.5^\circ$; $\alpha = 50^\circ$, $\beta = 40^\circ$; (i) $Re = 1.1 \times 10^5$, (ii) $Re = 3.3 \times 10^5$

This is some of the analysis carried out and presented as part of this study. The characteristics of the wake velocities behind the inclined circular cylinders are presented in the flow visualizations above to provide additional information to that provided by the time series for the cylinder wake velocities. By using the frequency domain analysis additional information about the wake vortices may be obtained [2].

To evaluate the results of this study in the frequency domain, the cross-coherence is calculated between coefficient of lift, the pressure coefficient along the leeward side of the cylinder, and the velocity fluctuation along the leeward side of the cylinder. It is assumed that the sampled variables used are all ergodic processes. The bispectrum

is used in statistics to search for nonlinear interactions and bicoherence builds on this as a squared normalized version of the bispectrum. The relationship between three sets of variables is measured by the cross-bicorrelation in the time domain [13] and gives an indication of the persistence of that interaction. The measurement in the frequency domain of such interaction is presented as the cross-bispectrum density. In the use of this analysis, the three data sets are segmented into possibly overlapping records where the mean from each record is removed, and then the time-domain window is applied.

For the same four cases outlined above, the results of the cross-coherence between the coefficient of lift, the pressure coefficient along the leeward side of the cylinder, and the velocity fluctuation along the leeward side of the cylinder are presented in Figs. 8 and 9. The lower the cross-coherence present between the variables the darker the colour shown, and the lighter the colour the more intensive coherence is between the variables for the given Strouhal (St) number, as shown in the colour scale in the right of the figures below. The cases presented in this section show varying levels of cross-coherence between the three variables with the cross-coherence intensity increasing with the increase in Reynolds number including more Strouhal numbers taken into consideration with the increase in Reynolds number.

The results for the overall study were categorized under three cases, low non-linear interaction, intermediate non-linear interaction, and high non-linear interaction, as illustrated by the cross-coherence. The case $\alpha = 50^\circ, \beta = 40^\circ, \phi = 60.5^\circ$, for $Re = 1.1 \times 10^5$ presented shows low non-linear interaction, and $\alpha = 60^\circ, \beta = 0^\circ, \phi = 60^\circ$, for $Re = 1.1$ and 3.3×10^5 , and case $\alpha = 50^\circ, \beta = 40^\circ, \phi = 60.5^\circ$, for $Re = 3.3 \times 10^5$ presented of the inclined circular cylinder shows intermediate non-linear interaction between the three variables mentioned.

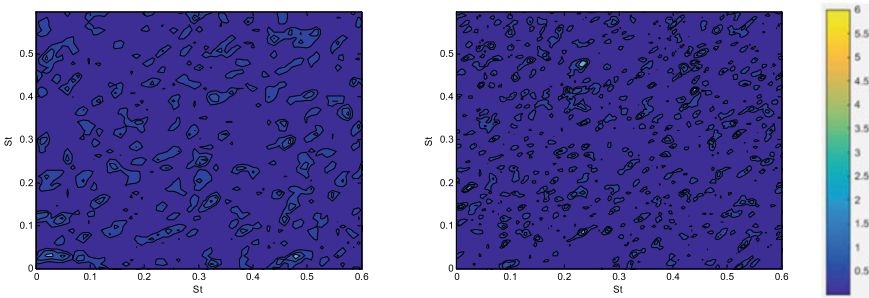


Fig. 8 Cross-coherence between C_L -Pressure-Total Velocity: $\phi = 60^\circ; \alpha = 60^\circ, \beta = 0^\circ$; (i) $Re = 1.1 \times 10^5$, (ii) $Re = 3.3 \times 10^5$

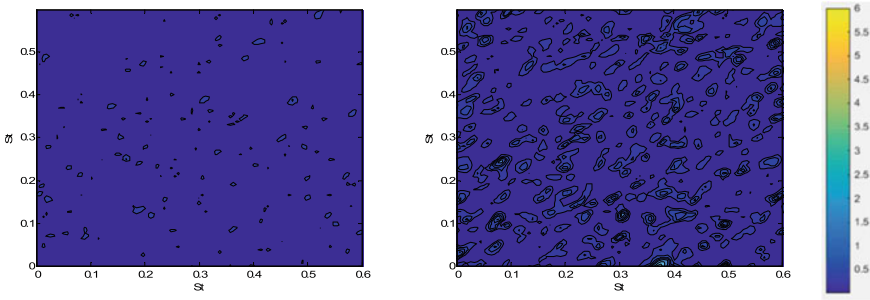


Fig. 9 Cross-coherence between C_L -Pressure-Total Velocity: $\phi = 60.5^\circ$; $\alpha = 50^\circ$, $\beta = 40^\circ$; (i) $Re = 1.1 \times 10^5$, (ii) $Re = 3.3 \times 10^5$

7 Conclusions

The focus of the current study is to numerically investigate the flow behaviour around the inclined and yawed circular cylinders. The objective was to clarify the occurrence and properties of the axial flow along on the leeward side of an inclined circular cylinder with the influence this could have on dry inclined cable galloping phenomenon of inclined cables for cable-stayed bridges. Several cases of inclined (α) and yawed (β) circular cylinders with angles between 0° and 60° , and 0° and 40° respectively were studied with the results for cases $\alpha = 60^\circ$, $\beta = 0^\circ$, $\phi = 60^\circ$; and case $\alpha = 50^\circ$, $\beta = 40^\circ$, $\phi = 60.5^\circ$; with Reynolds numbers of 1.1×10^5 and 3.3×10^5 presented here.

The pressure distributions for the cases presented noted that regions of weak layers of pressure variation along the leeward length of the cylinder including a non-periodic variation in the pressure distribution, or rotational formations of low velocity intensity generated along the leeward side of the cylinder with closely spaced formations cases resulting in high negative pressures.

The velocity distributions show the rotational formations of low velocity intensity generated along the leeward side of the cylinder, or low intensity rotational formations with widely spaced gaps between them noted in areas of lower negative pressure. These formations are closely spaced for the cases where there are high negative pressures.

When capturing the pressure distribution along the length of the leeward side of the cylinder some cases showed low-pressure intensity alternating with high intensity pressure along the length of the cylinder. Continuous shear layers detachment occurs as the flow is directed along the length of the cylinder creating lower pressure.

The cross-coherence results are presented above between the coefficient of lift, the pressure coefficient along the leeward side of the cylinder, and the velocity fluctuation along the leeward side of the cylinder are presented.

The results presented in the current paper add to the database of flow visualizations for flow around the inclined circular cylinder to help understand the flow-structure interaction for inclined cables of cable-stayed bridges. Further clarification is required for the influence of the yaw angle for flow around a circular cylinder inclined to the flow especially around the relative angle of 60° .

References

1. Cheng S, Larose GL, Savage MG, Tanaka H, Irwin PA (2008) Experimental study on the wind-induced vibration of a dry inclined cable—Part I: phenomena. *J Wind Eng Ind Aerodyn* 96:2231–2253
2. Elgar S, Van Atta CW, Gharib M (1990) Cross-bispectral analysis of a vibrating cylinder and its wake in low Reynolds number flow. *J Fluid Struct* 4:59–71
3. FHWA/HNTB (2005) Wind induced vibration of stay cables. Interim final report, RDT 05-004
4. Hoftyzer MS, Dragomirescu E (2022) Three-dimensional flow patterns of yawed inclined circular cylinders for cable-stayed bridges. In: Proceedings of the fourteenth America's conference on wind engineering, Lubbock, TX
5. Katsuchi H, Yamada H (2009) Surface pressure and axial flow measurements for indented-surface stay cable. In: Proceedings of 8th international symposium on cable dynamics '09, Paris, France, pp 215–222
6. Larose GL, Savage MG, Jakobsen JB (2003) Wind tunnel experiments on an inclined and yawed circular cylinder in the critical Reynolds number range. In: Proceedings of the eleventh international conference on wind engineering, Lubbock, TX, pp 1705–1712
7. Macdonald JHG, Larose GL (2003) Two-degree-of-freedom inclined cable galloping—Part 1: general formulation and solution for perfectly tuned system. *J Wind Eng Ind Aerodyn* 96:291–307
8. Matsumoto M, Shiraishia N, Kitazawab M, Kniselya C, Shiratoa H, Kimc Y, Tsujijia M (1990) Aerodynamic behaviour of inclined circular cylinders-cable aerodynamics. *J Wind Eng Ind Aerodyn* 33(1–2):63–72
9. Matsumoto M, Shirato H, Yagi T, Goto M, Sakai S, Ohya J (1995) Field observation of the full-scale wind-induced cable vibration. *J Wind Eng Ind Aerodyn* 91:13–26
10. Matsumoto M, Yagi T, Hatsudab H, Shimac T, Tanaka M, Naitoa H (2010) Dry galloping characteristics and its mechanism of inclined/yawed cables. *J Wind Eng Ind Aerodyn* 98:317–327
11. Saito T, Matsumoto M, Kitazawa M (1994) Rain-wind excitation of cables on cable-stayed Higashi-Kobe Bridge and cable vibration control. In: Proceedings of the international conference A.I.P.C.-F.I.P. Cable-stayed and suspension bridges, pp 507–514
12. Simiu E, Scanlan RH (1987) *Wind effect on structures*, 1st edn. John Wiley & Sons, New York, NY, USA
13. Swami A, Mendel JM, Nikias CL (1998) Higher-order spectral analysis toolbox for use with Matlab, The MathWorks
14. Zdravkovich MM (1997) *Flow around circular cylinders Vol 1: fundamentals*. 1st ed., Oxford University Press, New York, NY, USA
15. Zuo D (2014) Full-scale measurement of wind pressure on the surface of an oscillating circular cylinders. *J Wind Eng Ind Aerodyn* 133:65–72

Propagation of the Uncertainty in the Dynamic Behavior of OPGW Cables Under Stochastic Wind Load



Damián Campos , Andrés Ajas , and Marcelo Piovan 

Abstract In power transmission lines, conductors and guard wires are subjected to different types of mechanical vibrations, such as galloping, aeolian vibrations, and in the case of conductor bundles, sub-span oscillations. In this paper, a calibrated finite element model (FEM) is developed to evaluate the dynamic response due to aeolian vibrations of a single OPGW (Optical Ground Wire) cable with Stockbridge dampers. The model included the geometric, material, and damping characteristics of the OPGW cable and dampers, calibrated in previous work. The wind power input was simulated using a stochastic wind model based on Wiener processes, which allowed for a more realistic representation than deterministic models available in the literature. In addition, a Polynomial Chaos-Kriging (PCK) metamodel of the FEM model was constructed to reduce the computational cost of the model evaluation. The uncertainty of the wind load was propagated through the metamodel to obtain the distributions of the variables regarding the dynamic response, including the antinode and bending amplitudes, as a function of the Von Karman vortex shedding frequency. This was achieved using a Monte Carlo simulation approach, in which a large number of random simulations based on the wind model probability distribution were generated. The results were aggregated to obtain the distributions of the variables of interest. Field measurements were recorded with specific equipment to validate the simulation results. The results obtained in this study provide valuable insights into the dynamic behavior of cable-damper systems under aeolian vibrations, which are of great importance in their robust design.

Keywords Aeolian vibration · Stochastic wind model · Uncertainty propagation · Polynomial Chaos-Kriging · Stockbridge damper · OPGW cable

D. Campos (✉) · A. Ajas

Conductor Testing Laboratory, Department of Applied Mechanics, Faculty of Engineering, Universidad Nacional del Comahue, Buenos Aires 1400, 8300 Neuquén, Argentina
e-mail: damian.campos@fain.uncoma.edu.ar

M. Piovan

Center for Theoretical and Applied Research in Mechanics, Universidad Tecnológica Nacional FRBB, 11 de Abril 461, 8000 Bahía Blanca, Argentina

1 Introduction

The Optical Ground Wire (OPGW) cables protect the phase conductors of overhead power transmission lines from two main problems: high discharge currents caused by lightning strikes and instantaneous current surges generated by short circuits or faults. They are also used to provide data transmission for telecommunication purposes [1]. Overhead transmission lines are the mechanical structures with the most considerable extension of slender and flexible elements, which makes the cables highly exposed to wind. Under the action of this phenomenon, cables can vibrate and oscillate due to different types of aerodynamic and aeroelastic instabilities [2].

The problem of wind-induced vibration can be analyzed, in principle, according to the configuration of the line. If the line has only one conductor per phase or in the guard wire, the fundamental cause of vibration is vortex shedding, called aeolian vibration. If a bundle of conductors per phase forms the line, the primary cause of the oscillation is the vortex wake effect, known as sub-span oscillations. Finally, galloping is a self-excited vibrational phenomenon characterized by low frequency and large amplitude. Its occurrence is commonly associated with cables with surface ice formation in winter.

Due to the stochastic nature of wind speed, random phenomena arise that make it difficult to evaluate. Mainly, they produce harmful dynamic effects and damage to the lines. In the particular case of aeolian vibration, being the most frequent phenomenon, without proper protection, it causes fatigue problems, which can lead to breakage in the cables themselves and in the fittings and supports, and can also cause failures due to wear of the fittings. In order to mitigate these harmful effects and prevent probable failures, it is necessary to reduce vibrations and dynamic stresses within tolerable limits, which is achieved by increasing the damping of the system. This can be achieved by installing energy absorbers or Stockbridge-type dampers in the line [3].

Generally, in the design of transmission lines, the manufacturer recommends a specific type of damper and specifications on the distances of its positioning on the cable, guaranteeing a reduction of vibration amplitudes to the required levels. In this sense, projects should contemplate higher requirements for vibration damping employing Stockbridge dampers since the fiber optic cable is more sensitive to the consequences of vibrations due to the micro-curvatures of the fibers that occur during oscillations with the consequent possibility of signal attenuation. A vibration modeling and study are required to limit the maximum values and to set the damping conditions. In addition, the conditions for measuring vibrations after commissioning must be established to verify the calculations performed.

In this paper, a energy balance model based on a non linear finite-element formulation was used to analyze the dynamic behavior of a system composed of a single OPGW cable and Stockbridge dampers. In this case, since the finite element model (FEM) was calibrated in previous works, we intend to analyze the propagation of uncertainty in the system's response to the excitation of a stochastic wind

model. In order to alleviate the computational burden and propagate uncertainty more efficiently, the proposed simulation model is replaced by a metamodel based on Polynomial-Chaos-Kriging (PCK).

2 Deterministic Model

The Energy Balance Method (EBM) is the most popular concept used to predict the vibration of transmission lines. This method states that the cable self-damping and the dampers dissipate the wind's energy transferred by the wind to the conductor. The mathematical interpretation is given below:

$$P_W = P_{SD} + \sum_n (P_d)_n \quad (1)$$

Where (P_W) is the wind power input, (P_{SD}) is the power dissipated through cable self-damping, and $(P_d)_n$ is the power dissipated by the n th damper.

When implementing the EBM, a fundamental assumption is that steady-state cable vibration is a sinusoidal standing wave of the mode corresponding to the lock-in frequency and requires some experimental characterization of system parameters as indicated by International Standards. Several researchers have developed EBM-based calculation methods to predict the aeolian vibration level of the combined cable and damper system [4–6]. The EBM is simple to implement and does not involve a high computational cost. Nonetheless, this method is restricted since it does not consider the following issues: cable flexural rigidity, contributions from other vibration modes, traveling-wave effects, and damper mass. This implies that the cable is modeled as a string instead of a beam. Consequently, it can considerably influence the amplitude of cables vibration, affecting the clamps' bending stress. Also, the maximum amplitude of vibration is overestimated because of the negligible stiffness.

The motion equation, where the displacement vector is denoted by u , can be written in the following form:

$$[\mathbf{K}]u + [\mathbf{C}]\dot{u} + [\mathbf{M}]\ddot{u} = \mathbf{F} \quad (2)$$

where $[\mathbf{K}]$ and $[\mathbf{M}]$ are stiffness and mass matrix, whereas $[\mathbf{C}]$ is the Rayleigh damping matrix, whose calculation is explained later. The stiffness matrix has two main parameter EI and T that can affect the dynamics of the whole structure. Finally, the \mathbf{F} term relates to the system excitation force associated with the wind load.

In this work, the motion of the cable and the damper system is solved numerically using the finite element method (FEM), where the cable is modeled as a simply supported very slender beam under axial tension (T). The Euler-Bernoulli theory is applicable since the ratio of the length of the cable to its diameter (D) is smaller than the span length. The mass per unit length (ρA), is uniform across the cable span, since

the diameter is constant. The model accounts for the two-way coupling between the cable and the damper, the bending stiffness of both the damper and the cable, and the mass of the two counterweights of the damper [7].

The bending stiffness (EI) of the OPGW cable and the damper messenger cables is an important parameter in studying the dynamic response. Several models of the non-linear variation of this parameter with respect to the curvature have been developed [8, 9]. The non-linearity of bending stiffness creates a hysteresis that dissipates energy. In addition, the self-damping with hysteric characteristics depends on other factors such as the amplitude of vibration and axial tension.

To account for the self-damping of the cable, a Rayleigh damping model was used alongside the constant bending stiffness model. This damping model is a linear combination of the mass and stiffness matrix of the finite element method equations of motion (Eq. 3).

$$[\mathbf{C}] = \alpha[\mathbf{M}] + \beta[\mathbf{K}] \quad (3)$$

Where α and β are the Rayleigh damping coefficients related to the modal damping and frequency of the cable, respectively [10].

In order to solve the equations of motion of the system, a FEM model was developed using the open source CodeAster software [11]. The geometry proposed of the cable was a one dimensional discretization, where a density function was applied in order to increment the number of finite elements near the clamps. A non-linear solver was applied to evaluate the dynamic evolution of the cable. Energy balance equations are established for the Newmark time integration algorithm, forming a sequence applicable to balancing internal forces due to inertia, damping, and stiffness with the external forces constituting the wind load [12].

3 Uncertainty Propagation

Uncertainty propagation usually requires a large number of iterations of the deterministic model (M) for different values of the input parameters, e.g., by a Monte Carlo simulation procedure. In order to reduce the computational cost associated with this process, it was considered necessary to implement a metamodel to evaluate the system's dynamic behavior. In particular, Kriging models have gained popularity in recent years thanks to their great flexibility to approximate responses with a high degree of nonlinearity by providing statistical information on the error made in the prediction [17]. The Kriging feature is to interpolate the local variations of the computational model output as a function of neighboring experimental design points. In contrast, Polynomial Chaos Expansions (PCE) approximate the global behavior of M using a set of orthogonal polynomials [18].

Combining the two techniques is intended to capture the global behavior of the computational model with the set of orthogonal polynomials in the trend of a universal Kriging model and the local variability with the Gaussian process (σ^2). This approach, called Polynomial-Chaos-Kriging (PCK), combines these two different

metamodeling techniques and their characteristics and can be expressed in polynomial notation as follows:

$$M \approx M^{(PCK)}(x) = \sum_{\alpha \in A} a_{\alpha} \psi_{\alpha}(x) + \sigma^2 Z(x) \tag{4}$$

Where $\sum_{\alpha \in A} a_{\alpha} \psi_{\alpha}(x)$ is a weighted sum of orthonormal polynomials describing the mean value of the Gaussian process, and A is the set of polynomial indices. While $Z(x)$ is a stationary Gaussian process of zero mean and unit variance, defined by an autocorrelation function $R(|x - x'|; \phi)$ and parameterized by a set of hyperparameters ϕ . In brief, the construction of a PCK metamodel consists of two parts: the determination of the optimal set of polynomials contained in the regression part (i.e. truncation A) and the calibration of the correlation hyperparameters ϕ , as well as the Kriging parameters $\{\sigma^2, a_{\alpha}\}$. Finally, the model uncertainty was propagated by the generation of Monte Carlo samples.

4 Wind Model

As the function changes with time, we regard the force generated by the shedding of vortices as a stochastic process. There are numerous stochastic processes available to represent uncertainties in the flow field, which affect the system's external excitation. The normalized mean power input can be calculated using the time history signal of the signal force, as stated in the following equation [13]:

$$\frac{\bar{W}}{f^3 D^4} = \text{func} \left(\frac{u}{D} \right) = \frac{1}{n T_s} \frac{1}{f^3 D^4} \int_t^{t+nT_s} F_{L(t)} \dot{u}(t) dt \tag{5}$$

Where \bar{W} is the mean power input, n is the number of cycles in the time signal, T_s the period, $F_L(t)$ the time history of the lift force and $\dot{u}(t)$ the cable velocity. In addition, the uncertainties around the wind power input due to the flow field are modeled as a bounded, weakly stationary, narrowband random process $\eta(t)$ given [14]:

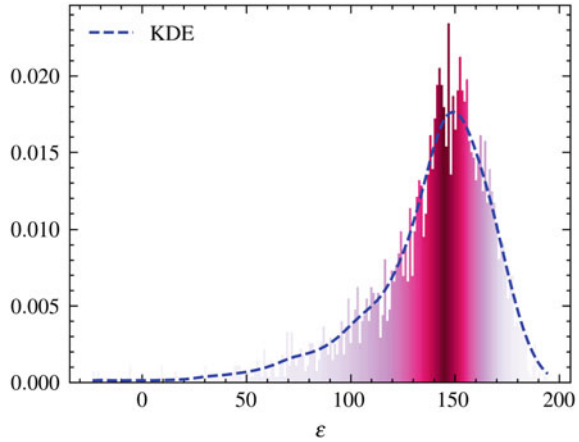
$$F_L = \frac{1}{2} \rho U^2 D C_L \eta(t) \tag{6}$$

$$\eta(t) = \cos(vt + \xi W(t) + \gamma)$$

Where v is the central vortex shedding frequency, $W(t)$ is the standard Wiener process, C_L is the non-dimensional lift coefficient, U is the free stream velocity, ρ the flow density, and ξ is the strength of the random process. The constant γ corresponds to the phase of the vortex-induced excitation. The lift coefficient is obtained from the following relationship [15]:

$$C_{L_r} = C_L r^2 \tag{7}$$

Fig. 1 Probability Density Function (**PDF**) of parameter ϵ and calculated KDE



Where r is the parameter that defines the wind velocity variations in the synchronous field. Assuming a harmonic motion and a linear relationship between u/D and C_L by the proportionality constant K_L , the following expression is obtained for the wind power input, for $\frac{u}{D} < 0.3$:

$$\epsilon = \frac{\pi \rho K_L}{n T_s S_t^2} \int_t^{t+nT_s} \eta(t) \cos(2\pi f t) dt \quad (8)$$

$$\text{func} \left(\frac{u}{D} \right) = \epsilon \left(\frac{u}{D} \right)^2$$

The parameter ϵ is dependent of the following random variables. The phase constant γ is a uniform random variable: $\gamma \sim U[0, 2\pi]$. In addition, S_t is Strouhal number and is assumed to distribute uniformly between values from the literature, such as $S_t \sim U[0.18, 0.2]$. Indeed, the K_L constant is set as a uniform random variable $K_L \sim U[3, 3.6]$, based on the experimental data from the literature [15]. The stochastic process samples are generated using the Monte Carlo simulation approach, generating a total of 100,000 samples. The Probability Density Function (PDF) of ϵ is presented and the corresponding Kernel Density Estimation (KDE) (see Fig. 1). The stochastic model is compared with the literature wind power models (see Fig. 2).

5 Case Study

The case study focuses on the OPGW cable of a high voltage power line (500kV) installed in the northern Patagonian region of Argentina, with more than 30 years of commercial operation. The characteristics of the OPGW cable and the dampers correspond to those described previously. The cable is composed of two layers of

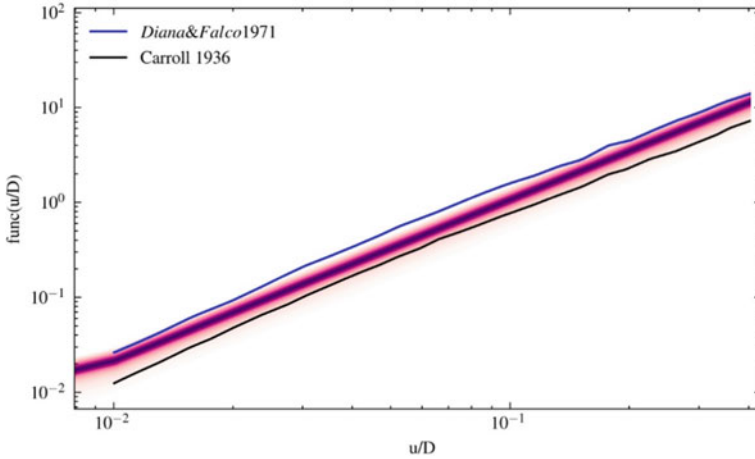


Fig. 2 Stochastic wind model contrast with specific power input literature data [16]

aluminum wrapping steel and aluminum alloy wire and a core where an aluminum casing surrounds several layers of polymeric materials and optical fiber wires. The Stockbridge dampers installed in the line are symmetrical with 0.64 kg of weight per mass. The parameters for the FEM model for the dynamical properties of the cable and the damper were calibrated in previous work by a Bayesian Inversion with experimental data [19, 20]. The analysis contemplates a span with a length of 500 m in which it is proposed the installation of two dampers at each end of the span (four dampers in total), at a distance of 0.6 m from the suspension clamps and 0.6 m from subsequent dampers. In this setup, a tension load of 10% UTS is specified.

The measurements of aeolian vibrations were made with a VIBREC 500 [21] aeolian vibration sensor and recorder (see Fig. 3). The processing of information was made through specific software. The recorder measures the differential displacement (vertical movement) between the suspension clamp and the cable during vibration



Fig. 3 VIBREC 500 installation detail (a) VIBREC 500 sensor, (b) Input arm of the recorder, (c) OPGW cable and Stockbridge damper system, and (d) Suspension clamp

activity. The input arm of the recorder is secured to the cable at a specified distance from the suspension hardware. In this sense, the IEEE recommends 89 mm distance from the last contact point of the cable with the bolted suspension clamp and the vibration sensor. In this case, given the type of clamp installed (armor rod), the sensor is installed 200 mm from center to clamp, standardizing the measurement to 89 mm from the correction proposed by the specific measurement software.

Recording periods have a three-week established duration. Because of this, continuously measuring vibrations becomes unfeasible due to hardware limitations. The recorder must then take 10 s measurements every 15 min to provide the desired resolution in the data [22]. The technical specifications consider maximum amplitude values to 150 μm peak-to-peak for 95% of the total cycles registered and 250 μm peak-to-peak for the remaining cycles. The analysis of the aeolian vibrations records showed that the maximum value reached in 95% of cycles was 125 μm peak-to-peak.

6 Results and Discussion

This section presents the results obtained from the application of the proposed methodology in the case study. The vibration amplitude for the standardized Y_b is presented and contrasted with the field measurement records. Uncertainty propagation due to stochastic wind excitation is observed in the band up to the 95% percentile of the PCK metamodel. Good agreement with the records is seen, particularly for the excitation frequencies that produce the maximum displacements (See Fig. 4).

Some of the observed discrepancies may be due to the following phenomena. The modeling of the cable is done for a stationary condition, however, due to the complex effects between the turbulence of the flow and the cable-wind interaction, this condition is hardly encountered, and multiple frequencies are excited. Also, the calibration of the Stockbridge damper properties was performed using data obtained on a shaker and not in situ on the cable line.

Due to the high computational cost of the model evaluation, the design of the experiment for the construction of the metamodel contemplated the implementation of a Docker container which was evaluated in a parallelized configuration on an on-demand cloud computing provider. The number of model evaluations for the metamodel construction was 1000, and demanded a computational cost of 10,800 vCPU processing hours. By means of the proposed parallelization, the results were obtained in a few hours.

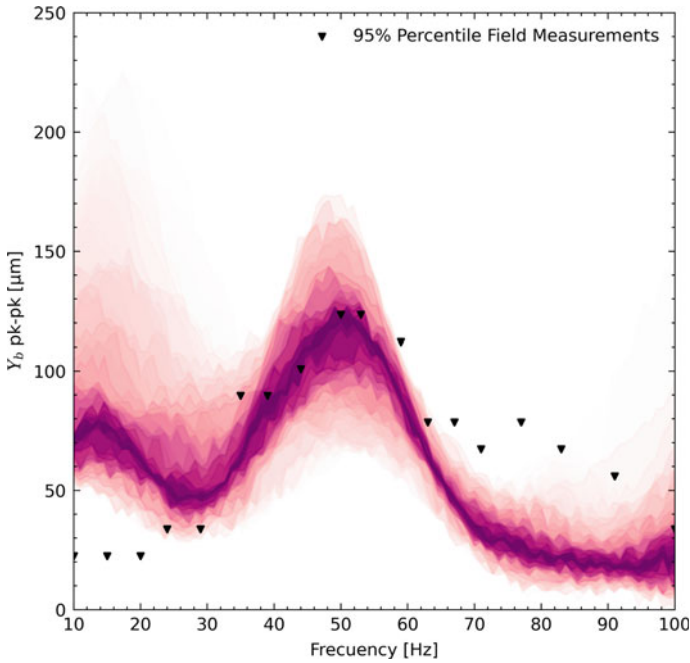


Fig. 4 Uncertainty propagation of vibration amplitude (Y_b at 89 mm) as a function of frequency. A colormap (RdPu) is applied from increasing percentiles up to the 95th, where the strongest shade of purple color corresponds to the median for every frequency

7 Conclusion

This work proposes a stochastic wind model based on the specific power absorbed as a function of vibration amplitude. Its implementation allows propagating the uncertainty associated with the large scatter evident in the curves obtained by various research groups over the last decades (see Fig. 2).

The methodology is a powerful tool to evaluate models of increasing complexity by studying the interaction of the stochastic variables involved. The application of surrogate modeling techniques considerably reduces the cost of assessing the proposed models, making this analysis technically feasible. In short, the methodology provides more accurate information about the parameters of interest for designing and verifying power transmission lines.

References

1. Günday A, Karlık S (2013) Optical fiber distributed sensing of temperature, thermal strain and thermo-mechanical force formations on OPGW cables under wind effects. In 2013 8th international conference on electrical and electronics engineering (ELECO), pp 462–467
2. Cosmai U, Van Dyke P, Mazzola L, Lillien JL (2017) Conductors motions. In Papailiou K (Ed) Overhead lines. Springer International Publishing, pp 559–711
3. Wang Z, Li H-N, Song G (2021) Aeolian vibration control of power transmission line using Stockbridge type dampers - a review. *Int J Struct Stab Dyn* 21(01):2130001. <https://doi.org/10.1142/S0219455421300019>
4. Claren R, Diana G (1969) Mathematical Analysis of Transmission Line Vibration. *IEEE Trans Power Apparatus Syst PAS-88(12):1741–1771* (1969). <https://doi.org/10.1109/TPAS.1969.292291>
5. Hagedorn P (1982) On the computation of damped wind-excited vibrations of overhead transmission lines. *J Sound Vib* 83(2):253–271. [https://doi.org/10.1016/S0022-460X\(82\)80090-4](https://doi.org/10.1016/S0022-460X(82)80090-4)
6. Lu M (2004) A practical approach to the Aeolian vibration of overhead power lines. In: Proceedings of 15th conference electric power supply industry, pp 1–8
7. Langlois S (2013) Prediction des vibrations eoliennes d'un systeme conducteur-amortisseur avec une methode temporelle non lineaire. PhD dissertation Universite de Sherbrooke (Canada)
8. Papailiou K (1997) On the bending stiffness of transmission line conductors. *IEEE Trans Power Deliv* 12:1576–1588
9. Foti F, Martinelli L (2016) An analytical approach to model the hysteretic bending behavior of spiral strands. *Appl Math Model* 40(13):6451–6467
10. Zhu Z, Meguid S (2007) Nonlinear FE-based investigation of flexural damping of slacking wire cables. *Int J Solids Struct* 44:5122–5132
11. Finite element *code_aster*, Analysis of Structures and Thermomechanics for Studies and Research. <http://www.code-aster.org>. Accessed 28 March 2023
12. Krenk S (2006) Energy conservation in Newmark based time integration algorithms. *Comput Methods Appl Mech Eng* 195(44–47):6110–6124. <https://doi.org/10.1016/j.cma.2005.12.001>
13. Muggiasca S, Belloli M, Diana D (2018) Specific power input: comparison among rigid and flexible models. *J Wind Eng Ind Aerodyn* 173:180–186. <https://doi.org/10.1016/j.jweia.2017.12.004>
14. Adhikari S, Rastogi A, Bhattacharya B (2020) Piezoelectric vortex induced vibration energy harvesting in a random flow field. *Smart Mater Struct* 29(3) (2020). <https://doi.org/10.1088/1361-665X/ab519f>
15. Diana G, Falco M (1971) On the forces transmitted to a vibrating cylinder by a blowing fluid. *Meccanica* 6(1):9–22
16. Tavano F, Cloutier L, Claren R, Ervik M, Hagedorn P, Hardy C, Kern G, Krispin H-J, Möcks L, Rawlins CB, Dulhunty PW, Manenti A, Tunstall M, Asselin JM, Bückner W, Havard DG, Hearnshaw D, Diana G (2018) Modelling of aeolian vibrations of single conductors. In: Diana G (eds) Modelling of vibrations of overhead line conductors. CIGRE Green Books. Springer, Cham. https://doi.org/10.1007/978-3-319-72808-7_1
17. Tong C, Wang J, Liu J (2019) A Kriging-based active learning algorithm for mechanical reliability analysis with time-consuming and nonlinear response. *Math Probl Eng*. <https://doi.org/10.1155/2019/7672623>
18. Schöbi R, Sudret B, Wiart J (2015) Polynomial-Chaos-based Kriging. *Int J Uncertainty Quantification*, Begell House Publishers 5:171–193
19. Campos D, Ayras A, Piovan M (2021) Bayesian model calibration for bending stiffness assessment in OPGW cables. In: International conference on electrical, computer and energy technologies (ICECET), Cape Town, South Africa, 2021, pp 1–5. <https://doi.org/10.1109/ICECET52533.2021.9698575>

20. Campos D, Ajas A, Goytiño L, Piovan M (2022) Inversión bayesiana de un modelo dinámico no lineal para amortiguadores tipo Stockbridge., XV Congreso Iberoamericano de Ingeniería Mecánica. In: Universidad Politécnica de Madrid
21. Pfisterer Vibrec 500 Recorders, <http://www.pfisterer.com>. Accessed 30 March 2023
22. IEEE Guide for Aeolian Vibration Field Measurement of Overhead Conductors. In: IEEE Std 1368-2006, pp 1–35 (2006). <https://doi.org/10.1109/IEEESTD.2006.371267>

Investigation of Ice Accretion Conditions in Observed Galloping Events of Four-Bundled Conductor



Saki Taruishi  and Hisato Matsumiya 

Abstract Ice accretion characteristics and the relationship between ice accretion and tension fluctuations caused by galloping were investigated based on 28 icing events observed in the test line located on a mountain ridge in Japan. The details of three significant ice accretion and galloping events that were well available from the data and photographs regarding ice accretion were discussed. Observation results showed that ice accretion grows when the temperature ranges from -2.0 to -0.5 °C. It melts at a temperature above -0.5 °C or a humidity beneath 100%. The wind speed during galloping is greater when the ice accretion height is greater. Additionally, galloping becomes less steady when the ice accretion shape is rougher. The average tension correlates well with the ice accretion amount during no galloping and weak wind conditions. Building a method for removing the influence of wind from the average tension is also important for estimating the ice accretion amount of the event without weak wind.

Keywords Ice accretion · Galloping · Four-bundled conductor · Field observation

1 Background and Objective

The galloping of transmission lines is a self-excited vibration that occurs under ice and snow accretion and strong wind. Galloping may lead to severe electrical faults and equipment fatigue. To prevent galloping, various galloping countermeasure devices are developed and verified [1]. However, this is costly if countermeasures are installed on all conductors. It is important to clarify the galloping occurrence mechanisms and conditions (for example, wind speed and direction; and amount and shape of ice accretion) to identify the conductors requiring galloping countermeasures.

S. Taruishi (✉) · H. Matsumiya
Central Research Institute of Electric Power Industry, Tokyo 270-1104, Japan
e-mail: taruishi@criepi.denken.or.jp

H. Matsumiya
Kyoto University, Kyoto 615-8530, Japan

For understanding galloping characteristics, various galloping observations were conducted, for example, observations of various single conductors by Rawlins [2] and observations of various single and bundle conductors by Lilien [3]. The authors also have been conducting long-term galloping observations of four-bundled conductors that are frequently observed galloping in Japan [4, 5]. The relationship between the wind speed and tension fluctuation caused by galloping determined through observations showed that galloping occurred when the wind speed exceeded a specific value during ice accretion. In addition, the tension fluctuation reached the maximum value at a particular wind speed. However, galloping did not always occur, even under the above conditions. Galloping seems to be influenced not only by the wind speed and existence of ice accretion but also by the ice amount and shape.

This study investigated the relationship between the ice accretion conditions and tension fluctuations caused by galloping based on ice accretion events observed in two winter seasons. The observation was conducted in the “Tsuruga test line” in Japan, which was the same test line used in [4] and [5].

2 Observation Method

Figure 1 shows the location and an overview of the Tsuruga test line. It is located in central Japan, approximately 10 km from the Sea of Japan. The towers are built on a mountain ridge, approximately 700–800 m above sea level. Because of this terrain condition, ice accretion and galloping of the conductor are frequently caused by strong north winds during the winter. The observation target in this study was Phase C in Fig. 1. It consisted of four-bundled aluminum steel-reinforced ACSR conductors with a nominal cross-sectional area of 410 mm^2 , which are normally used in Japan. The span length, sag, and height difference between two support points were 345, 10.8, and 95 m, respectively. The support points are at the arm of the tower, 40 m from the ground.

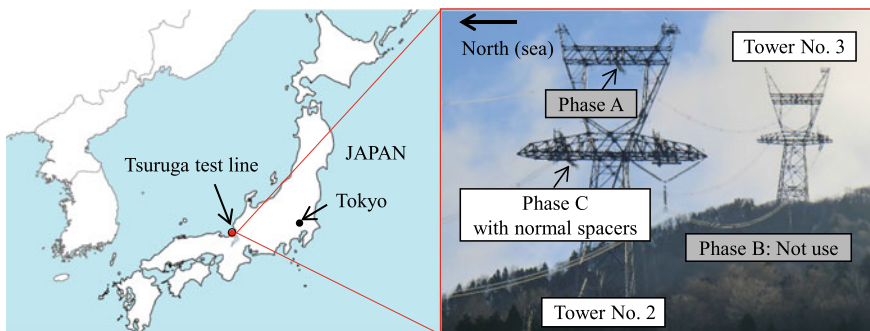


Fig. 1 Location and overview of Tsuruga test line

Observations were conducted from 2018 to 2019 (fiscal years). In this period, normal spacers, which are always installed on bundled conductors to keep distance between sub-conductors, were installed in Phase C. It should be noted that galloping countermeasure devices were not installed in this period.

Figure 2 shows the layout of the measurement equipment. The data presented in Table 1 was obtained from this equipment. From tension data measured during each ice accretion event, tension fluctuations were calculated as the difference of the maximum and minimum tension in 10 min data. Tension data averaged for the four conductors, that represents the tension per one sub-conductor, with a band-pass filter and cut-off frequencies of 0.6 and 0.8 Hz were used because this value is proven to be correlated with the peak-to-peak vertical amplitude caused by galloping [5]. Additionally, average wind speeds orthogonal to the direction of the span (orthogonal wind speed) were calculated from the 10 min wind speed and direction data.

Ice accretion characteristics (for example, the time when the ice accretion starts and stops growing, the time when the dropping or melting of ice occurs, and ice accretion height to conductor diameter and shape) were estimated using photographs captured by a camera installed at the 1/4 position of the span. Although the ice accretion characteristics should be measured at various positions of the span in the future, the relationship between galloping and ice accretion characteristics can be evaluated to a certain extent by comparing the data in various icing events obtained through the same position. Note that the ice accretion characteristics were unavailable at night (from 17:36 to the next 6:36); and when the conductors were not visible due to poor weather conditions. Additionally, the average tension (increment from the no-ice condition), used as an indicator of the ice accretion amount in the author’s previous research [4], is calculated to evaluate the relationship with ice accretion characteristics.

Fig. 2 Layout of the measurement equipment

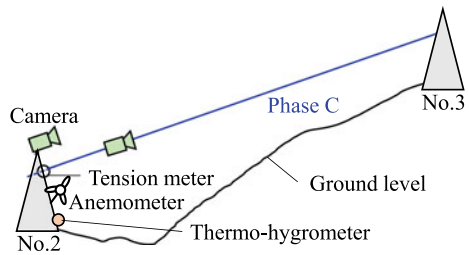


Table 1 List of observation data

	Equipment	Sampling frequency
Tension	Tension meters	20 Hz
Wind direction and speed	Anemometer	20 Hz
Temperature and humidity	Thermo-hygrometer	Every 10 min
Image of ice accretion	Cameras	Every 10 min (6:36–17:36)

3 Observation Result

3.1 Overview of Observed Ice Accretion Events

From two winter observations, 28 ice accretion events were obtained. They were determined based on the tension and photograph data. Only in-cloud icing occurs in these events. Figure 3 shows the relationship between the average orthogonal wind speeds and tension fluctuations in all events. Galloping starts to occur at wind speeds above 5 m/s. The tension fluctuation gradually increases as the wind speed increases and reaches a peak value when the wind speed is around 10 m/s. At wind speeds above 10 m/s, the tension fluctuation decreases as the wind speed increases, although some examples show that the tension fluctuation exceeds 8 kN around the wind speed of 15 m/s. Generally, the average orthogonal wind speeds and tension fluctuations have the same relationship as in previous research [5].

Of many observed events, three typical ice accretion and galloping events are emphasized in Fig. 3. Table 2 shows their characteristics. The date of each event was determined by the time just before ice accretion started and after the ice completely dropped. The icing height was estimated by the photograph of the ice accretion that seems to be closest to the condition during galloping. The icing height was averaged for the two sub-conductors on the leeward side, in which the whole ice accretion was visible. These events have similar characteristics regarding the maximum tension fluctuation, approximately 8 kN. However, the ice height and wind speed at the maximum tension fluctuation depend on the event.

In Sect. 3.2, the details of icing and the galloping process in these events and the relationships between icing and galloping characteristics will be explained using the meteorological and tension data and photographs of ice accretion on the conductors.

Fig. 3 Relationship between the average orthogonal wind speeds and tension fluctuations

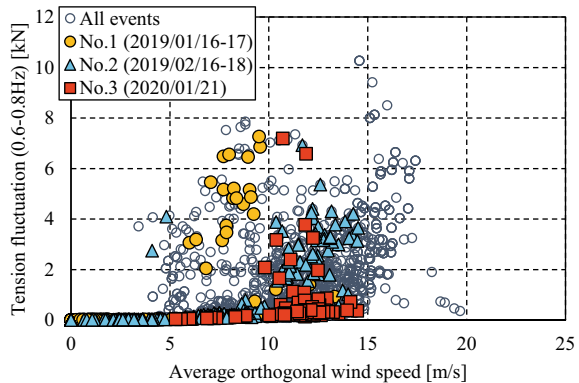


Table 2 Typical ice accretion and galloping events

No	Date	Icing height at 1/4 span	Max. tension fluctuation [kN]	Wind speed at max. Tension fluctuation [m/s]
1	2019/01/16 08:30 –01/17 11:00	0.4D	7.9	9.5
2	2019/02/16 11:30 –02/18 08:30	0.7D	7.7	11.7
3	2020/01/21 06:30 –01/21 21:00	0.4D	7.7	11.1

* D: conductor diameter

3.2 Ice Accretion and Galloping Characteristics in Typical Three Events

Event No. 1 (2019/01/16–17) Figures 4 and 5 show the observation data and process of icing of event No.1. The left side is the upwind side in the following photographs of ice accretion. Icing started at around 8:30 (see Fig. 4a) when the temperature and humidity were $-0.8\text{ }^{\circ}\text{C}$ and 100%, respectively. It continued until around 15:00 (see Fig. 4b), when the temperature decreased to $-2.0\text{ }^{\circ}\text{C}$. Then, the temperature continued to decrease, reaching the minimum value of $-2.5\text{ }^{\circ}\text{C}$ at 21:00. In contrast, ice accretion stopped growing from 15:00 and remained constant until the next morning (see Fig. 4c). Ice accretion started to melt at 10:00 when the temperature increased to $-0.5\text{ }^{\circ}\text{C}$ and had completely dropped by 11:00 when the temperature increased to $0\text{ }^{\circ}\text{C}$ (see Fig. 4d). The humidity remained 100% until the end of the event. Additionally, the ice accretion angles were always diagonally downwards towards upwind directions.

Galloping started at around 13:00 when the wind speed was 9 m/s and stopped at around 13:30 when the wind speed decreased and the ice accretion slightly increased. However, galloping started again at around 15:00 and it continued until 17:00 while the wind speed decreased to around 7 m/s and the ice accretion increased more. According to the previous study, galloping occurs when the rotational angle of the conductor reaches a certain value due to the action of the moment of ice accretion and buffeting caused by wind [4]. It indicates that the rotational angle of the conductor reached the same angle in the above two conditions.

The average tension was near 0 kN at 8:30 before the icing started, and it gradually increased until 20:00 although the ice accretion stopped growing at 15:00. This phenomenon is owing to galloping and buffeting. Galloping seems to increase the average tension because it is larger during galloping than a previous instance. Additionally, buffeting caused by wind decreases the average tension. This is because the wind blows upwards at an angle of around 10° from the horizontal direction in the Tsuruga test line and it lifts up the conductors. The average tension increased until 20:00 because the wind speed decreased from 15:00 to 20:00. Although the average

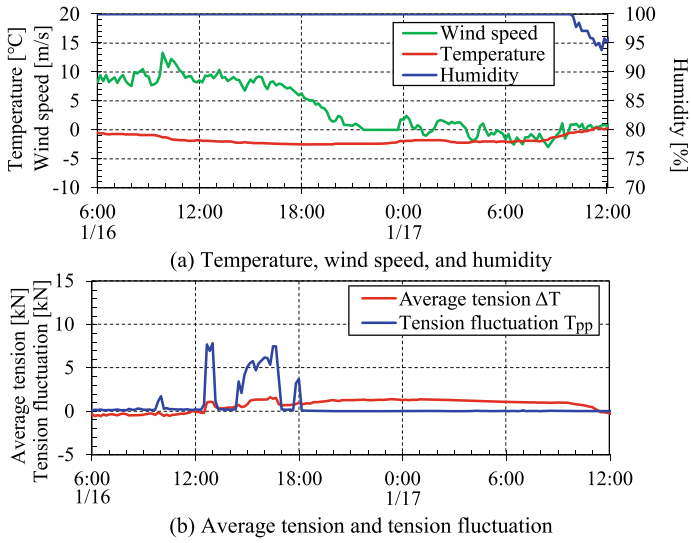


Fig. 4 Observation data of event No.1 (2019/01/16–17)

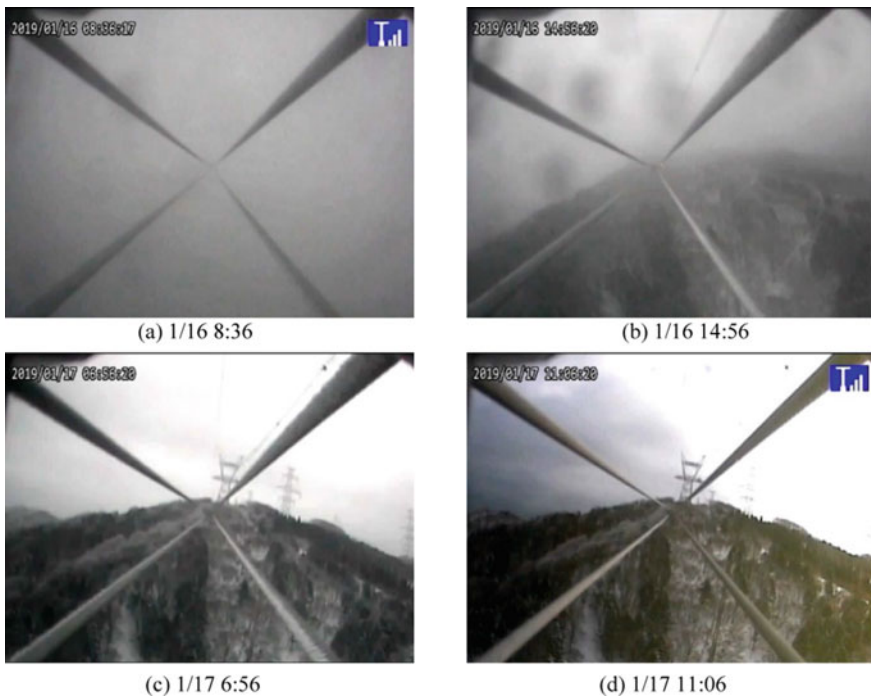


Fig. 5 Process of ice accretion of event No.1 (2019/01/16–17)

tension correlates with the ice accretion amount, it is affected not only by the ice accretion amount but also galloping and buffeting.

Event No. 2 (2019/02/16–18) Figures 6 and 7 show the observation data and process of ice accretion of event No. 2. Icing started at 11:46 (see Fig. 7a) when the temperature and humidity were $-0.3\text{ }^{\circ}\text{C}$ and 100%, respectively. Ice accretion continued growing until at around 17:36 (see Fig. 7b) and it seems to increase a little at night because ice accretion height in the next morning became a little greater (see Fig. 7c). Ice accretion gradually melted on 2/17 (see Fig. 7d) because of solar radiation although the temperature was in the range of -3.0 to $-2.0\text{ }^{\circ}\text{C}$. On 2/18, ice accretion melted further (see Fig. 7e) and completely dropped at 8:36 (see Fig. 7f) when the temperature increased to $-0.2\text{ }^{\circ}\text{C}$. As with event No. 1, the humidity kept around 100% and the ice accretion angles were always diagonally downwards towards an upwind direction.

Galloping occurred from 2/16 17:00 to 2/17 2:00 when the wind speeds were 11–14 m/s and it stopped by 8:50 when the wind speed decreased to 7 m/s. However, the correct time when galloping stopped is unclear because of missing values due to the battery outage of observation equipment. As far as available data, the maximum tension fluctuations is 7.7 kN, which is close to the value of event No.1. It indicates that greater wind speed is required to reach the rotation angle that galloping is expected to occur when there is much ice accretion on the conductor.

The average tension was near 0 kN at 11:30 before the icing started, and it gradually increased until around 17:00. While the change of the ice accretion amount during night is small, average tension increased and decreased significantly. Additionally, the average tension from 2/17 8:30 to 19:00 seems to change with increasing and

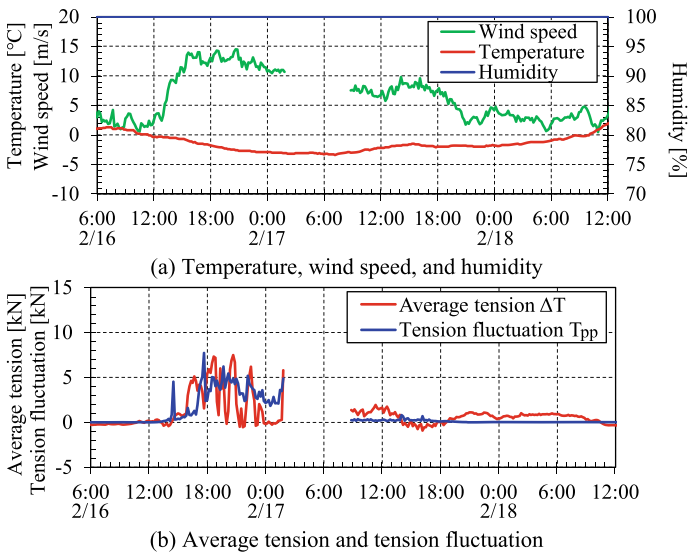


Fig. 6 Observation data of event No. 2 (2019/02/16–18)

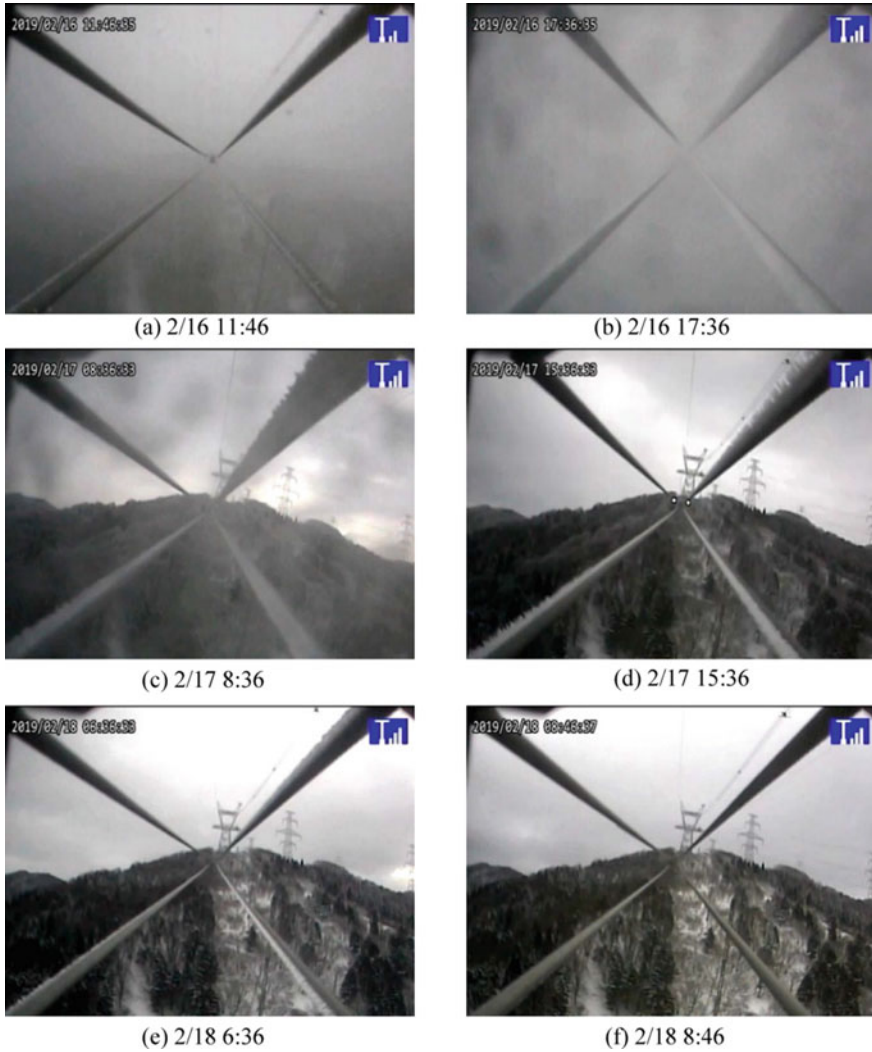


Fig. 7 Process of ice accretion of event No. 2 (2019/02/16–18)

decreasing wind speed. As with event No.1, average tension fluctuation is affected by the ice accretion amount, galloping, and wind speed.

Event No. 3 (2020/01/21) Figures 8 and 9 show the observation data and process of ice accretion of event No. 3. Icing started at 6:46 (see Fig. 9a) when the temperature and humidity were $-0.5\text{ }^{\circ}\text{C}$ and 100%, respectively. Ice accretion gradually grew until 16:56 (see Fig. 9b-d) when the temperature was -1.3% . Whereas there was no clear photograph after 17:00, ice accretion seemed to completely melt by around

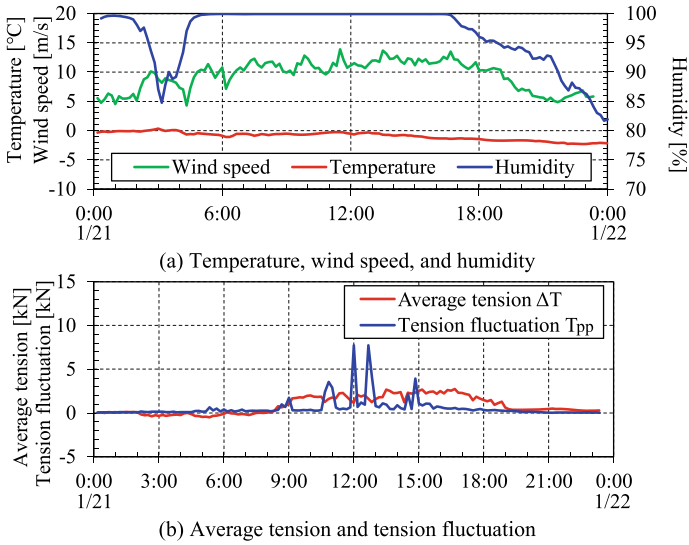


Fig. 8 Observation data of event No. 3 (2020/01/21)

21:00 because of decreasing humidity (see Fig. 8). As with events No. 1 and 2, the ice accretion angles were diagonally downwards towards an upwind direction.

Galloping occurred occasionally from 10:30 to 15:00, unlike event No. 1 where the galloping was relatively steady. Although the height of ice accretion in events No. 1 and 3 were equivalent, the shape of ice accretion in event No. 3 is rougher than that in event No. 1 (see Fig. 5b and Fig. 9c). It is estimated that the moment of ice accretion in event No. 3 was smaller than that in event No. 1 because of the rough ice shape, and more wind speed might be required for galloping to occur.

The average tension was near 0 kN at around 6:30 before the icing started, gradually increasing until around 17:00. Although the average tension correlates with the ice accretion amount, it is affected by wind speed. However, the ice accretion already melted when the wind speed decreased to around 5 m/s at 21:00. It is difficult to determine the average tension equivalent to the ice accretion amount of this event unless the influence of wind speed is appropriately removed from the average tension.

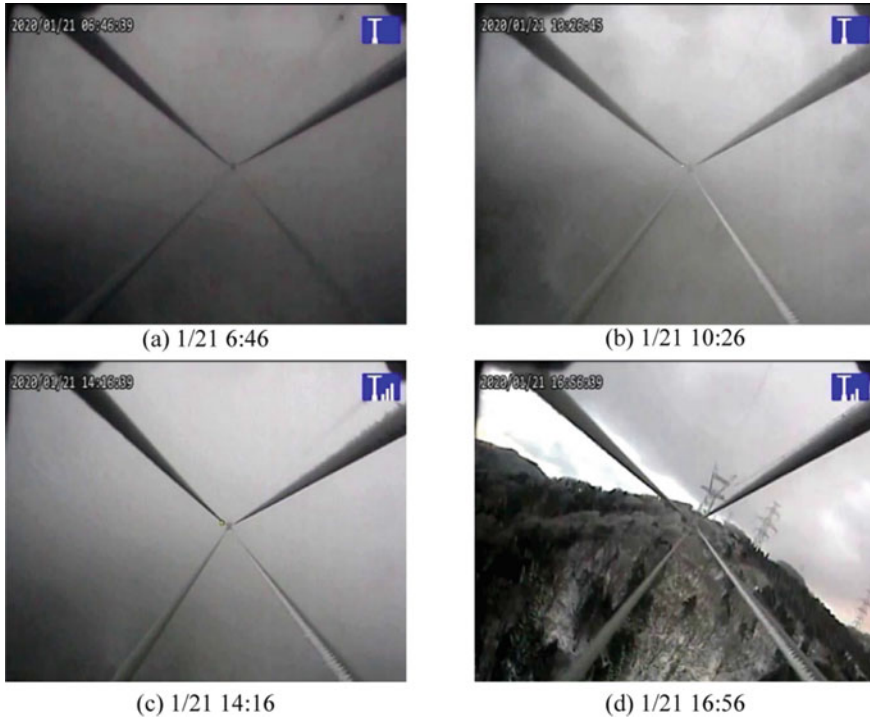


Fig. 9 Process of ice accretion of event No. 3 (2020/01/21)

4 Conclusion

Ice accretion characteristics and their relationship with tension fluctuations caused by galloping were investigated based on 28 icing events observed in the Tsuruga test line. Among these events, the data and photographs regarding ice accretion were well available in three significant events. The details of ice accretion and galloping in those events were discussed, and the following characteristics were obtained:

- Icing starts when the temperature reaches approximately $-0.5\text{ }^{\circ}\text{C}$, and ice accretion stops growing at $-2.0\text{ }^{\circ}\text{C}$. Ice accretion drops or melts when the temperature exceeds $-0.5\text{ }^{\circ}\text{C}$ or the humidity remains below 100%. Solar radiation also contributes to the dropping or melting of ice accretion.
- When the ice accretion height is greater, more wind speed is required for galloping to occur because increasing ice weight might stabilize the conductor. Additionally, galloping becomes less steady when the ice accretion shape is rougher.
- The average tension correlates with not only the ice accretion amount but galloping and buffeting as well. The average tension during no galloping and weak wind can be a reliable indicator of the ice accretion amount. It is also important to build a method for removing the influence of wind from the average tension.

Acknowledgements The investigations were performed with the cooperation of Kansai Transmission and Distribution, Inc. and Sumitomo Electric Industries, Ltd. The authors would also like to thank the members of the Research Committee of Snow Damage of Electric Power Transmission Facilities (chaired by Professor Emeritus Takeshi Ohkuma, Kanagawa University and organized by Central Research Institute of Electric Power Industry) for their direction and advice regarding this study.

References

1. CIGRE (2007) State of the art conductor galloping. CIGRE technical brochure, No 322, TF B2.11.06
2. Rawlins CB (1981) Analysis of conductor galloping field observations—single conductors. *IEEE Trans Power Appar Syst PAS-100(8):3744–3753*
3. Lilien JL, Havard DG (2000) Galloping database on single and bundle conductors prediction of maximum amplitudes. *IEEE Trans Power Delivery 15(2):670–674*
4. Matsumiya H, Yukino T, Shimizu M, Nishihara T (2022) Field observation of galloping on four-bundled conductors and verification of countermeasure effect of loose spacers. *J Wind Eng Ind Aerodyn 220:104859*
5. Taruishi S, Matsumiya H (2022) Investigation of effect of galloping countermeasure for four-bundled conductor through field observation. In: *Proceedings of 19th international workshop on atmospheric icing of structures*

The Influence of Ice Accretion Thickness on the Aerodynamic Behaviour of Stay Cables of Bridges



Annick D'Auteuil, Sean McTavish, Arash Raeesi, and Krzysztof Szilder

Abstract Several cable-stayed bridges in the world are exposed to freezing rain conditions. Ice that accretes at the surface of the stay cable modifies the circular cross-section of the cable sheath. Storms resulting in a few millimeters of ice accretion occur more frequently, but thick ice accretion on the order of 60 mm of precipitation can be associated with freezing rain events in Eastern Canada with a return period of 50 years. Both cases could affect the aerodynamics of the stay cables and could lead to potential cable instability. A wind tunnel study was carried out to investigate the influence of ice accretion thickness on the aerodynamic behaviour of stay cables. Two freezing rain precipitation levels were investigated: 2.5 and 60 mm. Four stay cable models were fabricated in SLS: a baseline cable model without ice, cable models with ice accretion corresponding to 2.5 mm and 60 mm of freezing rain at -1.5°C ambient temperature and a fourth cable model with 60 mm of freezing rain at -5°C ambient temperature. The ice accretion shapes were generated based on the National Research Council Canada (NRC) morphogenetic numerical simulation model of ice accretion on stay cables. Aerodynamic forces acting on the static models were measured for different wind speeds, cable-wind angles and cable axial rotation angles, for Reynolds numbers (Re) up to 5×10^5 . The wind-tunnel test was done in smooth flow and in turbulent flow. The results indicated that the drag coefficient increased in magnitude with the ice thickness from 0.75 to 1.2 at high Re but the highest drag coefficient value of 1.38 that was observed in the study occurred at Re of 0.5×10^5 for the cable with thick ice accretion. The aerodynamic response of cables with thick ice was largely dictated by the shape of the ice and the cable-wind angle but a limited effect of the wind turbulence was also observed. Exposing the cable without ice to wind turbulence or adding thin ice accretion had a similar impact with a shift of the drag crisis to lower Re . Large negative values associated with the variation of the lift coefficient with the cable axial rotation angle suggest that cables with thin and thick ice accretion may show the potential for cable instability.

Keywords Ice accretion · Aerodynamics · Stay cables · Bridges

A. D'Auteuil (✉) · S. McTavish · A. Raeesi · K. Szilder
National Research Council Canada, Ottawa, Canada
e-mail: annick.dauteuil@nrcnrc.gc.ca

© Crown 2024

V. Gattulli et al. (eds.), *Dynamics and Aerodynamics of Cables*, Lecture Notes in Civil Engineering 399, https://doi.org/10.1007/978-3-031-47152-0_13

145

1 Introduction

Cable-stayed bridges are exposed to weather conditions including freezing rain precipitations. Ice accretion can form at the surface of inclined stay cables leading to a modification of the circular cross-section of the cable sheath. Ice accretion affects the aerodynamic forces acting on the stay cables and can affect their stability leading to potential cable ice-wind-induced vibrations. Several cable-stayed bridges around the world are experiencing ice accretion on the stay cables due to their geographic location where lower ambient temperatures that occur for part of the year can be around the freezing point such as in Canada, USA, Europe and Asia. Some bridges had to be closed due to ice fragments detaching and falling from the cables on to the bridge traffic lanes including the Port Mann bridge in the Western Canada, the Pierre-Laporte bridge in Eastern Canada and the Russky Bridge in Russia [1–3]. Ice accretion on cables became an important topic of research in the last decade [4–7]. While a few millimeters of freezing rain precipitation can translate into a thin layer of ice at the surface of the cable, freezing rain storms with more than 60 mm of precipitation lead to thick ice accretion.

Canada's Changing Climate Report (CCCR) [8] has identified that significant parts of Canada are predicted to experience more winter precipitation and warmer average winter temperatures due to the effects of climate change. The change in winter precipitation and temperature predicted under two warming scenarios present ideal conditions for the occurrence of more frequent freezing rain events. Additionally, an ice accretion thickness of 66 mm is the value specified in the Canadian Highway Bridge Design Code (CHBDC) [9] for part of Eastern Canada for freezing rain events with a return period of 50 years. Work conducted previously by NRC identified that the aerodynamic drag of stay cables could increase by as much as 50% in conditions that were less severe, i.e. 25 mm of freezing rain, than for the design criteria for 66 mm of freezing rain [7]. A wind tunnel study was carried out to investigate the influence of ice accretion thickness on the aerodynamic behaviour of stay cables, including drag coefficient (C_D) and lift coefficient (C_L). Two freezing rain precipitation levels were investigated: 2.5 and 60 mm. The paper describes the experimental conditions and presents the results of the drag and lift force coefficients and their variation with Reynolds number, yaw angle and axial rotation angle of the cable.

2 Experimental Conditions

Experimental tests were performed in the NRC 2×3 m Wind Tunnel. The ice shapes were obtained from the NRC morphogenetic numerical simulation model [10, 11] and printed using the Selective Laser Sintering (SLS) method. The use of the morphogenetic simulation model for stay cables has been validated based on digital scans of several cases involving physical freezing rain accretion [11]. The four cable models were painted to obtain a surface roughness similar to a High-Density Polyethylene

(HDPE) cable (see Fig. 1, left image). The ice shapes were also painted, since the surface roughness of the painted ice more closely resembled that of ice compared to the surface roughness of the as-printed SLS. Each ice shape was fabricated as a sleeve to slide over the main core of the cable model. The outer diameter of the physical cable models was 96.15 mm which represents a sub-scale model size of approximately 30% to 60% of a full size stay cable. The physical diameter of the cable was used as the reference dimension for the Reynolds number. All cables were equipped with a double helical fillet at the surface of the cable with a helix angle of 45° and cross-sectional dimensions of 1×3 mm. Table 1 provides a summary of the characteristics of the cables and conditions used for the formation of the ice shapes. Figure 2 shows the three cables with simulated ice mounted in the test section of the wind tunnel. The right-side image in Fig. 1 illustrates a schematic of the cable orientation where θ , β , and ϕ are respectively the inclination, yaw, and cable-wind angle relative to the wind vector, U . A yaw angle of 0° is defined as the condition when the wind is aligned with the cable main axis. A negative yaw angle corresponds to a counterclockwise rotation of the turntable when viewed from above. The freestream wind speed (U) has a component that is normal to the cable axis, but still aligned in the cable-wind plane ($U_N = U \sin \phi$). The angle between the vertical cable plane and the wind component normal to the cable axis is α_N . The tests were carried out for a cable inclination of 60° from the horizontal, which represents well the inclination for many stay cables on existing bridges. Aerodynamic forces acting on the static cable models were measured for Reynolds numbers (Re) from 0.4×10^5 to 5.3×10^5 in smooth flow conditions. Tests were also performed in turbulent flow with a longitudinal turbulence intensity, I_u , that varied between 3.3% and 5.6% for Re up to 3.3×10^5 . The details of the turbulent-flow setup are described in [7]. In the first set of measurements, the axial rotation angle (α) was set to 0° when $\beta = 0$ and then the cable response was evaluated at yaw angles of 0° , -30° , -60° , -90° , -120° , -135° , -150° . The corresponding α_N for each cable-wind angle in the first phase of the measurements is shown in Fig. 3. The second set of measurements were performed for a cable at 0° yaw angle ($\phi = 60^\circ$) and for axial rotation angles (α) that ranged from -90° to $+90^\circ$ in increments of 15° . A negative axial rotation angle of the cable corresponds to a clockwise rotation of the cable when viewed from above.

3 Results

A comparison of the results for C_D and C_L as a function of Re for the cable without ice, with thin ice (cable 1), with thick ice (cable 2) and with thick ice and cold air temperature (cable 3) is presented in Fig. 4. Following the terminology used by Zdravkovich [12], it can be observed that for the cable without ice, the C_D varies significantly with the change in yaw angle; at 0° ($\phi = 60^\circ$) the critical Re regime which is characterized by a large variation of the drag coefficient with Re (drag crisis) is present from a Re of 0.5×10^5 to 2.5×10^5 while at a yaw angle of 90° ($\phi = 90^\circ$), the critical- Re regime is present for a Re of 2.0×10^5 to 3×10^5 with

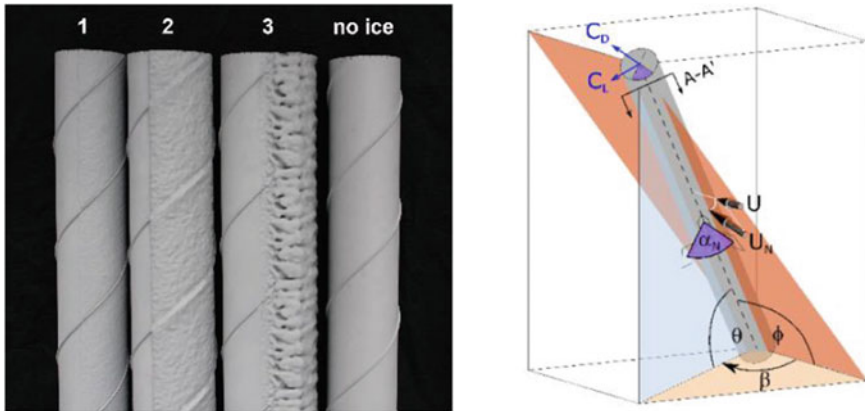


Fig. 1 Left: Four cables tested: one without ice and three with ice accretion. Right: schematic of the cable-wind relative angles θ , β , and ϕ with respect to wind vector U

Table 1 Cable characteristics

Cable	Cable surface geometry	Freezing rain precipitation	Freezing rain air temperature
No ice	Double Helical fillet, right-handed 45° helix angle, 1 × 3 mm	–	–
1	Double Helical fillet, right-handed 45° helix angle, 1 × 3 mm	2.5 mm	–1.5 °C
2	Double Helical fillet, right-handed 45° helix angle, 1 × 3 mm	60 mm	–1.5 °C
3	Double Helical fillet, right-handed 45° helix angle, 1 × 3 mm	60 mm	–5 °C



Fig. 2 Views of the cables with simulated ice in the NRC 2 × 3 m Wind Tunnel: cable 1 (left), cable 2 (center) and cable 3 (right)

a small reduction of C_D compared to the case at 0° yaw. The variation in C_D over the entire Re range and the C_D at high Re are consistent with values for HDPE cable models with helical fillet observed in literature [6].

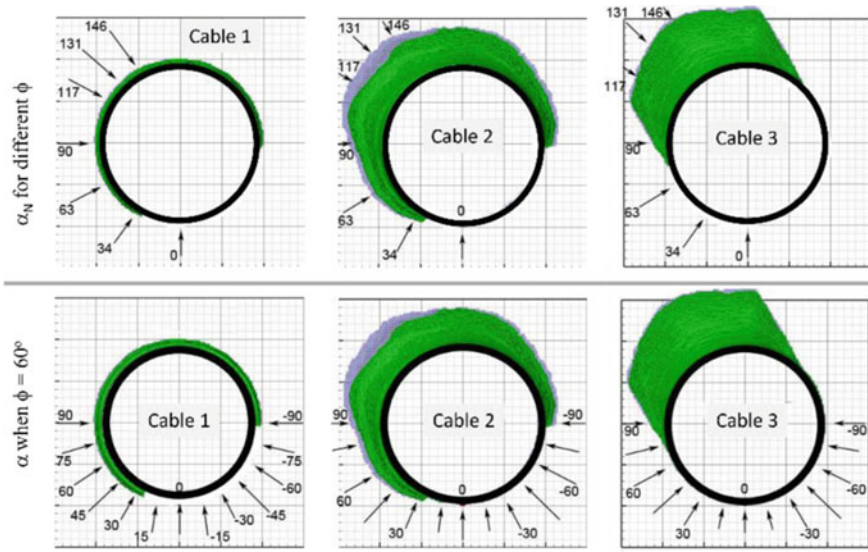


Fig. 3 Cross-sectional view of the cable (black) with ice (green). α_N is shown for different ϕ (top) and α is shown for the case where $\phi = 60^\circ$ (bottom). Minor gridlines represent 5.08 mm

When ice accretion is present at the surface of the cable, the critical-Re regime and the corresponding drag crisis for the three iced cables shifts to below a Re of 1.5×10^5 . For cable 1 and cable 2, minimal correlation between C_D and Re was observed for all the cable-wind angles tested. However, results for cable 3 indicated a large variation of C_D with cable-wind angle due to the ice shape that changes significantly from one yaw angle to another with respect to the wind direction. For thick and localized ice accretion at the surface of the cable, the trend of the C_D curve versus Re and its magnitude are largely dictated by the ice shape geometry. The maximum C_D at maximum Re increased with ice accretion thickness; 0.76 for cable without ice, 0.8 for cable 1 with 2.5 mm of freezing rain, 0.96 for cable 2 with 60 mm of freezing rain and 1.2 for cable 3 with 60 mm of freezing rain and cold temperature. However, the highest C_D value observed in the study was 1.38 at low Reynolds numbers for cable 3. Whether the sign of the lift coefficient for the cable without ice (Fig. 4, top) is negative or positive is a result of the flow asymmetry created by the direction of the double helical fillet right-handed. The variation of C_L was within -0.6 – 0.7 . With a thin layer of ice (cable 1), the variation in C_L was reduced compared to the cable without ice and comprised between -0.4 and 0.45 . The variation in C_L was observed for low Re in the critical-Re regime followed by more-or-less constant values in the supercritical-Re regime. For the two thicker ice shapes, the direction of C_L is influenced by the relative position of the un-iced portion of the cable on the cable circumference. The relative orientation of the un-iced portion of the cable for each cable-wind angle (and α_N) can be seen in Fig. 3, top.

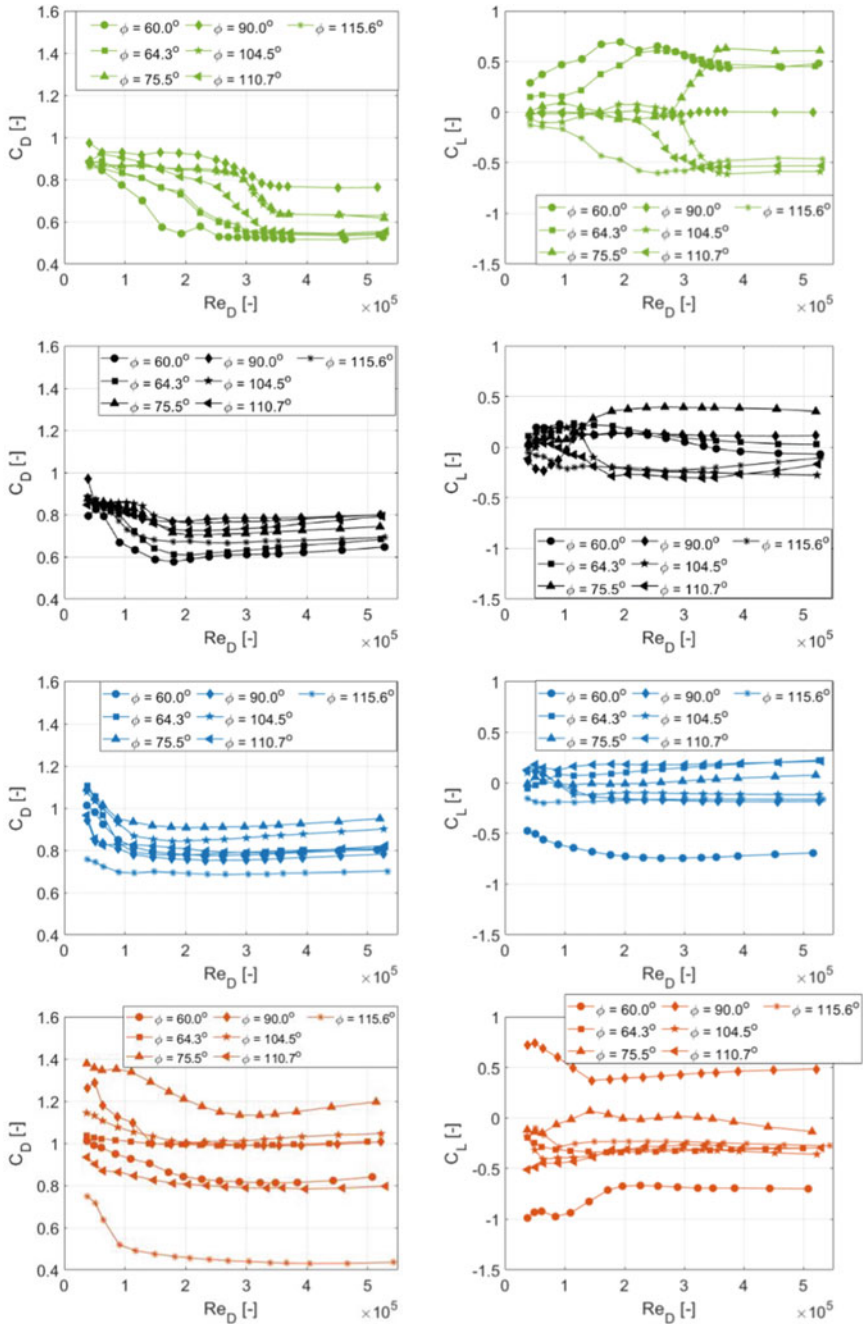


Fig. 4 Drag and lift force coefficients as a function of Reynolds number for different cable-wind angles for cable without ice (top), for cable 1 (second row), for cable 2 (third row) and for cable 3 (bottom) in smooth flow

Measurements of the static aerodynamic forces at different cable axial rotation angles, α , provided insight into the aerodynamics and could be used to predict potential cable instability. Based on the Den Hartog galloping criterion [13], a cable may have the potential for instability when $C_D + \delta C_L/\delta\alpha < 0$. Figure 5 shows the drag and lift coefficients as a function of the axial angle of rotation of the cable, along with their derivatives, for two different Re (in the critical and supercritical regimes, respectively) for cables 1, 2 and 3. The derivatives were calculated using the gradient function in Matlab. Results are shown for two Re , but the variation and magnitude of the force coefficients and their derivatives were similar at the other Re investigated. It can be observed that the largest magnitude of $\delta C_L/\delta\alpha$ was greater than -3.5 at $\alpha = -30^\circ$ to -45° for cable 3. This value is significantly larger than the drag coefficient value and therefore, according to the criteria, the cable could be subjected to wind-induced vibrations. The results for cable 1 and cable 2 also indicated a $C_D + \delta C_L/\delta\alpha < 0$ with values between 0 and -1 around $\alpha = -15^\circ$ suggesting that even with thin ice or more evenly distributed thick ice on the circumference, the cable may be prone to wind-induced vibrations. The design recommendations for stay cables under ice-wind conditions are based on the Post-Tensioning Institute (PTI): Recommendations for Stay-Cable Design, Testing and Installation [14]. A value of the drag coefficient of 1.0 and a value of the derivative of the lift coefficient $\delta C_L/\delta\alpha$ of -2.0 are suggested in the design guidelines to calculate the minimum structural damping required to mitigate the galloping due to ice-wind conditions. Based on the results obtained in the current study, higher values in magnitude for the $\delta C_L/\delta\alpha$ term should be considered. A value of -3.8 has been observed in this study but it is expected that higher values could be measured if the axial rotation angle increment were on the order of 5° instead of 15° .

The experimental tests were also conducted under turbulent flow conditions with longitudinal turbulence intensity, I_u , that varied between 3.3% and 5.6% compared to 0.14% in smooth flow. Results for C_D and C_L as a function of Re for the cable without ice, with thin ice (cable 1), with thick ice (cable 2) and with thick ice and cold temperature (cable 3) are presented in Fig. 6. For the cable without ice, the turbulence shifted the drag crisis to a lower Re range. For cables with ice (1, 2, 3), the turbulence did not impact the Re range at which drag crisis occurred, but overall, the magnitude of C_D was increased with wind turbulence. Results at high Re indicated an increase of the C_D of 10–12% for the cable without ice and cable 1 and 2.5–5% for cable 2 and 3. However, at low Re in the drag crisis, the increase in C_D was up to 15% for cable 3. Adding turbulence or adding thin ice accretion on a cable with a helical fillet had a similar impact on the drag and lift coefficients with a shift of the drag crisis to lower Re . Similar results were obtained in turbulent flow for the variation of the drag coefficient and the derivative of the lift coefficient with the angle of rotation of the cable (α) compared to smooth flow conditions. Figure 7 shows the results in turbulent flow for the drag coefficient and the derivative of the lift coefficient. Comparable results were obtained in turbulent flow compared to smooth flow conditions for cables 1, 2, 3 with the minimum $\delta C_L/\delta\alpha$ that occurred for the

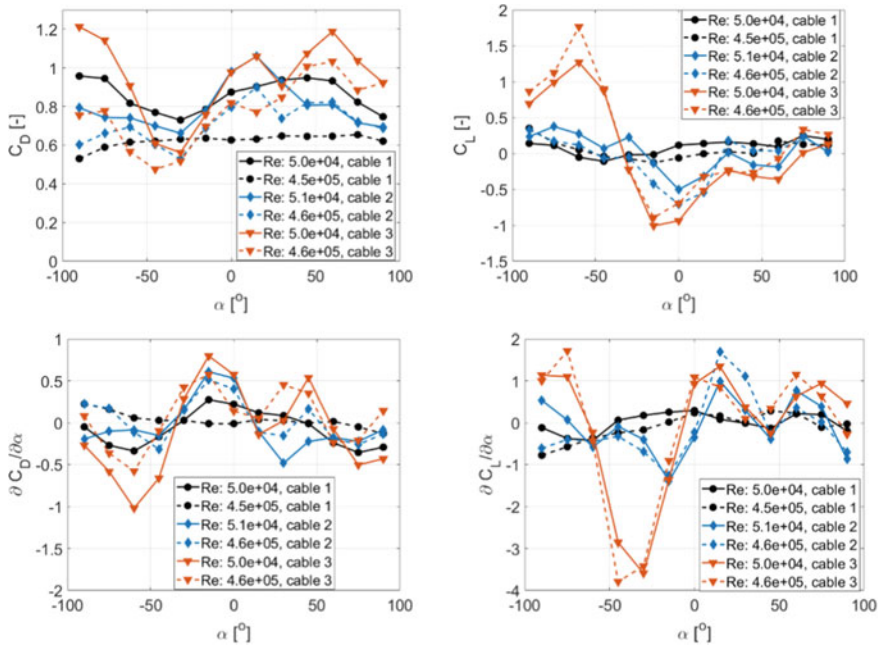


Fig. 5 Drag and lift force coefficients (top row) and drag and lift coefficient derivatives (bottom row) as a function of the axial angle of rotation of the cable for two different Reynolds numbers and for the three cables with ice in smooth flow

same range of angles of rotation of the cable α . The magnitude was slightly different but it could be due to the larger increment in angle of rotation (step of 30° in turbulent flow versus 15° in smooth flow). Based on the Den Hartog criterion, cables 1, 2 and 3 may be prone to wind-induced vibrations.

4 Conclusions

This paper has described experiments conducted in the NRC 2×3 m wind tunnel to evaluate the aerodynamic force coefficients for cable models without ice, with thin ice and with thick ice. The cable models all had a double helical fillet and were painted to represent a surface roughness similar to HDPE cables and tests were completed under smooth and turbulent flow conditions. The maximum drag coefficient (C_D) observed under the current study revealed values up to 1.2 at high Reynolds number (Re) and 1.38 at low Re for cable with thick ice (cable 3) in smooth flow conditions. Design C_D value used in common practice is 1.0 which is smaller than what has been measured in the current study. Based on the Den Hartog criterion, the results indicated that cable 3 (thick ice with low temperature) may be prone to wind-induced vibrations with $\delta C_L / \delta \alpha$ smaller than -2.5 in smooth and turbulent flows for a range

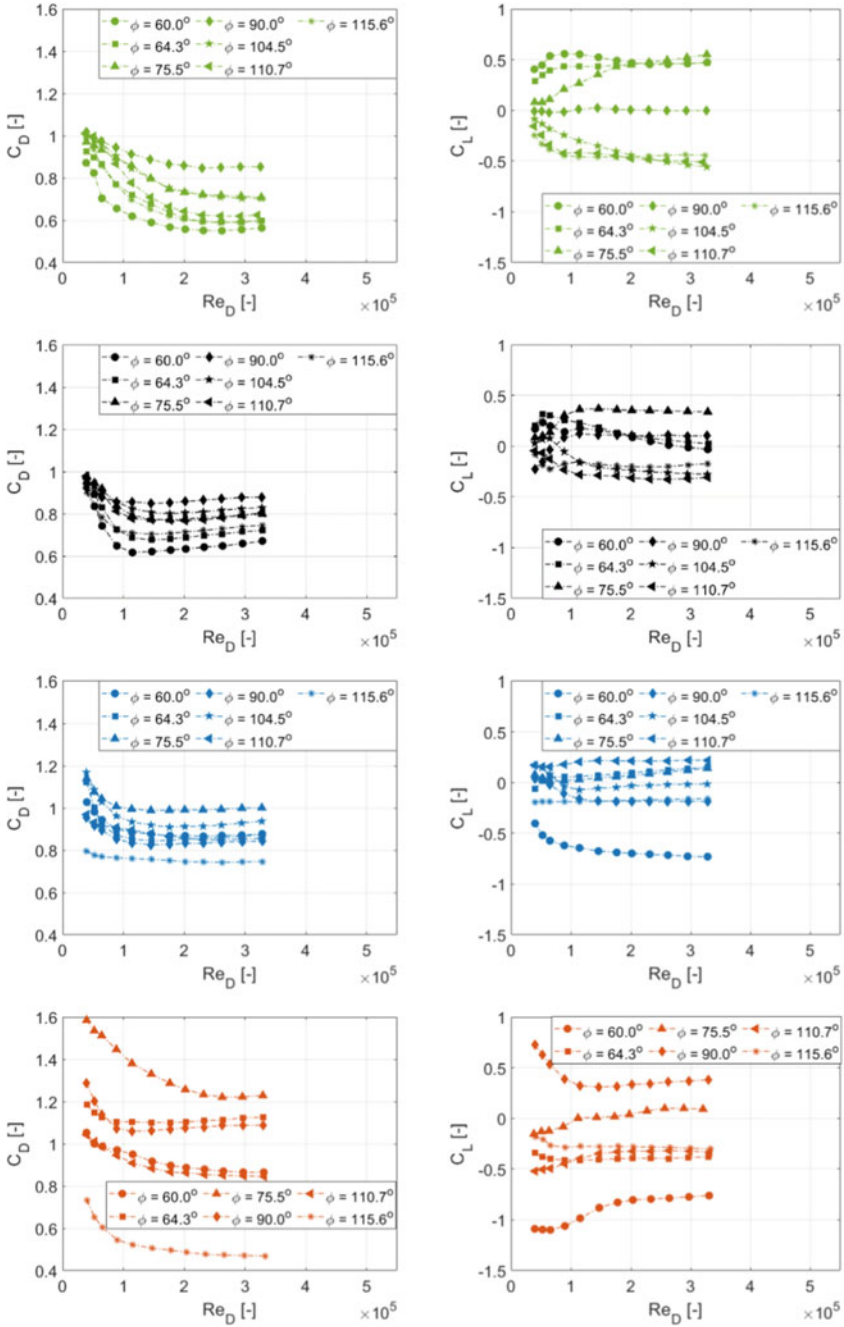


Fig. 6 Drag and lift force coefficients as a function of Reynolds for different cable-wind angles for cable without ice (top), for cable 1 (second row), cable 2 (third row) and cable 3 (bottom row) in turbulent flow

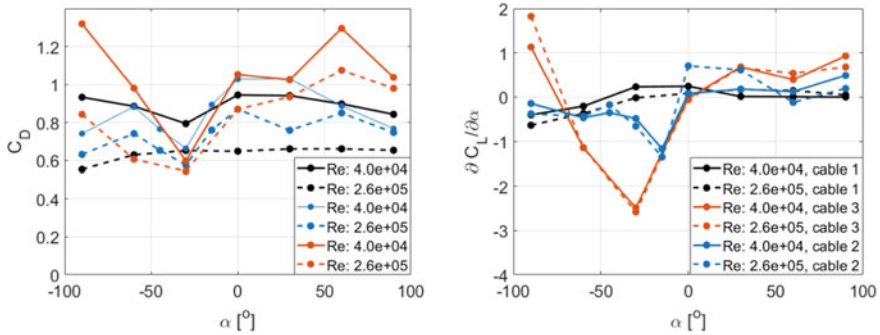


Fig. 7 Drag force coefficient (left) and lift coefficient derivative (right) as a function of the axial angle of rotation of the cable for two different Reynolds numbers and for the three cables with ice in turbulent flow

of axial cable rotation angles. Cable 1 (thin ice) and cable 2 (thick ice) also presented conditions for cable instability for a narrower range of cable axial rotation angles. The aerodynamic response of cables with thick ice was largely dictated by the shape of the ice and the cable-wind angle but a limited effect from the wind turbulence was also observed. Exposing the cable without ice to wind turbulence or adding thin ice accretion had a similar impact with a shift of the drag crisis to lower Re.

Acknowledgements The authors acknowledge the financial support of Infrastructure Canada through the Climate Resilient Built Environment Project. The authors would like to thank the technical team in the NRC Aerodynamics Laboratory for their support.

References

1. Global News (2020) Ice bombs damage vehicles on Port Mann, Alex Fraser bridges during snowfall. <https://globalnews.ca/news/6395011/bc-snow-ice-bombs-bridges/>
2. CBC (2017) Driver glad to be alive after ice falls through windshield off pierre-laporte bridge. <https://www.cbc.ca/news/canada/montreal/pierre-laporte-bridge-ice-falls.14045703>
3. The Siberian Times (2020) Call for extra hands to clear the Russky Bridge still shut after last week's disastrous ice rain. <https://siberiantimes.com/other/others/news/call-for-extra-hands-to-clear-russky-bridge-in-vladivostok-still-shut-after-last-weeks-disastrous-ice-rain/>
4. Demartino C, Koss HH, Georgakis CT, Ricciardelli F (2015) Effects of ice accretion on the aerodynamics of bridge cables. *J Wind Eng Ind Aerodyn* 138:98–119. <https://doi.org/10.1016/j.jweia.2014.12.010>
5. Demartino C, Ricciardelli F (2015) Aerodynamic stability of ice-accreted bridge cables. *J Fluids Struct* 52:81–100. <https://doi.org/10.1016/J.JFLUIDSTRUCTS.2014.10.003>
6. Kleissl K, Georgakis CT (2012) Comparison of the aerodynamics of bridge cables with helical fillets and a pattern-indented surface. *J Wind Eng Ind Aerodyn* 104–106:166–175. <https://doi.org/10.1016/J.JWEIA.2012.02.031>
7. McTavish S, D'Auteuil A, Raesi A, Szilder K (2021) Effect of cable surface geometry and ice accretion shapes on the aerodynamic behaviour of inclined stay cables. *J Wind Eng Ind Aerodyn* 216

8. Bush E, Lemmen DS (2019) Canada's changing climate report. Government of Canada, Ottawa, p 444p
9. CSA Group (2019) Canadian highway bridge design code No S6-19
10. Szilder K (2018) Theoretical and experimental study of ice accretion due to freezing rain on an inclined cylinder. *Cold Reg Sci Technol* 150:25-34
11. Szilder K, D'Auteuil A, McTavish S (2021) Predicting ice accretion from freezing rain on bridge stay cables. *Cold Reg Sci Technol*, 187
12. Zdravkovich MM (1997) Flow around circular cylinders, vol 1. Oxford University Press, Oxford, UK
13. Den Hartog JP (1985) Mechanical vibrations. Courier Dover Publications
14. PTI Guide Specification (2018) Recommendations for stay cable design, testing and installation DC45.1-18, 7th ed Post-Tensioning institute committee on cable-stayed bridges

Non-linear Dynamic Response of a Small-sag Cable Model of a Guy Line of a Guyed Tower to Stochastic Wind Excitation



Hanna Weber , Anna Jabłonka , and Radosław Iwankiewicz 

Abstract A cable with small-sag is considered as a simplified model of guy line of a guyed tower. The strong dynamic wind action leads to the transverse vibrations of the guyed tower that causes the base-motion excitation of the cable and its axial and lateral vibrations. Because of strong gusts of wind the significant displacements of the tower can be observed, wherefore the geometrical non-linear effects arise. In the considered model the axial non-linear vibrations of the cable with small-sag are coupled with transverse ones. The set of ordinary differential equations is obtained by using the Galerkin method. The single-fundamental-mode response of the tower to a wide-band stochastic wind excitation is considered as the narrow-band stochastic process. Therefore the base motion excitation for the guy line is assumed as an idealized response of an auxiliary linear filter to a Gaussian white noise excitation. The obtained state vector of the system is expressed by the original state variables augmented by the filter state variables. The equivalent linearization technique is then used to convert the original non-linear system into the equivalent linear one with coefficients obtained from the condition of minimization of the mean square error between the both systems. As a result the mean values, variances and cross-covariances of particular random state variables are determined and verified by Monte Carlo simulation.

Keywords Stochastic dynamics · Nonlinear system · Small-sag cable · Equivalent linearization technique · Gaussian white noise process

H. Weber (✉) · A. Jabłonka
West Pomeranian University of Technology in Szczecin, Szczecin, Poland
e-mail: Hanna.Weber@zut.edu.pl

A. Jabłonka
e-mail: Anna.Jablonka@zut.edu.pl

R. Iwankiewicz
Calisia University, Kalisz, Poland
e-mail: r.iwankiewicz@uniwersytetkaliski.edu.pl

1 Introduction

Nowadays, vibrations can be observed in many various structural elements and their correct analysis is slowly becoming an inseparable element of design process [1]. A strong dynamic wind action leads to the excitation of slender structures for example cable-stayed bridges, high-rise buildings, masts or guyed towers. Bending deformation of the structure and its displacements cause excitation of the transportation systems [2] or the supporting cables [3, 4]. Due to the non-deterministic nature of the load these problems should be solved by using the stochastic methods [5].

In presented paper the nonlinear model of a guy line in the guyed tower, treated as small-sag cable is considered. The horizontal displacements of the tower under stochastic wind action leads to the coupled longitudinal and lateral vibrations inside the cable. The nonlinear set of ordinary differential equations of motion is obtained, where the base-motion excitation for the guy-line is modelled as a response of an auxiliary linear filter to the Gaussian white noise excitation. To convert the original system into the approximate linear one the equivalent linearization technique is used. This method has been implemented in many problems of stochastic dynamics e.g. [6, 7]. Main advantages of this approach are easy application to numerical calculations and much lower time needed to perform calculations compared to other methods.

2 Static Behaviour of a Small-sag Cable

In the considered problem the initial tension H in the guy line is assumed to be very high in the comparison to the effect of its own weight (gravity forces), therefore the line is considered as a small-sag cable. The cable mass per unit length is assumed as μ while its axial stiffness and total length equal EA and L , respectively. For the sake of simplification the motion is executed only in the cable plane. Let us denote that $u(x, t)$ and $w(x, t)$ are the longitudinal and the transverse displacements of the cable resulting from its deformation, respectively. The initial shape of the cable in its plane in the direction perpendicular to the guy line caused by the gravity forces is denoted as $z(x)$ (see Fig. 1a).

Initial, small-sag shape $z(x)$ of the cable is governed by the equation:

$$\frac{d^2z}{dx^2} = -\frac{\mu g}{H} \cos \gamma \quad (1)$$

where g is the gravity acceleration. Equation (1) is satisfied when the ratio of the sag to the length of the cable is equal or less than 1:8 [8]. For the small-sag cable we can assume the initial shape of the guy line in the form of parabola. Therefore for mid span where $x = L/2$ we can adopt that $dz/dx = 0$. Furthermore, at the support

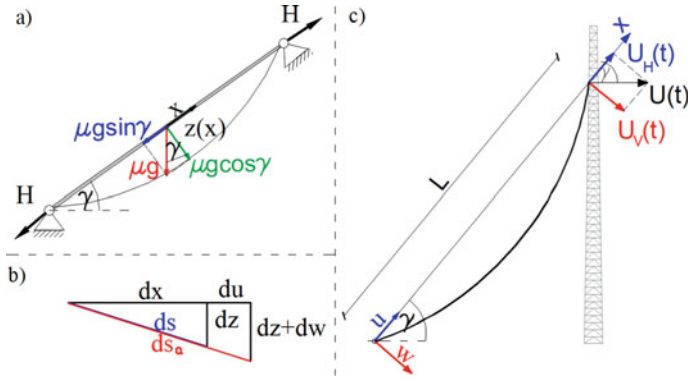


Fig. 1 a Small-sag cable model of the guy line under gravity forces, b Differential element of the small-sag cable, c Guy line base motion excitation

point where $x = 0$ we can assume that $z(x = 0) = 0$. Using these two conditions in the integration process leads to the following expression:

$$z = \frac{\mu g}{2H} x(L - x) \cos \gamma. \tag{2}$$

3 Nonlinear Equations of Motion for a Small-sag Cable

Using the Hamilton’s principle we can write that

$$\int_0^t \delta(V - T)dt = 0, \tag{3}$$

where V and T are the potential and kinetic energies, respectively. If only a planar motion of a cable with a small sag is considered, the kinetic energy can be expressed by the following equation

$$T = \frac{\mu}{2} \int_0^L \left(\left(\frac{\partial u}{\partial t} \right)^2 + \left(\frac{\partial w}{\partial t} \right)^2 \right) ds. \tag{4}$$

Considering the initial shape of the cable under the gravity forces that is presented in Fig. 1b, the following expression can be obtained

$$ds = \sqrt{dx^2 + dz^2} = \sqrt{dx^2 \left(1 + \left(\frac{dz}{dx} \right)^2 \right)} = \sqrt{1 + (z')^2} dx. \tag{5}$$

Using Eqs. (4) and (5) the variation of the kinetic energy can be obtained as

$$\delta T = \frac{1}{2}\mu \int_0^L \delta \left(2\frac{\partial u}{\partial t} \delta \dot{u} + 2\frac{\partial w}{\partial t} \delta \dot{w} \right) \sqrt{1 + (z')^2} dx. \quad (6)$$

Taking into account that variation of the derivative equals the derivative of the variation, i.e. $\delta \dot{u} = (\delta \dot{u}) = \frac{\partial}{\partial t} (\delta u)$, $\delta \dot{w} = (\delta \dot{w}) = \frac{\partial}{\partial t} (\delta w)$ and the fact that at the initial time 0 and at the final time t the variations δu and δw vanish, because the states at these times are fixed, the final result is

$$\int_0^t \delta T = -\mu \int_0^t \int_0^L \left(\frac{\partial^2 u}{\partial t^2} \delta u + \frac{\partial^2 w}{\partial t^2} \delta w \right) \sqrt{1 + (z')^2} dx dt. \quad (7)$$

Elastic potential energy can be expressed as

$$V = \underbrace{\int_0^L N(x)\varepsilon(u', w') ds}_{V^{(1)}} + \underbrace{\frac{EA}{2} \int_0^L \varepsilon^2(u', w') ds}_{V^{(2)}} + V^{(g)}, \quad (8)$$

where $N(x)$ is the initial static tension in the cable and $V^{(g)}$ is the gravitational potential energy. The normal strain is expressed as (see Fig. 1b)

$$\varepsilon = \frac{ds_a - ds}{ds}, \quad (9)$$

with the term ds_a given by

$$ds_a = \sqrt{(dx + du)^2 + (dz + dw)^2} \cong dx \sqrt{1 + 2\frac{\partial u}{\partial x} + \left(\frac{\partial u}{\partial x}\right)^2 + 2\frac{\partial z}{\partial x} \frac{\partial w}{\partial x} + \left(\frac{\partial w}{\partial x}\right)^2}, \quad (10)$$

where the term $\left(\frac{\partial z}{\partial x}\right)^2$ has been neglected. For the small-sag cable, the following simplification is used $1/\sqrt{1 + \left(\frac{\partial z}{\partial x}\right)^2} \approx 1$. Consequently, the normal strain is obtained as

$$\varepsilon \cong \sqrt{1 + 2\frac{\partial u}{\partial x} + \left(\frac{\partial u}{\partial x}\right)^2 + 2\frac{\partial z}{\partial x} \frac{\partial w}{\partial x} + \left(\frac{\partial w}{\partial x}\right)^2} - 1. \quad (11)$$

Using the Taylor series expansion leads to the following expression

$$\varepsilon \cong \frac{\partial u}{\partial x} + \frac{1}{2} \left(\frac{\partial u}{\partial x}\right)^2 + \frac{\partial z}{\partial x} \frac{\partial w}{\partial x} + \frac{1}{2} \left(\frac{\partial w}{\partial x}\right)^2 = u' + \frac{1}{2}(u')^2 + z'w' + \frac{1}{2}(w')^2. \quad (12)$$

Assuming that $\frac{N(x)}{\sqrt{1+(z')^2}} = H(x)$, the variation of the first term of potential energy can be given by

$$\delta V^{(1)} = \delta \int_0^L N(x) \varepsilon(u', w') ds = \int_0^L H(x) (\delta u' + u' \delta u' + z' \delta w' + w' \delta w') dx. \quad (13)$$

The terms of the Eq. (13) that depend on $u(x, t)$ and $w(x, t)$, respectively are given by

$$\begin{aligned} & \int_0^L H(x) (\delta u' + u' \delta u') dx = \int_0^L H(x) ((\delta u)' + u' (\delta u)') dx \\ & = H(x) (\delta u) \Big|_0^L - \int_0^L \frac{\partial H}{\partial x} dx \delta u + H u' \delta u \Big|_0^L - \int_0^L \frac{\partial}{\partial x} (H u') dx \delta u, \\ & \int_0^L H(x) (z' \delta w' + w' \delta w') dx = \int_0^L H(x) (z' (\delta w)' + w' (\delta w)') dx \\ & = H(x) z' (\delta w) \Big|_0^L - \int_0^L \frac{\partial}{\partial x} (H(x) z') dx \delta w + H(x) w' \delta w \Big|_0^L - \int_0^L \frac{\partial}{\partial x} (H(x) w') dx \delta w. \end{aligned} \quad (14)$$

Effect of the gravity forces - gravitational potential energy can be defined as

$$V^{(g)} = - \int_0^L \mu g w ds = - \int_0^L \mu g w \sqrt{1 + (z')^2} dx. \quad (15)$$

The variation of the gravitational potential energy is consequently obtained by

$$\delta V^{(g)} = - \int_0^L \mu g \sqrt{1 + (z')^2} dx \delta w. \quad (16)$$

Self-satisfied equation of equilibrium

$$- \frac{\partial}{\partial x} (H(x) z') - \mu g \sqrt{1 + (z')^2} = 0 \quad (17)$$

is subtracted from the final form of equations of motions. Variation of the second term of potential energy can be written as

$$\begin{aligned} \delta V^{(2)} &= \frac{EA}{2} \delta \int_0^L \varepsilon^2(u', w') ds = EA \int_0^L \varepsilon(u', w') \delta \varepsilon(u', w') ds \\ &\cong EA \int_0^L (u' + \frac{1}{2}(u')^2 + z' w' + \frac{1}{2}(w')^2) \cdot (\delta u' + u' \delta u' + z' \delta w' + w' \delta w') dx. \end{aligned} \quad (18)$$

Taking into account that $\delta u' = (\delta u)' = \frac{\partial}{\partial x} (\delta u)$ and $\delta w' = (\delta w)' = \frac{\partial}{\partial x} (\delta w)$, leads to the terms in equation of motion governing $u(x, t)$ and $w(x, t)$, respectively:

$$EA \int_0^L \left(u' + \frac{1}{2}(u')^2 + z'w' + \frac{1}{2}(w')^2 \right) (1+u') \delta u' dx = EA \frac{\partial}{\partial x} \left[\left(u' + \frac{1}{2}(u')^2 + z'w' + \frac{1}{2}(w')^2 \right) (1+u') \right],$$

$$EA \int_0^L \left(u' + \frac{1}{2}(u')^2 + z'w' + \frac{1}{2}(w')^2 \right) (z'+w') \delta w' dx = EA \frac{\partial}{\partial x} \left[\left(u' + \frac{1}{2}(u')^2 + z'w' + \frac{1}{2}(w')^2 \right) (z'+w') \right]. \quad (19)$$

Using Hamilton's principle for Eqs.(14) together with Eqs.(19) and simplification for the small-sag cable $\sqrt{1+(z')^2} = 1$ leads to the equations of motion in the form as presented below

$$-\frac{\partial}{\partial x} (H(x)u') - EA \frac{\partial}{\partial x} \left[\left(u' + \frac{1}{2}(u')^2 + z'w' + \frac{1}{2}(w')^2 \right) (1+u') \right] + \mu \frac{\partial^2 u}{\partial t^2} = 0,$$

$$-\frac{\partial}{\partial x} (H(x)w') - EA \frac{\partial}{\partial x} \left[\left(u' + \frac{1}{2}(u')^2 + z'w' + \frac{1}{2}(w')^2 \right) (z'+w') \right] + \mu \frac{\partial^2 w}{\partial t^2} = 0. \quad (20)$$

4 Vibrations of a Guy Line Due to a Base Motion Excitation

The horizontal displacement $U(t)$ of the guyed tower at the point of attachment of the guy line (see Fig. 1c) plays the role of the base motion (kinematic) excitation for the guy line (cable). The components of the excitation in the longitudinal and transverse directions are defined as $U_H(t) = U(t) \cos \gamma$ and $U_V(t) = U(t) \sin \gamma$, respectively. The absolute motions $\bar{u}(x, t)$ and $\bar{w}(x, t)$, expressed in terms of the base motion due to $U(t)$ and the relative motions $u(x, t)$ and $w(x, t)$, which are related with the elastic deformations, are defined as

$$\bar{u}(x, t) = \frac{x}{L} U(t) \cos \gamma + u(x, t), \quad \bar{w}(x, t) = \frac{x}{L} U(t) \sin \gamma + w(x, t). \quad (21)$$

The Eq. (20) written down in terms of the absolute motions is

$$\int_0^L \left(-\frac{\partial H(x)}{\partial x} \frac{\partial \bar{u}}{\partial x} - H(x) \frac{\partial^2 \bar{u}}{\partial x^2} - EA \frac{\partial}{\partial x} \left[\left(\frac{\partial \bar{u}}{\partial x} + \frac{3}{2} \left(\frac{\partial \bar{u}}{\partial x} \right)^2 + \frac{\partial z}{\partial x} \frac{\partial \bar{w}}{\partial x} + \frac{1}{2} \left(\frac{\partial \bar{w}}{\partial x} \right)^2 \right. \right. \right. \\ \left. \left. \left. + \frac{1}{2} \left(\frac{\partial \bar{u}}{\partial x} \right)^3 + \frac{\partial \bar{u}}{\partial x} \frac{\partial z}{\partial x} \frac{\partial \bar{w}}{\partial x} + \frac{1}{2} \frac{\partial \bar{u}}{\partial x} \left(\frac{\partial \bar{w}}{\partial x} \right)^2 \right) \right] + \mu \frac{\partial^2 \bar{u}}{\partial t^2} \right) \delta \bar{u} dx \\ + \int_0^L \left(-\frac{\partial H(x)}{\partial x} \frac{\partial \bar{w}}{\partial x} - H(x) \frac{\partial^2 \bar{w}}{\partial x^2} - EA \frac{\partial}{\partial x} \left[\left(\frac{\partial \bar{u}}{\partial x} \frac{\partial z}{\partial x} + \frac{1}{2} \left(\frac{\partial \bar{u}}{\partial x} \right)^2 \frac{\partial z}{\partial x} + \left(\frac{\partial z}{\partial x} \right)^2 \frac{\partial \bar{w}}{\partial x} \right. \right. \right. \\ \left. \left. \left. + \frac{3}{2} \frac{\partial z}{\partial x} \left(\frac{\partial \bar{w}}{\partial x} \right)^2 + \frac{\partial \bar{u}}{\partial x} \frac{\partial \bar{w}}{\partial x} + \frac{1}{2} \left(\frac{\partial \bar{u}}{\partial x} \right)^2 \frac{\partial \bar{w}}{\partial x} + \frac{1}{2} \left(\frac{\partial \bar{w}}{\partial x} \right)^3 \right) \right] + \mu \frac{\partial^2 \bar{w}}{\partial t^2} \right) \delta \bar{w} dx = 0, \quad (22)$$

where the following relationships are valid $\delta \bar{u}(x, t) = \delta u(x, t)$, $\delta \bar{w}(x, t) = \delta w(x, t)$. The time derivatives are given by the following expressions

$$\frac{\partial^2 \bar{u}}{\partial t^2} = \frac{x}{L} \ddot{U}(t) \cos \gamma + \frac{\partial^2 u}{\partial t^2}, \quad \frac{\partial^2 \bar{w}}{\partial t^2} = \frac{x}{L} \ddot{U}(t) \sin \gamma + \frac{\partial^2 w}{\partial t^2}. \quad (23)$$

In the derivatives with respect to x the base motion term disappears. However the damping forces assumed as dependent on the relative velocity are included as $-c_h \frac{\partial u}{\partial t}$ and $-c_v \frac{\partial w}{\partial t}$. If the Galerkin method and the single-mode approximation are used the particular displacements are defined by the following terms:

$$u(x, t) = p(t) \sin \frac{\pi x}{L}, \quad w(x, t) = q(t) \sin \frac{\pi x}{L}, \quad (24)$$

and their variations are given by

$$\delta u(x, t) = \delta p(t) \sin \frac{\pi x}{L}, \quad \delta w(x, t) = \delta q(t) \sin \frac{\pi x}{L}. \quad (25)$$

If the initial tension is much higher than the own weight of the cable, the tension may be assumed as constant: $H = \text{const}$. Using Eqs. (23)–(25) in Eq. (22), after integrating process and multiplying the results by $\frac{2}{\mu L}$ leads to the set of nonlinear equations

$$\begin{aligned} \ddot{p}(t) + EA \left[\frac{\pi^2}{\mu L^2} p(t) + \frac{3\pi^4}{8\mu L^4} p^3(t) + \frac{3\pi^4}{8\mu L^4} p(t)q^2(t) + \frac{28g\pi}{9HL^2} \cos \gamma p(t)q(t) \right] \\ + \frac{c_h}{\mu} \dot{p}(t) + H \frac{\pi^2}{\mu L^2} p(t) = -\frac{2}{\pi} \cos \gamma \ddot{U}(t) \\ \ddot{q}(t) + EA \left[\frac{3\pi^4}{8\mu L^4} p^2(t)q(t) + \frac{3\pi^4}{8\mu L^4} q^3(t) + \frac{14g\pi}{9HL^2} \cos \gamma p^2(t) + \frac{14g\pi}{3HL^2} \cos \gamma q^2(t) \right] \\ + \left(\frac{\mu g}{H} \cos \gamma \right)^2 \left(\frac{6 + \pi^2}{12\mu} \right) q(t) + \frac{c_v}{\mu} \dot{q}(t) + H \frac{\pi^2}{\mu L^2} q(t) = -\frac{2}{\pi} \sin \gamma \ddot{U}(t) \end{aligned} \quad (26)$$

5 Stochastic Model

The response $U(t)$ of a guyed tower to the stochastic wind excitation is assumed to be dominated by the fundamental mode shape, with the corresponding natural frequency Ω_o . The stochastic wind excitation is a stationary wide band process, therefore the process $U(t)$ is narrow-band, with central frequency Ω_o . It is idealized as the Gaussian white noise of the spectral density S_0 passed through the first-order linear filter, yielding the process $X(t)$, which is subsequently passed through the second-order linear filter. Hence the stochastic governing equations are defined by

$$\ddot{U} + 2\zeta_f \Omega_o \dot{U} + \Omega_o^2 U = X(t), \quad \dot{X} + \alpha X = \alpha \sqrt{2\pi S_o} \xi(t), \quad (27)$$

where $\xi(t)$ is a Gaussian white noise process. The stationary stochastic process $U(t)$ need to be twice differentiable, which is satisfied if $\omega^4 S_{UU}(\omega)$ is integrable

over $(-\infty, \infty)$. In the present case the spectral density $S_{UU}(\omega)$ of the process $U(t)$ equals

$$S_{UU}(\omega) = \frac{S_0 \alpha^2}{(\omega^2 + \alpha^2)[(\Omega_0^2 - \omega^2)^2 + (2\zeta_f \Omega_0 \omega)^2]}. \quad (28)$$

The steady-state variance of the process $U(t)$ equals

$$\sigma_U^2 = \frac{\alpha \pi S_0 (2\zeta_f \Omega_o + \alpha)}{2\zeta_f \Omega_o^3 (2\alpha \zeta_f \Omega_o + \alpha^2 + \Omega_o^2)}. \quad (29)$$

The stochastic process $U(t)$ is assumed to be mean-square equivalent to the harmonic process with amplitude A_0 and frequency Ω_0 . When the equivalence condition is adopted as $\sigma_U^2 = A_0^2/2$, the parameter α is determined as

$$\alpha = \Omega_o \left\{ -\zeta_f + \sqrt{\zeta_f^2 + \frac{\zeta_f \Omega_o^3 A_0^2}{\pi S_0 - \zeta_f \Omega_o^3 A_0^2}} \right\}. \quad (30)$$

The equations of motions that are taken into further consideration are given by the following expressions:

$$\begin{aligned} \ddot{p}(t) &= -a_1 p(t)(EA + H) - a_2(p^3(t) + p(t)q(t)^2) + 2a_3 p(t)q(t) - \frac{c_h}{\mu} \dot{p}(t) - \beta_h \ddot{U}(t), \\ \ddot{q}(t) &= -a_2(p^2(t)q(t) + q^3(t)) + a_3(p^2(t) + 3q^2(t)) + a_4 q(t) - \frac{c_v}{\mu} \dot{q}(t) - a_1 H q(t) - \beta_v \ddot{U}(t), \\ \ddot{U}(t) &= X(t) - 2\zeta_f \Omega_o \dot{U}(t) - \Omega_o^2 U(t), \end{aligned} \quad (31)$$

where the particular constant terms are denoted as:

$$\begin{aligned} \beta_h &= \frac{2}{\pi} \cos \gamma, & \beta_v &= \frac{2}{\pi} \sin \gamma, & a_1 &= \frac{\pi^2}{\mu L^2}, \\ a_2 &= EA \frac{3\pi^4}{8\mu L^4}, & a_3 &= -EA \frac{14g\pi}{9HL^2} \cos \gamma, & a_4 &= -EA \left(\frac{\mu g}{H} \cos \gamma \right)^2 \left(\frac{6+\pi^2}{12\mu} \right). \end{aligned} \quad (32)$$

If $W(t)$, $\mathbf{c}(\mathbf{Y}(t), t)$ and $\boldsymbol{\sigma}$ denote the standard Wiener process, the drift vector and the diffusion vector, respectively, the stochastic equations of motion in state space form are

$$d\mathbf{Y}(t) = \mathbf{c}(\mathbf{Y}(t))dt + \boldsymbol{\sigma}dW(t). \quad (33)$$

If the state vector is defined as $\mathbf{Y}(t) = [p(t) \dot{p}(t) q(t) \dot{q}(t) U(t) \dot{U}(t) X(t)]^T$, the particular elements of drift vector are consequently expressed as

$$\begin{aligned} c_1(\mathbf{Y}(t)) &= \dot{p}(t); \\ c_2(\mathbf{Y}(t)) &= -a_1(EA + H)p(t) - a_2(p^3(t) + p(t)q(t)^2) + 2a_3 p(t)q(t) - \frac{c_h}{\mu} \dot{p}(t) \\ &\quad + \beta_h(\Omega_o^2 U(t) + 2\zeta_f \Omega_o \dot{U}(t) - X(t)); \\ c_3(\mathbf{Y}(t)) &= \dot{q}(t); \end{aligned} \quad (34)$$

$$\begin{aligned}
c_4(\mathbf{Y}(t)) &= -a_2(p^2(t)q(t) + q^3(t)) + a_3(p^2(t) + 3q^2(t)) + a_4q(t) - \frac{c_v}{\mu}\dot{q}(t) - a_1Hq(t) \\
&\quad + \beta_v(\Omega_o^2U(t) + 2\zeta_f\Omega_o\dot{U}(t) - X(t)); \\
c_5(\mathbf{Y}(t)) &= \dot{U}(t); \\
c_6(\mathbf{Y}(t)) &= -\Omega_o^2U(t) - 2\zeta_f\Omega_o\dot{U}(t) + X(t); \\
c_7(\mathbf{Y}(t)) &= -\alpha X(t),
\end{aligned}$$

and the diffusion vector is

$$\boldsymbol{\sigma} = [0 \ 0 \ 0 \ 0 \ 0 \ 0 \ \alpha\sqrt{2\pi S_o}]^T. \quad (35)$$

6 Application of the Equivalent Linearization Technique

To convert the original nonlinear set of differential equations into the linear one, the augmented state vector needs to be transformed to the centralized state vector, that is defined as $\mathbf{Y}^0(\mathbf{t}) = [Y_1^0 \ Y_2^0 \ Y_3^0 \ Y_4^0 \ Y_5^0 \ Y_6^0 \ Y_7^0]^T$. The particular elements of $\mathbf{Y}^0(\mathbf{t})$ are determined in general form as $Y_i^0(t) = Y_i(t) - E[Y_i(t)]$. The differential equations for the mean values are given by

$$\frac{d}{dt}E[\mathbf{Y}(t)] = E[\mathbf{c}(\mathbf{Y}^0(t))]. \quad (36)$$

The centralized state vector leads to the stochastic equation of motion

$$d\mathbf{Y}^0(t) = \mathbf{c}^0(\mathbf{Y}^0(t), t)dt + \boldsymbol{\sigma}(t)dW(t), \quad \text{with } \mathbf{c}^0(\mathbf{Y}^0(t), t) = \mathbf{c}(\mathbf{Y}^0(t), t) - E[\mathbf{c}(\mathbf{Y}^0(t), t)]. \quad (37)$$

In further considerations the original nonlinear system described by Eq.(33) is replaced by the equivalent linear one expressed by

$$d\mathbf{Y}^0(t) = \mathbf{B}\mathbf{Y}^0(t)dt + \boldsymbol{\sigma}dW(t), \quad (38)$$

where the centralized drift terms are replaced by the linear function of the state variables and equivalent coefficients B_{im} , that are obtained from the condition of mean-square minimizations the difference between the Eqs.(37) and (38)

$$c_{i,eq}^0(\mathbf{Y}^0(t)) = B_{im}Y_m^0, \quad \text{where } B_{im}\kappa_{mj} = E[Y_j^0 c_i^0(\mathbf{Y}^0)], \quad (39)$$

with κ_{mj} being the covariance function of the state variables m and j . Because of the jointly Gaussian distribution of the centralized state variables \mathbf{Y}^0 the following relationship for zero-mean Gaussian random vector \mathbf{X} given by [9] is used

$$E[\mathbf{X}f(\mathbf{X})] = E[\mathbf{X}\mathbf{X}^T]E[\nabla f(\mathbf{X})], \quad (40)$$

where $f(\mathbf{X})$ is the non-linear function while $\nabla = \left[\frac{\partial}{\partial X_1}, \frac{\partial}{\partial X_2}, \dots, \frac{\partial}{\partial X_n} \right]^T$. Using Eqs. (40) in (39) gives

$$\kappa(t)\mathbf{B}^T = \kappa(t)\mathbf{E}[\nabla \mathbf{c}^{0T}(\mathbf{Y}^0(t))], \text{ where } \mathbf{B}^T = \mathbf{E}[\nabla \mathbf{c}^{0T}(\mathbf{Y}^0(t))], \quad (41)$$

and $\kappa(t)$ is the covariance matrix. Equation (41) describes the components of matrix \mathbf{B} . Applying Eq. (41) to the elements of the drift vector defined by the Eqs. (34) after transformation to the centralized state variables leads to the matrix B in the following form

$$\mathbf{B} = \begin{bmatrix} 0 & 1 & 0 & 0 & 0 & 0 & 0 \\ b_1 - \frac{c_h}{\mu} & b_2 & 0 & \beta_h \Omega_o^2 & 2\beta_h \zeta_f \Omega_o & -\beta_h \\ 0 & 0 & 0 & 1 & 0 & 0 & 0 \\ b_2 & 0 & b_3 - \frac{c_v}{\mu} & \beta_v \Omega_o^2 & 2\beta_v \zeta_f \Omega_o & -\beta_v \\ 0 & 0 & 0 & 0 & 0 & 1 & 0 \\ 0 & 0 & 0 & 0 & -\Omega_o^2 & -2\zeta_f \Omega_o & 1 \\ 0 & 0 & 0 & 0 & 0 & 0 & -\alpha \end{bmatrix}, \quad (42)$$

where the particular terms are given by:

$$b_1 = -a_1(EA + H) - a_2(3\mathbf{E}[(Y_1^0)^2] + 3(\mathbf{E}[p(t)])^2 + \mathbf{E}[(Y_3^0)^2] + (\mathbf{E}[q(t)])^2) + 2a_3\mathbf{E}[q(t)],$$

$$b_2 = -2a_2(\mathbf{E}[Y_1^0 Y_3^0] + \mathbf{E}[q(t)]\mathbf{E}[p(t)]) + 2a_3(\mathbf{E}[p(t)]),$$

$$b_3 = -a_2(\mathbf{E}[(Y_1^0)^2] + (\mathbf{E}[p(t)])^2 + 3\mathbf{E}[(Y_3^0)^2] + 3(\mathbf{E}[q(t)])^2) + 6a_3\mathbf{E}[q(t)] + a_4 - a_1 H.$$

The covariance matrix $\kappa(t)$ is governed by the following set of differential equations

$$\frac{d}{dt} \kappa(t) = \mathbf{B}\kappa(t) + \kappa(t)\mathbf{B}^T + \boldsymbol{\sigma}\boldsymbol{\sigma}^T, \quad (43)$$

which should be solved together with the differential equations for the mean values defined by the Eq. (36). As a result the set of 35 differential equations is obtained that is solved numerically.

7 Numerical Results

In the numerical analysis the guyed tower with the single guy line is considered. The cable with the total length $L = 300$ m is attached to the guyed tower on the level 254.4 m, which gives the slope of the guy-line $\gamma = 58^\circ$. The mass per unit length of the rope is equal to $\mu = 7.47$ kg/m while its longitudinal stiffness $EA = 195$ MN. The assumed initial tension is $H = 300$ kN. The fundamental frequency and the amplitude of the structural response process $U(t)$ are assumed as $\Omega_0 = 8.65$ rad/s and $A_0 = 0.25$ m, respectively. The damping coefficients are

adopted as $c_h = c_v = 0.03 \text{ Ns/m}^2$. The spectral density of the Gaussian white noise process and the damping of the linear filter are assumed as $S_0 = 1$ and $\zeta_f = 0.005$, respectively.

Firstly, the numerical solution of set of 35 differential equations determined by Eqs. (36) and (43) was obtained during 60s of motion. Afterwards, the results of expected values and variances of particular random state variables were verified by the Monte Carlo simulation conducted for Eqs. (27) and (31), with the number of sample functions equal to 1000. In the Monte Carlo simulation of the white noise process it is important to introduce the correct value of its standard deviation, that should be equal to $1/\sqrt{\Delta t}$, where Δt is the value of the time step that is taken in the analysis [10]. This will make the obtained results independent of the value of the time step. Otherwise, the received results may be misinterpreted.

Figure 2 shows a good match between the results of the expected values obtained from both methods. Due to the high frequency of the $p(t)$ variable, for better visibility, the results are shown only for the first 10 s of the motion. However, for the rest of the time, the diagram course is analogous. The variances of particular random state variables presented on Fig. 3 show also good agreement. A better matching of the diagrams could be achieved by increasing the number of simulations in the Monte Carlo method, however, this significantly increases the time needed to obtain results. Calculations of the equivalent linearization technique conducted for a set of 35 differential equations take a few seconds, while the Monte Carlo simulation carried out for a set of 7 differential equations with using 1000 simulations requires about 7 h. This indicates a significant advantage of the proposed approach. The bigger differences can be observed for $\text{Var}[p(t)]$, where the values of the equivalent linearization technique show a greater vibration amplitude, but they oscillate around the results obtained from the Monte Carlo simulation. On the other hand, the order of these quantities is very small, so the course of the diagram may also be affected by some numerical errors.

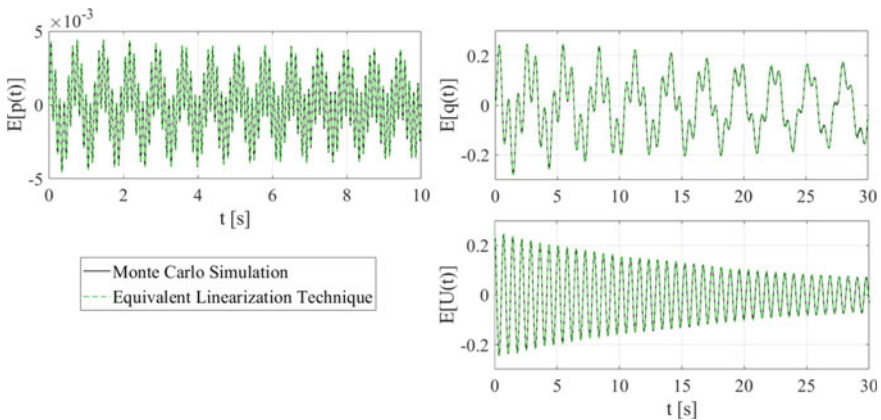


Fig. 2 Expected values of the particular random state variables

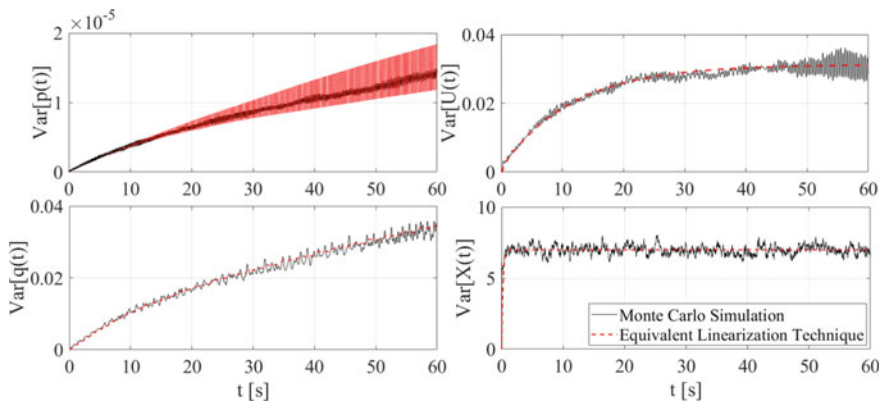


Fig. 3 Variances of the particular random state variables

8 Conclusions

The results presented in this paper show that equivalent linearization technique allows to obtain expected values, variances and cross-covariances of particular random state variables with good accuracy. These complex results give a better view on the behaviour of the entire system. In the case of guy line in the guyed tower with significant height the small-sag cable model seems to be more appropriate than using the string model, because in reality it is almost impossible to apply enough initial tension to the steel rope, to fully compensate the sag caused by its own weight. The presented approach can be easily implemented in computer codes by using numerical techniques and results in much shorter time needed to receive the values comparable with the Monte Carlo simulation.

Acknowledgements Supported by West Pomeranian University of Technology in Szczecin.

References

1. Hagedorn P, DasGupta A (1990) *Vibrations and waves in continuous mechanical systems*. Wiley, New York
2. Weber H, Kaczmarczyk S, Iwankiewicz R (2020) Non-linear dynamic response of a cable system with a tuned mass damper to stochastic base excitation via equivalent linearization technique. *Meccanica* 55(12):2413–2422
3. Berlioz A, Lamarque C-H (2005) A non-linear model for the dynamics of an inclined cable. *J Sound Vib* 279:619–639
4. Giaccu GF, Caracoglia L, Barbiellini B (2017) Higher-order moments of eigenvalue and eigenvector distributions for the nonlinear stochastic dynamics of cable networks. *Procedia Eng* 199:637–642
5. Roberts JB, Spanos PD (1990) *Random vibration and statistical linearization*. Wiley, New York

6. Proppe C, Pradlwarter HJ, Schuëller GI (2003) Equivalent linearization and Monte Carlo simulation in stochastic dynamics. *Probab Eng Mech* 18:1–15
7. Spanos PD, Zhang YF (2019) Formulation of statistical linearization for MDOF systems subject to combined periodic and stochastic excitations. *J Appl Mech* 86(10):101003
8. Irvine HM (1981) *Cable structures*. The MIT Press, Cambridge, MA and London
9. Atalik TS, Utku S (1976) Stochastic Linearization of Multi-degree-of-freedom Nonlinear Systems. *Earthq Eng Struct Dyn* 4:411–420
10. Weber H, Kaczmarczyk S, Iwankiewicz R (2021) Non-linear response of cable-mass-spring system in high-rise buildings under stochastic seismic excitation. *Materials* 14(22):6858

Review Study on Nonlinear Modeling Issues Associated with the Dynamics of In-Plane Cable Networks



Luca Caracoglia  and Gian Felice Giaccu 

Abstract This study summarizes a decade-long research activity, devoted to the examination of the nonlinear dynamics of in-plane cable networks on cable-stayed bridges. Nonlinearity is triggered by amplitude-dependent, internal restoring force behavior of the cross-ties, connecting two adjacent stays. The work originates from an earlier study by the first author. The study reviews the main contributions that include the derivation of the Equivalent Linearization Method to solve the amplitude-dependent eigenvalue-eigenvector problem of the network, and the use of Stochastic Approximation to examine stochastic dynamics, induced by random amplitudes at the onset of aeroelastic vibrations. A random amplitude parameter is used to characterize the nonlinear behavior in the restrainer, and to simulate imperfections, malfunctioning and modeling simplifications. A three-stay, one-restrainer network, installed on the Fred Hartman Bridge (Houston, Texas, USA) is employed to illustrate the main results.

Keywords Cable-stayed bridges · Stays · Nonlinear vibration · Wind load effects · Stochastic Approximation · Monte Carlo methods

1 Introduction

Cross-ties are often employed as passive devices for the mitigation of stay cable vibrations, which have been observed in the field under the excitation of wind and rain/wind.

L. Caracoglia (✉)

Department of Civil and Environmental Engineering, 400 Snell Engineering Center, Northeastern University, 360 Huntington Avenue, Boston, MA 02115, USA
e-mail: lucac@coe.neu.edu

G. F. Giaccu

Department of Architecture, Design and Urban Planning, University of Sassari, 07041 Alghero, Italy
e-mail: gf.giaccu@uniss.it

The “basic module” of an in-plane cable network is composed of two stays connected by a transverse cross-tie [2]. These systems can become very complex if the basic module is repeated to form a large, complex cable structure. These systems exhibited engineering failures. Several models have been proposed by the Authors [4–7], originating from a linear dynamic formulation of the cable network, up to the exploration of cases in which the use of a nonlinear cross-tie element is introduced to more realistically simulate the dynamic behavior under non-negligible vibration amplitudes in the stays [11]. Structural nonlinearity can be used to describe various phenomena, from the simplest case, in which one non-linear element anchors the stay to the deck, to more complicated cases in which the non-linear linkages are multiple and replicate a large cable network geometry.

The nonlinearity is examined by utilizing the Equivalent Linearization Method (ELM), derived to compare nonlinear performance to that of the corresponding linear case. Either a frequency increment or a decrement can be observed in the system as a function of a generalized vibration amplitude parameter, at least for the fundamental “modes”. Subsequently, the ELM is coupled with the Stochastic Approximation (SA) [9, 12, 13] to account for the presence of parameter variability and systematic uncertainty during aeroelastic vibration.

Although not summarized herein, an extended model has been presented [4] to analyze the effects of a loss in the pre-tensioning force imparted to the cross-ties; the model investigates the “unilateral” free-vibration response of the network, simulates an incipient slackening of the connector and determines an appropriate level of pretension force in the cross-tie.

2 Theoretical Background

2.1 Nonlinear Cable Network Dynamics

The case study is a three-cable system, installed on the Fred Hartman Bridge (Houston Ship Channel, Texas, USA) and labeled as BSL network (Fig. 1). The system is composed of three stays (BS13, BS14 and BS15) and one cross-tie. The reference stay is BS15 with index $j = 1$. The properties of the stays (j) are: tension T_j , length L_j and mass per unit length μ_j . The fundamental, native cable frequencies of the three stays are 1.30 Hz (BS15), 1.36 Hz (BS14) and 1.89 Hz (BS13). Description of the stay properties may be found in previous studies [1]. The ELM can be used to examine the free-vibration, in-plane dynamics of the system in Fig. 1. The model employs the wave equation to analyze the vibration of taut-cables [10] (with $j = 1, 2, 3$ and $p = 1, 2$ in Fig. 1), where $x_{j,p}$ and $y_{j,p}$ respectively represent the position and vertical displacement of the considered cable element (Fig. 1).

$$T_j \frac{\partial^2 y_{j,p}}{\partial x_{j,p}^2} = \mu_j \frac{\partial^2 y_{j,p}}{\partial t^2} \quad (1)$$

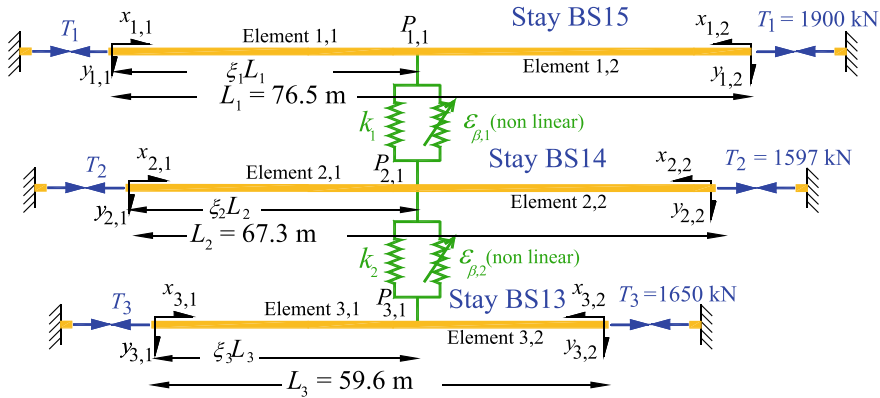


Fig. 1 Cable network with nonlinear restrainers—F. Hartman Bridge as a case study (figure reproduced from [1])

Each segment of the stays is simulated as a continuous taut-string element, with transverse oscillation at a generic point of coordinates along the segment and time t . The nonlinearity is concentrated in the internal restoring force transferred by the cross-ties. In the case of cable-cross-tie systems, flexural stiffness and nonlinear sag effects can be usually neglected in practical applications.

In this review study, the following properties of the BSL network are considered: cross-tie position $x_{1,1} = 0.52L_1$ with $L_1 = 76.5$ m (except for Sect. 3.2 where $x_{1,1} = 0.35L_1$ is used); linear stiffness properties in both cross-tie segments with $d_k = d_{k,1} = d_{k,2}$ with $d_{k,1} = T_1/(k_1L_1)$, $d_{k,2} = T_2/(k_2L_2)$. The “dimensionless stiffness parameter” $d_{k,j} = T_j/(k_jL_j)$, with $j = \{1, 2\}$, compares the stiffness in a linear restrainer element with the geometric stiffening effect, which is proportional to T_j/L_j . The assumption used on $d_k = d_{k,1} = d_{k,2}$ is not restrictive, since a small relative difference among stiffness parameters typically has a secondary influence on the cable network dynamics [6].

In the ELM, the constitutive relationship that simulates the internal restoring force effect in the cross-tie (Fig. 1) is linearized. For example, the internal force in the restrainer connecting stays j and $j + 1$ is, with $x_{j,1} = \xi_{j,1}L_j$ on stay j :

$$F_{j,j+1} = - [k_j (y_{j,1} - y_{j+1,1}) + \epsilon_{\beta,j} |y_{j,1} - y_{j+1,1}|^\beta \text{sign} (y_{j,1} - y_{j+1,1})] \quad (2)$$

In Eq. (2) a linear spring of stiffness k_j is used in parallel with a nonlinear element of generalized stiffness $\epsilon_{\beta,j}$; $\epsilon_{\beta,j} > 0$ simulates a stiffening effect after initial pre-tension of the wire connector, whereas $\epsilon_{\beta,j} < 0$ corresponds to a degradation of cross-tie properties. Quantities $y_{j,1}$ and $y_{j,1+1}$ in Eq. (2) are the transverse vibrations of the stays at the anchorage points of the restrainer. Quantity β is an integer number (power-law coefficient).

The ELM allows substituting the nonlinear internal restoring force effect in Eq. (2) with an equivalent linearized effect. In a dimensionless formulation, a linearized

dimensionless stiffness parameter is designated, similar to $d_{k,j} = T_j/(k_j L_j)$. For example, the inverse of the linearized parameter, pertaining to the nonlinear effect in the restrainer between nodes $P_{j,1}$ and $P_{j+1,1}$ and the j -th cable in Fig. 1, is:

$$\frac{1}{d_{k_{\text{ELM}},j}} = 2\nu_{\beta,j}\lambda L_1(\beta + 1)^{-1}|S_{j,1} - \delta_j S_{j+1,1}|^{\beta+1} \quad (3)$$

In Eq. (3) $d_{k_{\text{ELM}},j} = T_j/(k_{\text{ELM},j} L_j)$ and $k_{\text{ELM},j}$ are dimensionless and dimensional equivalent stiffness terms; $\nu_{\beta,j} = \epsilon_{\beta,j} L_j^\beta / T_j$ quantifies the nonlinear stiffness effect contribution in the cross-tie. Eq. (3) depends on dimensionless vibration amplitude parameter $\lambda \geq 0$, the local displacement field at nodes $P_{j,1}$ and $P_{j+1,1}$ designated by quantities $S_{j,1} = \sin(\alpha\pi \tilde{f}_j \xi_j)$ and $S_{j+1,1}$ (depending on frequency ratio \tilde{f}_j and generic dimensionless frequency α) and the “modal amplitude ratio” δ_j [5, 6]. The scalar λ measures the ratio between anticipated vibration amplitude in the reference stay ($j = 1$ or BS15), mode by mode, and the length L_1 .

The total equivalent stiffness parameter $1/d_{k_{\text{E}},j}$ of each cross-tie segment, combining the nonlinear spring model with the linear one of stiffness k_j or $d_{k,j} = T_j/(k_j L_j)$, is:

$$d_{k_{\text{E}},j} = \frac{d_{k,j} d_{k_{\text{ELM}},j}}{d_{k,j} + d_{k_{\text{ELM}},j}} \quad (4)$$

By ELM and Eq. (4), the nonlinear dynamic differential equations are transformed to a system of linearized homogeneous algebraic equations, similar to an equivalent eigenvalue/eigenvector problem. The solution is expressed using the definition of “equivalent frequency” α_{E} , referenced to $\omega_{01} = \pi/L_1 \sqrt{T_1/\mu_1}$ first-mode pulsation of stay $j = 1$ (BS15 in Fig. 1), and “modes” $y_{j,p}(x_{j,p}, t) = \exp(\iota \alpha_{\text{E}} \omega_{01} t) Y_{j,p}(x_{j,p})$, with ι imaginary unit; the mode shapes $Y_{j,p}(x_{j,p})$ are real trigonometric functions.

The term $d_{k_{\text{E}},j}$ in Eq. (4) depends, mode by mode, on real, dimensionless frequency α_{E} (unknown), exponent β , and the generalized scalar amplitude parameter λ .

2.2 Stochastic Approximation

The variable λ is random to account for the inadequate knowledge of the stay vibration mechanism, influenced by irregular wind load features and aeroelasticity. Modeling uncertainty can be simulated by a uniformly distributed λ variable between 0 and λ_u ; λ_u is inferred from the anticipated level of vibration [14]. The problem consequently becomes a random eigenvalue problem, which requires stochastic methods to obtain the solution. The SA [12, 13] is an iterative method for finding the root of a function, even if the function’s equation is unknown due to unavoidable errors. The SA method, firstly used in [3] to evaluate the mean value of the amplitude-dependent random frequency of a cable network, is briefly described in this section.

The nature of the stochastic free vibration can be represented through the random sequence of λ , which generates a corresponding sequence of equivalent frequencies α_E . These frequencies are found by ELM from the roots of the polynomial associated with the equivalent eigenvalue/eigenvector problem. Given that the true value of the expected frequency $\bar{\alpha}_E = \mathbb{E}[\alpha_E]$ is not known, the SA determines its estimator (mode by mode) by a recursive search and successive iterations from an approximate sequence; the SA avoids expensive root finding for each realization of λ . The approximate solution is found by iterations using SA, in which a “damping parameter” and a “relaxation parameter” are used to facilitate the numerical convergence [13]. Special situations are possible for closely-spaced roots of the characteristic polynomial [3].

2.3 Layered SA Algorithm

The standard SA enables estimation of expectations (i.e., average roots of the characteristic polynomial or $\bar{\alpha}_E$ (ELM frequencies or eigenvalues). Extensions of the SA paradigm have been proposed [1] to allow evaluating higher statistical moments. The *layered* SA algorithm considers replacing the continuous random variable α_E , with a discrete equivalent random eigenvalue variable, for which the probability mass function can be found recursively. Since there is a nonlinear relationship between random λ and random output α_E , the problem is reduced to a transformation of random variables [8]. This relationship is replaced, in the SA setting, by a stratified discrete equivalent (DE) variable. Quantity λ is sampled from m equal-probability independent intervals, Λ_r with $r = 1, \dots, m$, in each of which the frequency converges to a representative discrete point $\alpha_{E,r}^{(DE)}$.

Each discrete point $\alpha_{E,r}^{(DE)}$ is evaluated as the expected value of the continuous variable by restricting the sampling of λ to each sub-set r or $\alpha_{E,r}^{(DE)} = \mathbb{E}[\alpha_E | \lambda \in \Lambda_r]$. Expectation estimation is repeated m times, by layering the sampling to $\lambda \in \Lambda_r$. Mean and standard deviation of the frequency α_E are evaluated from the first and second moments of the corresponding, approximate discrete variable, with probability mass function $\mathcal{PMF} = 1/m$ and with symbol “.” designating simple multiplication:

$$\mathbb{E}[\alpha_E] \approx \sum_{r=1}^m \alpha_{E,r}^{(DE)} \cdot (\mathcal{PMF}) \tag{5}$$

$$\mathbb{E}[\alpha_E^2] \approx \sum_{r=1}^m \left(\alpha_{E,r}^{(DE)}\right)^2 \cdot (\mathcal{PMF}) \tag{6}$$

3 Simulation Results

3.1 BSL Network—Deterministic Linear Analysis

The SA has been deployed to study the BSL network under stochastic disturbance, simulated through random amplitude variable uniformly distributed $0 < \lambda \leq \lambda_u$. The upper limit λ_u investigates various vibration levels; $\lambda_u = 1/200 = 0.005$ corresponds to amplitude of 1/200th of the reference cable length. First, linear analysis is conducted by neglecting effects of amplitude λ .

Parametric investigations are carried out to study the dynamics of the BSL network in Ref. [3].

In Ref. [3] simulations considered the analysis of Mode II and Mode III of the BSL network (Fig. 1) since the modal dynamics has special features. Following the same motivation, this study mainly examines the behavior of Modes II and III. In the studied system, the cross-tie located at $x_{1,1} = 0.52L_1$ with $d_k = d_{k,1} = d_{k,2} = 0.0018$ equal to design values and $\epsilon_{\beta,j} = 0$.

3.2 ELM Analysis of the BSL Network with Non-linear Cross-Tie

In the case of simulations with power-law-stiffness cross-tie, the main consequence of nonlinearity in the restoring-force mechanism is the “shift” in the equivalent frequencies of the entire system [3]. The variation of equivalent frequency, mode by mode, is a function of the type of nonlinearity and vibration amplitude, treated as a constant, deterministic parameter in this subsection $\lambda = \lambda_u$.

Even though both a stiffness increment ($\nu_{\beta j} = \epsilon_{\beta j} L_j^\beta / T_j > 0$) and reduction ($\nu_{\beta j} < 0$) can be considered, the case $\nu_{\beta j} > 0$ with cross-tie at $x_{1,1} = 0.35L_1$ is exclusively analyzed in this sub-section. For comparison of the results at other β values, a “similarity ratio” may be introduced [6].

Stay BS15 is designated as the reference stay, i.e., “stay 1”. Nonlinear restoring effects are replicated in both segments of the restrainer (between BS13 and BS14, and between BS14 and BS15 in Fig. 1) through generalized, positive power-law model. The case with $\beta = 2$ and parameter $d_k \approx d_{k1} = T_1 / (k_1 L_1)$ uses both design values $d_k = 0.008$ and extends the analysis by parametric investigation to various d_{k1} . The vibration parameter $\lambda = 0.005$ corresponds to amplitudes equal to 0.38 m, compatible with the diameter of BS15 (140 mm).

Figure 2 illustrates the normalized frequency α_E vs. $d_k = d_{k1} = T_1 / (k_1 L_1)$ and a stiffening effect exerted by the quadratic power-law restoring mechanism in the cross-tie segments. Figure 2a also considers numerical results for the first and second in-plane network modes, whereas Fig. 2b shows the frequency evolution for Mode III. The cross-tie induces a beneficial frequency increment $\alpha_E > 1.0$ (Mode I) in comparison with the fundamental native-cable frequency of the longest stay, BS15.

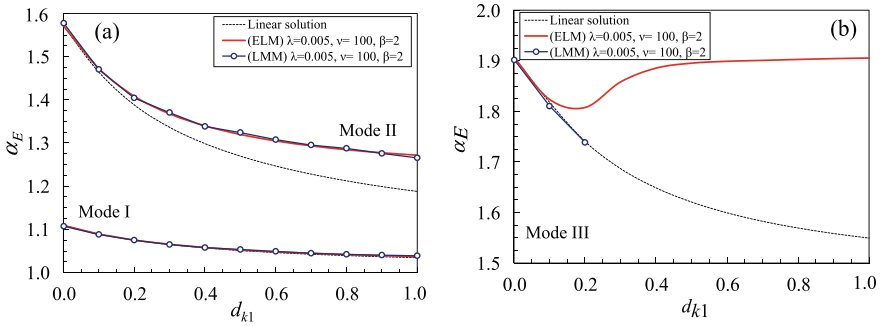


Fig. 2 Normalized frequency as a function of $d_k = d_{k1} = T_1/(k_1L_1)$ for the nonlinear BSL network with quadratic-stiffness cross-tie, $\nu_{\beta 1} = \nu_{\beta 2} = 10^2$, cross-tie at $x_{1,1} = 0.35L_1$, and constant deterministic amplitude parameter $\lambda = 0.005$: **a** First and second “equivalent modes”; **b** third mode. Comparison between ELM, LMM and linear case (reproduced from [6])

The graph also exhibits a drastic diminution of frequency for weak linear restrainer and $d_k > 0.5$. The nonlinear resorting effect is more pronounced for Mode II with a relative frequency increment approximately equal to +10% at $d_k > 0.5$. We note that Mode I is a global network mode.

By contrast, when the three stays tend to vibrate with opposite phase (e.g., Mode II), the force transmitted through the cross-tie increases and the presence of a nonlinear restoring effect is important, especially for relatively weak restrainers with $d_k > 0.1$, but also in the design case ($d_k = 0.008$).

In Fig. 2b the numerical results indicate no significant variation of α_E between linear-restrainer and nonlinear-restrainer case for Mode III at low $d_k = d_{k1}$. A discrepancy between ELM and LMM (lumped-mass or finite-element model) solutions can be observed for $d_k = d_{k1} > 0.1$. In this range of values, the finite-difference scheme tends to follow the linear solution with a progressive diminution of α_E , while the ELM predicts an increment of frequency compared to the linear case, and a horizontal asymptotic frequency at large d_k , coincident with the solution for a rigid cross-tie. Since the proposed linearization is based on the dimensional vibration amplitude λL_1 of the BS15 stay, which marginally contributes to Mode III, the ELM is less efficient at assessing the nonlinear dynamics for moderately nonlinear, flexible cross-tie.

Figure 3 shows the “equivalent” shapes of Modes II and III, computed via ELM for a positive increment of equivalent stiffness, and corresponding to the frequency results depicted in Fig. 2 for $d_k = d_{k1} = 0.8$.

The “scale” of Y_r is normalized so that the modal amplitude is the same for all modes, both linear and nonlinear. The figure confirms that, nonlinear effects are particularly important for Mode III. A drastic change in the mode shapes is noted: the equivalent mode denotes contributions from all the stays.

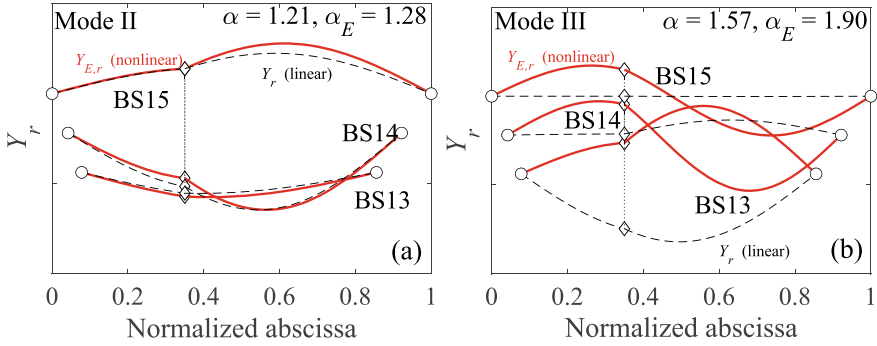


Fig. 3 Normalized eigen-functions (mode shapes) of the BSL network - comparison between linear solution $d_k = d_{k1} = 0.8$ and ELM “equivalent modes”, derived for quadratic-stiffness cross-tie at $x_{1,1} = 0.35L_1$ with $\nu_{\beta 1} = \nu_{\beta 2} = 10^2$ and $\lambda = 0.005$; **a** second mode, **b** third mode (reproduced from [6])

4 BSL Network—Stochastic Approximation

In this section, the location of the cross-tie is $x_{1,1} = 0.52L_1$, i.e., the full-scale design configuration. Results are plotted as a function of the cross-tie normalized stiffness $d_k = d_{k1}$, with $d_k = 0.0018$ corresponding to the design configuration. For Mode III ELM mode and ELM frequency are particularly sensitive to random λ . The case with moderate positive nonlinearity is studied. The amplitude parameter is random, uniformly distributed in the interval $0 \leq \lambda \leq (1/400)$, simulating aeroelastic vibration of one or two cable diameters (140 mm for BS15).

Even though the mean value can be found by standard SA algorithm, a better approximation of the mean values can be achieved through the layered SA algorithm in Eq. (5). The standard deviation is determined from Eq. (6).

Verification of the layered SA algorithm is presented in Fig. 4, illustrating mean and standard deviation of the random frequency of Mode III.

The approximate numerical results are compared with “exact” values, obtained by Monte Carlo sampling with 500 realizations (graphs labeled as BFM or “Brute Force Method”). In Fig. 4b the standard deviation of α_E tends to increase with the decrement of linear stiffness in the cross-tie. In fact, flexible restrainers not only reduce the beneficial effect of a frequency increment but also drastically enhance the sensitivity to randomness. Further examination suggests that the order of magnitude of the standard deviation is quite different as a result of the nonlinearity. We note the coefficient of variation is small, about 7%. Estimation of $SD(\alpha_E)$ is influenced by the selection of equally-probable sets m , with $m = \{2, 4, 6\}$. The estimation error is large (20%) with $d_k = 1.0$ (unrealistically large value). In the range $0.0 < d_k < 0.6$, $m \geq 4$ is needed for accuracy.

Further inspection also reveals that only a modest improvement effect is obtained by increasing the sets above $m = 6$. In all the simulations a drastic reduction of computing time is achieved by sequential application of the SA. The approximate

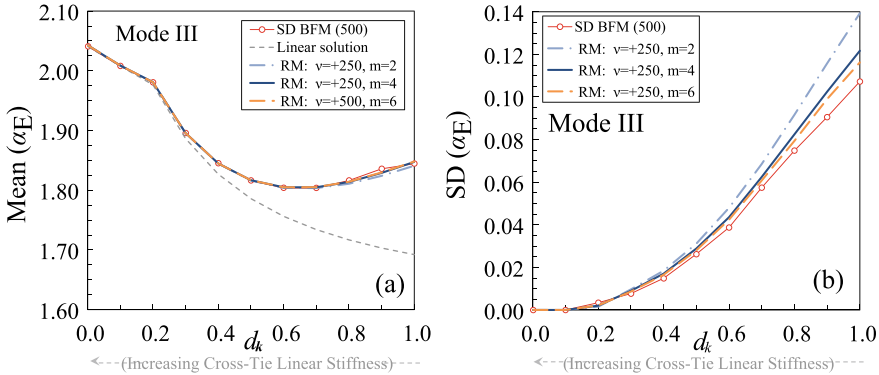


Fig. 4 Layered SA algorithm examining random α_E of the BSL network’s third mode with nonlinear cross tie located at $x_{1,1} = 0.52L_1$ ($\beta = 3, \nu_{\beta 1} = \nu_{\beta 2} = +250$), induced by uniform stochastic vibration (random amplitude $0 \leq \lambda \leq (1/400)$): **a** mean value, **b** standard deviation (SD); reproduced from [1]

$SD(\alpha_E)$ is consistently larger than the reference value (BFM). This discrepancy can be influenced by the non-negligible frequency shift between linear and nonlinear solution in terms of mean values (Fig. 4a). This result is not unexpected since the continuous probability distribution of $SD(\alpha_E)$ is essentially replaced by a discretely sampled (or stratified) output random variable.

5 BSL Network—Random Eigenvector Analysis

It is useful to investigate the variations in the modal amplitudes due to randomness of amplitude λ . A modified BSL network with cubic stiffness nonlinear cross-tie ($\nu_{\beta 1} = \nu_{\beta 2} = +250$), located at $x_{1,1} = 0.52L_1$ on the stay BS15, as in Sect. 4. We have used an “eigenvector cloud”, found by generating a sample population of $0 \leq \lambda \leq (1/400)$ and by computing the ELM frequency output random sample and the corresponding eigenvectors. If the brute force Monte Carlo method is used, this operation requires solving the characteristic polynomial many times and finding the amplitudes of the mode shapes in the six segments of the BSL network. This task is achieved by describing the mode shapes as $Y_{E,j,p} = A_{E,j,p} \sin(\alpha_E \pi \tilde{f}_j x_{j,p} / L_j)$, where $j = 1, 2, 3$ and $p = 1, 2$ designate the various segments in Fig. 1. We note that $\tilde{f}_j = \omega_{01} / \omega_j$ and ω_j is the native cable fundamental pulsation of stay j . The unknown mode shape amplitudes $A_{E,j,p}$ are real and random because of the random λ .

Figure 5a illustrates the eigenvector cloud; 100 random eigenvectors, found by BFM, are compared to the linear solution. Figure 5a shows that the linear eigenvector of Mode III with deterministic $\lambda = 0$ is not representative of the nonlinear behavior, resulting from stochastic variability in the system. Since calculation of the

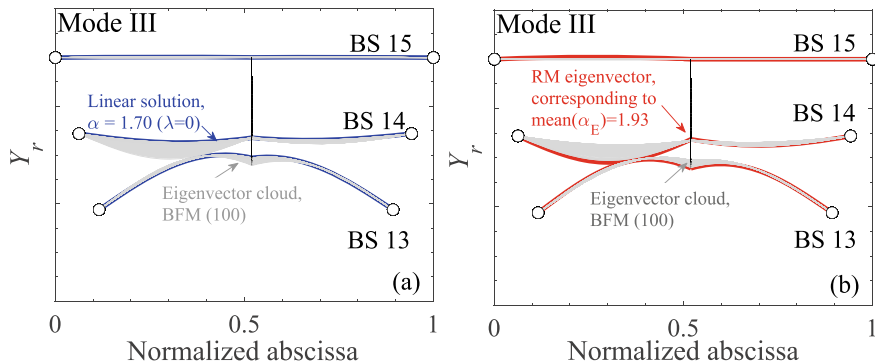


Fig. 5 BSL network with nonlinear cross tie ($\beta = 3, \nu_{\beta 1} = \nu_{\beta 2} = +250$) at $x_{1,1} = 0.52L_1$, subject to uniform stochastic vibration ($0 \leq \lambda \leq (1/400)$)—random eigenvector of Mode III : **a** linear deterministic eigenvector vs. random eigenvector “cloud” (BFM—brute force Monte Carlo), **b** RM eigenvector versus random eigenvector cloud

eigenvector cloud requires significant computational effort, the SA is advantageously used to evaluate an average, nonlinear mode shape, designated as “RM eigenvector”. Figure 5b presents the comparison between the eigenvector cloud, previously examined in Fig. 5a, and the new RM eigenvector. The RM eigenvector reproduces the main features of the cloud.

6 Conclusions

Numerical results demonstrate that it is possible to simulate the rich dynamic behavior of in-plane cable networks through appropriate modeling of the internal, restoring force effect in the cross-ties. By contrast, other sources of geometric nonlinearity (e.g., shallow stay-cable configuration) can be ignored since one of the cross-tie functions is to eliminate cable sag in the long stays. Despite the research advancements and contributions, there are still possibilities for improving the analysis through generalization of the methods described herein.

Dedication This paper is dedicated to the late Professor John H. G. Macdonald and his numerous contributions to the field of nonlinear cable dynamics.

References

1. Caracoglia L, Giaccu GF, Barbiellini B (2017) Estimating the standard deviation of eigenvalue distributions for the nonlinear free-vibration stochastic dynamics of cable networks. *Meccanica* 52:197–211
2. Ehsan F, Scanlan RH (1989) Damping stay cables with ties. In: 5th US-Japan bridge engineering workshop, pp 203–217
3. Giaccu GF, Barbiellini B, Caracoglia L (2015) Parametric study on the nonlinear dynamics of a three-stay cable network under stochastic free vibration. *J Eng Mech-ASCE* 141(6), 04014166
4. Giaccu GF, Barbiellini B, Caracoglia L (2015) Stochastic unilateral free vibration of an in-plane cable network. *J Sound Vib* 340(15):95–111
5. Giaccu GF, Caracoglia L (2012) Effects of modeling nonlinearity in cross-ties on the dynamics of simplified in-plane cable networks. *Struct Control Health Monit* 19(3):348–369
6. Giaccu GF, Caracoglia L (2013) Generalized power-law stiffness model for nonlinear dynamics of in-plane cable networks. *J Sound Vib* 332(8):1961–1981
7. Giaccu GF, Caracoglia L, Barbiellini B (2014) Modeling unilateral response in the cross-ties of a cable network: deterministic vibration. *J Sound Vib* 333(19):4427–4443
8. Grigoriu M (2002) Stochastic calculus. Applications in science and engineering. Birkhäuser, Boston, MA, USA
9. Harju A, Barbiellini B, Siljamäki S, Nieminen RM, Ortiz G (1997) Stochastic gradient approximation: an efficient method to optimize many-body wave functions. *Phys Rev Lett* 79(1997), 1173–1177
10. Irvine HM (1981) Cable structures. MIT Press, Cambridge, MA, USA
11. Macdonald JHG (2014) Response amplitudes of non-linear stay cable vibrations (keynote lecture). In: Symposium on the dynamics and aerodynamics of cables (SDAC). Technical University of Denmark
12. Robbins H, Monro S (1951) Stochastic approximation method. *Ann Math Stat* 22(3):400–407
13. Spall JC (2003) Introduction to stochastic search and optimization: estimation, simulation and control. Wiley, Hoboken, NJ, USA
14. Zuo D, Jones NP (2010) Interpretation of field observations of wind- and rain-wind-induced stay cable vibrations. *J Wind Eng Ind Aerodyn* 98(2):73–87

Monitoring and Testing

Force Measurements on Flexible Sagged Cable Undergoing Forced Vibration at a Single Point



Dániel Dorogi  and László E. Kollár 

Abstract Force measurements using load cell are carried out at one suspension point of a horizontal sagged cable periodically excited at given amplitude and frequency at the position of 0.25 times the spanwise length of the structure measured from the load cell. The excitation amplitude is fixed at 1 mm and the steady excitation frequency is varied between 5 Hz and 70 Hz. Two response types have been identified. For excitation frequency values below approximately 50 Hz the longitudinal and vertical forces have frequency components at the whole number multiples of the excitation frequency. In contrast, at high excitation frequency values, i.e., above 50 Hz, a low-frequency component that is significantly lower than the excitation frequency also occurs. For such cases a transient time domain is identified in the spectrograms of the force components. Within this interval the instantaneous frequency spectra dynamically changes. It was shown that the width of the transient domain is affected by the time rate change of the excitation frequency.

Keywords Force measurement · Frequency · Horizontal sagged cable · Periodic excitation

1 Introduction

Suspended flexible cables occur in many engineering fields, such as in transmission lines, cable-stayed bridges, or risers. For transmission lines two basic configurations are distinguished. The single-span arrangement where the flexible structure is stretched between two suspension points [1], and the multi-span configuration where the intermediate suspension points are mounted on elastic supports [7]. This study focuses on the investigation of single-span flexible cables.

D. Dorogi (✉) · L. E. Kollár
Savaria Institute of Technology, Faculty of Informatics, ELTE Eötvös Loránd University,
Budapest, Károlyi Gáspár square 4, Szombathely 9700, Hungary
e-mail: dorogi@inf.elte.hu

L. E. Kollár
e-mail: kl@inf.elte.hu

When placing a flexible structure into a high-velocity fluid flow vortex shedding occurs which means periodic excitation on the body. For cases when the vortex shedding frequency and the natural frequency of the structure are close to each other the cable starts to vibrate. If the vibration is caused by the wind, the phenomenon is referred to as wind-induced vibration (WIV). Relevant results on WIV are summarized in the recent review paper of Jafari and Abdelkefi [2]. Wind-induced vibration is an extremely complex coupled fluid mechanics and structural mechanics phenomenon. As a model, cable motion is often investigated without the fluid flow, i.e., when periodic excitation is imposed on the particular point of the structure. Several studies focused on the theoretical investigation of cable vibrations. Irvine and Caughey [1] developed a linear model for the computation of free vibrations of a horizontal (the suspension points are at the same level) sagged cable. In their nonlinear model N. Srinil with co-authors took the effects of geometric nonlinearities (i.e., the initial curvature) into account. Their approach is suitable for both horizontal [11] and inclined [10] cables. Based on the nonlinear structural mechanics model, Srinil [9] and Srinil and Ma [5] developed an approach which is able to accurately predict vibrations of inclined flexible sagged cables induced by external fluid flow.

In order to further understand the vibration phenomenon and also to validate the theoretical models, laboratory measurements have been carried out. Very often, experiments are performed for the case when one support of the cable is subjected to harmonic motion. Perkins [6] and Koh and Rong [3] carried out such experiments for horizontal sagged cables. When comparing the measurement and computational results, they obtained good agreements. Rega et al. [8] performed similar laboratory experiments for an inclined cable. Much less attention has been paid to the effects of periodic forcing of the cable at a specific point. Lee and Perkins [4] considered such type of excitation whose direction was normal to the cable.

The aim of the present study is to experimentally investigate the forces acting on one suspension point of a cable while the structure is periodically excited at a single point in the vertical direction. The excitation amplitude is fixed at 1 mm and the (steady) vibration frequency is varied between 5 Hz and 70 Hz. Short-time and full fast Fourier transformation approaches are used to analyze the data.

2 Experimental Setup

The experiments are carried out using the small-scale laboratory model of a transmission line at the Savaria Institute of Technology. Figure 1 shows the physical setup of the experimental configuration. As can be seen in the figure, a horizontal sagged flexible cable stretched between two suspension points is considered. The x , y , and z axes shown in Fig. 1 point in the longitudinal, vertical, and transverse horizontal directions, respectively. The length of the cable span is $X_H = 16.62$ m and the sag length (i.e., the distance between the lowest part of the cable and the line that connects the two suspension points) is $s = 0.6$ m. The core of the cable is reinforced steel around which Aluminum wires are twisted. The cross-section area

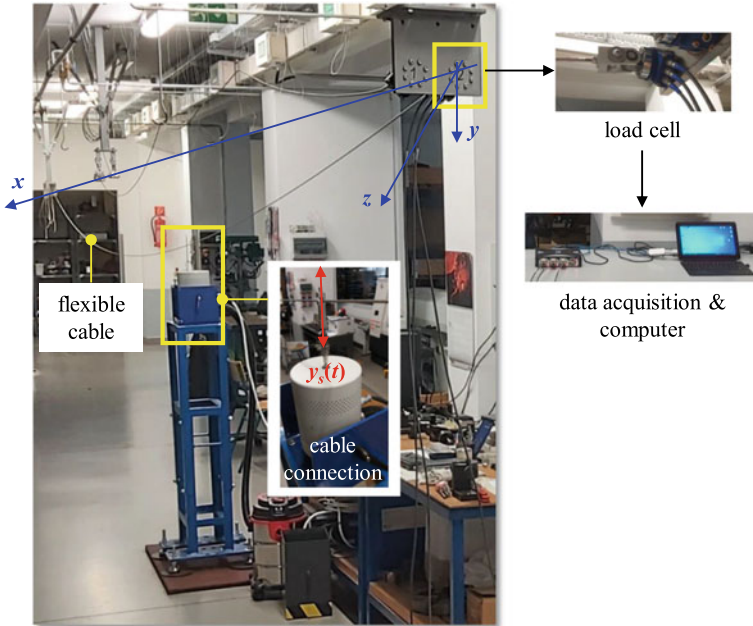


Fig. 1 Physical setup of the experiments

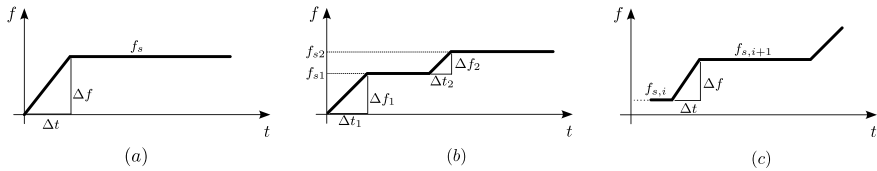


Fig. 2 Time variation trends of the excitation frequency

and the outer diameter of the cable are $A = 7.428 \text{ mm}^2$ and $D = 4 \text{ mm}$, respectively, the mass per unit length of the cable is $m = 0.061 \text{ kg/m}$, and the Young's modulus is $E = 60 \text{ GPa}$. The horizontal component of the cable tension is 31.25 N which value compares fairly well with the theoretical value of $T_H = mgX_H^2/(8s) = 34.44 \text{ N}$ [1]. Irvine and Caughey's parameter $\lambda^2 = (8s/X_H)^2 EA/T_H/[1 + 8(s/X_H)^2]$ has the value of 1177.3 for this experimental configuration.

As can be seen in Fig. 1, the cable is periodically excited at the longitudinal position of $x/X_H = 0.25$ in vertical direction as $y(t) = A_s \sin[2\pi f(t)t]$. Here t is the time, A_s is the excitation amplitude, and $f(t)$ is the time-dependent forcing frequency. The time variation trends of the excitation frequency considered in this study are shown in Fig. 2 (see description in Sect. 3). For the periodic excitation the ESD-045 modal shaker is used which is connected to the cable using an Aluminum holding device (see Fig. 1). The maximum amplitude, velocity, and acceleration of the shaker are

12.5 mm, 1.6 m/s, and 981 m/s², respectively, and the frequency range in which it can operate is 5–6000 Hz. Three unsteady force components $F_x(t)$ (longitudinal), $F_y(t)$ (vertical), and $F_z(t)$ (transverse horizontal) acting on the suspension point at $x/X_H = 0$ are measured by using a load cell. The sampling frequency is fixed at the value of 19.2 kHz which is more than two orders of magnitude greater than the maximum steady excitation frequency considered in this study.

The raw experimental data are low-pass filtered in order to remove propagation errors due to measurement noise. For this purpose a seventh-order Butterworth filter is used with the cutoff frequency value of 4800 Hz. The filtered longitudinal and vertical force signals obtained from the experiments are analyzed by using the short-time Fourier Transform (SFFT) approach. The whole signals are divided into windows of width 0.8 s; the overlap between two neighboring windows is 50%. Spectrograms are created based on the SFFT spectra in order to visualize the time variation of the frequency spectra of forces.

3 Results and Discussion

In this study the effects of steady excitation frequency f_s is investigated at constant forcing amplitude value of $A_s = 1$ mm on the standard deviation of longitudinal and vertical force components, and the frequency content of force signals. The steady excitation frequency is varied in the domain of $f_s = 5$ –70 Hz. Before the systematic measurements, preliminary investigations are carried out to analyze the roles of the time variation of the forcing frequency. In these tests the spectrograms of force components are analyzed.

3.1 Types of Response

In the first preliminary tests the excitation frequency is varied from 5 Hz (the minimum frequency of the shaker, see Sect. 1) within the time interval Δt at the end of which f reaches f_s , i.e., the steady excitation frequency. Then, the forcing frequency is kept constant at f_s for approximately $3\Delta t$. The schematics of the time variation of $f(t)$ is shown in Fig. 2a. The time rate change of the forcing frequency $\Delta f/\Delta t$ is used as a parameter to characterize the frequency variation trends, where $\Delta f = f_s - 5$ Hz. The excitation frequency values of $f_s = 20$ Hz, 40 Hz, and 70 Hz are considered here and $\Delta f/\Delta t$ is kept constant at 3 Hz/s.

Figure 3 shows the spectrograms of the longitudinal (left-column plots) and vertical (right) force components for different f_s values. On the vertical axis frequency normalized by the excitation frequency f/f_s is shown; the axis is scaled logarithmically. Color represents the instantaneous amplitude of the signals. As the colorbar shows, the darker the color, the greater the amplitude of the signal. It can be seen in Fig. 3 that initially, f/f_s corresponding to peak amplitudes; i.e., the most dominant

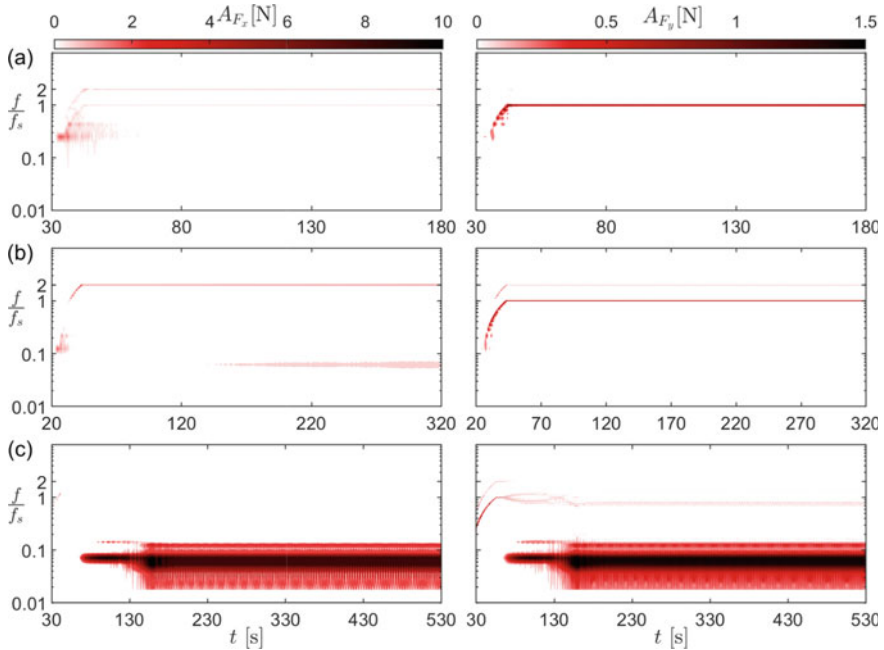


Fig. 3 Spectrogram of F_x and F_y force components (left and right-column plots, respectively) for $f_s = 20$ Hz (a), 40 Hz (b), and 70 Hz (c)

frequency components (seen visually as red rising stripes) increase with time. This domain coincides with the range within which the excitation frequency increases. Beyond this interval, for $f_s = 20$ Hz and 40 Hz, two dominant frequency components both constant in time occur at f_s and $2f_s$. In contrast, the spectrograms presented in Fig. 3c for $f_s = 70$ Hz display completely different characteristics. In the range of $t \approx 58-169$ s (right after the point where the steady excitation frequency is reached) the frequency content of F_x and F_y display strong variations. This regime will be referred to as the ‘transient domain’. Above $t \approx 169$ s the frequency spectra of the signals are roughly constant in time. As can be seen in Fig. 3c, the highest amplitudes are captured at a frequency far below f_s ; i.e., at 4.9 Hz. To the best knowledge of the authors, such high-amplitude and low-frequency component in the force signals has not yet been presented when applying low-amplitude and relatively high-frequency excitation. In addition to the low-frequency component, much lower amplitude peaks are observed roughly at 55 Hz; at a value slightly lower than the steady excitation frequency.

3.2 Effects of Time Rate Change of Excitation Frequency

The transient domain identified for $f_s = 70$ Hz (see Fig. 3c) can cause issues when calculating the statistical properties of the signals (e.g. time-mean value and standard deviation). These quantities are obtained for the steady part of the force data; thus, the transient domain has to be excluded from the evaluation. For the sake of accurate data processing, information are needed on the parameters which influence the width of the transient domain. The time rate change of the excitation frequency can be such a parameter whose effect on the transient domain is investigated here more in depth. Experiments are performed for $f_s = 40$ Hz and 70 Hz by using $\Delta f/\Delta t = 0.1$ Hz/s, 1 Hz/s and 3 Hz/s. Note that although the transient domain was not observed for low f_s values (i.e., for $f_s = 20$ Hz and 40 Hz, see Fig. 3a, b, respectively), considering different $\Delta f/\Delta t$ values may result in its occurrence. Thus, the authors think it is important to be checked.

Figure 4 shows the spectrograms of F_y for $f_s = 40$ Hz (left-column plots) and 70 Hz (right) for different $\Delta f/\Delta t$ values. It can be seen that in the range where the excitation frequency increases, the dominant frequency components of F_y increase. As expected, for $f_s = 40$ Hz, independently of the value of $\Delta f/\Delta t$ no transient domains are observed (see the left plots in Fig. 4) which finding is in agreement

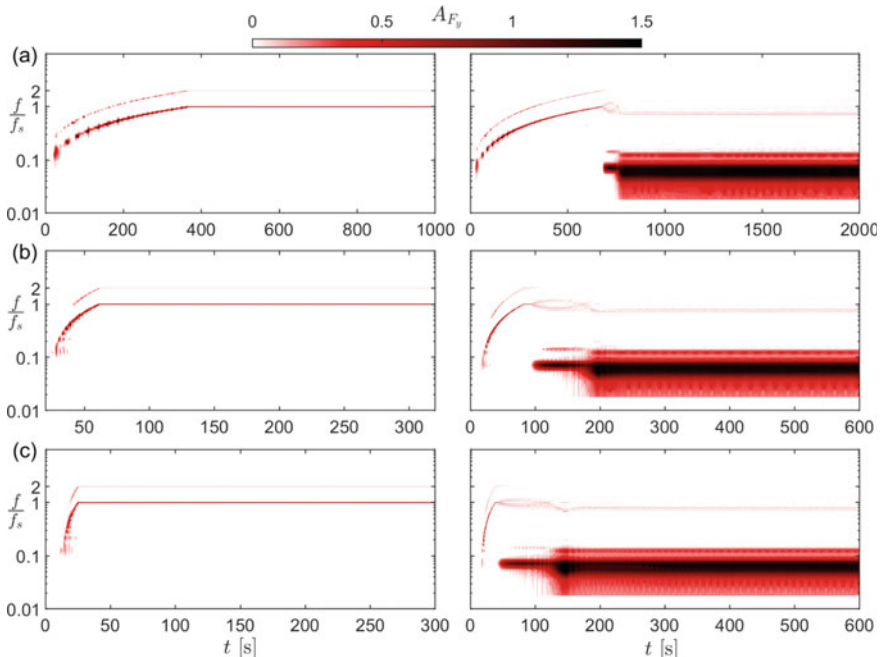


Fig. 4 Spectrogram of F_y for $f_s = 40$ Hz and 70 Hz (left and right-column plots, respectively) using $\Delta f/\Delta t = 0.1$ Hz/s (a), 1 Hz/s (b) and 3 Hz/s (c)

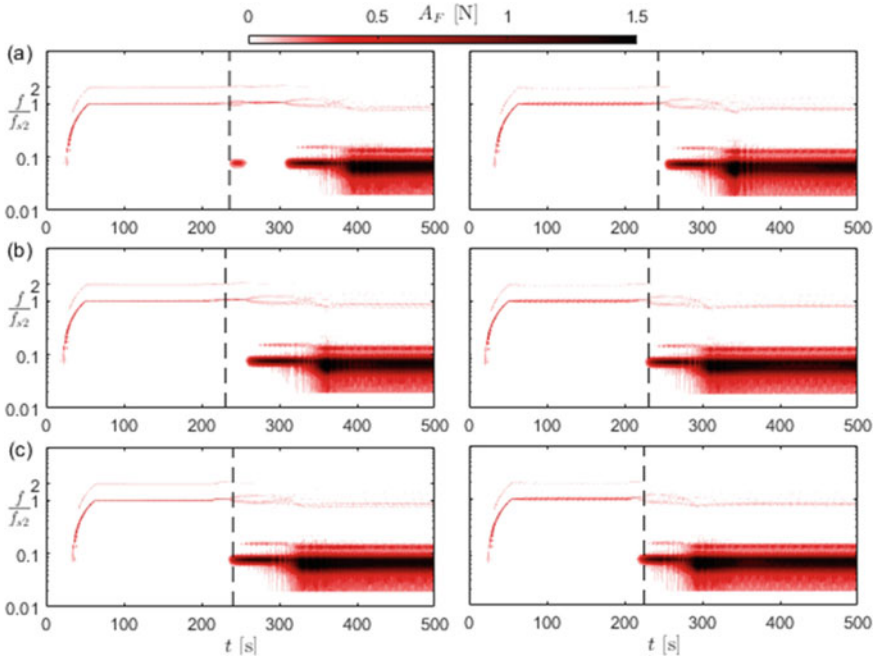


Fig. 5 Spectrogram of F_y for $f_{s1} = 65$ Hz (left) and 68 Hz (right) using $\Delta f_2/\Delta t_1 = 0.05$ Hz/s (a), 0.1 Hz/s (b) and 0.5 Hz/s (c)

with that presented in Fig. 3. However, for $f_s = 70$ Hz the transient range occurs for each $\Delta f/\Delta t$ value, and its time interval seems to widen with $\Delta f/\Delta t$. Similarly to the spectrogram shown in Fig. 3c, beyond the transient domain the signals include strongly repeatable cycles.

In order to further study the effects of time rate change of excitation frequency on the transient domain, another measurement scenario is performed; its schematic is shown in Fig. 2b. As can be seen, the excitation frequency is increased to $f_{s2} = 70$ Hz in two stages. First, it is increased up to f_{s1} by using a time rate change of frequency value of $\Delta f_1/\Delta t_1 = 2$ Hz/s. Afterwards, the excitation frequency is kept constant at f_{s1} for 200 s. As the second stage, the forcing frequency is increased up to f_{s2} ; the time rate change of frequency in the second stage is $\Delta f_2/\Delta t_2$. Figure 5 shows the spectrograms of F_y for $f_{s1} = 65$ Hz (left-column plots) and 68 Hz (right) for different $\Delta f_2/\Delta t_2$ values. Black dashed lines represent the onset of the second frequency variation stage. Similarly to previous results, the f/f_s value belonging to amplitude peaks displays increasing trends at the beginning of the investigated time domain. Afterwards, in the time interval where the frequency of the shaker is $f(t) = f_{s1}$ two amplitude peaks develop at once and twice the steady excitation frequency. This finding holds true for both $f_{s1} = 65$ Hz and 68 Hz and each $\Delta f_2/\Delta t_2$ value. It can also be observed in Fig. 5 that right after the second frequency variation

stage (i.e., where $f(t) = f_{s2}$) the transient domain occurs independently of the value of $\Delta f_2/\Delta t_2$. Moreover, its width seems to be only slightly sensitive to $\Delta f_2/\Delta t_2$. This finding implies that the transient domain occurs independently of how much the excitation frequency changes.

3.3 Effects of Steady Excitation Frequency

The effects of steady excitation frequency is investigated in the domain of $f_s = 5\text{--}70$ Hz with frequency step of 1 Hz at constant amplitude value $A_s = 1$ mm. Figure 2c shows the time variation schematics of $f(t)$. It can be seen in the figure that the excitation frequency is held constant at the value of $f_{s,i}$ for 200 s which time interval is sufficiently wide for the transient domain to decay (if it is present). Then, $f(t)$ is varied by a time rate change value of 0.1 Hz/s between $f_{s,i}$ and $f_{s,i+1}$, where $f_{s,i+1} = f_{s,i} + 1$ Hz. This process is repeated until $f_{s,i+1}$ reaches 70 Hz. The last 60-s-long time interval is analyzed to result in the frequency spectra and the standard deviation of the longitudinal and vertical forces.

Figure 6a, b shows the frequency spectra contour map of longitudinal and vertical force components, respectively. Yellow circles correspond to the most dominant frequency of the forces at a particular f_s values, i.e., at which the highest amplitude

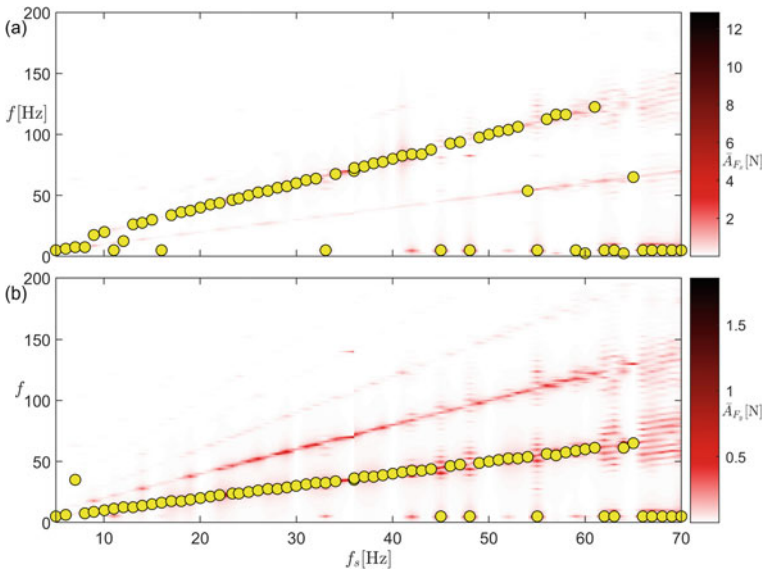


Fig. 6 (Contour outline) Frequency spectra of longitudinal (a) and vertical (b) forces against the excitation frequency. Yellow circles indicate the frequency values belonging to the peak force amplitudes

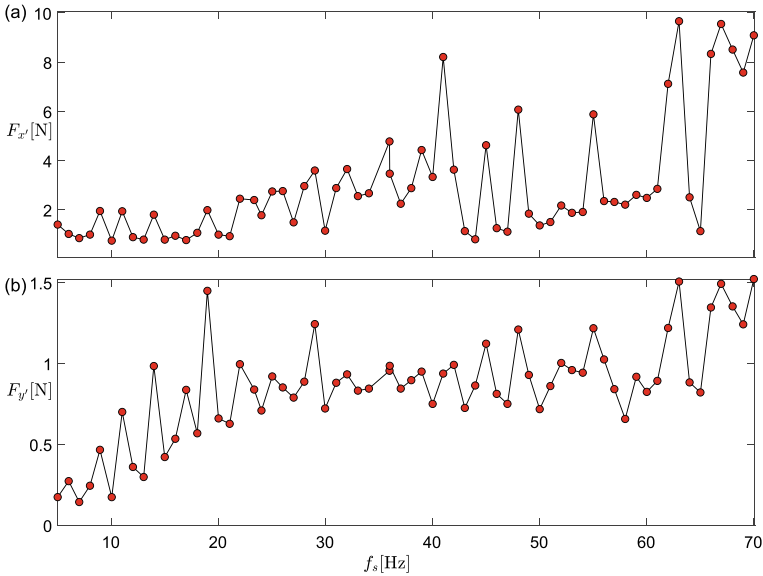


Fig. 7 Standard deviation of longitudinal (a) and vertical (b) forces against the steady excitation frequency

is identified. It can be seen in Fig. 6 that in the frequency spectra of F_x and F_y the whole number multiples of the steady excitation frequency play important roles. In most cases, the most dominant component in the spectra of the longitudinal force is $2f_s$ (see Fig. 6a) and that in the spectra of vertical force is f_s (see Fig. 6b). However, there are some cases typically above $f_s = 50$ Hz where the frequency component significantly lower than f_s has the highest amplitude. This low-frequency component was investigated more in details in Sect. 3.1. In case the low-frequency component is present at a given f_s value, many other peaks can also be observed which are not the whole number multiples of the steady excitation frequency.

Figure 7a, b shows the standard deviation std of longitudinal and vertical force components $F_{x'}$ and $F_{y'}$, respectively. It can be seen in the figure that $F_{x'}$ is approximately 1–8 times higher than $F_{y'}$. Both force std curves involve thin intervals within which they gradually increase and after peaking they decrease. Presumably the location of peaks correspond to the natural frequency of the cable which needs further measurements (with finer steps in f_s) and analyses. It can also be seen in Fig. 7 that at the higher end of the f_s domain $F_{x'}$ and $F_{y'}$ reach much higher values than in other ranges. This phenomenon is associated to the occurrence of the low-frequency components in the signals.

4 Conclusions

In this study a horizontal flexible sagged cable is considered which is periodically excited at prescribed amplitude and frequency at the position of 0.25 times the span-wise cable length. The excitation amplitude is fixed at the value of 1 mm and the excitation frequency is chosen to be in the domain of 5–70 Hz. The three components of unsteady forces acting on a suspension point are measured. It was shown that in most cases the frequency spectra of longitudinal and vertical forces include components at the whole number multiples of the excitation frequency. At high forcing frequency values (typically above 50 Hz) a component significantly lower than the excitation frequency is observed. For such cases, the spectrograms of forces involve a time interval within which the frequency content displays strong fluctuations. The width of this transient domain is found to be affected by the time rate change of excitation frequency. The standard deviation std of longitudinal force occurs to be 1–8 times larger than that of the vertical force. For cases when the low-frequency signal components are present, the std of forces are higher compared to other excitation frequency values.

Acknowledgements Project no. TKP2021-NVA-29 has been implemented with the support provided by the Ministry of Ministry of Culture and Innovation of Hungary from the National Research, Development and Innovation Fund, financed under the TKP2021-NVA funding scheme.

References

1. Irvine HM, Caughey TK (1974) The linear theory of free vibrations of a suspended cable. *Proc R Soc London A* 341:299–315
2. Jafari M, Hou F, Abdelkefi A (2020) Wind-induced vibration of structural cables. *Nonlinear Dyn* 100:351–421
3. Koh C, Rong Y (2004) Dynamic analysis of large displacement cable motion with experimental verification. *J Sound Vib* 272(1–2):187–206
4. Lee CL, Perkins NC (1995) Experimental investigation of isolated and simultaneous internal resonances in suspended cables. *J Vib Acoust* 117(4):385–391
5. Ma B, Srinil N (2023) Prediction model for multidirectional vortex-induced vibrations of catenary riser in convex/concave and perpendicular flows. *J Fluids Struct* 117:103826
6. Perkins N (1992) Modal interactions in the non-linear response of elastic cables under parametric/external excitation. *Int J Non-Linear Mech* 27(2):233–250
7. Qi L, Xu A, Liu X (2019) In-plane free vibrations of multi-span transmission lines. *Canadian J Civil Eng* 46(12):1114–1127
8. Rega G, Srinil N, Alaggio R (2008) Experimental and numerical studies of inclined cables: free and parametrically-forced vibrations. *J Theor Appl Mech* 46(3):621–640
9. Srinil N (2010) Multi-mode interactions in vortex-induced vibrations of flexible curved/straight structures with geometric nonlinearities. *J Fluids Struct* 26(7):1098–1122
10. Srinil N, Rega G, Chucheepsakul S (2003) Large amplitude three-dimensional free vibrations of inclined sagged elastic cables. *Nonlinear Dyn* 33(2):129–154
11. Srinil N, Rega G, Chucheepsakul S (2004) Three-dimensional non-linear coupling and dynamic tension in the large-amplitude free vibrations of arbitrarily sagged cables. *J Sound Vib* 269(3):823–852

Wave Propagation-Based Assessment of Damage in Laboratory Samples of a Cable



João Rodrigues , Elsa Caetano , Carlos Moutinho ,
and Raphael Mendonça 

Abstract The assessment of structural degradation from modal characteristics has a long tradition in engineering practice. For the specific case of bridge cables, such features (most notably, natural frequencies) are often employed in the identification of the installed axial force. However, low-order modal properties may be relatively insensitive to small, localised damage, and the effects of the latter are, in many cases, hindered by the epistemic uncertainty in the boundary conditions. As such, an alternative approach for evaluating the integrity of these members is being pursued within the CTWAVE research project based on the dispersive velocities of transverse waves propagating along a cable. In contrast with modal characteristics, these features are independent of end restraints and can be assessed along wide frequency ranges, thus enhancing their sensitivity to small defects. To investigate the adequacy of the method in detecting and quantifying damage, this study introduces the results from laboratory tests conducted on a 5.10 m-long cable made from a tensioned, solid bar with distinct levels of cross-section loss. The effect of such damage is examined in terms of both modal properties and the velocities of travelling waves. The results obtained in this particular case study demonstrate that cable degradation is indeed associated with a local variation in the wave velocities and that these features are of interest for damage quantification.

Keywords Cable dynamics · Wave propagation · Phase velocity · Inverse problem · Damage identification

1 Introduction

The assessment of the condition of civil engineering structures is typically framed into four levels of increasing complexity, which correspond to the detection, localisation and quantification of damage, and the prognosis of the remaining service

J. Rodrigues (✉) · E. Caetano · C. Moutinho · R. Mendonça
CONSTRUCT, Faculty of Engineering, University of Porto, Rua Dr. Roberto Frias, 4200-465
Porto, Portugal
e-mail: jmcr@fe.up.pt

life [1]. Modal characteristics have long been employed in this domain, as they are directly related to the stiffness and mass distribution of the members under inspection. However, low-order natural frequencies and mode shapes represent the global behaviour of the structure and may be relatively insensitive to the presence of small, localised damage. Full-scale applications addressing the first three levels of damage assessment are scarce and generally require dense sensor networks and advanced data processing techniques [2]. For the specific case of bridge cables, the usual integrity assessment approach involves identifying the installed axial force from a set of measured natural frequencies and fitting some model representing the dynamic behaviour [3]. Nevertheless, damage-induced variations in the axial force are only significant when the load paths within the structure are altered [4]. In addition, especially for short cables, the accuracy of the inverse problem largely depends on the proper characterisation of the restraints at the member supports and the free vibration length [3].

In such a context, an alternative strategy for the condition assessment is being pursued within the CTWAVE research project based on the velocities of transverse waves travelling along a cable. These quantities are frequency-dependent, but unlike modal features they are exclusively determined by the stiffness characteristics of the propagation medium and not influenced by its boundary conditions. Moreover, they can be identified along wide frequency ranges, thus enhancing damage sensitivity. Previous studies towards the goal mentioned above focused on the analytical derivation of such velocities (by regarding cables as tensioned Timoshenko beams) and the development of algorithms for their automated extraction, using sparse response measurements to an impact hammer excitation. Therefore, it is pertinent to demonstrate that cable degradation is associated with a local variation in the wave velocities and to explore if such features are also of interest for the third level of the condition assessment (damage quantification).

An extensive laboratory campaign was designed within the research project to fulfil these purposes, considering two typologies of cable cross-section and damage scenarios of varying nature, location, extension and magnitude. In particular, and after outlining in Sect. 2 the fundamentals of the approach, this study introduces, in Sect. 3, the results from experimental tests performed on a 5.10 m-long solid bar with a diameter of 20 mm, representing a possible cable solution for short span pedestrian bridges. Besides the healthy condition, two levels of cross-section loss are defined over an extension of 1.00 m. In Sect. 4, the effect of such damage is investigated in terms of both the resulting modal characteristics (natural frequencies and mode shapes) and the velocities of transverse-propagating waves to examine the adequacy of the method in detecting and quantifying damage. Finally, the conclusions of the study are summarised in Sect. 5.

2 Transverse Wave Propagation in Bridge Cables

The dynamic behaviour of bridge cables is often explored from analytical models that may account for the influence of axial extensibility and non-negligible sag, either in healthy [5] or damaged conditions [6]. In this work, to include the effects of bending stiffness and shear rigidity in wave propagation, a cable with a given mass per unit length μ , area moment of inertia I and cross-sectional area A is assimilated to a Timoshenko beam subject to a tensile force T [7]. In the absence of external loading, if u represents the transverse displacement and φ denotes the rotation due to bending (both as functions of the position s and the time t), the equilibrium of a segment with constant properties yields the partial differential equations:

$$\begin{aligned} c_s^2 \left(\frac{\partial^2 u}{\partial s^2} - \frac{\partial \varphi}{\partial s} \right) + c_t^2 \frac{\partial^2 u}{\partial s^2} &= \frac{\partial^2 u}{\partial t^2} \\ c_s^2 \left(\frac{\partial u}{\partial s} - \varphi \right) + c_f^2 \frac{\partial^2 \varphi}{\partial s^2} &= r^2 \frac{\partial^2 \varphi}{\partial t^2} \end{aligned} \quad (1)$$

in which c_t , c_f and c_s are defined by $\sqrt{T/\mu}$, $\sqrt{EI/\mu}$ and $\sqrt{GAK/\mu}$, while r is the radius of gyration $\sqrt{I/A}$. E and G designate the Young's and shear moduli, respectively, and K symbolises the shear coefficient.

The system of equations above evidences the physical coupling between the member responses along u and φ . By substitution in (1), these functions only admit nontrivial, harmonic and positive-propagating solutions of type $C_1 e^{i(\gamma s - \omega t)}$ and $C_2 e^{i(\gamma s - \omega t)}$, with wavenumber γ and angular frequency ω , at the roots of the characteristic equation:

$$\tau_3 \gamma^4 - (\tau_2 \omega^2 - c_t^2) \gamma^2 + (\tau_1 \omega^2 - 1) \omega^2 = 0 \quad (2)$$

the auxiliary parameters τ_1 , τ_2 and τ_3 being expressed by:

$$\tau_1 = \frac{r^2}{c_s^2} \quad (3)$$

$$\tau_2 = \left(1 + \frac{c_t^2}{c_s^2} \right) r^2 + \frac{c_f^2}{c_s^2} \quad (4)$$

$$\tau_3 = \left(1 + \frac{c_t^2}{c_s^2} \right) c_f^2 \quad (5)$$

In general, phase velocities c_{ph} represent the speed of carrier waves, being defined by the ratio ω/γ [7]. Therefore, replacing γ for ω/c_{ph} in (2), one obtains two positive solutions for c_{ph} , in accordance with the modes of deformation of the Timoshenko theory. The root c_{pht} associated with transverse-dominant waves is given by:

$$c_{phl}(\omega) = \sqrt{\frac{\tau_2\omega^2 - c_t^2 - \sqrt{(\tau_2\omega^2 - c_t^2)^2 - 4\tau_3(\tau_1\omega^2 - 1)\omega^2}}{2(\tau_1\omega^2 - 1)}} \tag{6}$$

This expression constitutes the dispersion relation of the cable medium. It reveals that each frequency component travels with a specific phase velocity, controlled by the axial force and the stiffness properties of the member. In particular, c_{phl} approaches c_t as $\omega \rightarrow 0$ and $\sqrt{c_t^2 + c_s^2}$ when $\omega \rightarrow \infty$. The solid bar from the experimental tests is now used as an example to assess the sensitivity of phase velocities to the various cable parameters. For this type of cross-section, the diameter ϕ determines the values of μ , I and A , while the shear coefficient is approximately equal to 0.886, assuming a Poisson’s ratio of 0.3 [8]. As the material is isotropic and the Young’s and shear moduli are related, only T , E and ϕ subsist as independent parameters. In Fig. 1, such properties take the reference values of 20 kN, 200 GPa and 20 mm, respectively, and 10% variations in each (from 50 up to 150%) are also introduced. One can observe that the phase velocities are largely unresponsive to the axial force, except in the low-frequency range. On the contrary, these features appear very sensitive to both the Young’s modulus and the diameter as $\omega \rightarrow \infty$, with a general trend of greater c_{phl} in stiffer media. It should be noted that when $\omega \rightarrow 0$ the mass loss associated with the lower values of ϕ dominates over the reduction in I and A , and phase velocities increase, as can be observed in Fig. 1c.

The procedure to assess phase velocities can be derived from the representation in Fig. 2. Accordingly, by applying an impact hammer excitation at a location S0 and by measuring the cable response at two sections S1 and S2, the computed time–frequency distributions enable the calculation of wave velocities from the difference of arrival times to S1 and S2. For the sake of conciseness, the reader interested in such an approach should consider the works of Kishimoto et al. [9] and Park and Kim [10].

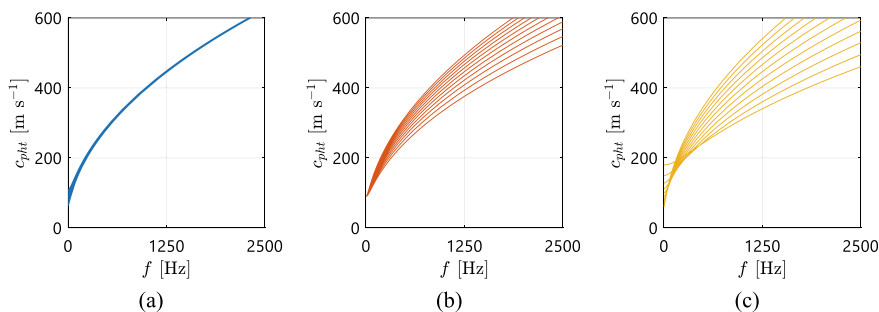


Fig. 1 Sensitivity of the analytical phase velocities associated with the Timoshenko model (solid bar) to 10% variations in the parameters: **a** T ; **b** E ; **c** ϕ

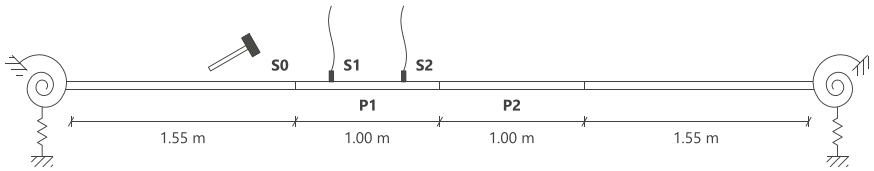


Fig. 2 Schematic procedure for the experimental assessment of wave velocities

3 Laboratory Setup and Tests

The laboratory setup designed to pursue the study's objectives comprises two steel anchoring modules roughly 5 m apart, illustrated in Fig. 3a, and, for tensioning purposes, a hydraulic cylinder with a hand pump. Such geometry defines a free vibration length of 5.10 m for the cables. Due to restrictions in manufacturing the damaged samples and to enhance the diversity of the experimental scenarios, the option was made to cut the solid bar into four parts. The free lengths of 1.55 m at the extremities, represented in Fig. 2, possess a fixed diameter of 20 mm. The segments identified in this figure by P1 and P2 can be exchanged to represent different levels of section loss over an extension of 1.00 m each. Details of the connection between adjacent portions are shown in Fig. 3c and d. In the experimental tests reported in this work, segment P1 was kept with a diameter of 20 mm. For the P2 segment, samples with diameters of 18, 19 and 20 mm were considered, as indicated in Table 1.

For each configuration presented herein, both the modal characteristics and the velocities of propagating waves were identified. These two types of experiments involved a set of piezoelectric accelerometers with a sensitivity of 0.1 V g^{-1} , depicted in Fig. 3b, and an impact hammer. For the modal identification tests (MIT), the sensors were placed with a spacing of 0.50 m from the mid-span and at the locations delimiting the free vibration length. As for wave propagation tests (WPT), the pair of accelerometers was alternately positioned over the P1 and the P2 segments to characterise the different wave propagation velocities. To control the tension of the samples, the installed axial force was recorded using a load cell, being the average values obtained during each experiment (T_{MIT} and T_{WPT} , respectively) also presented in Table 1. It should be noted that, although targeted to the same value, the manual tensioning of the cable and the non-simultaneous performance of the tests determined the slightly different forces.

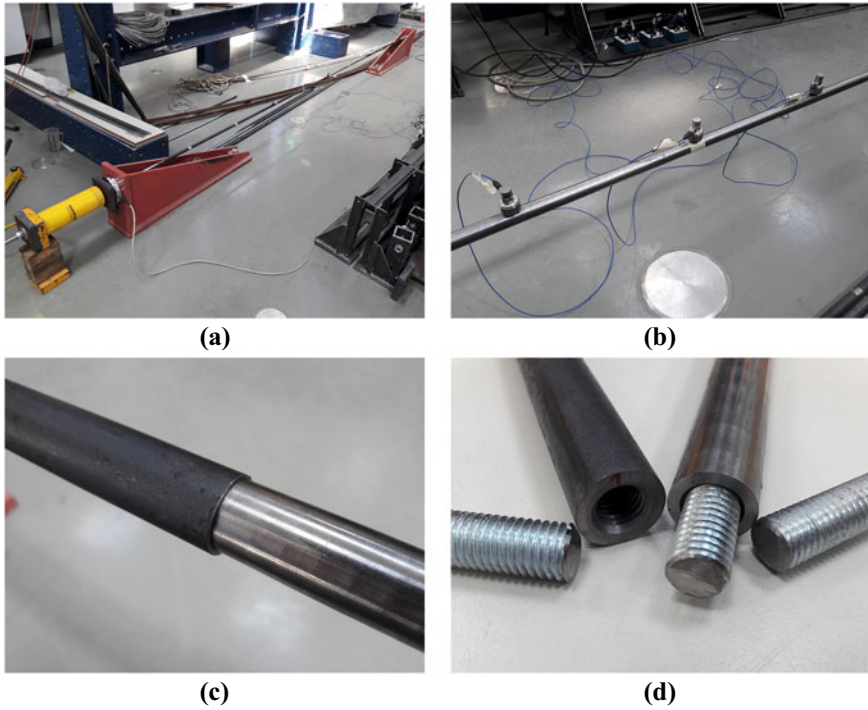


Fig. 3 Laboratory tests on a solid bar: **a** general perspective of the experimental setup and the sensing solution; **b** set of piezoelectric accelerometers fixed with magnetic bases; **c** transition from damaged to undamaged segments; **d** bolted connection between segments

Table 1 Geometric definition and load characteristics of the laboratory tests on a solid bar

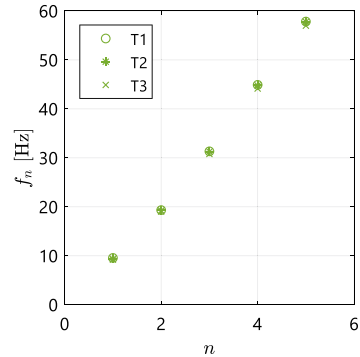
Test	ϕ_{P1} [mm]	ϕ_{P2} [mm]	T_{MIT} [kN]	T_{WPT} [kN]
T1	20	18	20.254	19.980
T2	20	19	20.115	20.003
T3	20	20	20.076	20.023

4 Results and Discussion

4.1 Modal Properties

The identification of natural frequencies and mode shapes was based on a conventional operational modal analysis in which a reference sensor was maintained in a section while the remaining two were successively mounted in other locations. The simultaneous response to impact excitation enabled the construction of transfer functions relating the acceleration measured at each section and the acceleration

Fig. 4 Natural frequencies identified from operational modal analysis of cables T1, T2 and T3



at the reference location. Applying the peak-picking method permitted to identify the natural frequencies and mode shapes displayed in Figs. 4 and 5 for the three cables. Taking the test T3 (intact cross-section) as a baseline, it can be observed that the reduction of diameter leads to observable variations of natural frequency in the range of 3.8–1.5% for the case of maximum reduction of cross-section (T1) and 1.9–1.2% for the other (T2). It should be noted that the increase of natural frequency for a so-called damaged cable results from the predominance of the mass loss with regard to the stiffness reduction in low-order modes, which agrees with the trend recorded in Fig. 1c. Regarding the mode shapes represented in Fig. 5, evident variations can be visually registered for the first mode over the P2 segment (between 1.55 and 2.55 m). However, quantification of the observed damage would not be straightforward.

4.2 Transverse Wave Velocities

Following the procedure outlined at the end of Sect. 2, the dispersive phase velocities were identified over the P1 and the P2 segments for the three cable tests. A total of 36 measurements were performed in each case, being such observations employed to construct 95% confidence intervals for c_{phl} . In this operation, robust estimators (the median and the median absolute deviation) were considered for the location and scale parameters to minimise the effect of outliers. Figures 6 and 7 depict the resulting intervals for the P1 and P2 samples, respectively. For comparison purposes, a dashed line with the analytical phase velocities for a diameter of 20 mm is also included.

As a general trend, one can observe that the experimental phase velocities found in undamaged conditions (P1 samples of all three tests and P2 segment of T3) are consistent and agree well with the analytical reference. Moreover, the reduction of cross-section conducts to spatial variations in c_{phl} that are statistically significant, as can be recognised in Fig. 7a and b.

The obtained phase velocities can be employed at last at the inverse problem of estimating a set of cable parameters, in order to quantify the observed damage. The

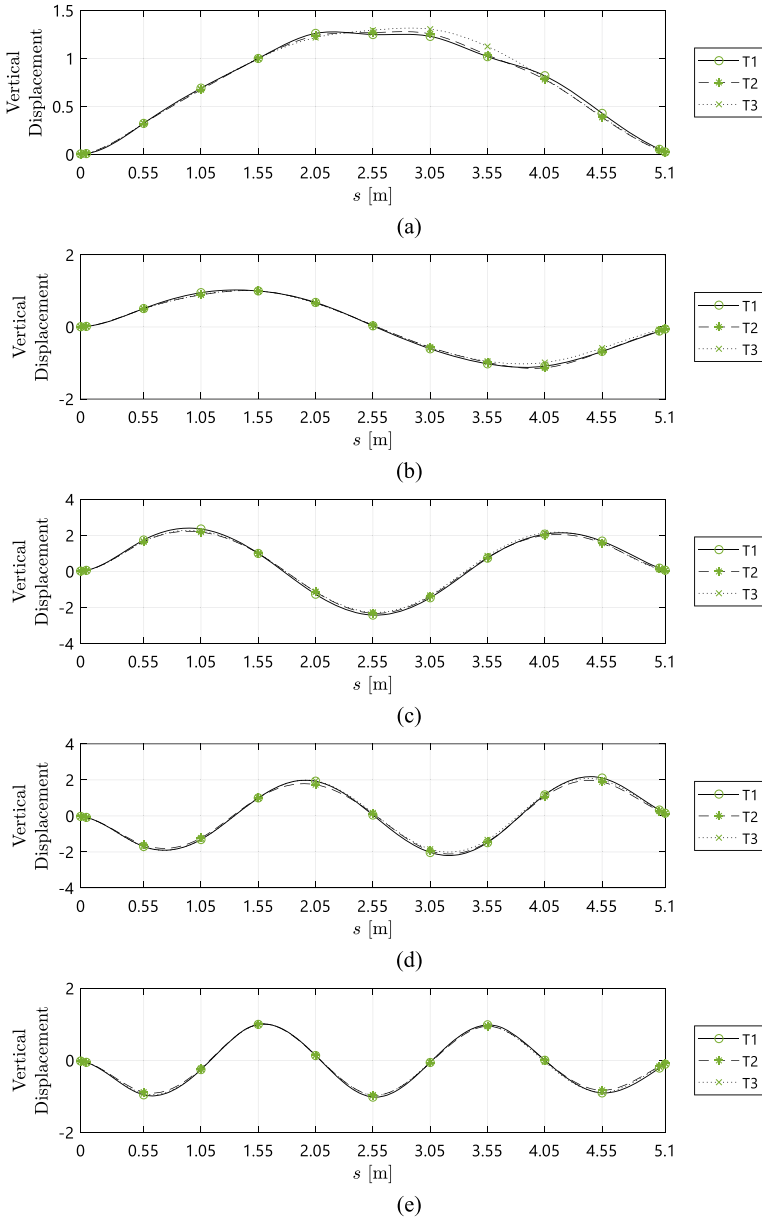


Fig. 5 Mode shapes identified from operational modal analysis of cables T1, T2 and T3: **a** first mode; **b** second mode; **c** third mode; **d** fourth mode; **e** fifth mode

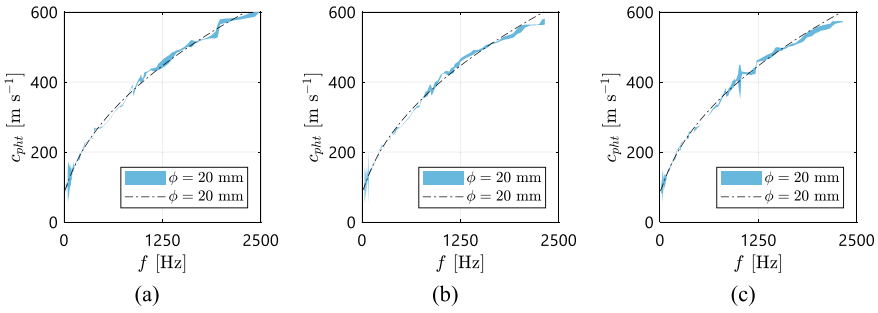


Fig. 6 Experimental phase velocities (95% confidence intervals) obtained through wave propagation tests on the P1 segment of cable: **a** T1; **b** T2; **c** T3

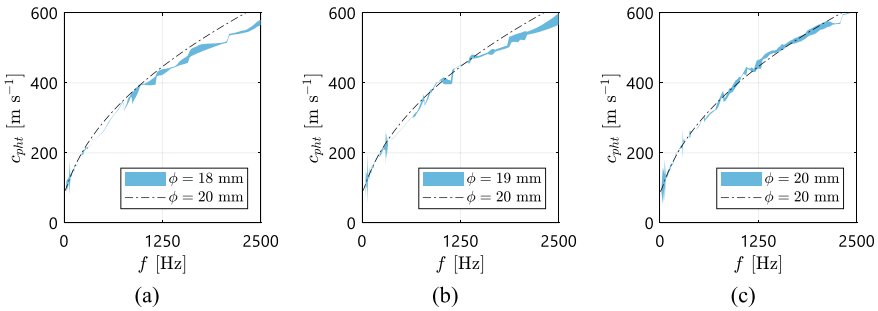


Fig. 7 Experimental phase velocities (95% confidence intervals) obtained through wave propagation tests on the P2 segment of cable: **a** T1; **b** T2; **c** T3

study documented in Fig. 1 advises against the simultaneous optimisation of the Young’s modulus and the diameter of the solid bar because the frequency ranges of sensitivity are similar. Therefore, in this work, the results from the P1 segments were first used to estimate and verify the value of E , assuming a known diameter of 20 mm. Then, the phase velocities found in the P2 samples enabled the identification of the respective ϕ , taking for the Young’s modulus the mean of the point estimates recorded at the P1 segments. In general terms, for a fixed-regressor nonlinear model built upon n observations $(\omega_i, c_{pht_i}^{exp})$, the least-squares estimate $\hat{\theta}$ of θ^* (here interchangeably denoting the true value of E or ϕ) minimises the objective function:

$$S(\theta) = \sum_{i=1}^n \left(c_{pht_i}^{exp} - c_{pht}(\omega_i, \theta) \right)^2 \tag{7}$$

over $\theta \in \Theta$, a subset of \mathbb{R} . Since S evaluates the closeness of the observations to the fitted equation, it can also be employed to build a $1 - \alpha$ confidence interval for the cable parameters, using the upper α critical value of the $F_{1,n-1}$ distribution [11].

Table 2 Point estimates and 95% confidence intervals of the Young's modulus and diameter identified on the P1 and P2 segments of cables T1, T2 and T3

Test	E_{P1} [GPa]		ϕ_{P2} [mm]	
	Point estimate	95% confidence interval	Point estimate	95% confidence interval
T1	199.11	[195.70, 202.56]	17.79	[17.62, 17.97]
T2	196.13	[192.53, 199.79]	18.66	[18.43, 18.90]
T3	193.14	[189.75, 196.56]	20.01	[19.83, 20.19]

The results from such methodology are presented in Table 2, including the point estimates and the 95% confidence intervals obtained for the Young's modulus and the diameter in the segments P1 and P2, respectively. It should be noted that even though in only two of the six cases the true value of the parameters lies inside the confidence interval, the relative errors associated with the point estimates are small, with maximum differences of 3.4% for E and 1.8% for ϕ .

5 Conclusions

The experimental work documented in this paper has confirmed that natural frequencies constitute valuable indicators of the presence of damage and that mode shapes can assist, to some degree, in its localisation. However, the interpretation of modal-based features is not straightforward for the following level of the condition assessment (quantification). Being controlled by the stiffness characteristics of the propagation medium, phase velocities can offer a relevant contribution in this domain. The results of this study demonstrated that a cross-section loss is associated with a local variation of such velocities and that they can be employed for damage quantification. One should note, in any case, that these findings are not readily generalisable, and further studies with more demanding cross-section typologies and other degradation scenarios are required.

Acknowledgements The first author would like to acknowledge the PhD scholarship SFRH/BD/129183/2017 awarded by FCT.

This work was financially supported by: base funding (UIDB/04708/2020) and programmatic funding (UIDP/04708/2020) of the CONSTRUCT–Instituto de I&D em Estruturas e Construções, funded by national funds through the FCT/MCTES (PIDDAC); project CTWAVE–Identification of Cable Damage from Transverse Wave Propagation (EXPL/ECI-EGC/1324/2021), funded by national funds through the FCT/MCTES (PIDDAC).

References

1. Doebling SW et al (1998) A summary review of vibration-based damage identification methods. *Shock Vib Dig* 30(2):91–105. <https://doi.org/10.1177/058310249803000201>
2. Zhang C et al (2022) Vibration feature extraction using signal processing techniques for structural health monitoring: a review. *Mech Syst Signal Process* 177. <https://doi.org/10.1016/j.ymssp.2022.109175>
3. d. S. Caetano E (2007) Cable vibrations in cable-stayed bridges. IABSE-AIPC-IVBH, Zürich
4. Caetano E (2022) Characterisation and assessment of damage in cable structures. *J Civil Struct Health Monit* 12(6), 1267–1283. <https://doi.org/10.1007/s13349-022-00614-z>
5. Behbahani-Nejad M, Perkins NC (1996) Freely propagating waves in elastic cables. *J Sound Vib* 196(2):189–202. <https://doi.org/10.1006/jsvi.1996.0476>
6. Lepidi M et al. (2007) Static and dynamic response of elastic suspended cables with damage. *Int J Solids Struct* 44(25–26):8194–8212. <https://doi.org/10.1016/j.ijsolstr.2007.06.009>
7. Graff KF (1991) Wave motion in elastic solids. Dover Publications, Mineola
8. Cowper GR (1964) The shear coefficient in Timoshenko's beam theory. *J Appl Mech Trans ASME* 33(2):335–340. <https://doi.org/10.1115/1.3625046>
9. Kishimoto K et al (1995) Time frequency analysis of dispersive waves by means of wavelet transform. *J Appl Mech Trans ASME* 62(4):841–846. <https://doi.org/10.1115/1.2896009>
10. Park HC, Kim DS (2001) Evaluation of the dispersive phase and group velocities using harmonic wavelet transform. *NDT and E Int* 34(7):457–467. [https://doi.org/10.1016/S0963-8695\(00\)00076-1](https://doi.org/10.1016/S0963-8695(00)00076-1)
11. Seber GAF, Wild CJ (2003) Nonlinear regression. Wiley, Hoboken

Full-Size Testing of Stay Cable Damping for the Assessment of Viscous Damper Efficiency



Max Vollmering  and Werner Brand

Abstract Full-scale stay cable tests for viscous damping assessment at the Guadiana International Bridge are presented and discussed in this article. The tests carried out involved a pull-and-release method which allowed a repeatable damping assessment. Based on this, stay cable damping was identified by an exponential function fit to acceleration data. Measured stay cable damping ratios confirmed the viscous damper design, achieving a minimum of 4% logarithmic decrement total damping in accordance with fib89.

Keywords Full-size testing · Stay cable damping · Viscous damper · Damper efficiency

1 Introduction

Cable-stayed bridges have become a popular construction type over the last few decades, resulting in increased span lengths, tower heights, and cable lengths. For the design of cable-stayed bridges, cable vibrations must be limited to avoid structural damage. Therefore, the risk of excessive cable vibrations due to parametric excitation and various wind phenomena (such as buffeting, vortex shedding, galloping and rain-wind induced vibrations) can be investigated. To limit the cable amplitudes, a required stay cable damping can be defined for each investigated case (sometimes by using the Scruton number). To achieve the required damping, the use of viscous dampers is state of the art [1].

For damper design, analytical solutions for the eigenvalue analysis of the partial differential equation of the cable provide a well-established basis for predicting the stay cable damping achieved by viscous dampers [2, 3]. However, based on full-scale test results on various cable-stayed bridges, it is known that the actual damping provided is lower than the predictions based on the above theory, which is sometimes referred to as damper efficiency. This leads to two important issues: (a) how to perform

M. Vollmering (✉) · W. Brand
DYWIDAG-Systems International GmbH, Neuhofweg 5, 85716 Unterschleißheim, Germany
e-mail: Max.Vollmering@Dywidag.com

reliable full-scale damping assessment tests and (b) what damping efficiencies can be considered for damper design.

For some cable-stayed bridges, the theoretically calculated damping is just above the damping requirements. Therefore, further development of accurate damping assessment methods and full-scale damping assessment examples are needed by the industry. Therefore, this article presents damping assessment tests carried out by DYWIDAG-Systems International GmbH (in the following DYWIDAG) at the Gadiana International Bridge (Spain-Portugal). The tests were carried out in 2021 after replacement of the stay cables. A pull-and-release method was used to assess the stay cable damping by viscous dampers. Measurements were analyzed using an exponential function fit of free vibrations and tests were performed three times to show repeatability. In conclusion, the calculated damper efficiency results are within the range reported in the scientific community for other cable-stayed bridges.

2 Damping Tests at Gadiana Bridge (Spain-Portugal)

The Gadiana International Bridge is located on the border between Spain and Portugal (between the towns of Ayamonte, in the district of Huelva, and Castro Marim, in the district of Faro). It has a total length of 666 m, a central span of 324 m, and the structure consists of two 100 m high pylons. The bridge deck is supported by 128 stay cables, made up of between 22 and 55 strands, ranging in length from 50 to 170 m. Built between 1985 and 1991, the Gadiana International Bridge remains one of the most iconic cable-stayed bridges on the Iberian Peninsula (see Fig. 1).



Fig. 1 Aerial view of Gadiana International Bridge during stay cable replacement works [4]



Fig. 2 During inspection water leakage at deck anchorages was found (left); Deck anchorages after removal (middle); Installation of new stay cables with ConTen system (right)

2.1 Inspection and Stay Cable Replacement at Guadiana International Bridge

After two strands broke in recent years (a third broke in March 2019), inspections and non-destructive testing were carried out in 2018. The inspection results suggested a complete replacement of the stay cable system (originally installed by a competitor). The following work was therefore carried out by DYWIDAG (see Fig. 2 and [4]):

1. Removal of the existing stay cables and anchorages.
2. Adjustments in existing elements.
3. Installation of new stay cables, including external viscous dampers.
4. Installation of cable force monitoring system.

After replacing the stay cables, the Guadiana International Bridge has been repaired and is safe again.

2.2 Damping Tests

Newly installed stay cables were also equipped, where necessary, with external viscous dampers based on a conducted viscous damper design. After the installation of the dampers, damping tests were carried out to check the validity of the damping system in order to comply with fib89 [5], which recommends 3–4% logarithmic decrement total damping (0.48–0.64% damping ratio) for cables longer than 80 m. Standard testing methods for stay cable damping are (a) rhythmic pulling (e.g. by hand or machine) and (b) the pull-and-release method. The latter was used on the Guadiana International Bridge, where the cable was pulled with a rope and then released (see Fig. 3). The rope was attached at a height of approximately 11 m above

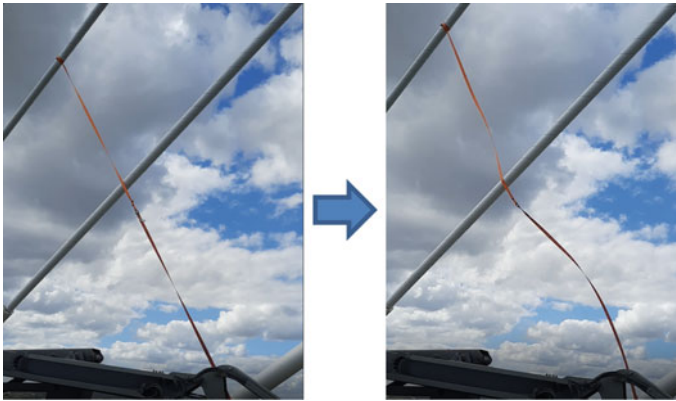


Fig. 3 Pull-and-Release method for damping assessment at Guadiana International Bridge

Table 1 Parameters of tested stay cables

Cable	Chord length L [m]	Chord angle θ [°]	Strands [-]	Unit mass m [kg/m]	Tension H [kN]	Damper c -value [kNs/m]	Damper position x_c/L [-] (%)
2N28	132.800	29.4	37	51.45	3091	65	3.13
2N29	141.550	28.2	37	51.45	2948	65	3.03
2N30	150.360	27.1	37	51.45	3246	65	2.93
2N31	159.220	26.1	37	51.45	3300	65	2.87
2N32	168.120	25.3	55	75.38	4873	95	2.79

deck and the rope was pulled until the cable moved at least 10 mm at the damper position (to ensure damper activation). Once released, the free vibrations of the stay cable were measured using an accelerometer attached on top of the stay cable at approximately 10 m height.

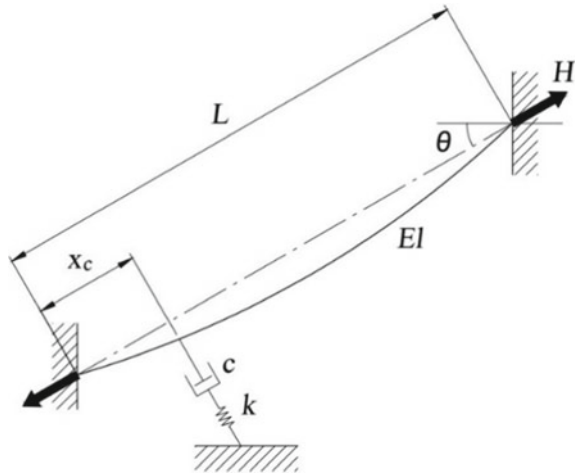
For cables 2N28...2N32, damping tests were carried out three times (see Table 1), which are analyzed in Sect. 4. The tests were carried out under similar environmental conditions (approximately 25 °C air temperature).

3 Assessment of Viscous Damper Efficiency

3.1 Viscous Damper Design

State-of-the-art damper design theory is based on the work of Krenk et al. [2, 3] and is well-known for its high accuracy and applicability. This theory is based on the mechanical model shown in Fig. 4. The damper is modelled as a Maxwell element to

Fig. 4 Mechanical model of viscous damper design



incorporate the damper support stiffness [1]. The mechanical model “cable-damper” allows for the calculation of the additional damping ratio ζ (the cable itself is modelled without inherent damping).

From this model, the reduction in damper efficiency due to bending stiffness, cable sag, and equivalent damper support stiffness are derived. For the analyzed stay cables of the Guadiana International Bridge, the sag has a negligible influence and is therefore not considered in the following.

Based on the stay cable parameters, a curve of the achievable damping ratio ζ is calculated, based on the universal damping curve [1]. For a chosen viscous damping coefficient c , several curves separately show the damping ratio for different vibration modes of the stay cable.

An example of the universal damping curve for cable 2N28 is shown in Figs. 5 and 6. The design curves are shown using a security coefficient $\gamma_\zeta = 0.75$ (see Sect. 4). Importantly, there is no linear damper with an optimal damper configuration for all modes. Within this detailed design, it is shown that dampers with a chosen damping coefficient c lead to different damping ratios for each mode.

It is well known that the actual damping provided is less than the predictions based on the above theory, sometimes referred to as damper efficiency [1]. Therefore, full-scale test results are required for accurate damper design.

3.2 Damping Assessment

To calculate the stay cable damping, the measured data must be processed, usually using free vibration acceleration measurements (see Sect. 2.2). At the Guadiana International Bridge, the mechanical system “cable-damper” acts almost linear, therefore the free decay of the cable $w(t)$ due to an initial deflection is theoretically known as

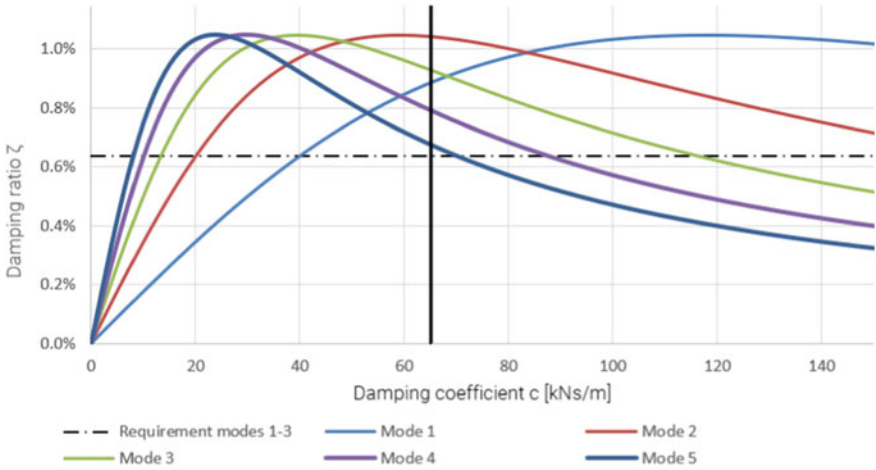


Fig. 5 Viscous damper design for stay cable 2N28: Additional design damping ratio can be seen at the intercepts of design curves at the chosen damper c -value of 65 kNs/m (vertical black line)

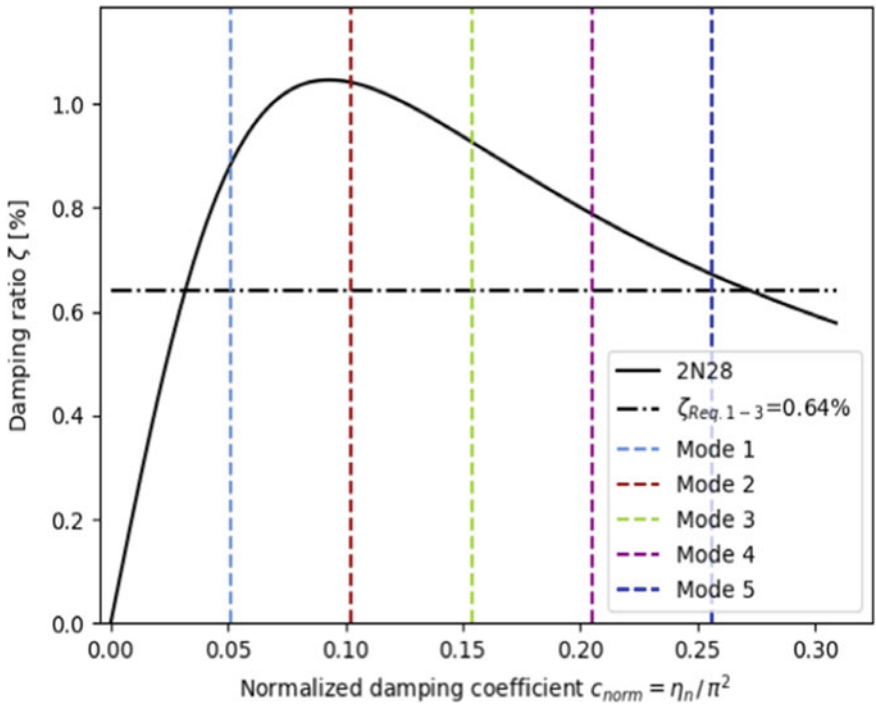


Fig. 6 Normalized viscous damper design for stay cable 2N28: Additional design damping ratio can be seen at the intercepts of design curve and normalized c -values following $c = 65\text{kNs/m}$ ($\eta_n = n\pi(x_c/L)c/\sqrt{Hm}$; vertical colored line for mode n); Identical calculated damping ratios as in Fig. 5

$$w(t) = e^{-\omega_0 \zeta t} (A \cdot \sin(\omega_d t) + B \cdot \cos(\omega_d t)), \omega_d = \omega_0 \sqrt{1 - \zeta^2} \tag{1}$$

A and B indicate general factors and are not required to calculate the damping ratio ζ . Further, undamped and damped angular frequencies ω_0/ω_d are very similar for small damping ratios ζ , vibration “peaks” can be modelled by

$$g(t) = a \cdot e^{-bt} + c \tag{2}$$

By identifying $g(t)$, it is straightforward to estimate ζ . Since the stay cable vibrates at several frequencies (modes), it is necessary to analyse each frequency separately. Hence the following procedure for damping assessment has been used (see Figs. 7 and [6]):

1. Bandpass filtering with FIR filters (filter design by window method with Hamming window) to extract a single mode (modes 1–5 were analysed).
2. Identification of half-wave maxima (“peaks”).
3. Fitting the “peaks” with an exponential function.
4. Damping ratio ζ follows from the exponential function fit.

As damping assessment can lead to scattered results [6], damping tests were performed three times per cable and the average is used below.

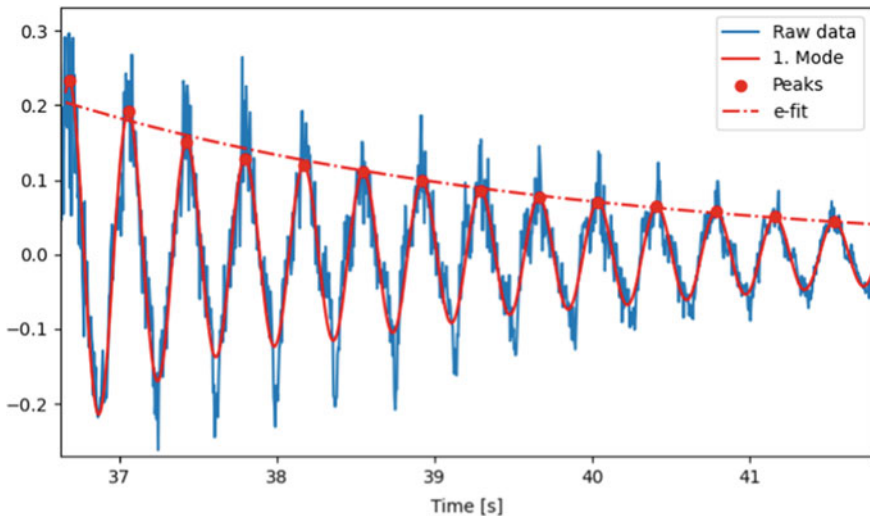


Fig. 7 Principle of damping assessment by exponential function fitting

4 Results: Damper Efficiency at Guadiana International Bridge

This section brings together the viscous damper design from Sect. 3.1 and the test results from Sect. 3.2 to show the measured damper efficiency.

Viscous damper design. For the viscous damper design, a security coefficient $\gamma_\zeta = 0.75$ has been used by $\zeta_{\text{design}} = \gamma_\zeta \cdot \zeta_{\text{calculation}}$ following general recommendations [1]. Further, the stiffness of the damper support was chosen based on experience. For comparison with measured “total” damping ratios, the design values have been increased by an assumed inherent damping of 0.1%.

Damping test results. Measured mean damping ratios are so-called “total damping ratios” (damper + inherent damping). For some modes, damping ratios could not be analyzed (and therefore are not shown), probably due to test conditions (the reasons could not be fully explained).

As can be seen in Fig. 8, all measured damping ratios are above the design universal damping curve (to be comparable an inherent damping of 0.10% is added; security coefficient has been applied). Therefore, the damping tests carried out confirm that

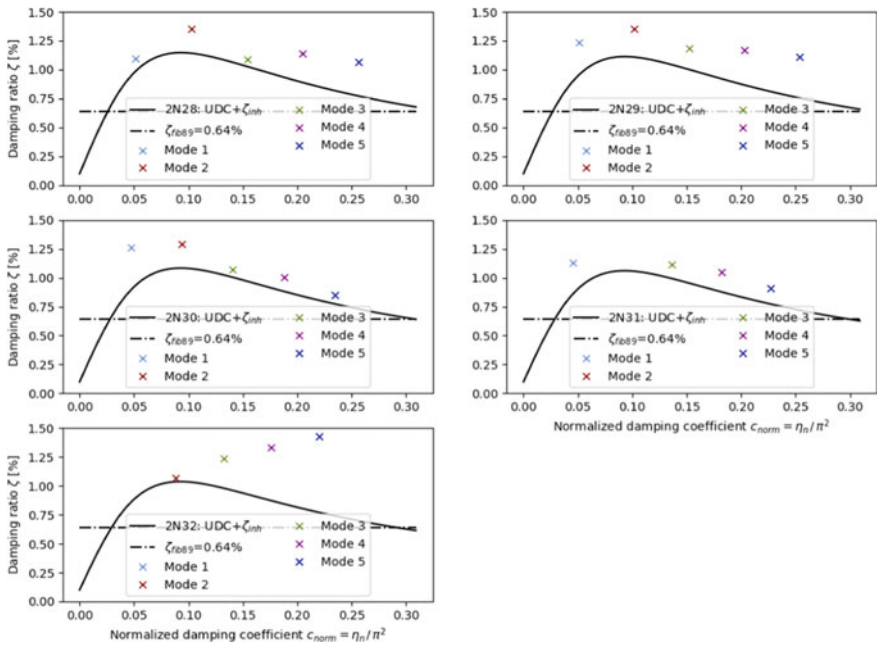


Fig. 8 Results of damper efficiency at Guadiana International Bridge: Measured “total” damping ratios (colored crosses) are above the universal design curve (to be comparable an inherent damping of 0.10% is added; black line, see Sect. 3.1) for each tested cable (subplot)

the viscous damper design complies with fib89 [5] (total damping larger than 4% logarithmic decrement).

From a theoretical point of view, it is important to note that the measured damping ratios follow the general shape of the universal damping curves for stay cables 2N28, 2N29, 2N30 and 2N31, which reinforces the conducted viscous damper design.

5 Conclusions

This paper presents and discusses full-scale stay cable tests carried out at the Gadiana International Bridge to assess viscous damping. A pull-and-release method was used to allow repeatable damping tests. The measured data were then processed using exponential function fitting to identify the stay cable damping. Considering the test results, all measured damping ratios confirmed the viscous damper design to achieve a minimum of 4% logarithmic decrement according to fib89 [5].

The security coefficient applied is a pragmatic and simple approach to considering damper efficiency and is consistent with the damping efficiencies reported by Caetano [1]. The identified damping efficiency is considered specific to the Gadiana International Bridge and may not be general for other cable-stayed bridges. Therefore, it is recommended that the scientific community publishes more measurement data (i.e., further full-scale damping assessment involving different test methods and other cable-stayed dampers) to allow for even more accurate damper design and improved cable-stayed bridge design.

References

1. Caetano E (2007) Cable vibrations in cable-stayed bridges, vol 9. IABSE, Structural Engineering Documents. ISBN 978-3-85748-115-4.
2. Krenk S (2000) Vibrations of a taut cable with an external damper. *J Appl Mech* 67(4):772–776
3. Krenk S, Høgsberg JR (2005) Damping of cables by a transverse force. *J Eng Mech* 131(4):340–348
4. Martínez F, Abecasis D (2021) Gadiana International Bridge new generation stay cables. In: Concrete structures: new trends for eco-efficiency and performance. Proceedings for the 2021 fib symposium, Lisbon, Portugal, 14–16 Jun 2021.
5. fib Bulletin No. 89 (2019) Acceptance of cable systems using prestressing steels. Fédération internationale du béton (fib), ISBN 978-2-88394-130-4
6. On-Site Vibration Testing of Stay Cables and Damping Evaluations, Contract No. C-7800, Task No. 29, Florida Department of Transportation (2005).

Vibration Excitation and Damping of Suspension Bridge Hanger Cables



Allan Larsen

Abstract The paper presents full-scale observations and wind tunnel tests carried out to clarify the mechanisms driving the hanger vibrations observed in the final phases of completing the 1915 Çanakkale suspension bridge. It is found that high frequency low amplitude vibrations were caused by rhythmic vortex shedding whereas large amplitude low frequency vibrations were caused by rain wind galloping. Stockbridge dampers were introduced to mitigate the hanger vibrations but were found to fail due to fatigue of the messenger wire. Taut string theory is reviewed and combined with the wind tunnel test results and damper characteristics to explain the likely cause for damper failure. It is concluded that Stockbridge dampers are well suited for mitigation of vortex induced vibrations if properly designed but are insufficient for mitigation of rain wind vibrations of the hanger cables. Mitigation of rain wind vibrations requires hydraulic dampers connecting the hanger cables to the bridge deck structure.

Keywords Hanger cable vibrations · Wind tunnel tests · Taut string modal damping · Stockbridge dampers · Hydraulic dampers

1 Introduction

Hanger cables in suspension bridges are important structural elements which transfer the dead load of the bridge girder to the main cables. Over time various designs of the hangers and anchorages have been favored. The hangers of older suspension bridges are composed of galvanized stranded wire loops set into grooves in the cable bands and attached to the deck top chord by means of threaded bolts. Newer hanger designs feature locked coil or parallel wire strands painted or sheathed by high density polyethylene HPDE coating. The cable ends of the newer type hangers are commonly attached to the cable bands and deck anchor plates by means of fork socket/eye plate connections. While the older types of stranded wire hangers do not

A. Larsen (✉)
COWI AS, 2800 Lyngby, Denmark
e-mail: Aln@COWI.com

© The Author(s), under exclusive license to Springer Nature Switzerland AG 2024
V. Gattulli et al. (eds.), *Dynamics and Aerodynamics of Cables*, Lecture Notes in Civil Engineering 399, https://doi.org/10.1007/978-3-031-47152-0_19

217

appear to be particularly sensitive to wind effects, wind induced vibrations of the newer types of hangers are reported on a regular basis. A situation raising questions to structural fatigue and visual discomfort with the public crossing the bridges. A way of mitigating suspension bridge hanger vibrations is by adding mechanical damping in the form of mechanical resonant dampers (Stockbridge dampers) or hydraulic dampers [1].

A field measurement campaign of vortex induced vibrations (VIV) of the locked-coil fork socket/eye plate hangers of the Hålogaland suspension bridge, Norway [2], identified the lower bound structural damping of the hangers to be in the range 0.0015–0.002 log. dec. It was also found that the VIV were efficiently mitigated by Stockbridge dampers.

2 1915 Çanakkale Suspension Bridge Hanger Vibrations

The world record 1915 Çanakkale suspension bridge (2023 m main span length), Türkiye, features hangers having fork socket/eye plate connections similar to the Hålogaland suspension bridge. The 1915 Çanakkale bridge hanger cables are composed of parallel wire strands and are sheathed by HPDE coating similar to the Hålogaland bridge. The longest hangers of the 1915 Çanakkale bridge are twice as long (220–240 m) as the longest hangers on the Hålogaland bridge.

In view of the similar hanger design, it was not surprising that the hangers of the 1915 Çanakkale bridge displayed low amplitude cross wind vibrations at high frequencies increasing with the wind speeds as is expected for VIV. During the final phases of completion of the bridge it was decided to add Stockbridge dampers to the hangers for mitigation of the hanger VIV. The Stockbridge dampers, which are of similar design to the Hålogaland dampers, were doubled in number from 2 to 4 for the longest hangers to match the longer hanger length. The dampers proved efficient for mitigation of VIV which had been observed previously mostly on days with clear skies. However, the longest hangers were observed to be set into large amplitude vibrations during weather situations with both high wind speeds and rainfall. The dampers on the longest hangers failed after about two months of service, Fig. 1.

Before failure of the Stockbridge dampers, it was noted that the vibrations of the longest hangers changed character when the weather changed from dry conditions to high winds and rain. The high frequency VIV largely mitigated by the Stockbridge dampers switched into crosswind low frequency, high amplitude vibrations displaying 4 to 6 half-waves along the cable length, Fig. 1 (left). Close up examination of the vibrating hangers revealed a water rivulet forming and running along the hanger and draining of at the lower socket. A similar phenomenon referred to as rain wind induced vibrations (RWIV) is well known for inclined cables of cable-stayed bridges [3] but has not been observed for vertical cables to the knowledge of the present author.



Fig. 1 RWIV and VIV of longest hangers (left and middle) wind normal to the hanger plane. Overlay of two video frames at the extreme excursions of the cable. Failed stockbridge dampers displaying empty clamps and damper masses scattered on the bridge deck (right)

2.1 Wind Tunnel Tests

Two types of wind tunnel tests were carried out at the FORCE Technology 2×2 m cross section climatic wind tunnel [4] to clarify the aerodynamic excitation of the hanger cables associated with VIV and RWIV.

The VIV set-up involved a classical elastically suspended horizontal 1:1 scale section model composed of a carbon fiber shaft clad by cylindrical foam elements reproducing the external shape and roughness of the 0.108 m diameter hanger cable HPDE shroud, Fig. 3 left. The model was fitted with 0.138 m diameter end plates to secure two-dimensional flow. This model design allowed a minimum weight of the section model to allow maximum self-induced response. Different levels of mechanical damping were introduced to the model by an eddy current mechanism composed of permanent magnets moving across an aluminum plate. This setup allowed the

Scruton Number to be varied in the range $5.8 < Sc < 32.5$. For the present discussion the Scruton Number is defined as:

$$Sc = \frac{2\delta_s m}{\rho d^2} \quad (1)$$

where δ_s is the structural damping level (log. dec.), m is cable model mass/unit length, ρ is air density and d is external cable model diameter.

The VIV experiment started by mapping the model amplitudes as function of wind speed. The test then proceeded by systematically increasing Sc by stepping up the damping level and recording the peak amplitude of the VIV response at lock-in. The 82 mm peak-peak amplitude of the model at $Sc = 5.8$ may be appreciated from Fig. 2, left.

The RWIV set-up involved a vertical 0.11 m diameter cylindrical HPDE pipe suspended from a flexure at the roof of the wind tunnel, Fig. 2, right. The flexure allowed the model to oscillate with a linear mode shape in the crosswind and along wind direction at an eigen frequency $f_m = 2.2$ Hz. Damping could be introduced to the model by adding a paddle submerged in an oil bath situated at the free end of the model on the wind tunnel floor. A water sprinkler system was installed upwind of the model to allow simulation of rainfall. This test set-up allowed the Scruton Number to be varied in the range $13.5 < Sc < 69.9$.

Prior to turning on the wind, the RWVI experiment started by treating the surface of the model by polyvinyl alcohol to simulate the full-scale surface condition caused by pollution and UV exposure. Then the test proceeded by turning on the wind

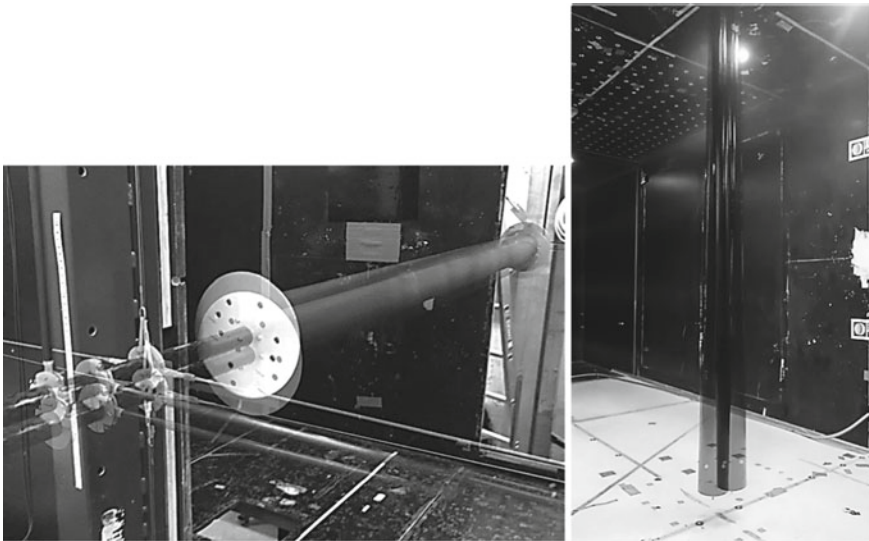


Fig. 2 VIV model (left) and RWIV model (right) in the wind tunnel. Overlay of two video frames captured at the extreme excursions of the cable models

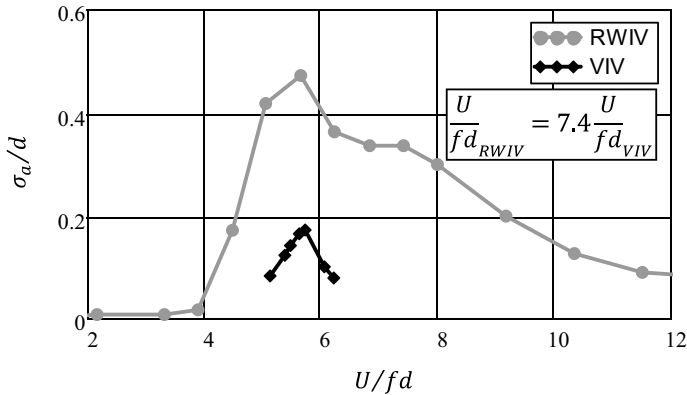


Fig. 3 Non-dim std. dev. of model responses as function of non-dim. VIV wind speed

and sprinkler system to identify the rainfall rate that yielded the largest crosswind response of the free end of the model. For this rainfall rate the standard deviation of the amplitude of the free end was recorded as function of wind speed. For the rainfall rate and wind speed setting yielding the largest model response, Sc was systematically increased by stepping up the damping level and recording the peak amplitude. The 235 mm peak-peak amplitude of the model at $Sc = 13.5$ can be seen from Fig. 2, right. It was found that the polyvinyl alcohol coating was partly washed off during the run of an experiment resulting in a decrease of the RWIV response of the model. Thus, the experiment was repeated 4 times for each Sc with renewed coating before each test run to allow assessment of the variability of the model response caused by the variability of the model surface condition.

2.2 Wind Tunnel Test Results

The standard deviation of the model amplitudes made non-dimensional by the model diameter, σ_a/d are plotted as function of the non-dimensional wind speed U/fd , Fig. 3. The non-dimensional wind speeds for the RWIV are divided by a factor 7.4 to align the peaks of the RWIV and VIV responses on the wind speed axis for easy illustration.

From Fig. 3 it is noted that the maximum of the VIV response falls at $U/fd = 5.73$ yielding a Strouhal Number $St_{VIV} = 0.175$ in good agreement with Eurocode ($St = 0.18$). The maximum of the RWIV response falls at $U/fd = 5.73 \cdot 7.4 = 42.4$ corresponding to a Strouhal Number $St_{RWIV} = 0.024$. In the present context VIV and RWIV are treated in a similar way due to the similarity of the shapes of the σ_a/d versus U/fd curves although fluid dynamics processes controlling VIV (von Kármán vortex shedding) and RWIV (flow separation caused by the water rivulet) are likely to be different.

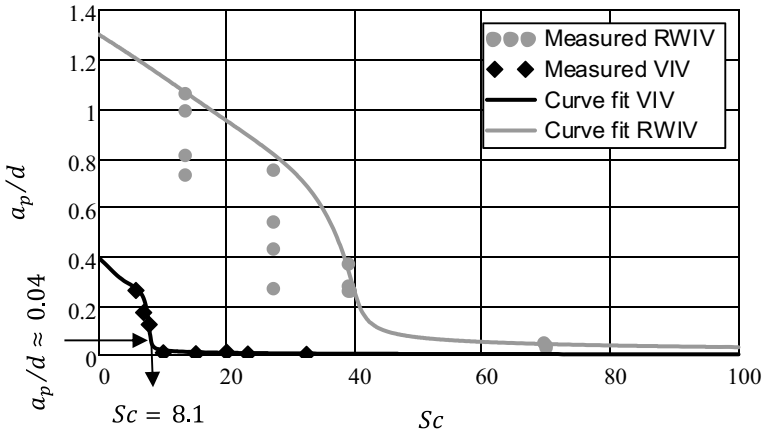


Fig. 4 Measured VIV and RWIV peak amplitude envelopes as function of Sc

In order to investigate the effect of increasing Scruton Numbers on the VIV and RWIV responses on the cable models the structural damping was increased systematically for $U/fd = 5.73$ for VIV and $U/fd = 42.4$ for RWIV. The measured non-dimensional peak responses as function of Sc are shown in Fig. 4 along with envelope curves fitted following the EN1991-1-4 method 2 model [5]. For RWIV the test was repeated 4 times at each Sc as the peak responses displayed a certain variation possibly due to variations of the adhesion of water to the model surface in the individual test runs.

It is observed that damping of VIV to low amplitudes beyond the self-excited response range requires a Scruton Numbers $Sc > 10-15$. For RWIV, Fig. 4 indicates that $Sc > 60-70$ for effective mitigation of the vibrations.

The response curve for VIV, Fig. 4, was used for estimation of the inherent structural damping of the hangers. Video recordings of for the vibrating hangers without Stockbridge dampers allowed estimation of the non-dimensional peak amplitudes $a_p/d \approx 0.04$ as indicated in Fig. 1 (middle). From Fig. 4 the corresponding $Sc = 8.1$ yielding $\delta_s \approx 0.0013$ in good agreement with the Hålogaland bridge damping estimates [2].

3 Hanger Cable Dynamics

Hanger cables behave dynamically much like a taut string. The modal damping resulting from a viscous damper attached to the hanger at a position x_c above the anchorage and having a damping constant C [Ns/m] is well predicted by Krenk’s closed form asymptotic formula [3], which is considered accurate if the number of modal waves n are less than 10. This approximation is often sufficient for RWIV of stay- and hanger cables. In the case of VIV of a 200 m long hanger cable excited at

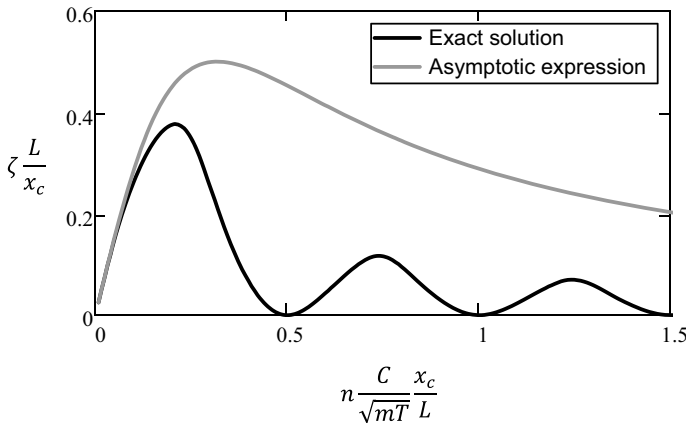


Fig. 5 Comparison of non-dimensional modal damping as function of non-dimensional viscous damping constant multiplied by mode number. $C/\sqrt{mT} = 0.5$

a wind speed of 15 m/s, the theoretical number of half waves is about $n \approx 100$ in which case the asymptotic formulation breaks down.

A suitable formulation for the numerical solution of the exact formulation of the string equation by iteration is given by Krenk and reproduced as Eq. (6.21) in [3]. A comparison of the non-dimensional modal damping relative to critical $\zeta L/x_c$ as function of the non-dimensional mode number and viscous damping constant $nC/\sqrt{Tm}x_c/L$ is shown in Fig. 5. It is noted that the asymptotic expression predicts the modal damping well for $nC/\sqrt{Tm}x_c/L < 0.1$ but overpredicts the modal damping at higher values. Also, it is noted that the modal damping is zero at $nC/\sqrt{Tm}x_c/L \approx 0.5, 1.0, 1.5$ for the exact expression. Here the damper is located at a node of the mode shape without displacement in which case the damper is not activated. This observation is important to keep in mind when considering positioning of dampers for mitigation of VIV of hanger cables.

4 Stockbridge Dampers

Stockbridge dampers are mechanical resonant devices usually composed of two masses or counterweights attached to a fastening clamp via a common messenger wire, Fig. 6 (left). The messenger wire acts as the elastic element as well as it provides damping through friction between the individual strands of the wire. Stockbridge dampers may be built symmetric yielding two distinct resonance peaks or asymmetric having a larger and a smaller mass to provide four resonance peaks depending on the application. The damping capacity of a Stockbridge damper is usually presented in a characteristics curve obtained from forced vibration testing. The characteristic

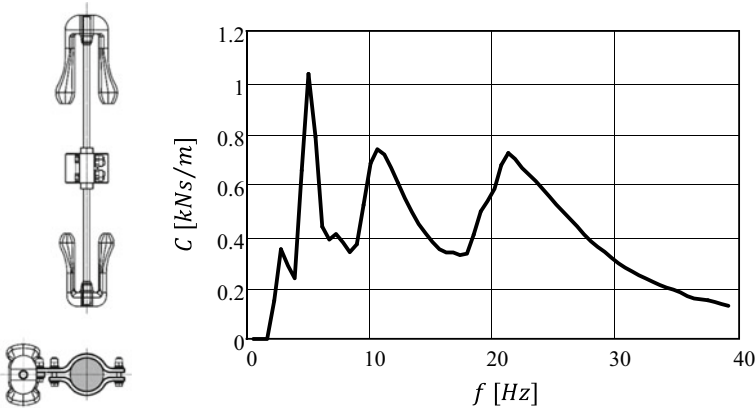


Fig. 6 Stockbridge damper (left). Damping constant characteristic (right)

presents the damper's ability to dissipate power P_D [W] as a function of frequency f [Hz], [2].

To calculate the modal damping of a hanger cable fitted with a Stockbridge damper, the P_D characteristic must be converted into an equivalent damping constant C as a function of frequency. This can be done by regarding the Stockbridge damper as a base excited damped oscillator for which the relationship between dissipated power, driving force F_0 and vibration velocity v is:

$$P_D = \frac{1}{2} F_0 v \sin(\varphi) = \frac{1}{2} C v^2 \sin(\varphi) \quad \frac{1}{2} C = \frac{2P_D}{v^2} \sin(\varphi) \quad (2)$$

where φ is the phase angle between the driving force and the damping force. As the Stockbridge damper is mainly working at its resonances it is fair to assume a phase shift $\varphi \approx 90^\circ$.

The Stockbridge dampers for the 1915 Çanakkale bridge were tested following the IEEE specifications adopted by the power supply industry. This standard specifies that the driving velocity at the clamp is kept constant at $v_0 = 0.1$ m/s. Application of (2) yields the damping constant characteristic shown in Fig. 6 (right) obtained from the P_D supplied by the manufacturer. The damper characteristic displays four peaks. The two peaks at 2.8 and 5.0 Hz are associated with the first cantilever bending mode of the messenger wire connecting the larger and smaller mass to the clamp. These modes cause bending stresses in the messenger wire at the clamp. The peaks at 10.8 and 21.2 Hz are associated with a rotary motion of the larger and smaller masses about their centers of gravity. These modes cause bending stresses in the messenger wire at the attachments to the masses.

5 Example: Hanger 111 of the 1915 Çanakkale Bridge

Hanger no. 111 (Fig. 1) is a double hanger composed of two individual cables set at a spacing of 1.5 m. The average length of the individual hanger cables is $L = 221$ m, the axial tension force due to deadload $T = 2.72$ MN and the cable mass/unit length is 46 kg/m. Each of the individual cables of hanger 111 were equipped with two pairs of Stockbridge dampers situated at $x_{c1} = 4.6$ m and $x_{c2} = 5.5$ m above the pin bolts anchoring the cable sockets to the bridge deck, Fig. 1. The frequency for $n = 1$ is 0.56 Hz.

The Scruton Number obtained by combining the modal damping obtained using the numerical exact solution to the string equation, the estimated inherent damping $\delta_s = 0.0013$ and the above physical cable parameters are shown in Fig. 7 (black graph). The horizontal axes display the mode number n and the frequency f .

The following observations are made from Fig. 7:

For low mode numbers $n = 1, 2, 3$, the vortex shedding frequency falls below the first resonance of the Stockbridge dampers in which case the dampers are not activated. Thus, VIV may occur.

For mode numbers $4 \leq n < 7$, $10 < Sc < 70$ in which case VIV is mitigated but RWIV is highly possible. $4 \leq n < 7$ corresponds to wind speeds in the range 10–18 m/s in good agreement with the observations of RWIV shown in Fig. 1.

For mode numbers $8 \leq n \leq 26$, $Sc > 70$ in thus neither VIV nor RWIV are expected.

Comparing Figs. 6 and 7 it is noted that the damping effect of the 4th resonance peak of the damper at about 21 Hz (rotation of the small mass) is almost completely lost due to the dynamics of the cable.

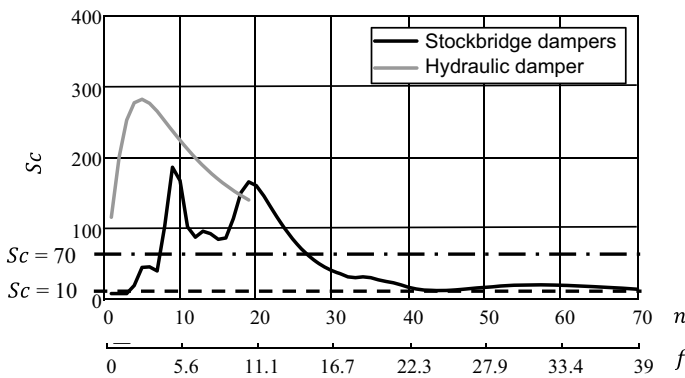


Fig. 7 Scruton number as function of mode number n /frequency f [Hz] for hanger no. 111

6 Failure of the Stockbridge Dampers

Figure 7 demonstrates that the Stockbridge dampers supplies insufficient damping to prevent RWIV of hanger 111 at mode numbers less $n < 7$. Mode 4–6 of hanger 111 having frequencies between 2.2 and 3.3 Hz coincides with the first resonance peak of the Stockbridge damper indicating a risk for large bending stresses in the messenger wire. A forced vibration test of the damper was carried out to establish the amplification of the amplitude of the masses relative to the forced displacement of the clamp, Fig. 8 (left) and the risk for encountering fatigue related rupture of the messenger wire.

Comparing the magnitude of the peak-peak displacement of the clamp to the displacement of the mass yields an amplification ≈ 2.5 . Thus, a clamp movement of one cable diameter = 0.11 m (Fig. 1 left) will result in 0.25 m deflection of the attachment point of the mass causing considerable dynamic bending stresses in the messenger wire at the clamp, Fig. 8 (right). The test demonstrated rupture of the first wire strand at the clamp after 6 hours of testing and complete rupture of the messenger wire after 11 hours. Wire rupture at the mass end of the messenger wire is likely to be due to VIV resonating with the high frequency second mode of the smaller mass, Fig. 8 (right).

The failure of the Stockbridge dampers on the longest hangers of the 1915 Çanakkale bridge due to RWIV lead to the design of a hydraulic damper assembly composed of two individual hydraulic damper cylinders having a compound damping constant $C = 50$ kNs/m and attached to the hanger $x_c = 3.2$ m above the anchor point. The Scruton Number for hanger 111 fitted with the hydraulic damper as is plotted in Fig. 7 (grey graph). It is noted that $Sc > 70$ for all mode numbers up to $n = 19$.

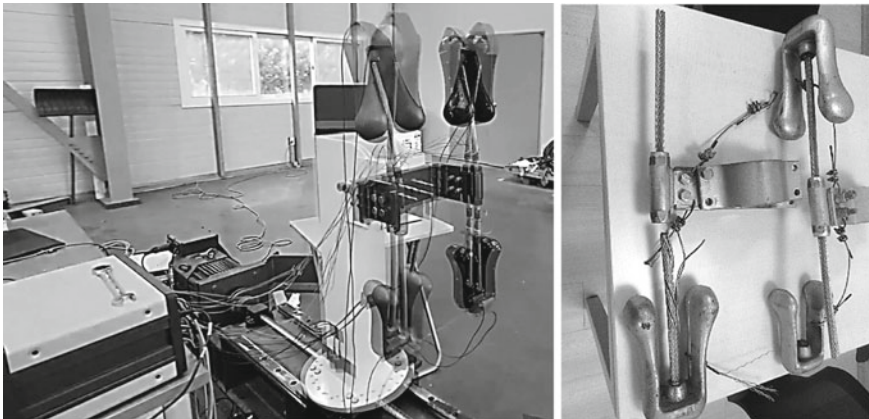


Fig. 8 Forced motion test of stockbridge dampers (left). Overlay of two video frames captured at the extreme excursions of the clamp and mass. Failed dampers displaying rupture of messenger wire at the clamps and at the masses (right)

7 Conclusions

Field observations and wind tunnel simulation of the vibration of parallel wire or locked-coil suspension bridge hangers sheathed by HPDE tubes and mitigation by means of mechanical dampers is discussed. The following conclusions are highlighted:

- Vertical parallel wire or locked-coil hanger cables sheathed by HPDE tubes are found to have very low structural damping in the range 0.001–0.002 log. dec.
- These types of hanger cables are expected to receive high frequency excitation by rhythmic vortex shedding or low frequency rain wind effects. Rain wind excitation is considerably stronger than vortex induced vibrations.
- The classical wave theory for a taut string fitted with a viscous damper must be solved numerically for accurate prediction of the resulting modal damping for high wave numbers.
- Stockbridge dampers are efficient for damping of vortex induced vibrations of the hanger cables but are likely to fail due to fatigue of the messenger cable when subjected to rain/wind vibrations.
- Hydraulic dampers are likely to present a more efficient and durable alternative to Stockbridge dampers as they can be designed to yield higher modal damping and are less vulnerable to fatigue.

References

1. Sluszka P (2017) Long-term performance of suspension bridge main cables and hangers. In: Caetano E (ed) ISDAC2017 symposium. FEUP Porto, pp 91–98
2. Larsen A (2021) Wind induced hanger vibrations—Hålogaland bridge. In: Jakobsen JB (ed) ISDAC2021 symposium. University of Stavanger, Norway, pp 91–98
3. Caetano E (2007) Cable vibrations in cable-stayed bridges, structural engineering documents. IABSE, Zürich, Switzerland
4. Geogakis CT, Koss HH, Ricciardelli F (2009) Design specifications for a novel climatic wind tunnel for the testing of structural cables. In: Proceedings of the 8th international symposium on cable dynamics
5. Larsen A (2017) Cable aerodynamics in eurocode—an engineering point of view. In: Caetano E (ed) ISDAC2017 symposium. FEUP Porto, pp 91–98

Cable-Stayed Bridge Model Updating Through Analytical Formulation, Finite Element Model and Experimental Measurements



Cecilia Rinaldi^{ID}, Marco Lepidi^{ID}, Francesco Potenza^{ID},
and Vincenzo Gattulli^{ID}

Abstract The evaluation of the dynamic response of cable structures is a topic of relevant interest for both researchers and designers working in the civil engineering field. For the implementation of reliable numerical models able to simulate the actual mechanical behaviour of such structures, the cable tension is a fundamental variable to be assessed accurately. This contribution describes methods and procedures aiming to enhance the reliability of finite element models in reproducing the dynamic response of a cable-stayed pedestrian bridge, through the fusion of static and dynamic experimental data from different technologies. First, the experimental evaluation of the cable static configuration has been used for identifying the cable tension. Indeed, by virtue of a low-order approximation of the catenary suspended cable model (obtained by a perturbation method), a cubic function of the cable static configuration under self-weight has been determined. In this formulation, the quadratic and cubic coefficients have been recognized as tension-sensitive quantities and have been used to analytically evaluate the cable tension. Then, traditional output only dynamic tests, under environmental noise, have been exploited to evaluate the reliability of the computational model of the bridge and to analyze the deck modes mainly involved in the dynamic behaviour. The subsequent manual model updating, targeted at reducing the difference between the experimental and numerical frequen-

C. Rinaldi (✉) · V. Gattulli
Department of Structural and Geotechnical Engineering, Sapienza University of Rome,
via Eudossiana 18, 00184 Rome, Italy
e-mail: cecilia.rinaldi@uniroma1.it

V. Gattulli
e-mail: vincenzo.gattulli@uniroma1.it

M. Lepidi
Department of Civil, Chemical and Environmental Engineering, University of Genoa,
Via Montallegro 1, 16145 Genoa, Italy
e-mail: marco.lepidi@unige.it

F. Potenza
Department of Engineering and Geology, University “G. d’Annunzio” of Chieti-Pescara,
Viale Pindaro 42, 65127 Pescara, Italy
e-mail: francesco.potenza@unich.it

cies, showed higher effectiveness if the designed cable tensions are replaced by the identified values in the computational model.

Keywords Suspended cable · Perturbation methods · Tension identification · Modal analysis

1 Introduction

Along the years, the cable, as structural element, constitutes one of the most useful and efficient solutions to guarantee high material strength, functionality, low-weight and aesthetic fineness of a mechanical systems. In the last decades, several researches have provided interesting contributions, mainly concerning the description of the cable mechanical behaviour [6, 11, 15]. Moreover, reduced analytical models have been also developed to explain some experimental evidences [3–5]. To exemplify, the model proposed in [4] describes the free dynamics of a system composed by beam-cable-beam. Such description aimed to classify the parameters intervals where global, local and hybrid modes occurred. The analysis allowed to justify some unpredictable dynamic interactions observed during some experimental tests conducted on the damaged masonry walls of the Basilica of Collemaggio, heavily damaged during the 2009 L'Aquila Earthquake.

The reliability of these models can be improved through an appropriate identification of the parameters that are mainly involved in the structural dynamic behaviour. The procedure used to reach this objective is commonly named *model updating* that aims to increase the accuracy of a model (analytical or computational) based on the information coming by experimental measurements. These latter, in the last years, have been for the most part vibration-based [12] and so, in this case, the model updating process is oriented to a proper evaluation of the modal properties (especially frequencies and modal shapes). Dynamic tests are usually carried out measuring the structural response induced by ambient excitation (output-only, i.e. without direct knowledge of the input), and the structural identification procedure is called in this case operational modal analysis. In the last decades, have been developed consolidated procedures able to accurately identify the modal parameters, as the ones reported in [13, 14]. A lot of examples concern structural systems in which the cables are of primary importance as in the case of suspended or stay-cables bridges or walkways [1, 7]. Such updated models constitute a base for continuous structural health monitoring and quickly identifying the triggering of critical trends.

Regarding the cable, beyond the classical mechanical damage indicators usually depending by a combination of the modal features [8–10], the evaluation of its axial force (cable tension) is one of the most important. It can be directly measured through a dedicated instrumentation or assessed by indirect methods, solving inverse problems. In this case, the identification results depend by both the measurements accuracy and the refinement of the analytical model used in the inverse procedure. Such models can be included in the simplest class (taut-string that neglects the flex-

ural stiffness and sag) or in ones more complicated particularly suitable for long cables [2, 16, 19].

The aim of this research activity is the accuracy enhancement of a finite element model to analyze the dynamic behaviour of the cable-stayed bridge described in Sect. 2, exploiting both geometric (static) and vibration (dynamic) experimental data. First, the actual cable tensions are evaluated through a low-order polynomial approximation of their experimental static configuration under self-weight (Sect. 3). Then, a preliminary finite element model is implemented according to design values of cable forces and it is subsequently improved by considering the identified cable tensions. Computational model accuracy is evaluated in Sect. 4 by a comparison with operational modal analysis results and concluding remarks are reported in Sect. 5.

2 Bridge Description and Experimental Tests

The cable-stayed bridge under investigation is the pedestrian walkway in Beinasco (province of Turin, Italy) depicted in Fig. 1. The cycle-pedestrian walkway was built in 2004 and it was named to Albano Zuin, a partisan of Beinasco killed during the second world war. It is composed by three main elements: (1) deck, (2) access ramp and (3) pylon (Fig. 1a, b). As it can be noted in the longitudinal view in Fig. 1c, such three substructures interact each other by a system of 26 stay cables all connected to the pylon at different heights. In particular, seven cables (steel, 42 mm diameter, pretensioned) constitute a fan system bearing the deck that is further sustained by three supports two located at the ends and the third one at about one third of the total length. The deck is a steel truss-type beam 80 m long, 3 m wide and 1.65 m tall showing a slight curvature in its horizontal plane (Fig. 1d). Moreover, such substructure is

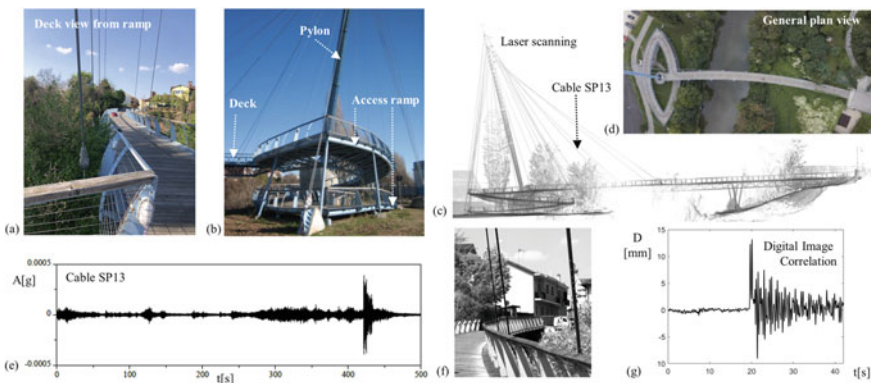


Fig. 1 Overview of the Albano Zuin cable-stayed bridge and experimental tests: deck (a) and access ramp (b) picture; lateral view of the 3D point cloud model (c); general plan view (d); measured accelerations of SP13 cable (e); image (f) and displacement (g) data by high-speed camera

composed by three main elements connected together through smaller crossbeams. Similar to the deck, the access ramp is a truss-type beam, with an ovoid shape in plan, which is sustained by both supports and stays (steel, 28 mm diameter). The two ends of the access ramp are connected to the ground and deck, respectively. Finally, the pylon is a steel tubular 45 m tall showing a slight inclination. For the stabilization of the whole system, nine stays connect the pylon to the ground.

Different experimental surveys have been carried out to obtain an accurate knowledge of the as-built structure and to improve the numerical model describing the walkway structural behaviour. The specifications of the instrumentation used for the acquisition of experimental data are listed in Table 1. To faithfully describe the geometry of the whole system, a terrestrial laser scanner has been used to obtain a 3D point cloud model of the bridge (Fig. 1c). Due to the large dimensions of the structure, the geometry reconstruction needed of 26 stations and 7 h of acquisition. To investigate the dynamic behaviour of the deck and cables supporting the deck, dynamic tests (output-only) under environmental noise have been conducted, for which three vibration measurement systems (high-speed camera, uniaxial wired accelerometers, uni- and tri-axial wireless accelerometers) have been used. Examples of acquisitions carried out on the cables are showed in the Fig. 1e, f, g. It is worth to highlight that, to measure an appreciable amplitude level for the cable dynamic response, some manual light input have been applied (see, for example, the last part of the time history in Fig. 1e). The camera has been installed on the concrete cantilever in the central aerea of the access ramp and it has been able to record the vibration of cables SP15 and SP16 (see Fig. 2a where the attachment points of the seven stay cables supporting the deck are also reported), while for SP10–SP14 cables PCB accelerometers have been used. The displacement time histories of SP15 and SP16 were obtained by processing the acquired images using the Digital Image Correlation as visual tracking algorithm [17]. The positions of uni- and tri-axial MEMS accelerometers installed on the deck are illustrated in Fig. 2b.

Table 1 Data acquisition systems for geometry and vibration measurements

Geometry	3D point cloud	Cam2 Laser Scanner Focus Faro × 130 0.6–130 m Range, ± 2 mm Distance error
Vibrations	Cable disp.	Camera IO Industries Flare 12M125 × CL 4096 × 3072 Resolution, 100 fps Sampling frequency
		Cable accel.
	Deck accel.	Wireless Lumentek Sentinel MEMS accelerometers 1350 mV/g Sensitivity, 250 Hz Sampling frequency

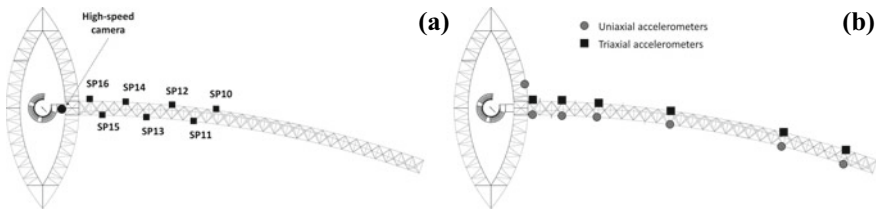


Fig. 2 Setup plan view: **a** position of the high-speed camera and anchorage points of the cables supporting the deck; **b** setup for the dynamic tests conducted on the deck by using uniaxial and triaxial accelerometers

3 Analytical Cable Model and Tension Identification

Let consider an inclined and inextensible cable hanging between two fixed supports. The nonlinear ordinary differential equation governing the static equilibrium of the cable under self-weight w , constant per unit natural length, reads in nondimensional form

$$\frac{d^2z}{dx^2} = -8\delta \left[1 + \left(\tan \vartheta + \frac{dz}{dx} \right)^2 \right]^{1/2} \quad \text{with} \quad \delta = \frac{wL}{8H} \quad (1)$$

and the boundary conditions read $z(0) = 0$ and $z(1) = 0$, where x variable describes the span L between the two supports, the coordinate function $z(x)$ describes the dip of the cable below the chord, ϑ is inclination angle of the chord and H is the unknown horizontal reaction at support. The exact solution of this equation is the catenary function which can be challenging to handle for cable tension identification purposes. Under the assumption of cable shallowness, a classic perturbation scheme can be pursued. The parameter δ is considered small and, introducing the ordering $\delta = \epsilon \delta_1$, where $\epsilon \ll 1$ is a nondimensional smallness parameter, the unknown variable $z(x)$ can be approximated by $z_{[n]}(x) = \sum_{i=1}^n \epsilon^i z_i(x)$. The functions $z_i(x)$ are independent unknown variables which are determined substituting the parameter ordering and the variable expansion $z_{[n]}$ in the equilibrium equation (1), expanding and collecting terms of the same ϵ -power, and solving the obtained system of linear equations up to second order. The second order reconstructed solution is a cubic function reading

$$z_{[2]}(x) = 4\delta \sec \vartheta \left(1 + \frac{4}{3}\delta \sin \vartheta \right) x - 4\delta \sec \vartheta \left(1 + 4\delta \sin \vartheta \right) x^2 + \frac{32}{3}\delta^2 \tan \vartheta x^3 \quad (2)$$

where δ can be analytically assessed by solving a compatibility equation. In the inverse problem for tension identification, the cable tension $N = H / \cos \vartheta$ (and consequently the parameter δ) is the primary unknown and the geometric static configuration is an experimentally known information. If the parameter δ is unknown and the geometric configuration of the cable \hat{z} is known and described as function of the span variable ξ as

$$\hat{\zeta}(\xi) = -(\hat{\kappa}_1 + \hat{\kappa}_0)\xi + \hat{\kappa}_1\xi^2 + \hat{\kappa}_0\xi^3, \tag{3}$$

the direct comparison of Eq. (3) with the cubic function (2) allows to identify $\hat{\delta}$ by equating the respective quadratic and cubic coefficients. As the quadratic coefficient $\hat{\kappa}_1$ is larger than the cubic coefficient $\hat{\kappa}_0$, according to the perturbation scheme, the identification is based on $\hat{\kappa}_1$ which can be determined with higher accuracy. Once $\hat{\delta}$ is obtained, considering the Eq. (1), \hat{H} can be identified and, consequently, \hat{N} can be determined as

$$\hat{N} = \frac{wL}{8\hat{\delta} \cos \vartheta} = -\frac{1 + \sqrt{1 - 2\hat{\kappa}_1 \sin(2\vartheta)}}{4\hat{\kappa}_1 \cos^2 \vartheta} wL \tag{4}$$

where the overhat indicates directly measured quantities, or quantities identified from measures. The accuracy of this tension identification strategy has been evaluated in [18] through a comparison with the forces evaluated through the dynamic (frequency-based) output-only identification method.

The experimentally measured geometric configuration of the cable is a three dimensional point cloud model which needs to be post-processed to obtain a description consistent with the analytical formulation of the tension identification problem. These post-processing operations consist of determining the vertical mid-plane where cable is hanging on and roto-translating the reference system. Then, the coefficient $\hat{\kappa}_1$ can be obtained and substituted in the formula (4). To reduce computational effort in estimating parameters for the description of geometric configuration, the point cloud model can be reduced by considering two suited subset of points, according a proper selection criterion as described in [18]. Identification results obtained for the Albano Zuin footbridge following the described strategy showed a change in relation to the design values of cable tensions as reported in Table 2.

Table 2 Deck cable data and tension identification results

Cable	L^{chord} [m]	ϑ	$\hat{\kappa}_1$	$\hat{\kappa}_0$	\hat{N} [kN] (Ident.)	N [kN] (Design)
SP10	52.66	0.572	-3.30E-02	4.50E-04	94.82	175
SP11	49.56	0.648	-5.21E-02	8.44E-03	58.41	122
SP12	46.38	0.731	-1.18E-01	1.51E-04	27.00	30
SP13	44.45	0.826	-1.74E-01	2.76E-03	18.49	30
SP14	42.07	0.941	-6.28E-02	3.14E-03	53.05	30
SP15	40.93	1.036	-2.47E-01	1.76E-02	16.46	33
SP16	39.03	1.112	-1.01E-01	5.78E-04	40.96	36

4 Bridge Models

4.1 Computational Model

A computational model of the cable-stayed bridge has been implemented in a finite element environment, based on the information available from the original structural design. Since the 3D point cloud model obtained through the laser scanner showed that the position of the monitored pylon top point (44 m above the ground) has 1.18 m distance from its design position (probably due to limited control during construction phase), the FEM model has been implemented taking into account the scanned geometry. As showed in Fig. 3a, the deck structure has been modeled by beam elements, while the cables by tension-only elements defined with the pretension available in the design documentation. The external nodes have been fixed (in some cases only one rotation has been fixed) except for the node at the base of the pylon which is hinged. To investigate the dynamic behaviour of the structure, a modal analysis has been performed and, to obtain an accurate description of the local modes of the stays supporting the deck, each cable element has been subdivided in 30 parts. Modal analysis results highlighted, for low frequencies, the prevalence of local modes (cable dominant) of the type shown in Fig. 3b. The first global mode (deck dominant), reported in Fig. 3c, can be found at 0.837 Hz. The overall description of the modal properties is reported in Table 3 and in Fig. 4. As regards deck dominant modes, it can be noted that the first 5 of them (up to 5 Hz) are vertical and horizontal bending modes, while for frequencies higher than 6 Hz bending-torsional modes can be found.

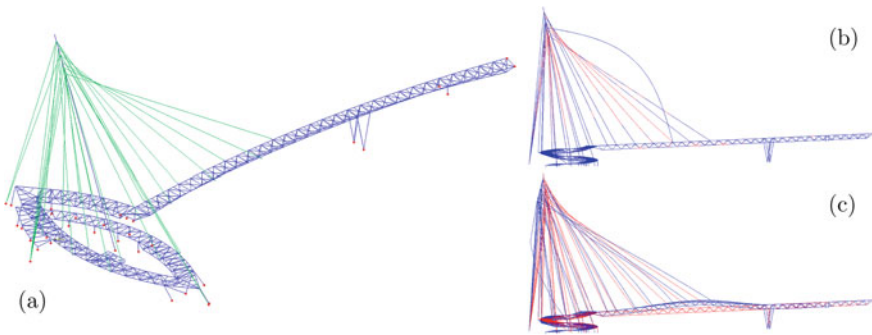


Fig. 3 FEM model of the Albano Zuin bridge: **a** 3D view of the model consisting of beam and cable elements and external constraints; **b** first local mode (0.56 Hz); **c** first global mode (0.837 Hz)

Table 3 Frequencies in Hz of the first mode of cables supporting the deck

Cable	Exp.	Num.—Design force	Num.—Ident. force
SP10	0.923	1.194	0.879
SP11	0.770	1.057	0.731
SP12	0.546	0.560	0.531
SP13	0.495	0.582	0.457
SP14	0.763	0.611	0.812
SP15	0.500	0.652	0.461
SP16	0.840	0.652	0.755

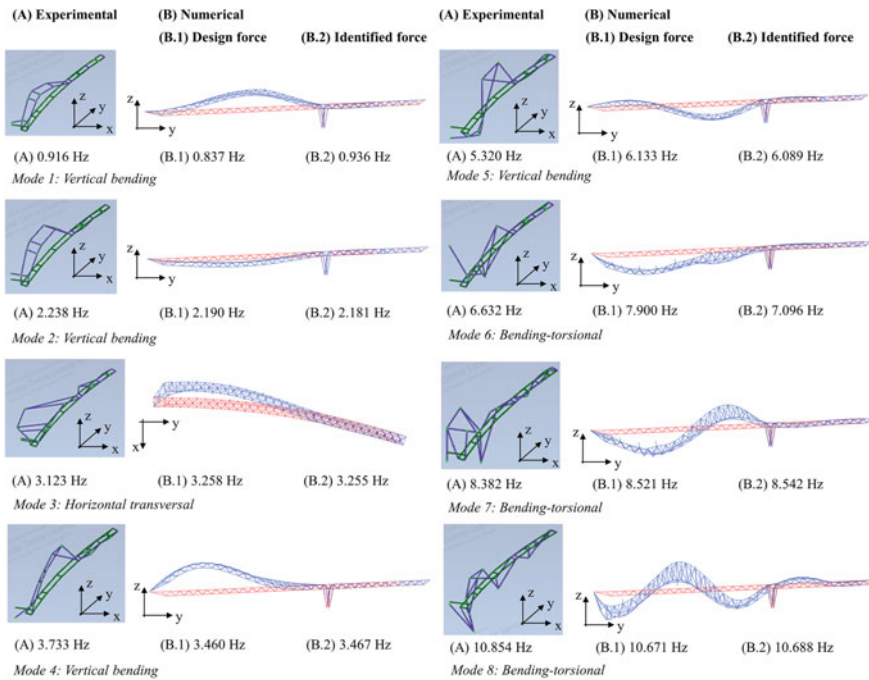


Fig. 4 Comparison of experimental and numerical (considering both design and identified cable tensions) deck dominant modes

4.2 Modal Identification and Model Updating

To identify the main global modes of the deck, the wireless sensor nodes have been installed according to the setup reported in Fig. 2b and the acquired signals have been processed through the Frequency Domain Decomposition technique to evaluate natural frequencies and mode shapes. Since triaxial accelerometers have also been used, such layout allowed to identify different type of modal configurations, vertical

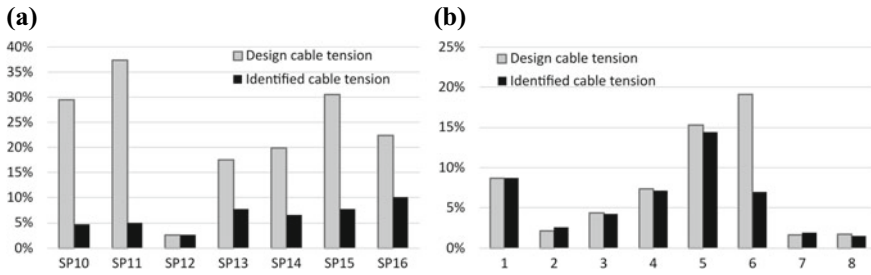


Fig. 5 Frequency difference between experimental results and numerical results based on design and identified cable tensions for the first mode of cables supporting the deck (a) and for deck dominant modes (b)

bending, horizontal transversal, bending-torsional, as reported in Fig.4 compared with numerical modes. FEM results have been improved considering cable forces identified through the static method described in Sect. 3. As it can be noted in Table 3, the replacement of design cable forces with identified tensions allowed to obtain an estimate of the local mode frequencies which is more consistent with the experimental frequencies evaluated through the spectral content of the acquired vibration signals. In the analysis of cable modes, a relevant improvement of the computational model, obtained through the identification of the actual cable tensions, can be noted for all cables. For deck mode frequencies, a significant improvement can be found mainly for mode 6, which is the first bending-torsional mode, and it is due to the high difference between design and identified cable tension encountered for cables SP10 and SP11 which support the part of deck affected by the torsional deformation of mode 6. Such results can be clearly observed in Fig. 5, where the frequency difference of deck, Δf^d , and cables, Δf^c , evaluated as

$$\Delta f^d = \frac{f_{num}^d - f_{exp}^d}{f_{exp}^d}, \quad \Delta f^c = \frac{f_{num}^c - f_{exp}^c}{f_{exp}^c}, \quad (5)$$

are reported.

5 Conclusions

The paper describes the procedures pursued to increase the reliability of a finite element model in simulating the dynamic behaviour of a cable-stayed pedestrian bridge. The improvement of the computational model of the structure has been focused on an accurate assessment of the actual tensions of cables supporting the deck, based on an identification strategy which exploits a low-order approximation of the catenary solution of the suspended cable under self weight and the experimental measurement of its geometric static configuration. The accuracy of the finite element models has

been evaluated through a comparison between numerical and operational modal analysis results. Considering the identified tensions allowed to obtain, for local modes (cable dominant), an estimate of the natural frequencies which is more consistent with the experimental frequencies and, for global modes (deck dominant), a significant improvement mainly for the frequency of the first bending-torsional mode involving the cables which have showed the highest tension variation from design values. Such results highlighted the significance to accurately assess the cable forces in cable structure modeling, fusing static and dynamic experimental data coming from different technologies.

Acknowledgements This study was carried out within the MOST—Sustainable Mobility National Research Center and received funding from the European Union Next-GenerationEU (PNRR)—MISSIONE 4 COMPONENTE 2, INVESTIMENTO 1.4—D.D. 1033 17/06/2022, CN00000023). This manuscript reflects only the authors' views and opinions, neither the European Union nor the European Commission can be considered responsible for them.

References

1. Cunha Á, Caetano E, Magalhães F, Moutinho C (2018) Dynamic identification and continuous dynamic monitoring of bridges: different applications along bridges life cycle. *Struct Infrastruct Eng* 14(4):445–467
2. Foti F, Geuzaine M, Denoël V (2021) On the identification of the axial force and bending stiffness of stay cables anchored to flexible supports. *Appl Math Model* 92:798–828
3. Gattulli V, Cunha A, Caetano E, Potenza F, Arena A, Di Sabatino U (2021) Dynamical models of a suspension bridge driven by vibration data. *Smart Struct Syst, Int J* 27(2):139–156
4. Gattulli V, Lepidi M, Potenza F, Di Sabatino U (2016) Dynamics of masonry walls connected by a vibrating cable in a historic structure. *Meccanica* 51(11):2813–2826
5. Gattulli V, Lepidi M, Potenza F, Di Sabatino U (2019) Modal interactions in the nonlinear dynamics of a beam-cable-beam. *Nonlinear Dyn* 96(4):2547–2566
6. Irvine HM (1981) Cable structures. The MIT Press
7. Koo KY, Brownjohn J, List D, Cole R (2013) Structural health monitoring of the Tamar suspension bridge. *Struct Control Health Monit* 20(4):609–625
8. Lardies J, Minh-Ngi T (2011) Modal parameter identification of stay cables from output-only measurements. *Mech Syst Signal Process* 25(1):133–150
9. Lepidi M, Gattulli V (2012) Static and dynamic response of elastic suspended cables with thermal effects. *Int J Solids Struct* 49(9):1103–1116
10. Lepidi M, Gattulli V, Vestroni F (2009) Damage identification in elastic suspended cables through frequency measurement. *J Vib Control* 15(6):867–896
11. Luongo A, Zulli D (2013) Mathematical models of beams and cables. Wiley
12. Mottershead JE, Link M, Friswell MI (2011) The sensitivity method in finite element model updating: a tutorial. *Mech Syst Signal Process* 25(7):2275–2296
13. Peeters B, Van der Auweraer H et al (2005) Polymax: a revolution in operational modal analysis. In: *Proceedings of the 1st international operational modal analysis conference, Copenhagen, Denmark, vol 820*, pp 1–12
14. Peeters B, De Roeck G (2000) Reference based stochastic subspace identification in civil engineering. *Inverse Probl Eng* 8(1):47–74
15. Rega G (2004) Nonlinear vibrations of suspended cables-part i: modeling and analysis. *Appl Mech Rev* 57(6):443–478

16. Ren WX, Chen G, Hu WH et al (2005) Empirical formulas to estimate cable tension by cable fundamental frequency. *Struct Eng Mech* 20(3):363–380
17. Rinaldi C, Ciambella J, Gattulli V (2022) Image-based operational modal analysis and damage detection validated in an instrumented small-scale steel frame structure. *Mech Syst Signal Process* 168:108640
18. Rinaldi C, Lepidi M, Potenza F, Gattulli V (2023) Identification of cable tension through physical models and non-contact measurements. *Mech Syst Signal Process* 205:110867
19. Zhang X, Xu H, Cao M, Sumarac D, Lu Y, Peng J (2023) In-plane free vibrations of small-sag inclined cables considering bending stiffness with applications to cable tension identification. *J Sound Vib* 544:117394

Identification and Control

Bayesian Identification of the Axial Forces, the Bending Stiffnesses, and the Connecting Point in Crossed Cables



D. Piciuccio, F. Foti, V. Denoël, T. Auguste, S. Hoffait, and M. Geuzaine

Abstract In this paper, an asymptotic expression is derived for the natural frequencies of two interconnected cables with small but non-negligible bending stiffness. This simple analytical formulation serves as a starting point for solving the inverse problem. First, it ensures that it is possible to univocally identify five parameters: the axial force and the bending stiffness in each of the two cables, as well as the position of the crossing point. A Bayesian framework based on the Metropolis-Hasting sampling algorithm is then used to calculate the most probable values and posterior distributions of these five parameters. The methodology is finally verified on a lab experimental setup, and applied to vibration data collected on an actual bridge.

Keywords Cable network · Structural health monitoring · Bayesian regression · Vibrations · Cable force · Natural frequencies

1 Introduction

One of the simplest and fastest strategies to assess the health state of cable-supported structures is to monitor the evolution of forces in their constitutive elements over time. Regarding stays and hangers, vibration-based identification techniques are

D. Piciuccio · F. Foti
Dipartimento di Ingegneria Civile e Ambientale, Politecnico di Milano, Milan, Italy
e-mail: francesco.foti@polimi.it

V. Denoël
Structural & Stochastic Dynamics, University of Liège, Liège, Belgium
e-mail: v.denoel@uliege.be

T. Auguste
SPW, Walloon Public Services, Liège, Belgium

S. Hoffait
V2i, Belgium, Liège, Belgium

M. Geuzaine (✉)
NatHaz Modeling Laboratory, University of Notre Dame, South Bend, IN, USA
e-mail: mgeuzaine@uliege.be

particularly convenient and affordable. Acceleration measurements are recorded on each cable, then processed to extract their natural frequencies, which finally provide an estimate of their tensile forces. But first, their relationship needs to be established through the formulation of explicit expressions, the solution of characteristic equations, or the construction of finite element models.

In order to perform identifiability studies, it is useful to understand how the natural frequencies of cables are affected by their axial force, bending stiffness, or sag extensibility for instance. Methods based on analytical formulas are particularly appreciated in this context because they have a clearer domain of applicability than others. But except for a few specific cases [1], the closed-form expressions devoted to the dynamic analysis of two-cable networks rely on taut string models [2]. The flexural rigidity of the cables is therefore ignored although it can significantly modify the values of the natural frequencies and reveal the effects of rotational end restraints [3, 4].

Despite this lack of mathematical developments, Furukawa et al. [5] tried to identify simultaneously the tensile forces, the bending, and the axial stiffnesses of two cables connected by an intersection clamp while considering their extremities as hinged. To do so, the governing equations were solved in a numerical way and the input parameters were modified to minimize the difference (in the least square sense) between calculated and measured natural frequencies. However, it appeared that the objective function was much more sensitive to changes in the tensile forces, which thus were the only parameters to be estimated with a sufficient accuracy.

Section 2 of this work therefore aims at deriving analytical formulas for the in-plane natural frequencies of any two-cable network with small but non-negligible bending stiffness, as represented in Fig. 1. To do so, perturbation methods are applied on single cables with an intermediate support. Hence, the approach is similar to what was done for bi-supported cables in [3, 4] but the application is different. Although approximate, the resulting expressions provide a clear understanding of the effects that the most influential parameters have on the natural frequencies, which is useful for determining their identifiability.

In Sect. 3, a Bayesian identification strategy is developed according to the previous findings. This algorithm is used to estimate the axial forces and the bending stiffness of the cables but also for refining initial estimates of the crossing point location. Contrary to the classical least square method, the proposed procedure provides the most probable values of the cable parameters and their posterior distributions, which are conditioned on observed frequencies. This gives access to credible intervals and helps to gain confidence in the results.

In Sect. 4, this identification method is finally verified with laboratory experiments and validated with on-site measurements of cable vibrations collected on an actual bridge.

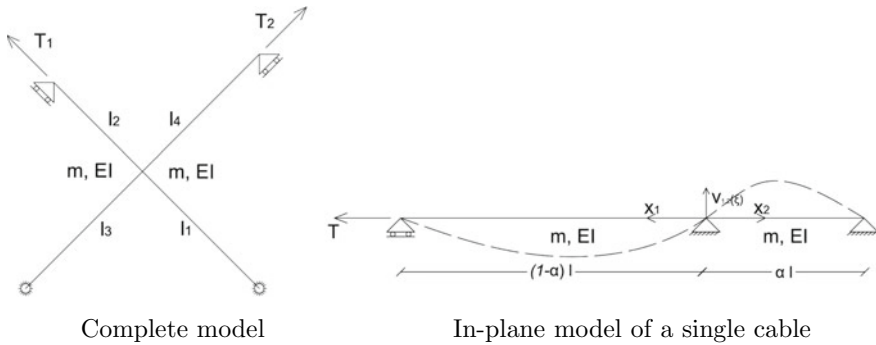


Fig. 1 Cable network model

2 In-Plane Analytical Model

This part of the paper discusses the direct analysis of a cable network constituted by two crossing hangers, as represented in Fig. 1a. For the sake of modeling, the end restraints are supposed to be transversely rigid and the connector at the crossing point position is assumed to enforce the continuity of the displacement. The in-plane free vibrations of each cable are then considered separately as shown in Fig. 1b where an intermediate fixed support simulates the restraining action exerted by the transversal cable.

2.1 Problem Formulation

The total length of the considered cable is l and the distance of the intermediate support from the right end is denoted as αl , $\alpha \in [0; 1]$. The cable is subjected to the tensile force T and has a uniform mass per unit length m and bending stiffness EI . The limited length of the four cable elements makes the bending stiffness effect non-negligible while the shear deformability, rotational inertia, and vertical sagging effects are discarded on the basis that the cable elements are sufficiently slender, extensible, and tensioned.

In the following, the problem is examined in its non-dimensional form. A reference system is considered at the intermediate support, from which two different coordinates (x_1 and x_2) depart. The non-dimensional variables describing the transversal displacement and the position are respectively $\nu_1 = \frac{v_1}{(1-\alpha)l}$, $\nu_2 = \frac{v_2}{\alpha l}$, $\xi_1 = \frac{x_1}{(1-\alpha)l}$ and $\xi_2 = \frac{x_2}{\alpha l}$. Following the same derivations as in [3, 4], the problem is governed by the system

$$\begin{cases} \varepsilon_1^2 \frac{\partial^4 \nu_1}{\partial \xi_1^4} - \frac{\partial^2 \nu_1}{\partial \xi_1^2} + \frac{\partial^2 \nu_1}{\partial \tau^2} = 0 \\ \varepsilon_2^2 \frac{\partial^4 \nu_2}{\partial \xi_2^4} - \frac{\partial^2 \nu_2}{\partial \xi_2^2} + \frac{\partial^2 \nu_2}{\partial \tau^2} = 0 \end{cases} \quad \text{with} \quad \begin{cases} \varepsilon_1 = \sqrt{\frac{EI}{T(1-\alpha)^2 l^2}} \\ \varepsilon_2 = \frac{1-\alpha}{\alpha} \varepsilon_1 = a \varepsilon_1 \end{cases} \quad (1)$$

to which the boundary conditions $\nu_1(0) = 0$, $\nu_1(1) = 0$, $\nu_2(0) = 0$, $\nu_2(1) = 0$, $\varepsilon_1^2 \nu_1''(1) = 0$, $\varepsilon_2^2 \nu_2''(1) = 0$, $\varepsilon_1 \nu_1'(0) = -\varepsilon_1 \nu_2'(0)$ and $\varepsilon_1^2 \nu_1''(0) = \varepsilon_1 \varepsilon_2 \nu_2''(0)$ are associated.

As the symbol ' indicates differentiation in space, these boundary conditions actually correspond to zero displacements at the sub-span ends, zero bending moments at the cable ends, and continuity of the slope and moment at the intermediate support. The problem can be solved through the classical separation of variables leading to the following algebraic eigenvalue problem:

$$\mathbf{B}(\omega_{2,n}; \varepsilon_2; \alpha) \boldsymbol{\varphi}_n = 0 \quad \forall n \in \mathbb{N} \quad (2)$$

The boundary condition matrix \mathbf{B} is of size 8×8 and the vector $\boldsymbol{\varphi}_n$ contains the 8 integration constants $\boldsymbol{\varphi}_n = (\varphi_{1,n}; \dots; \varphi_{8,n})^T$ of the n-th mode shapes. The symbol $\omega_{2,n}$ represents the n-th dimensionless natural frequency obtained by dividing the n-th natural frequency of the system, Ω_n , by the characteristic frequency of the taut string model related to the shorter sub-span, Ω_b :

$$\omega_{2,n} = \frac{\Omega_n}{\Omega_b} \quad \text{with} \quad \Omega_b = \sqrt{\frac{T}{m\alpha^2 l^2}} \quad \text{and} \quad \tau = \frac{1}{\Omega_b} \quad (3)$$

2.2 Solution of the Eigenvalue Problem

Exact solutions of the eigenvalue problem (2) can be found for some simple configurations only, e.g. two sub-span of equal lengths. Otherwise, the problem has to be solved numerically. Nevertheless, asymptotic solutions can be developed through a standard perturbation approach hinging on the smallness of the bending stiffness parameter [3, 4]. They are convenient to define the set of parameters that can be identified based on measured eigenfrequencies. The approach proposed in [3, 4] for isolated cable elements is therefore extended in this paper to get second-order accurate asymptotic expressions for the eigenfrequencies of two-cable networks, which thus read as follows

$$\hat{\omega}_{a,k} = \frac{k\pi}{a} \left(1 + \frac{\varepsilon_2}{2a} + \frac{1 + 2k^2\pi^2 + k\pi \cot(\frac{k\pi}{a})}{4a^2} \varepsilon_2^2 \right) \quad (4)$$

$$\hat{\omega}_{b,k} = k\pi \left(1 + \frac{\varepsilon_2}{2} + \frac{1 + 2k^2\pi^2 + k\pi \cot(k\pi a)}{4} \varepsilon_2^2 \right) \quad (5)$$

Please note that these solutions are valid when $\varepsilon_2 \ll 1$ and finally need to be sorted in ascending order to recover the set of $\hat{\omega}_{2,n}$ which contains the approximate natural frequencies to compare with the exact numerical values. These results have been validated with a finite element model but this is not shown in this paper for the sake of conciseness.

Overall, these in-plane eigenfrequencies appear to depend on two dimensionless parameters: the bending stiffness ε_2 and the crossing point position $a = \frac{1-\alpha}{\alpha}$ or equivalently ε_2 and ε_1 . These parameters can be separately identified as no symmetric combination of the two can be observed in the formulation. For symmetry reasons, the eigenfrequencies are also insensitive to the swapping of the sub-span lengths. As evidence, by replacing ε_2 with $a\varepsilon_1$ and a with $1/a$, the same set of dimensional frequencies is obtained. Therefore, the identification procedure can be implemented by limiting α between 0 and 0.5 and estimating separately the bending stiffness, the cable force, and the crossing point location.

3 Non-linear Bayesian Regression

The mathematical model and the information provided by the closed-form solutions are used to implement an inverse identification strategy for determining the cable forces and bending stiffness, and for refining initial estimates of the crossing point location. This latter parameter is difficult to measure on-site and plays a major role in the dynamics of cable networks, as it can induce reordering of the eigenmodes because of the associated wavelength variation. The proposed identification algorithm relies on the Bayesian non-linear regression [6, 7] to estimate the posterior distributions of the model parameters, that maximize their likelihood. The probability distributions are computed exploiting a *Metropolis-Hasting* sampling algorithm [8]. This sampling technique, starting from initial values of the model parameters $\beta^{(0)}$, samples from a proposed distribution of the candidate values $\beta^{(cand)}$, that are accepted or rejected depending on the values of their likelihoods. The Monte Carlo simulations are repeated up to an established maximum number of samples and an initial transient phase (*burn-in period*) is discarded. This latter is the number of samples required for the algorithm to reach its steady state (i.e. to converge towards more likely values). The obtained distributions are used to compute the final estimates of the model parameters as the mean values ($\beta_{est} = \text{mean}[\beta_i]$) and the credible intervals (CI) from the standard deviation ($CI = \beta_{est} \pm 2\sigma$). The credible intervals are associated with the 95% probability that the true value falls within this range and provide confidence bounds useful for decision-making.

The main input parameters of the identification algorithm [9] are:

- the *range of admissible values* that should be sufficiently wide to contain the solution of the problem. It does not affect either the accuracy or the convergence rate;
- the *initial values* which strongly affect the convergence rate, that is halved when moving from starting values set to 1% the true values to initial guesses equal to 85% the nominal values [9];
- the number of *frequencies* used for the identification. When it increases, the error in the final estimates reduces and the CI shrinks. The suggested number of frequencies is between 6 and 15;
- the number of *samples* or iterations. They should be enough to get sufficient resolution in the final distributions, but their effect on the accuracy is not significant. The minimum suggested iterations are about one thousand.

4 Application

4.1 Small-Scale—Lab Setup

In order to verify the identification method presented above for the axial forces, a two-stage experimental campaign is conducted on a scaled model. A single cable is first installed as shown in Fig. 2a. It is attached to a fixed support on one side. On the other side, a pulley and a mass are used to control the axial force. Droplet piezoelectric accelerometers are then placed on the cable to record the vibrations obtained under a hammer impact. The FFT of the signal is finally calculated to extract

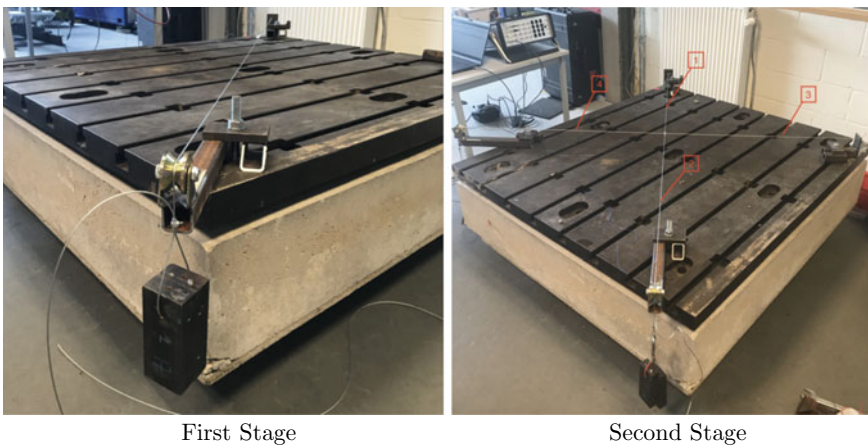


Fig. 2 Setup

Table 1 Input parameters for modeling and processing purposes

Name	Unit	Value	Name	Unit	Value
Cable length	[m]	2	Initial value (T_0)	[kN]	100
Cable diameter	[mm]	2	Admissible range	[kN]	[10;1000]
Lineic mass	[g/m]	12.5	Initial value ($E I_0$)	[Nm ²]	0.1
Elastic modulus	[GPa]	185	Admissible range	[Nm ²]	[0.0001;100]
Frequency rate	[Hz]	5	Iteration number	[-]	2000
Record duration	[s]	12	Burn-in region	[-]	500

Table 2 Axial forces identified in [kN] for a single cable

Mass (kg)	Nominal value	Estimated value	Credible interval
2	19.8	18.2 (-7.8%)	[18.05, 18.45]
4	39.3	36.6 (-6.9%)	[36.35, 36.80]
10	98.2	90.8 (-7.4%)	[90.53, 91.10]

Table 3 Cable length configurations

Configuration	l_1 in [m]	l_2 in [m]	l_3 in [m]	l_4 in [m]
1	0.97	1.03	0.91	0.99
2	0.75	1.25	0.85	1.05

the natural frequencies of the element by peak-picking. Additional information on the experimental setup and on the input parameters used for the processing of the measurements can be found in Table 1.

From there on, it is possible to evaluate the axial force and the bending stiffness of the cable as explained before, provided that the lines related to the boundary conditions at the middle support are discarded from the matrix \mathbf{B} . The expected and obtained results are shown in Table 2. Overall, the estimated values are about 7% lower than the weight of the masses. This difference is attributed to a torque resistance effect of the pulley and will consequently be taken into account in the sequel. It also appears that f_n over n is approximately equal to 21.3 Hz for all mode numbers n , meaning that the flexural rigidity of the cable is negligible. It is therefore not possible to identify this parameter.

In the next stage, a second cable is installed and is subjected to the same masses as the first one via an additional pulley. These two cables are clamped to each other as shown in Fig. 2b and according to the configurations detailed in Table 3. Accelerometers are then placed on the first and the second segment of the network to record vibrations due to hammer impact on each of these two sub-spans. Being of almost equal length in the first configuration, their natural frequencies subsequently form pairs. Their respective modal amplitudes however show that the hit part vibrates much more than the other, which indicates that the bending stiffness is still negligible.

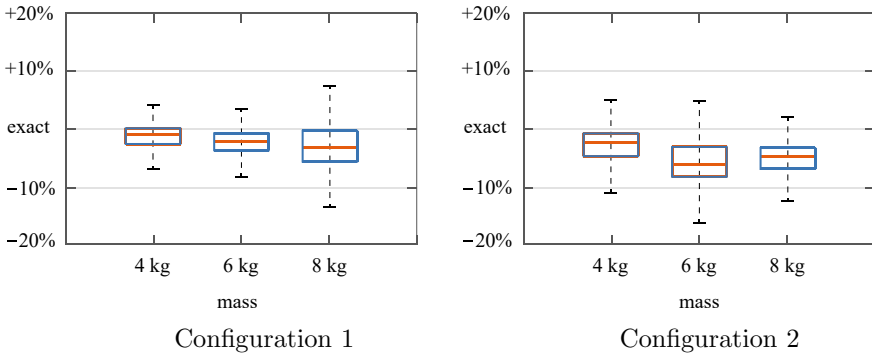


Fig. 3 Relative errors on the axial forces identified by the proposed procedure

Once converged, the axial forces sampled at each iteration by the Metropolis-Hasting algorithm are finally processed to get the probabilistic properties of the parameter after identification. These results are summarized for each configuration in Fig. 3a and b. Boxplots are used to illustrate the applicability and accuracy of the procedure proposed in this paper. They are indeed quite narrow as there is always less than a 10% difference between the first and third quartiles. Meanwhile, the relative errors attributed to the median values are also less than a few percent. They are all negative as well, which can indicate compensation from the fact that the model is a bit lighter or stiffer than the actual setup in some places.

4.2 Full-Scale—Haccourt Bridge

The identification strategy is here applied to the data collected on a real bridge (Haccourt Bridge, Belgium—1985) as a proof of concept. It is an arch-shaped cable-stayed bridge of 142 m in length and 23 m in height (Fig. 4). The steel arch has a thin-walled rectangular cross-section with a thickness of 30 and 36 mm and a size of 167×170 mm. The identification is performed on the first six in-plane eigenfrequencies of a cable whose sub-span lengths are respectively $l_1 = 6.65$ m and $l_2 \approx 2l_1$. The eigenfrequencies have been measured through accelerometers having a sensitivity of 10000 mV/g placed at the midspan of each sub-span. The bridge was tested in low traffic conditions under ambient and traffic excitations. The values of the natural frequencies have been extracted from the FFT of the signal by peak-picking.

The nominal values reported in the design drawings are used as starting values of the procedure ($T_0 = 640$ kN, $EI_0 = 331.4$ kNm², $\alpha_0 = 0.352$). The range of admissible values is set in between one-tenth and ten times the initial values for the cable force and bending stiffness while α is limited to 0.5. The distributions obtained after 6000 iterations are reported in Fig. 5.



Fig. 4 Tested bridge—Haccourt bridge

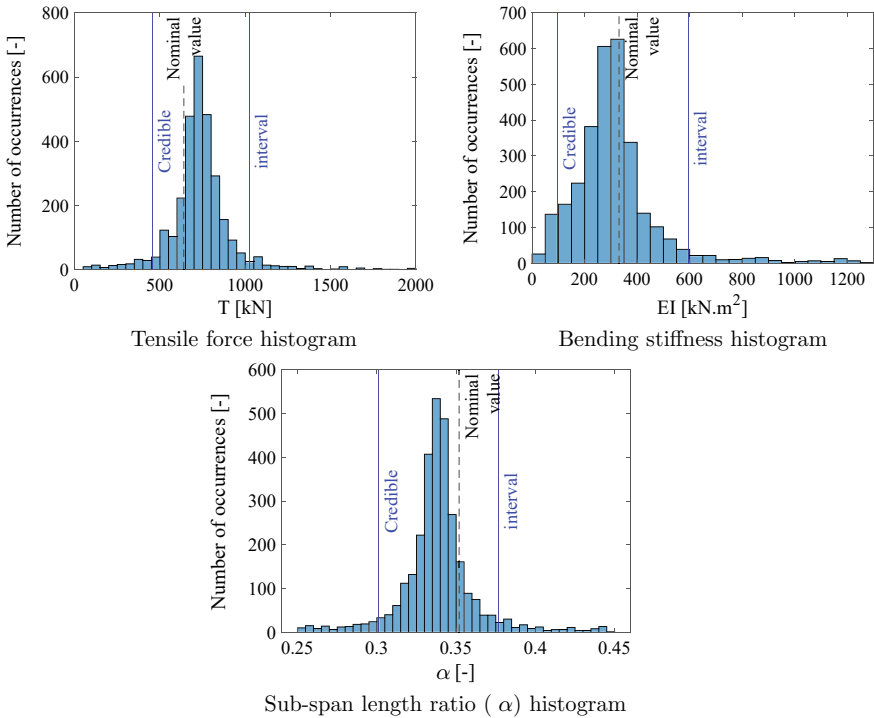


Fig. 5 Histograms, In-plane identification in the Haccourt bridge

The eigenfrequencies computed before and after identification are listed in Table 5 while the estimated parameters and their credible intervals are reported in Table 4. The identification provides an improvement of the fifth eigenfrequency at the price of a very slight worsening of the fundamental mode. Overall, the Root Mean Square Error (RMSE) in the eigenfrequencies reduces from 0.785 before identification to 0.324 after identification, proving the appropriateness of the identification strategy.

Table 4 Parameters identified in the Haccourt bridge

Name	Unit	Nominal value	Estimated value	Credible interval
T	[kN]	640	739.1	[455.3, 1023.8]
EI	[kNm ²]	331.4	315.9	[96, 595]
α	[–]	0.352	0.339	[0.301, 0.377]

Table 5 In-plane natural frequencies in [Hz]

	Experimental data	Before identification	After identification
f_1	5.83	5.79 (+0.69%)	6.05 (+3.70%)
f_2	11.86	11.15 (+6.17%)	12.12 (+2.17%)
f_3	12.63	12.39 (+1.92%)	13.07 (+3.42%)
f_4	19.72	19.47 (+1.27%)	19.98 (+1.31%)
f_5	27.37	25.66 (+6.45%)	27.48 (+0.40%)
f_6	29.09	28.71 (+1.31%)	29.58 (+1.67%)

5 Conclusions

This study proposes a Bayesian identification strategy for the cable forces, bending stiffnesses, and crossing point position of cable networks. Closed-form solutions of the in-plane eigenfrequencies are proposed, showing that the cable parameters can be separately identified. The accuracy of the algorithm is assessed through experimental tests which prove that the identification provides very reliable results as the error in the predicted parameters is always less than a few percent. The identification is finally applied to the data collected on a real bridge, leading to an improvement of the RMSE on the eigenfrequencies compared to the results obtained when nominal values are used.

Acknowledgements This work was supported by the Service Public de Wallonie. Special thanks go to T. Auguste and the V2i Company for providing assistance with the collection of experimental data on the Haccourt Bridge and in the lab.

References

1. Younespour A, Cheng S (2021) In-plane modal responses of two-cable networks considering cable bending stiffness effect. *Eng. Struct.* 230:111691
2. Caracoglia L, Jones NP (2005) In-plane dynamic behavior of cable networks. Part 1: formulation and basic solutions. *J. Sound Vib.* 279:969–991

3. Geuzaine M, Foti F, Denoël V (2021) Minimal requirements for the vibration-based identification of the axial force, the bending stiffness and the flexural boundary conditions in cables. *J. Sound Vib.* 511:116326
4. Foti F, Geuzaine M, Denoël V (2021) On the identification of the axial force and bending stiffness of stay cables anchored to flexible supports. *Appl. Math. Model.* 92:798–828
5. Furukawa A, Yamada S, Kobayashi R (2022) Tension estimation methods for two cables connected by an intersection clamp using natural frequencies. *J. Civ. Struct. Heal. Monit*
6. Clyde M et al (2019) An introduction to Bayesian thinking. In: *A companion to the statistics with R course*, vol 197
7. Koehrsen W (2018) Introduction to Bayesian linear regression. Online referencing. Accessed 25 Oct 2021
8. Yıldırım I (2012) Bayesian inference: Metropolis-Hastings sampling technical report, vol 6
9. Piciuccio D, Foti F, Geuzaine M, Denoël V (2023) Bayesian forces identification in cable networks with small bending stiffness. In: *Structural health monitoring*

Comparison of Fatigue Lifetime Estimation of a Conductor Based on a Standard Vibration Device and Other Structural Health Monitoring System Sensors



Raphael Mendonça , Elsa Caetano , Carlos Moutinho, Omar As Saadi, and João Rodrigues

Abstract This article presents an experimental work developed in the context of the study of conductors' fatigue due to the turbulent effect of wind on an overhead high-voltage transmission line. The research is centred on the laboratory study of a conductor segment with a 17 m length. The cable model, fitted with typical anchorages adopted in transmission lines, is mounted on a specially designed anchoring system following the normative prescriptions of CIGRÉ. An extensive monitoring system is installed, including a load cell, several accelerometers, LVDTs and fibre optic sensors to assess the conductor's dynamic properties and the corresponding dynamic response to the wind loads, here simulated by a random excitation applied from a shaker. Based on the conductor response measured with the different sensors, with and without a Stockbridge damper, the fatigue lifetime of the conductor is calculated. A comparison is made of the fatigue lifetime estimated from acceleration, strain or LVDT measurements, the latter simulating the procedure typically used based on the VIBREC measurements. Finally, the Stockbridge damper's dissipation capacity in increasing the conductivity lifetime subject to aeolian vibrations is analysed as a function of the position of the damper.

Keywords Aeolian vibrations · Stockbridge best position · Conductor lifetime · Structural health monitoring · Overhead high-voltage transmission line

R. Mendonça · E. Caetano (✉) · C. Moutinho · O. A. Saadi · J. Rodrigues
CONSTRUCT-VIBEST, Faculty of Engineering – FEUP, University of Porto, Rua Dr. Roberto Frias s/n, 4200-465 Porto, Portugal
e-mail: ecaetano@fe.up.pt

R. Mendonça
e-mail: raphael.mendonca@fe.up.pt

1 Fatigue of Conductors

In overhead high-voltage transmission lines, maintenance is essential to increase the lifetime of the conductors and save electricity distributor companies' investments. However, these structures are prone to one of the most complicated mechanical problems related to damage and failure: fretting fatigue. Fretting results from relative motion between the internal conductor wires and their contact with clamps and dampers. This phenomenon is mainly caused by aeolian vibrations, also known as vortex-shedding resonance. These vibrations are caused by the development of alternate vortices at the top and bottom of the conductor, which induce a vertical cable movement that results in bending at the anchorage point near the tower for specific wind velocities. Combining bending and tension loads at the cable could lead to wire fatigue.

Aeolian vibrations in cable conductors occur at low wind velocities between 0.5 and 7 m/s, at a frequency range between 3 and 120 Hz, with amplitudes ranging from 0.01 to 1 diameter [1].

2 S–N Curves and CIGRÉ's Safe Border Line (CSBL)

The fatigue performance of a material is often characterised by utilising the stress-life approach and S–N curves, which plot the cyclic stress (S) vs the number of cycles until failure (N) during a laboratory test. The conditions for stopping the test are either the failure of 10 per cent of the cable's wires or of the three outer layer wires. Due to the problematic execution and high costs associated with this type of test, the International Council for Large Electric Systems (CIGRÉ) developed a Safe Border Line curve (CSBL) to assist in determining the lifetime of conductors from a simplified method. The following equation expresses the Safe Border Line curve

$$\sigma_a = A \cdot N_i^B \quad (1)$$

The constants A and B are related to the number of fatigue cycles N_i for a specified level of stress and the number of aluminium wire layers in a conductor. The stress amplitude is denoted by the symbol σ_a and is measured in MPa. According to [1], the values of these parameters are shown in Table 1.

Table 1 Constant values A and B for the CSBL curve

# of layers	$N < 2 \times 10^7$		$N > 2 \times 10^7$	
	A	B	A	B
1	730	−0.2	430	−0.17
>1	450	−0.2	263	−0.17

2.1 Poffenberger and Swart Equation

The precise evaluation of stress and strain on conductors is a challenging undertaking. Poffenberger and Swart [2] found a direct correlation between the dynamic bending stress (σ_{PS}) at the wires' outer layer and the peak-to-peak vibration amplitude (Y_b) via an analytical formulation. The Poffenberger-Swart equation is as follows

$$\sigma_{PS} = K \cdot Y_b \quad (2)$$

The constant K in this equation converts the vertical amplitude measured at 89 mm from the last point of contact (LPC) into bending stress (0-to-peak).

In this study, the bending amplitude of vibration Y_b is calculated using different procedures to compare the results of a standard vibration device (VIBREC) with the structural health monitoring calculations using accelerometers and fibre optical sensors. The VIBREC is simulated here using a linear variable differential transformer (LVDT).

3 Stockbridge Dampers

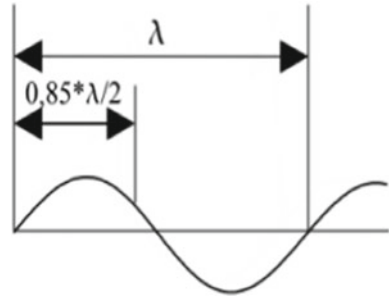
To mitigate aeolian vibrations on conductors of overhead high-voltage transmission lines, the correct position of the Stockbridge damper is crucial. The damper position is associated with its capacity to dissipate wind-induced energy in the structural system. Installing the Stockbridge dampers in improper locations might increase mechanical overload on the cable, resulting in a shorter lifetime.

The Stockbridge generally consists of two rigid masses connected to both ends of a messenger cable. A rigid clamp ensures the connection between the conductor and the damper, which allows displacement transmission from the conductor to the Stockbridge. The vibration of the inertial masses connected to the messenger cable induces bending, which dissipates energy through the friction caused by the relative movement of the cable's internal wires. Maximum levels of energy dissipation occur in a frequency band close to their natural frequency when the Stockbridge is excited at that frequency [3]. If the conductor and Stockbridge damper dissipate more energy than that imparted by the wind, the conductor will vibrate with less amplitude and for a shorter period.

To guarantee the system efficiency, CIGRE recommends that the Stockbridge damper should be placed at a distance of $0.85\lambda/2$ from the last point of contact, as shown in Fig. 1, where λ is the wavelength of the highest mode to be mitigated, and can be expressed as follows

$$\lambda = \frac{1}{f_n} \cdot \sqrt{\frac{T}{m}} \quad (3)$$

Fig. 1 CIGRE's recommended distance of the Stockbridge installation from the cable clamp



In Eq. (5), f_n is the cable's natural frequency in Hz, T is the tension force, expressed in N , and m is cable mass per unit of length, expressed in kg/m .

Resonance occurs when the frequency of wind excitation (Strouhal frequency) approaches the natural frequency of the conductor. The expression for the critical wind frequency can be derived from the Strouhal number of 0.185, which is the recommended number for the specific case of cables in overhead high-voltage transmission lines.

$$f_n = \frac{0.185 \cdot U}{d} \quad (4)$$

where U is the wind velocity in m/s , and d is the diameter of the conductor, expressed in m .

4 VIBREC500 Vibration Recorder

VIBREC (Fig. 2) is the most widely used device for measuring aeolian vibrations. The device records peak-to-peak relative vibration amplitudes between two sections and has an autonomy of approximately one year, depending on the ambient temperature and the acquisition time interval.

VIBREC does not continually record data due to the need to manage the battery life and memory. The standard acquisition consists of saving 10 s of active-time data within 15 min of an inactive interval, per CIGRÉ's recommendation, establishing a minimum monitoring duration of three months.

This standard device is capable of calculating the remaining lifetime of the conductor. The equipment analysis follows the most recent CIGRÉ [4] and IEEE [5] standards. The data are expressed through an S–N curve relating each block of stress to the number of cycles, and the damage at the conductor is determined using the Miner's rule using the expression

Fig. 2 VIBREC500-WT device at suspension clamp



$$D = \sum_{i=1}^m \frac{n_i}{N_{fi}} \tag{5}$$

and the procedure shown in Fig. 3. The S–N curve obtained with the recorded data is compared with the CIGRÉ’s Safe Border Line [1], bringing the final damage value, which is extrapolated to a one-year period.

Finally, the lifetime is given by the following equation

$$V = \frac{1}{D} \tag{6}$$

where D is the accumulated damage, and V is the lifetime in years.

As stated before, the VIBREC device was simulated in this study using a pair of LVDT sensors to measure the relative vibrations at two sections, recording peak-to-peak amplitudes.

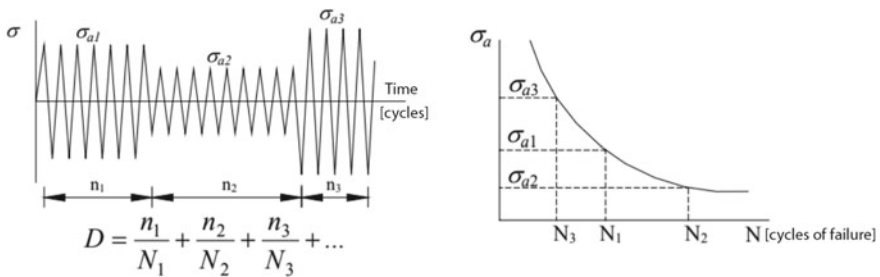


Fig. 3 Damage calculation procedure

5 Laboratory Setup

A setup was created to accommodate the conductor and the anchoring systems within the space of the FEUP laboratory to conduct the tests correctly and replicate the conductor's behaviour on site (Fig. 4).

The setup comprises the conductor, which is roughly 17 m in length, and two steel-plate anchoring modules. For this experiment, the maximum tension at the supports is 23,3kN, which is 20% of the conductor's RTS.

The analysed conductor is a BEAR-325 type ACSR (Aluminum Conductor Steel Reinforced) cable with 30 aluminium wires, seven steel wires in the reinforcement core, and an external diameter of 23 mm.

5.1 Instrumentation

To realise the fatigue experiments and find the best position of the Stockbridge to mitigate aeolian vibrations, a group of sensors was installed along the conductor. As cable tension control is essential in this kind of dynamic experiment, a force transducer is positioned at the active anchorage point to measure the tension force applied to the conductor by a jack. Three piezoelectric accelerometers were used in the experiments to characterise the structural response of the conductor subjected to forced vibrations: one was installed near the anchorage point to permit the calculation of the bending amplitude of vibration using a double integration procedure to transform accelerations into displacements. To simulate the VIBREC device behaviour, a pair of LVDTs were installed at the end of the cable (Fig. 4). The first sensor was

Fig. 4 Setup and instrumentation prepared for tests at the conductor



placed 42 mm from the LPC and the second sensor 89 mm from the other. Figure 5 shows the scheme of installation.

Finally, a group of fibre optical sensors were installed on the conductor better to understand the conductor's behaviour at low frequencies. The sensors were previously tested and calibrated before the tests. They were installed in the section closest to the position chosen for the Stockbridge (72 cm from the last point of contact LPC), near the end anchorage point. Figure 6 shows the applied setup, which consists of a fiberglass sleeve with a "1/4 cane" shape and an interior diameter equal to the conductor's diameter incorporating three FBG optical transducers. Two are strain gauges arranged longitudinally at the ends of the sleeve, and the other is a temperature transducer insulated from strain located in the middle zone.

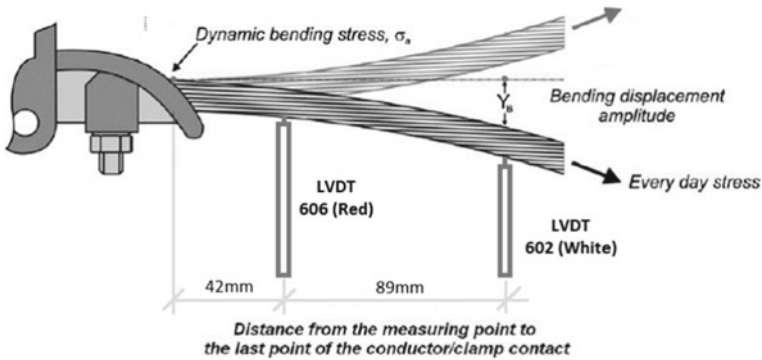


Fig. 5 LVDTs position relative to the Last Point of Contact (LPC)



Fig. 6 Fiber optical sensors installed on the conductor

6 Best Stockbridge Position Along the Cable

6.1 Tests Description

To determine the best position of the Stockbridge damper that minimises the vibration amplitudes and, consequently, the bending stresses at the anchorages, four tests were carried out using a shaker to simulate the wind-induced action. The tests consisted of 1 h measurement of the conductor response under excitation close to the midspan with a random force. This force was generated with a frequency content defined from 3 to 80 Hz to simulate Aeolian vibrations. A first test was carried out without the presence of the damper, and the other three were conducted with the Stockbridge installed at three different positions. The position recommended by CIGRE was defined considering the maximum wind speed that produces wind vibrations, which is 7 m/s. Using Eq. (6), it is possible to determine the vortex-shedding frequency associated with such wind speed for a Strouhal number of 0.185

$$f_n = \frac{0.185 \cdot U}{d} = \frac{0.185 \cdot 7 \text{ m/s}}{0.023 \text{ m}} = 56 \text{ Hz}$$

The Stockbridge frequency range recommended in the literature is between 0.7 and 1.3 f_n , where f_n is the previously calculated maximum. In this way, the range of frequencies where the damper will act is from 42 to 80 Hz, approximately. In addition, as wind-induced vibrations occur more frequently at low speeds, a frequency referring to the wind speed of 3 m/s was also added, corresponding to a frequency of 24 Hz. Table 2 presents the calculation parameters used in the tests.

As a result of the tests, it is possible to determine the bending amplitude of vibrations according to the Stockbridge positions. The position which leads to a minimum amplitude of vibration is considered the best position to install the damper, which means that at this position, the Stockbridge dissipates more energy. Figure 7 shows the amplitudes calculated using different sensors, which are also systematised in Table 3. “Acc” is the accelerometer, and “FBG” is the fibre optical sensor.

It is possible to observe that the minimum amplitudes are reached when the damper is installed at 72 cm from the last contact point, as recommended by CIGRE. Position 0 indicates the test without the presence of the damper.

Table 2 Parameters for Stockbridge best position tests

Wind velocity [m/s]	Strouhal frequency [Hz]	Wavelength λ [m]	Stockbridge Pos. [m]
3.0	24.0	5.77	2.31
5.2	42.0	3.29	1.37
10.0	80.0	1.73	0.72 (CIGRE)

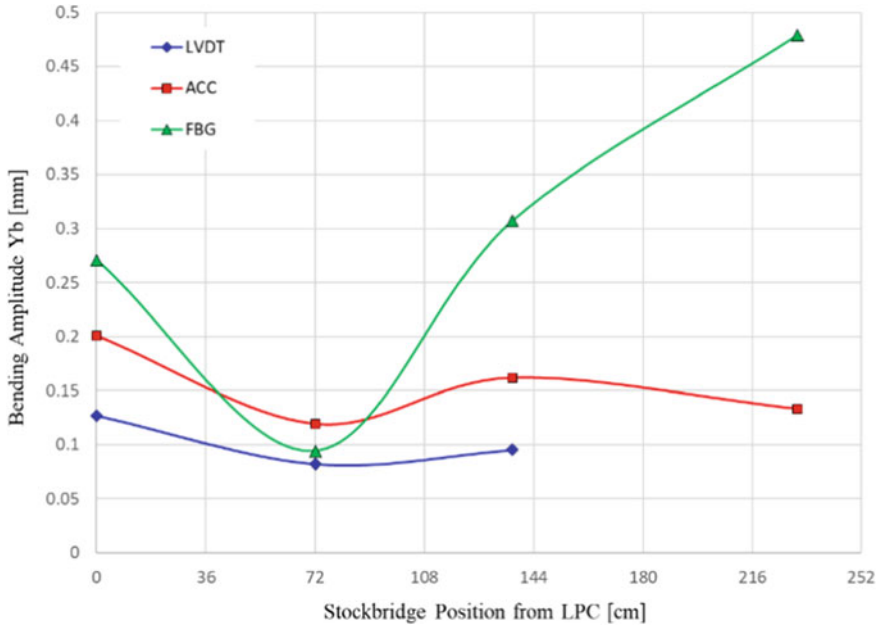


Fig. 7 Bending amplitude of vibration according to the Stockbridge position

Table 3 Amplitudes of vibration Y_b according to the Stockbridge position

Stockbridge Pos. [cm]	LVDT— Y_b [mm]	ACC— Y_b [mm]	FBG— Y_b [mm]
Without damper	0.127	0.201	0.271
72.0 (CIGRE)	0.082	0.119	0.094
137.0	0.095	0.162	0.307
231.0	–	0.133	0.479

7 Lifetime Estimation

After defining the best position for the Stockbridge installation, the estimates of the lifetime due to fatigue of the conductor subjected to wind actions were calculated. Finally, the total damage was estimated using the Rainflow method for counting fatigue cycles and the procedure described in Sect. 5, simulating the calculation made by VIBREC.

Figure 8 and Table 4 present the lifetime calculation expressed in years for each type of sensor according to the position of the Stockbridge. As expected, the position that leads to the most extended lifetime is the position 72 cm from the last point of contact, which is in accordance with the proposition established by CIGRE. It is also possible to observe that all sensors present the same result for the best position of the damper, indicating that structural health monitoring using several types of sensors

is feasible and reliable compared to the standard device VIBREC. Nevertheless, it is observed that the calculations made using different sensors lead to very different fatigue life estimations, which is consistent with the different impact of the response frequency content in the different measured quantities, such as displacement, strain or acceleration.

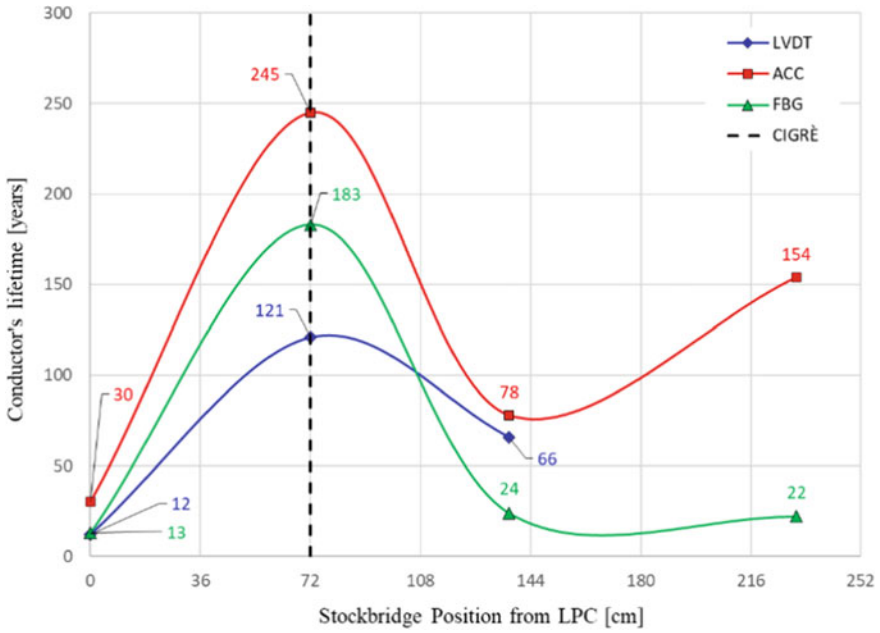


Fig. 8 Lifetime estimation according to the Stockbridge position

Table 4 Lifetime estimation calculated using different sensors

Stockbridge Pos. [cm]	LVDT—V [years]	ACC—V [years]	FBG—V [years]
Without damper	12.0	30.0	13.0
72.0 (CIGRE)	121.0	245.0	183.0
137.0	66.0	78.0	24.0
231.0	—	154.0	22.0

8 Conclusions

In overhead high-voltage transmission lines, the correct damper position is an important variable to consider in the conductor's design. In general, the manufacturers design the Stockbridge positions, and the lifetime estimations are made using standard recording devices like VIBREC. This work presented an alternative using structural health monitoring with accelerometers and fibre optical sensors positioned along the conductor. The calculations follow the CIGRE recommendation, which defines that the best position for the damper is at $0.85\lambda/2$, considering the wavelength for the highest frequency in the range of Aeolian vibrations. This study also indicates that other quantities measured with a structural health monitoring system could be used to determine the dampers' best position and calculate the conductor's estimated lifetime. Nevertheless, a calibration of the fatigue lifetime estimates is required.

Acknowledgements This work was financially supported by: base funding (UIDB/04708/2020) and programmatic funding (UIDP/04708/2020) of the CONSTRUCT—Instituto de I&D em Estruturas e Construções, funded by national funds through the FCT/MCTES (PIDDAC); project CTWAVE—Identification of Cable Damage from Transverse Wave Propagation (EXPL/ECI-EGC/1324/2021), funded by national funds through the FCT/MCTES (PIDDAC). The financial support granted by FCT to the first author through the doctoral scholarship 2020.07461.BD is also acknowledged.

References

1. EPRI (2006) EPRI transmission line reference book: wind-induced conductor motion. Palo Alto, CA, p 1012317
2. Poffenberger JC, Swart RL (1965) Differential displacement and dynamic conductor strain. IEEE transactions paper, vol PAS-84, pp 281–289
3. CIGRE SCB2–08 WG30 TF7 (2007) Fatigue endurance capability of conductor. Conductor/Clamp systems-update of present knowledge. CIGRE-TB 332
4. CIGRE: modelling of vibrations of overhead line conductors (2018) (CIGRE Green Books)
5. IEEE: Guide for Aeolian vibration field measurements of overhead conductors (2006)

On the Assessment and Mitigation of Vortex-Induced-Vibrations of Overhead Electrical Conductors



F. Foti and L. Martinelli

Abstract In the present work, an extension of the Energy Balance Method (EBM) is investigated, by considering both the dynamic interaction between a conductor and the support system, and the coupling in the dynamic response of two adjacent spans. The presence of dampers in each span to control aeolian vibrations is also taken into account. The modal properties of the line are studied within a rigorous mathematical setting and used as the input to apply the EBM. The parameters that control the dynamics of the structural system are clearly identified, paving the way to the definition of simple yet effective criteria for the design of the mechanical characteristics of the damping devices connected to the line. The proposed procedure allows also to investigate the effects of energy dissipation within flexible supports.

Keywords Aeolian vibration · Electrical transmission lines · Energy balance method

1 Introduction

Vibrations induced by the shedding of vortices have been since long recognized as a major source of wear damage and fatigue failures of overhead electrical line conductors and of other line components [1, 2]. Assessment and mitigation of such vibrations, hence, is of paramount importance for both design of new lines and retrofitting of existing ones. Damping devices, such as Stockbridge [3, 4] or Bretelle dampers [5] are typically installed along the line to control aeolian vibrations.

F. Foti (✉) · L. Martinelli

Department of Civil and Environmental Engineering, Politecnico di Milano, Milan, Italy

e-mail: francesco.foti@polimi.it

L. Martinelli

e-mail: luca.martinelli@polimi.it

The practical approach, commonly adopted to estimate the amplitude of aeolian vibrations, is based on the Energy Balance Method (EBM). In this context, for one or more reference sections of the line between two support towers, the conductors are modeled as taut cables restrained by rigid supports. Under the hypothesis of a modal steady-state oscillation, the antinodal vibration amplitude is then evaluated for each natural frequency of the conductor to impose the balance between the average energy per cycle supplied by the wind and that dissipated within the cable and in the added damping devices (e.g. [2]).

In spite of being widely used, EBM is open to criticisms. First of all, it can be observed that typical aeolian vibration records clearly show that several natural modes of the conductors can be simultaneously excited due to space- and time-variations of the wind velocity along the line [6, 7]. To overcome this drawback, stochastic models based on the modeling of the vortex-induced lift force as an incompletely homogeneous bidimensional random field have been recently proposed by the authors' research group [8, 9]. Since these novel approaches are at the research stage, however, there is still a considerable interest in improving the capabilities of the EBM. Within this context, it is worth noting that, being based on the definition of a reference section of the line, current implementations of the EBM available in the literature do not take into account the potentially relevant effects of: (a) dynamic interaction between the cable and the support system (suspension clamps, tower, etc.), (b) of the coupling in the dynamic response of two or more adjacent spans. Moreover, since Bretelle dampers connect adjacent spans of the conductor, their contribution cannot be taken into account within the EBM.

The present work aims to extend the applicability of the EBM by removing the aforementioned limitations (a) and (b) of current EBM implementations, also paving the way for the definition of a rational methodology to include Bretelle dampers in the description of the line. A reference line section made of two adjacent spans with a flexible intermediate support and attached damping devices is considered to keep the presentation of the proposed methodology as simple as possible. Generalization to the case of a generic number of spans is, however, straightforward. The conductor is described according to the classic taut-string model and the dampers are described as single-degree-of-freedom (sdof) linear systems. The latter assumption can be considered as an approximate description of the behavior of real Stockbridge dampers (see e.g. [4] for a more detailed discussion on the topic). The modal properties of the line are studied within a rigorous mathematical setting and used as the input to apply the EBM. The parameters that control the dynamics of the structural system are clearly identified, paving the way to the definition of simple yet effective criteria for the design of the mechanical characteristics of the damping devices connected to the line.

2 Formulation of the Problem

2.1 Equations of Motion

Let us consider the two span line section schematically depicted in Fig. 1. The conductor is strung at the constant tension T , the left (R_{sl}) and right (R_{sr}) support are assumed to be perfectly rigid and the intermediate one is modeled as a flexible support (F_s), with known impedance or dynamic stiffness function. The dynamic stiffness function provides a synthetic description of the linear dynamic behavior of the intermediate support (herein regarded as the assembly of tower, insulator string, suspension clamp, etc.) and can be in general characterized by multiple poles corresponding to the dominant natural modes of the support system. To keep the presentation as simple as possible, a single mode of the intermediate support will be herein retained, which amounts to model the support as a sdof system with mass m_s , stiffness k_s and damping ratio ν_s . Dampers are assumed to be located both in the left (D_l) and right (D_r) span, at a distance L_{i1} ($i = l, r$) from the intermediate support. Each damper is modeled as a sdof linear system with mass m_i , stiffness k_i and damping ratio ν_i ($i = l, r$). In spite of its simplicity, the adopted modeling approach allows to capture fairly well the effect of the fundamental mode of Stockbridge dampers, which is often the most important in practical applications, as it has been shown e.g. in [10].

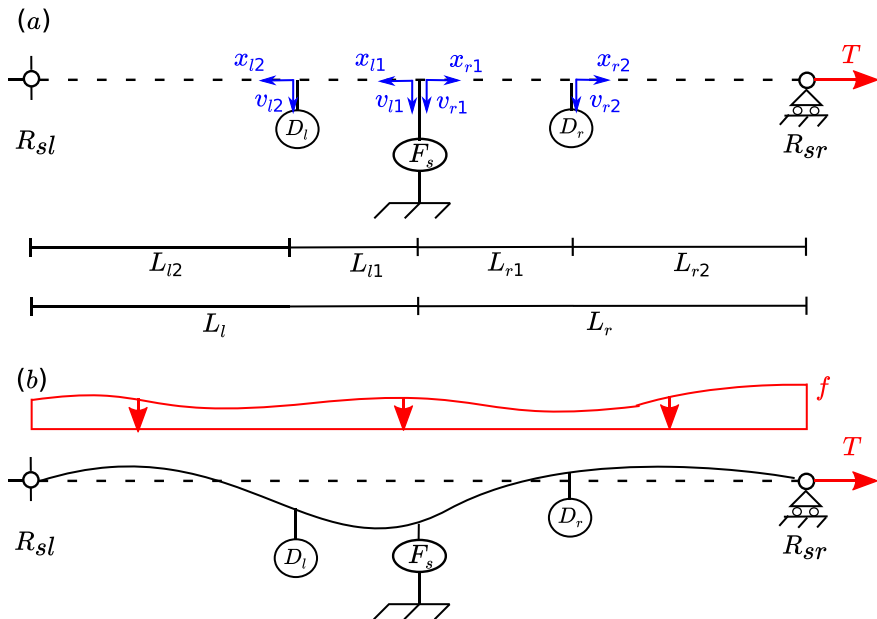


Fig. 1 Schematic representation of the two-span line section

Generalization to the case of both linear and non-linear multi-degree-of-freedom dampers is relatively straightforward and has been presented e.g. in [4].

Aeolian vibrations of transmission line conductors may develop under light or moderate steady wind conditions. They occur mostly in the cross-wind direction and are characterized by low-amplitude (less than one cable diameter) and frequency in the broad range of 3–200 Hz [2]. Typical span length and axial force values lead to a fundamental frequency of transmission line conductors in the order of 0.1 Hz. It can be concluded, hence, that aeolian vibrations tend to excite high-order modes, which are not significantly affected by the static sag of the cable (see e.g. [11, 12]). Based on this observation, the conductor can be modeled as a straight flexible system. Classic models of the literature include the taut string model, which neglects the effects of the bending stiffness, and the tensioned beam model. Inclusion of bending stiffness terms is of crucial importance for the evaluation of stresses and strains in the neighborhood of supports and damping devices (i.e. in the boundary layers of the cable, see e.g. [13–16]), but has minor effects on the global dynamics of the conductor [17]. In the present work, small planar vibrations of the conductor are described by neglecting both sag-extensibility effects and bending stiffness terms, and the following linear partial differential equation of motion (taut-string model) is introduced:

$$\gamma \partial_t^2 v_{ki} - T \partial_{x_{ki}}^2 v_{ki} + f_D = f, \quad \text{with : } k = l, r \text{ and } i = 1, 2 \quad (1)$$

where $x_{ki} \in [0, L_{ki}]$ are the abscissae defined in Fig. 1, $v_{ki} = v_{ki}(x_{ki}, t)$ are the displacements of the conductor centerline, γ is the mass per unit of length, f_D is a distributed damping force and f is the lift force per unit of length imparted by the wind to the vibrating conductor. The Eqs. of motion (1) can be integrated under suitable initial conditions and boundary conditions that impose compatibility and equilibrium both at the supports and at the interface between the conductor and the dampers.

The governing equations can be re-written by introducing the following non-dimensional variables:

$$\xi_{ki} = \frac{x_{ki}}{L_c} \in \left[0, \alpha_{ki} = \frac{L_{ki}}{L_c} \right], \quad \tau = \omega_c t, \quad v_{ki} = \frac{v_{ki}(x_{ki}(\xi_{ki}), t(\tau))}{L_c} \quad (2)$$

where L_c and ω_c are, respectively, a characteristic length and frequency of the problem, that can be conveniently defined as the average span length $L_c = \frac{L_l + L_r}{2}$ and $\omega_c = \frac{1}{L_c} \sqrt{\frac{T}{\gamma}}$. Substitution of Eqs. (2) in (1) yields the Eqs. of motion:

$$\partial_\tau^2 v_{ki} - \partial_{\xi_{ki}}^2 v_{ki} + \bar{f}_D = \bar{f}, \quad \text{with : } k = l, r \text{ and } i = 1, 2 \quad (3)$$

that can be integrated along with suitable initial and boundary conditions, whose full expressions are herein omitted for the sake of conciseness. In the Eq. (3) the symbols \bar{f}_D and \bar{f} denote the non-dimensional distributed damping and external forces ($\bar{f}_D = \frac{L_c f_D}{T}$ and $\bar{f} = \frac{L_c f}{T}$).

2.2 Natural Frequencies and Mode Shapes

Application of the EBM to assess aeolian vibration severity requires preliminary calculation of the natural frequencies and mode shapes of the line section. The presence of concentrated sources of dissipation (i.e. the dampers and the intermediate flexible support) makes the structure non-proportionally damped. Experimental evidence (see e.g. [18]), however, suggests that, being the structure very lightly damped, modal coupling induced by non-proportional damping terms can be neglected.

Undamped natural frequencies and mode shapes can be calculated by setting $\bar{f}_D = \bar{f} = 0$ in Eq. (3) and searching for stationary oscillatory solutions in the form: $v_{ki} = \phi_{ki}(\xi_{ki}) \exp(j\bar{\omega}\tau)$ ($k = l, r$ and $i = 1, 2$), where j denotes the imaginary unit and $\bar{\omega}$ is the non-dimensional vibration frequency. The mode shape functions satisfy the ordinary differential equations:

$$\frac{d^2\phi_{ki}}{d\xi_{ki}^2} + \bar{\omega}^2\phi_{ki} = 0, \quad \text{with : } k = l, r \text{ and } i = 1, 2 \tag{4}$$

along with the boundary conditions:

$$\left\{ \begin{array}{l} \phi_{l2}(\alpha_{l2}) = 0 \\ \phi_{r2}(\alpha_{r2}) = 0 \\ \phi_{l1}(0) - \phi_{r1}(0) = 0 \\ \phi_{l1}(\alpha_{l1}) - \phi_{l2}(0) = 0 \\ \phi_{r1}(\alpha_{r1}) - \phi_{r2}(0) = 0 \\ \phi'_{l1}(0) + \phi'_{r1}(0) - \mu_s \bar{H}_s^{-1}(\bar{\omega}; \nu_s = 0) \phi_{l1}(0) = 0 \\ -\phi'_{l1}(\alpha_{l1}) + \phi'_{l2}(0) + \mu_{dl} \bar{\omega}^2 (1 + \bar{\omega}^2 \bar{H}_{dl}(\omega; \nu_{dl} = 0)) \phi_{l2}(0) = 0 \\ -\phi'_{r1}(\alpha_{r1}) + \phi'_{r2}(0) + \mu_{dr} \bar{\omega}^2 (1 + \bar{\omega}^2 \bar{H}_{dr}(\omega; \nu_{dr} = 0)) \phi_{r2}(0) = 0 \end{array} \right., \quad \forall \tau \tag{5}$$

where a prime denote differentiation with respect to the non-dimensional space coordinates and the following definition apply: $\mu_q = \frac{m_q}{\gamma L_c}$, $\nu_q = \frac{c_q}{2\sqrt{k_q m_q}}$, $\omega_q = \sqrt{\frac{k_q}{m_q}}$,

$\delta_q = \frac{\omega_q}{\pi\omega_c}$, $\bar{H}_q(\bar{\omega}; \nu_q) = (-\bar{\omega}^2 + j 2\pi\nu_q \delta_q \bar{\omega} + \pi^2 \delta_q^2)^{-1}$, with $q = s, dl, dr$.

The non-dimensional natural frequencies $\bar{\omega}_{(n)}$ and mode shapes $\phi_{ki(n)} = a_{ki(n)} \sin(\bar{\omega}_{(n)} \xi_{ki(n)}) + b_{ki(n)} \cos(\bar{\omega}_{(n)} \xi_{ki(n)})$, with $n \in \mathbb{N}^+$, can be easily found by solving the boundary value problem defined by Eqs. (4) and (5). The natural frequencies of the conductor are then obtained through the re-scaling equation:

$$\omega_{(n)} = \omega_c \bar{\omega}_{(n)}.$$

2.3 Energy Balance Equation

The EBM relies on the assumption of steady-state mono-modal vibrations of the cable. For each natural vibration frequency of the conductor $\omega_{(n)}$, determined as in Sect. 2.2, the maximum expected vibration amplitude is obtained by imposing the balance between the average power per unit of length per vibration cycle imparted by the wind to the cable (expressed as $P_w = P_{wl} + P_{wr}$, i.e. as the sum of the contributions coming from the left and right spans) and the average dissipated power per unit of length and per vibration cycle within the structure. The latter term is herein expressed as the sum of the power per unit of length dissipated in the conductor (also known as cable “self-damping” and expressed as $P_c = P_{cl} + P_{cr}$, i.e. as the sum of the contributions coming from the left and right spans), the power dissipated in the intermediate flexible support divided by the total length of the conductor ($\frac{P_s}{L_l+L_r}$) and the power dissipated within the dampers divided by the total length of the conductor ($\frac{P_{dk}}{L_l+L_r}$, with $k = l, r$).

$$\lambda_l (P_{wl} - P_{cl}) + \lambda_r (P_{wr} - P_{cr}) - \frac{P_s}{L_l + L_r} - \frac{P_{dl}}{L_l + L_r} - \frac{P_{dr}}{L_l + L_r} = 0 \quad (6)$$

where $\lambda_k = \frac{L_k}{L_l+L_r}$, $k = l, r$.

The wind input power acting on each span can be evaluated as:

$$P_{wk} = D^4 \left(\frac{\omega}{2\pi} \right)^3 F \left(\frac{y_{max,k}}{D} \right), \quad k = l, r \quad (7)$$

where D is the conductor diameter, ω is the circular vibration frequency, $y_{max,k}$ is the maximum modal amplitude of vibration in the k -th span and F is a non-linear function of the non-dimensional vibration amplitude $\frac{y_{max,k}}{D}$. Different expressions have been proposed in the literature for the function F , based on the outcomes of wind tunnel tests. Without loss of generality, the expression recommended in [19] is adopted in the present work.

The conductor self-damping can be expressed by means of power laws based on both empirical and theoretical approaches (see e.g. [20, 21]). Without loss of generality, the theoretical expression derived in [21] under the assumption of micro-slip conditions on the contact surfaces between adjacent wires of the conductor is adopted in the present work and re-stated in a slightly modified form:

$$P_{ck} = \mathcal{K}_{ms} \frac{y_{max,k}^3 \omega^7}{T^4}, \quad k = l, r \quad (8)$$

where \mathcal{K}_{ms} is a proportionality coefficient that only depends on the mechanical and geometric properties of the conductor cross section (please see [21] for further details).

It is worth noticing that, since the dampers are usually located very close to the supports (i.e. $L_{l1} \ll L_l$ and $L_{r1} \ll L_r$), the maximum modal amplitude of vibration

entering in Eqs. (7) and (8) is herein approximately assumed to be defined in the longer subspans of the section (i.e. the ones with length L_{l2} and L_{r2}). This simplifying assumption is in the spirit of the background of Eqs. (7) and (8), that make reference to “far-field” values of the maximum modal vibration amplitude, i.e. values defined in a region of the conductor far from the supports.

The power dissipated in the flexible support can be evaluated as:

$$P_s = \frac{1}{2} \omega \operatorname{Im} [G_s(\omega)] y_s^2 \tag{9}$$

where the symbol Im denotes the imaginary part of a complex quantity, while $G_s(\omega) = m_s \omega_c^2 \bar{H}_s^{-1}(\bar{\omega}(\omega); \nu_s)$ and y_s are, respectively, the dynamic stiffness and the modal amplitude of vibration of the support.

The power dissipated in dampers can be evaluated as:

$$P_{dk} = \frac{1}{2} \omega \operatorname{Im} [G_{dk}(\omega)] y_{dk}^2, \quad k = l, r \tag{10}$$

where $G_{dk}(\omega) = m_{dk} \omega_c^2 \left[1 + \bar{H}_{dk}(\bar{\omega}(\omega); \nu_{dk}) \left(\frac{\omega}{\omega_c} \right)^2 \right]$ and y_{dk} are, respectively, the dynamic stiffness and the modal amplitude of vibration of the k th damper.

Preliminary knowledge of the mode shape functions (see Sect. 2.2), allows to express all modal displacement amplitudes entering Eqs. (7)–(10) as a function of a single modal amplitude parameter A . Substitution of Eqs. (7)–(10) in (6), hence, yields for a given vibration frequency of the conductor (ω) a scalar non-linear algebraic equation that can be numerically solved to get the unknown modal amplitude $A = A(\omega)$. Once A is known, the expected vibration amplitude of any point of the conductor can always be easily retrieved. Results of the EBM are often reported by plotting the maximum expected modal vibration amplitude of a span as a function of the vibration frequency, i.e. with the notation adopted in the present paper $y_{max,k} = y_{max,k}(\omega)$.

3 Application Example

The proposed formulation is applied to a Aluminum Conductor Steel Reinforced (ACSR) Bersfort (diameter $D = 35.6$ mm, mass per unit of length $\gamma = 2.375$ kg/m, Rated Tensile Strength $RTS = 180$ kN) strung at a tension $T = 0.2 RTS$. The case of a single-span of length $L = 450$ m has been already studied elsewhere by the authors [21] and the outcomes of the EBM have been compared to experimental data coming from [22].

As a first example of application, a symmetric two-span configuration with $L_l = L_r = 450$ m is considered. Figure 2 reports the maximum value of the non-dimensional vibration amplitude ($\frac{y_{max}}{D}$) under the assumption of “stiff” and non-

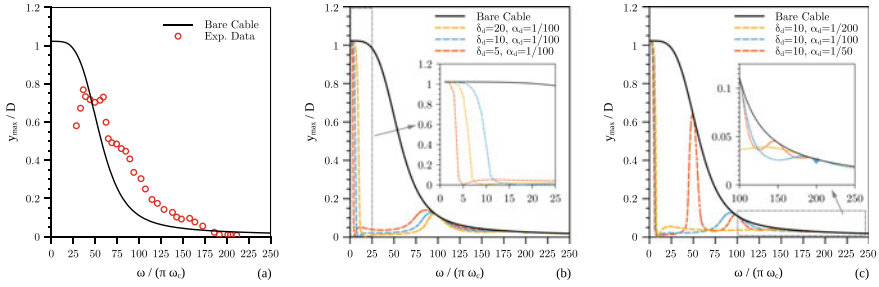


Fig. 2 Maximum non-dimensional vibration amplitude for a symmetric two-span configuration with $L_l = L_r = 450$ m and a “stiff” non dissipative support ($\delta_s = 200, \nu_s = 0, \mu_s = 0.1$). Notice that $y_{max,l} = y_{max,r}$ due to symmetry. **a** Bare cable. Experimental results for a single-span conductor from [22]. **b** Damped cable, with $\nu_{dl} = \nu_{dr} = 0.01, \mu_{dl} = \mu_{dr} = 0.01, \alpha_{dl} = \alpha_{dr} = 1/100$ and different values of the tuning parameter $\delta_d = \delta_{dl} = \delta_{dr}$. **c** Damped cable, with $\nu_{dl} = \nu_{dr} = 0.01, \mu_{dl} = \mu_{dr} = 0.01, \delta_d = \delta_{dl} = \delta_{dr} = 10$ and different values of $\alpha_d = \alpha_{dl} = \alpha_{dr}$

dissipative intermediate support (i.e. $\delta_s = 200, \nu_s = 0, \mu_s = 0.1$). It is worth noting that, due to symmetry, the vibration amplitude of the left and right span is strictly equal, i.e. $y_{max} = y_{max,l} = y_{max,r}$. The solid black line refers to the case of single-span bare cable and is reported for comparison purposes. As Fig. 2a shows, the predicted amplitudes reproduce reasonably well the experimental results published in [22] for a single-span undamped conductor (“bare cable”). Figure 2b and c report the results for a damped conductor and a symmetric position of the dampers around the intermediate support. The two figures shed some light on the effect of the tuning of the dampers (parameter $\delta = \delta_{dl} = \delta_{dr}$) and on the position of the dampers in the span (parameter $\alpha = \alpha_{l1} = \alpha_{r1}$). As depicted in Fig. 2b, decreasing the value of δ shifts the curves to the left, so increasing the effectiveness of the damper in the low frequency range. Instead, as depicted in Fig. 2b, as α is decreased the frequency at which the damper first becomes ineffective is shifted to the right.

In Fig. 3 results for a non-symmetric two-span configuration (with $L_l = 225$ m and $L_r = 450$ m) are reported. In this case no dampers are added to the line, while the stiffness of the intermediate support is varied by considering different values of the tuning parameter δ_s . A damping ratio $\nu_s = 0.01$ and a mass ratio $\mu_s = 0.1$ are considered in all calculations. Figure 3a depicts the maximum non-dimensional vibration amplitude for the left-span, while Fig. 3b shows the same quantity for the right span. The broken black line reports the values computed for a single span of corresponding length (hence disregarding coupling between the non symmetric spans). As Fig. 3 depicts, disregarding this coupling leads to an underestimation of the extreme amplitude of motion in the short (the left) span while the extreme value for the long span (the right) can be correctly predicted.

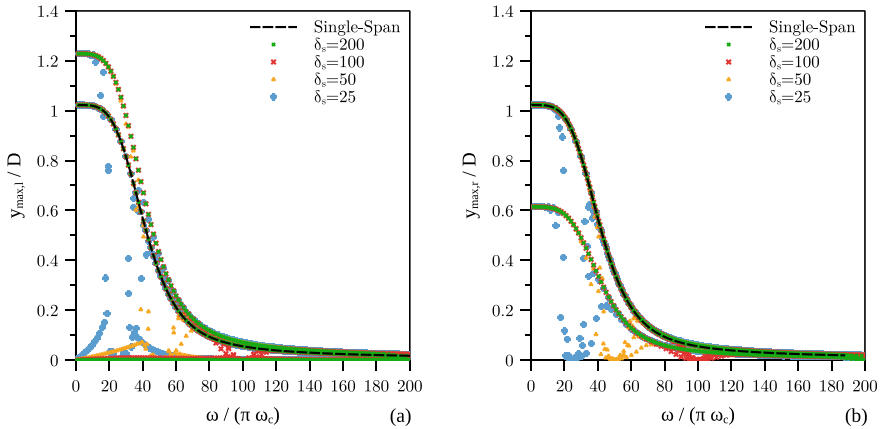


Fig. 3 Maximum non-dimensional vibration amplitude for a non-symmetric two-span configuration with $L_l = 225$ m and $L_r = 450$ m ($\omega_c = 0.3648$ rad/s). No dampers added to the line. The intermediate support is characterized by $\nu_s = 0.01$, $\mu_s = 0.1$ and different values of the tuning parameter δ_s . **a** Left-span. **b** Right span. The results obtained for a single-span conductor on rigid supports and length $L = 225$ m (Fig. a) and $L = 450$ m (Fig. b) are plotted for comparison purposes

4 Conclusions

In the present work, an extension to the EBM has been proposed. The formulation allows to take explicitly into account both the dynamic interaction between the cable and the support system, and the coupling in the dynamic response of two adjacent spans. The presence of dampers in each span to control aeolian vibrations is also considered. The modal properties of the line are studied within a rigorous mathematical setting and used as the input to apply the EBM.

Application to test cases shows the potential of the proposed formulation, that allows to clearly identify the effect of the main geometrical and mechanical parameters controlling the aeolian vibrations of the line. Reported results hint to a simple yet effective criteria for the design of the mechanical characteristics both of the damping devices and of the intermediate support in order to mitigate the severity of aeolian vibrations.

References

1. Ervik M et al (1986) Report on aeolian vibrations. Electra 124:40–77
2. EPRI - Electric research power institute: transmission line reference Book: Wind- induced conductor motion. Palo Alto, USA (2006)
3. Foti F, Martinelli L (2018) Hysteretic behaviour of Stockbridge dampers: modelling and parameter identification. Math Probl Eng 2018(8925121):17

4. Bogani F, Sosio A, Foti F, Martinelli L (2023) A reduced hysteretic model of Stockbridge dampers. *Res Proc* 26:417–422
5. Hautefeuille P, Porcheron Y (1964) Field experiments on mechanical behaviour of overhead lines. In: Proceedings of the: conference internationale des grands reseaux electriques a haute tension, June 1–10, Paris (France), Paper 236, 46 p
6. Diana G, Cheli F, Fossati F, Manenti A (1993) Aeolian vibrations of overhead transmission lines: computation in turbulence conditions. *J Wind Eng Ind Aerodyn* 46–47:639–648
7. Denoël V, Andrianne T (2017) Real-scale observations of vortex induced vibrations of stay-cables in the boundary layer. *Procedia Eng* 199:3109–3114
8. Foti F, Denoël V, Martinelli L, Perotti F (2020) A stochastic and continuous model of aeolian vibrations of conductors equipped with Stockbridge dampers. In: Proceedings of the XI international conference on structural dynamics (EURODYN 2020), vol 1, pp 2088–2102
9. Foti F, Denoël V, Martinelli L, Perotti F (2023) A probabilistic approach to the Poffenberger-Swart bending stress of conductors subject to aeolian vibrations. In: Submitted for presentation at the XII international conference on structural dynamics (EURODYN 2023)
10. Di Cello G (2023) On the modelling of aeolian vibrations of damped multi-span suspended cables. M.Sc. thesis, Politecnico di Milano, Milano, Italy
11. Irvine HM, Caughey TK (1974) The linear theory of free vibrations of a suspended cable. *Proc R Soc, Ser A* 341:299–315
12. Irvine HM (1981) Cable structures. MIT Press Series in Structural Mechanics
13. Denoël V, Detournay E (2010) Multiple scales solution for a beam with a small bending stiffness. *J Eng Mech* 136:69–77
14. Denoël V, Canor T (2013) Patching asymptotics solution of a cable with a small bending stiffness. *J Struct Eng* 139:180–187
15. Foti F, Denoël V, Martinelli L (2021) Analytical modelling of the varying bending stiffness inside the boundary layer of cables. In: Bugonovic Jakobsen J (ed) Proceedings of the second international symposium on dynamics and aerodynamics of cables - ISDAC 2021, Sept 16–17, Stavanger, Norway, pp 199–206
16. Arena A, Pacitti A, Lacarbonara W (2016) Nonlinear response of elastic cables with flexural-torsional stiffness. *Int J Solids Struct* 87:267–277
17. Hagedorn P (1987) On the computation of damped wind-excited vibrations of overhead transmission lines. *J Sound Vib* 83:253–271
18. Claren R, Diana G (1969) Mathematical analysis of transmission line vibrations. *IEEE Trans Power Appar Syst* 88:1741–1771
19. Diana G et al (2005) Modelling of aeolian vibrations of a single conductor plus damper: assessment of technology. *Electra* 223:28–36
20. Foti F, Martinelli L (2018) A unified analytical model for the self-damping of stranded cables under aeolian vibrations. *J Wind Eng Ind Aerodyn* 176:225–238
21. Foti F, Martinelli L (2018) An enhanced unified model for the self-damping of stranded cables under aeolian vibrations. *J Wind Eng Ind Aerodyn* 182:72–86
22. Langlois S, Legeron F (2014) Prediction of aeolian vibration of transmission-line conductors using a nonlinear time history model - Part II: conductor and damper model. *IEEE Trans Power Delivery* 29:1176–1183

A Numerical Investigation on the Dynamic Response of Short Slack Cables



S. Corazza, F. Foti, and L. Martinelli

Abstract Short span cables subject to vary small values of axial force are encountered in several technical engineering applications such as flexible-bus electrical conductors and Bretelle dampers. Whenever dealing with short and slack cables, the bending stiffness contributions to the overall dynamic response are not negligible. Bending behavior of metallic cables is non-linear and non-holonomic due to the onset and propagation of relative sliding phenomena between the wires. As a consequence, the dynamic response of the envisaged applications turns out to be affected by strong geometrical and mechanical non-linearities. In this paper, a numerical approach is adopted to study the dynamics of short slack cables subject to support motion. The stranded cables are modeled as co-rotational beam finite elements with a non-linear bending moment-curvature relation based on a phenomenological model, previously developed by the research group. Results of both quasi-static and dynamic analyses are discussed.

Keywords Slack cables · Cable dynamics · Seismic motion · Bending stiffness

1 Introduction

There are several technical applications in which metallic stranded cables cover short spans, in the order of few meters, and are subject to very small values of axial force compared to their Rated Tensile Strength (*RTS*). This is the case, for example, of flexible-bus conductors used in high-voltage electrical substations to connect electrical equipment and Bretelle dampers, that in their most simple design

S. Corazza (✉) · F. Foti · L. Martinelli
Department of Civil and Environmental Engineering, Politecnico di Milano, Milan, Italy
e-mail: stefano.corazza@polimi.it

F. Foti
e-mail: francesco.foti@polimi.it

L. Martinelli
e-mail: luca.martinelli@polimi.it

are made of a short stretch of conductor connecting two adjacent spans of an overhead transmission line (see [13]).

However, quasi-static and dynamic analyses of short slack cables have been seldom addressed in the literature. Few studies on the behavior of such structures under dynamic loading conditions are available (see e.g. [3–5, 9, 14]). Most of results highlight a significant dynamic amplification of the conductor reaction forces, especially in the presence of small “slackness”, i.e. whenever the static sag is small in comparison to the span [11]. Moreover, experimental results related to parametrically-excited conductors show typical slackening and re-tensioning phenomena and the possible occurrence of dynamic instability regions [5]. A recent work’s findings highlight the tension-stiffening behavior of the conductors under quasi-static harmonic parametric excitation tests [9].

On the contrary, the bending behavior of metallic stranded cables has been widely studied in the past years, and different modeling strategies are nowadays available [6, 8]. As highlighted by extensive analytical and numerical investigations (see, e.g., [14, 17, 19]), whenever a strand is bent, an axial force gradient is generated along the length of the wires. Such gradient makes the wires prone to sliding with respect to the neighboring ones and is counteracted by the tangential friction forces acting on the internal contact surfaces between the wires. The possible activation of these sticking-sliding frictional interfaces makes the bending behavior of strands inherently non-linear and non-holonomic.

The present paper presents a novel methodology for the modeling of short slack stranded cables subject to imposed motion of the supports, by accounting for both geometrical non-linearities and their inherent nonlinear bending behavior. The latter is considered through a smooth phenomenological Bouc-Wen hysteretic model of the moment-curvature relationship. The parameters of such model are calibrated according to experimental results of the literature and quasi-static tests are then performed. Preliminary results of dynamic analyses are also presented.

2 Numerical Model

This section describes the methodology that has been adopted in the present paper to carry out both quasi-static and dynamic numerical analyses of short-span stranded cables subject to imposed motion of the supports. A finite element user-coded program has been developed, involving co-rotational beam finite elements ([7]) and fully accounting for both the geometrical non-linearities of the structure and the material non-linearity. The latter have been addressed throughout the nonlinear moment-curvature relationship presented in Sect. 2.1.

2.1 Moment-Curvature Law

Material nonlinearities have been described by means of the well-known smooth endochronic Bouc-Wen model, which was already adopted by the research group to describe the hysteretic bending behavior of metallic stranded cables in [8]. By interpreting the input-output characteristic of the system as a non-holonomic relation between a pair of work conjugated mechanical variables, one can express the model's relations in terms of a bending curvature $\chi(t)$ and of a bending moment $M(t)$. The so-called "minimal" or "normalized" Bouc-Wen model, which was proposed by Ikhouane and Rodellar (see [15, 16]), is herein rewritten in a slightly modified form, which allows for a clear and direct interpretation of the parameters governing the hysteretic behavior of stranded cables:

$$M(\chi(t), t) = EI_{min} \chi(t) + (EI_{max} - EI_{min}) \chi_0 z(t) \quad (1)$$

$$\dot{z}(t) = \frac{1}{\chi_0} \left(\dot{\chi}(t) - \sigma |\dot{\chi}(t)| |z(t)|^{n-1} z(t) + (\sigma - 1) \dot{\chi}(t) |z(t)|^n \right) \quad (2)$$

where $P = \{EI_{min}, EI_{max}, \chi_0, \sigma, n\}$ is the set of parameters of the model and $z(t)$ is a non-dimensional hysteretic variable. The parameters σ and n affect the shape of the nonlinear transition curve between the maximum (full-stick state, see [6]) and minimum (full-slip state, see [6]) tangent stiffness of the moment-curvature diagram, respectively denoted as EI_{max} and EI_{min} . The parameter χ_0 can be conveniently regarded as the first-yielding curvature value that characterizes the transition from the full-stick to the full-slip state.

2.2 Model Calibration

The non-linear moment-curvature law (see Sect. 2.1) requires calibration based on quasi-static bending tests on slack conductors. Results of experiments conducted by Chen et al. (see [2]) for a steel cable are used, as an example, to show the viability of the proposed formulation and model calibration strategy. A monotonic three-point bending test has been performed on a Galfan steel spiral strand with zero tension (see Fig. 1). The latter has an outer diameter equal to $D = 38$ mm and it is formed by 37 equal steel wires. It is characterized of a mass per unit of length $\gamma = 6.373$ kg/m and, consequently of a weight per unit of length $w = 62.50$ N/m. The rated tensile strength is set to $RTS = 359$ kN. By considering a Young's modulus of the steel wires $E = 206$ GPa and a Poisson's ratio $\nu = 0.3$, one obtains an axial stiffness $EA = 167.8$ MN and a torsional stiffness $GJ = 1410$ Nm².

As per the parameters EI_{max} , EI_{min} and χ_0 , a SET (A) of values has already been proposed for this specific application case (see [10]). In the present work, a novel calibration of χ_0 is also proposed, basing on the values of maximum and minimum

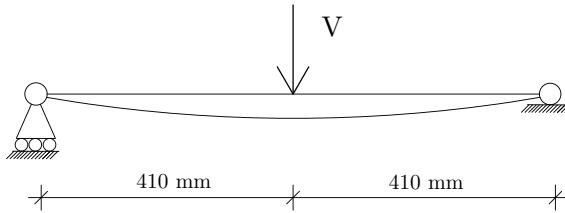
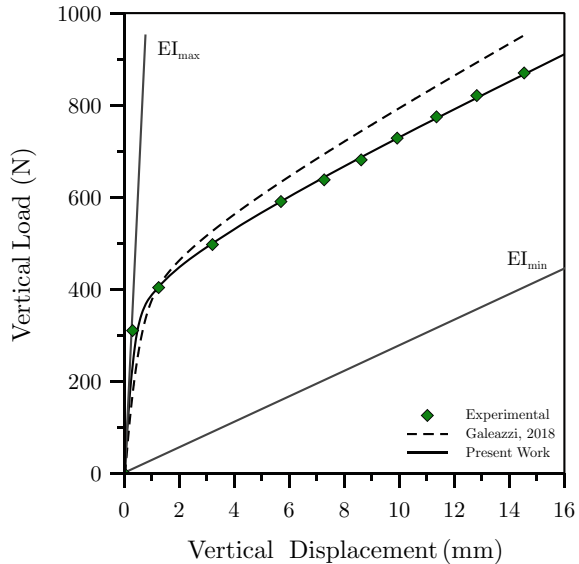


Fig. 1 Schematic representation of the bending test

Table 1 Set of the parameters for the Bouc-Wen hysteretic model

Reference	SET	$EI_{max} (Nm^2)$	$EI_{min} (Nm^2)$	$\chi_0 (m^{-1})$	$n (-)$	$\sigma (-)$
Galeazzi, 2018 [10]	A	4649	369	0.008	1.00	1.00
Present work	B	14613	318	0.005	1.00	1.00

Fig. 2 Vertical load as a function of the vertical midspan displacement for the Galfan steel strand ($D = 38$ mm) tested in [2]



bending stiffness obtained through analytical expression derived in [6]. This new set of values is referred to as SET B (see Table 1).

Figure 2 compares the numerical results of the cable response obtained for the two sets of parameters, with the experimental measurements from [2].

The elastic stiffness (analytically computed) are also shown. As it can be clearly appreciated, SET B allows for a more precise characterization of the bending response of the Galfan conductor tested in [2], being the experimental results excellently reproduced (cf. Fig. 2).

3 Quasi-static Analyses

This section collects the results of quasi-static analyses obtained for the so-called Galfan stranded cable. The maximum and minimum bending stiffness, as well as the first-yielding curvature to be adopted in the Bouc-Wen hysteretic model (see Eqs. 1 and 2) have been calibrated in Sect. 2.2. Since the aim of the present section is to show the main qualitative features of the non-linear slack cable model, and both the set of values previously obtained are describing with sufficient accuracy the experimental results (errors below 10%), the results hereafter presented have been obtained by considering the SET A of parameters. However, analogous results, from the qualitative point of view, would be obtained by using the SET B of parameters (see Table 1).

3.1 Cable Slackness

In order to investigate the effect of cable's slackness on its behavior, two static configurations of the cable have been considered, namely the slack profile (characterized by a significant sag-to-span ratio) and the taut profile (i.e. the static profile of the cable under the well-established small-sag cable theory).

Both of them are obviously characterized by the same value of the cable span l , i.e. the distance between the two supports and, hence, the difference between the two approaches is dictated by the initial length of the cable L_0 , which remarkably differs between the two cases, due to the sag d .

3.2 Loading Conditions

Two main cases of excitation due to the relative motion of supports can be identified, namely the direct support excitation (due to a relative displacement in the direction orthogonal to the cable's centerline) and the parametric excitation (due to a relative displacement in the direction along the cable's centerline) (see Fig. 3). The static scheme of the structure can be regarded to as a doubly-clamped beam with an additional displacement-controlled degree of freedom on the movable end, which was respectively selected as the axial displacement for the parametric excitation case and as the vertical in-plane displacement for the direct excitation case (see again Fig. 3).

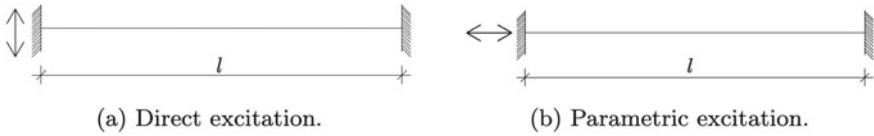


Fig. 3 Schematic representation of the excitation typologies

3.3 Numerical Results

The span l of the cable is set equal to 3 m, whereas the mid-span sag attained for the slack and taut configuration is equal to $d = 432$ mm and $d = 7$ mm, respectively. A quasi-static cyclic support displacement loading history of amplitude A_{qs} is then imparted.

Figure 4 depicts the hysteresis cycles of the cable subject to quasi-static direct excitation for both the slack (a) and the taut (b) configurations. Both diagrams start from a nonzero vertical reaction force at the movable end-section, which is induced by the self-weight of the cable.

Figure 4a outlines a symmetrical hysteresis cycle (with respect to the initial static configuration), which is characterized by a softening behavior essentially due to material nonlinearities (see also the $M - \chi$ diagram of the clamped-end section for the slack configuration, depicted in Fig. 6a).

Although being symmetric with respect to the initial static configuration, the hysteresis cycle depicted in Fig. 4b denotes an hardening-type behavior which is due to the activation of the geometrical nonlinearities.

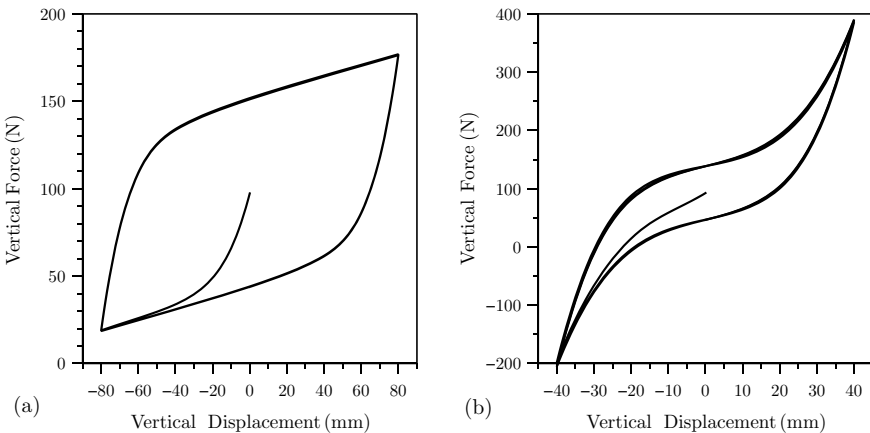


Fig. 4 Hysteresis cycles for the direct excitation case. Slack configuration, $A_{qs} = 80$ mm (a) and taut configuration, $A_{qs} = 40$ mm (b)

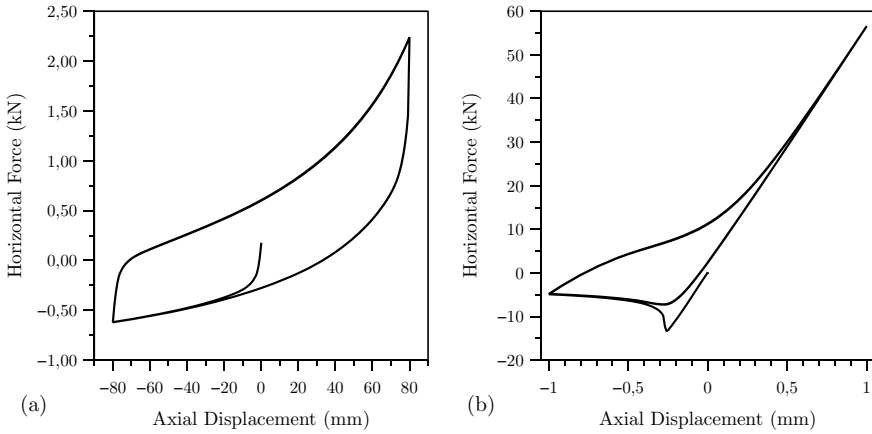


Fig. 5 Hysteresis cycles for the parametric excitation case. Slack configuration, $A_{qs} = 80$ mm (a) and taut configuration, $A_{qs} = 1$ mm (b)

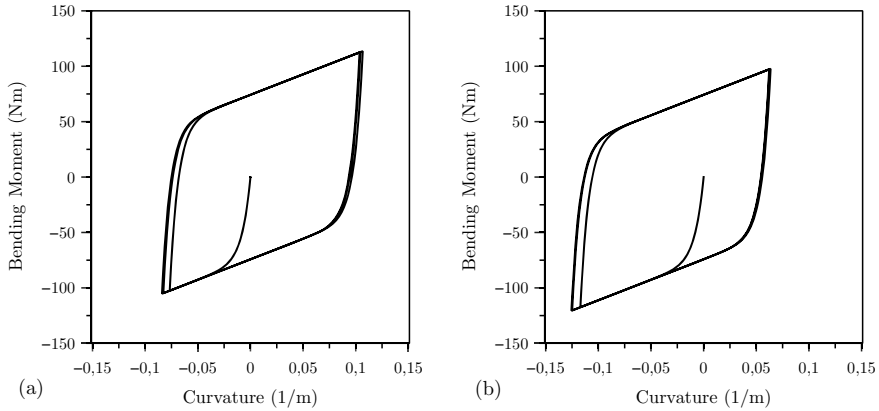


Fig. 6 Moment-curvature diagram at the clamped-end for the direct excitation case. Slack (a) and taut (b) configurations

In addition, material hysteretic behavior is also present, as clarified by Fig. 6b (i.e. the $M - \chi$ diagram of the clamped-end section in the case of taut configuration).

Figure 5 depicts the hysteresis cycles of the cable subject to quasi-static parametric excitation for both the slack (a) and the taut (b) configurations.

Figure 5a clearly illustrates the non-linear and non-holonomic nature which affects the bending behavior of stranded cables. In fact, remarkable geometrical nonlinearities influence the response of such structures by making the cycle non-symmetric and prone to the development of an hardening-type branch in the tension-side and of a softening-type branch in the compression side.

These features are in excellent qualitative agreement with experimental results of quasi-static tests of electrical substation flexible conductors (see, e.g., [4, 9]).

Figure 5b depicts the occurrence of instability phenomenon in the compression region, and a recovery of the linear elastic behavior in the tension one (after the post-buckling branch). The response of the cable under this peculiar loading condition can be assimilated to the one experimentally observed for cyclically loaded steel bracings (cf. [1]).

Moreover, as a general comment, very low displacements are admitted in the case of parametrically-excited taut cables. In fact, in such situation, the structure is not able to accommodate the relative displacements which can arise due to the seismic axial motions of the support. This behavior was also highlighted in [11].

4 Dynamic Analyses

Similarly to the case of static analyses (see Sect. 3), dynamic analyses have been performed by controlling displacements, velocities and accelerations of the movable end-section of the cable. The discretized equation of motion in a classical finite-element dynamic analyses procedure reads:

$$\begin{bmatrix} \mathbf{m}_{ff} & \mathbf{0} \\ \mathbf{0} & \mathbf{m}_{rr} \end{bmatrix} \begin{bmatrix} \ddot{\mathbf{U}}_f \\ \ddot{\mathbf{U}}_r \end{bmatrix} + \begin{bmatrix} \mathbf{c}_{ff} & \mathbf{c}_{fr} \\ \mathbf{c}_{rf} & \mathbf{c}_{rr} \end{bmatrix} \begin{bmatrix} \dot{\mathbf{U}}_f \\ \dot{\mathbf{U}}_r \end{bmatrix} + \begin{bmatrix} \mathbf{P}_f(\mathbf{U}_f, \mathbf{U}_r) \\ \mathbf{P}_r(\mathbf{U}_f, \mathbf{U}_r) \end{bmatrix} = \begin{bmatrix} \mathbf{0} \\ \mathbf{R} \end{bmatrix} \quad (3)$$

where $\mathbf{U}_f(t)$ and $\mathbf{U}_r(t)$ denote respectively the unknown nodal generalized displacements of the load-controlled degrees of freedom and the know nodal generalized displacements imposed at the movable end-section of the cable. Dots denote derivation with respect to time t , while the vectors \mathbf{P}_f and \mathbf{P}_r denote the nonlinear restoring forces work-conjugated to $\mathbf{U}_f(t)$ and $\mathbf{U}_r(t)$, whereas \mathbf{R} denotes the unknown vector of reactions forces at the movable end-section of the cable. Both mass and damping matrices have been introduced in a partitioned form, with obvious meaning of the terms.

The Hilbert-Hughes-Taylor (HHT) time stepping algorithm was adopted for the solution procedure (see [12]) and the parameters were chosen as is it follows: $\alpha = 0.1$, $\beta = 0.3025$, $\gamma = 0.6$. The unknown nodal generalized displacements $\mathbf{U}_f(t)$ are solved from the first row of Eq. 3, and then substituted in the second row, from which the reaction forces \mathbf{R} are then obtained.

A mono-harmonic input signal at the fundamental natural frequency of the cable (i.e. 36.42 Hz for the slack configuration and 12.44 Hz for the taut configuration) has been considered. Both an initial and a final ramp have been added to the input signal. The amplitude of the dynamic cyclic motion will be hereafter denoted with the symbol A_d . Viscous-type damping was accounted for by considering a constant modal damping coefficient $\xi = 1\%$ on the first 10 modes of the cable.

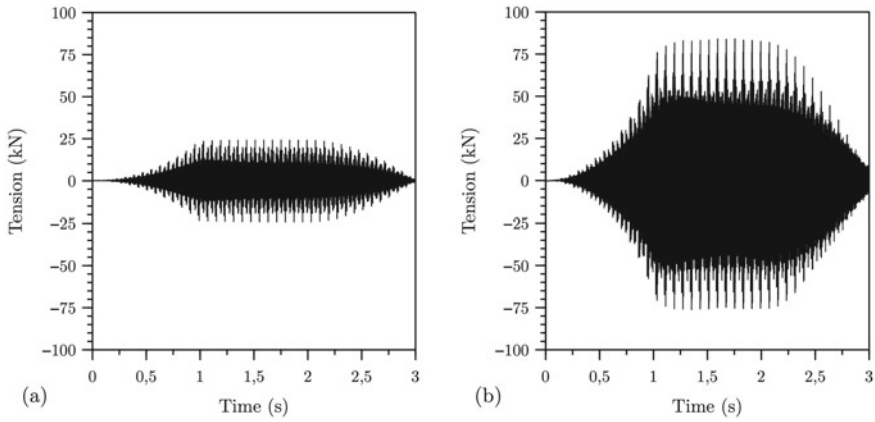


Fig. 7 Time histories of the tension for the slack configuration with $A_d = 20$ mm, for the direct (a) and parametric (b) excitation case

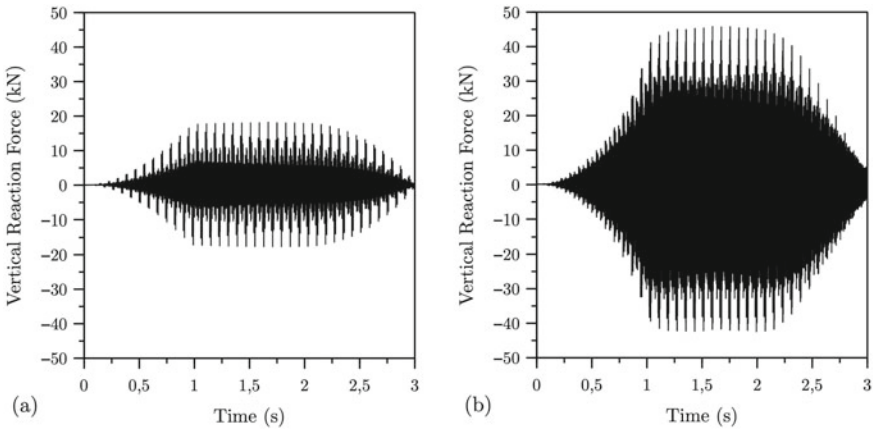


Fig. 8 Time histories of the vertical force for the slack configuration with $A_d = 20$ mm, for the direct (a) and parametric (b) excitation case

The duration of dynamic analyses has been set equal to 3 s, while the adopted time step was particularly demanding in terms of computational burden, i.e. $\Delta t = 10^{-6}$ s, but necessary to capture with good accuracy the first significant modes of the structure, due to the high frequency of excitation.

As an example, results of dynamic analyses for the case of Galfan steel cable in the slack configuration are hereafter reported. Figure 7 depicts the time histories of the cable tension for both direct (a) and parametric (b) excitation case. Figure 8 depicts, instead, the time histories of the vertical reaction force at the movable end, for both direct (a) and parametric (b) excitation case.

Strong dynamic amplification of both vertical and horizontal reaction forces is observed during the motion of the structure. Moreover, parametric excitation leads, as expected, to significantly higher maximum and minimum values of the two response quantities, compared to the direct excitation case.

Application of the proposed methodology to a more rigorous characterization of the dynamic response of short slack cables through extensive parametric analyses is subject of the ongoing research.

5 Conclusions

In this paper, a methodology for the description of both the quasi-static and the dynamic response of short slack cables subject to imposed support motion has been presented. As an application example, the quasi-static and dynamic response of a short slack cable for both direct and parametric excitation cases was numerically investigated. The stranded cable was modeled through co-rotational beam finite elements with a non-linear bending moment-curvature relation based on the smooth Bouc-Wen phenomenological model. Results of quasi-static tests highlight a remarkably different behavior both for the two different initial static configurations (i.e. slack and taut) and for the two different excitation typologies (i.e. direct and parametric) which were considered. Highly geometrically nonlinear behavior was observed, with the developing of hardening-type branches. As per the dynamic analyses, two main sources of nonlinearities, which tend to compete, can in principle affect the response of the cable: the geometrical nonlinearities, which tend to produce a hardening behavior in the response, and the material nonlinearities, which, on the contrary, lead to a softening response of the cable. Activation of each source of nonlinearity strongly depends on both the system parameters (geometric and material properties of the cable) and on the loading conditions. Ongoing research is devoted to an in-depth investigation of the rich nonlinear dynamics of this system. Although further numerical analyses and experimental validation are still needed, the proposed methodology can be a viable tool for the simulation of short slack metallic cables and electrical apparatus such as flexible bus conductors and Bretelle dampers.

References

1. Ballio G, Perotti F (1987) Cyclic behaviour of axially loaded members: numerical simulation and experimental verification. *J Constr Steel Res* 7(1):3–41
2. Chen Z, Yu Y, Wang X, Wu X, Liu H (2015) Experimental research on bending performance of structural cable. *Constr Build Mater* 96:279–288
3. Dastous JB, Paquin JY (2003) Testing and development of alternative flexible-bus geometries for interconnected substation equipment subjected to earthquakes. *IEEE Trans Power Deliv* 18(3):772–780

4. Dastous JB, Pierre JR (1996) Experimental investigation on the dynamic behavior of flexible conductors between substation equipment during an earthquake. *IEEE Trans Power Deliv* 11(2):801–807
5. Filiatrault A, Stearns C (2005) Flexural properties of flexible conductors interconnecting electrical substation equipment. *J Struct Eng* 131(1):151–159
6. Foti F, Martinelli L (2016) Mechanical modeling of metallic strands subjected to tension, torsion and bending. *Int J Solid Struct* 91:1–17
7. Foti F, Martinelli L (2018) Finite element modelling of cable galloping vibrations. Part I: Formulation of mechanical and aerodynamic co-rotational elements. *Arch Appl Mech* 88(1):645–670
8. Foti F, Martinelli L (2018) Hysteretic behaviour of Stockbridge dampers: modelling and parameter identification. *Math Probl Eng* 2018:Article ID 8925121, 17
9. Fu Y, Sivaselvan MV (2023) Nonlinear dynamics of short-span electrical conductor cables under uniaxial periodic excitation. *J Sound Vibr* 543:Article ID 117319, 16
10. Galeazzi J (2018) Hysteretic behavior of wire rope isolators: numerical modelling and parameter identification. Msc Thesis, Politecnico di Milano, Milan
11. He C, Xie Q, Yang Z, Xue S (2019) Modelling large planar deflections of flexible bundled conductors in substations using a modified chained-beam constraint model. *Eng Struct* 185:278–285
12. Hilbert HM, Hughes TJR, Taylor RL (1977) Improved numerical dissipation for time integration algorithms in structural dynamics. *Earthquake Eng Struct Dynam* 5:283–292
13. Hautefeuille P, Porcheron Y (1964) Field experiments on mechanical behavior of overhead lines. In: *Proceedings of the conference Internationale des Grands Reseacux Electriques a Haute Tension*, June 1–10, Paris (France), Paper 236, 46
14. Hong KJ, Der Kiureghian A, Sackman JL (2005) Bending behavior of helically wrapped cables. *J Eng Mech* 131:500–511
15. Ikhouane F, Rodellar J (2005) On the hysteretic Bouc-Wen model. part i: Forced limit cycle characterization. *Nonlinear Dyn* 42:63–78
16. Ikhouane F, Rodellar J, Hurtado JE (2006) Analytical characterization of hysteresis loops described by the Bouc-Wen model. *Mech Adv Mater Struct* 13(16):463–472
17. Lalonde S, Guilbault B, Légeron F (2017) Modeling multilayered wire strands, a strategy based on 3D finite element beam-to-beam contacts - Part I: model formulation and validation. *Int J Mech Sci* 126:281–296
18. Lanteigne J (1985) Theoretical estimation of the response of helically armored cables to tension, torsion and bending. *J Appl Mech* 52:423–432
19. Papailiou KO (1997) On the bending stiffness of transmission line conductors. *IEEE Trans Power Deliv* 126:1576–1588

Comparing Different Techniques of Determining Cable Forces from Vibration Measurements on a Cable-Stayed Arch Bridge



Stefan Verdenius

Abstract As part of a reassessment of a cable-stayed arch bridge in The Netherlands, cable forces need to be determined. To this end vibration measurements are performed on each cable individually, from which the natural frequencies are derived. This paper describes three methods to determine cable forces from these vibration measurements, all using the relation between force and frequency according to the taut-string formula. In the first method the cable length as-is is used as vibrating length. A second method uses information on the mode shapes to determine the vibrating length and a third method uses the change in frequency due to an added point mass as a way to derive the vibrating length. Measurements on the shortest cable of the arch bridge show that using modal shapes leads to a vibrating length of almost one meter shorter than the full cable length (13.29 m instead of 14.32 m), while the third method leads to a much lower vibrating length (12.32 m) and thus to a different cable force. The two latter methods have as big advantage that they can be applied independent of the boundary condition of the cables, but the measurements have shown that their success is strongly related to the accuracy with which different parameters can be determined.

Keywords Cable force · Natural frequency · Vibration measurements

1 Introduction

Finite element models play an essential role in assessing the remaining life time of steel bridges [1, 2]. When creating a finite element model of an arch bridge, the cable forces are an important measure in tuning the model [3]. Cable forces cannot be measured directly if no load cells are installed during construction, but many alternative measurement techniques are proposed in literature [4, 5]. By measuring

S. Verdenius (✉)

Unit of Mobility and Built Environment, TNO, Delft, The Netherlands

e-mail: stefan.verdenius@tno.nl

vibrations, the so-called taut-string method, one of the most common ways to determine cable forces, can be used [6, 7]. When applying this method, cable forces are calculated based on the measured natural frequencies of the cable, in combination with the estimated vibration length, mass and stiffness of the cable.

These measurements have been performed numerous times in The Netherlands and in other countries [8]. Although this method is straight-forward and easy to perform, the downside of this method is that the necessary cable parameters are sometimes hard to determine and that the applicability is strongly related to the boundary conditions of the cables, thereby leading to an uncertainty band on the resulting cable forces [9]. This experience is shared by the author based on earlier measurements performed in The Netherlands.

In literature multiple experiments are listed to gain additional information on the different cable parameters. In [10] it is shown that extra information on the vibration length can be gathered by performing a modal analysis, leading to a more accurate determination of cable forces. This modal analysis can easily be applied on the conventional taut-string measurement set-up when paying attention to the exact location of the accelerometers as described in [10]. A second paper describes how the vibration length can be estimated by adding a point mass to the cable and by evaluating the change in natural frequency of the cable due to this extra mass [11].

During the reassessment of the ‘Brug over de Beneden Merwede’, a steel arch bridge of ca. 200 m with four lanes of traffic in The Netherlands, the forces in all 28 stay-cables are determined using vibration measurements. This work elaborates on the determination of the force in the shortest cable (14.32 m) using three methods. Firstly the cable force is determined using the conventional taut-string method, with an estimate of some cable parameters and by using the full cable length as vibrating length. Hereafter, the cable force is recalculated by adding the data from the modal analysis. As a third step the cable force is determined by using the change in natural frequency due to additional tests with an added point mass.

This paper describes how the tests are performed and how the three evaluation techniques lead to different cable forces.

2 Assessment of Cable Forces

2.1 Taut-String Method

Different studies describe how the force in a cable can be determined from the measured natural frequency depending on the boundary conditions of the cable [12]. The formulas that describe this relation for a clamped and hinged connection between cable and bridge are given in Eqs. (1) and (2) respectively.

$$f_k = \frac{k}{2L} \sqrt{\frac{F}{\mu}} \left(1 + 2\sqrt{\frac{EI}{FL^2}} + \left(4 + \frac{k^2\pi^2}{2} \right) \frac{EI}{FL^2} \right) \quad (1)$$

$$f_k = \frac{k}{2L} \sqrt{\frac{F}{\mu}} \sqrt{1 + \frac{k^2 \pi^2 EI}{L^2 F}} \quad (2)$$

In these equations f_k is the natural frequency [Hz] of mode k , L is the vibrating length of the cable [m], μ is the mass of the cable per meter [kg/m], EI is the bending stiffness of the cable [N/m²] and F is the force in the cable [N].

In previous measurements performed in The Netherlands, the natural frequencies of the cable are measured while all other parameters are determined using e.g. design drawings. The force in the cable can then be determined by solving the minimization problem as stated in Eq. (3) for different values of cable force F .

$$\operatorname{argmin} \left(\sum_{k=1}^{k_{max}} \frac{f_{k,meas} - f_{k,calc}}{f_{k,meas}}, F \right) \quad (3)$$

In this equation $f_{k,meas}$ is the measured natural frequency of mode k , $f_{k,calc}$ is the natural frequency of mode k according to Eqs. (1) or (2) and k_{max} is the highest mode measured. The length L is, when no additional information is present, taken equal to the length of the cable.

2.2 Modal Analysis

The work reported in [10] describes how the cable force can be estimated more accurately by including information on the mode shape ratios. When evaluating the mode shape ratios one can determine the vibrating length L_k by solving the minimization problem as stated in Eq. (4).

$$\operatorname{argmin} \left(\sum_{k=1}^{k_{max}} \sum_{j=1}^n \left\{ a_k \cosin \left[k\pi \frac{x_j - d_k}{L_k} - \widehat{\phi}_{jk} \right] \right\}^2, \{d_k, a_k, L_k\} \right) \quad (4)$$

In Eq. (4) x_j is the location of accelerometer j with respect to the middle of the cable [m], L_k is the vibrating length of the cable for mode k and a_k is the amplitude coefficient of mode k . The parameter d_k is introduced in order to include asymmetry of the cable, representing an origin shift [m] and the term \cosin represents a cosine-function for all odd modes and a sine-function for all even modes. The value $\widehat{\phi}_{jk}$ denotes the real part of the measured mode shape value of the k -th mode at accelerometer j , determined by normalizing the Discrete Fourier Transform using the value at one of the n accelerometers.

Minimizing the error-function stated in Eq. (4) with three unknowns (d_k , a_k and L_k) leads to a best guess of the vibrating length, which thereafter can replace parameter L in Eq. (2) to determine the cable force.

2.3 Additional Point Mass

In [11] a method is derived to determine the effective length of cables by adding a point mass to the cable. The first natural frequency of a cable (ω_1) changes when adding a point mass M [kg], where the first natural frequency after addition of the point mass (ω_{m1}) is described as

$$\left(\frac{\omega_1}{\omega_{m1}}\right)^2 = 1 + \frac{2M}{mL_{eq}} \sin^2 \frac{\pi(2L_m - L + L_{eq})}{2L_{eq}} \quad (5)$$

In Eq. (5) m is the mass per length of the cable [kg/m], L denotes the total length of the cable [m], L_m the location of the added point mass [m] and L_{eq} the equivalent length [m]. When the additional mass is placed exactly in the middle of the cable length, Eq. (5) can be simplified as

$$\left(\frac{\omega_1}{\omega_{m1}}\right)^2 = 1 + \frac{2M}{mL_{eq}} \quad (6)$$

The parameter L in Eq. (2) can then be replaced by the effective length L_{eq} after which the force in the cable can be determined.

3 Field Measurements

3.1 Brug Over de Beneden Merwede

Measurements are performed at the Brug over de Beneden Merwede (Fig. 1). This bridge has a main span of 203 m and an arch with a height of ca. 30 m above deck. Arch and deck are connected through 28 diagonal cables, 14 on each side of the bridge, with lengths varying from 14.32 m to 30.87 m. The cables are wire ropes with a diameter of 78 mm and a mass of 34.68 kg/m. The first ca. 2.9 m of the cables above deck are protected against vandalism through a cover bolted around the cable; however, this cover is removed prior to the measurements to prevent it influencing the free vibration of the cable. Cables are measured one after another; in this paper only the measurements of cable 1 (14.32 m) are discussed.

3.2 Measurement Set-Up

Based on the work in [10] each cable is instrumented with four wireless accelerometers (Lord Microstrain, G-Link-200), of which two are at the outer ends of the cable



Fig. 1 Brug over de Beneden Merwede [13]

(Fig. 2, left). The position of the other two accelerometers is kept equal to the position used in [10]. A lashing strap is used to pretension the cable, being attached to the cable on one end (at an arbitrary location) and at the barrier on deck on the other end (Fig. 2, right). An HBM U9C load cell (range 5000 N) is used to determine the tension in the lashing strap.

For the measurements described in Sect. 2.3 an additional point mass is added to the cable. This point mass is placed in the middle of the cable length, as depicted in Fig. 3. The additional point mass consisted of two aluminum ‘shields’ (5.42 kg each)

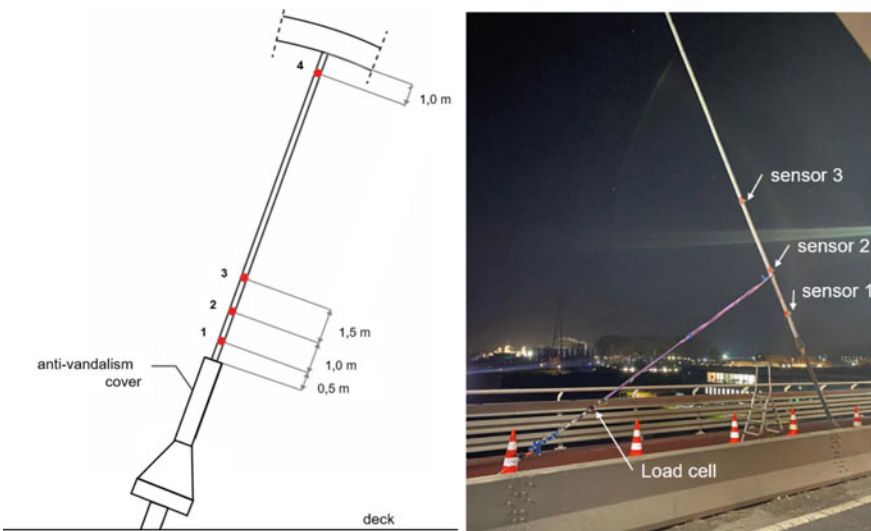


Fig. 2 Schematic depiction of the four accelerometers along the length of the cable (left). Picture during the measurement indicating the load cell on the lashing strap between cable and barrier (right). Do note that the anti-vandalism shield is removed before the measurements



Fig. 3 Additional point mass attached to the cable. The left figure indicates the light weight (46.56 kg) and the right picture the heavy weight (82.28 kg)

that are clamped around the cable. On top of these shields additional steel plates (4.47 kg each) could be placed to increase the mass. The amount of mass is chosen such that the addition of the mass leads to a measurable change in natural frequency ($>5\%$) for all hangers. The ratio between added mass and cable mass is comparable with the ratio in [11].

3.3 Measurement Procedure

Vibration measurements are performed during a closure of the bridge (no traffic). Using the lashing strap, the force perpendicular to the cable is increased to 2 kN, after which the force is released at once, leading to vibration of the cable. When the cable vibrations are damped, the lashing strap is tensioned again in order to repeat this measurement. In total 5 measurements are performed.

After these 5 measurements the point mass is added. At first all steel plates are added to the aluminum shields, leading to a total point mass of 82.28 kg. Again, five measurements are performed as described above. After these five measurements, half of the plates are removed and five new measurements are performed (with a total added mass of 46.56 kg).

4 Data Evaluation

To determine the natural frequencies of the cable, the measured accelerations of the cable and the force in the lashing strap are evaluated. Note that for determining the natural frequencies either one of the four accelerometers can be used. The force in the lashing strap and the measured acceleration of accelerometer 1 (the lowest sensor) are shown synchronous in time in Fig. 4 for all five consecutive excitations (without additional point mass). Data was sampled with a rate of 256 Hz. In Fig. 4 the different stages of the step-relaxation excitation (tightening the strap, releasing the strap and free vibration of the cable) can clearly be distinguished.

The five individual excitations are indicated in Fig. 4 using red lines as the start of the excitation (releasing the lashing strap) and black lines as the end of the cable vibration and the start of a new excitation (tensioning the lashing strap). Only the time segments between the red and black lines were used for data evaluation; the period of tightening the lash is thus not evaluated.

All five segments from Fig. 4 are combined into one continuous signal and the transfer function of the applied force in the lashing strap and the measured acceleration is determined. The transfer function is determined using the built-in Matlab Fourier Transform function ‘tffestimate’ in combination with a Hanning window and zeropadding. The resulting spectral image of accelerometer 1 of cable 1 is shown in Fig. 5, in which the individual natural frequencies can clearly be distinguished as peaks in the amplitude.

To determine the mode shapes necessary for applying the method as described in Sect. 2.2 a Fast Fourier Transform is made, using the built-in Matlab function ‘fft’.

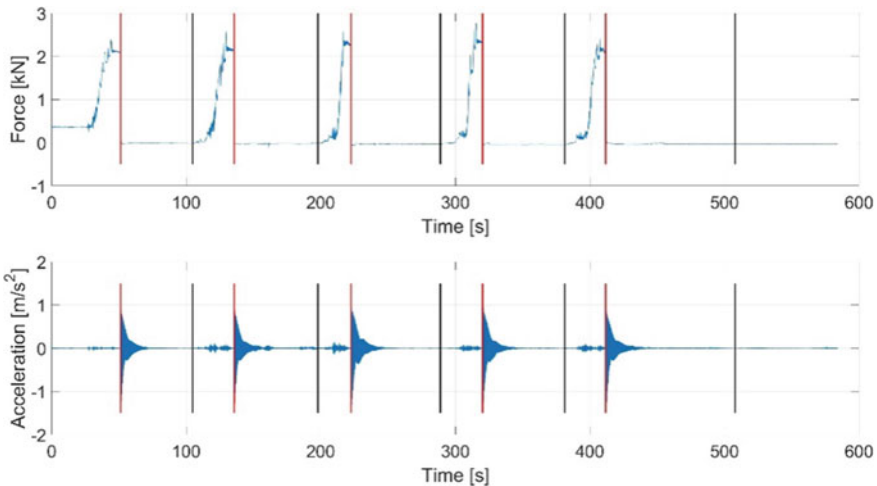


Fig. 4 Measurement signal from excitation of cable 1. The top figure shows the force in the lashing strap, the bottom figure the acceleration measured by sensor 1. The red and black lines indicate the sections that are used for evaluation

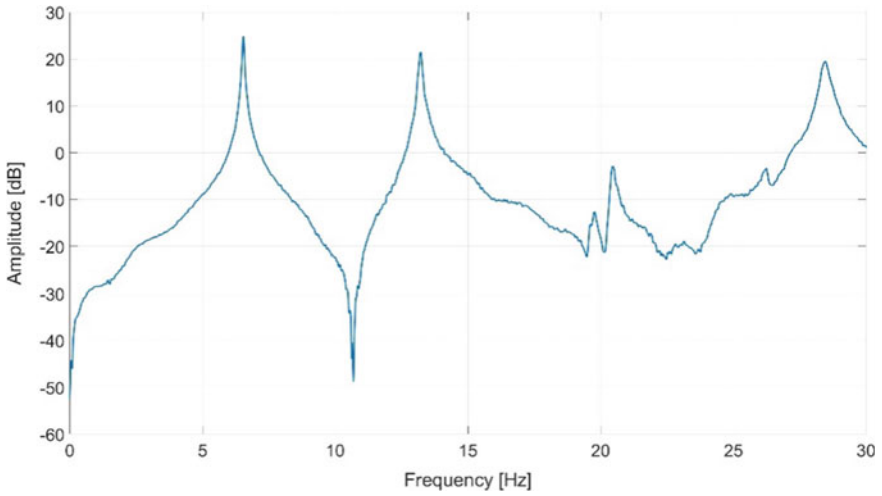


Fig. 5 Visualization of the natural frequencies found when evaluating the transfer function of the force and the acceleration (sensor 1) for excitation of cable 1

A similar procedure is followed to determine the natural frequencies in case of an added point mass, as described in Sect. 2.3.

5 Results

5.1 Frequencies

Based on the analysis described in Sect. 4, the natural frequencies are determined as listed in Table 1.

In order to apply the method listed in Sect. 2.2, the mode shapes for all accelerometers are determined for the first natural frequency as listed in Table 2.

Table 1 Natural frequencies for cable 1 per added mass

Added mass	Natural frequency (1st mode)
No mass	6.50 Hz
46.56 kg	5.89 Hz
82.28 kg	5.53 Hz

Table 2 (Normalized) mode shape parameters for the first natural frequency per sensor

Accelerometer	Mode shape	Normalized mode shapes
1	12.2016	1.0000
2	13.4537	1.1026
3	13.6381	1.1177
4	3.91129	0.3206

Table 3 Resulting vibration lengths and cable forces

Method	Vibrating length [m]	Cable force [kN]
'Basic' taut-string	14.32	1202
Mode shape analysis	13.29	1035
Added point mass (ω_0/ω_{46})	12.34	892
Added point mass (ω_0/ω_{82})	12.34	892
Added point mass (ω_{46}/ω_{82})	12.32	890

5.2 Vibration Length and Cable Force

When applying the procedure as described in Sect. 2.2 and using the data from Table 2, a vibrating length of 13.29 m results. Hereto the results of accelerometer 3 had to be omitted, since it turned out that this accelerometer was placed too far in the middle of the cable, thereby preventing convergence of Eq. (4). In applying the method from Sect. 2.3, distinction is made between three different analyses since two different masses were added. These analyses all use a different relation between frequencies, namely ω_0/ω_{46} , ω_0/ω_{82} and ω_{46}/ω_{82} , where the number in the subscript indicates the added mass. With these three analyses equivalent lengths of 12.34 m, 12.34 m and 12.32 m are found.

Using Eq. (2) the corresponding cable force can be determined. For now this equation is applied neglecting the bending stiffness and only evaluating the first natural frequency.

All results are summarized in Table 3.

5.3 Evaluation of the Results

When reviewing the numbers from Table 3 it can be seen that all methods lead to a different result. The vibrating length resulting from Sect. 2.2 is about 1 m shorter than the full cable length, which might be explained due to the part of the cable that is clamped within the arch and below the deck. However, the length found when applying an additional point mass (Sect. 2.3) is about 2 m shorter than the full cable

length, which is hard to explain when looking at the bridge structure. However, it cannot be said which length from Table 3 is the correct vibration length.

A possible explanation for the large difference between the length found using the added mass and the full cable length, is the limited accuracy in the measured natural frequencies. A sensitivity study is performed investigating the effect of a measurement error in the natural frequency on the resulting equivalent lengths (not reported in this paper). This study has shown that in case a measurement error of only 0.5% was made in only the natural frequency measured with an added mass of 46.56 kg (e.g. 5.92 Hz instead of 5.89 Hz), the three analyses lead to completely different lengths (13.21 m, 12.54 m and 11.42 m). This shows that the procedure based on added masses is extremely sensitive to the determined natural frequencies.

6 Conclusion

This paper describes the determination of cable forces of an arch bridge in the Netherlands based on vibration measurements. Results of the shortest cable are given when using three different evaluation technique. The first technique assumes the vibration length is equal to the full cable length, leading to a cable force of 1202 kN when assuming a hinged connection with the bridge and when neglecting the bending stiffness of the cable. The other two evaluation techniques base the vibration length on the mode shape ratio or the change in natural frequency due to an added point mass respectively. This first technique leads to a cable force of 1035 kN, the latter results in a cable force of circa 890 kN.

Differing results between methods can be possibly caused by inaccuracy of determining the natural frequency, or by inaccuracy in measuring locations of sensors and added masses. The method using modal shapes seems to give accurate results in this measurement, although more measurements should be performed in order to conclude on its accuracy. At first sight the proposed method of adding a point mass seems too sensitive to be applied during field measurements. It is suggested to perform a sensitivity study on the exact positions of the added point mass and the accelerometers on the resulting vibrating length. On top of this, it would be beneficial to invest in signal processing techniques in order to increase the quality of the measurement signal.

Acknowledgements The author would like to thank colleague Linda Abspoel and the experimental team of TNO that performed the measurements on the bridge. Additionally the author would like to thank Rijkswaterstaat and Movares for their help and assistance in the measurements.

References

1. Schlune H, Plos M, Gylltoft K (2009) Improved bridge evaluation through finite element model updating using static and dynamic measurements. *Eng Struct* 31(7):1477–1485
2. Icke P, Margheriti C (1993) The benefits and use of FE modelling in bridge assessment and design. *Elastic* 1
3. Benedettini F, Gentile C (2011) Operational modal testing and FE model tuning of a cable-stayed bridge. *Eng Struct* 33(6):2063–2073
4. Zhang L, Qiu G, Chen Z (2021) Structural health monitoring methods of cables in cable-stayed bridge: a review. *Measurement* 168:108343
5. Yao Y, Yan M, Bao Y (2021) Measurement of cable forces for automated monitoring of engineering structures using fiber optic sensors: a review. *Autom Construct* 126:103687
6. Geier R, De Roeck G, Flesch R (2006) Accurate cable force determination using ambient vibration measurements. *Struct Infrastruct Eng* 2.1:43–52 (2006)
7. Caetano E (2011) On the identification of cable force from vibration measurements. IABSE-IASS Symposium, London
8. Verdenius S, Bronkhorst O, Geurts C (2022) Vibration measurements on a cable-stayed cyclist arch bridge for assessment of the dynamic behaviour. In: *Experimental Vibration Analysis for Civil Engineering Structures: Select Proceedings of the EVACES 2021*. Springer International Publishing, Cham, pp 125–135
9. Ma L (2017) A highly precise frequency-based method for estimating the tension of an inclined cable with unknown boundary conditions. *J Sound Vib* 409:65–80
10. Chen C-C et al (2016) Tension determination of stay cable or external tendon with complicated constraints using multiple vibration measurements. *Measurement* 86:182–195
11. Li S et al (2021) An accurate measurement method for tension force of short cable by additional mass block. *Adv Mater Sci Eng* 2021:1–10
12. Ren W-X, Chen G, Hu W-H (2005) Empirical formulas to estimate cable tension by cable fundamental frequency. *Struct Eng Mech* 20.3:363–380
13. PZC, <https://www.pzc.nl/dordrecht>. Accessed 24 Apr 2023

Models

On the Seismic Response of Anchoring Elements for Submerged Floating Tunnels



S. Corazza, M. Geuzaine, F. Foti, V. Denoël, and L. Martinelli

Abstract Submerged Floating Tunnels (SFTs) are interesting modular structures that lend themselves well to the crossing of water bodies. In a widespread design configuration the SFTs retain positive buoyancy and are kept at a fixed depth under the water surface by anchoring devices connected to the seabed. Different technological solutions have been proposed for the anchoring devices. They all share the properties of being slender, axially stiff and very flexible in transverse direction. The positive buoyancy of the SFT is typically tailored such to avoid detensioning (slackening) of the anchoring elements under design loading conditions, e.g. wave and earthquake loading. Whenever the tunnel is located in seismic prone areas, the seismic loading can be the dominant one. The present paper focuses on the local dynamic response of anchoring elements of a proposal for the Messina Strait crossing. The seismic input is modeled according to a suitable power spectral density of the ground acceleration and a reduced-order model of anchoring element is set up according to the classic theory of small-sag cables. The seismic working conditions are assessed with respect to slackening requirements.

Keywords Submerged floating tunnels · Cable dynamics · Seismic loading · Slackening

S. Corazza (✉) · F. Foti · L. Martinelli
Department of Civil and Environmental Engineering, Politecnico di Milano, Italy
e-mail: stefano.corazza@polimi.it

F. Foti
e-mail: francesco.foti@polimi.it

L. Martinelli
e-mail: luca.martinelli@polimi.it

M. Geuzaine
NatHaz Modeling Laboratory, University of Notre Dame, Notre Dame, USA
e-mail: mgeuzaine@uliege.be

V. Denoël
Structural & Stochastic Dynamics, University of Liège, Liège, Belgium
e-mail: v.denoel@uliege.be

1 Introduction

Since the last decades of the past century, Submerged Floating Tunnels (SFTs) have been considered as a viable alternative to bridges and immersed tunnels for crossing waterways [1]. Although a first realization is still missing, many preliminary design proposals have been drafted and reported in the literature for sea strait, fjord and lake crossing (see e.g. [2, 15, 18]). The main design parameter of SFTs is the Buoyancy to Weight Ratio (BWR), i.e. the ratio between the buoyancy force and weight per unit of length of the tunnel. Seabed anchored SFTs, on which the present paper focuses, are always characterized by values of the BWR greater than one and the net buoyancy force is transferred to the foundations by means of a spread system of anchoring elements (mooring system), that are typically realized with structural cables or tubular steel profiles closely spaced along the tunnel length. The BWR of the tunnel controls the tensile load acting in the tethers under static loading conditions and can be tailored such to avoid detensioning (slackening) under design dynamic loading conditions, e.g. wave and earthquake loading [19]. Increasing the BWR, however, leads to an increase of the tensile loads that must be counteracted by the foundations. Optimal design of the BWR, hence, implies searching for a trade-off between these competing design objectives.

Within this context, an accurate prediction of the dynamic response of the SFTs anchoring elements is of paramount importance.

Dynamics of SFTs has been studied in the literature mostly by means of numerical simulations based on applications of the Finite Element (FE) method, e.g. [9, 10, 16, 17]. However, computationally efficient FE models able to simultaneously capture the main features of both global and local vibration modes with the same degree of accuracy, are inherently hard to set up. As a consequence, anchoring elements are often modeled as mass-less tendons and their local dynamics is disregarded or considered on a separate note under simplified loading conditions (see, e.g. [4]).

Global-local mode interaction has been extensively studied with reference to cable-supported bridges, such as stayed bridges, and different ad-hoc modeling strategies have been proposed [8, 13, 21]. Although potentially promising, application of such formulations to the analysis of SFTs requires addressing the following issues that specifically distinguish SFTs anchoring elements from stay cables: (1) SFT anchoring elements are immersed in water, and (2) they are directly connected to the foundations.

The aim of the present paper is to make a first step in this direction. A reduced-order geometrically nonlinear dynamic model for the anchoring elements of a SFT is first formulated by generalizing the stay cable model originally proposed by Warnitchai et al. [21]. The model relies on the small-sag cable theory and allows for a generic motion of the end sections. The cable model is then applied to investigate the seismic response of the tethers of a SFT designed to cross the Messina strait, in Italy [10]. To this aim, a simplified two-step procedure that neglect coupling between global and local vibration modes of the structure is herein adopted. Results are then discussed with respect to the possible occurrence of slackening phenomena.

2 Local Dynamics of the Anchoring Element

In the present section, a reduced-order model for the dynamic response of inclined anchoring elements is presented. The latter accounts for both geometrical nonlinearities and a generic form of support motion, basing on the formulation firstly presented in [21] for inclined cables. The main hypothesis of the model is that the total motion of the element can be decomposed into the sum of a quasi-static component and of the modal motions of the cable. The former are the displacements of the cable which moves as an elastic tendon due to the support motion, while the latter are expressed as a combination of the linear undamped modes of a cable with fixed ends. The model developed in [21] for the local analysis of the cable response, with applications related to cable-stayed bridges, is here extended to the case of a water immersed tether.

Due to space constraints, the reduced-order model formulation is here presented focusing only on the in-plane vibrations. Generalization to the case of three-dimensional motion is, however, straightforward.

2.1 Preliminaries

Let us consider a tether inclined with an angle θ with respect to the horizontal plane, having initial chord length L_0 , mass per unit of length γ_s , axial stiffness EA_0 and subject to a static tension $T_0 > 0$ (leading to a static stress $\sigma_s = T_0/A_0$). The self-weight per unit of length of the tether is denoted by w_s (i.e. $w_s = \gamma_s g$), while the symbol br indicates its buoyancy ratio, namely the ratio of the hydrostatic forces and the self-weight per unit of length. Furthermore, as usual in the context of small-sag cable theory [14], let us denote by λ^2 the well-known elasto-geometric Irvine's parameter, defined according to the following equation:

$$\lambda^2 = \Gamma^2 \cos^2(\theta) \frac{1}{\varepsilon_0} \quad (1)$$

where $\Gamma = w_s(1 - br)L_0/T_0$ and $\varepsilon_0 = T_0/EA_0$. The maximum sag (d) of the tether can be computed, according to the classic parabolic approximation, as:

$$d = \frac{w_s(1 - br) L_0^2}{8 T_0} \quad (2)$$

It is also convenient for the following developments to introduce the non-dimensional load parameter as $\eta_0 = T_0/T_y$, where $T_y = f_y A_0$ is the yielding tensile force and f_y is the yielding stress of the steel. The non-dimensional load parameter is directly proportional to the BWR of the tunnel.

Moreover, in the case of submerged tethers, the so-called virtual mass per unit of length enters into play:

$$\gamma_v = \gamma_s + C_A \gamma_w \tag{3}$$

where γ_w represents the weight per unit of length of the fluid which is moved due to the presence of the anchoring element. In fact, γ_v takes into account the presence of the fluid around the cable that acts as an added mass when dealing with its dynamic response. The added-mass coefficient C_A depends on the cable cross-section and, in the case of a circular cross-section, the unit value is usually adopted (see e.g. [5, 22]).

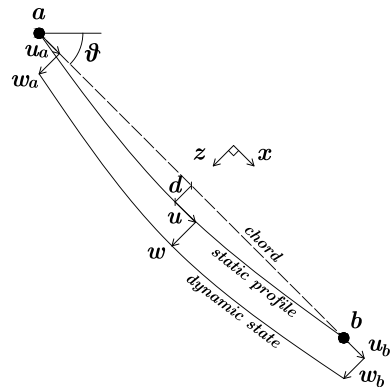
2.2 Equations of Motion

Let us consider the reference system depicted in Fig. 1, in which the x axis spans the whole chord length, i.e. $0 < x < L_0$, and the dynamic displacements along x , and z directions are denoted by u and w , respectively. Let us also consider a generic form of support motion, by expressing the in-plane displacements at support a and b as u_a, u_b, w_a and w_b . The total time-dependent displacements are separated into two parts: quasi-static displacements (denoted by the subscript q), which are depending only on the support displacements (see [21]), and modal displacements (denoted by subscript m). By employing the usual separation of variables and neglecting the axial modal motion (i.e. $u_m(x, t) \ll w_m(x, t)$), one has:

$$w_m(x, t) = \sum_{m=1}^M \psi_m(x) z_m(t) \tag{4}$$

where M denotes the total number of in-plane modes retained in the reduced model. The time functions z_m can be interpreted as a generalized modal coordinate for the

Fig. 1 Schematic representation of the inclined anchoring element



in-plane motion, whereas ψ_m is the associated shape function, herein defined as the m th mode of the tether under the assumption of fixed end sections. The derivation of the reduced-order model relies on a standard application of the Lagrange's equation of motion. Both potential (U_c) and kinetic (T_c) energies are written as a function of the quasi-static and modal components of displacements and the same procedure developed in [21] is adopted. A non-dimensional form of the equations of motion can be obtained by introducing the following non-dimensional variables:

$$\bar{z}_m = \frac{z_m}{L_c} \quad \bar{t} = \frac{t}{t_c} = \omega_c t \quad \bar{u}_i = \frac{u_i}{L_c} \quad \bar{w}_i = \frac{w_i}{L_c} \quad i = a, b \quad (5)$$

where L_c is a characteristic length, hereafter set equal to the maximum sag d (see Eq. 2), while ω_c is a characteristic circular frequency, hereafter set equal to the fundamental natural circular frequency of the tether calculated according to a taut-string model, i.e.:

$$\omega_c = \frac{\pi}{L_0} \sqrt{\frac{T_0}{\gamma_v}} \quad (6)$$

The sought final non-dimensional expression is then readily obtained:

$$\begin{aligned} & \ddot{\bar{z}}_m + 2\xi_{zm}\bar{\omega}_{zm}\dot{\bar{z}}_m + \bar{\omega}_{zm}^2\bar{z}_m + \sum_{k=1}^M \bar{\nu}_{mk}\bar{z}_m\bar{z}_k^2 + \sum_{k=1}^M 2\bar{\beta}_{mk}\bar{z}_m\bar{z}_k + \\ & - \sum_{k=1}^M 2\bar{\beta}_{mk}\bar{z}_m\bar{z}_k(\bar{u}_b - \bar{u}_a) + \sum_{k=1}^M \bar{\beta}_{km}\bar{z}_k^2 - \sum_{k=1}^M \bar{\beta}_{km}\bar{z}_k^2(\bar{u}_b - \bar{u}_a) + \\ & + 2(\bar{\eta}_m - \bar{\mu}_m)(\bar{u}_b - \bar{u}_a)\bar{z}_m + \bar{\zeta}_m[\ddot{\bar{w}}_a + (-1)^{m+1}\ddot{\bar{w}}_b] + \\ & - \bar{\alpha}_m(\ddot{\bar{u}}_b - \ddot{\bar{u}}_a) = \bar{F}_{z_m} \end{aligned} \quad (7)$$

which holds for $m = 1, 2, \dots, M$.

The expressions of the non-dimensional coefficients that appear in Eq. 7 are reported in Appendix 5. Such coefficients are slightly different with respect to the ones presented in [21], because the hypothesis related to the small magnitude of the quasi-static axial stress σ_q with respect to the static stress σ_s (i.e. $\sigma_q \ll \sigma_s$), which was enforced by Warnitchai et al., is here removed, since its validity to the case of SFT anchoring elements needs to be preliminary assessed. Once the non-dimensional modal coordinates have been solved from Eq. 7, the total stress $\sigma_{tot}(t)$ acting on the tether is computed by linear superposition between the static component σ_s and the dynamic one $\sigma_d(t)$ (which is straightforwardly retrieved by direct application of the constitutive law), i.e. $\sigma_{tot}(t) = \sigma_s + \sigma_d(t) = \sigma_s + E\epsilon(t)$, where E and $\epsilon(t)$ denote the Young's modulus of the tether and the dynamic axial strain, respectively.

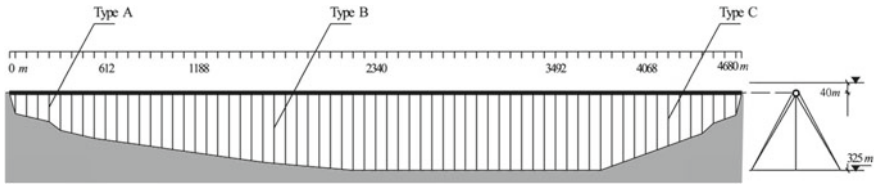


Fig. 2 Schematic representation of the SFT example. Side view and cross-section

3 Application Example

In this section, the applicability of the reduced-order model previously presented is investigated by considering the dynamic behavior of an inclined anchoring element of a SFT proposed for the crossing of the Messina Strait, in Italy [10].

The considered SFT is designed to connect Sicily to the mainland, crossing a strait characterized by a maximum seabed depth of 325 m. The total length of the SFT is 4680 m and the tunnel axis is placed 40 m below the water table. The tunnel is anchored to the seabed (having variable depth) through a mooring system made of inclined hollow core circular cross-section tethers (see Fig. 2). In the original proposal three types of cross-sections (types A, B and C) are considered for the tethers along the length of tunnel, while their spacing is assumed to be constant and equal to 72 m. In the present work, simplified analyses have been carried by assuming that all anchoring elements are characterized by the same cross-section type B, defined by the following parameters: $D_o = 1.950$ m, $s = 0.065$ m, $A_0 = 0.3849$ m², $\gamma_v = 6005$ kg/m, $br = 0.986$, where the symbols D_o and s denote respectively the outer diameter and the thickness of the circular cross-section. The meaning of the other parameters has been introduced in Sect. 2.1. Due to space constraints, results will be shown for a single anchoring element, located at a distance 2772 m from the left shore (see Fig. 2) and characterized by the parameters: $L_0 = 403.05$ m, $\theta = 45^\circ$ and $\lambda^2 = 0.0259$, the latter being computed for a value $\eta_0 = 20\%$.

3.1 Modeling of the Seismic Motion

For illustrative purposes, the case of horizontal seismic loading is herein considered. The procedure can be applied also to the case of vertical seismic motion. In the latter case, however, seaquake effects should be properly considered being, in principle, not negligible (see [16]).

The ground acceleration is modeled as a stationary zero-mean Gaussian random process described by a real symmetric Power Spectral Density (PSD) function defined according to the Modified Kanai-Tajimi (MKT) model [6].

The parameters of the MKT model were selected to give a response spectrum satisfying on average the horizontal acceleration response spectrum in Eurocode 8

for far field earthquakes and a soil type C for a Peak Ground Acceleration (PGA) of 1 m/s^2 (see [16]). Two additional values of PGA were also considered in the analyses, namely: 4 m/s^2 and 7 m/s^2 (the latter value being representative of design values of PGA at the considered site) and the PSD of the seismic input was re-scaled according to the criteria presented in [3].

3.2 Global Response of the SFT

The global response of the SFT is evaluated by neglecting the local vibration modes of the anchoring elements, through an application of the semi-analytical continuous model previously developed and described in [11, 12]. The SFT is modeled as a Euler-Bernoulli beam with constant cross section continuously supported by distribution of mass-less linear elastic springs (non-homogeneous Winkler-type soil), which represents the mooring system. The seismic motion is assumed acting in the horizontal direction, perfectly correlated along the tunnel and described according to the criteria presented in Sect. 3.1. Hydrodynamic effects are modeled in an equivalent linearized form and neglecting seaquake effects. An ad-hoc numerical simulation code was developed to perform both the global tunnel analyses and the local analyses of the anchoring elements through the application of the reduced-order model presented in Sect. 2.

3.3 Local Response of the Cable

Starting from knowledge of the PSD of the seismic acceleration and the transfer functions from the ground motion to tunnel displacements and accelerations, a set of $N_s = 100$ realizations of displacement and acceleration time histories of the end sections of the tether have been generated through a standard approach (see [20]). These realizations have been used as an input ($\bar{u}_i, \ddot{u}_i, \ddot{w}_i$, for $i = a, b$ and with $\bar{F}_{zm} = 0$; see Eq. 7) to analyze the local dynamic response of the anchoring elements. The non-linear equations of motion (7) have been numerically integrated by using a standard implicit Runge-Kutta time stepping algorithm (ode45 solver in Matlab). The results reported in the following were obtained by considering the first ten modes in the reduced-order model (i.e. $M = 10$).

Figure 3 depicts the Root Mean Square (RMS) value of the total stress σ_{tot} normalized with respect to the static stress σ_s as a function of the non-dimensional loading parameter η_0 (i.e. the ratio between the static stress of the tether and the yielding strength of the material). A box plot representation is adopted. Values in the box are comprised between the 25th and 75th percentile, whiskers refer to the 9th and 91th, while a “x” marker and circles identify respectively the mean and the outliers. Figure 3a refers to a PGA of 7 m/s^2 , while Fig. 3b shows a comparison among results calculated for three increasing PGA values, namely: 1 m/s^2 , 4 m/s^2

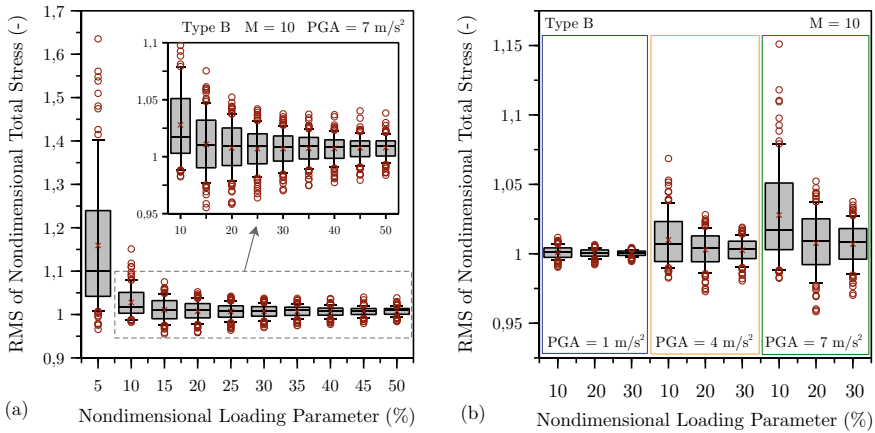


Fig. 3 RMS of the non-dimensional total stress σ_{tot}/σ_s

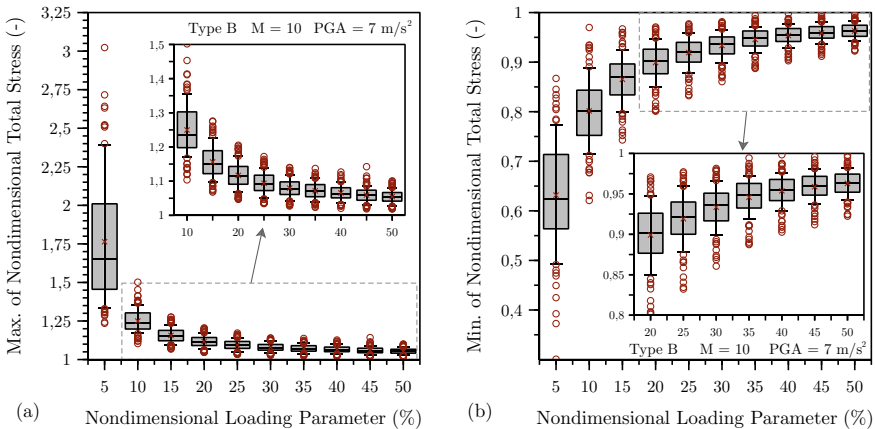


Fig. 4 Max. (a) and min. (b) values of the non-dimensional total stress σ_{tot}/σ_s

and 7 m/s². As it can be appreciated from the figures, by increasing the value of the non-dimensional loading parameter the mean value of the RMS tends, as expected, to the unit and the dispersion of the results decreases. The dependence of the axial stress on the input intensity, schematically depicted in Fig. 3b, turns out to be almost linear for this specific application.

Figures 4a and b depict, respectively, the maximum and minimum values of the total stress σ_{tot} normalized with respect to the static stress σ_s as a function of the non-dimensional loading parameter η_0 and for a PGA of 7 m/s². As expected, at the increase of η_0 , the maximum (minimum) values of σ_{tot}/σ_s approach the unit from above (below). Lower values of η_0 make the tether more prone to slackening phenomena, as the increase in dispersion and number of outliers point out (see Fig. 4b).

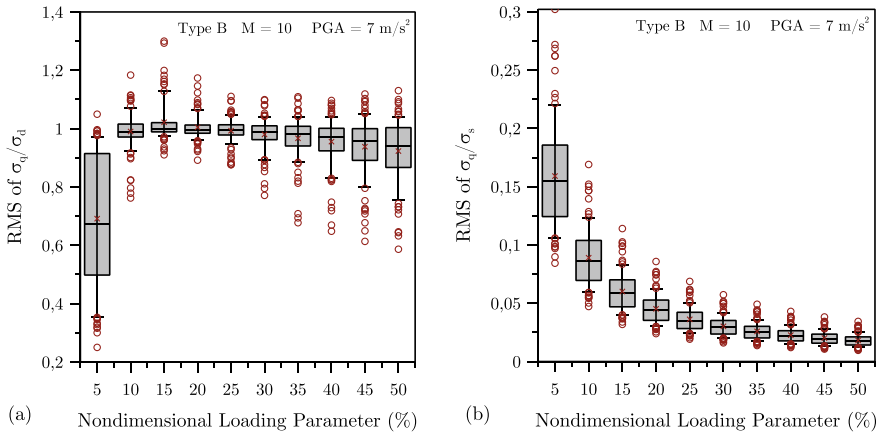


Fig. 5 **a** RMS of the ratio between the quasi-static and total dynamic stress. **b** RMS of the ratio between the quasi-static and static stress

This result highlights the importance of controlling the static tension in the tethers through selection of an appropriate value of the BWR, as already reported in the literature [19].

Figure 5a depicts, as a function of the non-dimensional loading parameter η_0 and for a PGA of 7 m/s^2 , the RMS of the ratio between the quasi-static component of the stress (σ_q) and the total dynamic stress ($\sigma_d = \sigma_q + \sigma_m$, where σ_m denotes the contribution of the local vibration modes of the tether—cf. [21]). Values close to one denote that the total dynamic stress is contributed mostly by the quasi-static component. For the application herein considered, this happens almost for the whole range of non-dimensional loading parameter η_0 .

Figure 5b reports the RMS of the ratio between the quasi-static component of the stress (σ_q) and the static stress (σ_s). In the original formulation, developed with reference to inclined stay cables in air, this ratio is assumed much smaller than one, and hence disregarded, while it has been fully included with its value in the herein proposed formulation. In fact, depending on the value of the loading parameter, the original assumption ($\sigma_q/\sigma_s \ll 1$) is not always justified.

4 Conclusions

In this paper, a reduced order model for inclined mooring cables has been developed and applied to study the local dynamic response of a SFT anchoring element through a simplified two-step procedure. The proposed formulation extends to the case of tethers immersed in water a model of the literature originally developed for inclined stay cables in air. Most notably, the proposed reduced-order model fully accounts for the contribution of the quasi-static stress, that, differently than for stay cables in

air, is shown to be in general not negligible compared to the static stress (i.e. the one due to the cable static tension).

The preliminary results reported in the paper highlight once more the importance of selecting an appropriate value of the tunnel BWR already stated in the literature. The BWR indeed controls the static tension in the elements and, hence, permits to limit the occurrence of slackening phenomena under design dynamic loading conditions. The proposed formulation can be regarded to as a simple yet accurate tool to investigate the local dynamics of the anchoring elements without resorting to complex and computationally expensive finite element models. Further research, however, is still needed and is currently ongoing to extend the proposed formulation to deal with different dynamic loading conditions, such as current-induced loads and seaquake effects, which may cause a more severe nonlinear response.

5 Coefficients of the Equation of Motion

$$\begin{aligned} \bar{\alpha}_m &= \frac{24 w_s(1 - br)L_0 \cos \theta}{(12 + \lambda^2)T_0\varepsilon_0 m^3 \pi^3} [1 + (-1)^{m+1}] & \bar{k}_m &= \frac{2\lambda^2}{\pi^4 m^4} [1 + (-1)^{m+1}]^2 \\ \bar{\beta}_{mk} &= \frac{w_s(1 - br) \cos \theta m^2 d}{2\pi T_0\varepsilon_0} \left[\frac{1 + (-1)^{k+1}}{k} \right] & \bar{\omega}_{zm} &= m \sqrt{1 + \bar{k}_m} \\ \bar{\beta}_{km} &= \frac{w_s(1 - br) \cos \theta k^2 d}{2\pi T_0\varepsilon_0} \left[\frac{1 + (-1)^{m+1}}{m} \right] & \bar{\zeta}_m &= \frac{2}{m\pi} \\ \tilde{\beta}_{mk} &= \frac{6w_s(1 - br) \cos \theta m^2 d^2}{(12 + \lambda^2)\pi L_0 T_0 \varepsilon_0^2} \left[\frac{1 + (-1)^{k+1}}{k} \right] & \bar{\eta}_m &= \frac{6m^2 d}{(12 + \lambda^2)L_0 \varepsilon_0} \\ \tilde{\beta}_{km} &= \frac{6w_s(1 - br) \cos \theta k^2 d^2}{(12 + \lambda^2)\pi L_0 T_0 \varepsilon_0^2} \left[\frac{1 + (-1)^{m+1}}{m} \right] & \bar{\nu}_{mk} &= \frac{\pi^2 m^2 k^2 d^2}{4\varepsilon_0 L_0^2} \\ \bar{\mu}_m &= \frac{24 w_s^2(1 - br)^2 d L_0 \cos^2 \theta}{(12 + \lambda^2)T_0^2 \varepsilon_0^2 m^2 \pi^4} [1 + (-1)^{m+1}]^2 & \bar{F}_{zm} &= \frac{2L_0 \int_0^{L_0} Z A_0 \psi_m dx}{\pi^2 T_0 d}. \end{aligned}$$

References

1. Ahrens D (1997) Submerged floating tunnels - a concept whose time has arrived. *Tunn Undergr Space Technol* 12:318–336
2. Bruschi R, Giardinieri V, Marazza R (1990) Merletti T (1990) Submerged buoyant anchored tunnels: technical solutions for the fixed link across the strait of Messina, Italy. In: Krokeborg J (ed) *Strait crossings*. Balkema, Rotterdam, pp 605–612
3. Buchholdt H (1997) *Structural dynamics for engineers*. Thomas Telford, London

4. Cantero D, Rønnquist A, Naess A (2017) Tension during parametric excitation in submerged vertical taut tethers. *Appl Ocean Res* 65:279–289
5. Chakrabarti SK (1987) *Hydrodynamics of offshore structures*. Computational Mechanics Publications, Springer, Berlin
6. Clough R, Penzien J (2003) *Dynamics of structures*, 3rd edn. Computers and Structures Inc, Berkeley
7. Denoël, V, Degee, A (2008) Comparison of parametric excitation and excitation of an elastic stay cable. In: *Proceedings of the seventh european conference on structural dynamics*, p 11
8. Desai YM, Punde S (2001) Simple model for dynamic analysis of cable supported structures. *Eng Struct* 23:271–279
9. Di Pilato M, Perotti F, Fogazzi P (2008) 3D dynamic response of submerged floating tunnels under seismic and hydrodynamic excitation. *Eng Struct* 30(1):268–281
10. Fogazzi P, Perotti F (2000) The dynamic response of seabed anchored floating tunnels under seismic excitation. *Earthquake Eng Struct Dynam* 29:273–295
11. Foti F, Martinelli L, Perotti F (2023) A semi-analytical model for the design and optimization of SFTs under seismic loading. In: *Bridge safety, maintenance, management, life-cycle, resilience and sustainability (IABMAS 2022)*, pp 1117–1121
12. Foti F, Martinelli L, Morleo E, Perotti F (2023) Dynamic response of submerged floating tunnels: an enhanced semi-analytical approach. *Submitted to Ocean Engineering*, p 24
13. Gattulli V, Lepidi M (2007) Localization and veering in the dynamics of cable-stayed bridges. *Comput Struct* 85(21–22):1661–1678
14. Irvine HM (1981) *Cable structures*. The MIT Press series in structural mechanics, The MIT Press Cambridge, Massachusetts
15. Jakobsen B (2010) Design of the submerged floating tunnel operating under various conditions. *Proc Eng* 4:71–79
16. Martinelli L, Barbella G, Feriani A (2011) A numerical procedure for simulating the multi-support seismic response of submerged floating tunnels anchored by cables. *Eng Struct* 33(10):2850–2860
17. Martinelli L, Domaneschi M, Shi C (2016) Submerged floating tunnels under seismic motion: vibration mitigation and seaquake effects. *Proc Eng* 166:229–246
18. Mazzolani FM, Landolfo R, Faggiano B, Esposito M, Perotti F, Barbella G (2008) Structural analyses of the submerged floating tunnel in Qiandao lake (Pr of China). *Adv Struct Eng* 11:439–454
19. Perotti F, Foti F, Martinelli L, Tomasin M (2018) SFTs under dynamic loads: new design issues and numerical simulation. In: *Maintenance, safety, risk, management and life-cycle performance of bridges (IABMAS 2018)*, pp 885–892
20. Shinozuka M (1971) Simulation of multivariate and multidimensional random processes. *J Acoust Soc Am* 49:357–368
21. Warnitchai P, Fujino Y, Susumpow T (1995) A non-linear dynamic model for cables and its application to a cable-structure system. *J Sound Vib* 187(4):695–712
22. Wilson JF (1984) *Dynamics of offshore structures*. Wiley Inc, Hoboken

3D Finite Element Modelling of Conductor-Clamp Assemblies Under Cyclic Bending: Sensitivity Analysis of Wire Contact Coefficient of Friction



Sébastien Lalonde , Leticia Kared, Raynald Guilbault, and Sébastien Langlois

Abstract Recent advances in numerical modelling now allow 3D analysis of complete conductor-clamp assemblies under multiaxial loading, while considering all wire interactions. In-depth studies simulating complex problems, such as wind-induced overhead conductor fatigue, are now possible. Providing detailed wire stresses and contact load distributions in the vicinity of suspension clamps, these models lead to refined conductor service life estimations. However, owing to its stranded configuration and multiple wire interactions, conductor kinematics is intricate and depends on material tribological properties. On the other hand, applications of conductor-clamp models commonly assume a uniform and constant adhesion coefficient of friction (μ_a). In reality, μ_a may vary over time with surface degradation. Therefore, numerical solutions that use a single μ_a value could provide incomplete information and thus, lead to inaccurate conclusions. Using an efficient and proven multilayered strand modelling strategy based on 3D beam-to-beam contacts, this study investigates the influence of the coefficient of friction (μ_a) on full conductor-clamp model solutions. Mapped distributions of wire stresses and local contact conditions are used to characterize the overall influence of the coefficient of friction on the model solution. Exploiting a factorial design approach, the analyses also highlight the cross-influence between the μ_a level and conductor axial tension and cyclic bending amplitude.

Keywords Overhead conductors · 3D conductor-clamp modelling · Wind-induced cyclic bending · Inter-wire contact · Coefficient of friction

S. Lalonde (✉) · L. Kared · R. Guilbault
Department of Mechanical Engineering, École de Technologie Supérieure, Montreal, QC, Canada
e-mail: sebastien.lalonde@etsmtl.ca

S. Langlois
Department of Civil Engineering, Université de Sherbrooke, Sherbrooke, QC, Canada

1 Introduction

Overhead conductors are highly vulnerable to wind-induced vibrations, especially near restraining fixtures such as the suspension clamps [1]. At these critical locations, vibrations produce cyclic bending loads promoting fretting fatigue and wear at inter-wire contact interfaces (Fig. 1). These degradation mechanisms can compromise conductor integrity and progressively lead to wire failures. Predicting and preventing conductor damage is therefore crucial to ensure the reliability of electrical transmission lines.

The stranded conductor geometry combined to its loading conditions in the clamped region is intricate to analyze, but recent progress in computer-assisted engineering now offers the capabilities to simulate such complex systems [2, 3]. Usually developed with the Finite Element (FE) method, conductor-clamp models account for all wire-to-wire and wire-to-clamp contact interactions. The FE modelling of the clamp is generally similar in all models, whereas the conductor geometry can be modelled using 3D solid elements [2] or beam elements [3]. In both cases, each individual wire is discretized and all inter-wire contacts are included by means of contact elements. Conductor loading usually considers first, an axial tension (T) applied at the conductor extremities with a static sag angle (β_0). The wind-induced dynamic loading is then added through a cyclic variation of T application angle ($\pm\Delta\beta$), usually targeting a specified deflection amplitude, computed at 89 mm from the clamp exit (Y_b) [3]. From the simulation results, wire stresses and contact forces are obtained and can therefore be used for detailed fretting analysis [4, 5] or to estimate conductor fatigue damage [6].

However, conductor-clamp FE models involve many geometric, load and material parameters that may influence the precision of the obtained numerical solutions. With the conductor kinematics being directly related to frictional interactions at wire contacts, the adhesion coefficient of friction (μ_a) used in conductor-clamp FE models is particularly important. On the other hand, most conductor-clamp FE model

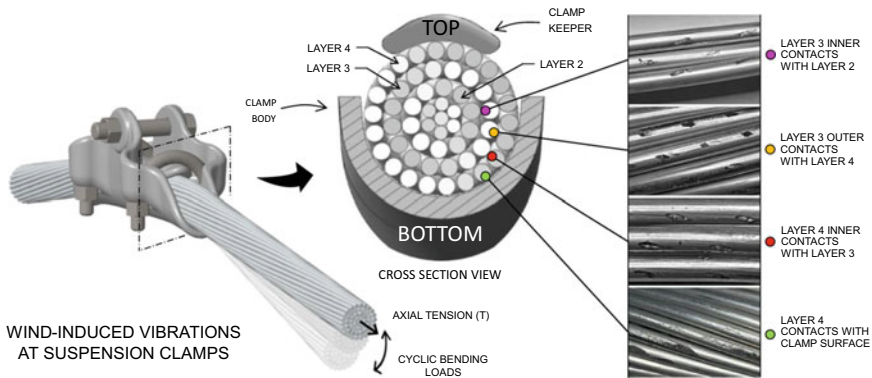


Fig. 1 Wind-induced vibrations at suspension clamps and examples of inter-wire contact marks

applications assume a constant μ_a value at all contact points [2, 3, 6]. This modelling assumption does not account for the effects of contact loading, surface degradation and other environmental factors that may result in fluctuation of μ_a over time [7].

A preliminary investigation on the influence of μ_a on the conductor FE model results is proposed in [8]. The study revealed an increasing effect on local wire stress amplitude (σ_a) for higher μ_a values, especially at the outer layer wires and for high deflection amplitudes (i.e., $Y_b > 0.5$ mm). Although the work presented in [8] is based on a 3D conductor FE model using beam elements, it does not include the clamp effect and the study was limited to a single conductor tension (T) level.

Therefore, the sensitivity of conductor-clamp FE models to the coefficient of friction parameter (μ_a) needs to be assessed, to ensure cautious interpretations of simulation results. This work thus extends the numerical characterization proposed by the authors in the present proceedings [9] with the integration of the coefficient of friction (μ_a) effect on the conductor-clamp FE model response. The study focuses on the μ_a influence regarding the local wire solicitation at the contact points.

2 Numerical Modelling and Analysis Approach

As with the previous numerical characterization performed in [9], the ACSR Bersfort case study is considered in this analysis. Therefore, both the conductor and the short-radius metallic suspension clamp have the same geometric and material configurations presented in [9].

2.1 Conductor-Clamp Finite Element Model

General FE modelling approach. The beam element-based modelling strategy [3] is also exploited in this study to model the conductor-clamp assembly. Since the methodology has been thoroughly demonstrated in [3] and also briefly covered in [9], details of the FE modelling are omitted here.

Inter-wire contact modelling. The applied conductor-clamp model uses a line-to-line contact algorithm to account for all wire-to-wire and wire-to-clamp interactions. Contact friction is considered with the Coulomb frictional law, relating the computed normal (P) and tangential (Q) contact forces to the adhesion coefficient of friction (μ_a). Wires are thus in stick condition for $|Q| \leq \mu_a P$ and start sliding when $|Q|$ reaches $\mu_a P$.

Boundary conditions and load applications. The applied conductor loads and constraints are presented in Fig. 2. Details of their application process are also given in [9], simply recalling here that the static sag angle (β_0) is set to 5° and the clamping force (F_c) to 74.5 kN. Specifications on the conductor tension (T) and deflection

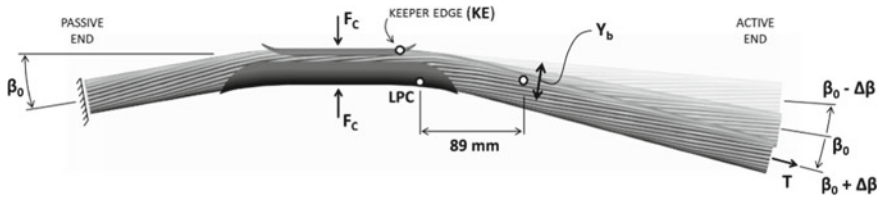


Fig. 2 ACSR Bersfort loading configuration

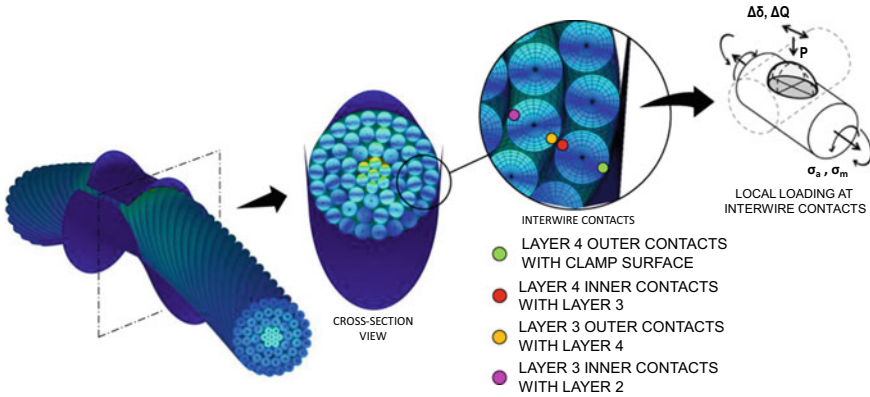


Fig. 3 Wire stresses and contact loads post-processing at inter-wire contact points

amplitude (Y_b) at 89 mm from the Last Point of Contact (LPC) are discussed in Sect. 2.2.

Simulation results post-processing. In this work, the influence of μ_a is characterized with respect to the local loading conditions at inter-wire contact points. Figure 3 illustrates the inter-wire contact locations where local loads and stresses are extracted from the simulations results. The retrieved information includes the normal (P) and tangential (Q) contact forces, along with the relative contact displacement (δ). The wire stress amplitude (σ_a) and mean stress (σ_m) at inter-wire contacts are also extracted.

2.2 Factorial Design Approach

This study builds upon the characterization results obtained in [9], which employed a two-factor and three-level full factorial design, considering the conductor axial tension (T) and the bending amplitude (Y_b) as factors. To analyze the influence of the coefficient of friction, this design of experiments (DOE) used in [9] is extended

Table 1 DOE factors and levels

Levels	Factors		
	T (% RTS)	Y _b (mm)	μ _a
1	15	0.3	0.7
2	25	0.5	0.9
3	35	0.7	1.1

*ACSR Bersfort Rated Tensile Strength (RTS) = 180.1 kN

with the introduction of μ_a as a third factor, including also 3 levels. The new full factorial design thus requires 3³ simulations to cover all factor combinations.

Table 1 presents the factor values for each level, with tensions (T) and Y_b amplitudes remaining unchanged from the initial DOE. It is to be reminded that Y_b amplitudes are indirectly induced through the variation of T application angle (±Δβ). Levels for μ_a were defined to encompass the range of the coefficient of friction values observed experimentally and reported in published fretting tests on conductor wires [2, 10].

3 Coefficient of Friction Analysis

3.1 Relation Between Δβ and Y_b

The influence of the coefficient of friction is first examined macroscopically through global conductor dynamics. Thus, Fig. 4 shows the evolution of the Δβ angle required to achieve each Y_b level at the three tensions (T).

From the results in Fig. 4, a smaller impact of μ_a can be observed at low Y_b and high T values. This is explained with the low deflection amplitudes being insufficient to initiate wire sliding and the high tensions increasing the inter-wire normal contact

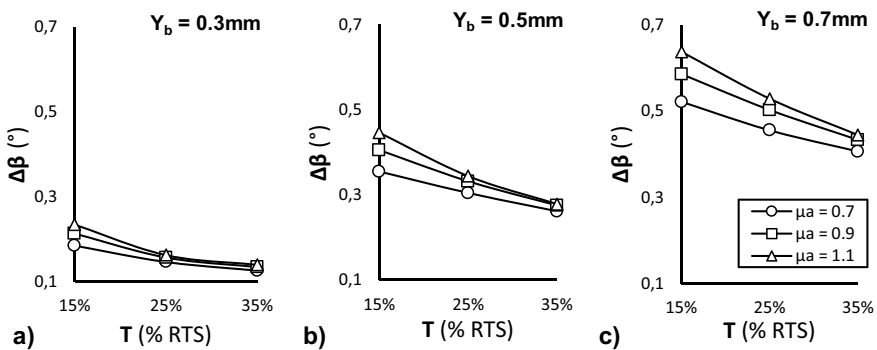


Fig. 4 Δβ variation with tension T at **a** Y_b = 0.3 mm, **b** Y_b = 0.5 mm and **c** Y_b = 0.7 mm

forces (P), also preventing sliding. Conversely, μ_a has a greater effect at low-tension values. Overall, the impact of the coefficient of friction on conductor dynamics appears to be moderate at a macroscopic level, though it seems to amplify as μ_a decreases.

3.2 Coefficient of Friction Influence on Local Loading Distribution

The effect of the coefficient of friction on the local loading distribution of the wires is investigated using the same inter-wire contact mapping representation developed in [9]. Figures 5 and 6 present the wire stress amplitudes (σ_a) computed at $Y_b = 0.3$ and 0.7 mm respectively, for mid-level tension (T) at 25% RTS and μ_a levels at 0.7 and 1.1. Stress mappings are given for layers 3 and 4 inter-wire contacts, which are located between 0 and 100 mm from the clamp center.

The mappings include the contact statuses established from the prevailing local contact forces (i.e. P and Q) at each contact point. As explained in [9], four contact state conditions are possible: sticking, sliding, slipping and no contact. The contact point marker shape indicates the contact status in Figs. 5 and 6. This combined representation enables refined wire stresses interpretations in conjunction with the contact conditions, making it an effective way to identify critical contact locations susceptible to fatigue damage.

Consequently, the Smith–Watson–Topper criterion (σ_{SWT} —Eq. 1) is used in this work to locate the most critical contacts. The ten most critical points are circled in red and ranked in order of criticality in Figs. 5 and 6.

$$\sigma_{SWT} = \sqrt{\langle \sigma_{max} \rangle \cdot \sigma_a} = \sqrt{\langle \sigma_m + \sigma_a \rangle \cdot \sigma_a} \quad (1)$$

As noted in [9], the SWT criterion predicts no damage for compressive maximum stress (i.e. $\sigma_{max} < 0$), which does not concur with observations during conductor fatigue tests [11]. Therefore, the SWT evaluation is adapted in this study to neglect the effect of compressive mean stresses (i.e. σ_m is set to 0 for $\sigma_m < 0$), but to always account for the σ_a effect. The implemented critical contact point detection is also limited to a single critical point per wire, assuming the wires can only fail at a single point.

A first examination of the results in Figs. 5 and 6 indicates slightly higher maximum stress amplitudes (σ_a) for $\mu_a = 0.7$. Conversely, the high stress region is dispersed over a larger number of contact points with $\mu_a = 1.1$, resulting in a slightly reduced stress amplitude (σ_a).

At lower bending amplitudes ($Y_b = 0.3$ mm), the μ_a effect on the contact statuses is minimal, whereas it becomes more significant as Y_b increases, resulting in a higher number of inter-wire contacts in sliding and slipping mode at $\mu_a = 0.7$.

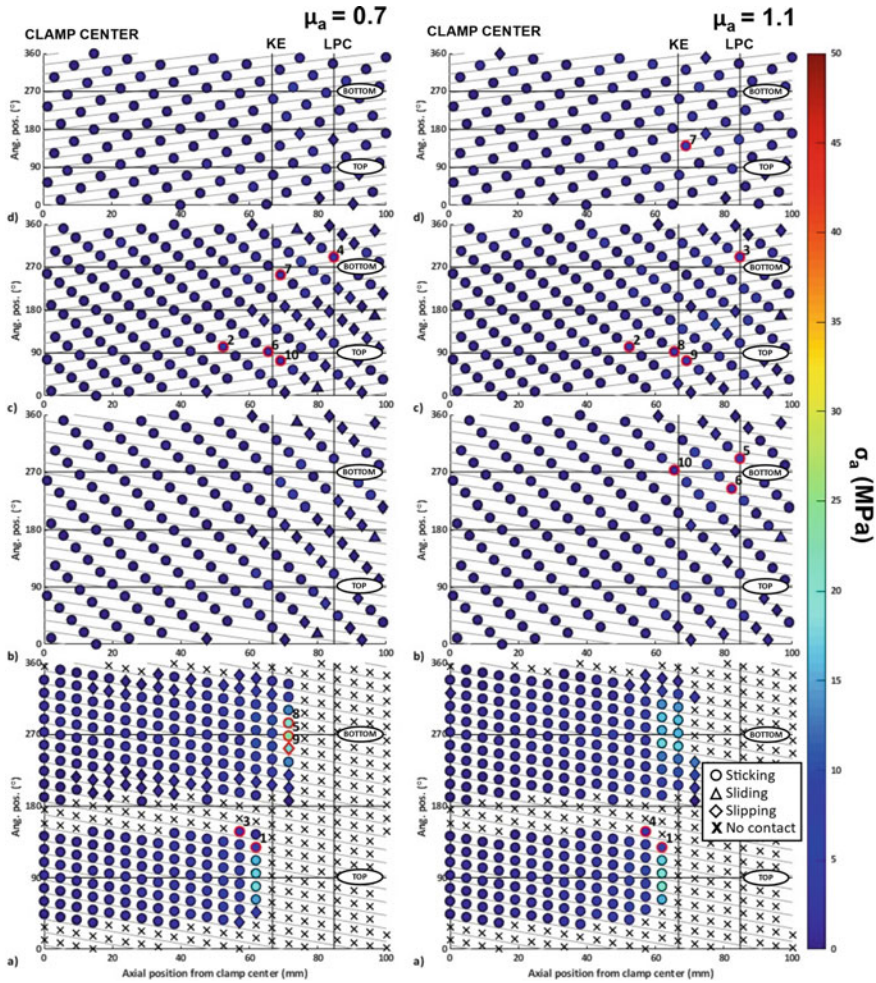


Fig. 5 Wire stress amplitude (σ_a) at **a** layer 4 outer contacts with clamp surface, **b** layer 4 inner contacts with layer 3, **c** layer 3 outer contacts with layer 4 and **d** layer 3 inner contacts with layer 2, for $T = 25\%$ RTS and $Y_b = 0.3$ mm ($\mu_a = 0.7$ —left charts, $\mu_a = 1.1$ —right charts)

The distributions of critical points are similar for $\mu_a = 0.7$ and 1.1, but lower values of μ_a lead to more critical points at wire-to-clamp contacts on the conductor’s bottom side.

As pointed out in [9], the SWT criterion always predicts the first critical point to be at a wire-to-clamp contact on the conductor top side, which is mainly due to the high mean stresses in this region.

To provide a comprehensive overview of the wire stress distribution across the entire DOE, Fig. 7 presents the variation of σ_{SWT} and σ_a with respect to μ_a , for all

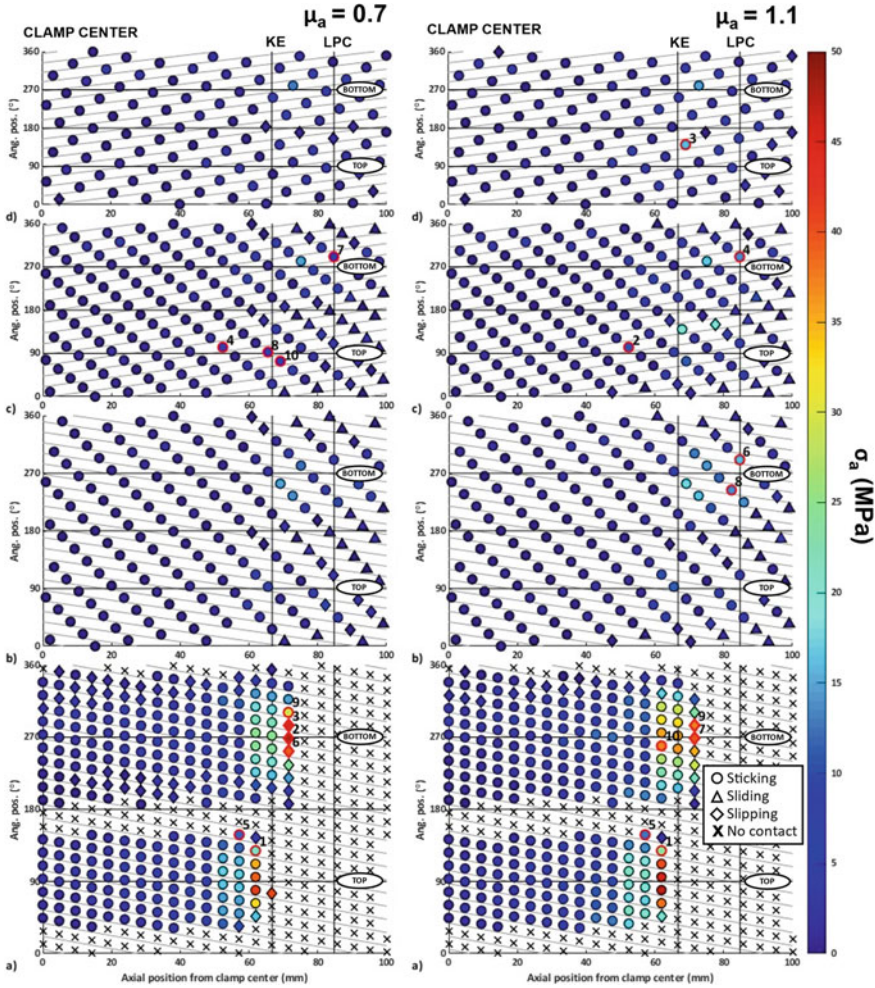


Fig. 6 Wire stress amplitude (σ_a) at **a** layer 4 outer contacts with clamp surface, **b** layer 4 inner contacts with layer 3, **c** layer 3 outer contacts with layer 4 and **d** layer 3 inner contacts with layer 2, for $T = 25\%$ RTS and $Y_b = 0.7$ mm ($\mu_a = 0.7$ —left charts, $\mu_a = 1.1$ —right charts)

Y_b - T combinations. The curves that correspond to the top five σ_{SWT} and σ_a values are plotted in Fig. 7 and identified as ranked critical contact points.

The curves associated with σ_{SWT} in Fig. 7 demonstrate an increasing effect of μ_a on the criterion, but only for the most critical point (1st), while the other four points have much lower σ_{SWT} values. The situation is quite different for critical contact points based solely on σ_a values. Globally, the μ_a effect is less important for σ_a and leads to a more uniformed variation of the criterion from the 1st to the 5th critical contact points. These observations suggest that the influence of μ_a on fatigue damage

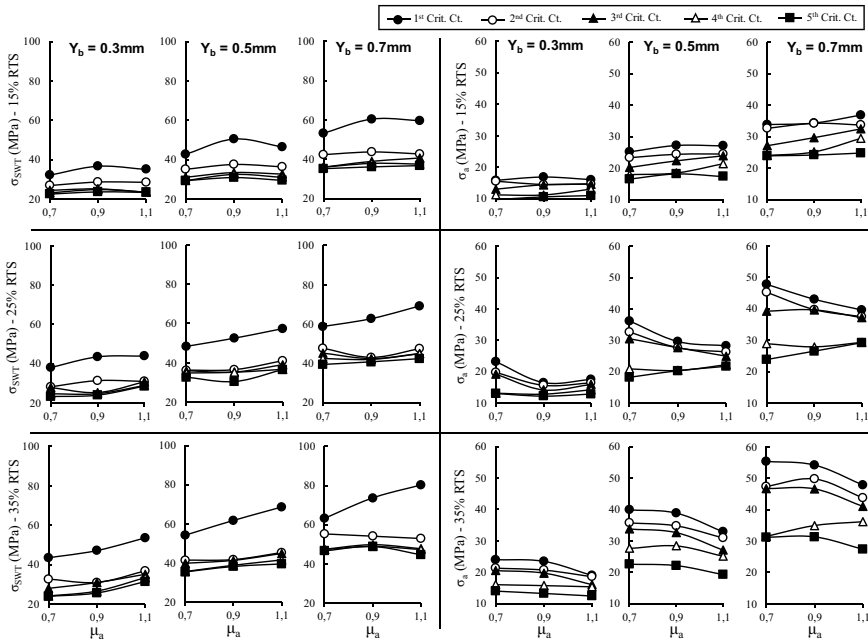


Fig. 7 Influence of μ_a on the SWT criterion (σ_{SWT} —left charts) and the wire stress amplitude (σ_a —right charts) variation for all Y_b - T combinations at the five most critical contact points

prediction may be greater for a fatigue criterion that accounts for the mean stress (σ_m).

3.3 Coefficient of Friction Interrelations with Loading Parameters

This section examines the interrelations between the DOE factors. As highlighted in the previous characterization study [9], factor cross-influence analysis is more informative when considering the local loading at the critical contact points. Thus, first-order interrelation plots between μ_a and Y_b are given at Fig. 8 for all T levels, with respect to the local loading conditions of the same critical wire-to-clamp contact point investigated in [9].

Figure 8 demonstrates a significant interactions between Y_b and μ_a , for tangential contact loading (ΔQ) and slip ($\Delta\delta$) variations. Similar interaction levels are also observed between factors T and μ_a , but in this case, for all local loading parameters. From Fig. 8 results, it can also be concluded that μ_a has a general influence on all local contact load and stress parameters, for most Y_b - T combinations.

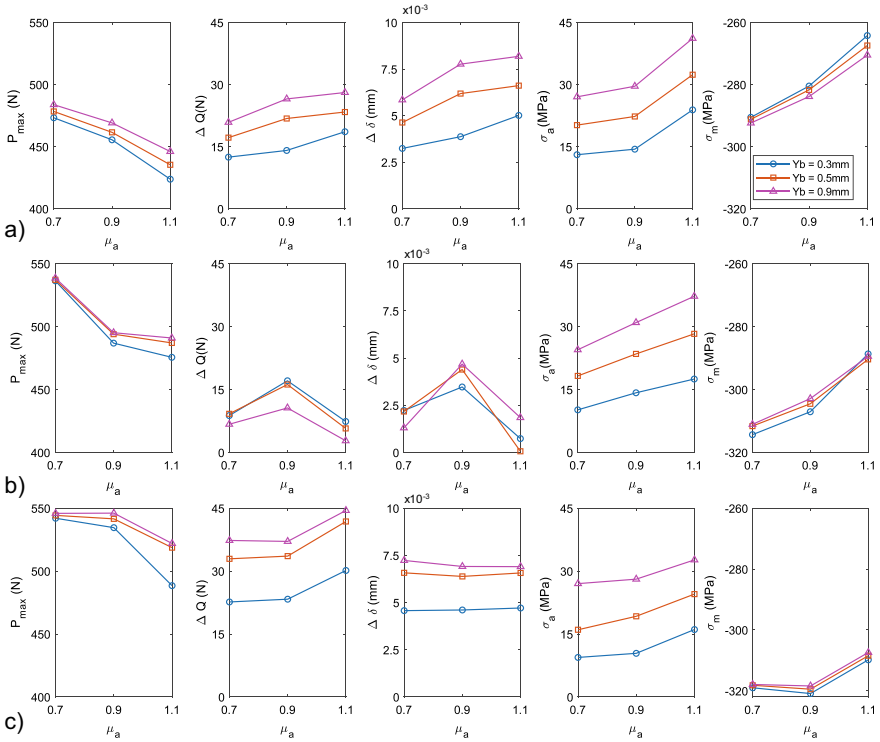


Fig. 8 Two-Factor interrelations between Y_b and μ_a for local loads and stresses at a critical contact point for **a** $T = 15\%$ RTS, **b** 25% RTS and **c** 35% RTS

3.4 Coefficient of Friction Influence on Local Loading Variation

Local loading conditions of the critical contact point depicted in Fig. 8 is examined over a full bending cycle (i.e., $\pm \Delta\beta$). Figure 9 plots the variation of P , Q and σ obtained with $\mu_a = 0.7$ and 1.1 at the mid-level tension $T = 25\%$ RTS.

From Fig. 9 a constant normal force (P) is noticed with $\mu_a = 0.7$, while it varies moderately at higher μ_a level. The tangential force (Q) variation profile is more affected by μ_a , particularly as Y_b increases. Meanwhile, the wire stress variation is essentially influenced in terms of the magnitudes of σ_a and σ_m , as shown in Fig. 8.

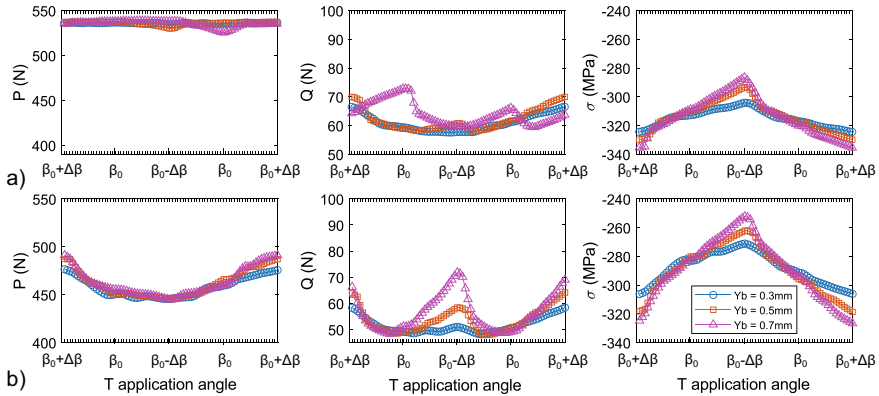


Fig. 9 Critical point cyclic loading variation at $T = 25\%$ RTS with **a** $\mu_a = 0.7$ and **b** $\mu_a = 1.1$

4 Conclusion

This study investigated the effect of the coefficient of friction (μ_a) on the conductor local loading conditions near the suspension clamp, based on FE models and a three-factor DOE including factors Y_b , T and μ_a . Using wire stress and contact load mappings, along with detailed load variation analysis at a critical location, the study revealed the general influence of μ_a on all local solicitation parameters. Therefore, it appears crucial to carefully consider the chosen value of μ_a when modelling conductor-clamp assemblies, as it can directly affect conductor fatigue life estimations.

Acknowledgements The authors acknowledge the support of the Natural Sciences and Engineering Research Council of Canada (NSERC).

References

1. Ouaki B (2003) Fretting fatigue analysis of aluminium conductor wires near the suspension clamp. *J Strain Anal Eng Des* 38(2):133–147
2. Said J (2020) A multi-scale strategy to predict fretting-fatigue endurance of overhead conductors. *Tribol Int* 143:106053
3. Lalonde S (2018) Numerical analysis of ACSR conductor-clamp systems undergoing wind-induced cyclic loads. *IEEE Trans Power Del* 33(4):1518–1526
4. Said J (2023) A global–local approach to predict the fretting-fatigue failure of clamped aluminum powerline conductors: from mono-contact crossed wires to full conductor vibrational tests. *Eng Fail Anal* 146:107073
5. Omrani A (2021) Fretting fatigue life assessment of overhead conductors using a clamp/conductor numerical model and biaxial fretting fatigue tests on individual wires 44(6), 1498–1514

6. Rocha PHC (2022) A general life estimation method for overhead conductors based on fretting fatigue behavior of wires. *Theo Appl Frac Mech* 121:103443
7. Hintikka J (2019) Stable and unstable friction in fretting contacts. *Tribol Int* 131:73–82
8. Lalonde S (2017) Modeling multilayered wire strands, a strategy based on 3D finite element beam-to-beam contacts—Part II. *Intl J Mech Sci* 126:297–307
9. Kared L (2023) Numerical characterization of overhead conductor local loading conditions at wire contact points in the vicinity of suspension clamps. In: 3rd international symposium on dynamics and aerodynamics of cables proceedings. Springer, Rome, p 10
10. Omrani A (2022) Friction properties at the contact interfaces of overhead line aluminium conductors. *IEEE Trans Power Del* 37(1):442–448
11. Levesque F (2005) Étude de l'applicabilité de la règle de Palmgren-Miner aux conducteurs électriques sous chargements de flexion cyclique par blocs. Université Laval, Québec

Numerical Characterization of Overhead Conductor Local Loading Conditions at Wire Contact Points in the Vicinity of Suspension Clamps



Liticia Kared, Sébastien Lalonde , Sébastien Langlois, and Raynald Guilbault

Abstract Wind-induced vibration is one of the main causes of overhead conductor fatigue, especially at the suspension points. These critical locations involve several inter-wire contact points prone to fretting damage due to conductor cyclic bending. Assessing the severity of these local loading conditions is therefore essential to better understand, predict, and prevent conductor failures. Available numerical models allow full 3D representations of conductor-clamp systems under cyclic bending, while considering all local contact interactions. Exploiting a recent finite element model based on an efficient beam-to-beam contact modelling strategy, this paper proposes a complete numerical characterization of conductor local loading conditions in the vicinity of suspension clamp. The study considers an ACSR Bersfort conductor installed in a short-radius metallic suspension clamp and subjected to cyclic bending loads associated to Aeolian vibrations. Using a factorial design of experiments (DOE), the characterization considers two key factors: the bending amplitude (Y_b) and the conductor axial tension (T), each at three levels. From the DOE simulation results, the analyses highlight the parameter interactions with respect to the local loading conditions: wire mean (σ_m) and alternating (σ_a) bulk stresses, normal (P) and tangential (Q) inter-wire contact forces and the contact slip (δ). Results from the DOE thus provide a global and detailed description of the relationships between the external loads and local loading conditions being at the origin of conductor fretting fatigue damage. Under given Y_b and T conditions, the proposed characterization therefore allows the identification of the critical contact points and their associated local solicitation for further in-depth and targeted investigations.

Keywords Overhead conductors · Suspension clamp · Wind-induced vibrations · Local loading conditions · Wire contact points · Finite element · Factorial design

L. Kared · S. Lalonde (✉) · R. Guilbault
Department of Mechanical Engineering, École de Technologie Supérieure, Montreal, Canada
e-mail: sebastien.lalonde@etsmtl.ca

S. Langlois
Department of Civil Engineering, Université de Sherbrooke, Sherbrooke, Canada

1 Introduction

Overhead power lines are aging in many countries and this is becoming a major concern for Transmission System Operators (TSO). Assessing conductor residual strength and life is therefore crucial for in order to prioritize maintenance and replacement operations on electrical transmission networks.

Exposed to wind-induced vibrations, overhead conductor degradation mostly originates from cyclic bending loads, producing fretting fatigue damage at inter-wire contacts near the suspension clamps (Fig. 1) [1]. These mechanisms are complex and difficult to quantify, especially considering the stranded geometry involving hundreds of inter-wire contacts in the clamped region. Therefore, conductor fatigue is commonly assessed indirectly from the axial tension (T) and the double-bending amplitude Y_b , measured at 89 mm from Last Point of Contact (LPC) at the clamp exit. Interpreted with the well-known Poffenberger-Swart (P-S) relation (Eq. 1), an idealized stress amplitude (σ_a) can be estimated.

$$\sigma_a = \frac{d_c E_c (T/4EI)}{e^{-\sqrt{T/EI}z} - 1 + \sqrt{T/EI}z} Y_b \tag{1}$$

In Eq. 1, d_c , E_c , EI and z refer to the wire diameter and its elastic modulus, the conductor minimum bending stiffness and the axial position from the LPC (i.e. 89 mm), respectively. Despite the P-S simplifications, it correlates well with experimental fatigue test data and thus, represents a useful indicator to assess the vibration severity. However, it does not provide any direct and detailed information related to the inter-wire local loadings leading to conductor fatigue damage. Indeed, depending on the wire normal (P) and tangential (Q) contact loads, combined to bulk static (σ_m) and dynamic (σ_a) stresses, fretting-induced damage may vary from fatigue cracking to surface wear.

Thus, to better describe and quantify conductor fretting, detailed Finite Element (FE) models of wire-to-wire [2] and wire-to-clamp [3] contacts are proposed in the literature. These models provide complete stress field descriptions at the contact interfaces from local loading inputs (e.g. P , Q , σ_m and σ_a), allowing then refined interpretations of the damaging mechanisms. However, the prediction quality of these

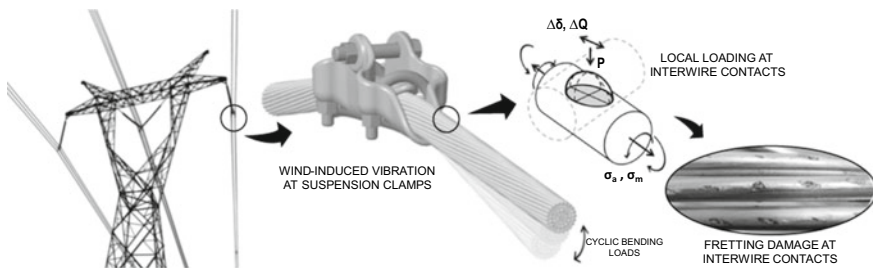


Fig. 1 Overhead conductor wind-induced fretting damage at suspension clamps

models highly depends on the representativeness of the considered local loading conditions, for a given conductor-clamp geometry and load configuration.

Precise estimations of local loading conditions are usually limited with available analytical and semi-analytical approaches. Due to the advances in numerical analysis, recent studies are now proposing full 3D conductor-clamp FE models simulating the effects of wind-induced cyclic bending, while including all wire contact interactions [4–6]. The local loading conditions (i.e. σ_a, σ_m, P, Q and δ) can therefore be extracted from simulation results at any of the inter-wire interfaces.

Towards a better understanding of the relations between the contact points conditions under given conductor static (T) and dynamic (Y_b) solicitations, this work proposes a numerical characterization of wire local loading in the vicinity of suspension clamp. The study is based on the application of a conductor-clamp FE model developed by Lalonde et al. [5] and considering the ACSR Bersfort conductor case study. The correlations between conductor local loading distributions and external loads (i.e. Y_b, T) are analyzed through a factorial DOE.

2 Numerical Design of Experiments

2.1 Conductor-Clamp Configuration

The characterization study is conducted on an ACSR Bersfort mounted in a short-radius metallic suspension clamp, schematically represented in Fig. 2. Additional geometric information on this conductor-clamp configuration can be found in [7].

Figure 2 also indicates the LPC reference location as per observations in [8]. The ACSR Bersfort stranding configuration is given in Table 1 with n_i, d_i, α_i, E_i and

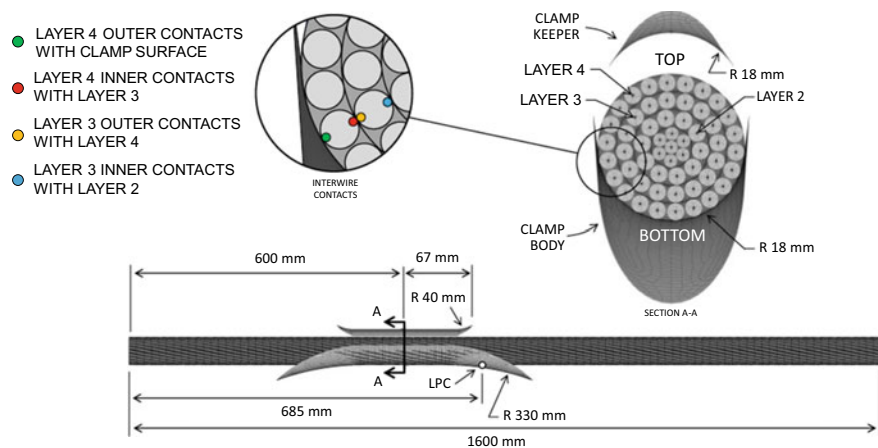


Fig. 2 ACSR Bersfort conductor-clamp configuration and inter-wire contacts identification

Table 1 ACSR* Bersfort stranding configuration

Layer	n_i	d_i (mm)	α_i (°)	E_i (GPa)	ν_i
Core	1	3.32	–	207 (steel)	0.3
1	6	3.32	6.2	207 (steel)	0.3
2	10	4.27	9.7	69 (alu.)	0.33
3	16	4.27	10.7	69 (alu.)	0.33
4	22	4.27	11.7	69 (alu.)	0.33

*ACSR: Aluminium Conductor Steel Reinforced

Table 2 DOE factors and levels

Levels	Factors	
	T (% RTS)	Y_b (mm)
1	15	0.3
2	25	0.5
3	35	0.7

ν_i referring to the layer i wire number, the wire diameter, the lay angle, the elastic modulus and the Poisson ratio. This conductor has a Rated Tensile Strength (RTS) of 180.1 kN.

2.2 DOE Factors and Levels

The proposed factorial design includes two important factors related to conductor fatigue: 1—the conductor axial tension T and 2—the double-bending amplitude Y_b . Each factor is considered at 3 levels, whose values are presented in Table 2.

Axial tensions are expressed in percentage of the conductor RTS and covers the usual range of tensions seen in overhead power lines [7]. On the other hand, the Y_b levels were defined to ensure they correspond to a vibration intensity sufficient to produce fatigue damage. Thus, Y_b level 1 was set just above the ACSR Bersfort endurance limit estimated between 0.20 and 0.25 mm, using the P.S. formulation (Eq. 1) as per the methodology defined in [7]. The other two Y_b levels correspond to the amplitudes used in fatigue tests published on the same conductor [9]. Therefore, the factorial design needs 3^2 simulations to cover all factor combinations.

2.3 Conductor-Clamp Finite Element Model

FE modelling approach. Numerical simulations are performed using a 3D conductor-clamp FE modelling strategy developed by Lalonde et al. [5, 10]. The

formulation and validation of the approach are fully detailed in these references. Therefore, only basic principles are recalled here.

Implemented within the commercial FE software Ansys®, the approach is based on an effective use of 3-nodes beam elements to model each conductor wire, while the clamp geometry is represented with rigid quadratic surface elements (Fig. 3). Beam elements are 10 mm long and surface elements have an average size of 2.5 mm.

Wire lateral and radial contact interactions are handled with a 3D line-to-line algorithm using master–slave contact pairs. Similarly, a 3D line-to-surface algorithm handles wire-to-clamp contacts. In all cases, frictional effects are considered with the Coulomb law and an adhesion friction coefficient (μ_a) [10]. In the present model, $\mu_a = 0.9$ for aluminium-aluminium contacts [4], whereas values of 0.3 and 0.5 are used for steel-steel and aluminium-steel contacts [5], respectively.

Boundary conditions and load application. Conductor loads and constraints are induced at both of its extremities, modelled as rigid surfaces through node DOF coupling [5]. Using a pilot node on each rigid clamp surface, the clamp body is fully constraint, while the keeper has only its vertical translation allowed.

Conductor static and dynamic loads, shown in Fig. 4, are induced within a multiple-step process in quasi-static mode. First, the axial tension T is applied at both conductor ends with a static sag angle (β_0), set to 5° in the present study. Once force T is fully applied at β_0 , the conductor passive end is fixed in place and a clamping force F_c of 74.8 kN is induced to the keeper, reproducing a clamping torque of 47.5 Nm. When F_c is reached, the keeper surface is locked in place.

The next load steps are related to the dynamic loading induced through a $\pm \Delta\beta$ variation of T application angle, from its static position β_0 . The angle variation $\Delta\beta$ is determined iteratively to produce the desired Y_b bending amplitude. In order to

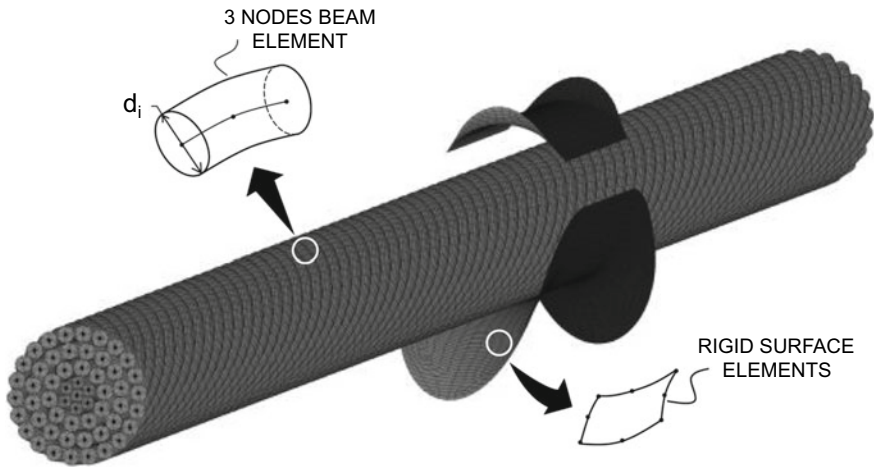


Fig. 3 Conductor-clamp FE model

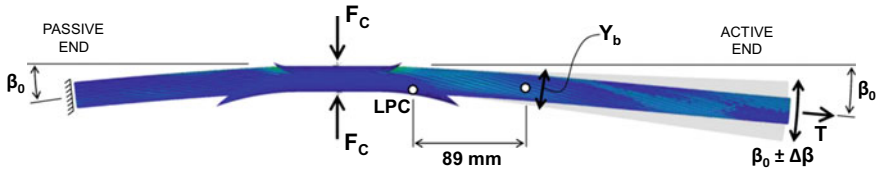


Fig. 4 Conductor-clamp external load configuration

fully capture the local loading evolution during cyclic bending, each angle variation ($\Delta\beta$) is applied within 20 load increments.

3 DOE Response Analysis

From DOE simulation results, the wire local loading conditions are analyzed through all inter-wire contacts. The analysis focuses on the clamped region, including contact points located between 0 and 100 mm from the clamp center, along the conductor axis.

3.1 Local Loading Distribution

To provide a global perspective on the local loading severity, the wires stress amplitude (σ_a) distributions are analyzed first. Stress amplitudes values (σ_a) are thus retrieved from FE results at each wire contact points and mapped onto each interlayer interfaces (see contact identifications in Fig. 1), using a layout similar to [5, 11].

The maps also include the contact points statuses according to four state conditions: sticking, sliding, slipping (i.e. partial relative displacement) and no contact. Contact statuses are established based on the computed normal (P) and tangential (Q) forces. Sticking condition is detected for $|Q| \leq \mu_a P$, sliding when $|Q| > \mu_a P$ and no contact for $P = 0$. Slipping is indirectly determined for contact points experiencing a status change from sticking to sliding over a full bending load cycle (i.e., $\pm \Delta\beta$).

Figures 5 and 6 present mappings obtained for $Y_b = 0.3$ and 0.7 mm, at $T = 15\%$ RTS and $T = 35\%$ respectively. To identify the critical contact points, stress distributions are also interpreted with the stress-based Smith–Watson–Topper (σ_{SWT}) criterion (Eq. 2), recently applied in conductor fatigue analyses [12].

$$\sigma_{SWT} = \sqrt{\langle \sigma_{max} \rangle \cdot \sigma_a} = \sqrt{\langle \sigma_m + \sigma_a \rangle \cdot \sigma_a} \tag{2}$$

In Eq. 2, the Macauley brackets $\langle \rangle$ are defined as $\langle x \rangle = (x + |x|)/2$. SWT is thus accounting for the mean stress effect, but also predicts no damage when σ_{max} is

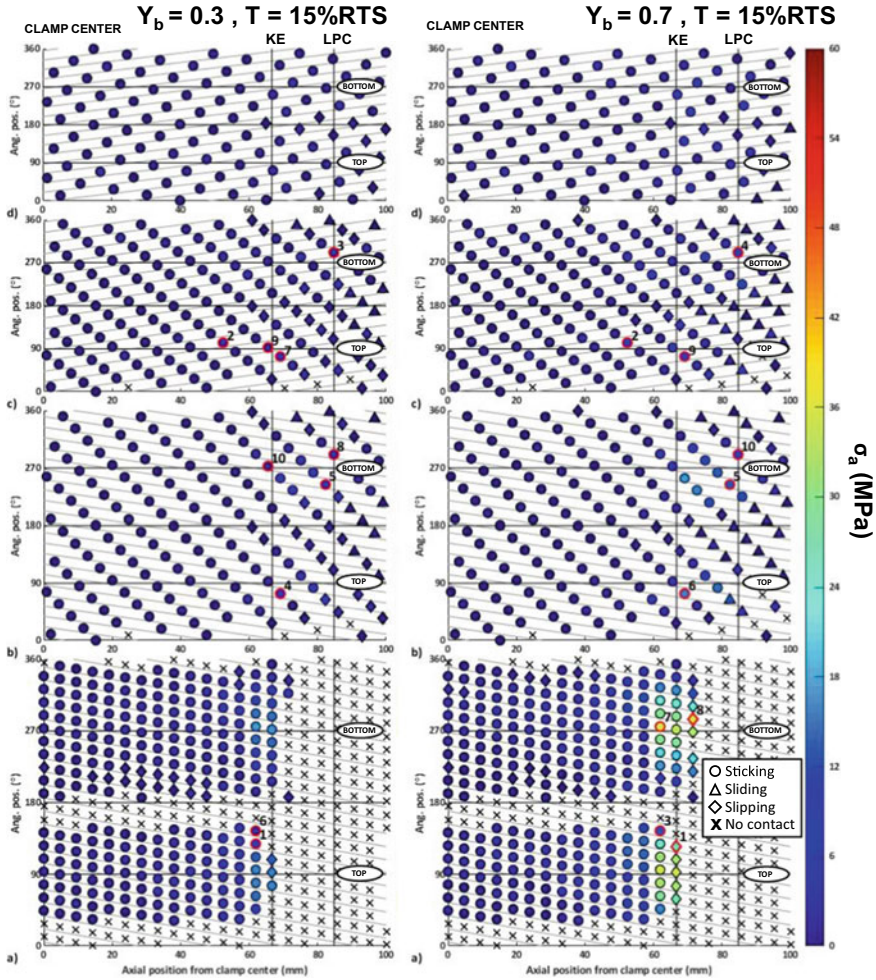


Fig. 5 Wire stress amplitude (σ_a) at (a) layer 4 outer contacts with clamp surface, (b) layer 4 inner contacts with layer 3, (c) layer 3 outer contacts with layer 4 and (d) layer 3 inner contacts with layer 2, for $T = 15\%$ RTS with $Y_b = 0.3$ mm (left charts) and 0.7 mm (right charts)

negative. The latter is not reflecting the observations from [13] revealing a majority of wire failures underneath the conductor, where mean stresses are mainly compressive.

Therefore, to account for the damage on the bottom side, σ_m is set to 0 in Eq. 2 for $\sigma_m \leq 0$, thus assuming no damage contribution for compressive mean stresses. Based on this adapted SWT evaluation, the ten (10) most critical contact points having the highest σ_{SWT} values are ranked and circled in red in Figs. 5 and 6.

The mappings first reveal maximum stress amplitudes (σ_a) always located at outer contact points of the external layer, on the bottom side near the LPC. It should be noted the obtained LPCs in Figs. 5, 6 are not matching exactly the reference value due

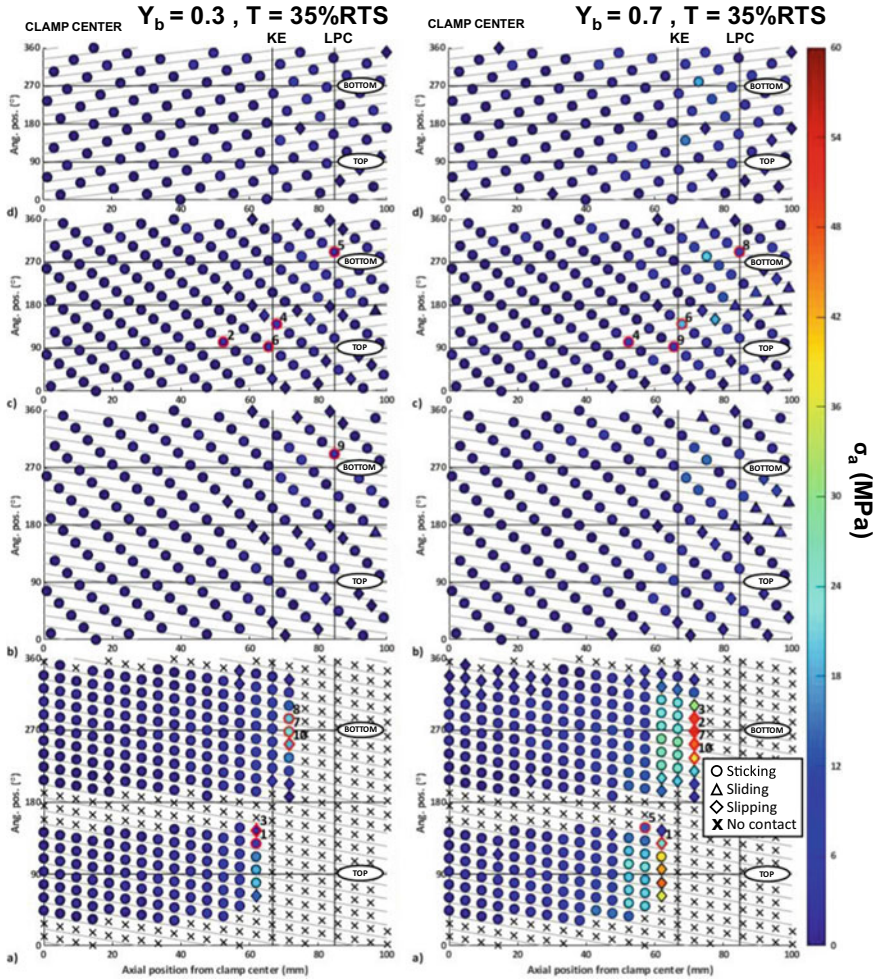


Fig. 6 Wire stress amplitude (σ_a) at **a** layer 4 outer contacts with clamp surface, **b** layer 4 inner contacts with layer 3, **c** layer 3 outer contacts with layer 4 and **d** layer 3 inner contacts with layer 2, for $T = 35\%$ RTS with $Y_b = 0.3$ mm (left charts) and 0.7 mm (right charts)

to slight load differences with [8] and probable imprecisions on LPC measurements [5]. The vibration amplitude (Y_b) also contributes to important σ_a increases in the high stress region, but also to contact status change from sticking to slipping near the KE and LPC. The Y_b effect on contact statuses is also seen at contact points inward, with more slipping and sliding contact points on layer 3 as Y_b increases. This observation is amplified for lower tensions (T) levels. The axial tension (T) also influences the wire-to-clamp contact distribution. Contact points with the clamp body are extending further away from the clamp center at $T = 35\%$ RTS, while it is the opposite for contact points with the clamp keeper.

Regarding the σ_{SWT} evaluation, critical points are essentially located near the conductor top and bottom region. Load configurations at $T = 15\%$ RTS led to critical point distributions more dispersed through layer interfaces, either for outer and inner contact points. While at $T = 35\%$, critical points are concentrated on the outer contacts near the KE and LPC. These predictions are in general agreement with the experimental wire failure observations [13]. However, the most critical point is always predicted at near the KE at the conductor top, which differs from the 1st wire break locations observed at the bottom during fatigue tests in [13]. The SWT criterion not accounting directly for the contact stresses induced by loads P and ΔQ , may explain this difference.

3.2 Factor Interrelations

DOE factors interrelations are studied in this section to better understand their combined influence on local loading conditions.

Interrelations based on averaged local loading. To first interpret Y_b and T global effects, Fig. 7 presents the first-order interactions using averaged local loads values, computed over all contact points within the aforementioned 0–100 mm zone.

P_{max} is the maximum normal contact force, ΔQ the tangential contact force variation and $\Delta\delta$ the contact relative displacement variation. Figure 7 reveals practically no influence of Y_b on normal contact forces (P), being essentially driven by T . However, Y_b has a direct effect on the tangential contact force (ΔQ), while the influence is lower for T , although it slightly increases at higher deflection amplitudes. The more significant Y_b - T interaction is observed with the relative displacement ($\Delta\delta$).

Interrelations based on critical point local loading. As factors interrelations may be attenuated from averaged values, Fig. 8 repeats the same interaction analysis, but

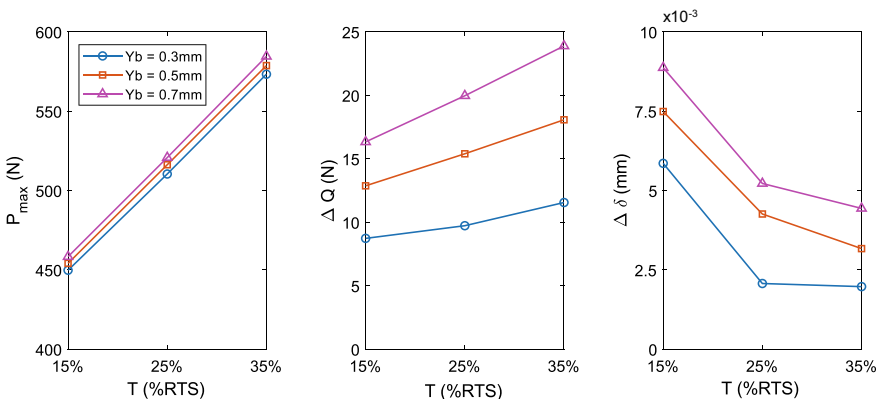


Fig. 7 Factor interrelations for averaged local loads

for local loads and stresses at critical contact point #7 in Fig. 5, for $Y_b = 0.7$ mm. Wire stress amplitude (σ_a) and mean stress (σ_m) are also included in the analysis. At the critical contact point level, Fig. 8 shows an influence of both factors on all local loads and stresses. Also, Y_b - T interactions is noticed for all loading parameters, although it is more pronounced for ΔQ and $\Delta \delta$.

Local loading variation at critical contact point. The conductor-clamp FE model also allowed full descriptions of contact point loading history, useful for in-depth analysis of fretting damage analysis. Figure 9 thus presents the local loading variation at the contact point illustrated in Fig. 8, for all DOE combinations.

Figure 9 first reveals an almost constant normal contact force (P) through all the load cycle, especially at higher tensions (T). On the other hand, the tangential

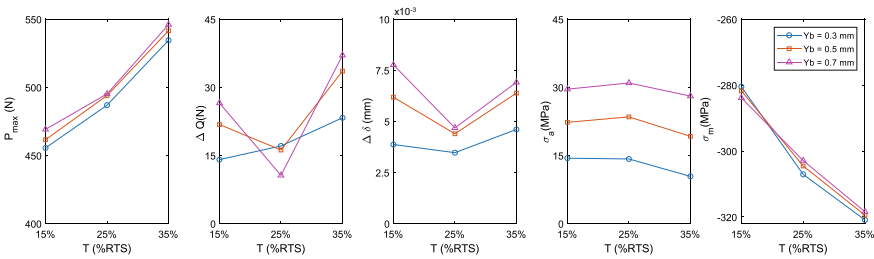


Fig. 8 Factor interrelations for local loads and stresses at a critical contact point #7

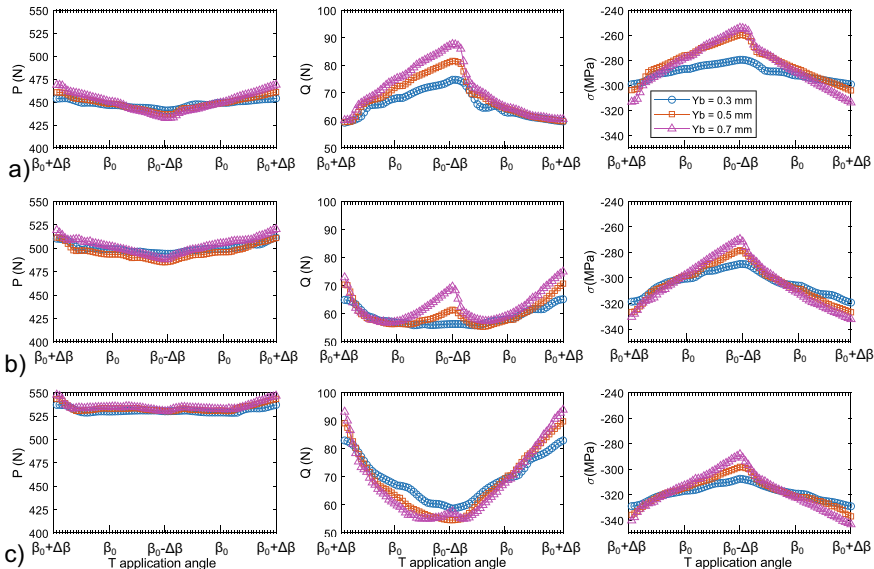


Fig. 9 Local loading variation at critical point for one bending cycle at **a** $T = 15\%$ RTS, **b** 25% RTS and **c** 35% RTS

load spectrum varies considerably from one factor combination to another. Finally, the wire stress variation at this contact point appears to stay in phase with the T application angle cycle $\pm \Delta\beta$. This detailed local loading description, available for all contacts, could therefore be very useful for in-depth contact stress analysis with refined FE wire models [2, 3].

4 Conclusion

This study proposed a numerical characterization of the local loading conditions at contact points, responsible for conductor damage. Using a factorial design, the investigation depicted the influence of two major parameters in conductor fatigue: Y_b and T .

Distribution mappings first exposed the combined wire stresses and contact statuses distribution in an effective representation of the local loading conditions. With an adapted SWT criterion, the mappings allow a precise identification and tracking of the critical contacts points locations. Globally in-line with experimental observations, the prediction could be refined by including the contact stress effects.

The two-factor interaction plots also showed the interrelations between Y_b and T with respect to the local loading, which is especially significant at critical contacts points. Being limited to only two factors, the local loading characterization could be enriched from sensitivity analysis to other conductor-clamp design, load or material parameters.

Acknowledgements The authors acknowledge the support of the Natural Sciences and Engineering Research Council of Canada (NSERC).

References

1. Azevedo CRF (2009) Fretting fatigue in overhead conductors: rig design and failure analysis of a Grosbeak al. cable steel reinforced conductor. *Eng Failure Anal* 16(1):136–151
2. Matos IM (2022) Fretting fatigue performance and life prediction of 1120 aluminum alloy wires of overhead conductors, *Theor Appl Fract Mech* 121(103521):13
3. Levesque F (2011) (2011) Finite element model of the contact between a vibrating conductor and a suspension clamp. *Tribol Int* 44(9):1014–1023
4. Said J (2020) A multi-scale strategy to predict fretting-fatigue endurance of overhead conductors. *Tribol Int* 143:106053
5. Lalonde S (2018) Numerical analysis of ACSR conductor-clamp systems undergoing wind-induced cyclic loads. *IEEE Trans Power Del* 33(4):1518–1526
6. Belkhabbaz A (2021) Surrogate model based approach to predict fatigue stress field in multi-stranded cables. *Int J Solids Struct* 230:111168
7. Cloutier L, Diana G, Goel A (2006) EPRI transmission line reference book: wind-induced conductor motion, Palo Alto

8. Goudreau S (2010) Strain measurements on ACSR conductors during fatigue tests III—strains related to support geometry. *IEEE Trans Power Del* 25(4):3007–3016
9. Levesque F (2010) Strain measurements on ACSR conductors during fatigue tests I—experimental method and data. *IEEE Trans Power Del* 25(4):2825–2834
10. Lalonde S (2017) Modeling multilayered wire strands, a strategy based on 3D finite element beam-to-beam contacts - part I. *Int J Mech Sci* 126:281–296
11. Zhou ZR (1994) Fretting patterns in a conductor-clamp contact zone. *Fatigue Fract Eng Mater Struct* 17(6):661–669
12. Rocha PHC (2022) A general life estimation method for overhead conductors based on fretting fatigue behavior of wires. *Theo Appl Frac Mech* 121:103443
13. Levesque F (2005) Étude de l'applicabilité de la règle de Palmgren-Miner aux conducteurs électriques sous chargements de flexion cyclique par blocs. Université Laval, Québec

General Modelling of Cable Vibrations Using Data Extracted from Physical Simulation



John A. Redford , Maxime Gueguin , Fikri Hafid , Matthieu Ancellin ,
and Jean-Michel Ghidaglia 

Abstract A methodology has been put in place to allow simulation data to be correlated and used to model cable vibrations. Computational Fluid Dynamics (CFD) was used to create a database of lift force data on cylinders subjected to forced vibrations at a range of amplitudes and frequencies. Linear regression was found to be suitable for the correlation of the lift force with respect to the local cylinder displacement and velocity when lock-in occurs. The approach has been tested on a cylinder attached to a mass-spring-damper system and compared to fluid-structure interaction simulations that use CFD. After this, the correlated data was used to demonstrate lock-in of a cable vibration, where the classical sinusoidal lift did not lock-in. This approach will allow for a more realistic simulation tool for cable vibrations to be developed, while maintaining a low computational cost relative to the use of CFD. Having such a tool will make study of cable vibrations under a wide range of conditions simpler, which would include the role of multi-mode vibrations and the transient growth of vibrations.

Keywords Fluid structure interaction · Linear regression · Model reduction

J. A. Redford (✉) · M. Gueguin · M. Ancellin
Eurobios Mews Labs, 61 avenue du Président Wilson, 94235 Cachan, France
e-mail: jredford@eurobios.com
URL: <http://www.eurobios.com>

F. Hafid
Rte, Direction R&D, Immeuble Window, 7c place du Dôme, 92800 Paris La Défense, France

F. Hafid · J.-M. Ghidaglia
Centre Borelli, ENS Paris-Saclay, 4, avenue des Sciences, 91190 Gif-sur-Yvette, France

MSDA, University Mohammed VI Polytechnique (UM6P) Benguerir, Benguerir, Morocco

1 Introduction

Overhead lines are subject to vibrations that are caused by an interaction with the wind [4]. The case of a vibrating string in a constant wind flow is well understood, however, the real case is not like this as the wind varies in time and space due to turbulence and the topography of the surrounding environment. Real cables are also more complicated with non-constant rigidity and difficulties in quantifying the damping. A step in the right direction would therefore be to experiment with various wind profiles and structure models to try and improve understanding of the effect on the cable vibrations. The problem is that using Computational Fluid Dynamics (CFD) tools make this a costly task due to the long running time and the potential number of different configurations [2, 13]. Previous attempts to replace the CFD models with wake oscillators have not been fruitful in the sense that the cable vibrations did not grow realistically [5], so it would be good to search for an alternative that sufficiently captures the fluid-structure interaction.

In order to model the interaction, the hypothesis could be made that the lift force can be correlated with a certain number of local characteristics at a given point along the span, for example, the local cable displacement, speed and acceleration. The data required to make this empirical correlation comes from simulations of cylinders that are forced to oscillate in a wind flow at a range of frequencies and amplitudes [7], where the relationship between the fluid forces and the structure movement is learnt from these simulations.

This work forms part of the efforts by Rte (Réseau de transport d'électricité) to develop prediction tools for the ageing of conductor cables. It is thought that the ageing is largely due to the vibrations induced by the wind, but the variability of the weather conditions makes it difficult to quantify the likely full history of cable vibrations. The ultimate goal of this work is to make this possible.

In this article, first the methodology for the generation of the data using forced vibration CFD simulations is described. Then a linear regression that allows the lift force to be found from the cable displacement history is put in place. Finally, the approach is tested in the context of a mass-spring-damper and cable vibrations.

2 Methodology

It is proposed that the fluid part of the fluid structure interaction is replaced by the linear regression of forced cylinder vibration data. An overview of the process is shown in Fig. 1. First, CFD analysis of forced cylinder vibrations yields lift and displacement data over a converged vibration cycle for a given vibration amplitude and frequency. Linear regression of this data is used to create a function that relates lift force to displacement which can then be used to replace the CFD simulation for modelling of a fluid structure interaction.

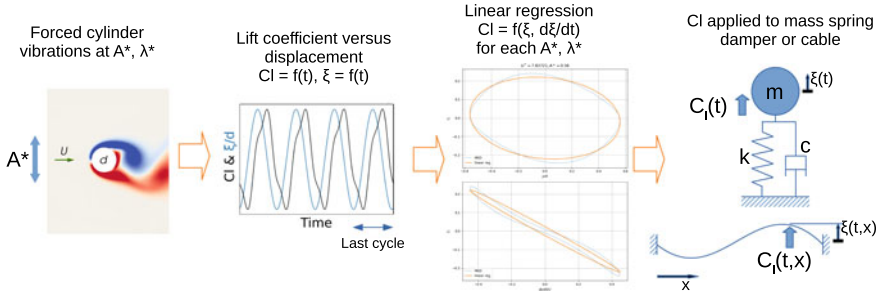


Fig. 1 Methodology overview

For the fluid flow, the incompressible Navier-Stokes equations are solved. The displacement of the cable is applied to the fluid flow using a moving reference frame attached to the rigid body [8, 13].

$$\nabla \cdot \mathbf{u} = 0, \tag{1}$$

$$\frac{\partial \mathbf{u}}{\partial t} + \mathbf{u} \cdot \nabla \mathbf{u} = -\nabla P + \nabla \cdot \sigma + \frac{d\mathbf{u}^S}{dt}, \tag{2}$$

where \mathbf{u} is the velocity vector and P is the pressure. For the moving frame, rotation is neglected and only translation with velocity \mathbf{u}^S is considered.

It has been shown that forced vibrations can be used to better understand the nature of free vibrations. This includes being able to find the free vibration amplitude [6, 7]. Here the cylinder displacement ξ is vibrated in time t following

$$\xi(t) = A \sin(2\pi ft), \tag{3}$$

where A is the vibration amplitude and f is the forcing frequency. Forced and free vibrations at $Re = 100$ have already been investigated by [6], where the same Reynolds number is used here to simplify the generation of the data, and their results correspond well with those found here.

A mass-spring-damper model will be used for comparison of the linear regression and the CFD. The mass-spring-damper is defined as

$$m_l \frac{d^2 \xi}{dt^2} + c \frac{d\xi}{dt} + k\xi = F_y(t), \tag{4}$$

where m_l is the mass per unit length of the cylinder, c is the damping coefficient and k is the spring stiffness. The natural frequency of (4) is $f_N = \frac{1}{2} \sqrt{k/m_l}$ and the damping ratio is $\zeta = c/2\sqrt{m_l k}$. In this respect, the non-dimensional groups that are important are, respectively, the normalised amplitude, the normalised velocity and the normalised wavelength

$$A^* = \frac{A}{d}, \quad U^* = \frac{U}{fNd}, \quad \lambda^* = \frac{U}{fd}, \quad (5)$$

where d is the cylinder diameter, U is the free stream velocity and f is the oscillation frequency.

A laminar cylinder flow does not depend on the use of turbulence modelling and two-dimensional flow can be assumed. Hence, all simulations are made on a two-dimensional mesh with 10,359 cells, where a smooth cylinder of diameter d is placed at the centre of a domain $26d$ in length and $22d$ in width. The inlet velocity is U while symmetry conditions are used on the lateral boundaries and a Neumann boundary condition is applied at the exit. Grading is used to place more cells near the cylinder surface in a circular refined zone of radius $\sqrt{9.68}d$, where the maximum wall coordinate $y_{\max}^+ = 1.6$ at the first grid point. More cells are placed in the wake region to capture the re-circulation zone that can influence the flow around the cylinder itself [12]. The Strouhal number was measured to be 0.167, which corresponds to the value found in the literature. The peak skin-friction coefficient is 0.41 at 49° , which is about 3% less than that found by [10], the stagnation pressure coefficient is $C_p = (p - p_\infty)/(\frac{1}{2}\rho U^2) = 1.05$ and the base pressure coefficient is 8% less than [10] at $C_p = -0.681$.

The fluid exerts a drag and lift force on the cylinder which here will be presented in the form of drag $C_d = 2F_x/\frac{1}{2}\rho U^2 A_c$ and lift $C_l = 2F_y/\frac{1}{2}\rho U^2 A_c$ coefficients, where A_c is the frontal area of the cylinder. For the fixed cylinder test at $Re = 100$, mean $C_d = 1.39$ and max $C_l = 0.34$ ([9] found respectively 1.37 and 0.34 for C_d and C_l).

In future, Large Eddy Simulation (LES) could be used if the approach is to be applied to more realistic Reynolds numbers [3].

3 Linear Regression

A linear regression of $C_l = f(\xi, \dot{\xi})$, where a dot denotes a derivative with respect to time, could be used to replace the CFD calculation, with the benefit that calculation time will be significantly reduced.

The simulation code that used the Navier-Stokes equations to resolve the fluid flow for forced oscillations (3) was run for fixed values of A^* and λ^* . Sufficient time was given to allow the flow to fully develop and then a sample over a complete vibration cycle was taken, where the position and velocity of the body $\xi(t_i)$, $\dot{\xi}(t_i)$ were extracted, as well as the lift coefficient $C_l(t_i)$. Passing this data to the `scikit-learn` library, we looked for a linear relation that is able to predict the lift coefficient from the position and velocity of the body:

$$a_{\text{opt}}, b_{\text{opt}} = \operatorname{argmin}_{a,b} \sum_{i=1}^N \|C_l(t_i) - a\xi(t_i) - b\dot{\xi}(t_i)\|^2.$$

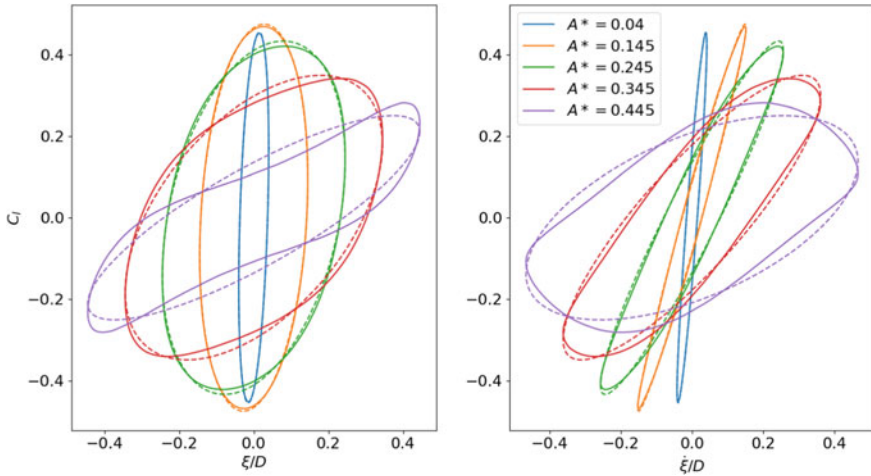


Fig. 2 Example linear regression of lift coefficient for range of A^* at $\lambda^* = 6$. Left plot show $C_l = f(\xi)$ and right plot shows $C_l = f(\dot{\xi})$. Solid lines are selected forced CFD results and dashed lines are the corresponding linear regressions

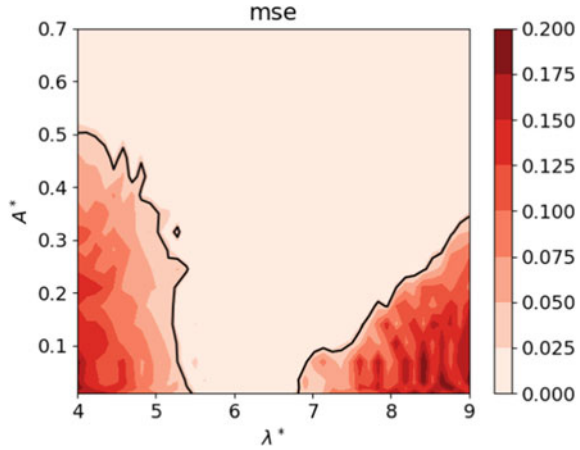
Afterwards, the $\tilde{C}_l(t) = a_{opt}\xi(t) + b_{opt}\dot{\xi}(t)$ relationship has been used in the mass-damper-spring model (4) and a cable model [4] to predict the actual motion of the body.

The forced vibration simulations provide a database that can be used to find regressions over the (A^*, λ^*) space. A range of example linear regressions are shown in Fig. 2, which demonstrates how a close match with the simulation data was obtained for low A^* values. At higher values of A^* , the lift-displacement paths deviate from the elliptic form observed at low vibration amplitude, meaning that the chosen linear regression is less accurate.

The example given in Fig. 2 is only for a single λ^* value. As with A^* , the phase angle difference between the cylinder movement and the lift force also alters with λ^* , which makes collapse over the whole space using linear regression difficult. Instead, to prove the concept behind this approach, the regression coefficients for all discrete values in the (A^*, λ^*) space were stored, where the nearest point can be found and applied to the simulation. In future work, it would be good to investigate the possibility of a global correlation, where the increased flexibility in the application of the approach would be the principal advantage of such a development.

The linear regression does not work when lock-in does not occur. This is because the vortex shedding frequency does not correspond to the vibration frequency and the loops shown in Fig. 2 are not closed. The decision over whether lock-in has occurred was made using the mean squared error (MSE) of the linear regression. This can be done because the MSE is high when the lift force and the cylinder motion are decorrelated, as shown in Fig. 3. The threshold of $MSE < 0.03$ was chosen. If there is no lock-in, it is assumed that the overall effect is that no time mean energy passes

Fig. 3 Mean squared error for all (A^*, λ^*) . Black line marks $MSE < 0.03$, where lock-in threshold is applied



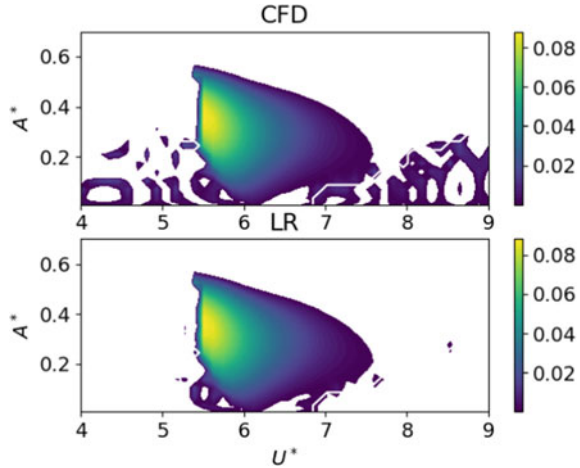
between the wind and the cable, so the lift force is set to zero. More work needs to be done here because there will be lift forces due to the vortex shedding, which could be modelled using a fixed cylinder function [1].

The power input is important because this is what is responsible for the growth of the vibrations, but at certain λ^* , U^* power input can also be negative. The structural dissipation will also remove energy. The power input can be found by multiplying the lift force F_y by the velocity $\partial\xi/\partial t$. Integrating over the cable length and finding the mean over a complete vibration cycle gives the mean power per cycle. The mean power from the forcing over a cycle is thus found from

$$P_{\text{force}} = \frac{1}{t_2 - t_1} \int_{t_1}^{t_2} \int_0^{L_z} F_y \frac{\partial\xi}{\partial t} dz dt, \tag{6}$$

where t_1 and t_2 are t at the beginning and end of a vibration cycle. The powers in the other terms of (4) can be calculated in a similar way and the sum total can be used to check that the calculated energy is well conserved. In Fig. 4, it can be seen that the power input is roughly the same for the forced CFD and the linear regression within the region of low MSE seen in Fig. 3. Outside, where there is no lock-in, the comparison between the CFD and linear regression breaks down because the relationship between the lift force and displacement is no longer cyclic. Hence, the differences between the linear regression and the forced simulations seen at high A^* are not seen in this statistic, meaning that vibration growth for the linear regression may be reasonably correct at high amplitudes.

Fig. 4 Power input from the forced CFD simulations (top) and the linear regression (bottom). Only positive power inputs are retained



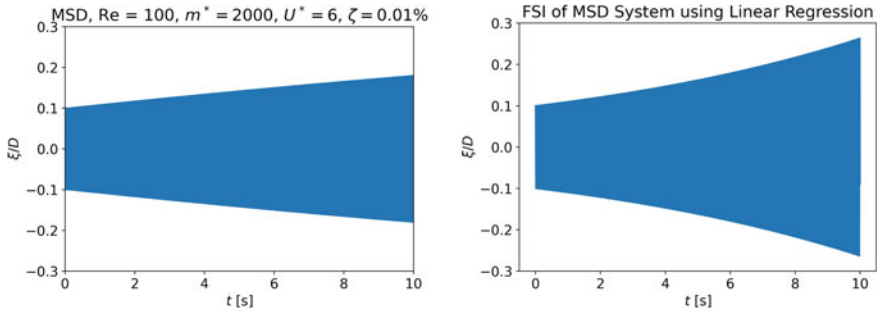
4 Cylinder Flow Vibrations Using Linear Regression

To demonstrate the feasibility of this approach, example simulations have been run for a mass-spring-damper (MSD) and a comparison is made with results under the same conditions for CFD of a cylinder coupled to a MSD system (4). Secondly, the linear regression has been implemented into existing cable vibration software to demonstrate the improvement with respect to the classical fixed-cylinder lift coefficient [1].

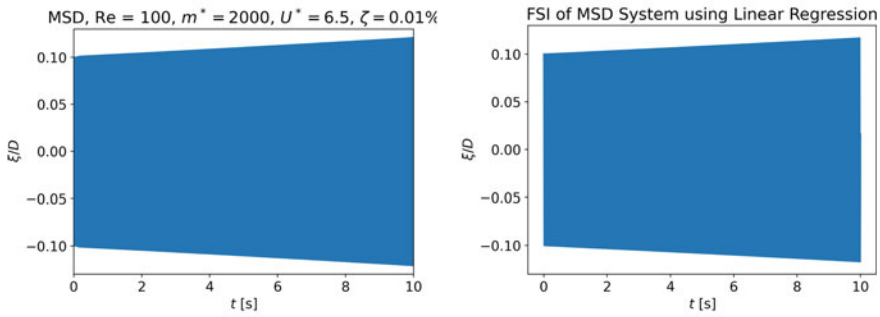
In Fig. 5, a comparison is made between CFD and the linear regression. The Reynolds number is 100, mass ratio $m^* = m_l / \rho d^2 = 2000$, which is typical for overhead lines, and the structural damping $\zeta = 0.01\%$. Simulations are run for a range of λ^* because it is known that the classical approach does not work when the frequencies of the structure and the fixed cylinder vortex shedding are different. In this case, where $Re = 100$, $U^* = 6$ is where the resonance would occur without lock-in. Depending on the vibration amplitude, the vortex shedding frequency is adjusted at higher values of U^* to widen the possibility of resonance. This is what is seen in Fig. 5, where growth is observed in all cases but the CFD at $U^* = 7$. The power input at $U^* = 7$ is positive, but the structural damping will have a greater effect.

There is growth in all the linear regression simulations, demonstrating that this approach tends to overestimate the vibration amplitude, and that some effect may be missing. This may be a result of finite time to make changes in the vortex shedding as the vibration amplitude increases, which is not captured by the linear regression. However, the growth trend observed for the linear regression is roughly the same as for the CFD. Note that, the fixed cylinder lift coefficient would have given no growth in the $U^* = 6.5$ and 7.0 cases.

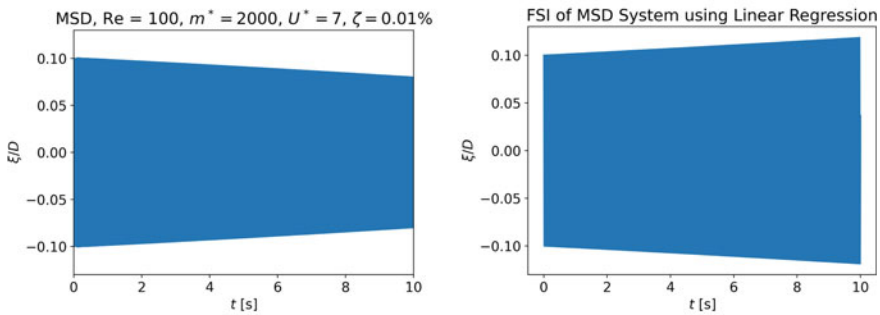
To demonstrate this approach in the context of overhead line cable vibrations, the linear regression has been implemented into software developed to solve cable



(a) $U^* = 6$



(b) $U^* = 6.5$



(c) $U^* = 7$

Fig. 5 Comparison of CFD (left) with linear regression (right) when applied to cylinder attached to a mass-spring-damper

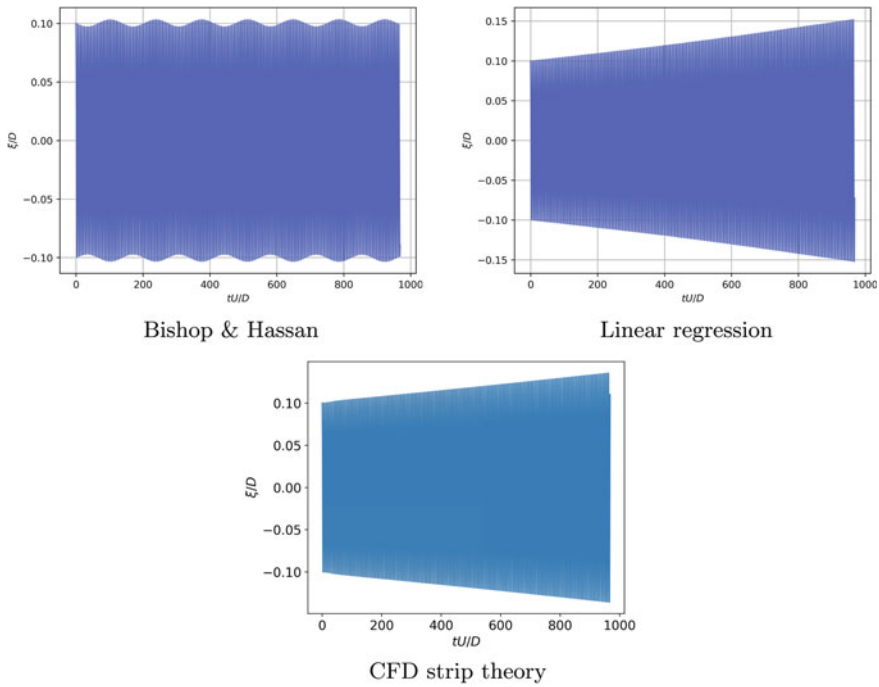


Fig. 6 Cable displacement at the mid-span location. Fixed cylinder law (left) and linear regression (right) applied to cable vibrations, strip theory for string vibrations with 7 strips (bottom)

vibrations [4]. The results shown in Fig. 6 are both for a short cable that should allow for the mode 1 vibration to be excited. The cable parameters are mass per unit length $m = 1.57 \text{ kg/m}$, diameter $d = 31 \text{ mm}$, stiffness $EA = 37.6 \text{ MN}$, length $L = 5 \text{ m}^2$, tension $H = 37 \text{ kN}$, while the wind is at 3 m/s . The Bishop & Hassan model [1] has a Strouhal number of 0.166 and a lift coefficient vibration amplitude $C_{l0} = 0.6$.

An initial vibration amplitude of $A^* = 0.1$ is imposed. The resulting frequency is about 15.3 Hz , which gives $U^* = 6.33$ where a lock-in would be expected at most amplitudes for the real flow. However, this does not correspond to the Strouhal frequency where $U^* = 6$ meaning that in Fig. 6 Bishop & Hassan does not have a growing vibration amplitude that would result from the lock-in effect. There is some beating, that suggests the resonance is at a frequency that is not too far away. However, the linear regression vibrations are growing, which suggests that lock-in has occurred. Also, Fig. 6 bottom shows a strip theory simulation of a simple string (i.e. $EA = 0$) which has growth that compares well with the linear regression. In future, the stiffness term will be added to allow direct comparisons with the linear regression model.

5 Conclusion

It has been demonstrated that linear regression of fluid simulation data can be used to replace the fluid simulation itself when simulating a fluid-structure interaction. This will reduce the time to run these problems from hours to minutes and the advantages of this are clear for the creation of a simulator that allows for a wide range of parameters and configurations to be investigated.

The results shown here are from a preliminary implementation of the approach and more work is required. Improvement may be possible for the linear regression itself, where it may be possible to capture the effect of the amplitude and frequency in the regression, instead of having a discrete range of regressions.

The use of converged cycles means that the details of how the system changes when the amplitude or frequency varies are not included, however, the vibrations grow in time due to the potential energy input. The effect of an evolving amplitude should be investigated, as it may be possible that there is a delay in the changing dynamics of the vortex shedding, which could be responsible for the over-prediction of the vibration amplitude by the linear regression.

When no lock-in occurs, there will still be a lift force that will correspond to the fixed cylinder case. At the moment, the lift is treated as zero in this case, but adding this effect consistently will improve the realism of the approach. It is also important to consider small and zero amplitude vibrations, as these would return a zero force in the current approach.

Acknowledgements The computations for this work were run on the Simlab Cluster at the University Mohammed VI Polytechnique (UM6P) in Morocco.

References

1. Bishop RED, Hassan A (1964) The lift and drag forces on a circular cylinder in a flowing fluid. *Proc R Soc Lond Ser A Math Phys Sci* 277(1368):32–50
2. Bourguet R, Karniadakis GE, Triantafyllou MS (2011) Vortex-induced vibrations of a long flexible cylinder in shear flow. *J Fluid Mech* 677:342–382
3. Breuer M (1998) Numerical and modeling influences on large eddy simulations for the flow past a circular cylinder. *Int J Heat Fluid Flow* 19(5):512–521
4. Cieren E, Redford J, Guéguin M, Allix O, Yang C, Hafid F, Ghidaglia JM (2020) On the validation and use of a simplified model of aeolian vibration of overhead lines for parametric studies. In: XI International conference on structural dynamics, pp 2011–2021
5. Facchinetti ML, De Langre E, Biolley F (2004) Coupling of structure and wake oscillators in vortex-induced vibrations. *J Fluids Struct* 19(2):123–140
6. Kumar S, Navrose N, Mittal S (2016) Lock-in in forced vibration of a circular cylinder. *Phys Fluids* 28(11):113605
7. Morse T, Williamson C (2009) Prediction of vortex-induced vibration response by employing controlled motion. *J Fluid Mech* 634:5–39
8. Newman D, Karniadakis G (1996) Simulations of flow over a flexible cable: a comparison of forced and flow-induced vibration. *J Fluids Struct* 10(5):439–453

9. Newman DJ, Karniadakis GE (1997) A direct numerical simulation study of flow past a freely vibrating cable. *J Fluid Mech* 344:95–136
10. Rajani B, Kandasamy A, Majumdar S (2009) Numerical simulation of laminar flow past a circular cylinder. *Appl Math Model* 33(3):1228–1247
11. Rigo F, Andrianne T, Denoël V (2022) Generalized lift force model under vortex shedding. *J Fluids Struct* 115:103758. <https://doi.org/10.1016/j.jfluidstructs.2022.103758>. www.sciencedirect.com/science/article/pii/S0889974622001505
12. Roshko A (1961) Experiments on the flow past a circular cylinder at very high Reynolds number. *J Fluid Mech* 10(3):345–356
13. Zhang L, Redford J, Hafid F, Ghidaglia JM, Gueguin M (2021) VIV modelled using simplified cable dynamics coupled to sub-critical cylinder flow simulations in a moving reference frame. *Eur J Mech B Fluids* 85:214–231. <https://doi.org/10.1016/j.euromechflu.2020.09.013>

Parametric Dynamic Modeling of Cable-Driven Parallel Manipulators



Andrea Arena , Erika Ottaviano , and Vincenzo Gattulli 

Abstract A two-dimensional parametric model for the study of the nonlinear dynamic response of cable-driven parallel manipulators is presented in this work. The model considers the distributed dynamical properties a generic number n of cables undergoing time-varying length. The cable equations of motion are obtained via a lagrangian formulation and the equations providing the connectivity between the end-effector and the cables are derived analytically; finally, the balance of the linear and angular momentum of the end-effector is enforced. The partial differential equations of motion of the system are reduced to a set of ordinary differential equations through a discretization procedure based on admissible trial functions, so as to couple the latter equations with the equations of motion of the end-effector. Finally, the direct dynamic problem is formulated and solved numerically for a selected case-study manipulator.

Keywords Cable-driven manipulator · Distributed mass cable · Direct dynamics

1 Introduction

Cable-Driven Parallel Manipulators (CDPMs) can be defined as parallel robots in which legs are replaced with extensible cables that allow to cover larger workspaces (WS) if compared to classical parallel robots. Cables are wound in actuated drums (i.e., the winches) that can be placed at a fixed frame, and the end-effector EE can be

A. Arena (✉) · V. Gattulli

Department of Structural and Geotechnical Engineering, Sapienza University of Rome,
Via Eudossiana 18, 00184 Rome, Italy
e-mail: andrea.arena@uniroma1.it

V. Gattulli

e-mail: vincenzo.gattulli@uniroma1.it

E. Ottaviano

Department of Civil and Mechanical Engineering, University of Cassino and Southern Lazio,
Via G. Di Biasio 43, 03043 Cassino (FR), Italy
e-mail: ottaviano@unicas.it

operated by controlling the cable lengths [13]. In the analysis and design of CDPMs, an aspect of great importance to be considered is related to the number of active cables and their arrangement. For this reason, CDPMs were classified into two main categories, namely, over-constrained and under-constrained robots, respectively.

Since CDPMs have shown inherent advantages over conventional parallel robots, many applications were developed in the past and their use is continuously increasing. Cables are the main components of CDPMs; therefore, a deep understanding of their static and dynamic behaviors is fundamental to properly design these devices. However, the mechanical modeling of cables can be very challenging if considering both their distributed mass, elasticity, and damping properties [8, 12]. Within this context, richest dynamical models of elastic cables, including the bending and the torsional stiffness, were proposed in [2, 6] and the identification of the axial and bending stiffness in stay cables was also performed in [5], while the effects of the temperature in the elastic response of cable were investigated in [11]. Those models have found suitable applications in the study and the characterization of the static and the dynamic behavior of CDPMs. In particular, the Irvine cable model [8] was adopted, as first, to formulate and solve the kinetostatic problem of CDPMs for studying the effect of the cables sag [14, 18], while more sophisticated nonlinear models, including the three-dimensional description of the finite kinematics and the large deformation of elastic cables, were proposed in [10, 16, 17] to solve the direct and the inverse kinematic problems of CDPMs working in a 3D space.

For what concerns the dynamics of CDPMs, in early studies, the distributed inertia and stiffness of cables were typically neglected since those were modeled via massless, rigid, links able at moving the EE in space [15]. The vibrations of the moving platform of CDPMs with large workspaces were studied in [3, 4], where cables were modeled by including their distributed mass and axial stiffness and the equations of motion were solved by using different numerical techniques, i.e., by using finite element method and by means of the assumed-mode method, respectively. Within this context, the correct modeling of the cable stiffness and inertia plays a fundamental role and has significant effects both in the static and in the dynamic response of CDPMs, such as in the correct kinematic description of the motion, the EE positioning accuracy, the forces distribution in the cables, and in the vibration and the control of the robot [7, 9].

In the present paper, a parametric nonlinear dynamic model of CDPMs undergoing two-dimensional motion is presented and discussed. The equations governing the in-plane dynamics of the CDPM are derived from a more general, three-dimensional, dynamic model formulated by the authors of this work and proposed in [1]. Finally, the solution of the direct dynamic problem is provided by means of a discretization procedure based on admissible trial functions.

2 Parametric Modeling

The model is formulated by considering a generic number n of cables whose length is varied in time to move and to change the orientation of an end-effector (EE) mass in a two-dimensional (2D) space by means of prescribed trajectories. Finite displacements and rotations of the end-effector are accounted for to provide an exact geometric formulation of the cable dynamics, and the equations of motion are then derived via a Lagrangian formulation.

2.1 Kinematics

The variable t and the cable arclength $s_i \in [0, L_i(t)]$ ($i = 1, \dots, n$) of the unstretched configuration are used to parametrize in time and space, respectively, the i -th elastic cable. Here, $L_i(t)$ represents the time-varying total unstretched length of the i th cable. Moreover, at time t , the minimum distance between the boundaries of the i th cable is given by $l_i(t)$. The geometry and the kinematics of the system are described by considering n fixed Cartesian frames having origin positioned at the boundary $s_i = 0$ of the corresponding cable. The origins of the n fixed frames are positioned in the frame $(\mathbf{e}_y, \mathbf{e}_z)$, being \mathbf{e}_z the gravity direction (positive upwards), and centered in the point O_1 of the first cable (i.e., at $s_1 = 0$), by the 2-by-1 position vector $\mathbf{x}_i = [y_i \ z_i]^\top$ ($i = 1, \dots, n$); therefore, it turns out that $\mathbf{x}_1 \equiv \mathbf{0}$, where $\mathbf{0}$ is the null vector. The vector describing, in the fixed frame $(\mathbf{e}_y, \mathbf{e}_z)$, the position of the point belonging to the end-effector and connected to the i -th cable is

$$\mathbf{r}_i(t) = [(r_{i,y}^0 \cos \theta(t) - r_{i,z}^0 \sin \theta(t)) \ (r_{i,y}^0 \sin \theta(t) + r_{i,z}^0 \cos \theta(t))]^\top, \quad (1)$$

where $r_{i,y}^0$ and $r_{i,z}^0$ are the components of the position vector in the mass-fixed local axes $\mathbf{b}_y(t)$ and $\mathbf{b}_z(t)$, respectively, centered in the EE center of mass O_M , while $\theta(t)$ is the EE rotation angle about the axis $\mathbf{e}_x \equiv \mathbf{b}_x$ orthogonal to the working plane. The vector $\mathbf{p}_i(s_i, t) = [p_{y,i}(s_i, t) \ p_{z,i}(s_i, t)]^\top$ is introduced to describe the position of the material point on the i -th cable, and its components are defined in the i -th fixed frame. The parameter s_i represents the unstretched arclength of the i -th cable. The stretch vector $\boldsymbol{\nu}_i(s_i, t) = \frac{d}{ds_i} \mathbf{p}_i(s_i, t)$, is defined to describe the strain state of the i -th cable and its norm can be calculated as: $\nu_i(s_i, t) = \sqrt{\left(\frac{dp_{y,i}}{ds_i}\right)^2 + \left(\frac{dp_{z,i}}{ds_i}\right)^2}$. Finally, the axial direction tangent to the dynamic configuration of the i -th cable is given by the unit vector as $\mathbf{a}_i(s_i, t) = \boldsymbol{\nu}_i(s_i, t) / \nu_i(s_i, t)$.

2.2 Equations of Motion

The equation of motion of the i -th cable can be derived according to the first Euler law of motion by enforcing the balance of linear momentum and can be written, in vector-valued form, as

$$\frac{d}{ds_i} \mathbf{n}_i(s_i, t) + \mathbf{f}_i(s_i, t) = \rho A_i \frac{d^2}{dt^2} \mathbf{p}_i(s_i, t) + c_i \frac{d}{dt} \mathbf{p}_i(s_i, t), \quad (i = 1, \dots, n), \quad (2)$$

where $\mathbf{f}_i(s_i, t)$ is the vector collecting the forces per unit length acting on the cable, $\mathbf{n}_i(s_i, t)$ is the axial force acting in the cable, while ρA_i is the mass per unit length of the i -th cable, respectively. Moreover, the Rayleigh dissipation function is considered to model the damping and the damping coefficient c_i is here assumed to be $c_i = 2\zeta\sqrt{EA_i\rho A_i/l_{0,1}^2}$, where ζ is the damping factor, E is the Young's modulus, and $l_{0,1}$ is the distance at time $t = 0$ between the boundary points of the first cable. Equation (2) must satisfy the kinematic boundary conditions $\mathbf{p}_i(0, t) = \mathbf{0}$, ($i = 1, \dots, n$) at $s_i = 0$ for assigned initial conditions. Moreover, the following relationship

$$\mathbf{x}_i + \mathbf{p}_i(L_i, t) - \mathbf{r}_i(t) = \mathbf{p}_1(L_1, t) - \mathbf{r}_1(t), \quad (i = 2, \dots, n), \quad (3)$$

which provides the compatibility condition ensuring that the material point at $s_i = L_i(t)$ of each cable is connected to the end-effector at the position $\mathbf{r}_i(t)$, must also hold. The balance of the linear and angular momentum of the end-effector mass M is provided by

$$-\sum_{i=1}^n \mathbf{n}_i(L_i, t) - Mg \mathbf{e}_z = M \left[\frac{d^2}{dt^2} (\mathbf{p}_1 - \mathbf{r}_1) \right]_{(s_1=L_1, t)}, \quad (4)$$

$$\sum_{i=1}^n \left[(n_{i,y}(L_i, t)r_{i,y} + n_{i,z}(L_i, t)r_{i,z}) \sin \theta - (n_{i,z}(L_i, t)r_{i,y} - n_{i,y}(L_i, t)r_{i,z}) \cos \theta \right] = J_M \frac{d^2}{dt^2} \theta(t), \quad (5)$$

where $n_{i,y}(L_i, t)$ and $n_{i,z}(L_i, t)$ are the components of the axial force vector along \mathbf{e}_y and \mathbf{e}_z , respectively, calculated at $s_i = L_i$, while J_M is the EE mass moment of inertia with respect to the local axis \mathbf{b}_x .

Trajectory of the EE. The trajectory of the end-effector, including its orientation, can be described through the position of the center of mass, given by the vector $\mathbf{p}_M(t)$, and the rotation about the axis \mathbf{b}_x given by the angle $\theta_M(t)$. Therefore, the position of each connected point of the end-effector is given, in the fixed frame $(\mathbf{e}_y, \mathbf{e}_z)$, by the vector $\mathbf{p}_{M,i}(t)$ whose expression can be calculated as:

$$\mathbf{p}_{M,i}(t) = \mathbf{p}_M(t) + \mathbf{r}_i(t) - \mathbf{x}_i, \quad (i = 1, \dots, n), \quad (6)$$

where $\mathbf{r}_i(t) = \left[\left(r_{i,y}^0 \cos \theta_M(t) - r_{i,z}^0 \sin \theta_M(t) \right) \left(r_{i,y}^0 \sin \theta_M(t) + r_{i,z}^0 \cos \theta_M(t) \right) \right]^\top$ in Eq. (6). Hence, at time t , the distance between the boundary points of the i -th cable can be calculated as $l_i(t) = \sqrt{\mathbf{p}_{M,i}(t)^\top \mathbf{p}_{M,i}(t)}$, ($i = 1, \dots, n$), whose norm $l_{0,i}$ represents the distance between the boundaries of the i th cable at time $t = 0$.

2.3 Nondimensional Form

The distance $l_{0,1}$ is adopted as characteristic length while the characteristic frequency $\omega_c = \sqrt{EA_1 / (\rho A_1 l_{0,1}^2)}$ is adopted to nondimensionalize the time, where EA_1 and ρA_1 are the axial stiffness and the mass per unit length of the first cable, respectively. Therefore, the following scalar and vector-valued nondimensional parameters can be introduced

$$\begin{aligned} \lambda_{0,i} &= \frac{l_{0,i}}{l_{0,1}}, \quad \bar{\mathbf{x}}_i = \frac{\mathbf{x}_i}{l_{0,1}}, \quad \bar{\mathbf{r}}_i^0 = \frac{\mathbf{r}_i^0}{l_{0,1}}, \quad \bar{\mathbf{r}}_i = \frac{\mathbf{r}_i}{l_{0,1}}, \\ \bar{\mathbf{p}}_M &= \frac{\mathbf{p}_M}{l_{0,1}}, \quad \bar{\mathbf{p}}_i = \frac{\mathbf{p}_i}{l_{0,1}}, \quad \bar{\mathbf{n}}_i = \frac{\mathbf{n}_i}{\rho A_1 \omega_c^2 l_{0,1}^2}, \quad (i = 1 \dots n). \end{aligned} \quad (7)$$

On the other hand, the nondimensional time τ can be calculated as $\tau = \omega_c t$. Finally, the following nondimensional time-varying parameters are defined: $\lambda_i(\tau) = \frac{l_i(\tau)}{l_{0,i}}$, $\Lambda_i(\tau) = \frac{L_i(\tau)}{l_{0,i}}$. It is then suitable to introduce the nondimensional arclength $\sigma = s_i / L_i(t)$, which varies into the nondimensional domain $[0, 1]$ for any time τ ; therefore, $L_i(\tau) = \Lambda_i(\tau) \lambda_i(\tau) l_{0,i}$. Due to the definition of ω_c , it turns out that the i -th axial force is given in nondimensional form as $\bar{N}_i(\sigma, \tau) = \kappa_i (\nu_i(\sigma, \tau) - 1)$, where $\kappa_i = (EA_i / EA_1)$ is the nondimensional axial stiffness of the i -th cable, defined as the ratio between the stiffness of the i -th cable and the first cable. Further nondimensional parameters governing the dynamics of the system are: the ratio between the mass per unit length of the i -th and the first cable $\varrho_i = \rho A_i / \rho A_1$, and the nondimensional damping coefficient $\bar{c}_i = c_i / (\rho A_1 \omega_c)$. Moreover, the nondimensional distributed load, calculated as $\bar{\mathbf{f}}_i = -\varrho_i \gamma \mathbf{e}_z$, is here considered to be the only cable self-weight $-\rho A_i g \mathbf{e}_z$, where $g = 9.81 \text{ m/s}^2$ is the gravity acceleration and $\gamma = g / (\omega_c^2 l_{0,1})$. Furthermore, after casting in nondimensional form the kinematic constraint equations, also the nondimensional form of the vector-valued balance equations of the end-effector linear and angular momentum is derived, in which $\mu = M / (\rho A_1 l_{0,1})$ represents the nondimensional EE mass and $\bar{J}_\mu = J_M [1 / (\rho A_1 l_{0,1}^3)]$. Finally, in the present work, the inertial and the elastic characteristics (i.e., ρA_i and EA_i , respectively) are assumed to be the same for all n cables, therefore $\kappa_i = 1$ and $\varrho_i = 1$, ($i = 1, \dots, n$).

2.4 Approximate Solution of the Equations of Motion

The discretization technique based on the Galerkin method is adopted to reduce the space-dependence of the cable equations of motion so as to reduce them into a set of ordinary differential equations, in the nondimensional time variable τ , coupled with the boundary equations of the balance of the end-effector linear and angular momentum. To this end, $m + 1$ trial functions are chosen so as to satisfy the kinematic boundary conditions; therefore, the approximate solution of the equations of motion is given by the 2-by-1 vector $\tilde{\mathbf{p}}_i(\sigma, \tau)$ ($i = 1, \dots, n$) expressed as the linear combination of the $m + 1$ trial functions as $\tilde{\mathbf{p}}_i(\sigma, \tau) = \mathbf{q}_{i,0}(\tau) \sigma + \sum_{j=1}^m \phi_{i,j}(\sigma) \mathbf{q}_{i,j}(\tau)$, where $\phi_{i,j}(\sigma) = \text{diag} \left(\varphi_{i,j}^{(y)}(\sigma), \varphi_{i,j}^{(z)}(\sigma) \right)$ is the ij -th 2-by-2 diagonal matrix collecting the j -th trial functions used to discretize the components of the i -th solution vector along the directions \mathbf{e}_y , and \mathbf{e}_z , respectively. In particular, it is assumed that $\varphi_{i,j}^{(y)}(\sigma) = \varphi_{i,j}^{(z)}(\sigma) = \sin(j \pi \sigma)$. Finally, $\mathbf{q}_{i,0}$ and $\mathbf{q}_{i,j}$ are the vectors collecting the unknown generalized coordinates.

Due to the trial functions adopted in the discretization, the approximate solution satisfies the kinematic constraint at $\sigma = 0$ (i.e., $\mathbf{p}_i(0, \tau) = \mathbf{0}$), whereas, to satisfy the compatibility equation at $\sigma = 1$, i.e., the nondimensional form of Eq. (3), the following relationship must hold: $\mathbf{q}_{i,0}(\tau) = \mathbf{q}_{1,0}(\tau) - \bar{\mathbf{r}}_1 + \bar{\mathbf{r}}_i - \bar{\mathbf{x}}_i$, ($i = 2, \dots, n$), since $\sin(j \pi \sigma) = 0$ at $\sigma = 1$ for all j . Therefore, only one out of n vectors $\mathbf{q}_{i,0}(\tau)$ is an effective set of unknown coordinates.

By now substituting the approximate solution into the equations of motion one obtains the vector of the unbalanced residual of the i -th equation of motion. By then collecting the n residual vectors into the $2n$ -by- $2n$ diagonal matrix $\tilde{\mathbf{H}}(\sigma, \tau)$, and by introducing the $2n$ -by- m matrix $\Phi(\sigma)$ collecting the sine functions, the matrix $\tilde{\mathbf{H}}(\sigma, \tau)$ of unbalanced residual can be minimized by ensuring that it is orthogonal in the nondimensional domain $[0, 1]$, to the trial functions adopted in the discretization.

3 Direct Approach to the Dynamic Problem

The system dynamics are governed by $2(nm + 1) + 1$ nonlinear balance equations of linear and angular momentum. On the other hand, the dynamic unknowns of the system are the $2(nm + 1)$ generalized coordinates collected in the 2-by-1 vectors $\mathbf{q}_{i,0}(\tau)$ and $\mathbf{q}_{i,j}(\tau)$ ($i = 1, \dots, n$, and $j = 1, \dots, m$), and the angle $\theta(\tau)$, respectively. Nevertheless, the system is characterized by further n unknown functions $\Lambda_i(\tau)$, providing the ratio, at time τ , between the unstretched length $L_i(\tau)$ and the distance $l_i(\tau)$ between the boundaries of the i -th cable. These time-dependent parameters play a crucial role in the calculation of the solution of the equations of motion of the system. Depending on the solution approach, those can be treated as known, pre-assigned, system parameters, or, conversely, as unknown functions to be calculated as part of the solution of the dynamic problem, in the direct and in the inverse

dynamic approach, respectively. Moreover, due to the generic number of cables that can be considered in the CDPM model, the latter may result to be under-, over-, or minimally-actuated, respectively. To classify the dynamic system, it is therefore convenient to introduce an additional parameter, namely, the degree of over-actuation o of the CDPM, defined as $o = n - d$ where d is the number of degrees of freedom. In this work the interest is not devoted to the study of the dynamics of under-actuated CDPM; therefore, by neglecting any possible under-actuated and minimally-actuated configuration, one scenario of interest is considered: namely, the over-actuated case, when $o > 0$. Moreover, only the direct approach will be investigated next.

The direct approach consists in assigning a priori the values of the n functions $\Lambda_i(\tau)$ and solving the system balance equations in terms of the $2(nm + 1) + 1$ unknown generalized coordinates and rotations. Unfortunately, this solution approach can not ensure that the effective motion of the end-effector, together with its orientation, matches exactly the expected trajectory. In fact, within the direct dynamic approach, only the balance equations of linear and angular momentum are verified and no kinematic relationship, providing the exact positioning in space and time of the EE, is satisfied. In particular, the target trajectory of the n connected points of the end-effector given by Eq. (6), is sought by assigning the n functions $\lambda_i(\tau)$ and solving the equations deriving from the minimization of the unbalanced residual and the balance equations of the linear and angular momentum of the EE mass, together with the initial conditions $\mathbf{q}_{1,0}(0) = \mathbf{q}_{1,0}^0$, $\mathbf{q}_{i,j}(0) = \mathbf{q}_{i,j}^0$, $\theta(0) = \theta^0$, and, $\dot{\mathbf{q}}_{1,0}(0) = \mathbf{0}$, $\dot{\mathbf{q}}_{i,j}(0) = \mathbf{0}$, $\dot{\theta}(0) = 0$, which can be calculated by solving the nonlinear equilibrium at time $\tau = 0$. Moreover, at the initial time step the n functions $\lambda_{0,i} = \lambda_i(0)$ ($i = 1, \dots, n$) can be calculated through the assigned trajectory, while an appropriate strategy must be used to calculate the ratios $\Lambda_{0,i} = \Lambda_i(0)$ ($i = 1, \dots, n$). To this end, $\Lambda_{0,i}$ can be determined by assuming the cables as massless linear springs and so as to satisfy the equilibrium equations of the end-effector mass as $\sum_{i=1}^n \hat{\mathbf{n}}_i + \mu \gamma \mathbf{e}_z = \mathbf{0}$, and $\sum_{i=1}^n (\bar{\mathbf{r}}_i \times \hat{\mathbf{n}}_i) = \mathbf{0}$, where $\hat{\mathbf{n}}_i = \kappa_i (1 - \Lambda_{0,i}) \hat{\mathbf{a}} = \bar{\mathbf{p}}_{M,i}(0)/\lambda_{0,i}$ is the vector of the axial force of the i -th massless spring directed as the unit vector $\hat{\mathbf{a}} = \bar{\mathbf{p}}_{M,i}(0)/\lambda_{0,i}$ tangent to the distance between the i -th cable boundary points at $\tau = 0$. Thus, to seek the solution of the direct dynamic problem, the n functions $\Lambda_i(\tau)$ can be assumed constant to the value attained at $\tau = 0$, that is $\Lambda_i(\tau) = \Lambda_{0,i}$. Although, it should be mentioned that the latter equations may provide values of $\Lambda_{0,i} \geq 1$ which imply that the i th cable is pre-compressed or stress-free; such conditions are unrealistic and, in that case, values of $\Lambda_{0,i} < 1$ must be assigned. Moreover, when the system is over-actuated (that is, when $o > 0$) the number of parameters $\Lambda_{0,i}$ is larger than the number of DoF (i.e., $n > d$); therefore, the solution depends on further o parameters $\Lambda_{0,k}$ ($k = 1, \dots, o$) which can be assigned ranging in the positive real number space \mathbb{R}^+ considering any value lower than 1. Finally, it is worth noting that, within the assumptions made to solve the direct problem, the parameters $\Lambda_i(\tau)$ ($i = 1, \dots, n$) do not represent, anymore, the effective cable aspect ratios, since the i th effective distance $l_i(\tau)$ does not coincide with that prescribed through the i th ratio $\lambda_i(\tau)$ and this is the consequence to the non-compatible solution calculated via direct approach.

3.1 Numerical Simulations on a Case-Study CDPM

The feasibility of the analytical model here developed is shown by performing numerical simulations on a selected CDPM configuration. By referring to [3], an EE having mass $M = 20$ kg and connected through a selected number n of elastic cables is considered in the simulations, together with the mechanical parameters reported in the above-mentioned work. In particular, all cables are characterized by the mass per unit length $\rho A_i = 4.19 \times 10^{-2}$ kg/m, the axial stiffness $EA_i = 150.36 \times 10^3$ N, ($i = 1, \dots, n$). A case-study simulation is performed by considering a selected CDPM configuration so as to discuss the case of over-actuated CDPM by considering $n = 4$ cables. Moreover, simulations are performed by assuming a weak dissipation function corresponding to a damping factor $\zeta = 0.5\%$. The coordinates of the cables boundaries at $s_i = 0$ are introduced in the model through the dimensional vector \mathbf{x}_i ($i = 1, \dots, n$). In particular: $\mathbf{x}_1 = [0 \ 0]^\top$, $\mathbf{x}_2 = [30 \ 0]^\top$, $\mathbf{x}_3 = [30 \ -10]^\top$, and $\mathbf{x}_4 = [0 \ -10]^\top$, where the components of the vectors are in meter (m). Finally, in the present case-study a square, having height of 1 m and the depth of 0.5 m, is considered. Therefore, the dimensional vectors describing the geometry of the end-effector mass are (dimensions are in meters): $\mathbf{r}_1^0 = [-0.25 \ 0.5]^\top$, $\mathbf{r}_2^0 = [0.25 \ 0.5]^\top$, $\mathbf{r}_3^0 = [0.25 \ -0.5]^\top$, $\mathbf{r}_4^0 = [-0.25 \ -0.5]^\top$, respectively. Finally, the EE principal mass moment of inertia with respect to the axis $\mathbf{b}_x(t)$ is $J_M = 2.08$ kg m². The end-effector is demanded to track a circular trajectory in the vertical plane ($\mathbf{e}_y, \mathbf{e}_z$) given by the vector $\mathbf{p}_M(t) = [(20 + \Delta_p \cos \Omega t) \ (-5 + \Delta_p \sin \Omega t)]^\top$ (components are in meters), where $\Delta_p = 1.5$ m and the angular velocity of the prescribed motion is assumed to be $\Omega = 0.314$ rad/s; therefore, the overall motion lasts 20 s. The orientation of the end-effector is demanded to vary according to the following time-law $\theta_M(t) = \frac{\pi}{18} \sin \Omega t$. Finally, at time $t = 0$ the position in space of the end-effector is given by the vector $\mathbf{p}_M(0) = [21.5 \ -5]^\top$ and its orientation by $\theta_M(0) = 0$. Simulations were performed by considering 5 trial functions (i.e., $m = 4$) to approximate the solution vector of each cable and the numerical computations were carried by implementing an in-house made code in the software Mathematica© [19].

In Fig. 1a and b is shown the motion of the EE mass simulated via direct approach in terms of the component along \mathbf{e}_y and \mathbf{e}_z of the position vector of cable 1 at $s_1 = L_1(t)$, Fig. 1a, and its orientation $\theta(t)$, Fig. 1 (b). The effective motion (black solid lines) was compared with the ideal trajectory represented by the black dashed lines. As expected, the motion of the end-effector shows oscillations near the ideal trajectory and this is due to the choice to keep constant in time the ratios $\Lambda_i(t)$ ($i = 1, \dots, 4$) by assuming those equal to the corresponding values $\Lambda_{0,i}$, calculated as discussed in the previous paragraph. The consequent error in the positioning of the EE along the directions \mathbf{e}_x and \mathbf{e}_z , is reported in Fig. 1c and d, respectively. The parametric model developed in this work allowed also to recover the time histories of the axial forces along the cable arclength and to monitor the change in time of the cable lengths. Such results are shown in Fig. 2a and b where are reported, at time t , the axial forces at $s_i = L_i(t)$ and the time histories of the total stretched and unstretched lengths of the four cables, respectively.

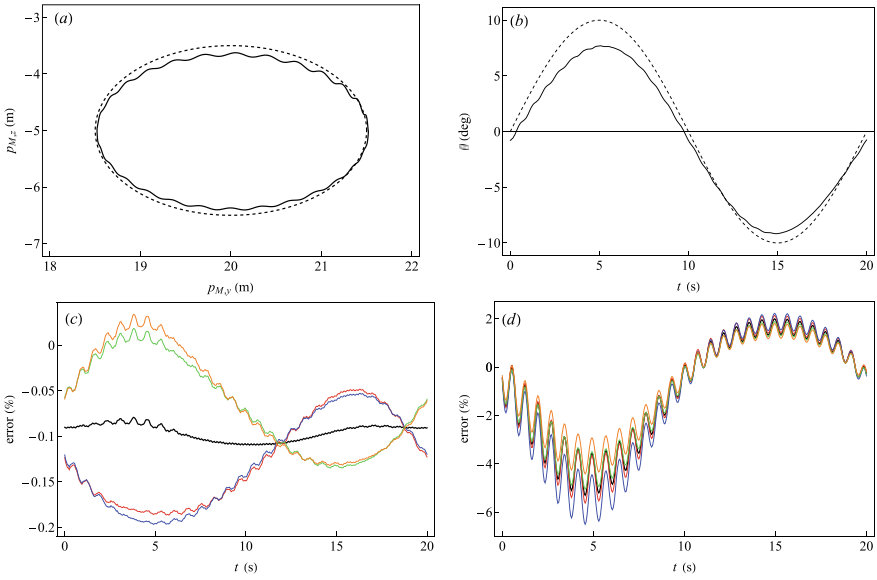


Fig. 1 Time history of the EE motion for a selected trajectory: **a** position vector $p_M(t)$ and **b** orientation $\theta(t)$. The dashed lines indicate the prescribed trajectory, while the solid black lines indicate the effective trajectory. Error in the positioning of the EE: component of p_i along e_x (**c**) and along e_z (**d**). Red, blue, green, orange, and black lines indicate the connection points of cables 1, 2, 3, 4, and of the EE center of mass, respectively

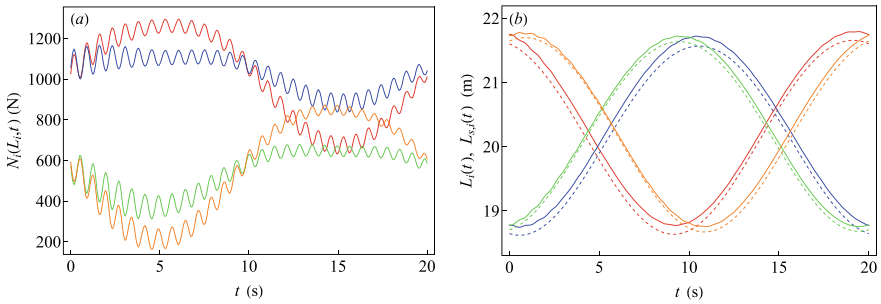


Fig. 2 Time history of the cable axial forces at $s_i = L_i(t)$ (**a**), and of the unstretched length $L_i(t)$ (solid lines) versus the stretched length $L_{s,i}(t)$ (dashed lines) (**b**) for $i = 1, \dots, 4$. Red, blue, green, orange, and black lines indicate the connection points of cables 1, 2, 3, 4, and of the EE center of mass, respectively

4 Conclusions

A parametric nonlinear dynamic model of CDPM undergoing two-dimensional motions was presented and discussed in this paper. Cables were modeled as elastic one-dimensional continua possessing distributed inertia and damping and characterized by time-varying lengths for the exact positioning (and orientation) in time of a two-dimensional end-effector mass. Simulations were carried out on a selected case-study to show the feasibility of the analytical model to investigate the dynamic response of over-actuated CDPMs endowed with an oriented mass, via the direct approach. It was shown that is possible to appropriately describe the dynamics of CDPM by a low-order dynamical model which, thus, can be suitably adopted for designing optimal control strategies.

Acknowledgements This research was in part sponsored by the NATO, Science for Peace and Security Programme Multi-Year Project Application, G5924–“IRIS–Inspection and security by Robots interacting with Infrastructure digital twinS”.

References

1. Arena A, Ottaviano E, Gattulli V (2023) Dynamics of cable-driven parallel manipulators with variable length vibrating cables. *Int J Non-Linear Mech* 151(104382):1–21
2. Arena A (2015) Free vibration of flexible cables. In: International design engineering technical conferences and computers and information in engineering conference, vol 57181. American Society of Mechanical Engineers, p V008T13A082
3. Du J, Agrawal SK (2015) Dynamic modeling of cable-driven parallel manipulators with distributed mass flexible cables. *J Vib Acoust* 137(2):1–8
4. Du J, Cui C, Bao H, Qiu Y (2015) Dynamic analysis of cable-driven parallel manipulators using a variable length finite element. *J Comput Nonlinear Dyn* 10(1)
5. Foti F, Geuzaine M, Denoël V (2021) On the identification of the axial force and bending stiffness of stay cables anchored to flexible supports. *Appl Math Model* 92:798–828
6. Foti F, Martinelli L (2016) Mechanical modeling of metallic strands subjected to tension, torsion and bending. *Int J Solids Struct* 91:1–17
7. Gómez GR, Arena A, Ottaviano E, Gattulli V (2023) Direct dynamics of 2D cable-driven parallel robots including cables mass effect and its influence in the control performance. In: Materials research proceedings, vol 26, pp 387–392
8. Irvine HM (1981) Cable structures. The MIT Press
9. Juárez-Pérez S, Martín-Parra A, Arena A, Ottaviano E, Gattulli V, Castillo-García FJ (2022) Dynamic control of a novel planar Cable-Driven parallel robot with a large wrench feasible workspace. *Actuators* 11(367)
10. Kozak K, Zhou Q, Wang J (2006) Static analysis of cable-driven manipulators with non-negligible cable mass. *IEEE Trans Robot* 22(3)
11. Lepidi M, Gattulli V (2012) Static and dynamic response of elastic suspended cables with thermal effects. *Int J Solids Struct* 49(9):1103–1116
12. Lepidi M, Gattulli V, Vestroni F (2007) Static and dynamic response of elastic suspended cables with damage. *Int J Solids Struct* 44(25–26):8194–8212
13. Merlet JP (2005) Parallel robots, vol 128. Springer Science & Business Media

14. Merlet JP (2015) The kinematics of cable-driven parallel robots with sagging cables: preliminary results. In: 2015 IEEE international conference on robotics and automation (ICRA). IEEE, pp. 1593–1598
15. Oh SR, Agrawal SK (2005) A reference governor-based controller for a cable robot under input constraints. *IEEE Trans Control Syst Technol* 13(4):639–645
16. Ottaviano E, Arena A, Gattulli V (2021) Geometrically exact three-dimensional modeling of cable-driven parallel manipulators for end-effector positioning. *Mech Mach Theory* 155(104102):1–20
17. Ottaviano E, Arena A, Gattulli V, Potenza F (2019) Slackening effects in 2D exact positioning in cable-driven parallel manipulators. In: Pott A, Bruckmann T (eds) *Mechanisms and machine science. Cable-driven parallel robots. CableCon 2019*, vol 74. Springer, Cham, pp 319–330
18. Riehl N, Gouttefarde M, Krut S, Baradat C, Pierrot F (2009) Effects of non-negligible cable mass on the static behavior of large workspace cable-driven parallel mechanisms. In: 2009 IEEE international conference on robotics and automation. IEEE, pp 2193–2198
19. Wolfram Research, Inc. (2016) *Mathematica*, Version 11. Champaign, IL. <https://www.wolfram.com/mathematica>

Catenary Solutions for Inextensible Cables: A Perturbation-Based High-Order Approximation



Marco Lepidi 

Abstract Cable structures are structurally efficient and architecturally elegant solutions for bearing and transferring loads across medium and large spans. The shape-finding problem related to the equilibrium configuration of suspended cables may present some algorithmic hurdles, related to the coexistence of analytical catenary solutions with nonlinear compatibility equations that need to be solved numerically. The catenary function describing the static equilibrium configuration for an inextensible cable suspended between displaceable supports is asymptotically expressed, using a proper perturbation method. The asymptotic configuration solution is described by an explicit polynomial function of the mechanical parameters and support displacements, automatically satisfying the compatibility condition. Fine approximation accuracy is achieved by extending the perturbation solution to high orders.

Keywords Cable structures · Catenary · Taut string · Inclined shallow cable · Perturbation methods

1 Introduction

Owing to a successful combination of extreme lightness, high strength and fine parametric designability, cable structures are considered unparalleled mechanical solutions for covering medium and large spans. By exploiting the limitless possibilities of combination with other structural elements (beams, arches, rings), cables are profitably used in a wide range of traditional and emerging engineering applications, including—among the others—suspension bridges, cable-stayed roofs, transmission lines, guyed masts, rigging systems, tethered vehicles, parallel manipulators.

M. Lepidi (✉)

DICCA - Department of Civil, Chemical and Environmental Engineering, University of Genoa,
Via Montallegro 1, 16145 Genoa, Italy

e-mail: marco.lepidi@unige.it

Genoa Section of INFN - National Institute for Nuclear Physics, Via Dodecaneso 33, 16146
Genoa, Italy

© The Author(s), under exclusive license to Springer Nature Switzerland AG 2024
V. Gattulli et al. (eds.), *Dynamics and Aerodynamics of Cables*, Lecture Notes in Civil
Engineering 399, https://doi.org/10.1007/978-3-031-47152-0_31

363

Over the past decades, numerous scientific publications and monographs have been focused on the topic, dealing with both the static and dynamic responses of horizontal or inclined cables [1–4].

Searching for the equilibrium configuration assumed by a suspended cable hanging between fixed supports at different levels can be regarded as a statically indeterminate shape-finding problem. Starting in the seventeenth century, the topic attracted the interest of many outstanding scientists, including Galileo, d’Alembert, Euler, Huygens, Bernoulli and many others. Specifically, if the ideal hypothesis of axial indeformability is introduced, the curved configuration assumed by a perfectly flexible cable under self-weight is mathematically described by a transcendental (non-polynomial) function, whose map in the vertical (gravitational) plane is known as *catenary* curve [1]. Admitting elastic axial deformability determines a slightly different configurational curve, mathematically described by a distinct transcendental function, analytically expressible in cartesian parametric form, whose map is known as *elastic catenary* curve. Both configurational functions depend on the horizontal reaction at the supports, playing the role of hyperstatic unknown, to be numerically determined by solving nonlinear equations expressing the indeformability constraint (for the catenary), or a pair of coupled compatibility boundary conditions (for the elastic catenary).

Within this well-established framework, mathematical difficulties in the analytical treatment of transcendental functions have inevitably led to the proliferation of approximate static solutions, mainly of the polynomial type (quadratic and cubic), which are more suitable for algebraic and differential manipulations. On the other hand, numerous studies have shown that the highest possible accuracy in the description of the static cable configuration, even if approximate, is a crucial aspect in direct and inverse mechanical problems, including—for instance—the assessment of the linearized modal properties [5–7], the description of nonlinear dynamic and aerodynamic phenomena [8–11], the evaluation of damage and temperature effects [12, 13], the performance of active control strategies [14, 15] and the reliability of identification procedures [16, 17]. Based to these considerations, the present contribution proposes a perturbation-based high-order solution for the asymptotic approximation of the catenary function that characterizes the static response of an inextensible cable to self-weight.

2 Static Equilibrium Problem

The quasi-static equilibrium of a suspended cable can be governed by formulating the mechanical model of a one-dimensional non-polar continuum, embedded in a three-dimensional space. The continuum is assumed homogeneous and linearly elastic, with natural length L_0 in the initial (undeformed and unstressed) configuration \mathcal{C}_0 . The kinematic hypotheses of perfectly flexibility in the transversal directions and axial indeformability are adopted. The latter can be introduced by ideally assuming infinite axial rigidity ($EA \rightarrow \infty$) in the elastic law $N = EA \varepsilon$, so that identically

null axial strain ε may correspond to finite-valued axial tensions N . In the absence of transversal (flexural and shear) rigidities, the axial tension is systematically required to be locally collinear to the equilibrium configuration. Therefore, searching the cable response under gravity loads consists in solving a geometric shape-finding problem, pursuing the unknown curvilinear configuration C_S satisfying the equilibrium in the vertical (gravitational) plane.

2.1 Governing Equations and Catenary Solutions

The suspended cable is supposed hanging between two distinct supports S_A and S_B , under the sole effect of uniform self-weight w per unit natural length (Fig. 1). Cables hanging between supports at different levels are referred to as *inclined* cables. Inclined cables are characterized by a *span* length L (horizontal inter-support distance) that differs from the *chord* length L_c (inter-support distance) according to the relation $L_c = L \sec \vartheta$, where ϑ expresses the *inclination angle*. Assuming the horizontal abscissa X as independent variable, the configurational function $Y(X)$ has to be determined to locate the cartesian position of each cable point $P(X)$ in the vertical plane. The horizontal and vertical reactions H and V at the support S_A , together with the axial tension $N(X)$, are also unknown.

The nonlinear coupled system of partial differential equations governing (i) the static equilibrium, (ii) the exact kinematics and (iii) the linear elastic law of the extensible cable can be manipulated to obtain—without approximations—the nonlinear ordinary differential equation governing the static vertical equilibrium of the

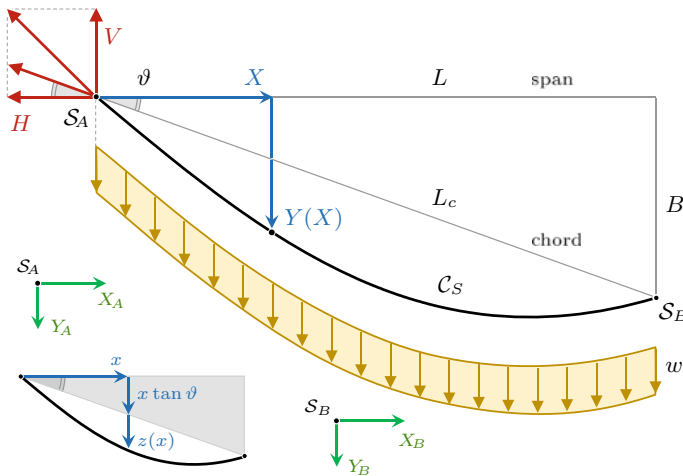


Fig. 1 Static equilibrium configuration C_S of a suspended cable under self-weight

infinitesimal cable element (see for instance [25]). Therefore, imposing the axial indeformability, the governing equation reads

$$\frac{d^2Y}{dX^2} = -\frac{w}{H} \left[1 + \left(\frac{dY}{dX} \right)^2 \right]^{1/2} \quad (1)$$

and is completely characterized by the constant coefficient w/H affecting the right-hand term. It is fundamental to remark that the horizontal reaction H plays the role of hyperstatic unknown, to be determined a posteriori by imposing a *compatibility condition*, according to a solution strategy resembling the force method used to solve statically indeterminate elastic problems.

The compatibility condition is imposed by requiring that the H -dependent arc-length L_e in the equilibrium configuration \mathcal{C}_S equates the natural length L_0 , to respect the cable inextensibility. Therefore, the *compatibility equation* is expressed as $L_e = L_0$. An admissible solution can exist only if the natural length exceeds the inter-support distance L_c . Thus, the *admissibility (inextensibility) inequality* $L_0 > L_c$ holds for fixed supports. If the supports undergo differential settlements $\Delta X = X_B - X_A$ and $\Delta Y = Y_B - Y_A$ (where X_A, Y_A and X_B, Y_B are displacements at supports \mathcal{S}_A and \mathcal{S}_B , respectively), the admissibility inequality becomes $L_0 > L_d$, where L_d is the distance between the displaced supports.

The governing equation can be expressed in a suited nondimensional form by introducing dimensionless independent and dependent variables, together with a minimal set of independent dimensionless parameters. To this purpose, by selecting the cable span L as (known) reference length and the horizontal reaction H as (unknown) reference force, the dimensionless quantities

$$x = \frac{X}{L}, \quad y = \frac{Y}{L}, \quad x_J = \frac{X_J}{L}, \quad y_J = \frac{Y_J}{L}, \quad \delta = \frac{wL_0}{8H}, \quad \Lambda = \frac{L_0}{L} \cos \vartheta \quad (2)$$

are defined, where the subscript $J = A, B$ refers to the left and right support. The geometric parameter Λ is known as *aspect ratio* and represents the ratio between the natural cable length and the inter-support distance L_c . The fundamental parameter δ expresses (one eighth of) the ratio between the approximate cable weight $wL \sec \vartheta$ and the approximate chord-aligned reaction $H \sec \vartheta$. The nondimensional form of the governing equation reads

$$y'' = -\delta [1 + (y')^2]^{1/2} \quad (3)$$

where the apex indicates differentiation with respect to the dimensionless coordinate x , spanning the domain $\mathcal{D} = [x_A, 1 + x_B]$. The role of dimensionless *hyperstatic unknown* is assumed by the parameter δ . The equation is complemented by boundary conditions $y(x_A) = y_A$ and $y(1 + x_B) = \tan \vartheta + y_B$.

The analytical solution of the nonlinear equation (3) is the well known catenary function $y_b(x) = y_A + \sinh(4\delta(x - x_A)) \sinh(\Psi_b - 4\delta(x + x_A)) / (4\delta)$, where Ψ_b is

a constant depending on the boundary conditions. Among all the statically determinable δ -dependent catenary functions satisfying the static equilibrium, the unique geometrically compatible solution $y_e(x)$ must be determined by assessing the hyperstatic unknown δ a posteriori. To this aim, the compatibility condition $\Lambda_e = \Lambda_0$ is imposed, where $\Lambda_e = L_e/L_c \sec \vartheta$ is the dimensionless δ -dependent arc-length of the catenary curve described by the function $y(x)$, reading

$$\Lambda_e = \cos \vartheta \int_{\mathcal{D}} [1 + (y')^2]^{1/2} dx \quad (4)$$

which depends on $x_B - x_A$ and $y_B - y_A$ only. In synthesis, the catenary function $y_e(x)$ must be regarded as a *quasi-analytical* solution, because the hyperstatic unknown δ has to be determined a posteriori, by solving numerically the transcendental compatibility condition. In the context of cable structures, the lack of *fully analytical* catenary solutions is an algorithmic hurdle that tends to slow down the development of parametric design tools—on the one hand—and often requires significant computational resources—on the other hand.

3 Perturbation Strategy for Fully-Analytical Solutions

A proper mathematical alternative to exact (but quasi-analytical) catenary solutions can be represented by fully analytical—although asymptotically approximate—polynomial solutions achievable by means of perturbation techniques. Perturbation methods are powerful asymptotic techniques that are widely used in a large variety of scientific research fields, ranging from direct problems concerning linear and nonlinear dynamics, stability and bifurcation [18–20] to inverse problems dealing with modal identification, optimal spectral design, damping and damage detection [21–23]. Perturbation methods are also classical and well-established strategies to study different problems in cable mechanics, including static behaviours [24, 25], linear and nonlinear dynamic phenomena [2, 26], aerodynamic instabilities [11, 27], active vibration control [28, 29].

Due to their typical lightness (small w) and high tensioning (large H), structural cables tend to be characterized by geometric closeness between the static equilibrium configuration and the inter-support chord. This geometric property is commonly referred to as cable *shallowness*. Consequently, the static problem for shallow cables can be reformulated by introducing the change of variables

$$y(x) = z(x) + y_d(x) = z(x) + a_0x + a_1 \quad (5)$$

where the linear function $y_d(x) = a_0x + a_1$ describes the chord between the *displaced* supports (Fig. 1). The coefficients of the function $y_d(x)$ depend on the set of boundary displacements $\mathbf{x} = (x_A, y_A, x_B, y_B)$ according to the relations

$$a_0 = \frac{y_B - y_A + \tan \vartheta}{1 - x_A + x_B}, \quad a_1 = \frac{y_A(1 + x_B) - x_A(y_B + \tan \vartheta)}{1 - x_A + x_B} \quad (6)$$

where $a_0 = \tan \vartheta$ and $a_1 = 0$ for fixed supports ($\mathbf{x} = \mathbf{0}$). From the physical viewpoint, the configuration variable $z(x)$ describes the small dip of the static cable profile below the extended chord. The dimensionless length of the extended chord between the displaced supports is $\Lambda_d = (L_d/L) \cos \vartheta$ and can be determined as $\Lambda_d = \cos \vartheta [(1 + \Delta_x)^2 + (\tan \vartheta + \Delta_y)^2]^{1/2}$, where $\Delta_x = x_B - x_A$ and $\Delta_y = y_B - y_A$. Applying the change of variable, Eq. (3) becomes

$$z'' = -\delta [1 + a_0^2 + 2a_0z' + (z')^2]^{1/2} \quad (7)$$

while the boundary conditions read $z(x_A) = 0$ and $z(1 + x_B) = 0$. An asymptotic form of the analytical solution is pursued for a cable with given aspect ratio Λ .

According to a standard perturbation strategy, the unknown solution $z(x)$ is postulated to be expressible as a finite series of n terms $z_i(x)$, scaled by increasing integer powers of a small nondimensional bookkeeping parameter $\epsilon \ll 1$, yielding

$$z_{[n]}(x) = \sum_{i=1}^n \epsilon^i z_i(x) = \epsilon z_1(x) + \epsilon^2 z_2(x) + \dots + \epsilon^i z_i(x) + \dots + \epsilon^n z_n(x) \quad (8)$$

where the functions $z_i(x)$ work as independent unknown variables.

Once all the functions $z_i(x)$ are determined for $i = 1, \dots, n$, the n -th approximate solution $z_{[n]}(x)$ is expected to asymptotically tend to the exact solution for growing n -values (increasing *approximation orders*). Although unknown a priori, the parameter δ can be considered small by hypothesis, coherently with the assumption of cable shallowness. Therefore, the parameter ordering

$$\delta_{[n]} = \epsilon \delta_1 + \epsilon^2 \delta_2 + \epsilon^3 \delta_3 + \dots + \epsilon^n \delta_n \quad (9)$$

can be postulated. As a minor difference from other perturbation approaches for the statics of inclined shallow cables, it can be noted that the a priori postulated ordering only concerns unknown variables and parameters.

Substituting the parameter ordering (9) and the variable expansion (8) in the nonlinear equation (7), expanding and collecting terms of the same ϵ -power, an ordered hierarchical system of linear *perturbation equilibrium equations* is obtained. Neglecting orders higher than the sixth ($n = 6$), the system reads

$$\epsilon^1 : z_1'' = -8c_0 \delta_1 \quad (10)$$

$$\epsilon^2 : z_2'' = -8c_0 \delta_2 - 8a_0 b_0 \delta_1 z_1' \quad (11)$$

$$\epsilon^3 : z_3'' = -8c_0 \delta_3 - 8a_0 b_0 [\delta_2 z_1' + \delta_1 z_2'] - 4b_0^3 \delta_1 (z_1')^2 \quad (12)$$

$$\begin{aligned} \epsilon^4 : z_4'' = & -8c_0 \delta_4 - 8a_0 b_0 [\delta_3 z_1' + \delta_2 z_2' + \delta_1 z_3'] \\ & - 4b_0^3 z_1' [\delta_2 z_1' + 2\delta_1 z_2'] + 4a_0 b_0^5 \delta_1 (z_1')^3 \end{aligned} \quad (13)$$

$$\begin{aligned} \epsilon^5 : z''_5 = & -8c_0\delta_5 - 8a_0b_0[\delta_4z'_1 + \delta_3z'_2 + \delta_2z'_3 + \delta_1z'_4] \\ & - 4b_0^3[\delta_3(z'_1)^2 + 2\delta_2z'_1z'_2 + 2\delta_1z'_1z'_3 + \delta_1(z'_2)^2] \\ & + 4b_0^5(z'_1)^2[c_0\delta_2z'_1 + 3a_0\delta_1z'_2 - \delta_1(z'_1)^2] + 5b_0^7\delta_1(z'_1)^4 \end{aligned} \tag{14}$$

$$\begin{aligned} \epsilon^6 : z''_6 = & -8c_0\delta_6 - 8a_0b_0[\delta_5z'_1 + \delta_4z'_2 + \delta_3z'_3 + \delta_2z'_4 + \delta_1z'_5] + \\ & - 4b_0^3[\delta_4(z'_1)^2 + 2\delta_3z'_1z'_2 + 2\delta_2z'_1z'_3 + 2\delta_1z'_1z'_4 + \delta_2(z'_2)^2 + 2\delta_1z'_2z'_3] + \\ & + 4b_0^5(z'_1)^2[c_0\delta_3 - 4\delta_1z'_2 - \delta_2(z'_1)] + 3a_0(\delta_1z'_1z'_3 + \delta_2z'_1z'_2 + \delta_1(z'_2)^2) + \\ & + b_0^7(z'_1)^3[4a_0\delta_1(z'_1)^2 + 5\delta_2z'_1 + 20\delta_1z'_2] - 7a_0b_0^9\delta_1(z'_1)^5 \end{aligned} \tag{15}$$

where the auxiliary parameters $c_0^2 = 1 + a_0^2$ and $b_0^2 = c_0^{-2}$. Homogeneous boundary conditions $z_i(x_A) = 0$ and $z_i(1 + x_B) = 0$ must be imposed at each order. Clearly, the hierarchy of perturbation equations can be extended to higher orders ($n > 6$), whenever a finer approximation accuracy is necessary.

The system solutions can be obtained straightforwardly by attacking the equations in cascade, starting from the lowest order, returning the *generating solution* $z_1(x)$. Thereafter (for $i > 1$), the i -th order systematically states an ordinary differential non-homogeneous linear equation involving only the second derivative of the i -th unknown variables $z_i(x)$ —at the left hand—and a known polynomial term, involving the first derivatives of all the lower-order variables—at the right hand. Since the generating solution is a second x -degree (quadratic) function, the higher ϵ -order solutions are polynomials of increasing x -degrees (cubic, quartic, quintic, ...). Specifically, the solution of the i -th order (power of the perturbation parameter ϵ) is a polynomial function including terms up to the $(i + 1)$ -th degree (power of the variable x), reading

$$\epsilon^i : z_i(x) = \sum_{j=0}^{i+1} c_{ij}x^j \tag{16}$$

where c_{ij} are auxiliary coefficients depending on the displacement set \mathbf{x} and the hyperstatic unknown coefficients δ_i (with $i = 1, \dots, n$).

After reconstruction, the hyperstatic unknown $\delta_{[n]}$ must be univocally assessed to identify the unique geometrically compatible solution $y_{[n]}(x) = z_{[n]}(x) + a_0x + a_1$ among all the statically determinable polynomial functions satisfying the perturbation equilibrium Eqs. (10)–(15). To this purpose, the compatibility equation can be imposed in the form $\Lambda_p = \Lambda_0$, where Λ_p is the dimensionless arc-length of the polynomial curve described by the function $y_{[n]}(x)$. According to differential geometry, the nondimensional arc-length is

$$\Lambda_p = \cos \vartheta \int_{\mathcal{D}} [1 + (y'_{[n]})^2]^{\frac{1}{2}} dx = \cos \vartheta \int_{\mathcal{D}} [1 + a_0^2 + 2a_0z' + (z'_{[n]})^2]^{\frac{1}{2}} dx \tag{17}$$

which tends to the catenary length Λ_e for growing n -values. By operating accordingly to the perturbation scheme ruled by Eqs. (8) and (9), the asymptotic arc-length takes the form $\Lambda_{p[n]} = \Lambda_{p0} + \epsilon \Lambda_{p1} + \epsilon^2 \Lambda_{p2} + \dots + \epsilon^i \Lambda_{pi} + \dots + \epsilon^n \Lambda_{pn}$, where

the lowest order series coefficients are $\Lambda_{p0} = \Lambda_d$ and $\Lambda_{p1} = 0$, while the higher order series coefficients read

$$\Lambda_{p2} = \frac{8}{3} b_0 \delta_1^2 \Sigma_x^3 \cos \vartheta \quad (18)$$

$$\Lambda_{p3} = \frac{16}{3} b_0 \delta_1 \delta_2 \Sigma_x^3 \cos \vartheta \quad (19)$$

$$\Lambda_{p4} = \left[\frac{8}{45} b_0 \Sigma_x^3 (32\delta_1^4 \Sigma_x^2 + 15(2\delta_1\delta_3 + \delta_2^2)) - \frac{32}{9} b_0^3 \delta_1^4 \Sigma_x^5 \right] \cos \vartheta \quad (20)$$

$$\Lambda_{p5} = \left[\frac{16}{45} b_0 \Sigma_x^3 (64\delta_1^3 \delta_2 \Sigma_x^2 + 15(\delta_1\delta_4 + \delta_2\delta_3)) - \frac{128}{9} b_0^3 \delta_1^3 \delta_2 \Sigma_x^5 \right] \cos \vartheta \quad (21)$$

$$\Lambda_{p6} = \left[\frac{8}{315} b_0 \Sigma_x^3 (64\delta_1^2 \Sigma_x^2 S_4 + 105S_6) - \frac{64}{135} b_0^3 \Sigma_x^5 \delta_1^2 R_4 + \frac{256}{27} b_0^5 \delta_1^6 \Sigma_x^7 \right] \cos \vartheta \quad (22)$$

where the auxiliary quantities $S_4 = 4\delta_1^4 \Sigma_x^2 + 7\Delta_4$, $R_4 = 32\delta_1^4 \Sigma_x^2 + 15\Delta_4$, $S_6 = 2\delta_1\delta_5 + 2\delta_2\delta_4 + \delta_3^2$, and $\Delta_4 = 2\delta_1\delta_3 + 3\delta_2^2$. It can be noted that the arc-length $\Lambda_{p[n]}$ is a function of the displacement differences $\Sigma_x = 1 + \Delta_x$ and Δ_y only, and also depends on the hyperstatic coefficients δ_i (up to $i = n - 1$).

In summary, determining the static equilibrium configuration requires (i) to assign the inclination angle ϑ and the aspect ratio Λ , (ii) to assign the support displacements x , defining the extended chord length Λ_d , and (iii) to enforce the compatibility equation $\Lambda_p = \Lambda$, to be solved in the hyperstatic unknown δ . The assigned aspect ratio must satisfy the *inextensibility condition* $\Lambda > \Lambda_d$. Furthermore, the postulate of cable shallowness (expressed by the smallness $\delta = \mathcal{O}(\epsilon)$) is respected if and only if the assigned aspect ratio Λ satisfies the same ordering $\Lambda = \Lambda_d + \mathcal{O}(\epsilon^2)$ of the arc-length $\Lambda_p = \Lambda_d + \mathcal{O}(\epsilon^2)$. This fundamental requirement is referred to as the *consistency condition* in the following. The consistency is automatically verified if the aspect ratio is ordered as $\Lambda = \Lambda_d + \epsilon^2 \Lambda_2$, where Λ_2 represents the natural extra-length. Physically, these mathematical requirements reflect the intuitive idea that the natural length of inextensible shallow cables must be greater (inextensibility condition), but not much greater (shallowness postulate) than the distance between the displaced supports.

According to the above considerations, the compatibility condition $\Lambda_p = \Lambda$ can be imposed in the asymptotic form $\Lambda_{p[n]} = \Lambda_d + \epsilon^2 \Lambda_2$. The resulting ordered hierarchy of algebraic *perturbation compatibility equations* returns the coefficients δ_i of the asymptotic hyperstatic unknown $\delta_{[n]}$, reading

$$\delta_1 = \frac{1}{4} \Lambda_1 \sec \vartheta \quad (23)$$

$$\delta_3 = - \left[\frac{3}{80} + \frac{1}{10} a_0^2 \right] b_0 \Lambda_1 \Lambda_2 \Sigma_x^{-1} \sec^2 \vartheta \quad (24)$$

$$\delta_5 = \left[\frac{321}{22400} + \frac{167}{1400} a_0^2 + \frac{17}{175} a_0^4 \right] b_0^2 \Lambda_1 \Lambda_2^2 \Sigma_x^{-2} \sec^3 \vartheta \quad (25)$$

while $\delta_2 = \delta_4 = \delta_6 = 0$ and $\Lambda_1 = (6c_0 \Lambda_2 \cos \vartheta)^{1/2} \Sigma_x^{-3/2}$. As major result, after reconstruction the hyperstatic unknown $\delta_{[n]}$ and the configuration function $y_{[n]}(x)$ are known analytical functions of the mechanical parameters and the support displacements. The high accuracy achievable in the asymptotic approximation is successfully verified in Figs. 2 and 3, in which the exact quasi-analytical (catenary-based) solu-

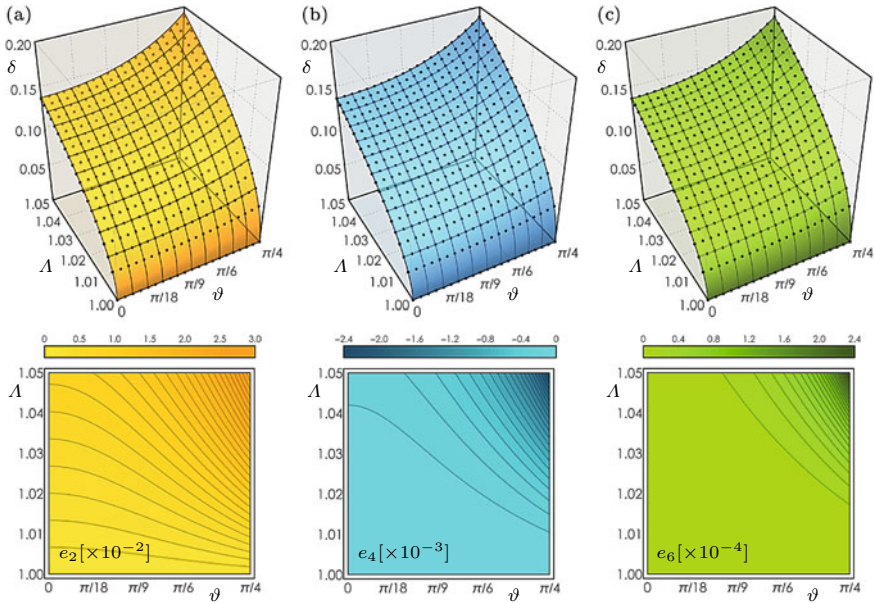


Fig. 2 Exact hyperstatic unknown δ (black dots) versus asymptotic approximations $\delta_{[n]}$ in the parameter ranges $\Lambda \in [100/100, 105/100]$ and $\vartheta \in [0, \pi/4]$ for boundary displacements $\Delta_x = 0$ and $\Delta_y = 0$: **a** $n = 2$ (yellow surface); **b** $n = 4$ (blue surface); **c** $n = 6$ (green surface). Relative errors are defined $e_n = (\delta_{[n]} - \delta)/\delta$

tions are compared with their fully analytical (perturbation-based) approximations within the technically significant range of mechanical parameters (with the exclusion of vertical or quasi-vertical cables).

4 Concluding Remarks

The catenary function representing the exact analytical solution of the static equilibrium problem for an inextensible cable suspended between displaceable supports has been asymptotically expressed by means of perturbation methods. The asymptotically approximate configuration function is an explicit function of the mechanical parameters and support displacements. Fine approximation accuracy has been achieved by extending the perturbation solution to high orders.

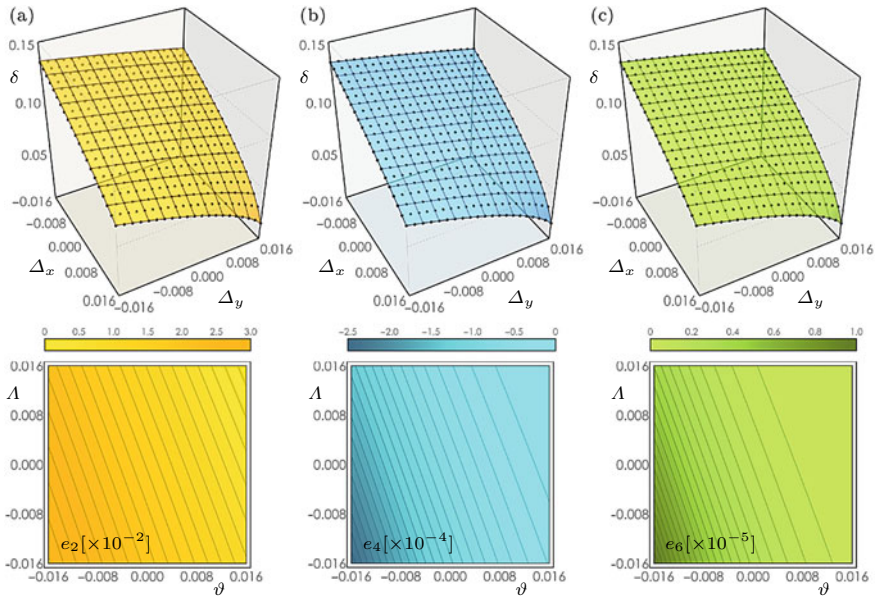


Fig. 3 Exact hyperstatic unknown δ (black dots) versus asymptotic approximations $\delta_{[n]}$ in the boundary displacement ranges $\Delta_x \in [-0.016, 0.016]$ and $\Delta_y \in [-0.016, 0.016]$ for parameters $\Lambda = 102/100$ and $\vartheta = \pi/8$: **a** $n=2$ (yellow surface); **b** $n=4$ (blue surface); **c** $n=6$ (green surface). Relative errors are defined $e_n = (\delta_{[n]} - \delta)/\delta$

References

1. Irvine H (1981) Cable structures. MIT Press
2. Rega G (2004) Nonlinear vibrations of suspended cables-part I: modeling and analysis. *Appl Mech Rev* 57(6):443–478
3. Rega G (2004) Nonlinear vibrations of suspended cables-part II: deterministic phenomena. *Appl Mech Rev* 57(6):479–514
4. Luongo A, Zulli D (2013) Mathematical models of beams and cables. Wiley
5. Wu Q, Takahashi K, Nakamura S (2005) Formulae for frequencies and modes of in-plane vibrations of small-sag inclined cables. *J Sound Vib* 279(3):1155–1169
6. Lacarbonara W, Paolone A, Vestroni F (2007) Elastodynamics of nonshallow suspended cables: linear modal properties. *J Vib Acoust* 129(4):425–433
7. Mansour A, Mekki OB, Montassar S, Rega G (2018) Catenary-induced geometric nonlinearity effects on cable linear vibrations. *J Sound Vib* 413:332–353
8. Srinil N, Rega G, Chucheepsakul S (2004) Three-dimensional non-linear coupling and dynamic tension in the large-amplitude free vibrations of arbitrarily sagged cables. *J Sound Vib* 269(3–5):823–852
9. Lacarbonara W, Paolone A, Vestroni F (2007) Non-linear modal properties of non-shallow cables. *Int J Non Linear Mech* 42(3):542–554
10. Gattulli V, Lepidi M, Potenza F, Di Sabatino U (2019) Modal interactions in the nonlinear dynamics of a beam-cable-beam. *Nonlinear Dyn* 96(4):2547–2566
11. Zulli D, Piccardo G, Luongo A (2021) On the nonlinear effects of the mean wind force on the galloping onset in shallow cables. *Nonlinear Dyn* 103(4):3127–3148

12. Lepidi M, Gattulli V, Vestroni F (2007) Static and dynamic response of elastic suspended cables with damage. *Int J Solids Struct* 44(25–26):8194–8212
13. Lepidi M, Gattulli V (2012) Static and dynamic response of elastic suspended cables with thermal effects. *Int J Solids Struct* 49(9):1103–1116
14. Gattulli V, Alaggio R, Potenza F (2008) Analytical prediction and experimental validation for longitudinal control of cable oscillations. *Int J Non Linear Mech* 43(1):36–52
15. Arena A, Ottaviano E, Gattulli V (2023) Dynamics of cable-driven parallel manipulators with variable length vibrating cables. *Int J Non Linear Mech* 151:104382
16. Lepidi M, Gattulli V, Vestroni F (2009) Damage identification in elastic suspended cables through frequency measurement. *J Vib Control* 15(6):867–896
17. Rinaldi C, Lepidi M, Potenza F, Gattulli V (2023) Identification of cable tension through physical models and non-contact measurements. *Mech Syst Signal Pr* 205:110867
18. Nayfeh AH (2007) *Perturbation methods*. Wiley-VCH Verlag GmbH
19. Rand RH, Armbruster D (2012) *Perturbation methods, bifurcation theory and computer algebra*, vol 65. Springer
20. Luongo A (2017) On the use of the multiple scale method in solving difficult bifurcation problems. *Math Mech Solids* 22(5):988–1004
21. Lepidi M (2013) Multi-parameter perturbation methods for the eigensolution sensitivity analysis of nearly-resonant non-defective multi-degree-of-freedom systems. *J Sound Vib* 332(4):1011–1032
22. Lacarbonara W, Carboni B, Quaranta G (2016) Nonlinear normal modes for damage detection. *Meccanica* 51(11):2629–2645
23. Lepidi M, Bacigalupo A (2018) Parametric design of the band structure for lattice materials. *Meccanica* 53(3):613–628
24. Denoël V, Detournay E (2010) Multiple scales solution for a beam with a small bending stiffness. *J Eng Mech* 136(1):69–77
25. Luongo A, Zulli D (2018) Statics of shallow inclined elastic cables under general vertical loads: a perturbation approach. *Mathematics* 6(2):24
26. Triantafyllou M (1984) The dynamics of taut inclined cables. *Q J Mech Appl Math* 37(3):421–440
27. Desai Y, Shah YA, Popplewell N (1996) Perturbation-based finite element analyses of transmission line galloping. *J Sound Vib* 191(4):469–489
28. Warnitchai P, Fujino Y, Pacheco B, Agret R (1993) An experimental study on active tendon control of cable-stayed bridges. *Earthq Eng Struct Dyn* 22(2):93–111
29. Gattulli V, Pasca M, Vestroni F (1997) Nonlinear oscillations of a nonresonant cable under in-plane excitation with a longitudinal control. *Nonlinear Dyn* 14(2):139–156

Author Index

A

Ajras, Andrés, [121](#)
Ancellin, Matthieu, [339](#)
Arena, Andrea, [351](#)
Aso, Teruo, [85](#)
Auguste, T., [243](#)

B

Brand, Werner, [207](#)

C

Caetano, Elsa, [195](#), [255](#)
Campos, Damián, [121](#)
Caracoglia, Luca, [171](#)
Cheng, Shaohong, [3](#)
Chouinard, Luc, [99](#)
Corazza, S., [277](#), [303](#)

D

Daniotti, Nicolo, [61](#)
Dao, Thu, [75](#)
D'Auteuil, Annick, [145](#)
Denoël, V., [243](#), [303](#)
Dorogi, Dániel, [185](#)
Dragomirescu, Elena, [109](#)
Dyke Van, Pierre, [99](#)

F

Foti, F., [243](#), [267](#), [277](#), [303](#)

G

Gattulli, Vincenzo, [229](#), [351](#)

Georgakis, Christos Thomas, [41](#)

Geuzaine, M., [243](#), [303](#)

Ghidaglia, Jean-Michel, [339](#)

Giaccu, Gian Felice, [171](#)

González Rodríguez, Antonio, [31](#)

Gueguin, Maxime, [339](#)

Guilbault, Reynald, [315](#), [327](#)

H

Hafid, Fikri, [339](#)

Hochrein, Gábor, [49](#)

Hoffait, S., [243](#)

Hoftyzer, Michael, [109](#)

I

Iwankiewicz, Radosław, [157](#)

J

Jablonka, Anna, [157](#)

Jakobsen, Jasna Bogunović, [61](#)

Juárez-Pérez, Sergio, [19](#), [31](#)

K

Kared, Liticia, [315](#), [327](#)

Kmet, Stanislav, [41](#)

Kollár, László E., [185](#)

L

Lalonde, Sébastien, [315](#), [327](#)

Langlois, Sébastien, [99](#), [315](#), [327](#)

Larsen, Allan, [217](#)

Lepidi, Marco, [229](#), [363](#)

M

Martinelli, L., [267](#), [277](#), [303](#)
Martín-Parra, Andrea, [19](#), [31](#)
Matsumiya, Hisato, [85](#), [133](#)
Matsushima, Hiroki, [85](#)
McTavish, Sean, [145](#)
Mendonça, Raphael, [195](#), [255](#)
Mohallem, Gabriel, [75](#)
Monje, Concepción A., [19](#)
Moutinho, Carlos, [195](#), [255](#)
Moya Fernández, Francisco, [19](#), [31](#)
Muñoz, Jorge, [19](#)

N

Noguchi, Kyohei, [75](#)

O

Ottaviano, Erika, [351](#)

P

Paradis, Josée, [99](#)
Piciucco, D., [243](#)
Piovan, Marcelo, [121](#)
Potenza, Francesco, [229](#)

R

Raeesi, Arash, [145](#)
Redford, John A., [339](#)

Rinaldi, Cecilia, [229](#)
Rodrigues, João, [195](#), [255](#)
Rodríguez Rosa, David, [19](#), [31](#)

S

Saadi, Omar As, [255](#)
Snæbjörnsson, Jónas Þór, [61](#)
Soltys, Robert, [41](#)
Szabó, Gergely, [49](#)
Szilder, Krzysztof, [145](#)

T

Taruishi, Saki, [85](#), [133](#)
Tomko, Michal, [41](#)

V

Verdenius, Stefan, [289](#)
Vollmering, Max, [207](#)

W

Wang, Ran, [3](#)
Weber, Hanna, [157](#)

Y

Yagi, Tomomi, [75](#)
Yang, Shaoqi, [99](#)